An exploratory assessment of the fourth and fifth carpometacarpal joints of humans, non-human great apes, and fossil hominins using three-dimensional geometric morphometric analysis

A thesis submitted in partial fulfilment of the requirements for the degree of Doctor of Philosophy

Tegid Arwyn Watkin

The University of Sheffield

Faculty of Arts and Humanities

Department of Archaeology

May 2024

Abstract

The range of motion afforded to the fourth and fifth metacarpals at their respective carpometacarpal joints are fundamental for the effective execution and utilization of uniquely-human grips and hand postures which are considered to have played a pivotal role in the deliberate manufacture and use of stone tools. However, despite their importance, functional morphological variation between humans, non-human primates, and hominin taxa contemporaneous with the earliest lithic tools are under-explored.

The aim of this project was to compare, using landmark-based three-dimensional geometric morphometric analysis, the morphology of the fourth and fifth carpometacarpal joints of modern humans and non-human great apes in order to identify functionally important morphologies that facilitate enhanced movements of these joints in modern humans. The hamate-metacarpal joint surfaces of available extinct hominin taxa were then compared to extant genera in order to identify human-like structures in the hominin fossil record, and to assess human-like movements of the hamate-metacarpal joints in selected hominin taxa.

This study identified several features of the fourth and fifth carpometacarpal joints of humans that are conducive to increased freedom of movement and load transmission compared with non-human taxa. Several of these features can be identified to varying extents in fossil hominin specimens contemporaneous with early Palaeolithic sites. However, the full suite of derived human features does not emerge until relatively late in the palaeontological record. The results and interpretations of this research indicate that the hamate-metacarpal joints of hominin taxa contemporaneous with the earliest-known lithic technology were not as mobile as those of modern humans and suggest that the fourth and fifth digits were utilized differently. Furthermore, hominin species known to make and use lithic tools display non-modern morphologies, suggesting that the full suite of human-like features of these joints developed relatively late in our evolutionary history.

Acknowledgements

I would like to thank my supervisors, Dr Kevin Kuykendall and Dr Elizabeth Craig-Atkins, for their guidance and patience throughout the course of this research. Their inputs to this project, and their feedback and suggestions, are greatly appreciated. I would also like to thank Dr Pia Nystrom for her support in the early stages of my Doctoral research, and Dr Sophie Newman for her assistance in locating and sourcing suitable human specimens from the University of Sheffield's Department of Archaeology's archaeological collections. I would also like to thank Yvette Marks for her support and friendship during my time as a Teaching Technician at the Department of Archaeology.

My thanks to Inbal Levine for her assistance during my time collecting non-human data at the Powell-Cotton Museum. I am especially grateful to members of staff at the Smithsonian Institution's National Museum of Natural History for their hospitality and assistance during my time as a Visiting Research Fellow. In particular, I am grateful to Professor Douglas Ubelaker for acting as my sponsor, and to Dr David Hunt for his assistance in navigating the Robert J. Terry human skeletal collection. I am also grateful to Dr Rick Potts and Dr Briana Pobiner for their guidance in locating non-human primate specimens at the Museum. The opportunity to conduct scientific research at the Smithsonian Institution was an experience that I will never forget.

I am extremely grateful to several individuals who were generous enough to share with me surface meshes of fossil hominin specimens, without whom the scope of this research would have lacked that which I had hoped for. My sincerest thanks to Drs Caley Orr and Matt Tocheri for providing me with their models of Neanderthal, *Homo floresiensis*, and early modern human hand fossils; to Professor Tracey Kivell for providing meshes of *Homo naledi*, *Australopithecus sediba*, *Australopithecus afarensis* and *Australopithecus africanus* material; and to Dr Guillelme Daver for his kind sharing of several other fossil hominin hand bone surface meshes.

I would like to acknowledge a number of people who assisted me throughout my career as a PhD researcher. My thanks to Dr Melissa Tallman for her advice on selection of landmarks during the planning phase of the project; to Professor Paul O'Higgins for kindly allowing me to sit in on his geometric morphometric lectures and practical sessions at the University of York; to

Professor Dean Adams for his advice regarding trouble-shooting coding issues pertaining to the geomorph program and R generally; to Dr Lorenzo Galletta for his assistance in R code writing and trouble-shooting for some of the statistical analysis; and to Dr Akinobu Watanabe for his advice regarding sliding semi-landmark densities and use of his LaSEC r package. I am also extremely grateful to Professor Tracy Kivell for her advice and encouragement during the early stages of this project.

Lastly, and most importantly, I would like to thank my family. I will be eternally grateful to my partner Nyssa for her support (both financial and emotional), encouragement, and patience during this long and arduous process. Her belief and confidence in my abilities were often the only motivation left to me in pursuing my ambition of finishing this PhD, and without her, this project may never have reached its conclusion. And to my daughter Aneira, whose spirited and joyful nature has kept me grounded throughout the process, and whose company always put the weight of significance I would too often put on my research career in perspective. Diolch, Aneira.

I Aneira

Table of Content

Abstract *ii*
Acknowledgements *iii*
Table of Content *vi*
List of Tables *viii*
List of Figures *xii*
Declaration *xvii*
Section I Introduction and Background
Chapter 1: Introduction 1
Chapter 2: Background 3
2.1 Historical and archaeological background 3
2.2 Tool-use in non-human primates 12
2.3 Uniquely-human manual dexterity and morphological features of the hand 18
2.4 Comparative functional morphology of the human hand 22
2.5 The human hypothenar digits 30
2.6 Summary and aims of the project 35
Section II Methods and Materials
Chapter 3: Methods 38
3.1 Geometric morphometrics 38
3.2 Methods used in this project 39
3.2.1 Digitization methods 40
3.2.2 Landmarks 42
3.3 Landmarks of the carpometacarpal articular surface of the hamate 45
3.4 Landmarks of the fourth metacarpal proximal articular surface 48
3.5 Landmarks of the fifth metacarpal proximal articular surface 51
3.6 Repeatability 54
3.7 Generalized Procrustes analysis protocol 55
3.8 Statistical analysis 56
Chapter 4: Materials 60
4.1 Extant dataset 60
4.2 Fossil Hominin sample 63
Section III Results 88
Chapter 5: The hamate-metacarpal articular surface 88
5.1 Hamate-metacarpal surface average shapes 88
5.2 Principal component analysis of the hamate-metacarpal surface 94
5.3 Canonical variate analysis of the hamate-metacarpal surface 115
5.4 Hamate-metacarpal Procrustes distances 130
Chapter 6: The hamate-metacarpal-4 articular surface 133
6.1 Hamate-metacarpal 4 surface average shapes 133
6.2 Hamate-MC4 principal component analysis 138
6.3 Hamate-MC4 canonical variate analysis 167
6.4 Hamate-MC4 Procrustes distances 182
Chapter 7: The Hamate-metacarpal-5 articular surface 185
7.1 Hamate-metacarpal 5 surface average shapes 185
7.2 Hamate-MC5 principal component analysis 190

7.3 Hamate-MC5 canonical variate analysis 213
7.4 Hamate-MC5 Procrustes distances 229
Chapter 8: The Metacarpal-4 proximal articulation results 232
8.1 Metacarpal-4 proximal articulation average shapes 232
8.2 Metacarpal-4 principal component analysis 236
8.3 Metacarpal-4 canonical variate analysis 254
8.4 Metacarpal-4 Procrustes distances 267
Chapter 9: The Metacarpal-V Proximal Articulation Results 270
9.1 Metacarpal-5 proximal articulation average shapes 270
9.2 Metacarpal-5 principal component analysis 275
9.3 Metacarpal-5 canonical variate analysis 295
9.4 Metacarpal-5 Procrustes distances 309
Section IV Discussion, limitations, and scope for future research 311
Chapter 10: Discussion 311
10.1 Comparisons between extant taxa 311
10.1.1 The hamate-metacarpal surface 311
10.1.2 The hamate-MC5 joint surface of extant taxa 315
10.1.3 The hamate-MC4 joint surface of extant taxa 319
10.2 Fossil specimens 326
10.3 Summary 357
10.4 Scope for future research and limitations of this project 361
Conclusions 365
Bibliography 367
Appendices 393
Appendix A: Dataset spreadsheets 393
Appendix B: Synopsis of human manual dexterity 398
Appendix C: Basic anatomical terminology and movements of the human hand 403
Appendix D: Skeletal anatomy of the hand 408
Appendix E: Muscular anatomy of the hand 410
Appendix F: Synopsis of Geometric Morphometrics 416
Appendix G: Repeatability tests results 425
Appendix H: Allometry tests results 431
Appendix I: PCA bivariate scatterplots of the hamate-MC4 surface 437

List of Tables

Table 3.3.1	Anatomical description and type of landmarks collected on the hamate's articular surface with the fourth and fifth metacarpals.	46
Table 3.4.1	Anatomical description and type of landmarks collected on the fourth metacarpal's proximal articular surface.	49
Table 3.5.1	Anatomical description and type of landmarks collected on the fifth metacarpal's proximal articular surface	52
Table 4.1	Extant great ape sample composition used in the study	60
Table 4.2	Fossil hominin samples used in the study	64
Table 5.1	Comparison of the mean hamate shape of each extant taxa	93
Table 5.2.1	Results of analysis of variance on principal component scores one through six on extant groups for the hamate-metacarpal surface	95
Table 5.2.2	Mean values and standard deviation of principal component 1-3 scores of extant groups compared with principal component 1-3 scores of fossil specimens for the hamate-metacarpal surface	97
Table 5.2.3	Tukey HSD *post-hoc* test results on PC 1 scores among extant groups for the hamate-metacarpal surface	100
Table 5.2.4	Tukey HSD *post-hoc* test results on PC 2 scores among extant groups for the hamate-metacarpal surface	103
Table 5.2.5	Tukey HSD *post-hoc* test results on PC 3 scores among extant groups for the hamate-metacarpal surface	107
Table 5.3.1	Cross-validation counts for a canonical variate analysis of the first 15 PCs of the hamate's metacarpal articulation	115
Table 5.3.2	Results of analysis of variance on canonical variate scores on extant groups for the hamate's metacarpal articulation	116
Table 5.3.3	*P*-values for Tukey's HSD pairwise comparisons of canonical variate scores along three CV axes for the hamate's metacarpal articulation	116
Table 5.3.4	Canonical variate analysis (CVA) classification results of fossil specimens based on scores of the first 15 principal components for the hamate's metacarpal articulation	117
Table 5.4.1	Procrustes distances between extant groups for the hamate's metacarpal articulation	130
Table 5.4.2	Procrustes distance of each fossil from the mean shape of each extant taxon group for the hamate's metacarpal articulation	130
Table 5.4.3	Results of the Shapiro-Wilk tests for normality tests performed on the Procrustes distances of each sample from their respective average group shapes group for the hamate's metacarpal articulation	131
Table 5.4.4	Distance in standard deviation of each fossil specimen from the mean shape of each extant group for the hamate's metacarpal articulation	132
Table 6.1	Comparison of the mean hamate-metacarpal 4 shape of each extant taxa	137
Table 6.2.1	Results of analysis of variance on principal component scores one through six on extant groups for the hamate-metacarpal 4 surface	139
Table 6.2.2	Mean values and standard deviation of principal component 1-4 scores of extant groups compared with principal component 1-3 scores of fossil specimens for the hamate-metacarpal 4 surface	140
Table 6.2.3	Tukey HSD *post-hoc* test results on PC 1 scores among extant groups for the hamate-metacarpal 4 surface	143
Table 6.2.4	Tukey HSD *post-hoc* test results on PC 2 scores among extant groups for the hamate-metacarpal 4 surface	147
Table 6.2.5	Tukey HSD *post-hoc* test results on PC 3 scores among extant groups for the hamate-metacarpal 4 surface	151
Table 6.2.6	Tukey HSD *post-hoc* test results on PC 4 scores among extant groups for the hamate-metacarpal 4 surface	155

Table 6.2.7	Tukey HSD *post-hoc* test results on PC 5 scores among extant groups for the hamate-metacarpal 4 surface	159
Table 6.3.1	Cross-validation counts for a canonical variate analysis of the first 12 PCs of the hamate's metacarpal-4 articulation	167
Table 6.3.2	Results of analysis of variance on canonical variate scores on extant groups for the hamate's metacarpal-4 articulation	168
Table 6.3.3	*P*-values for Tukey's HSD pairwise comparisons of canonical variate scores along three CV axes for the hamate's metacarpal-4 articulation	168
Table 6.3.4	Canonical variate analysis (CVA) classification results of fossil specimens based on scores of the first 12 principal components for the hamate's metacarpal-4 articulation	169
Table 6.4.1	Procrustes distances between extant groups for the hamate's metacarpal-4 articulation	182
Table 6.4.2	Procrustes distance of each fossil from the mean shape of each extant taxon group for the hamate's metacarpal-4 articulation	182
Table 6.4.3	Results of the Shapiro-Wilk tests for normality tests performed on the Procrustes distances of each sample from their respective average group shapes group for the hamate's metacarpal-4 articulation	183
Table 6.4.4	Distance in standard deviation of each fossil specimen from the mean shape of each extant group for the hamate's metacarpal-4 articulation	184
Table 7.1	Comparison of the mean hamate-metacarpal 5 shape of each extant taxa	189
Table 7.2.1	Results of analysis of variance on principal component scores one through six on extant groups for the hamate-metacarpal 5 surface	191
Table 7.2.2	Mean values and standard deviation of principal component 1-3 scores of extant groups compared with principal component 1-3 scores of fossil specimens for the hamate-metacarpal 5 surface	193
Table 7.2.3	Tukey HSD *post-hoc* test results on PC 1 scores among extant groups for the hamate-metacarpal 5 surface	196
Table 7.2.4	Tukey HSD *post-hoc* test results on PC 2 scores among extant groups for the hamate-metacarpal 5 surface	200
Table 7.2.5	Tukey HSD *post-hoc* test results on PC 3 scores among extant groups for the hamate-metacarpal 5 surface	204
Table 7.3.1	Cross-validation counts for a canonical variate analysis of the first nine PCs of the hamate's metacarpal-5 articulation	213
Table 7.3.2	Results of analysis of variance on canonical variate scores on extant groups for the hamate's metacarpal-5 articulation	214
Table 7.3.3	*P*-values for Tukey's HSD pairwise comparisons of canonical variate scores along three CV axes for the hamate's metacarpal-5 articulation	214
Table 7.3.4	Canonical variate analysis (CVA) classification results of fossil specimens based on scores of the first nine principal components for the hamate's metacarpal-5 articulation	215
Table 7.4.1	Procrustes distances between extant groups for the hamate's metacarpal-5 articulation	228
Table 7.4.2	Procrustes distance of each fossil from the mean shape of each extant taxon group for the hamate's metacarpal-5 articulation	229
Table 7.4.3	Results of the Shapiro-Wilk tests for normality tests performed on the Procrustes distances of each sample from their respective average group shapes group for the hamate's metacarpal-5 articulation	229
Table 7.4.4	Distance in standard deviation of each fossil specimen from the mean shape of each extant group for the hamate's metacarpal-5 articulation	231
Table 8.1	Comparison of the mean proximal metacarpal 4 shape of each extant taxa	235
Table 8.2.1	Results of analysis of variance on principal component scores one through five on extant groups for the metacarpal 4 proximal articular surface	237

Table 8.2.2	Mean values and standard deviation of principal component 1-3 scores of extant groups compared with principal component 1-3 scores of fossil specimens for the metacarpal 4 proximal articular surface	238
Table 8.2.3	Tukey HSD *post-hoc* test results on PC 1 scores among extant groups for the metacarpal 4 proximal articular surface	241
Table 8.2.4	Tukey HSD *post-hoc* test results on PC 2 scores among extant groups for the metacarpal 4 proximal articular surface	244
Table 8.2.5	Tukey HSD *post-hoc* test results on PC 3 scores among extant groups for the metacarpal 4 proximal articular surface	247
Table 8.3.1	Cross-validation counts for a canonical variate analysis of the first nine PCs of the metacarpal 4 proximal articular surface	254
Table 8.3.2	Results of analysis of variance on canonical variate scores on extant groups for the metacarpal 4 proximal articular surface	254
Table 8.3.3	*P*-values for Tukey's HSD pairwise comparisons of canonical variate scores along three CV axes for the metacarpal 4 proximal articular surface	255
Table 8.3.4	Canonical variate analysis (CVA) classification results of fossil specimens based on scores of the first nine principal components for the metacarpal 4 proximal articular surface	255
Table 8.4.1	Procrustes distances between extant groups for the metacarpal 4 proximal articular surface	268
Table 8.4.2	Procrustes distance of each fossil from the mean shape of each extant taxon group for the metacarpal 4 proximal articular surface	268
Table 8.4.3	Results of the Shapiro-Wilk tests for normality tests performed on the Procrustes distances of each sample from their respective average group shapes group for the metacarpal 4 proximal articular surface	269
Table 8.4.4	Distance in standard deviation of each fossil specimen from the mean shape of each extant group for the metacarpal 4 proximal articular surface	269
Table 9.1	Comparison of the mean proximal metacarpal 5 shape of each extant taxa	274
Table 9.2.1	Results of analysis of variance on principal component scores one through five on extant groups for the metacarpal 5 proximal articular surface	276
Table 9.2.2	Mean values and standard deviation of principal component 1-3 scores of extant groups compared with principal component 1-3 scores of fossil specimens for the metacarpal 5 proximal articular surface	277
Table 9.2.3	Tukey HSD *post-hoc* test results on PC 1 scores among extant groups for the metacarpal 5 proximal articular surface	280
Table 9.2.4	Tukey HSD *post-hoc* test results on PC 2 scores among extant groups for the metacarpal 5 proximal articular surface	283
Table 9.2.5	Tukey HSD *post-hoc* test results on PC 3 scores among extant groups for the metacarpal 5 proximal articular surface	287
Table 9.3.1	Cross-validation counts for a canonical variate analysis of the first nine PCs of the metacarpal 5 proximal articular surface	295
Table 9.3.2	Results of analysis of variance on canonical variate scores on extant groups for the metacarpal 5 proximal articular surface	296
Table 9.3.3	*P*-values for Tukey's HSD pairwise comparisons of canonical variate scores along three CV axes for the metacarpal 5 proximal articular surface	296
Table 9.3.4	Canonical variate analysis (CVA) classification results of fossil specimens based on scores of the first nine principal components for the hamate's metacarpal-5 articulation metacarpal 5 proximal articular surface	294
Table 9.4.1	Procrustes distances between extant groups for the metacarpal 5 proximal articular surface	309
Table 9.4.2	Procrustes distance of each fossil from the mean shape of each extant taxon group for the metacarpal 5 proximal articular surface	309

Table 9.4.3	Results of the Shapiro-Wilk tests for normality tests performed on the Procrustes distances of each sample from their respective average group shapes group for the metacarpal 5 proximal articular surface	310
Table 9.4.4	Distance in standard deviation of each fossil specimen from the mean shape of each extant group for the metacarpal 5 proximal articular surface	310
Table 10.1	Summary of notable features of the extant great ape groups	324
Table 10.2	Summary of notable features of the fossil hominin specimens	354

List of Figures

Figure 2.1	Examples of the Oldowan assemblage of Gona, Ethiopia	4
Figure 2.2	Examples of cut marks on fossil bones from Dikika	7
Figure 2.3	3.3-million-year-old cores and flakes from Lomekwi, Ethiopia	8
Figure 2.4	An adult chimpanzee cracks nuts with a stone hammer and anvil	16
Figure 2.5	An adult male capuchin monkey cracks nuts with a stone hammer	17
Figure 2.6	The three-jaw chuck grip and cradle grip	19
Figure 2.7	Power "squeeze" grip of a cylindrical tool.	21
Figure 2.8	Osteological features of the hand distinct to the human hand among extant taxa	23
Figure 2.9	The heads of the second to fifth metacarpals of the right hand of *Homo sapiens*	28
Figure 2.10	Representation of movements at the human fourth and fifth carpometacarpal joints	32
Figure 2.11	Flexion and supination of the fourth and fifth metacarpals at the hamate-metacarpal joints	34
Figure 3.3.1	Anatomical locations of the bounding landmark coordinates collected on the hamate-metacarpal articular surface	46
Figure 3.3.2	LasSEC Sampling curve for 221 landmarks placed on the hamate-metacarpal articular surface	47
Figure 3.3.3	Anatomical locations of landmark coordinates collected on the hamate-metacarpal articular surface,	48
Figure 3.4.1	Anatomical locations of landmark coordinates collected on the fourth metacarpal's proximal articular surface	49
Figure 3.4.2	LasSEC Sampling curve for 81 landmarks placed on the metacarpal-IV proximal articular surface	50
Figure 3.4.3	Anatomical locations of landmark coordinates collected on the metacarpal-IV proximal articular surface	51
Figure 3.5.1	Anatomical locations of landmark coordinates collected on the fifth metacarpal's proximal articular surface	52
Figure 3.5.2	LasSEC Sampling curve for 81 landmarks placed on metacarpal-V proximal articular surface	53
Figure 3.5.3	Anatomical locations of landmark coordinates collected on the metacarpal-V proximal articular surface	54
Figure 4.2.1(a)	The AL-333-50 *Australopithecus afarensis* hamate	65
Figure 4.2.1(b)	Surface mesh rendering of AL-333-50 with representative landmarks	65
Figure 4.2.2(a)	The AL-333-56 *Australopithecus afarensis* fourth left metacarpal	66
Figure 4.2.2(b)	Surface mesh rendering of AL-333-56 with representative landmarks	66
Figure 4.2.3(a)	The A.L. 333w-89 *Australopithecus afarensis* left fifth metacarpal	67
Figure 4.2.2(b)	Surface mesh rendering of A.L. 333w-89 with representative landmarks	67
Figure 4.2.4(a)	The A.L. 333-14 *Australopithecus afarensis* right fifth metacarpal	68
Figure 4.2.2(b)	Surface mesh rendering of A.L. 333-14 with representative landmarks	68
Figure 4.2.5(a)	The *Australopithecus cf. Australopithecus afarensis* KNM-WT 22944-I left hamate	69
Figure 4.2.5(b)	Surface mesh rendering of KNM-WT 22944-I with representative landmarks	70
Figure 4.2.6(a)	The StW 33 *Australopithecus africanus* fourth left proximal metacarpal	71
Figure 4.2.6(b)	Surface mesh rendering of StW 33 with representative landmarks	71
Figure 4.2.7(a)	The StW 65 *Australopithecus africanus* fourth right metacarpal	72
Figure 4.2.7(b)	Surface mesh rendering of StW 65 with representative landmarks	72
Figure 4.2.8(a)	The StW 63 *Australopithecus africanus* fifth left metacarpal	73
Figure 4.2.8(b)	Surface mesh rendering of StW 63 with representative landmarks	73
Figure 4.2.9(a)	The left (U.W. 88-106) and right (U.W. 88-95) hamates of *Australopithecus sediba* MH2 hand	74
Figure 4.2.9(b)	Surface mesh rendering of U.W. 88-95 with representative landmarks	74
Figure 4.2.10	The *Australopithecus sediba* MH2 right fourth metacarpal U.W. 88-117	75
Figure 4.2.10(b)	Surface mesh rendering of U.W. 88-117 with representative landmarks	75

Figure 4.2.11	The *Australopithecus sediba* MH2 right fifth metacarpal U.W. 88-118	76
Figure 4.2.11(b)	Surface mesh rendering of U.W. 88-118 with representative landmarks	76
Figure 4.2.12(a)	The *Paranthropus robustus /* early *Homo* SKW-2954 right fourth metacarpal	77
Figure 4.2.12(b)	Surface mesh rendering of SkW-2954 with representative landmarks	77
Figure 4.2.13(a)	The *Homo naledi* U.W. 101-1729 right hamate	78
Figure 4.2.13(b)	Surface mesh rendering of U.W. 101-1729 with representative landmarks	78
Figure 4.2.14(a)	The *Homo naledi* U.W. 101-1318 right fourth metacarpal	79
Figure 4.2.14(b)	Surface mesh rendering of U.W. 101-1318 with representative landmarks	79
Figure 4.2.15(b)	The *Homo naledi* U.W. 101-1309 right fifth metacarpal	80
Figure 4.2.15(b)	Surface mesh rendering of U.W. 101-1309 with representative landmarks	80
Figure 4.2.16(a)	The *Homo naledi* U.W. 102a-028 right fourth metacarpal	81
Figure 4.2.16(b)	Surface mesh rendering of U.W. 102a-028 with representative landmarks	81
Figure 4.2.17(a)	The LB21 and LB22 *Homo floresiensis* hamates, and the digital composite hamate	83
Figure 4.2.17(b)	Surface mesh rendering of LB-21/22 with representative landmarks	83
Figure 4.2.18	Surface mesh rendering of Kebara-2 with representative landmarks	84
Figure 4.2.19(a)	The Shanidar 4 *Homo neanderthalensis* left hand	84
Figure 4.2.19(b)	Surface mesh rendering of Shanidar 4 with representative landmarks	85
Figure 4.2.20	Surface mesh rendering of Tabun 1 with representative landmarks	85
Figure 4.2.21	Surface mesh rendering of Regourdou-1 with representative landmarks	86
Figure 4.2.22	Surface mesh rendering of Shanidar 4 with representative landmarks	86
Figure 4.2.23	Surface mesh rendering of Shanidar 4 with representative landmarks	87
Figure 5.1.1	The mean shape of the hamate's articular surface for the fourth and fifth metacarpals for the *Homo sapiens* population	89
Figure 5.1.2	The mean shape of the hamate's articular surface for the fourth and fifth metacarpals for the *Gorilla* sample	90
Figure 5.1.3	The mean shape of the hamate's articular surface for the fourth and fifth metacarpals for the *Pan troglodytes* sample	91
Figure 5.1.4	The mean shape of the hamate's articular surface for the fourth and fifth metacarpals for the *Pongo* sample	92
Figure 5.2.1	Percentage of variance accountable to the first 15 principal components of the principal component analysis of the hamate's articulation with the fourth and fifth metacarpal	94
Figure 5.2.2	Boxplot of the first principal component scores of the hamate's metacarpal articular surface for extant groups and fossil specimens with wireframe representations of the minimum and maximum shape.	99
Figure 5.2.3	Boxplot of the second principal component scores of the hamate's metacarpal articular surface for extant groups and fossil specimens with wireframe representations of the minimum and maximum shape.	102
Figure 5.2.4	Boxplot of the third principal component scores of the hamate's metacarpal articular surface for extant groups and fossil specimens with wireframe representations of the minimum and maximum shape.	106
Figure 5.2.5	Scatterplot of the first vs. second principal component of the hamate's metacarpal articular surface	110
Figure 5.2.6	Scatterplot of the first vs. third principal component of the hamate's metacarpal articular surface	112
Figure 5.2.7	Scatterplot of the second vs. third principal component of the hamate's metacarpal articular surface	114
Figure 5.3.1	Boxplot of the scores of the first Canonical Variate axis of the hamate's metacarpal articular surface for extant groups and fossil hominins with wireframe representations of the minimum and maximum shape.	119
Figure 5.3.2	Boxplot of the scores of the second Canonical Variate axis of the hamate's metacarpal articular surface for extant groups and fossil hominins with wireframe representations of the minimum and maximum shape.	121

Figure 5.3.3	Boxplot of the scores of the third Canonical Variate axis of the hamate's metacarpal articular surface for extant groups and fossil hominins with wireframe representations of the minimum and maximum shape.	123
Figure 5.3.4	Scatterplot of the first vs. second third canonical variates axis scores of extant groups and fossil specimens	125
Figure 5.3.5	Scatterplot of the first vs. third canonical variates axis scores of extant groups and fossil specimens	127
Figure 5.3.6	Scatterplot of the second vs. third canonical variates axis scores of extant groups and fossil specimens	129
Figure 6.1.1	The mean shape of the hamate's articulation for the fourth metacarpal for the *Homo sapiens* sample	133
Figure 6.1.2	The mean shape of the hamate's articulation for the fourth metacarpal for the *Gorilla* sample	134
Figure 6.1.3	The mean shape of the hamate's articulation for the fourth metacarpal for the *Pan troglodytes* sample	135
Figure 6.1.4	The mean shape of the hamate's articulation for the fourth metacarpal for the *Pongo* sample	136
Figure 6.2.1	Percentage of variance accountable to the first 15 principal components of the principal component analysis of hamate's articulation for the fourth metacarpal	138
Figure 6.2.2	Boxplot of the first principal component scores of the hamate's articulation for the fourth metacarpal for extant groups and fossil specimens with wireframe representations of the minimum and maximum shape.	141
Figure 6.2.3	Boxplot of the second principal component scores of the hamate's articulation for the fourth metacarpal for extant groups and fossil specimens with wireframe representations of the minimum and maximum shape.	146
Figure 6.2.4	Boxplot of the third principal component scores of the hamate's articulation for the fourth metacarpal for extant groups and fossil specimens with wireframe representations of the minimum and maximum shape.	150
Figure 6.2.5	Boxplot of the fourth principal component scores of the hamate's articulation for the fourth metacarpal for extant groups and fossil specimens with wireframe representations of the minimum and maximum shape.	154
Figure 6.2.6	Boxplot of the fifth principal component scores of the hamate's articulation for the fourth metacarpal for extant groups and fossil specimens with wireframe representations of the minimum and maximum shape.	158
Figure 6.2.7	Scatterplot of the first vs. second principal component of the hamate's articulation for the fourth metacarpal	162
Figure 6.2.8	Scatterplot of the first vs. third principal component of the hamate's articulation for the fourth metacarpal	164
Figure 6.2.9	Scatterplot of the second vs. fifth principal component of the hamate's articulation for the fourth metacarpal	166
Figure 6.3.1	Boxplot of the scores of the first Canonical Variate axis of the hamate-metacarpal 4 articular surface for extant groups and fossil hominins	171
Figure 6.3.2	Boxplot of the scores of the second Canonical Variate axis of the hamate- metacarpal 4 articular surface for extant groups and fossil hominins	173
Figure 6.3.3	Boxplot of the scores of the third Canonical Variate axis of the hamate's metacarpal 4 articular surface for extant groups and fossil hominins	175
Figure 6.3.4	Scatterplot of the first vs. second canonical variates axis scores of extant groups and fossil specimens for the hamate-metacarpal 4 articular surface	177
Figure 6.3.5	Scatterplot of the first vs. third canonical variates axis scores of extant groups and fossil specimens for the hamate-metacarpal 4 articular surface	179
Figure 6.3.6	Scatterplot of the second vs. third canonical variates axis scores of extant groups and fossil specimens for the hamate-metacarpal 4 articular surface	181
Figure 7.1.1	The mean shape of the hamate's articulation for the fifth metacarpal for the *Homo sapiens* sample	185
Figure 7.1.2	The mean shape of the hamate's articulation for the fifth metacarpal for the *Gorilla* sample	186

Figure 7.1.3	The mean shape of the hamate's articulation for the fifth metacarpal for the *Pan troglodytes* sample	187
Figure 7.1.4	The mean shape of the hamate's articulation for the fifth metacarpal for the *Pongo* sample	188
Figure 7.2.1	Percentage of variance accountable to the first 15 principal components of the principal component analysis of hamate's articulation for the fifth metacarpal	190
Figure 7.2.2	Boxplot of the first principal component scores of the hamate's articulation for the fifth metacarpal for extant groups and fossil specimens with wireframe representations of the minimum and maximum shape.	195
Figure 7.2.3	Boxplot of the second principal component scores of the hamate's articulation for the fifth metacarpal for extant groups and fossil specimens with wireframe representations of the minimum and maximum shape.	199
Figure 7.2.4	Boxplot of the third principal component scores of the hamate's articulation for the fifth metacarpal for extant groups and fossil specimens with wireframe representations of the minimum and maximum shape.	203
Figure 7.2.5	Scatterplot of the first vs. second principal component of the hamate's articulation for the fifth metacarpal	208
Figure 7.2.6	Scatterplot of the first vs. third principal component of the hamate's articulation for the fifth metacarpal	210
Figure 7.2.7	Scatterplot of the second vs. third principal component of the hamate's articulation for the fifth metacarpal	212
Figure 7.3.1	Boxplot of the scores of the first Canonical Variate axis of the hamate-metacarpal 5 articular surface for extant groups and fossil hominins	217
Figure 7.3.2	Boxplot of the scores of the second Canonical Variate axis of the hamate- metacarpal 5 articular surface for extant groups and fossil hominins	219
Figure 7.3.3	Boxplot of the scores of the third Canonical Variate axis of the hamate's metacarpal 5 articular surface for extant groups and fossil hominins	221
Figure 7.3.4	Scatterplot of the first vs. second canonical variates axis scores of extant groups and fossil specimens for the hamate-metacarpal 5 articular surface	223
Figure 7.3.5	Scatterplot of the first vs. third canonical variates axis scores of extant groups and fossil specimens for the hamate-metacarpal 5 articular surface	225
Figure 7.3.6	Scatterplot of the second vs. third canonical variates axis scores of extant groups and fossil specimens for the hamate-metacarpal 5 articular surface	227
Figure 8.1.1	The mean shape of the fourth metacarpal's proximal articulation for the *Homo sapiens* sample	232
Figure 8.1.2	The mean shape of the fourth metacarpal's proximal articulation for the *Gorilla* population	233
Figure 8.1.3	The mean shape of the fourth metacarpal's proximal articulation for the *Pan troglodytes* population	233
Figure 8.1.4	The mean shape of the fourth metacarpal's proximal articulation for the *Pongo* population	234
Figure 8.2.1	Percentage of variance accountable to the first 15 principal components of the principal component analysis of the fourth metacarpal's proximal articulation	236
Figure 8.2.2	Boxplot of the first principal component scores of the fourth metacarpal's proximal articulation for extant groups and fossil specimens with wireframe representations of the minimum and maximum shape.	240
Figure 8.2.3	Boxplot of the second principal component scores of the fourth metacarpal's proximal articulation for extant groups and fossil specimens with wireframe representations of the minimum and maximum shape.	243
Figure 8.2.4	Boxplot of the third principal component scores of the fourth metacarpal's proximal articulation for extant groups and fossil specimens with wireframe representations of the minimum and maximum shape.	246
Figure 8.2.5	Scatterplot of the first vs. second principal component of the fourth metacarpal's proximal articulation	249
Figure 8.2.6	Scatterplot of the first vs. third principal component of the fourth metacarpal's proximal articulation	251

Figure 8.2.7	Scatterplot of the second vs. third principal component of the fourth metacarpal's proximal articulation	253
Figure 8.3.1	Boxplot of the scores of the first Canonical Variate axis of the fourth metacarpal's proximal articulation for extant groups and fossil hominins	257
Figure 8.3.2	Boxplot of the scores of the second Canonical Variate axis of the fourth metacarpal's proximal articulation for extant groups and fossil hominins	259
Figure 8.3.3	Boxplot of the scores of the third Canonical Variate axis of the fourth metacarpal's proximal articulation for extant groups and fossil hominins	261
Figure 8.3.4	Scatterplot of the first vs. second canonical variates axis scores of extant groups and fossil specimens for the fourth metacarpal's proximal articulation	263
Figure 8.3.5	Scatterplot of the first vs. third canonical variates axis scores of extant groups and fossil specimens for the fourth metacarpal's proximal articulation	265
Figure 8.3.6	Scatterplot of the second vs. third canonical variates axis scores of extant groups and fossil specimens for the fourth metacarpal's proximal articulation	267
Figure 9.1.1	The mean shape of the fifth metacarpal's proximal articulation for the *Homo sapiens* population	270
Figure 9.1.2	The mean shape of the fifth metacarpal's proximal articulation for the *Gorilla* population	271
Figure 9.1.3	The mean shape of the fifth metacarpal's proximal articulation for the *Pan troglodytes* population	272
Figure 9.1.4	The mean shape of the fifth metacarpal's proximal articulation for the *Pongo* population	273
Figure 9.2.1	Percentage of variance accountable to the first 15 principal components of the principal component analysis of the fifth metacarpal's proximal articulation	275
Figure 9.2.2	Boxplot of the first principal component scores of the fifth metacarpal's proximal articulation for extant groups and fossil specimens with wireframe representations of the minimum and maximum shape.	279
Figure 9.2.3	Boxplot of the second principal component scores of the fifth metacarpal's proximal articulation for extant groups and fossil specimens with wireframe representations of the minimum and maximum shape.	282
Figure 9.2.4	Boxplot of the third principal component scores of the fifth metacarpal's proximal articulation for extant groups and fossil specimens with wireframe representations of the minimum and maximum shape.	286
Figure 9.2.5	Scatterplot of the first vs. second principal component of the fifth metacarpal's proximal articulation	290
Figure 9.2.6	Scatterplot of the first vs. third principal component of the fifth metacarpal's proximal articulation	292
Figure 9.2.7	Scatterplot of the second vs. third principal component of the fifth metacarpal's proximal articulation	294
Figure 9.3.1	Boxplot of the scores of the first Canonical Variate axis of the fifth metacarpal's proximal articulation for extant groups and fossil hominins	298
Figure 9.3.2	Boxplot of the scores of the second Canonical Variate axis of the fifth metacarpal's proximal articulation for extant groups and fossil hominins	300
Figure 9.3.3	Boxplot of the scores of the third Canonical Variate axis of the fifth metacarpal's proximal articulation for extant groups and fossil hominins	302
Figure 9.3.4	Scatterplot of the first vs. second canonical variates axis scores of extant groups and fossil specimens for the fifth metacarpal's proximal articulation	304
Figure 9.3.5	Scatterplot of the first vs. third canonical variates axis scores of extant groups and fossil specimens for the fifth metacarpal's proximal articulation	306
Figure 9.3.6	Scatterplot of the second vs. third canonical variates axis scores of extant groups and fossil specimens for the fifth metacarpal's proximal articulation	308

Declaration

I, the author, confirm that the Thesis is my own work. I am aware of the University's Guidance on the Use of Unfair Means (www.sheffield.ac.uk/ssid/unfair-means). This work has not previously been presented for an award at this, or any other, university.

1. Introduction

The evolution of the human hand has been a topic of great interest for over two centuries (Lamarck, 1809; Marzke, 1971). It was brought into focus the mid-19th century by Darwin's discussion of the subject in *The Descent of Man* (1871), and the significance of tool-using and tool-making to our evolutionary history has remained of great scientific and popular interest ever since. It has long been argued that the advent of tool-using behaviours resulted in easier access to nutrient-rich food resources through hunting and scavenging, fuelling a gradual increase in brain size, population size, and geographical range, and a greater ability to defend oneself against predators and competitors, thus resulting in a positive feedback loop where larger brains led to more advanced tools, further fuelling higher intelligence (Ambrose, 2001; Williams-Hatala, 2016). Such was the reverence placed upon the significance of tools in our evolutionary history that their use was long regarded as a uniquely-human endeavour, with tool-use and tool-manufacture considered defining characteristics of humanity, with statements about "Man the Tool Maker" being prevalent and ubiquitous (Nystrom and Ashmore, 2013; Oakley, 1956; Washburn, 1960). The development of tool-related behaviour was therefore inexorably linked to humans and our ancestral lineage (Harris, 1983; Leakey, Tobias and Napier, 1964).

However, a deeper understanding of the in-depth knowledge and understanding of fracture mechanics necessary for the repeated production of these tools, and ground-breaking discoveries of tool-use in extant non-human primates, challenged the notion that tool-associated activities were behaviours exclusive to members of the genus *Homo.* With the unearthing of more recent evidence for pre-*Homo* stone tool production and use from Dikika and Lomekwi (Harmand *et al.,* 2015; McPherron *et al.,* 2010), it is now accepted that such behaviour was not an innovation of *Homo*, and that these activities have their genesis far deeper in our evolutionary history than was previously appreciated. However, the discoveries of Lomekwi and Dikika are not definitively associated with specific contemporaneous hominin taxa. In the absence of unambiguous and conclusive evidence linking specific hominins to the earliest stone tools, indirect avenues of inquiry must be explored if we are to identify the hominin species responsible for the earliest archaeological record.

One such avenue is the comparison of the functional anatomy of the primate hand, pioneered in the mid-20th century by John Russell Napier (1955, 1956, 1960, 1961). Napier's work has been further elaborated upon and developed throughout the late 20th century and into the 21st century, and is increasingly relied upon to identify features considered essential for uniquely-human manipulative capabilities that may be identifiable in fossil hominin taxa. In that time, "traditional" methods of biological anthropology, palaeontology and archaeological sciences have been augmented with state-of-the-art research techniques which utilize advanced computational powers. Contemporary numerical and statistical methods complement and enhance traditional osteological methods of comparative anatomy, and novel imaging techniques allow us to analyse the surface structure of specimens of interest in greater detail, and even to peer into the internal structure of the hand bones of not only extant primates, but also of fossil hominins, when specimens permit (e.g. Orr *et al.,* 2013; Skinner *et al*., 2015).

Given its extraordinary agility, power and versatility, the human thumb has understandably received considerable attention by researchers who attempt to construct a narrative of the evolutionary development of the hand. Indeed, it was none other than Sir Isaac Newton, when contemplating the precision and perfection of its "design", who quipped: "*In the absence of any other proof, the thumb alone would convince me of God's existence*" (Copeland, 2002). However, the thumb would be of limited use in isolation. The fourth and fifth rays are on the periphery of the hand and have historically been largely peripheral in the focus of researchers whose work concerns the evolution of the human hand. It was the aim of this research project to employ modern methods of three-dimensional imaging and shape analysis to investigate the functional importance of these digits in hominin tool-making and tool-using behaviours by comparing the shape of the fourth and fifth carpometacarpal joints in humans, extant great apes, and available fossil hominins, and to contribute to our understanding of how our hands adapted to developing and using early technology.

2. Background

2.1 Historical and Archaeological Background

The development and use of stone tools in our evolutionary history has long been of considerable interest to the palaeontological community, with the advent of lithic technology considered of paramount importance in the advancement of humanity, and to the evolutionary success of the genus *Homo* (Lewis and Harmand, 2016). Throughout the late 19th and much of the 20th century, the manufacture and use of tools were behaviours so inexorably linked to humans that tool-production and tool-use were behaviours considered exclusive to, and definitive of, the genus *Homo* (Harris, 1983; Kivell, 2015; Leakey, Tobias and Napier, 1964; Nystrom and Ashmore, 2013). As such, when the fossil remains of Olduvai Hominid (OH) 7 were discovered in association with a well-defined living floor of stone tools in Olduvai Gorge, Tanzania in the early 1960s (Leakey, 1959, 1960; Napier, 1962), they were identified as the type-specimen of a previously undefined species of *Homo*: *Homo habilis*, or Handy/Skilful Man (Leakey, Tobias & Napier, 1964). It was concluded that *Homo habilis* was the maker and user of the tools discovered at Olduvai Gorge, while the previous candidate, *Paranthropus boisei* (originally classified as *Zinjanthropus boisei*), was demoted to the status of prey (Leakey, 1960, 1961; Napier, 1962; Leakey, Tobias & Napier, 1964). OH 7 was classified as *Homo* based not only on evidence of expanded cranial capacity and gnathic and dental reduction (Tobias, 1971), but significantly on the premise that it was members of the *Homo* lineage alone that took the evolutionary leap of hitting stones together to strike off sharp flakes for the purposes of using the resultant flakes as tools (Lewis & Harmand, 2016).

The stone tools discovered at Olduvai Gorge gave their name to what was at their time of discovery the earliest example of material culture in the archaeological record, now known as the Oldowan Industrial Complex. At its simplest, the Oldowan Industrial Complex is composed of cobbles and deliberately-modified stone flakes produced by conchoidal fracture of stones by way of deliberate percussive flaking. The defining feature of the Oldowan Industrial Complex is the "*production of flakes from pebbles, cobbles, and angular rock fragments by hard hammer percussion or knapping*" (Roche *et al.,* 2009; p. 138). The complex is characterized by "*simple flaked and battered artefact forms that clearly show patterned conchoidal fracture produced by*

high-impact percussion, that is unlike any found in the natural (non-hominin) world" (Schick and Toth, 2006: *p.* 4). Oldowan assemblages generally consist of three basic elements: cores, which are the parent rock from which flakes are removed, usually originating from cobbles; percussors, or hammerstones, which are used to hammer the cores, resulting in conchoidal fracturing of the cores; and flakes, which have been struck from the cores and are occasionally rudimentarily retouched (figure 2.1) (Schick and Toth, 2006; Toth and Schick, 2015). The large variety of forms found at Oldowan sites were likely produced by hard-hammer percussion, in which a core is reduced by striking it directly with a hammerstone, or rarely by placing a core on an anvil and striking it with a hammer (bipolar technique), or throwing one rock against another (Schick and Toth, 2006). In addition to the cores, hammerstones, and flakes, Oldowan sites also commonly contain an abundance of debitage, or waste pieces, which are the by-products of the manufacture and retouching of tools and utilized pieces.

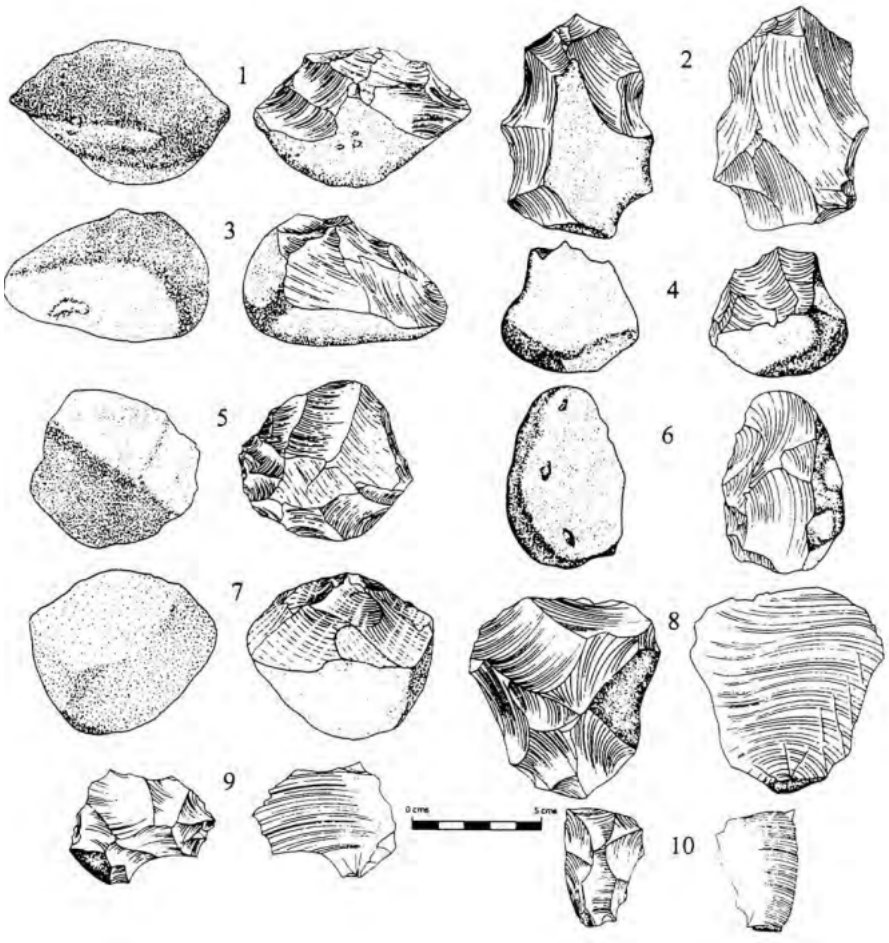

Figure 2.: Examples of the Oldowan assemblage of Gona, Ethiopia. From Semaw, 2006.

These Oldowan tools were likely used for a variety of purposes. Heavy duty cores such as large choppers may have been used as axes to cut branches into digging sticks, probes, or spears, with scrapers used to scrape the bark clean, or hollowed out with pointed tools such as awls (Toth and Schick, 2015). Microwear polishes on stone flakes demonstrate their use for cutting and scraping wood, as well as for cutting reeds and grasses (Keeley and Toth, 1981). Simple stone flakes with a sharp cutting edge would also, and perhaps most significantly, have effectively provided early hominins with stone "knives" that could have been used to procure meat resources, either from scavenging or hunting (Toth and Schick, 2015). The use of hammers and anvils in a bipolar technique (akin to a hammer-and-anvil method) also likely allowed for access of nutrient-rich bone marrow and nuts, with battered and pitted stones providing evidence of such activity. Indeed, Oldowan assemblages are frequently found alongside fragments of animal bones and teeth, hinting at such behaviour (Schick and Toth, 2013; Toth and Schick, 2015).

Until recently, the oldest examples the Oldowan Industrial Complex were those of Gona (figure 2.1) and Ledi-Geraru, in the Afar Triangle of Ethiopia, and which appear from around 2.6 Ma (Braun *et al.,* 2019; Semaw *et al.,* 1997, 2003). Zoological bone fragments with cut marks were also unearthed, suggesting that butchery was a significant function of the tools, in addition to cores being used as multipurpose tools such as hammerstones and for other pounding activities (Semaw *et al.,* 2003). Although the Ledi-Geraru tools appear to be more primitive than those of Gona, they exhibit understanding of sequential flake removal and systematic flake production that is characteristic of the Oldowan (Braun *et al.,* 2019). Currently, the earliest examples of Oldowan tools originate from Nyayanga, Kenya, dating from between 3.032 to 2.581 Ma (Plummer *et al.,* 2023). Flaked tools comparable to younger Oldowan sites, though with increased pounding activities, were used to cut, scrape, and pound large mammal and plant tissue. While dental material from two hominin individuals assigned to *Paranthropus sp*. were discovered in association with a hippapotimid butchery site, the Nyanyanga artifacts have not been definitively attributed to a specific hominin genus (Plummer *et al.,* 2023).

The tools found at these early Oldowan sites represent a lithic culture produced by toolmakers who had efficiently mastered the basic skills needed to flake cobbles to produce lithic tools (Schick and Toth, 2006). The makers of early Oldowan tools possessed an excellent empirical understanding of the mechanical properties of lithic raw materials, fracture mechanics, and

geometry, and were capable of a significant degree of planning (Ambrose, 2001). Oldowan artefacts reflect the considerable skill employed by their makers in efficiently removing large, sharp flakes from cores, and early Oldowan artifacts show a high degree of planning depth, coordination, and dexterity in their production. There is general consensus that the earliest Oldowan tools were produced by skilled toolmakers who had a clear understanding of the fracturing mechanics of different stone materials, and that Early Oldowan artefacts are too advanced to have been the first experiments by early hominins in producing sharp-edged stone flakes. The deliberate and systematic production of stone tools is therefore likely to have been a behaviour habitual to hominins prior to 2.6 Ma, with a simpler lithic reduction stage hypothesised to have existed prior to the Oldowan (Delagnes and Roche, 2005; Hovers, 2015; Schick and Toth, 2006; Semaw *et al.,* 2003; Putt, 2015). It is therefore highly unlikely that that the assemblages from Gona, Ledi-Geraru and Nyanyanga represent the earliest attempts of deliberate stone tool production by means of core reduction in the Hominin lineage. Rather, it is probable that a simpler lithic-reduction stage was employed prior to the production and deposition of stone tools at these early Oldowan sites (Delagnes and Roche, 2005; Haslam *et al.,* 2009; Putt, 2015).

Evidence of Pre-Oldowan Stone Tools

Evidence for a pre-Oldowan industry were first proposed by McPherron *et al.* (2010), who presented four bovid fossils with striation marks interpreted as being the result of butchery using sharp lithic flakes and stone hammers. Found at Dikika, in the Lower Awash Valley of Afar in Ethiopia, these four bones were dated to between 3.42 and 3.24 Ma. The bovid fossils exhibited, according to McPherron *et al.* (2010, p.857): "*unambiguous stone-tool cut marks for flesh removal and percussion marks for marrow access*". McPherron *et al.* (2010) concluded that a femur shaft (DIK-55-3) and rib fragment (DIK-55-2) showed evidence for the use of sharp-edged stones by hominins to remove flesh, while percussive marks on the femur were indicative of the use of hammerstones for marrow access (figure 2.2). The conclusions of McPherron *et al.* (2010), based on previous field observations conducted by Blumenschine *et al.* (1996), and subsequent optical and environmental scanning electron microscopy (ESEM), stated that the marks in question lacked the morphology indicative of trampling and biochemical marking, but rather

showed clear modifications resulting from hammering, scraping, and butchering activities using sharp-edged stone tools.

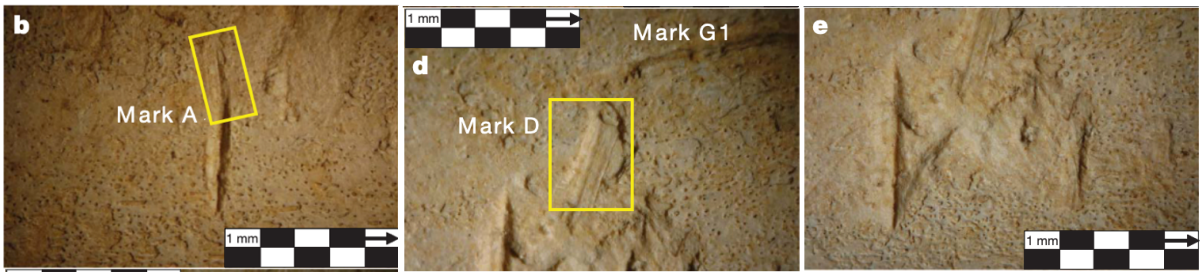

Figure 2.2: Examples of cut marks on the DIK-55-3 fossil bovid femur shaft from Dikika, interpreted to be made with the use of stone tools. B shows mark A, interpreted to be a high-confidence stone-tool-inflicted mark. d shows percussion damage (D), and e shows marks interpreted as high-confidence stone tool-inflicted marks. From McPherron *et al.,* 2010.

The conclusions of McPherron *et al.* (2010) are not universally accepted, and were disputed by Dominguez-Rodrigo *et al.* (2010, 2011, 2012; see also McPherron *et al.,* 2011), who argued that, rather than resulting from butchery using lithic tools, the marks were merely the product of trampling damage incurred during *"incidental movement of the de-fleshed specimens across and/or within their abrasive encasing sediments"* (Dominguez-Rodrigo *et al.,* 2010; p. 20929). Dominguez-Rodrigo *et al.* (2010) argued that McPherron *et al.* (2010) failed to address the stratigraphic and depositional context of the sandstone units from which the fossils originated, and that abrasional modifications such as random striations and trampling damage were to be expected on any fossil deposited within the unit. Furthermore, Dominguez-Rodrigo *et al.* (2010) considered the bases of the grooves interpreted by McPherron *et al.* (2010) as V-shaped to be commonly broader than the heights of the walls of the grooves, arguing that such morphologies were more likely to be the result of animal trampling than of hominin butchery (Dominguez-Rodrigo *et al.,* 2009; 2011). That the marked bones of Dikika were neither discovered *in situ,* nor accompanied by lithic artifacts, cast further doubt on McPherron *et al.*'s (2010) conclusions, and raised issues regarding not only their context, but also their age (Schick and Toth, 2013). Further, the absence of any lithic technological artefacts found in association with the marked bones precluded any inferences of whether the proposed tools were the result of deliberate knapping, or were rather naturally-occurring sharp-edged stones collected for that specific purpose (McPherron *et al.,* 2010). Nevertheless, were the conclusions of McPherron *et*

al. (2010) proven, Dikika would represent the earliest evidence of hominin lithic tool-use, expanding the antiquity of such behaviour by almost 800,000 years.

Despite the contextual uncertainty of the specimens discovered at Dikika, and the subsequent controversy surrounding their interpretation, in 2015 more conclusive evidence not only of pre-Oldowan tool-use, but of pre-Oldowan stone tool manufacture, were presented by Harmand *et al.* (2015). Lithic artefacts dating from 3.3 Ma were recovered at the Lomekwi-3 (LOM3) archaeological site in the West Turkana basin of Ethiopia, and consisted of 149 surface and *in situ* artifacts, including 83 cores and 35 flakes, as well as several anvils, hammerstones and worked cobbles (figure 2.3). Experimental analysis carried out by Harmand *et al.* (2015) concluded that the flake and core techno-morphology did not conform to observed patterns resulting from accidental rock fracture, but rather that the clear and repeating technological features of the flakes and flake fragments provided compelling evidence for their intentional production.

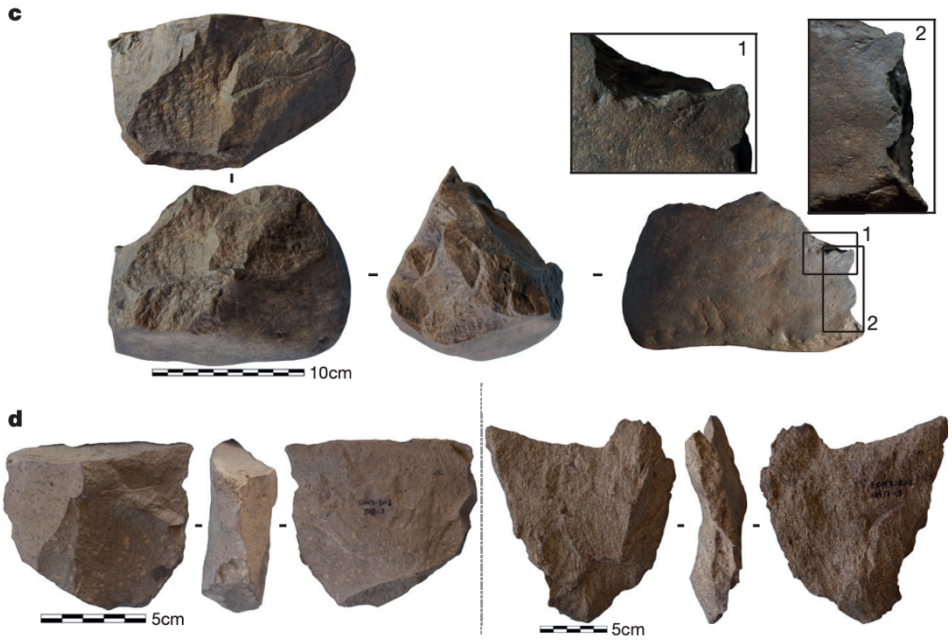

Figure 2.3: 3.3 million year-old cores and flakes from Lomekwi, Ethiopia, which represent the earliest-known evidence of stone tool production and use in the hominin lineage. From Harmand *et al.,* 2015.

The artefacts discovered at Lomekwi are significantly larger than traditional Oldowan tools and include extraordinarily large cores with relatively few flaking surfaces. Harmand *et al.*

(2015) concluded that rather than being produced through the hand-held core reduction techniques commonly used to make Oldowan tools, the flakes discovered at Lomekwi exhibited extensive evidence of being produced through less developed methods, such as bipolar percussive techniques, in which cores are rested on anvils and reduced by pounding them with hammer stones (Harmand *et al.* 2015; Hovers, 2015). Such methods of lithic reduction are rarely identified in the Oldowan (Braun *et al.,* 2019; Harmand *et al.* 2015). The lithic artefacts of Lomekwi contrast markedly from the early examples of Oldowan tools from Gona and Ledi-Geraru not only in their size, but also in their overall primitiveness, and while it is conceivable that some of the smaller flakes may have been produced by direct freehand percussive core-reduction, the average size and weight of the cores, and the apparently less-developed understanding of stone fracture mechanics and grammars of action associated with their production, indicate that such activity was unlikely, and the precision of the percussive motion by which these tools were made appear to have been less controlled than in the Oldowan (Harmand *et al.,* 2015; Hovers, 2015). Furthermore, the artefacts of Lomekwi indicate a degree of opportunism in their usage, with evidence of blank cores having been used for percussive activities prior to flake removal.

The chronological isolation of the Lomekwi artefacts suggest that though some contemporary hominins were capable of lithic tool-production through core reduction techniques, they would have done so sporadically (Williams-Hatala, 2016). The clear disconnect between the lithic technology represented at Lomekwi and those of later Oldowan sites led Harmand *et al.* (2015) to propose that their discovery signifies the first known example of a pre-Oldowan lithic industry representative of a technological stage intermediate between a hypothetical pounding-oriented stone tool use utilized by earlier hominins, and the more artisan methods of later Oldowan toolmakers.

The lithic artefacts of Lomekwi not only pre-date the earliest-known examples of Oldowan tools by more than 700,000 years (Harmand *et al.,* 2015), they also pre-date the earliest evidence of *Homo* in the fossil record by half a million years (Villmoare *et al.,* 2015). Based on current understanding, the artefacts discovered at Lomekwi provide evidence of tool-making and tool-using capabilities in pre-*Homo* hominins and challenges the paradigm that complex toolmaking and tool-using behaviours were unique to, and definitive of, the genus *Homo* (Callaway, 2015;

Harris, 1983; Kivell, 2015; Leakey, Tobias and Napier, 1964). Indeed, based on our current understanding of the fossil and archaeological record, it can be concluded that the deliberate manufacture and use of stone tools were behaviours prevalent in hominins prior to the evolution of the genus *Homo*, and that pre-*Homo* hominins were utilizing large-sized blocks of rock, and modifying them into sharp-edged tools, 500,000 years before the first occurrence of *Homo*, and 700,000 years before the earliest example of Oldowan technology (Ambrose, 2001; Balter, 2015; Callaway, 2015; Domalain, Bertin and Daver, 2017; Plummer, 2004; Semaw *et al.,* 1997; Villmoare *et al.,* 2015).

Such conclusions naturally lead to the issue of identifying pre-*Homo* hominin taxa capable of making and using the stone tool artefacts discovered at Lomekwi. However, to date, only indirect associations exist between the sporadic fossil hominin record and the archaeology of these early stone tools (Dunmore *et al.,* 2020). No inferences were made by McPherron *et al.* (2010) as to whether the proposed butchering behaviour at Dikika could be directly attributed to a specific taxon of contemporaneous hominin. The only hominin species currently known to have been in the Lower Awash Valley at 3.39 Ma is *Australopithecus afarensis* (Alemsgeled *et al.,* 2006; Callaway, 2015; Kimbel, Rak and Johanson, 2004). Likewise, no hominin species was discovered in direct association with the lithic technology of Lomekwi, though they were discovered in the same geographic and chronological ranges as the paratype of *Kenyanthropus platyops* (KNM-WT 38350) and other hominin fossils generally referred to as *cf*. *Kenyanthropus platyops* (Leakey *et al.,* 2001; Wood and Leakey, 2011). As such, Harmand *et al.* (2015) suggested that a pre-*Homo* taxon such as *Kenyanthropus platyops* or *Australopithecus afarensis* may have developed the ability to produce and use Lomekwian tools. While a *Paranthropus sp*. molar was discovered in direct association with a butchering site at Nyanyanga, *Homo* was also present in eastern Africa at the time of deposition, and the Nyayanga artefacts cannot therefore be definitively attributed to a specific hominin species (Plummer *et al.,* 2023). Likewise, no fossil hominins have been found in the sedimentary layers directly associated with the early Oldowan stone tools of Gona (Schick and Toth, 2013). However, a partial cranium and dentition was discovered in the Bouri Formation of the Middle Awash site region, approximately 60 miles to the south, which was dated to 2.5 Ma and assigned to *Australopithecus garhi* (Asfaw *et al.,* 1999). While *Australopithecus garhi* is considered by some to be a candidate for the manufacture of some of the earliest-known examples of Oldowan stone tools (Toth and Schick, 2015), two other hominin taxa – *Homo* and

Australopithecus aethiopithcus - are contemporaneously known elsewhere in eastern Africa from deposits that are chronologically comparable to Gona (Hill *et al.,* 1992; Semaw *et al.*, 1997; Walker *et al.,* 1986). Later Oldowan sites provide no more clarity. de Heinzelin *et al.* (1999), for example, attributed cut marks on 2.5-million-year-old bones to *Australopithecus garhi*, while tools from Swartkrans, South Africa, have been suggested to be the product of *Paranthropus robustus* (Backwell and d'Errico, 2001). The co-occurrence of several hominin taxa in the same geological horizons as many of the earliest archaeological sites inhibits a clear perception of which hominin species were making and using the earliest-known examples of lithic technology (Schrenk, 2013), assuming that such behaviour was not ubiquitous across the hominin clade. Furthermore, hominin taxa known to be chronologically and geographically contemporaneous with these sites almost invariably exhibit manual and upper limb skeletal morphologies that display adaptations for extensive use of the hand in suspensory locomotion and climbing.

Recent archaeological and palaeontological discoveries appear to conclusively demonstrate that the production and utilization of stone tools were not behaviours that originated in – and therefore were exclusive to – the genus *Homo*. Such conclusions naturally lead to several pressing questions: how did early hominins produce and effectively use early lithic technologies with hands that lacked a modern human form and exhibited functional features adapted for arboreal locomotion? Perhaps the most pressing question of all is, if the development of stone tools did not originate in the genus *Homo,* how then are we to identify contemporaneous species that were capable of their production and use? Lastly, was such behavior ubiquitous among contemporaneous early hominin taxa (Marzke, 2013; Kivell, 2015)?

In the absence of direct chronostratigraphic evidence linking contemporaneous hominin fossils with the earliest archaeological record, attempts to identify stone tool-making and tool-using capabilities in contemporaneous fossil hominin taxa must utilize multiple strands of inquiry, not only from the palaeontological and archaeological record, but also from comparative behavioral and morphological assessments of modern humans and extant non-human primates (Kivell, 2015). Marzke (2013) suggested that attempts to identify stone-tool related behaviours in extinct hominin taxa must draw a synthesis of results from the tests of two hypotheses: the first focusing primarily on behaviour and performance, the second on form and function. The first hypothesis posits that modern humans possess a unique pattern of grips, hand postures, and

hand movements that facilitate the effective production and use of stone tools, and that these have become prevalent through uniquely-human behaviors. Assuming the first hypothesis holds true, the second hypothesis predicts that, through millions of years of adaptive evolution, the modern human hand exhibits a unique pattern of functional morphologies that facilitate such capabilities (Marzke, 2013). To test these hypotheses, recent work has focused on identifying behaviors that are unique to humans among primates during manual manipulative activity, and the subsequent identification of morphological features in the human hand that facilitate such behaviors (Kivell, 2015). The presence or absence of human-like features in the hands of fossil hominin species may then inform conclusions on their ability to make and use lithic technology.

2.2 Tool-use in non-human primates

The recent discoveries of pre-*Homo* tool-making and tool-using behaviors are complemented by an increasing body of evidence that disprove the traditional paradigm that such activities are solely attributable to the genus *Homo*. However, prior to Jane Goodall's (1963, 1964) groundbreaking observations of tool-related behaviour in chimpanzees, tool-use was thought to be unique to humans, to the extent that such activities were a defining feature of humanity (Washburn, 1960; Dominguez-Rodrigo *et al.*, 2012). Goodall's observations that our closest living relatives were capable tool-users led her colleague and mentor Louis Leakey to proclaim that "*we must now redefine man, redefine tool, or accept chimpanzees as human*" (Surujnarain, 2019). Goodall's discoveries necessitated a paradigm shift in not only our understanding of non-human tool-use, but also of how we viewed ourselves within – and apart from – nature. Continued research over the last 60 years have demonstrated that many primates are capable, albeit episodic, tool-users, and are distinguished by the variation they show in tool-using contexts (Bentley-Condit and Smith, 2010). However, although tool-using behaviours in primates are varied and widespread, not all species are known to use tools. Strepsirrhines have not been reported to use tools in the wild, and while most captive haplorrhine primates will use tools when given the opportunity, only a few species have been observed doing so in the wild (Carvalho, Matsuzawa and McGrew, 2013; Gumert *et al*., 2009; Nystrom and Ashmore, 2008; Ottoni & Izar, 2008; Visalberghi and Fragaszy, 2013; Visalberghi *et al*., 2009).

Among non-human primates, only chimpanzees, orangutans, capuchins, and long-tailed macaques are currently known to habitually use tools in the wild (Luncz *et al*., 2022; Meulman and van Schaik, 2013). Long-tailed macaques (*Macaca fascicularis*) regularly crack open shellfish with naturally occurring stone tools to access food sources (Gumert, Kluck and Malaivijitnond, 2009; Malaivijitnoind *et al.,* 2007), while three species of capuchin monkeys (*Sapajus libidinosus, Sapajus xanthosternos, Cebus capucinus*) are also prolific and habitual tool-users (Barrett *et al*., 2018; Canale *et al*., 2009; Falotico and Ottoni, 2016; Fragaszy *et al*., 2004), employing a range of materials as tools which are used in various methods for numerous goals (Ambrose, 2001; Boinski, 1988; Visalberghi and Fragaszy, 2013). However, their causal understanding of what constitutes appropriate and inappropriate tools for certain outcomes appear to be lacking, and they appear to learn through trial-and-error what constitutes as an appropriate tool (Byrne and Russon, 1998; Visalberghi and Limongelli, 1994; Visalberghi and Trinca, 1989).

Hominidae are the most capable tool users among the primate families, with all genera having been observed to use tools in the wild, though significant variation in the frequency and proficiency of tool-using behaviours exist between the non-human great apes. Gorillas rarely use tools in the wild, and any tool-use that has been observed is simplistic in its nature (Breuer, Ndoundou-Hockemba and Fishlock, 2005). Prior to the observation of two adult female western lowland gorillas (*Gorilla gorilla gorilla*) using detached branches as postural support when crossing bodies of water, tool-use in wild gorillas had not been reported, and it was doubted whether wild gorillas used tools at all (Breuer *et al*., 2005). Several more observations of the use of tools by gorillas have since been reported, not only as transportation aids but also for food acquisition (Grueter *et al.,* 2013; Kinani & Zimmerman, 2015). Nevertheless, observational evidence of tool-use in wild gorillas remain rare, especially compared with other hominoids. Further, no indirect evidence for gorilla tool-use, such as discarded tools, have ever been discovered (McGrew, 1991). Their apparent lack of dependence on tools may simply be a consequence of their dental morphology and brute strength, which render extensive tool-use as an unnecessary endeavour (Breuer *et al*., 2005).

Tool-use in *Pongo* is more extensive than in gorillas, and orangutans have been observed using tools made of organic material for a range of purposes (Meulman and van Schaik, 2013). Wild Sumatran orangutans (*Pongo abelii*) have been observed using tools for a diverse array of

activities, from extracting honey to insect fishing, and for breaking fruit husk (Van Schaik, Fox and Sitompul, 1996; Bower, 2011). Furthermore, if a particular tool proves useful, the tool will often be retained, and overtime, individual orangutans will collect "toolboxes" (Van Schaik, Fox and Sitompul, 1996). However, while captive or rehabilitated orangutans frequently use tools, complex tool-use by wild orangutans is rare, and the behaviours that have been observed are simplistic (Fox, Sitompul & van Schaik, 1999; Kivell *et al.,* 2022; McGrew, 2004; Meulman & van Schaik, 2013; Nystrom and Ashmore, 2008; Whiten, Sanz & Morgan, 2007, 2009; Schick and Toth, 2009; Van Schaik, Fox and Sitompul, 1996).

Among non-human primates, chimpanzees (*Pan troglodytes*) are by far the most capable and sophisticated users of tools, possessing the richest tool-using repertoire of any non-human animal. Chimpanzees use tools for numerous goals, and in many varied formats across their geographical distribution (Toth and Schick, 2013). Organic material is the most commonly-used material for use as tools by chimpanzees (Boesch and Boesch, 1990), with ant and termite fishing using stripped and carefully-shaped twigs being among the most frequent behaviours, followed by the use of sponges made out of chewed leaves for water collection and cleaning (Toth and Schick, 2013). Chimpanzees have also been observed preparing sharpened sticks with their teeth to produce spear-like tools, which are then jabbed into the hollows of tree trunks in order to spear and kill small animals such as lesser bushbabies (*Galago senegalensis*) as a source of food (Pruetz and Bertolani, 2007).

Stone tool-use in non-human primates

Non-human primate tool use is not restricted to organic material. The use of lithic material as tools by chimpanzees is known from a number of locations in West Africa (Carvalho and McGrew, 2012). The foraging behaviour of Tai Forest chimpanzees (*Pan troglodytes verus*), for example, relies heavily on lithic material for use as hammers and anvils for the purposes of nut-cracking, and has produced an archaeological record dating back to at least 4.3 ka, indicating that the utilization of lithic material for the purposes of bipolar hammer-on-anvil nut cracking is a long-established behaviour in *Pan troglodytes verus* (figure 2.4) (Boesch and Boesch, 1990, 1993; Boesch and Boesch-Achermann, 2000; Carvalho et al., 2008; Mercader, Panger and Boesch,

2002; Mercader *et al*., 2007; Sakura and Matsuzawa, 1991). There have also been observations of chimpanzees propping up stone anvils with additional lithic material as wedges to obtain level anvil surfaces, argued by Matsuzawa (1991, 2001) as being proof that chimpanzees also use metatools (an object used to modify another object, which is in turn used as a tool), a behaviour not previously observed in non-human animals. There appears to be a strong degree of cultural transmission in the tool-using habits of chimpanzees, with different populations exhibiting preferences for different materials for the same tasks (Boesch and Boesch, 1990), as well as variation in tool-using habits between sexes and age groups (Boesch and Boesch, 1989; McGrew, 1979). However, lithic tool-use in chimpanzees is limited, and based on current evidence, is restricted to West African populations (Carvalo, Matsuzawa and McGrew, 2013; Proffit *et al.,* 2022).

During such use of lithic material as both hammers and anvils for the purposes of cracking open nuts, unintentional production of flake-like lithic detachments have been observed (Carvalho *et al*., 2008; Mercader *et al*., 2002; Mercader *et al*., 2007). However, stone breakages during chimpanzee tool use are unintentional, being the result of uneven or errant strikes, and are not the product of intent, nor are they used for any subsequent purposes (McGrew, 1992). And while the deliberate manufacture and use of flaked stone tools have been observed in three captive and encultured ape subjects – one orangutan and two bonobo chimpanzees (Schick *et al*., 1999; Toth, Schick, and Rumbaugh, 1993; Wright, 1972) – these behaviours were the results of extensive human training and interaction (Bandini *et al*., 2021), and should not be interpreted within the same context as wild and unhabitualized primates.

Figure 2.4: An adult chimpanzee cracks nuts with a stone hammer and anvil in a bipolar mode in Bossou, Guinea. From Haslam *et al.,* 2009.

Observations have been made of captive tufted capuchin monkeys (*Cebus apella*) producing stone-flakes by striking stones against hard surfaces, and infrequently through hard hammer percussion, as well as using stones as cutting tools in an experimental setting (Westergaard & Suomi, 1993). Wild bearded capuchins (*Sapajus libidinosus*) are also known to deliberately break stones through both hard hammer percussion and bipolar reduction methods (figure 2.5) (Proffit *et al*., 2016). To date, wild bearded capuchins are the only non-human primate known to deliberately engage in stone-reduction behaviours in the wild, with the intent being the deliberate reduction of the core. However, the primary aim of this behaviour appears to be either as an aggressive display (Moura, 2007), or for the ingestion of essential trace nutrients or lichens (Proffit *et al*., 2016). The production of sharp-edged flakes is not a primary objective of such activity, and any such objects are an unintentional product that are discarded and are not used in any subsequent behaviours.

Figure 2.5: An adult male capuchin monkey cracks nuts with a stone hammer and wood anvil. From Haslam *et al.,* 2009.

The use of tools – both lithic and organic – is no longer considered a defining attribute of the hominin lineage, let alone the genus *Homo*. However, while several taxa of extant non-human primates are known to habitually use tools, evidence for the deliberate production and subsequent use of sharp lithic cutting edges through percussive behaviour has not been observed in wild non-human primates. That chimpanzees have by far the most extensive tool-using repertoire of all the apes in the wild though do not display behaviours that involve the deliberate production and utilization of flaked stone tools suggests that such behaviour developed after the split of the last common ancestors of *Pan* and hominins (Bandini *et al*., 2021).

Evidence of non-human primate tool-use collated throughout the late 20th and early 21st centuries disprove the notion that tool-using behaviours are unique to *Homo*, and are certainly not a defining feature of the genus. Indeed, the abundance of observations of habitual tool-use among some primate clades suggests that generalized tool-using activities was a shared behavioural trait present in the last common ancestor of *Pan* and *Homo* (Braun *et al.,* 2019). However, while both lithic and organic material are used as tools in several primate taxa, the deliberate production of sharp cutting edges through controlled, conchoidal fracture involving the repeated removal of multiple flakes from a single core, with the edges of cores being clearly targeted, and these edges subsequently used for any purpose, does appear to be a uniquely

hominin behaviour that distinguishes the clade from other primates (Proffit *et al*., 2016). The significant role that the adoption of such behaviour played in our evolutionary history cannot be understated. However, in the absence of any direct and unambiguous associations of early lithic artefacts with certain fossil hominin species, the authorship of the earliest stone tools remains speculative.

2.3 Uniquely-Human Manual Dexterity and morphological features of the hand

In the absence of definitive evidence linking the earliest known examples of deliberately-flaked stone tools with contemporaneous fossil hominin species, it is necessary to infer the capacity for such behaviour in extinct hominin taxa through the testing of two hypotheses: the first hypothesis posits that modern humans have a unique repertoire of grips, hand movements, and postures compatible with the effective manufacture and use of stone tools; the second hypothesis proposes that if humans do indeed utilize distinctive hand grips and movements, these are facilitated by a unique repertoire of morphological adaptations in the hand that enable such movements (Marzke, 2013). Research into the evolution of human manipulative abilities in recent decades have focused on identifying manipulative behaviours that are unique to humans compared with other primates (a summary of the grips used during human manual behaviours is available in Appendix B). Subsequently, anatomical features of the human hand that facilitate such abilities can then be looked for in the hands of fossil hominins to infer their capacity for human-like grips and movements, and to inform research on the capabilities of extinct hominin taxa for making and using the earliest examples of deliberately-produced stone tools (Kivell, 2015; Marzke, 2013).

Non-human primate hands differ in their function significantly from the human hand due to the locomotive obligations of their hands during various forms of locomotion. Nevertheless, many primates are adept at manual manipulative behaviours, which overwhelmingly occur during feeding and grooming activities, and are characterized by a diversity of grip types, the extent, variety, and complexity of which vary through the order (Vereecke and Wunderlich, 2016). In an effort to identify grips and movements unique to the human hand, experimental stone knapping reconstructions have been compared with primate feeding behaviour, which present

many of the same challenges to stone tool-making in resisting strong external forces while exposing an adequate surface area of the manipulated object (Marzke, 2013). These studies have identified three manipulative behaviours that are considered unique to humans among extant primates: precision handling, forceful precision gripping, and power "squeeze" gripping (Kivell, 2015).

Precision handling is the ability to rotate and manipulate objects within a single hand using the thumb and fingertips alone, and without using the palm, another appendage, or the mouth to reposition the object (Kivell, 2015). While some non-human primates are capable of precision grips, secondary adjustment of the object is limited, and object rotation and repositioning is only achieved through the use of an additional anatomical region such as the palm of the hand, or a secondary appendage, such as the other hand, a foot, or the mouth (Boesch and Boesch, 1993; Christel, 1993; Kivell, 2015; Marzke and Shackley, 1986; Marzke and Wullstein, 1996). Precision handling allows the control and stabilization of objects by each hand simultaneously, for example during the application of strong percussive forces between two stones during core reduction activities (Marzke, 1997, 2013; Marzke & Shackely, 1986).

Forceful precision grips allow large forces to be applied on a manipulated object using only the pads of the thumb and one or more of the fingers, thereby enabling the stabilization and manipulation of an object while at the same time withstanding large external forces and keeping a significant portion of the surface of an object exposed (Kivell, 2015; Marzke, 1997, 2009, 2013; Marzke, Wullstein and Viegas 1992). During stone knapping, forceful precision grips allow for adequate exposure of a working surface, minimizing the portion of the stone that is covered by the hand and avoiding injury to the fingers, while at the same time withstanding the large external forces incurred during hard-hammer percussive activities (Kivell, 2015; Marzke, 1997, 2013). Examples of forceful precision grips which are employed exclusively by humans among extant taxa include the three-jaw-chuck grip (figure 2.6 (*a*)) and the cradle grip (figure 2.6 (*b*)), which cup manipulated objects by the thumb and finger pads – the second and third in the case of the three-jaw-chuck, and all four non-pollical fingers in the cradle grip (Marzke, 1997, 2013; Marzke & Wullstein, 1996). While other primates are capable of precision grips, typically the tip-to-tip or pad-to-side grips (see Appendix B), these grips are not executed with strong force, and

are therefore not capable of exerting as much power, or resisting as much external force, as those employed by modern humans (Kivell, 2015).

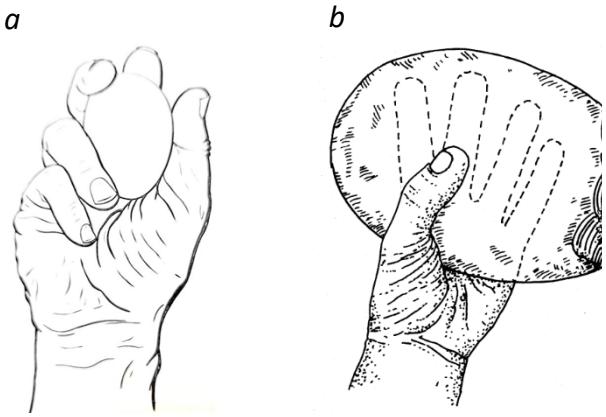

Figure 2.6: The three-jaw chuck grip (*a*) and cradle grip (b), which are examples of forceful precision grips. From Kapandji, 1982 and Marzke, 2013.

The power "squeeze" grip is utilized when a cylindrical object is held diagonally across the palm by strongly flexed fingers, with the thumb stabilizing the cylindrical object by either being wrapped around it or being in line with the forearm, such as when using a hammer (figure 2.7) (Kivell, 2015; Marzke, Wullstein and Viegas, 1992). During the power "squeeze" grip, the manipulated object is used as an extension of the forearm. While some non-human primates are capable of performing a variant of the power grip using the palm, or a diagonal hook grip with the fingers being stabilized against the palm, they are largely executed without major participation of the thumb, and when the posture becomes part of a dynamic activity, the power exerted in controlling the object is diminished relative to the human equivalent. The human power "squeeze" grip is therefore unique in the degree of power and control it exerts on an object (Kivell, 2015; Marzke, Wullstein and Viegas, 1992; Napier, 1960).

Figure 2.7: Power "squeeze" grip used on a cylindrical tool. From Marzke, 2013.

Comparative studies of modern human replication of stone knapping techniques and primate feeding behaviour have identified three manual actions which, based on current knowledge, are unique to modern humans among extant primates: precision handling; forceful precision grips; and use of the power "squeeze" grip. Following from the identification of these uniquely-human manual grips, postures, and movements, it is reasonable to theorize that such behaviours are facilitated by, and have resulted in, a suite of morphological features in the skeletal and muscular anatomy of the human hand that are unique among extant taxa.

In an effort to determine when these unique manipulative grips and postures evolved and became habitual to our ancestral lineage, comparative skeletal and muscular anatomical investigations, including comparative dissections, muscle architecture analysis, three-dimensional shape and biomechanical analysis of joint morphologies, and measurements of hand segment ratios have been conducted between modern humans, extant non-human primates, and, where possible, fossil hominin taxa (Vereecke and Wunderlich, 2016). Such investigations have indeed identified a suite of morphological features that are distinct to the human hand among extant primates, and which facilitate the effective execution of uniquely-human grips and hand postures, as well as enabling the resistance of powerful external pressures imposed upon the human hand during manual manipulative activities. While some specific features are found in other primates, such as a thumb-to-finger length ratio approaching the human condition in some primates (Almecija *et al.,* 2015), the complete suite of anatomical morphological features

are distinct to the human hand. Consequently, the identification of some or all of these morphological features in the hands of fossil hominin taxa can be used to infer human-like tool-making and tool-using behaviours in fossil hominin taxa, and provides an avenue of inquiry by which to discern authorship of the earliest-known examples of deliberately manufactured stone tools (Diogo, Richmond, and Wood, 2012; Kivell, 2015; Landsmeer and Long, 1965; Marzke, 1983; Marzke, 1983, 1997, 2013; Susman, 1998; Tocheri *et al.,* 2008).

2.4 Comparative functional morphology of the modern human hand

Despite its derived and specialized nature, the modern human hand is, at its most basic, primitive, retaining a plesiomorphic pentadactyl form (Napier, 1965). Paradoxically, subtle differences in the morphologies of the bones, articulations and muscles of the primate hand have transformed it into a highly specialized and sophisticated grasping organ used extensively in all aspects of primate life, from various modes of terrestrial and arboreal locomotion, to feeding, defence and infant care, through to social activities such as grooming and communication (Ankel-Simons, 2007). Subtle variations on an essentially primitive Bauplan have enabled primates to adapt to an extraordinary array of habitats, climates, locomotory modes, and behavioural and social structures (Fleagle, 1999). While the hands of most primates are constrained by locomotory obligations, the human hand, largely freed from such duties, has developed into an appendage which is not only capable of enhanced dexterity, but also of exerting as well as resisting substantial stresses and forces, resulting in a suite of distinctive morphological features. The capacity of the human hand to effectively perform unique forms of hand grips and prehensile movements is enabled by, and has resulted in, a suite of intrinsic skeletal and muscular anatomical features unique to modern humans (figure 2.8) (Diogo, Richmond, and Wood, 2012; Kivell, 2015; Landsmeer and Long, 1965; Marzke, 1983; Marzke, 1997; Susman, 1998; Tocheri *et al.,* 2008). A synopsis of the musculoskeletal anatomy of the human hand is available in Appendices D and E, and a detailed synopsis of the movements of the hand is available in Appendix C.

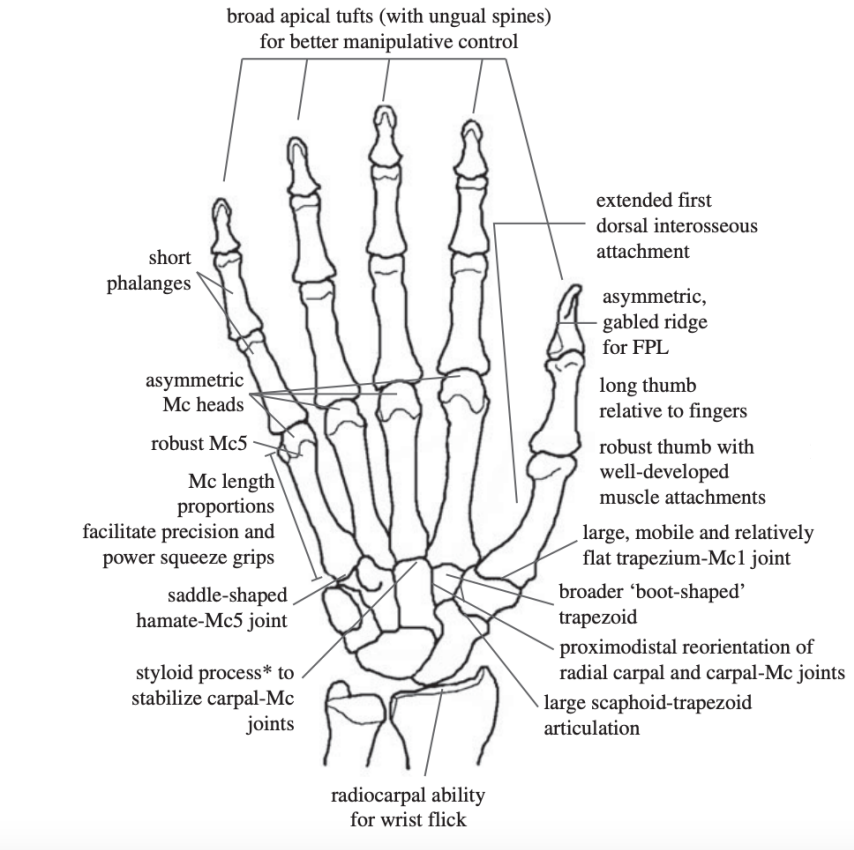

Figure 2.8: Selected features of the suite of osteological features generally considered distinct to the human hand and which facilitate uniquely-human grips and hand postures. From Kivell, 2015.

Many of the most obvious and critical features of the human hand relate to the skeletal and muscular anatomy of the thumb (Kivell, 2015). Compared with non-human primates, the human thumb is long and robust relative to the fingers (figure 2.8). A long and robust thumb is essential for the control of objects by effective execution of both power and precision grips (Aiello & Dean, 2006; Marzke, 2013). The extended length of the thumb relative to the fingers enables the distal pollical pulp to oppose the tip of the remaining digits more effectively, while the robusticity of the human thumb is a reflexion of the substantial external forces incurred upon it during tool use (Ruff, Holt and Trinkaus, 2006; Williams, Gordon and Richmond, 2012). A broad apical tuft, or distal tuberosity, relative to the base of the distal pollical phalanx further enhances object control and oppositional capacity in humans by providing a larger surface area of the distal pulp of the human pollex.

The trapeziometacarpal joint is of paramount importance in the various grips and postures performed by the human hand, with the majority of thumb movements occurring at this joint (Aiello & Dean, 2006). The wide range of motion of the human pollical metacarpal, including flexion-extension, adduction-abduction, and oppositional rotation, are facilitated by the sellar or saddle-shaped morphology of the trapeziometacarpal joint of the human hand. The large loads incurred by the human thumb during tool-related behaviour is also reflected in the relatively large size of the articular surfaces of the first carpometacarpal joint, and the broader and flatter articular surfaces of the joint. The joint surfaces of the trapeziometacarpal joint of humans are both dorsopalmarly broader and flatter than they are in apes, being only moderately curved compared to the marked curvature in chimpanzees (Aiello & Dean, 2006; Marzke *et al.,* 2010). Larger and flatter joint surfaces not only facilitate greater freedom of movement at the joint, but also provide a greater surface area for accommodation, resistance, and transferral of the increased joint compressive forces that are transferred through the joint when performing buttressing and oppositional obligations during forceful precision and power squeeze gripping (Marzke *et al.,* 2010; Tocheri *et al.*, 2007). The lower curvature of the carpometacarpal articular surface of the pollical metacarpal also reduces projection of its proximal volar beak, which lessens the potential for damage when it rides up on the trapezial saddle surface at the extreme ranges of opposition (Marzke *et al.,* 2010). However, despite the relatively flat surfaces, curvature is sufficient to maintain reasonable resistance to subluxation of the metacarpal with forces that tend to cause dorsal and radial displacement of the base (Marzke, 2013). Flexibility of the trapeziometacarpal joint is complemented by the positioning of the trapezium itself, which is positioned at an angle to its neighbouring carpal bones, automatically bringing the palmar surface of the thumb into opposition with the palmar surfaces of the remaining fingers (Aiello & Dean, 2006). Subtle asymmetry of the distal heads of the pollical metacarpal and proximal phalanx also enhance the oppositional capacity of the pollical distal pulp to effectively oppose those of the fingers (Shrewsbury *et al.*, 2003).

The musculature of the human thumb also reflects its enhanced capacity for strength and precision gripping, and though human pollical musculature is not unique, with every major muscle attached to the human thumb found in other primate taxa, these muscles are elaborated, with more muscles attaching to the human thumb than in almost all other primates (Diogo *et al*., 2012), and constitute a much larger proportion of total muscle mass of the hand in humans than

in other hominoids (Tuttle, 1969). Furthermore, all but one of the muscles of the human thumb have significantly larger moment arms and therefore enhanced mechanical advantages than those of chimpanzees (Kivell, 2015; Marzke *et al*., 1998, 1999; Richmond *et al*., 2016). The *opponens pollicis* muscle, which brings the pollical metacarpal and associated phalanges into opposition to the fingers, and is strongly recruited during tool-related behaviours, has a significantly larger potential torque and cross-sectional area, as well as significantly larger flexion and abduction moment arms in humans compared with other taxa, providing better leverage, and limiting fatigue during opposition of the thumb to the pads of the fingers (Marzke, *et al.,* 1998, 1999). The *adductor pollicis* also has a larger cross-sectional area and potential torque in humans compared with non-human primates (Marzke, *et al.,* 1998). Larger muscle attachments on the first metacarpal for the *opponens pollicis* and first dorsal interosseous muscles also help increase leverage and stabilize the trapezium-first metacarpal joint during opposition, which maintains forceful precision grips of stones during hard hammer percussive production of tools (Maki and Trinkaus, 2011; Tocheri *et al*., 2008). The attachment of the first dorsal interosseous muscle on the first metacarpal is also significantly longer in humans than it is in apes and is positioned to stabilize the base of the metacarpal, enhancing the ability for, and maintenance of, forceful precision grips (Marzke, 2013; Tocheri *et al.,* 2008).

Humans have two major extrinsic thumb muscles that are commonly absent in other great apes (although they are present in hylobatids): *flexor pollicis longus* and *extensor pollicis brevis* (Diogo*,* Richmond and Wood, 2012). The *flexor pollicis longus* muscle is not fully separated from *flexor digitorum profundis* in most non-human primates (*Hylobatidae* are a notable exception (Diogo, Richmond & Wood, 2012)), resulting in the involuntary flexion of the thumb during primary flexion of the fingers. In humans however, the *flexor pollicis longus* is more fully separated, allowing the thumb to be forcefully flexed independently from the other fingers, and *vice versa* (Richmond *et al*., 2016; Diogo, Richmond & Wood, 2012). The *flexor pollicis longus* muscle is important for precision control and manipulation, but it is particularly active in power "squeeze" grips rather than precision grips (Marzke, 2013). In humans, the *flexor pollicis longus* attaches onto the palmar surface of the distal pollical phalanx in a distinctively asymmetrical, gable-shaped pattern with a consistently long radial side. This asymmetry reflects a derived modern human pattern of loading on the pollical distal phalanx in manipulative behaviours and has been suggested to enhance opposition of the thumb to the fingers, together with an

asymmetrical pollical interphalangeal joint which slightly pronates the distal phalanx during flexion (Shrewsbury *et al*., 2003). A well-developed *flexor pollicis longus* muscle in humans helps to flex and stabilize the tip of the thumb and is particularly active during power "squeeze" grips, when the thumb acts as a buttress against an object (Kivell, 2015).

The carpal region of the human hand also displays distinct features that facilitate enhanced manipulative capabilities relative to other primates (Richmond *et al.,* 2016). Humans have a high degree of wrist mobility, particularly in extension, compared with other African apes (Tuttle, 1969). Increased extensive wrist mobility enhances the human capacity for hard-hammer percussion, as the increased extensional movement at the radiocarpal joint facilitates a wrist flick which is of particular importance in hard-hammer percussion, and which occurs just prior to a hammerstone strike of a core (figure 2.8) (Orr, 2012; Richmond *et al*., 2016; Williams, Gordon & Richmond, 2012).

In addition to a proportionately large joint surface on the trapezium for the first metacarpal, discussed above, the articulation of the trapezium for the scaphoid is also significantly larger in humans than in non-human great apes and baboons, and extends onto the scaphoid tubercle. This enlarged joint surface is capable of accommodating the larger joint compressive stresses associated with forceful precision and squeeze grips (Tocheri *et al.*, 2007). Most primates have a wedge-shaped trapezoid, with the narrow end of the wedge projecting palmarly, and an articulation with the capitate towards the dorsum of the hand. In humans, the palmar portion of the trapezoid is expanded, and the articulation between the trapezoid and capitate is situated at their corresponding palmar portions (Aiello & Dean, 2006; Tocheri *et al*., 2007). The palmar expansion of the human trapezoid effectively supinates the trapezium and brings the trapezium and the distal carpal row into greater radioulnar alignment (Tocheri, 2007). This realignment influences the morphology of many of the interphalangeal and carpometacarpal joints on the radial side of the hand and has been hypothesized to improve the biomechanics of resisting radioulnarly-oriented forces acting across the radial side of the wrist during forceful contraction of the enlarged thenar musculature (Tocheri, 2007; Tocheri *et al*., 2007, 2008). The palmar orientation of the modern human capitate-trapezoid articulation may be a direct adaptation to the compressive forces placed on the wrist by the thumb as it acts as a buttress during power grips, and facilitates transferral of considerable compressive forces from the base

of the thumb, through the trapezium and across the expanded anterior part of the trapezoid to the capitate (Lewis, 1977).

Reorientation of the scaphoid-trapezoid, trapezoid-second metacarpal, and capitate-second metacarpal joints in modern humans also work to better distribute the large loads incurred by the thumb during tool-related behaviours across the wrist and palm (Kivell, 2016; Lewis, 1989; Tocheri *et al*., 2005; Tocheri, 2007). The joints between the second metacarpal and the capitate and trapezium have a proximo-distal orientation in humans which allows a small degree of pronation when the second metacarpal is stressed by abduction and rotation of the index finger during the cupping of objects, and facilitates cupping of the human hand in adaptation to varying shapes of manipulated objects, acting to keep the trapezium-trapezoid and capitate-trapezoid joints in maximum contact during forceful precision and power grips (Marzke, 1997, 2013; Tocheri, 2007). A styloid process on the radiodorsal aspect of the base of the third metacarpal stabilizes the central part of the palm against external volar forces that accompany external loads acting on the third carpometacarpal joint (figure 2.8) (Marzke and Marzke, 1987). This styloid process has been hypothesised to have evolved to stabilise the carpometacarpal joint to prevent subluxation, especially in response to palmarly-oriented external forces experienced during stone tool use (Richmond *et al*., 2016).

The distal metacarpal heads of modern humans are also derived relative to non-human primates. The heads of the second and fifth (and minimally the third) metacarpals display an asymmetrical condyloid morphology, with the second metacarpal head being slightly bevelled dorso-radially, and the fifth metacarpal head being bevelled dorso-laterally (figure 2.9) (Lewis, 1977; Susman, 1979). No such asymmetry is observed in the metacarpal heads of *Gorilla* or *Pan*, though Susman (1979) did briefly note slight asymmetry of the second and fifth metacarpal heads of *Pongo.* The asymmetry of the second and fifth metacarpal heads modify movement in the flexion-extension plane, and result in conjunct, passive rotational movements of the fingers when flexed at their metacarpophalangeal joints. During flexion, the second proximal phalanx, and by extension the second digit as a whole, pronates and is abducted radially, while the converse movement occurs during flexion of the fifth digit, which is accompanied by passive and conjunct supination and adduction (ulnar deviation) (Lewis, 1977; Williams-Hatala, 2016).

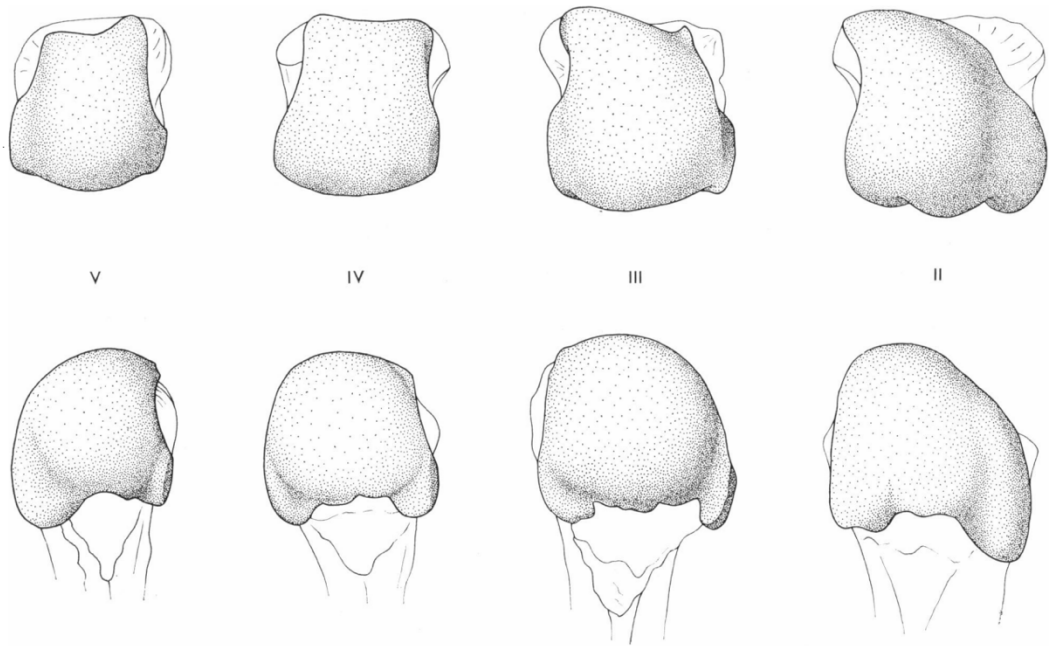

Figure 2.9: The heads of the second (right) to fifth (left) metacarpals of the right hand of *Homo sapiens* viewed from: top row, directly distally; bottom row, distoventrally. The second and fifth metacarpal heads are asymmetrical, which results in pronation of the second digit, and supination of the fifth, during flexion. From Lewis, 1977.

Humans also have the shortest and straightest phalanges among extant hominoids (figure 2.8) (Kivell, 2015; Richmond *et al*., 2016). Decreased length of the non-pollical phalanges result in a proportionally longer thumb which facilitates opposition to the fingers, and an ability for independent pad-to-pad touching between the distal pad of the thumb and each corresponding pad of the fingers. While not indicative of enhanced human-like manipulative abilities, longitudinal curvature of the proximal and distal phalanges is indicative of arboreal, and especially suspensory behaviour during life (Jungers *et al.,* 1997; Matarazzo, 2008; Rein, 2011; Stern & Susman, 1983). Curvature of the phalanges reduces bending stresses and diaphyseal strain during highly flexed finger postures, such as those employed when grasping branches during suspensory locomotion, and longitudinal curvature is sensitive to changes in behaviour during growth and is therefore a good indicator of arboreal behaviour during development (Richmond *et al*., 2016). Further reflecting the absence of arboreal and suspensory locomotory obligations of the human hand is the reduced development of flexor sheath ridges, which mark

the attachments of the flexor apparatus on the proximal and intermediate phalanges (Susman, 1979).

As with the distal pollical phalanx, the second-to-fifth distal phalanges of modern humans are characterized by broad distal tuberosities, or apical tufts, compared with other hominoids, which accommodate broad fingertips that enhance the control and manipulation of objects, especially during uni-manual behaviours (figure 2.8) (Kivell, 2015; Richmond *et al.*, 2016; Susman, 1979). Broader fingertips increase the surface area available for precision grips between the thumb and other digits (Richmond *et al.*, 2016), and the breadth of soft tissue of the fingertip is correlated with the breadth of the underlying distal tuberosity of the distal phalanx (Mittra *et al.,* 2007).

Comparative anatomy of the primate hand has revealed a suite of morphological features that, through adaptation to manual manipulation and a relaxation of the modern human hand's obligation for locomotion, facilitate the repertoire of grips and postures that enable our advanced dexterous capabilities. After the earliest hominins split from the last common ancestor with our closest living relatives, the chimpanzee and bonobo, two fundamental changes in function occurred. A transition to bipedality and reduced arboreality diminished the obligations of the hand for supporting weight through the forearm during locomotion. This freeing of the hominin hand from its locomotory obligations allowed for an intensification of manual manipulation, tool-use, and tool-making activities that required more precise and powerful fine motor actions (Richmond *et al*., 2016).

The comparative analysis of catarrhine hand morphologies has identified a suite of derived features in the modern human hand whose functions are consistent with the grips and stresses associated with habitual and effective manufacture and use of stone tools (Marzke, 2013). While each of the features discussed above may not facilitate uniquely-human hand movements and grips in isolation, the complete suite of morphological features is conducive to the effective execution of power "squeeze" grips, precision handling, and forceful precision gripping observed exclusively in modern humans among extant primate taxa. The identification of similar, human-like features in the hand bones of fossil hominin taxa may therefore provide information on the functional adaptation of their hands, and aid in the identification of extinct

hominin species that were capable of making and using the earliest lithic technologies (Lewis, 1977).

2.5 The human hypothenar digits

The identification of derived features in the hands of fossil hominins that are unique to humans among extant taxa is essential for assessing the stone tool-using and tool-making capabilities of extinct hominins. The importance of the thumb in human manipulative behaviours has long been acknowledged, and it is perhaps no surprise that research into the evolution of the human hand has focused extensively on the thumb (Key, Dunmore & Marzke, 2019). Due to their frequent utilization during grips used to wield hammerstones and flaked stone tools, the second and third digits have also been investigated in multiple important pieces of work. However, such focus has often been at the expense of research into the functional importance of the hypothenar (fourth and fifth) rays (Key, Dunmore & Marzke, 2019). Analysis of the fourth and fifth digits have, to date, been mostly limited to examining their lengths relative to the first digit (Alba, Moya-Sola & Kohler, 2003; Almecija, Smaers & Jungers, 2015; Key, Dunmore & Marzke, 2019; Key, Merritt and Kivell, 2018; Marzke, 1997; Marzke & Shackley, 1986). However, it is increasingly acknowledged that, rather than being passive actors during human manual manipulative activities, the two hypothenar digits – especially the fifth digit – are pivotal to the effective execution of many of the grips and postures essential for the enhanced dexterous activities performed by our species (Kivell, 2015; Marzke, 2013; Marzke, Wullstein & Viegas, 1983).

The importance of the hypothenar digits for stone tool-related activities were first discussed in detail by Marzke and Shackley (1986), who noted the significant role that the fourth and fifth digits played in resisting percussive forces during power squeeze gripping of stone tools. Marzke and Shackley (1986) noted that such activities were facilitated by strong flexion of the fourth and fifth digits, and by drawing the fifth metacarpal towards the first, thus enabling the cupping of the palm to squeeze and secure manipulated objects. A more recent study has demonstrated that the fifth digit is recruited in similar frequencies to the thumb and index finger during stone tool related behaviours, and incurs similar pressures during such activities (Key, Dunmore & Marzke, 2019). The dearth of research into the role of the fourth and fifth digits in

human tool-using behaviour between these two publications reflect the extent to which the hypothenar area of the hand has been overshadowed by the thumb with regards to research into the evolutionary development of the modern human hand. Nevertheless, while the functional importance of the fifth digit is poorly appreciated (Marzke, 2013), it probably has the greatest functional value after the thumb ray (Tubiana, Thomine & Mackin, 1996).

While there is no obvious difference between the basic morphologies of the four non-pollical digits of the hand, the fifth, and to a lesser extent fourth rays of the human hand exhibit significantly greater flexibility in their movements that reflect and facilitate their importance in human manipulative activities. While movements at the interphalangeal joints of all the fingers are to all extent and purposes restricted to the flexion-extension plane, a small amount of conjunct rotation occurs at the proximal interphalangeal joint of the fifth digit, facilitated by discrepancies in size and projection of the two condyles of the distal fifth proximal phalanx (Batmanabane and Malathi, 1985). Supination of the proximal phalanx of the fifth digit is also facilitated by asymmetry of the distal head of the fifth metacarpal (discussed above), which, in addition to adduction-abduction, flexion-extension, and circumduction, supinates the fifth finger during flexion to better oppose the thumb (Lewis, 1977; Susman, 1979). The conjunct movements of the fifth digit at its metacarpophalangeal and interphalangeal joints is complemented by a notably flexible fifth carpometacarpal joint. In contrast to the rigid and stable second and third carpometacarpal joints, the fourth and fifth carpometacarpal joints are relatively flexible, exhibiting an extensive range of motion in the flexion-extension plane, as well as passive conjunct rotational movements of supination-pronation that accompany flexion-extension, and a small amount of adduction-abduction (Hirt *et al.,* 2017; Kivell, 2016; Marzke, 1983; Marzke and Marzke, 1987). In this respect, the fourth and fifth carpometacarpal joints contribute significantly to hand mobility (El-Shennawy *et al.,* 2001; Nakamura *et al.,* 2001; Nanno *et al.,* 2001)

By some distance, the fifth carpometacarpal joint displays the most mobility of all the non-pollical carpometacarpal joints. While the second and third carpometacarpal joints are very limited in their freedom of motion, being restricted by the intrinsic interlocking shape of the bones themselves, when moving in concert with the fourth metacarpal, an astonishing amount of movement is permitted at the human fifth carpometacarpal joint (Bade, Koebke and Bilger,

1993). In isolation (when the fourth metacarpal is stationary), the movement at the fifth carpometacarpal joint permits an average of 28° of flexion of the fifth metacarpal, while the fourth carpometacarpal joint, which is more restrictive, permits an average of between 10° and 15° of flexion (Bade, Koebke and Bilger, 1993; El-Shennawy *et al.,* 2001; Lewis, 1977). However, the full range of motion of the fifth carpometacarpal joint is realized when the fourth metacarpal is unrestricted and moves in concert with the fifth (figure 2.10). In this scenario, flexion at the fifth carpometacarpal joint averages 44° (El-Shennawy *et al.,* 2001). These principal movements of flexion and extension at the fifth carpometacarpal joint of modern humans are also accompanied by conjunct movements of pronation (during extension) and supination (during flexion), as well as adduction and abduction, with the fifth carpometacarpal joint of modern humans permitting 13° of radial-ulnar deviation and 22° of supination (Bade, Koebke, and Bilger, 1993; El-shennawy *et al.,* 2001; Kivell, 2016). While no data is available on the kinematics of the hamate-metacarpal joints of non-human anthropoids, these joints in the non-human great apes are generally considered to lack any notable freedom of movement (Domalain, Bertin and Daver, 2017).

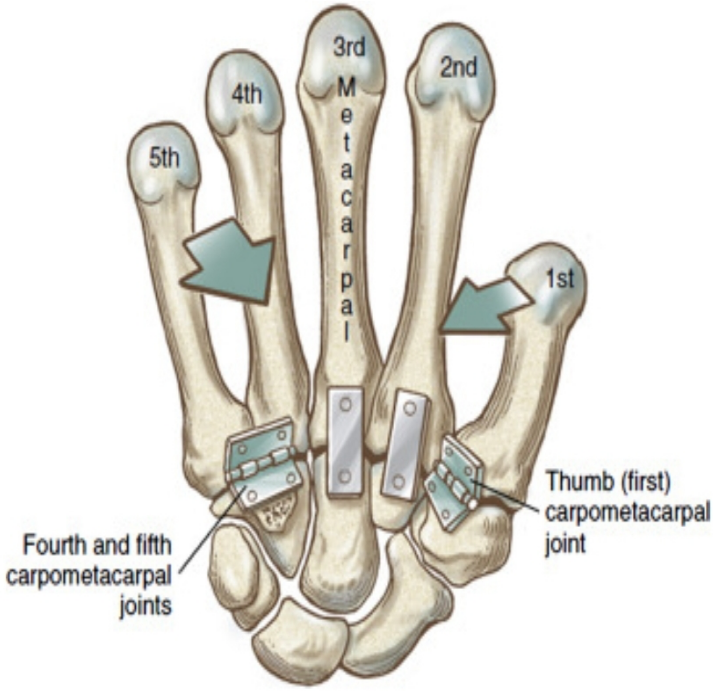

Figure 2.10: Representation of the movement capabilities of the carpometacarpal joints of *Homo sapiens*. From Ombregt, 2013.

The freedom of motion granted to the fourth and fifth metacarpals by their articulations with the hamate are pivotal for the effective execution of the power “squeeze” grips, precision grips, and cupping postures of the hand, all of which are essential to human manual dexterity. Flexion, supination, and abduction of the fifth metacarpal, augmented by similar movements of the proximal phalanx on the metacarpal head, enable the fifth digit to better oppose the rest of the hand, particularly the thumb (Lewis, 1977; Kivell, 2015). In conjunction with the more restricted movement of the fourth metacarpal, flexion and supination of the fifth metacarpal also brings the hypothenar area of the palm towards its centre, therefore allowing for a greater degree of curvature in the transverse metacarpal arch of the palm (figure 2.11). This movement not only aids in the capacity of the thumb to oppose the fourth and fifth digit, but also produces the distinctive cupping posture of the human palm (figure 2.11). Such movements and postures are an essential component of modern human manipulative capabilities, as they allow a better oriented pulp-to-pulp 5th digit grip force that substantially improves firm maintenance of a hammerstone (Kivell, 2015; Marzke, 1983, 1997, 2013; Marzke and Marzke, 2000; Marzke *et al*., 1998, 1999). They are also crucial for in-hand manipulation of objects, as well as for executing forceful cradle precision grips and effectively manipulating cylindrical objects during a power “squeeze” grip by bringing the hypothenar area of the palm towards its centre during flexion (Dubosset, 1981; Kapandji, 1982; Key, Dunmore & Marzke, 2019; Marzke, 1983 1997; Marzke, Wullstein & Viegas, 1992; Marzke *et al.,* 1998; Susman, 1979). Furthermore, as the most ulnar digit of the hand, the fifth digit plays an important role in power grips by clamping an object or the handle of a tool powerfully against the hypothenar eminence. Such an obligation is greatly facilitated by the ability of the fifth metacarpal to powerfully flex and supinate, initiated by the powerful hypothenar muscles (Tubiana, Thomine & Mackin, 1996).

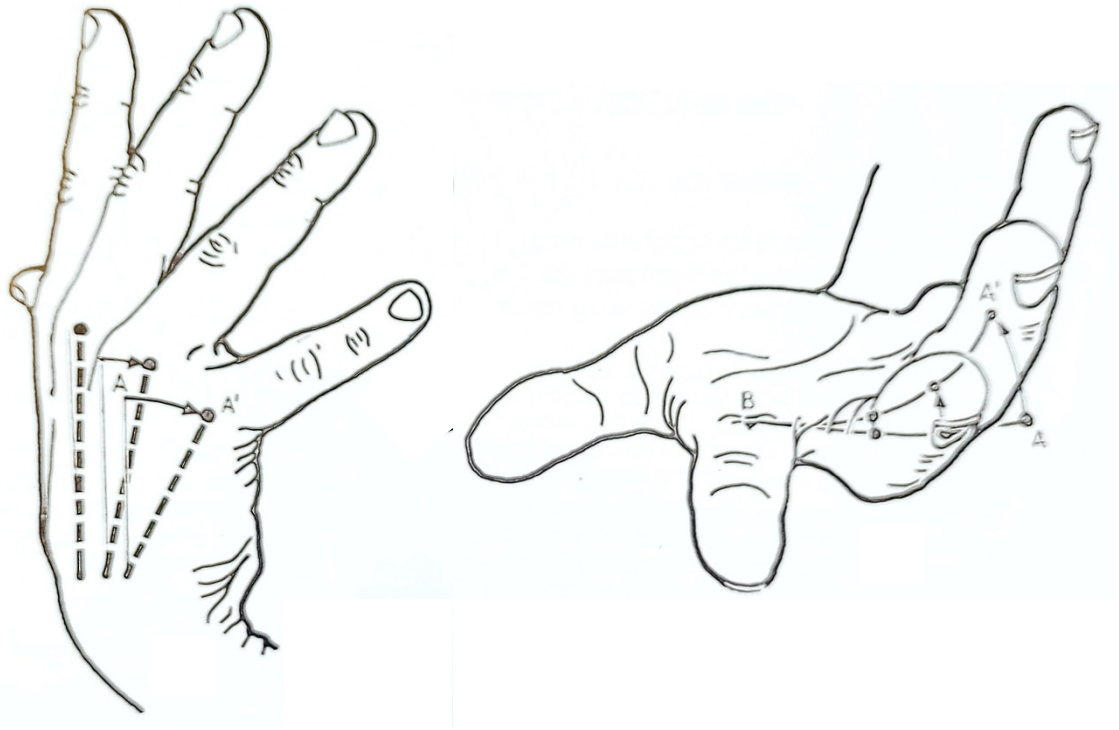

Figure 2.11: Flexion and supination of the fourth and fifth metacarpals at the hamate-metacarpal joints, which enable cupping postures of the palm and opposition of the fourth and fifth digits to the thumb, and enhance the transverse curvature of the distal metacarpal row. From Kapandji, 1982.

Mobility at the fourth and fifth carpometacarpal joints of modern humans is facilitated by a morphological architecture of the articular surfaces of the hamate-metacarpal joints that differ noticeably from those of extant non-human primates. While the proximal articulation of the human fourth carpometacarpal displays the most variation of all the carpometacarpal joints of the human hand, with up to five different morphologies recorded (El-Shennawy, 2001; El-Bacha, 1981; Viegas *et al*., 1991), the human fifth carpometacarpal joint is more regular, and as with the first, is generally of a saddle-shaped or sellar morphology, with the base of the fifth metacarpal exhibiting a slightly radioulnar convexity, and the facet of the fifth metacarpal exhibiting a complementary radioulnar convexity (Bade, Koebke and Bilger, 1993; El-Bacha, 1981; Lewis, 1989; Marzke and Marzke, 2000). Movement at the fourth and fifth carpometacarpal joints are facilitated not only by the architecture of the joint surfaces, but also by their placement with regards to the hamulus. The hamate articular facets for the fourth and fifth metacarpals do not extend onto the hamulus in modern humans, which is palmarly-projecting. Furthermore, the hamate articular surface is relatively smooth and flat, with only a

slight dorsopalmar concavity on the hamate in humans to match the correspondingly dorsopalmarly convex proximal facets of the metacarpals. In contrast to modern humans, the articular facet for both the fourth and fifth metacarpals in non-human hominoids are more complex and irregular, and generally extend onto a well-developed and distally-projecting hamulus (Bade, Koebke and Bilger, 1993; Kivell, 2016; Lewis, 1977). Such distally-projecting hamuli restrict the amount of flexion possible at the hamate-metacarpal joints, while a more palmarly-projecting hamulus, as is seen in modern humans, increases the mechanical advantage of the muscles that act on the fifth digit (Ward *et al*., 1999).

In addition to morphological variations of the hamate-metacarpal joints in hominoids, the relative sizes of the hamate's metacarpal articulations exhibit taxonomical variation. In humans, the hamate's facet for the fifth metacarpal is proportionately larger than that for the fourth metacarpal, while the opposite is true in African apes (though the condition in *Gorilla* is generally intermediate between humans and other great apes) (Marzke, Wullstein and Viegas, 1992; Orr *et al*., 2013). The relatively large and saddle-shaped MC5 facet of modern humans has been hypothesized to be an adaptation to greater loads experienced by the fifth digit during manipulatory and tool-using behaviours, as well as for enabling the slight rotational movements observed during flexion, with both capacities in concert enhancing the effectiveness of human forceful precision and power squeeze grips (Marzke, Wullstein and Viegas, 1992). Conversely, it has been argued that the apparent enlargement of the fifth metacarpal facet, rather than being the result of actual enlargement of the hamate-MCV joint surface, is in fact a reflection of a reduction in the size of the facet for the fourth metacarpal (Kivell, 2016). Orr *et al.* (2013) suggested that such a reduction of the MC4 facet reduces obstruction to movements of the fifth metacarpal, and more specifically, allows for greater rotation of the fifth metacarpal, further enhancing its ability to oppose the thumb.

2.6 Summary and aims of the project

Despite the increasingly evident role that the fourth and especially fifth digits played in the development and use of stone tools, investigations into the presence or absence of morphological features of the hamate-metacarpal joints that facilitate uniquely-human

movements of the digits remain under-explored in the hominin fossil record. Historically, focus of experimental biomechanics and biomechanical modelling has been limited to the radial side of the hand (Kivell *et al.,* 2022). And while more focus has been paid recently to the functional role of the second to fifth rays (Domalain, Bertin & Daver, 2017; Key, Dunmore & Marzke, 2019), the ulnar side of the hand remains largely underexplored (Kivell *et al.,* 2022; Marzke, 2013). Furthermore, previous comparisons of the hamate-metacarpal joints of modern humans, extant non-human primates, and fossil hominins have been overwhelmingly qualitative, and do not offer empirical, quantitative comparisons.

Such historical omissions can be explained, to an extent, by the limitations of traditional morphometric techniques in their ability to compare variations in the morphology of complex, three-dimensional joint architectures. However, recent advances in computational powers, three-dimensional imaging methods, and developments of statistical analysis provide new avenues of inquiry. Recent advances in geometric morphometric analysis, with the utilization of sliding semi-landmarks, provide new opportunities to quantitatively assess anatomical structures that previously, due to an absence of identifiable landmarks, were only capable of being compared qualitatively. A notable example of this is joint surface structures. Recent investigations have utilized three-dimensional geometric morphometric analysis to compare the shape of human, non-human primate, and fossil hominin hamates (Almécija *et al.,* 2015; Daver *et al.,* 2014; Orr *et al.,* 2013; Sollaccio *et al.,* 2019; Vanhoof *et al.,* 2021). However, these investigations concerned the overall shape of the hamate, and did not focus exclusively on the hamate's functionally important articulation with the fourth and fifth metacarpals. While Niewoehner (2001, 2007) compared the hamate-metacarpal and proximal fifth metacarpal articular surfaces of modern humans and Neanderthals, to date, there has been no quantitative investigations focusing exclusively on variation of the hamate-metacarpal joint surfaces between humans, non-human primates, and fossil hominin taxa contemporaneous with the earliest-recorded occurrence of incipient lithic technology.

This project aims to address such an omission by utilizing three-dimensional geometric morphometric methods to compare the articular surfaces of the hamate-metacarpal joints of modern humans with non-human primates in order to quantitively explore variations that have previously only been described qualitatively. In this project, the hamate-metacarpal joints of

extant great apes, including modern humans, were compared with those of fossil hominin specimens in order to ascertain if distinctly-human morphologies of these joints were present in earlier hominin taxa, and to assess their functional significance within the context of the development of early stone tools.

Section II: Methods and Materials

3 Methods

3.1 Geometric Morphometrics

To investigate shape variation of the hamate-metacarpal joints of great apes, modern humans, and fossil hominins, three-dimensional geometric morphometric analysis was considered the most suitable method. Results obtained through traditional multivariate morphometric analysis are mostly expressed numerically and graphically, and it is not possible to recover the shape of the original form from the results obtained, or to relate the results to the actual physical specimens upon which they are based (Rohlf and Marcus, 1993; Slice, 2005). Furthermore, the approximation of distances, ratios, and angles that complex, three-dimensional biological structures are reduced to during traditional morphometrics often fails to adequately encode all of the geometric information about the shape of the biological structures being studied. Traditional morphometric analysis may therefore neglect important geometric relationships among the structures under investigation, and important information on shape is often lost (Adams, Rohlf and Slice, 2004, 2013; Bookstein 1986; Bookstein *et al.,* 1985; Marcus, 1990; Rohlf and Marcus, 1993; Slice, 2005, 2007; Webster and Sheets, 2010).

Geometric morphometric analysis offers an alternative to traditional morphometrics that has many advantages and addresses many of the shortcomings of traditional morphometric analysis. It is a landmark-based method of shape analysis which utilizes two- or three-dimensional Cartesian coordinates of morphological landmark points in order to capture the overall shape of the structure being studied (Rohlf and Marcus, 1993). The use of landmark coordinates in preference to distance and angle measurements to represent shape allows for a more complete approximation of the shapes under study, as well as offering a three-dimensional approach to exploring shape variation within a population (Slice, 2007). Not only are the coordinates more versatile than traditional measurements, but the conservative distance measurements used in traditional morphometric analysis are retained and can be retrieved from

these coordinates (Rohlf and Marcus, 1993), allowing traditional morphometric analysis to be carried out in conjunction with geometric morphometric analysis, if so desired.

A major advantage that geometric morphometrics has over traditional multivariate morphometric analysis is that changes in shape can not only be expressed numerically and graphically, but also visually. Rather than simply reporting that shape has changed, geometric morphometrics enables the visual interpretation of how the shape of structures change within and between populations, and how certain structures vary relative to others (Rohlf and Marcus, 1993). By using landmark configurations, it is possible to generate the mean landmark configurations of each group within a sample, as well as the extremal morphologies within samples. The opportunity to visually investigate and describe shape allows for a more complete interpretation of how the shape of the structure under investigation has changed within the sample. A further advantage of geometric morphometrics is that it is possible to eliminate scale as a possible factor of variation. This ensures that it is variation in shape alone which is being investigated, though information on size of individual configurations is retained in the form of the centroid size (described in Appendix F), therefore allowing for comparison of size if desired (Bookstein 1986; Kendall 1989; Rohlf and Slice 1990). For these reasons, three-dimensional geometric morphometric analysis was considered most suitable method to address the aims of this project. An introductory summary into the theory and practical steps involved in geometric morphometric analysis is provided in Appendix F.

3.2 Methods used in this project

As a result of this project's focus on the morphology and variations in the shape of skeletal joint surfaces, and considering the benefits of the methods outlined above, geometric morphometric analysis was preferred to traditional morphometric analysis. Landmark data used in geometric morphometrics requires the use of points that have the same meaning and location in all specimens (Bookstein, 1991). However, joint surfaces have very few easily identifiable natural landmarks, and therefore present a challenge in identifying enough homologous landmarks suitable for the use of geometric morphometrics (Niewoehner, 2005). Furthermore, the articular surfaces of the hamate-metacarpal joints are relatively small, making the task of

collecting landmarks particularly challenging. For example, using a MicroScribe to digitize samples would be unsuitable, as not only would this lack a desired level of precision, but such a method would also risk displacement of the bone during the process of landmarking, thus reducing the reliability of the landmark coordinates collected (Proctor, 2010; Proctor, Broadfield and Proctor, 2008). It was therefore concluded that the most appropriate method for the collection of landmark data in this project was to produce virtual three-dimensional models, and to collect landmarks on these virtual models using bespoke software.

3.2.1 Digitization methods

The three-dimensional surface meshes of the hamate and fourth and fifth metacarpals used in this study were obtained through one of two primary methods: structured-light-scanning and photogrammetry. A small number of specimens (from the Smithsonian Institution's National Museum of Natural History) were also obtained through micro-CT scans by previous workers and are freely available upon request. Previous investigations have demonstrated that the modality used to generate polygon meshes has a negligible effect on the reliability and repeatability of landmark placement (Tocheri *et al.,* 2011; Robinson and Terhune, 2017; Shearer *et al.,* 2017). All models, regardless of the method by which they were produced, were therefore pooled into their respective component datasets (hamate, fourth or fifth metacarpal).

Structured Light Scanning

The collection of digital models through structured light scanning was achieved using an Artec Spider hand-held laser scanner. Each osteological component was placed on a rotating table, resting on a polyethylene foam square, and rotated slowly 360° while the hand-held scanner was kept stationary on a tripod. The bone was then rotated, and the newly exposed surface was scanned. This process was repeated six times, so that each bone was rotated 90° and scanned four times along its longitudinal axis, once while sitting vertically on its proximal articular surface, and once resting on its distal articular surface. These six surfaces were then cleaned of noise and aligned in the Artec Studio 18 software (Artec 3D, Luxembourg), and a 3D mesh with a

resolution of 0.1 mm was produced, simplified to a resolution of 700,000 polygons, and exported as an .OBJ file.

Photogrammetry

The meshes of the human and non-human sample from the Smithsonian National Museum of Natural History (Washington, D. C., USA) were obtained through photogrammetric methods. Each bone was placed on a rotating table with its proximal end facing upright and secured in position using museum putty. A Nikon D3500 DSLR camera with a resolution of 24.2 megapixels was placed on a tripod slightly below the horizontal level of the rotating table. The camera lens was fixed to 55 mm, and a photograph was taken remotely using the Bluetooth function of the camera. The table was rotated 15 degrees, and another photograph was taken. This process was repeated until a full 360° revolution of the table was completed, following which the tripod arm was raised and the process repeated. The tripod arm was raised a further four times, until the camera was positioned directly above the bone. From this position, the revolving table was moved 60° each time, so that six photograph were taken from directly above the bone. This process resulted in a total of 126 photographs, with the views of all the photographs relative to the bone resembling a hemisphere around the bone, with the bone located at its centre. The resultant photographs were edited in Photoshop (Adobe Inc., 2019) to mask the background, and then saved in .TIFF format. The masked photographs were imported into the Agisoft PhotoScan software (Agisoft LLC, St. Petersburg, Russian Federation), where a virtual model of the bone was produced, then scaled and cleaned. Each mesh was then simplified to a resolution of 700,000 pixels and exported in an .OBJ format.

In addition, a small number of specimens from the non-human Great Ape collection of the National Museum of Natural History, Washington, D. C., were previously digitised through computed tomographic scanning. These were scanned on a Siemens Somatom Emotion CT scanner (slice thickness 1 mm, slice increment 0.1 mm, voltage 110 kV, current 70 mA, reconstructing algorithm H50 moderately sharp kernel, pixel size 600 µm), and are freely available from the Smithsonian Institution's Human Origins Program, upon request.

3.2.2 Landmarks

Selected homologous landmarks as well as curve and surface sliding semilandmarks were placed on each bone using the Stratovan Checkpoint Version 2018.08.07 software (Stratovan Corporation, 2018). Stratovan Checkpoint was preferred over other software as it allows the placement of a grid of landmark points to be placed on a virtual surface which are anchored by nine discreet homologous, user-defined landmarks along the perimeter of the structure of interest (in this case, the articular surfaces of the fourth and fifth carpometacarpal joints) – four on each corner, with a further four placed between the corner points, and one point in the centre of the grid (Harcourt-Smith *et al.,* 2008). Furthermore, unlike other freely available software such as Landmark Editor (Wiley *et al.,* 2005) which allow the control of the landmark grid by a maximum of nine discrete landmarks, Stratovan Checkpoint offers the user a further eight anchor points (between each corner landmark and the middle landmark along the perimeters). These eight accessory anchor points can be manually or automatically placed, i.e., they are initially automatically placed onto the mesh surface at equidistant between their neighbouring two user-defined perimeter landmarks by the software itself, without the need for manual placement by the user. However, should these landmarks not be optimally placed, it is possible to manually adjust their locations accordingly. Stratovan Checkpoint therefore offers the user an unrivalled ability to control the shape of any landmark grid with 19 user-defined landmarks, thus allowing a higher degree of control over the placement of such landmark grids, and higher fidelity between the landmark configuration and the structure that these landmarks are intended to represent. Furthermore, Stratovan Checkpoint allows the merging of landmarks from separate landmark grids or curves. This feature was highly beneficial for this project, as it allowed the placement of two landmark grids on the hamate – one on its articular surface for the fourth metacarpal, and one on its fifth metacarpal articular surface. It was then possible to merge the central perimeter of the two grids along the border of the fourth and fifth metacarpal articular surfaces.

Stratovan Checkpoint allows each user-defined landmark grid or curve to be re-sampled to a three-dimensional mesh of *n* number of evenly-spaced points. In the case of landmark grids, the minimum number of points available to place along the perimeter of the grid is five, resulting in a grid of 25 points. This number increases in increments of four by adding an additional point

between each anchor point, so that the number of points available to place on a grid perimeter or curve is 5, 9, 13, 17, 21 etc., and the total number of points for each grid is 25, 45, 81, 111 etc. These points are evenly spaced along the perimeter or surface of the grid by the program itself, so that each non-user-defined landmark is equidistant from its neighbouring points.

As the relative location of these points are arbitrary, they are defined as semilandmarks, and only their variation in directions orthogonal to the surface reflect differences in the shape of the surface (Harcourt-Smith *et al.,* 2008). In order to minimize the effects of variation due to the arbitrary spacing in different specimens of the semilandmarks over the sampled surface, these semilandmarks were treated as sliding semilandmarks during Procrustes registration (see Appendix F) (Harcourt-Smith *et al.,* 2008; Tallman *et al.,* 2013). In addition, given the arbitrary nature of their definitions, all user-defined anchor points along a perimeter curve, as well as the central anchor point (type-III landmarks) were treated as sliding semilandmarks, which further minimized the effects of random human-generated variation caused by arbitrary placement of these type-III landmarks (Harcourt-Smith *et al.,* 2008; Tallman *et al.,* 2013). This method of projecting a grid comprising of landmarks and semi-landmarks enabled the sliding semi-landmarks to proxy as discreet, homologous landmarks universal to the entire dataset, therefore respecting Bookstein's (1991) necessitation that all landmarks in the dataset be representative of the same meaning and location between all specimens, and be homologous across all specimens. Furthermore, this method resulted in the production of landmarks that adequately and effectively described the overall three-dimensional forms of the articular surfaces of interest.

Landmark Density

The number and relative density of landmarks used in a geometric morphometric study is of critical importance, as using too few landmarks will fail to adequately represent the shape of structures, and risks overlooking local shape differences that drive global shape differences within a population, resulting in potentially spurious results biased by landmark choice (Watanabe, 2018). Conversely, using an excess of landmarks unnecessarily increases the dimensionality of the dataset, and may compromise the power of many standard statistical tests, as the number of shape variables may exceed the number of specimens (Gunz and Mitteroecker,

2013; Collyer, Sekora and Adams, 2015; Watanabe, 2018). As such, it was necessary to investigate the optimum number of surface and curve semilandmarks that adequately represented the shape variation of each articular surface studied.

It is not possible at present to determine *a priori* the number of landmarks necessary to adequately capture the shape variation of a given structure. However, by using the Landmark Sampling Evaluation Curve (LaSEC) function in the R package LaMBDA (Landmark Based Data Assessment) (Watanabe, 2018), a retrospective examination of how many landmarks required to capture the variation in the shape of a particular structure within a population is possible. The LaMBDA function firstly extracts shape information from a parent coordinate dataset, subsampling three randomly-selected landmarks, then calculates its fit of specimen distribution to that of the parent dataset based on Procrustes sum of squares (i.e. determining the fit of each reduced dataset compared to that of the complete dataset). Once the Procrustes sum of squares is recorded, one additional landmark is randomly selected, and the fit value is calculated between the new subsampled data and the parent dataset. This process is repeated until all landmarks in the parent dataset are sampled (Watanabe, 2018). Fit is based on Procrustes distance between the full and subsampled datasets with respect to position of the specimens in high-dimensional morphospace (i.e. not the spatial position of the landmarks). The function then generates a sampling curve, where a plateau in the curve signifies stationarity in the capturing of shape information. An absence of such a plateau indicates inadequate characterization of shape. In addition to the sampling curve, LaMBDA provides the median fit for each number of landmarks sampled. A fit of ≥ 0.95 indicates a high congruence between the variation in shape in the sample and the number of landmarks (Watanabe, 2018). The LaSEC R function is a useful tool in avoiding under- or over-sampling of landmarks (Watanabe, 2018; Baruda *et al.,* 2019), and was used in this study as a guide to determine how many surface and curve semilandmarks were necessary to adequately represent the variation in shape of the articular surfaces of the extant population.

In order to assess adequate semilandmark density in the articular surfaces of the fourth and fifth carpometacarpal joints, the datasets for the hamate's metacarpal surface, the fourth metacarpal's surface for the hamate, and the fifth metacarpal's surface for the hamate were individually assessed. For the hamate, the landmark patches of each individual bone were manipulated to a 13 x 9 patch on each articular facet of the metacarpals, resulting in a total of

225 landmarks (2(13x9)-9). For both metacarpal bases, landmark patches were manipulated to a 9 x 9 patch, resulting in 81 landmarks. Samples were considered to be represented by an adequate density of landmarks when fit reached ≥ 0.95, and the sampling curve terminated in a plateau.

3.3 Landmarks of the carpometacarpal articular surface of the hamate

For the carpometacarpal articular surface of the hamate, the landmark protocol was based upon and developed on the work of Almécija *et al.* (2015), Orr *et al.* (2013), Zeldich *et al.* (2012), Sollaccio *et al.* (2019), and Vanhoof *et al.* (2021). Two surface patches of 9 user-defined landmarks were applied to the articular surface of the hamate, with one patch placed on the hamate's articular surface for the fourth metacarpal, and one placed on the hamate's articular surface for the fifth metacarpal. These two landmark grids were then merged along the border of the fourth and fifth metacarpal articular surfaces. In their analysis of the overall shape of the anthropoid hamate, Almécija *et al.* (2015) identified seven type II landmarks and two type III landmarks which bounded and defined the hamate's articular surface with the metacarpals. In addition to these nine landmarks, an additional six type III landmarks were used to fully represent the shape of the articular surface and to define the limits of each landmark grid, resulting in a total of 15 user-defined landmarks – six type II and nine type III. Levels of landmark homogeneity were determined in accordance with Bookstein (1991) and O'Higgins (2000). The description and type of landmarks used to define the hamate articular surface are shown in table 3.3.1, while graphical representation of landmark locations is shown in figure 3.3.1 (*a*-*c*).

Table 3.3.1 Anatomical description and type of landmarks collected on the hamate's articular surface with the fourth and fifth metacarpals.

Landmark no.	Type	Description
1	II	Junction of the articular facets for metacarpals IV and V on the dorsal side.
2	III	Midpoint between landmarks 1 and 3 along the dorsal border of the MC-V facet.
3	II	The most medio-distal point of the MC-V articular facet.
4	III	Midpoint between 1 and 7 along the border between the articular surfaces for metacarpals IV and V.
5	III	Central point of the MC-V articular facet, equidistant between landmarks 2-8 and 4-6.
6	III	Midpoint between landmarks 3 and 9 along the medial border of the MC-V facet.
7	II	Junction of the articular facets for metacarpals IV and V on the palmar side.
8	III	Midpoint between landmarks 7 and 9 along the palmar border of the MC-V facet.
9	II	The most medio-palmar point of the MC-V articular facet.
10	II	The most latero-dorsal point of the MC-IV articular facet.
11	III	Midpoint between landmarks 1 and 10 along the dorsal border of the MC-IV facet.
12	III	Midpoint between landmarks 10 and 14 along the lateral border of the MC-IV facet.
13	III	Central point of the MC-IV articular facet, equidistant between landmarks 4-12 and 11-15.
14	II	The most latero-palmar point of the MCV articular facet.
15	III	Midpoint between landmarks 7 and 14 along the palmar border of the MC-IV facet.

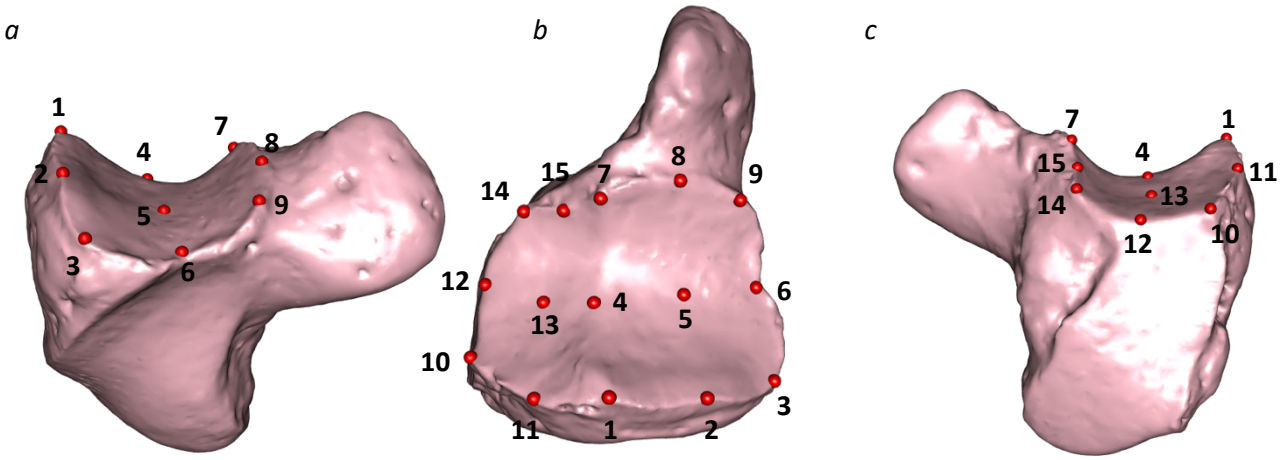

Figure 3.3.1: Anatomical locations of the bounding landmark coordinates collected on the hamate-metacarpal articular surface, shown on a human right hamate. The type II and type III landmarks acted as user-defined anchor points for the placement of a landmark patch on the hamate's articular surface with the fourth and fifth metacarpal, respectively. During generalized Procrustes analysis (GPA), type-III landmarks were treated as sliding semilandmarks, with landmarks 2, 4, 6, 8, 11, 13 and 15 treated as curve sliding semilandmarks, and landmarks 5 and 14 treated as surface sliding semilandmarks. Views presented are, from left to right: medial view (*a*), distal view (*b*), lateral view (*c*).

Results of the LaSEC testing on the hamate's articular surface indicate that the shape of the hamate-metacarpal articular surface was adequately described by a minimum of 91 landmarks (figure 3.3.2). Therefore, so as to adequately represent the shape of the hamate's articular surface for the fourth and fifth metacarpals, each patch was re-sampled into a 9x9 mesh of landmarks, with 9 landmarks traversing the palmodorsal length of the hamate, and 9 landmarks traversing the medio-dorsal length of each of the 4th and 5th metacarpal surfaces.

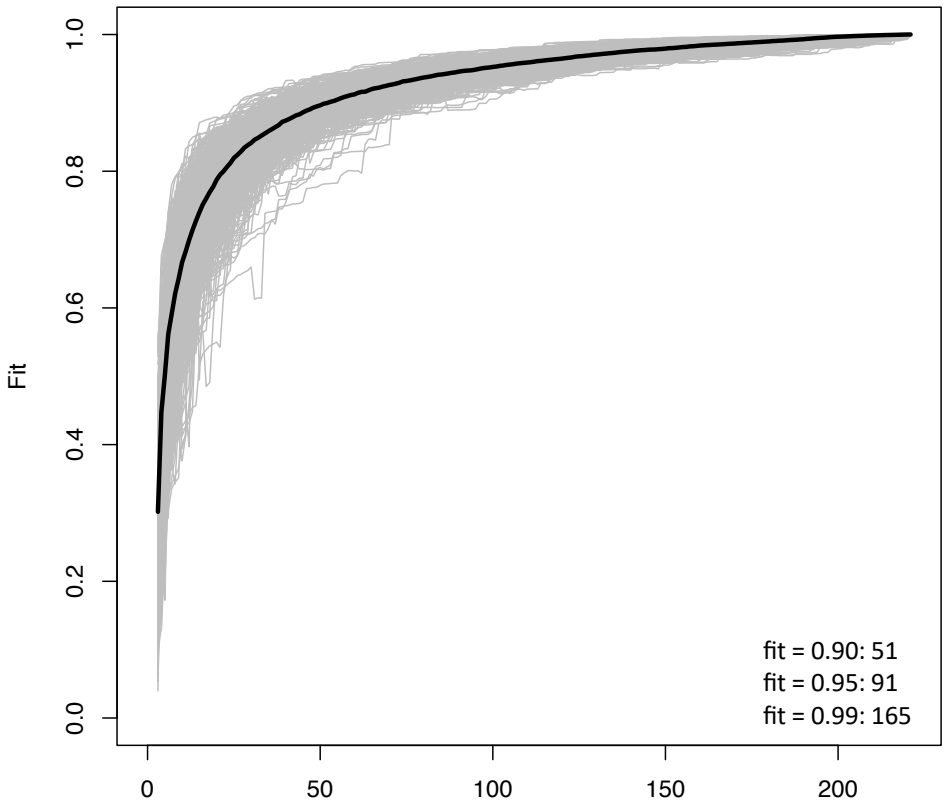

Figure 3.3.2: LasSEC Sampling curve for 221 landmarks placed on the hamate-metacarpal articular surface. Each grey line indicates fit values from one iteration of subsampling. Thick black line denotes median fit value at each number of landmarks. The numbers within the plot are the number of landmarks at median fit value of 0.90, 0.95. and 0.99.

Given the arbitrary nature of the user-defined landmarks on the perimeter of each grid, and that of the central landmark (the type-III landmarks defined in table 3.1.1, during the sliding process, these landmarks were treated as either curve or surface sliding semilandmarks (Hartcour-Smith *et al*., 2008; Tallman *et al*., 2013). This resulted in the hamate's metacarpal articular surface being represented by a total of 153 landmarks: six fixed landmarks, 63 curve

sliding semi-landmarks, and 84 surface sliding semi-landmarks, represented graphically in figure 3.3.3.

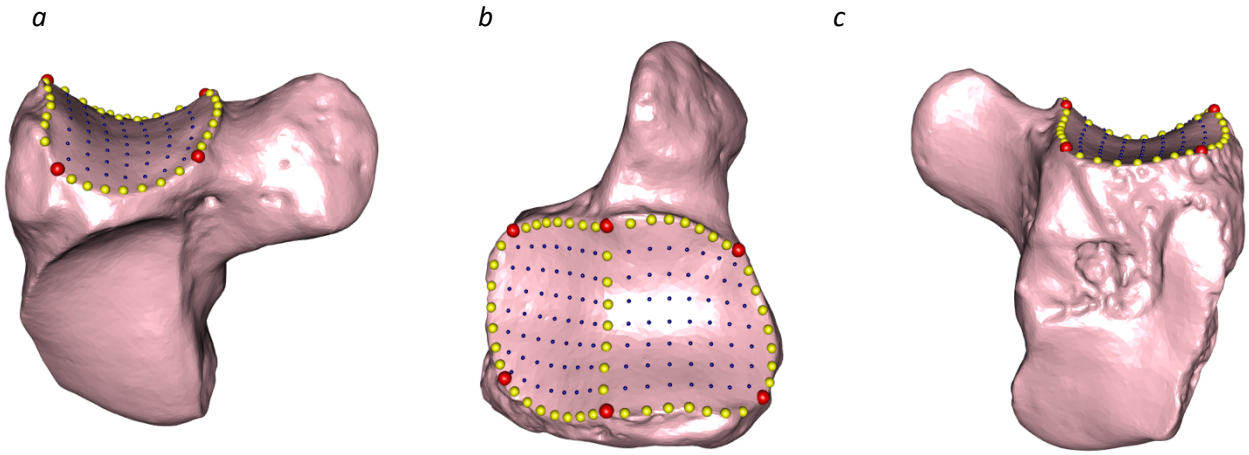

Figure 3.3.3: Anatomical locations of landmark coordinates collected on the hamate-metacarpal articular surface, shown on a human right hamate. Red spheres represent type II landmarks. Yellow spheres represent curve sliding semilandmarks, and dark blue spheres represent surface sliding semilandmarks. Views presented are, from left to right: medial view (*a*), distal view (*b*), lateral view (*c*).

3.4 Landmarks of the fourth metacarpal proximal articular surface

Landmarks used to define the proximal articular surface of the fourth metacarpal were based on previous work by Rein (2019) and Proctor (2010). Four type-II landmarks and five type-III landmarks were used to define and bound the fourth metacarpal's articular surface for the hamate. The description and type of landmarks used to define the fourth metacarpal's articular surface are shown in table 3.4.1, with graphical representation of landmark locations shown in figure 3.4.1 (*a*-*c*).

Table 3.4.1: Anatomical description and type of landmarks collected on the fourth metacarpal's proximal articular surface. Also shown is each landmark's corresponding equivalent on the hamate.

Landmark no.	Type	Description	Hamate LM
1	II	The most latero-dorsal point of the MC-IV's proximal articular facet	10
2	III	Midpoint between landmarks 1 and 3 along the dorsal border of the MC-IV's proximal facet	11
3	II	The most medio-dorsal point of the MC-IV's proximal articular facet	1
4	III	Midpoint between 1 and 7 along the lateral border of the MC-IV's proximal articular facet	12
5	III	Central point of the MC-IV's proximal articular facet, equidistant between landmarks 2-8 and 4-6	13
6	III	Midpoint between landmarks 3 and 9 along the medial border of the MC-IV's proximal facet	4
7	II	The most latero-palmar point of the MC-IV's proximal articular facet	14
8	III	Midpoint between landmarks 7 and 9 along the palmar border of the MC-IV's proximal facet	15
9	II	The most medio-palmar point of the MC-IV's proximal articular facet	7

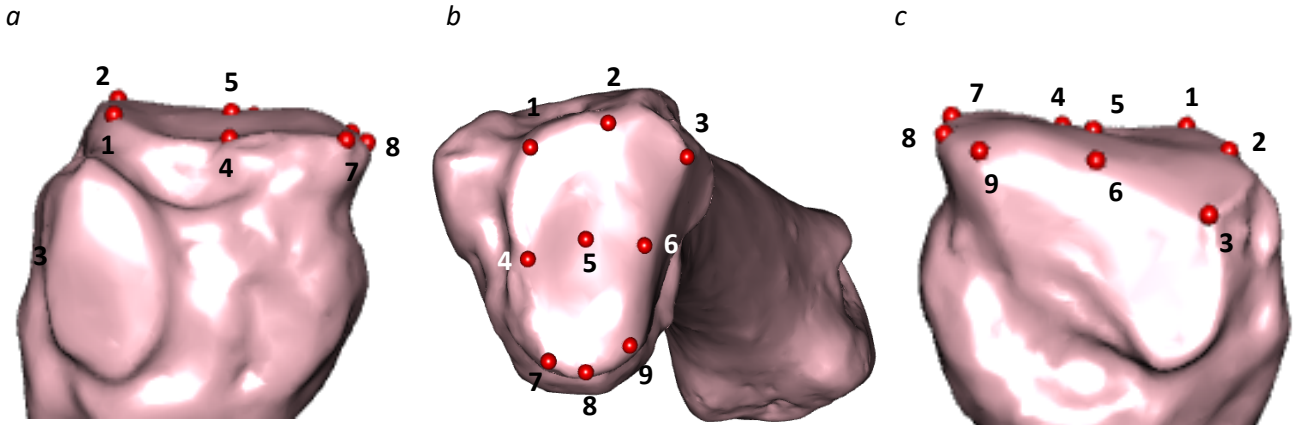

Figure 3.4.1: Anatomical locations of landmark coordinates collected on the fourth metacarpal's proximal articular surface, shown on a human right hamate. During generalized Procrustes analysis (GPA), the type-III landmarks (2, 4, 5, 6, and 8) were treated as sliding semi-landmarks, with landmarks 2, 4, 6, and 8 treated as curve sliding semi-landmarks. Landmark 5 was treated as surface sliding semi-landmarks. Views presented are, from left to right: lateral view (*a*), proximal view (*b*), medial view (*c*).

Results of the density study indicate that the shape of the metacarpal-IV proximal articular surface was adequately described by a minimum of 53 landmarks (fit $\geq$ 0.95) (figure 3.4.2). In order to adequately represent the surface's shape, and in order to retain fidelity with the landmarks of the hamate, as with the patches placed on each of the hamate's metacarpal articular surfaces, the patch placed on the fourth metacarpal's proximal articular surface was

manipulated into a 9x9 mesh of landmarks. As with the landmarks of the hamate, given the arbitrary nature of the type-III landmarks, during generalized Procrustes analysis these type-III landmarks were treated as either curve or surface sliding semilandmarks, with landmark 5 regarded as a surface sliding semi-landmark, and landmarks 2, 4, 6, and 8 treated as curve sliding semi-landmarks. (Hartcour-Smith *et al*., 2008; Tallman *et al*., 2013). This resulted in a total of 81 landmarks being placed on the fourth metacarpal's proximal articular surface with the hamate, four being fixed landmarks, 28 as curve sliding semi-landmarks, and 49 surface sliding semi-landmarks (figure 3.4.3).

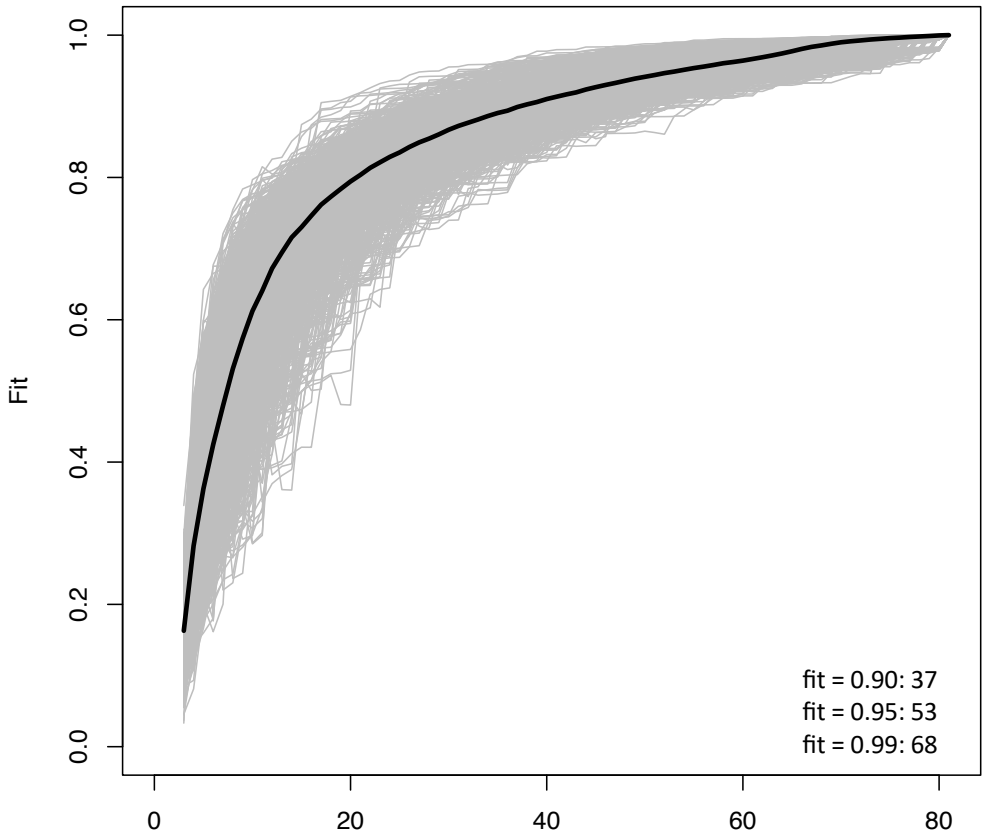

Figure 3.4.2: LasSEC Sampling curve for 81 landmarks placed on the metacarpal-IV proximal articular surface. Each grey line indicates fit values from one iteration of subsampling. Thick black line denotes median fit value at each number of landmarks. The numbers within the plot are the number of landmarks at median fit value of 0.90, 0.95, and 0.99.

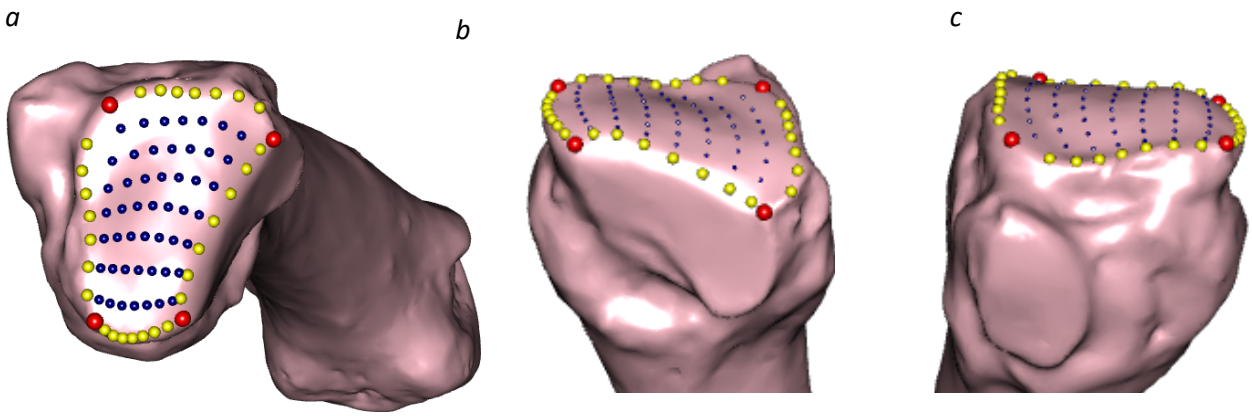

Figure 3.4.3: Anatomical locations of landmark coordinates collected on the metacarpal-IV proximal articular surface, shown on a human right fourth metacarpal. Red spheres represent type II fixed landmarks. Yellow spheres represent curve sliding semilandmarks, and dark blue spheres represent surface sliding semilandmarks. Views presented are, from left to right: proximal view (*a*), medial view (*b*), lateral view (*c*).

3.5 Landmarks of the fifth metacarpal proximal articular surface

The landmark protocol for the base of the fifth metacarpal was loosely drawn from the work of Rein (2019). Four type II landmarks and five type III landmarks bounded and defined the fifth metacarpal's basal articular surface for its articulation with the hamate. Again, levels of landmark homogeneity were determined in accordance with Bookstein (1991) and O'Higgins (2000). The description and type of landmarks used to define the fifth metacarpal's basal articular surface are shown in table 3.5.1, and visual representations of the landmarks are shown in figures 3.5.1.

Table 3.5.1: Anatomical description and type of landmarks collected on the fifth metacarpal's proximal articular surface. Also shown is each landmark's corresponding equivalent on the hamate.

Landmark no.	Type	Description	Hamate LM
1	II	The most latero-dorsal point of the MC-V's proximal articular surface	1
2	III	Midpoint between landmarks 1 and 3 along the dorsal border of the MC-V's hamate articular surface	2
3	II	The most medio-dorsal point of the MC-V's proximal articular surface	3
4	III	Midpoint between 1 and 7 along the lateral border of the MC-V's proximal articular surface with the hamate	4
5	III	Central point of MC-V's proximal articular surface, equidistant between landmarks 2-8 and 4-6	5
6	III	Midpoint between landmarks 3 and 9 along the medial border of the MC-V's proximal facet. Commonly corresponds to the most medial point of the articular surface	6
7	II	The most latero-palmar point of the MC-V's proximal articular surface	7
8	III	Midpoint between landmarks 7 and 9 along the palmar border of the MC-V's proximal articular surface	8
9	II	The most medio-palmar point of the MC-V's proximal articular surface	9

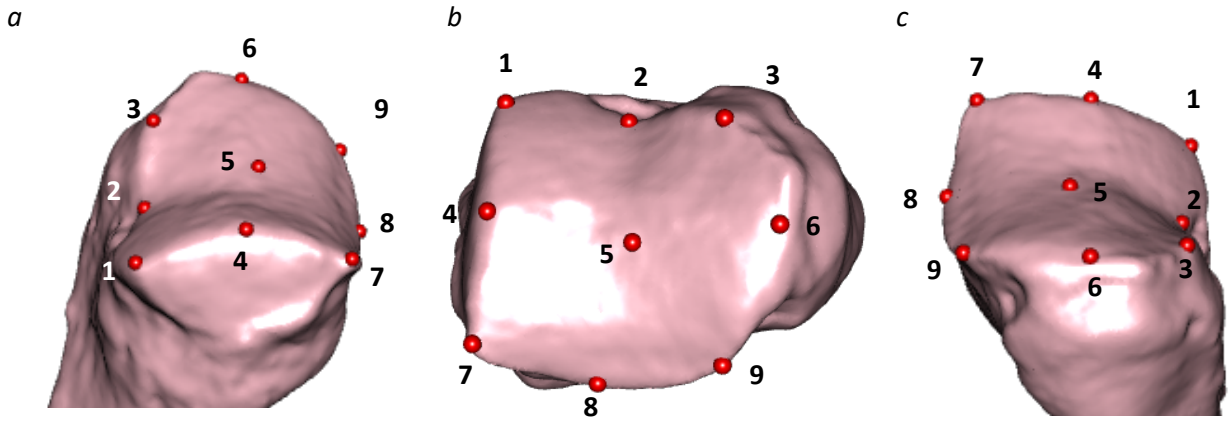

Figure 3.5.1: Anatomical locations of landmark coordinates collected on the fifth metacarpal's proximal articular surface, shown on a human right fifth metacarpal. During generalized Procrustes analysis (GPA), the type-III landmarks (2, 4, 5, 6, and 8) were treated as sliding semi-landmarks, with landmarks 2, 4, 6, and 8 treated as curve sliding semi-landmarks. Landmark 5 was treated as surface sliding semi-landmarks. Views presented are, from left to right: lateral view (*a*), proximal view (*b*), medial view (*c*).

The shape of the metacarpal-V proximal articular surface is adequately described (fit ≥ 0.95) by a minimum of 45 landmarks. As with the fourth metacarpal, the patch placed on the fifth metacarpal's proximal articular surface was manipulated into a 9x9 mesh of landmarks,

with type-III landmarks treated as either curve or surface sliding semilandmarks, and landmark 5 converted to a surface sliding semi-landmark, while landmarks 2, 4, 6, and 8 treated as curve sliding semi-landmarks. As with the landmark protocol used to define the fourth metacarpal's proximal articular surface, this resulted in a total of 81 landmarks being placed on the fifth metacarpal's proximal articular surface: four fixed landmarks, 28 curve sliding semi-landmarks, and 49 surface sliding semi-landmarks (figure 3.5.3).

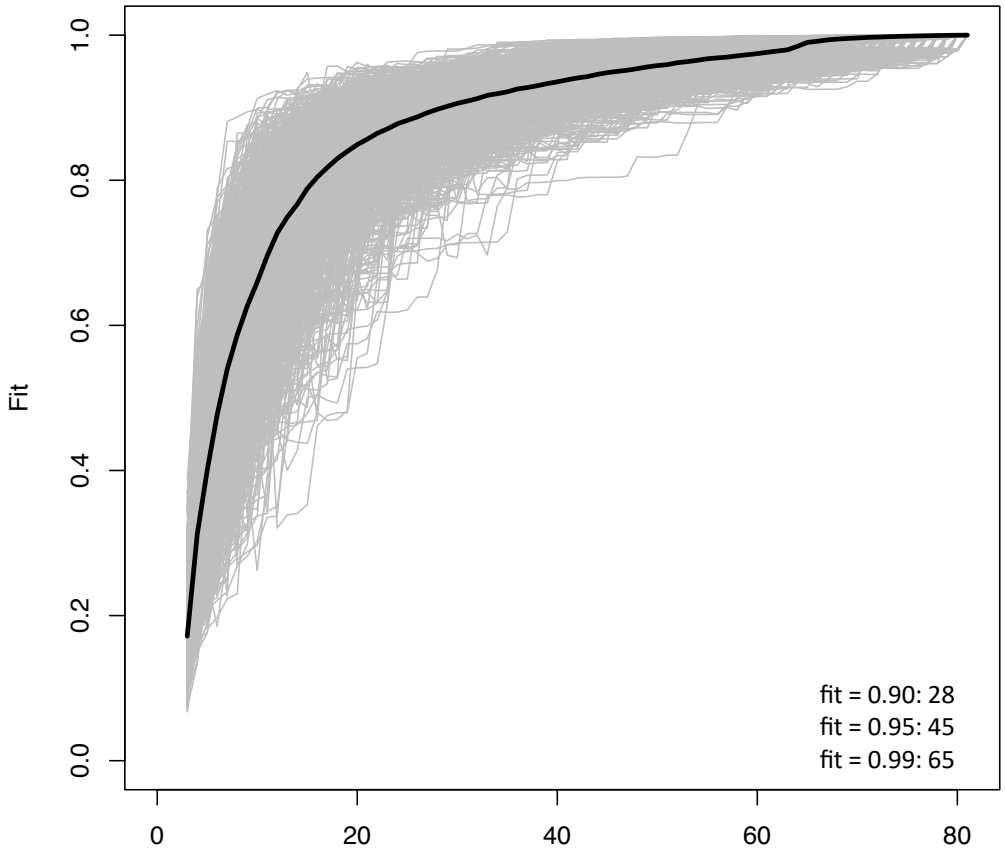

Figure 3.5.2: LasSEC Sampling curve for 81 landmarks placed on the metacarpal-V proximal articular surface. Each grey line indicates fit values from one iteration of subsampling. Thick black line denotes median fit value at each number of landmarks. The numbers within the plot are the number of landmarks at median fit value of 0.90, 0.95, and 0.99.

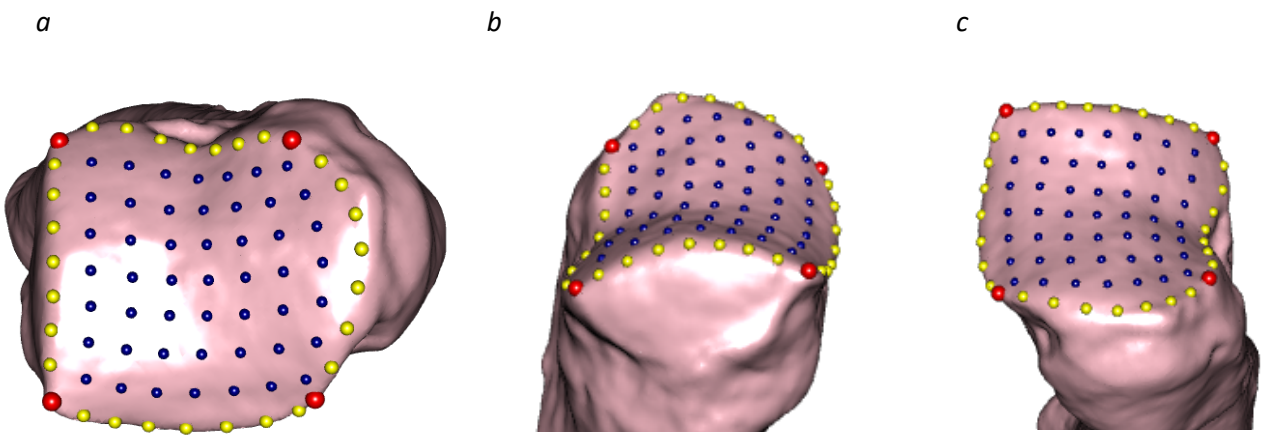

Figure 3.5.3: Anatomical locations of landmark coordinates collected on the fifth metacarpal's basal articular surface, shown on a human right fifth metacarpal. Red spheres represent type II landmarks, yellow spheres represent curve sliding semi-landmarks, and dark blue spheres represent surface sliding semi-landmarks. Views presented are, from left to right: proximal view (*a*), medioproximal view (*b*), lateroproximal view (*c*).

3.6 Repeatability

In order to ascertain the precision and repeatability of the landmarks selected to anchor the landmark grids on each surface, precision tests were performed on the dataset prior to any statistical analysis being conducted, in accordance with the methods established in previous research (Fernandez *et al*., 2015; Galleta *et al*., 2019; Proctor, 2010; Proctor, Broadfield and Proctor, 2008; Tallman, 2016; Vanhoof *et al.,* 2021). The methods set out below were conducted for the carpometacarpal articular surfaces of each osteological component assessed in the study (hamate; MCIV; MCV).

A hamate, fourth metacarpal, and fifth metacarpal were selected at random from each extant taxonomic group (*Gorilla, Homo sapiens, Pan troglodytes,* and *Pongo*). Each randomly-selected bone was landmarked six times according to the protocols outlined above, with at least three days elapsing between each landmark procedure (Galetta *et al.,* 2019). The six repeat landmark coordinates of each randomly-selected specimen were then pooled into their respective samples (osteological component and taxonomic grouping), and aligned through a generalized Procrustes analysis (see Appendix F), with the resultant Procrustes coordinates then subjected to a principal components analysis. The repeatability of each landmark coordinate

system was verified through assessing the relative clustering of the repeated measures compared to the clustering of the taxon as a whole for that specific osteological component. A substantial difference between the clustering of the repeat measures compared with the parent population reflected low variance between the different repeated measures and was considered as verification of the repeatability of the selected landmarks (Fernandez *et al*., 2015; Lockwood, Lynch and Kimbell, 2002; Proctor, 2010; Proctor, Broadfield and Proctor, 2008; Vanhoof *et al.,* 2021). The relative clustering of the repeated landmark coordinates compared with the whole genus was initially assessed visually by plotting a multivariate scatterplot of the first principal component against the second. Heterodacity between the repeated measures and their parent populations were further assessed using a multivariate correspondent of the Levene test along the first three principal components (Anderson, 2006; Galleta *et al*., 2019; Vanhoof *et al.,* 2021). Results of the repeatability tests conducted on the bounding landmarks of the hamate and fourth and fifth metacarpal bases are available in Appendix G.

3.7 Generalized Procrustes analysis protocol

Following repeatability testing, each block of landmark coordinates (hamate-metacarpal; fourth metacarpal; fifth metacarpal) were subjected to a generalized Procrustes analysis (GPA) (Dryden and Marida, 1998; Gower, 1975), which removed the effects of variation in location, orientation, and scale from the coordinates, and transposed the raw coordinates to a common coordinate system (see Appendix F for further detail). For the hamate-metacarpal articular surface, a GPA was initially performed on the entire landmark coordinate of 153 landmarks. Subsequently, in order to further investigate the morphology of each hamate-metacarpal articular surface individually, the 153 landmarks were separated into those which represented the hamate-MC4 and hamate-MC5 articular surfaces, with the 153 landmarks of the hamate-metacarpal coordinate system being divided along the border separating the two metacarpal articular surfaces, with the curve landmarks along this border included in both datasets, and subsequent GPAs conducted on these two landmark sets. This process resulted in a total of five Procrustes-aligned landmark coordinate configurations analysed in this project. During each GPA, curve- and surface-semilandmarks were slid using the minimized bending energy criterion (Bookstein, 1997; Gunz, Mitteroecker and Bookstein, F. L. 2005), though sliding by both

minimizing Procrustes distances and minimizing bending energy were explored and returned comparable results during subsequent principal components analysis. Previous research has shown that results using the two sliding criteria are comparable (Perez *et al.*, 2006).

3.8 Statistical analysis

Each block of Procrustes-aligned shape coordinates was subjected to a principal components analysis to quantify and explore patterns of shape variation of each articular surface within the dataset. Two methods were employed to assess how many principal components to investigate. While it is a common practice in geometric morphometrics to interpret principal components that represent more than 5% of the total variance, Bookstein (2014) suggested an alternative method for identifying principal components whose directions are meaningful and therefore entitled to interpretation, based on whether the ratio of a principal component and its successor is above a threshold based on a log-likelihood ratio, which is dependent on sample size. Both methods of identifying how many principal components were entitled to interpretation were used in this study, and after significant differences between groups were tested for each PC through use of an analysis of variance (ANOVA; discussed below), the PC axes remaining were largely comparable.

Investigating differences between extant non-human taxa

As an initial step, any potential differences between the constituent species or sub-species of the non-human groups were investigated. For the *Gorilla* and *Pongo* samples, a Hotelling's T^2 test for the multivariate difference of means were performed on all significant principal components, with each genus separated by their constituent species (*Gorilla*: *G. gorilla* and *G. beringei; Pongo*: *P. abelii* and *P.* pygmaeus). For the *Pan troglodytes* population, a multivariate analysis of variance (MANOVA) was performed on all significant principal components, with the species divided into the taxon's constituent sub-species (*P. troglodytes ellioti, P. troglodytes troglodytes, P. troglodytes verus*).

Allometry testing

Allometric signals in the data were tested on each of the landmark coordinate blocks. Allometry is commonly investigated when shape coordinates are involved by conducting regressions of a shape coordinate variable on a size variable. As body size was unknown for most specimens, allometric signals in the data were tested through multivariate linear regression of the first four PC scores using centroid size (CS) as a proxy of body size (Galletta *et al*., 2019; Vanhoof *et al.,* 2021). A multivariate analysis of covariance (MANCOVA) on the scores of the selected principal components were also conducted, with the extant taxon groups used as an independent categorical variable and natural log-transformed centroid size (lnCS) as a covariate (Galletta *et al*., 2019). Results of these allometry tests are shown in Appendix H.

Group comparisons

One-way analysis of variance (ANOVA) on scores along all significant principal components were conducted to test for significant differences between extant genera, with Tukey honestly significant difference (HSD) tests used for pairwise *post-hoc* comparisons between groups, subsequent to normality checks and Levene's tests being conducted to ensure normality and homoscedasticity of the data. The distribution of principal component scores were represented graphically using boxplots and scatterplots, and shape changes along each principal component were visualized as wireframe representations of the shapes corresponding to the minimum and maximum scores of each principal component of interest. Fossil hominin specimens were initially evaluated relative to the extant sample through visual comparisons of their locations relative to group distributions in the boxplots and scatterplots, and their relationship relative to the comparative extant sample were further evaluated by using extant group means and standard deviation of the PC scores of the extant groups to calculate the distance of each fossil specimen along all studied PCs by expressing the distance between each fossil specimen and the extant groups as the number of standard deviations from each group's mean. Differences were considered significant when the fossil specimens were more than one standard deviation from the mean of an extant group (Marchi *et al*., 2016, 2017; Galletta *et al*., 2019).

Canonical Variate Analysis

The dataset for each block of landmark coordinates representing the articular surfaces of the hamate-metacarpal joints were further analysed through a canonical variates analysis (CVA), which is also referred to as a linear discriminant analysis (LDA) or discriminant function analysis (DFA). In both CVA and PCA new axes are constructed, with each axis being a linear combination of the original variables and orthogonal to all others, with specimens then ordered along these new axes. However, while there are many similarities between canonical variates analysis and principal components analysis, they are complimentary, and the two tests do not necessarily yield the same results (Zeldich *et al.,* 2004; Tallman *et al.,* 2013). While PCA acts to maximize differences among individuals, CVA works to maximize difference among *a priori*-defined group means (Zeldich *et al.,* 2004). Furthermore, while both CVA and PCA construct new coordinate systems, and determine the scores along those axes for all individuals in a study, CVA uses the pattern of within-group variation to scale the axes of the new coordinate system, and distances in the CV space are not equal to the distances in the original coordinate system, and can therefore change the orientation of individuals within a morphospace (Zeldich *et al.,* 2004; Tallman *et al.,* 2013).

Initially, a CVA was performed with only the extant sample, with specimens categorized into their respective extant taxonomic group. Each CVA was performed using all the principal components that cumulatively accounted for $\geq$ 90% of the variation in order to reduce the dimensionality of the data (Daver *et al*., 2014). The efficacy of the CVA model was tested through a leave-one-out cross-validation, where each specimen was omitted from the analysis in turn, and then classified by the remaining sample (Tallman *et al.,* 2013). A multivariate analysis of variance (MANOVA) was then conducted, followed by the means equality between taxonomic groups being tested through an analysis of variance (ANOVA) along the scores of each CV axis. These were followed by *post-hoc* pairwise Hotelling's Honestly Significant Different (HSD) tests between all pairs of groups. Again, prior to the execution of (M)ANOVAs, normality checks and Levene's tests were carried out for each axis to ensure prerequisite assumptions were met. Shape change along each CV axis was then reconstructed and compared with the shape changes of the PC axes previously studied. The morphological affinities of the fossil specimens were then assessed by including them *a posteriori* into the CVA, with fossil specimens left ungrouped to be

classified by the analysis. Results of the canonical variate analysis and the locations of fossil specimens along CV axes relative to group samples were further interpreted visually through box-and-whisker plots and bivariate scatterplots of the CV scores.

Absolute Procrustes distances

While canonical variate analysis is a useful tool for the evaluation of the relative similarity of a fossil specimen to extant groups, as it classifies specimens into *a priori* defined groups, it does not provide information on the absolute similarity of an individual specimen to any specific group (Galletta *et al.,* 2019). In order to explore the absolute similarity of the fossil shapes to the extant groups, the mean shape of every extant group was defined and the Procrustes distance of each specimen of each extant group to its respective average shape was calculated. These distances were tested for normality using a Shapiro-Wilks test and visually using quintile-quintile (Q-Q) plots. Fossil Procrustes distance values were compared to the mean and standard deviation of every extant group, and the distance values (in standard deviations) from the mean were calculated. From these values the values of the upper-tail cumulative distribution function corresponding to the distance of the fossils from the mean of every extant group were calculated. This method derives from the work of Galletta *et al.* (2019), who used the linear distances of principal component scores as opposed to Procrustes distances. The values of the of the upper-tail cumulative distribution function of each fossil corresponded to the percentage of individuals in an extant group that are more different from the mean of the group itself than the fossil (Galletta *et al.,* 2019).

All statistical analysis were performed in the R environment (R Core Team, 2015) using the Geomorph v 4.0.6 (Adams and Otarola-Castillo, 2013; Adams *et al.,* 2023) and Morpho v 2.11 (Schlager, 2017) packages. All graphical outputs for results interpretation were also created in R using the package rgl v 1.2.1 (Murdoch and Adler, 2017). The significance value of all statistical test was set at $p = 0.05$.

4. Materials

4.1 Extant dataset

The extant great ape (including modern *Homo sapiens*) dataset used in this project was collected at three institutions: The University of Sheffield's Department of Archaeology, The Powell-Cotton Museum, and The Smithsonian Institution's National Museum of Natural History. The overall extant dataset used in this project is shown in Table 4.1, along with their collection of origin, total number, and number of each sex.

Table 4.1: Extant great ape sample composition used in the study, with total number, collection of origin and number of males and females of each taxon.

Taxon	*n*	Collection	Sex		
			Male	Female	Unknown
Homo sapiens	**60**	**PCM;NMNH; UoS**	**32**	**28**	**0**
Gorilla	**40**	**PCM;NMNH**	**20**	**18**	**2**
Gorilla gorilla	32	PCM; NMNH	18	14	2
Gorilla beringei beringei	6	NMNH	2	4	0
Pan troglodytes	**44**	**PCM; NMNH**	**17**	**22**	**5**
Pan troglodytes sp.	13	PCM	6	6	1
Pan troglodytes ellioti	7	PCM	3	4	0
Pan troglodytes schweinfurthii	3	NMNH	0	2	1
Pan troglodytes troglodytes	18	PCM; NMNH	7	8	3
Pan troglodytes verus	3	NMNH	1	2	0
Pongo	**21**	**NMNH; UoS**	**10**	**10**	**0**
Pongo abelii	8	NMNH	5	3	0
Pongo pygmaeus	13	NMNH; UoS	5	8	0
Total	**165**				

Abbreviations: NMNH = Smithsonian Institution National Museum of Natural History, Washington, D. C., USA; PCM = Powell-Cotton Museum, Birchington-on-Sea, Kent, United Kingdom; UoS = University of Sheffield Department of Archaeology, Sheffield, United Kingdom.

The bones of the right hand were preferred over the left hand in this study, given that functional laterality in the human hand results in a degree of bilateral asymmetry of the hand bones, and morphological characteristics resulting from manipulative functions may be better reflected in the right hand (Roy, Ruff and Plato, 1994). While significant bilateral asymmetry in the hands of chimpanzees and other apes have not been recorded (McFadden and Bracht, 2005; Sarringhaus *et al.,* 2005), for the sake of consistency, the right hand was also used where the relevant components of both the left and right hand were available. In specimens where it was not possible to digitize the bones of the right hand (either due to absence, taphonomic damage,

pathology or trauma, or the retention of soft body tissue on the bone), scans of the left hand were produced and landmarked, with the resultant landmark coordinates being mirrored by reflecting the landmark coordinates of the *x* axis in R (R Core Team, 2022).

Both male and female specimens of human and non-human primates were used in this investigation, with species divided as evenly as possible between males and females. As the morphology of the primate carpus is constrained mainly by the effects of high locomotor loads, and sexual dimorphism seems to have relatively little impact on carpal morphology (Kivell, Guimont and Wall, 2013), analyses were based on pooled sexes samples. All specimens were sexually mature, confirmed by the complete fusion of the epiphyses, and were also assessed for observable pathologies or skeletal trauma in the hand bones. Specimens were selected based on the absence of any such features. All non-human specimens were wild-shot.

The modern human sample (*n*=60: 32 male; 28 female) used in this study was collected from two collections: The University of Sheffield's Human Skeletal Collection, and The Smithsonian Institution's Robert J. Terry Skeletal Collection, held by the Department of Anthropology of the National Museum of Natural History of the Smithsonian Institution, Washington, D.C., United States of America. The University of Sheffield's Human Skeletal Collection is comprised of over 2,000 individuals from numerous archaeological sites. For this research project, specimens from the Coronation Street collection were used. The Coronation Street osteological collection comprises of skeletal remains from a working-class population interred at the burial ground of St Hilda's Parish Church, South Shields, between c.1816 to c.1855 AD, and excavated between 2006 and 2007 (Newman, 2016). The majority of the human dataset used for this project derive from the Robert J. Terry Skeletal Collection. The Terry Collection is composed of skeletons collected by Robert J. Terry during his time as professor of anatomy and head of the Anatomy Department at Washington University Medical School in St. Louis, Missouri from 1899 until his retirement in 1941. The majority of the remains that make up the collection came from local hospitals in the St. Louis area, as well as institutional morgues (Hunt and Albanesese, 2005).

The extant African great ape populations were collected from the Powell-Cotton Museum, Kent, and the Smithsonian Institution's Division of Mammals, also housed at the National Museum of Natural History, Washington D. C. The osteological sample of extant non-human great ape species used in this investigation consists of *Pan troglodytes* (*n*=44), (including *Pan troglodytes verus* (*n*=3), *Pan troglodytes troglodytes* (*n*=17), *Pan troglodytes ellioti* (*n*=7), and *Pan troglodytes schweinfurthi* (*n*=3) – the remaining 13 specimens were not assigned a taxonomic sub-species); *Gorilla gorilla gorilla* (*n*=35), *Gorilla beringei beringei* (*n*=7), *Pongo pygmaeus* (*n*=21), and *Pongo abelii* (*n*=8). 11 *Hylobates* and nine *Papio* specimens of various species were also collected from The Smithsonian Institution's Division of Mammals and The Powell Cotton Museum, respectively. These specimens were modelled and digitized in accordance with the methods above. However, the diminutive nature of the hamates and metacarpals of these taxa resulted in less-than-optimal three-dimensional modelling, especially when using photogrammetry. Furthermore, the small number of specimens for each species of *Papio* and *Hylobates* rendered their interpretation within the scope of the wider dataset challenging. As such, these specimens were omitted from the analysis.

Forty-four *Pan troglodytes* specimens were digitized at the National Museum of Natural History using photogrammetric methods (*Pan troglodytes verus; Pan troglodytes schweinfurthii*) and the Powell-Cotton Museum using structured-light-scanning methods (*Pan troglodytes troglodytes; Pan troglodytes ellioti; Pan troglodytes sp.*). Of the *Pan troglodytes* collection, seven were of the sub-species *Pan troglodytes ellioti* (3 male; 4 female), 18 were *Pan troglodytes troglodytes* (7 male; 8 female; 3 unknown), three to *Pan troglodytes verus* (1 male; 2 female), and three to *Pan troglodytes schweinfurthii* (2 female; 1 unknown), respectively. The remainder were not assigned to a specific sub-species.

Of the *Gorilla gorilla* sample used in this study, 30 were curated at the Powell-Cotton Museum in Kent, and were of the species *Gorilla gorilla gorilla* (18 male; 14 female). A further two specimens of *Gorilla gorilla* (2 female) were digitized at the NMNH, however these specimens were not categorized into a taxonomic sub-species. The six specimens of *Gorilla beringei beringei* used in this study were from the Smithsonian Institution's National Museum of Natural History in Washington, DC. Two were digitized using photogrammetric techniques, with

the remaining four being digitized using micro-CT scanning. Of the six specimens of *Gorilla beringei* used in this study, four were female and two were male.

A total of 13 specimens of *Pongo pygmaeus* were used in this project. A single female specimen from the University of Sheffield's Department of Archaeology was digitized using structured light scanning, and a further 12 specimens (5 male; 7 female) from the National Museum of Natural History in Washington, DC were digitized using photogrammetry. Eight specimens (5 male; 3 female) of *Pongo abelii* were sourced from the National Museum of Natural History's Mammalian Collection. Four were digitized by the author through photogrammetric methods, with the remaining four having been previously digitized through micro-CT scanning and made freely available from the Human Origins Program.

4.2 Fossil Hominin Sample

A total of 24 fossil hominin elements from eight taxa were used in this study, including 12 hamates, seven fourth metacarpals, and five fifth metacarpals. Table 4.2 denotes the taxa, catalogue reference, and element of all fossils used, as well as their collection of origin. Each fossil element used in this study is described in detail below. The fossil specimens used in this study comprise of several Australopiths and a number of *Homo* specimens. Several fossil specimens included in this analysis (*Homo naledi*, *Homo floresiensis*, *Homo neanderthalensis* and early *Homo sapiens*) are not directly pertinent to the issue of authorship of the earliest stone tools, as they are not chronologically contemporaneous with the early occurrence of lithic technology. However, they were included in this study as most are directly associated with lithic technology and are therefore known tool-makers, while their hands display a number of subtle variations on the modern human form. It was decided therefore that their inclusion in this project may provide valuable information on the evolution of the human hamate-metacarpal joints.

None of the virtual meshes of the fossil specimens used in this study were collected by the researcher. Rather, they were collected for previously-conducted research. The *Australopithecus, Paranthropus robustus/*early *Homo* and *Homo naledi* virtual material were produced by Kivell *et al.* (2015), while the *Homo floresiensis, Homo neanderthalensis,* and early

Homo sapiens material were digitized by Orr *et al.* (2013). While surface meshes of the fossil specimens were produced though various methods, as noted previously, it has been shown that the mode of digitization has a negligible effect on geometric morphometric results (Robinson and Terhune, 2017; Shearer *et al.,* 2017; Tocheri *et al.,* 2011). Each fossil specimen was landmarked in the same manner as the extant collection, explained in sections 3.3, 3.4, and 3.5.

Table 4.2: Fossil hominin samples used in the study.

Taxon	Element			Catalogue reference	Collection
	Hamate	MC-IV	MC-V		
Australopithecus afarensis	1	1	2	A.L. 333-50; A.L. 333-56; A.L. 333w-89; A.L. 333-14	NME
cf. *Australopithecus afarensis*	1	-	-	KNM-WT-22944-l	KNM
Australopithecus africanus	-	2	1	StW-330; StW-65; StW-63	WITS
Australopithecus sediba	1	1	1	U.W. 88-95; U.W. 88-117; U.W. 88-118	WITS
Australopithecus robustus / early *Homo*	-	1	-	SKW-2954	WITS
Homo naledi	1	2	1	U.W. 101-1729; U.W. 101-1318; U.W. 102a-028; U.W. 101-1309	WITS
Homo floresiensis	1	-	-	LB21+22	
Homo neanderthalensis	4	-	-	Kebara-2; Shanidar-4; Tabun-1; Regourdou-1	TAU; RM;
Early *Homo sapiens*	2	-	-	Tianyuan; Qafzeh-9	TAU
Total	**11**	**7**	**5**		

Abbreviations: MC-IV: fourth metacarpal; MC-V: fifth metacarpal; NME: National Museum of Ethiopia, Addis-Ababa; RM: Rockerfeller Museum, Israel; TAU: Tel Aviv University, Tel Aviv, Israel; WITS: University of the Witwatersrand, Johannesburg, South Africa; L: Left; R: Right

Australopithecus afarensis

The *Australopithecus afarensis* specimens used in this study were discovered at the A.L. 333 locality of the Hadar Formation, Ethiopia. All specimens date to ~3.2 Ma (Johanson *et al*., 1982). The specimens are curated at the National Museum of Ethiopia and digital renderings of these specimens were created by Zeray Alemseged, William Kimbel, Fred Spoor, Heiko Temming, and David Plotzki with the support of the Department of Human Evolution, Max Planck Institute for Evolutionary Anthropology.

A.L. 333-50 is an excellently-preserved right hamate (figure 4.2.1). The only defect on this bone is a post-fossilization fracture located at the base of the hamulus that involves the palmar part of the metacarpal facets (Bush *et al*., 1982).

Figure 4.2.1(a): The AL-333-50 *Australopithecus afarensis* hamate, viewed from, left to right: lateral, distal, medial, proximal, dorsal, and palmar views. From Bush *et al*., 1982.

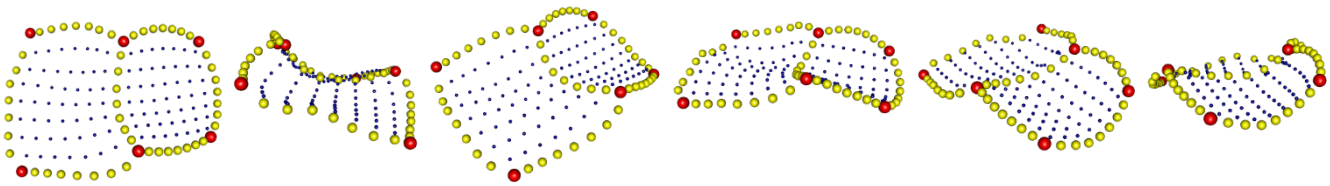

Figure 4.2.1(b): Landmark representation of the AL-333-50 *Australopithecus afarensis* hamate, viewed from, left to right: distal, lateral, laterodorsal, dorsal, mediodorsal, and medial views. Red spheres denote fixed landmarks, yellow spheres denote curve sliding semilandmarks, and blue spheres denote surface sliding semilandmarks.

A.L. 333-56 is a well-preserved and moderately robust left fourth metacarpal (figure 4.2.2). The metacarpal was recovered in two perfectly joining parts separated by a transverse break proximal to the midshaft (Bush *et al*., 1982).

Figure 4.2.2(a): The AL-333-56 *Australopithecus afarensis* fourth left metacarpal, viewed from, left to right: palmar, medial, dorsal, lateral views. From Bush *et al*., 1982.

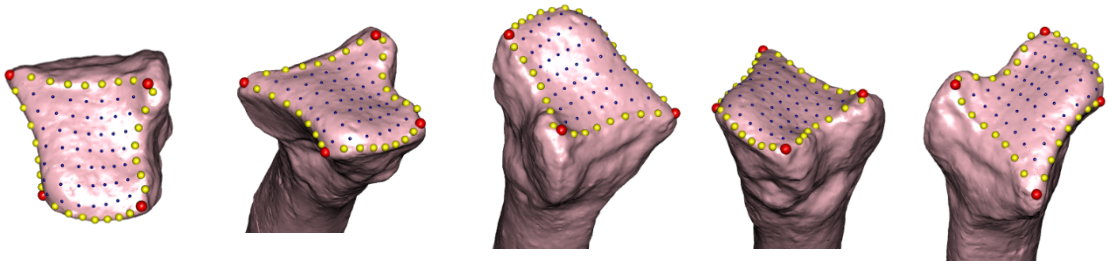

Figure 4.2.2(b): Surface mesh rendering of the AL-333-56 *Australopithecus afarensis* fourth metacarpal, with landmarks used to represent the specimen. Viewed from, left to right: distal, mediopalmar, laterodorsal, lateropalmar, and mediodorsal views. Red spheres denote fixed landmarks, yellow spheres denote curve sliding semilandmarks, and blue spheres denote surface sliding semilandmarks.

A.L. 333w-89 is a left adult fifth metacarpal that was discovered in three approximately equal segments separated by two traverse fractures (figure 4.2.3) (Bush *et al*., 1982). There is mild erosion along the medial aspect of the bone's hamate facet. The hamate facet tilts slightly to the radial side. The fourth metacarpal articulation is elliptical, palmodorsally elongate, convex, obliquely oriented, and inclined proximally and dorsally.

Figure 4.2.3 (a): The A.L. 333w-89 *Australopithecus afarensis* left adult fifth metacarpal, viewed from, left to right: palmar, medial, dorsal, lateral views. From Bush *et al*., 1982.

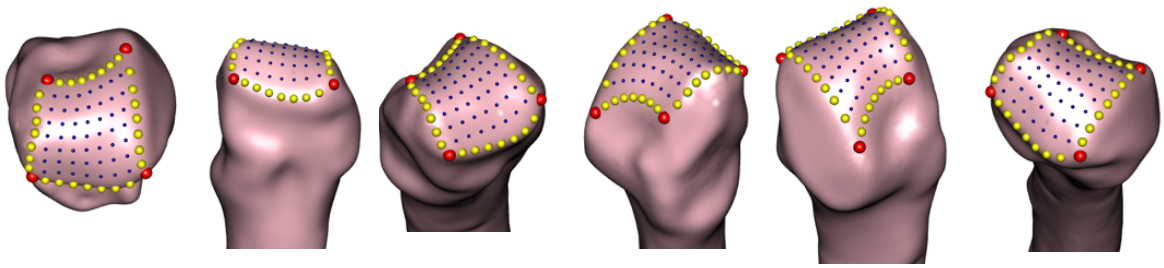

Figure 4.2.3 (b): Surface mesh rendering of the AL-333w-89 *Australopithecus afarensis* fifth left metacarpal, with landmarks used to represent the specimen. Viewed from, left to right: distal, palmar, mediopalmar, mediodorsal, laterodorsal, and lateropalmar views. Red spheres denote fixed landmarks, yellow spheres denote curve sliding semilandmarks, and blue spheres denote surface sliding semilandmarks.

A.L. 333-14 (figure 4.2.4) is a complete and essentially unblemished adult right fifth metacarpal, with the exception of minor erosional defect marks on the dorsal aspect of the fourth metacarpal articulation, and mild superficial erosion and microcracking.

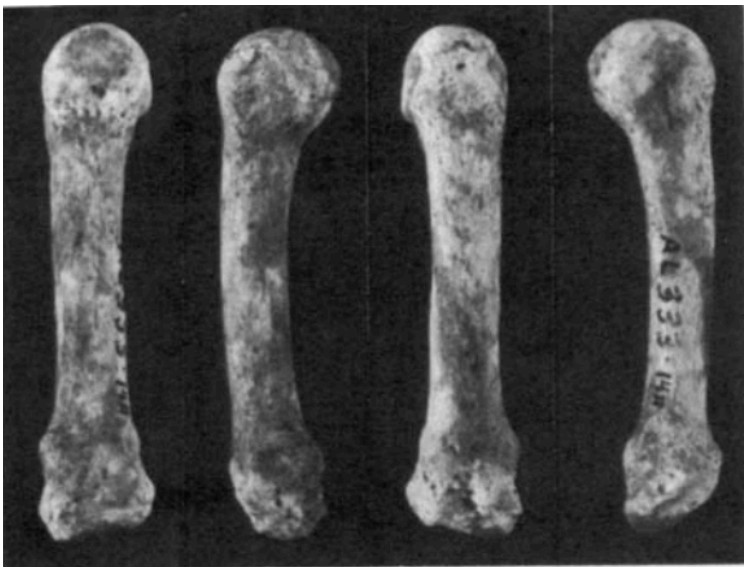

Figure 4.2.4(a): The A.L. 333-14 *Australopithecus afarensis* right adult fifth metacarpal, viewed from, left to right: palmar, medial, dorsal, lateral views. From Bush *et al*., 1982.

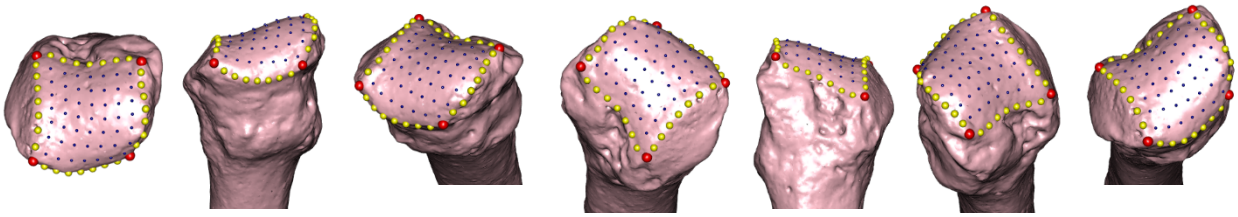

Figure 4.2.4 (b): Surface mesh rendering of the AL-333-14 *Australopithecus afarensis* right fifth metacarpal, with landmarks used to represent the specimen. Viewed from, left to right: distal, palmar, mediopalmar, mediodorsal, dorsal, laterodorsal, and lateropalmar views. Red spheres denote fixed landmarks, yellow spheres denote curve sliding semilandmarks, and blue spheres denote surface sliding semilandmarks.

Australopithecus cf. Australopithecus afarensis

KNM-WT 22944-I (figure 4.2.5) is a complete and well-preserved left hamate discovered in 1990 that was extracted from the Nachukui Formation of South Turkwel, Kenya, and dated to between 3.58 and 3.20 Ma (Grine *et a*l., 2022; Ward *et al*., 1999). KNM-WT 22944-I (alternatively given the catalogue designation KNM-ST 22944 (Wood and Leakey, 2011)) is well-preserved

except for an abrasion on its dorsal surface, with the margins of the MC-V facet being notably abraded. KNM-WT 22944-I is contemporaneous with *Au. afarensis* specimens found at Laetoli (Deino, 2011), the Hadar Formation (Campisano and Feibel, 2008), Woranso-Mille (Haile-Selassie *et al.*, 2016) and Dikika (Alemseged *et al*., 2006), though is also contemporaneous with fossils from the Nachukui Formation that have been attributed to or compared with *Kenyanthropus platyops* (Brown, McDougall and Gathogo, 2013; Leakey *et al.,* 2001; Wood and Leakey, 2011). Ward *et al.* (1999: *p*. 94) concluded that the KNM-WT 22944 fossils "*are not identical to Au. Afarensis*", though "*they exhibit no characters which would suggest that they necessarily belonged to a distinct species*." However, no hand bones known from penecontemporaneous taxa, such as *Australopithecus deyiremeda* and *Kenyanthropus platyops* have yet been discovered, and as such comparisons with these species is not possible (Grine *et al*., 2022). For the purposes of this study, KNM-WT 22944-I is taxonomically assigned to *Australopithecus cf. Australopithecus afarensis* (Kivell *et al.*, 2022)

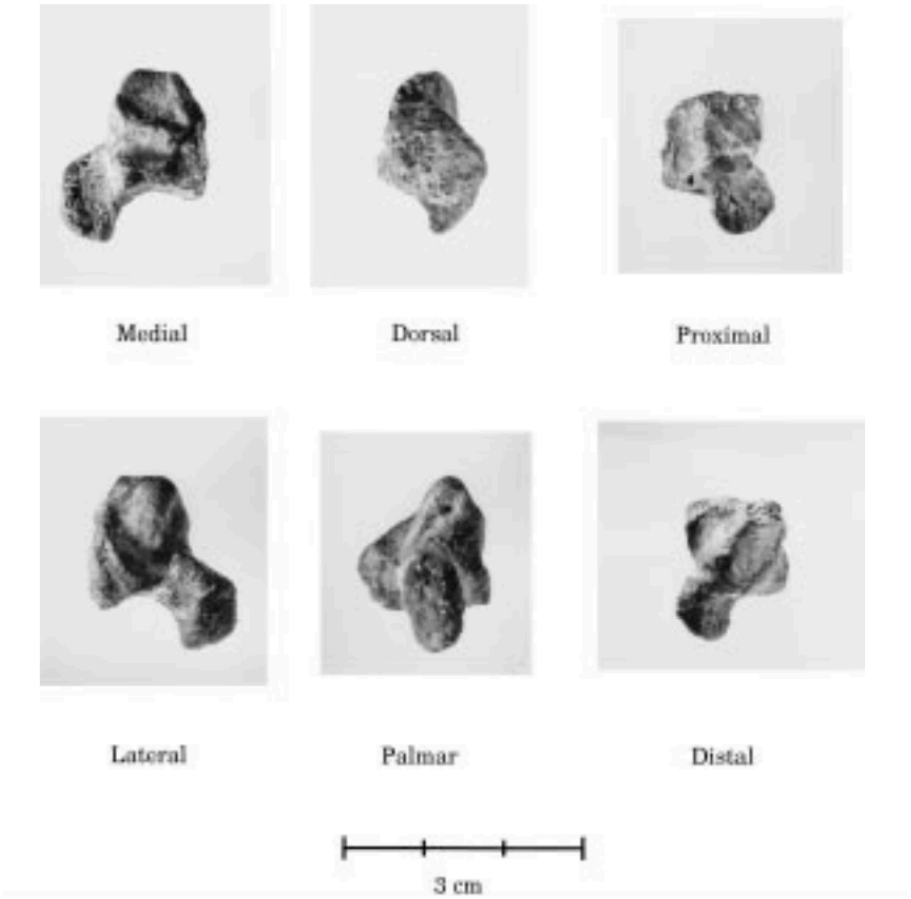

Figure 4.2.5(a): The *Australopithecus cf. Australopithecus afarensis* KNM-WT 22944-I left hamate, from a medial, dorsal, proximal, lateral, palmar, and distal view. From Ward *et al*., 1999.

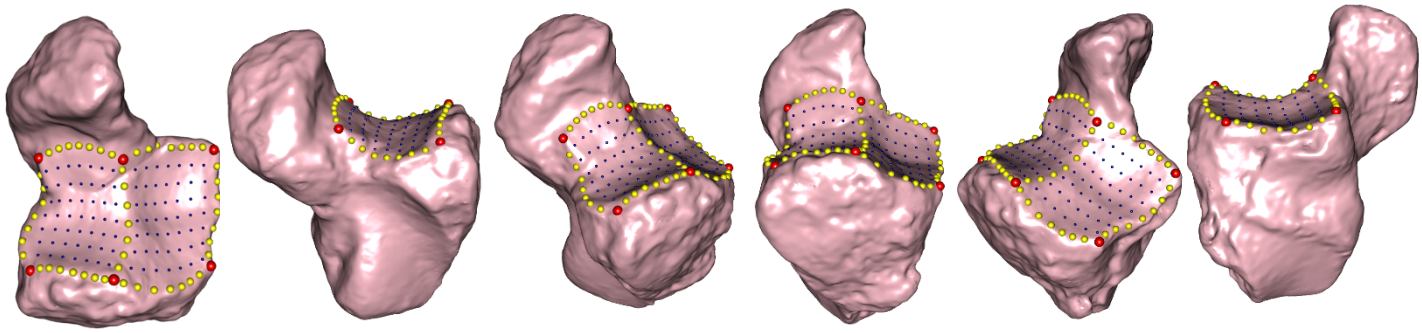

Figure 4.2.5 (b): Surface mesh rendering of the KNM-WT-22944-I *Australopithecus cf. Australopithecus afarensis* left hamate, with landmarks used to represent the specimen. Viewed from, left to right: distal, medial, mediodorsal, dorsal, laterodorsal, and lateral views. Red spheres denote fixed landmarks, yellow spheres denote curve sliding semilandmarks, and blue spheres denote surface sliding semilandmarks.

Australopithecus africanus

The *Australopithecus africanus* material used in this project originate from Sterkfontein, South Africa, and consist of a left fourth metacarpal (StW 330), a right fourth metacarpal (StW 65), and a left fifth metacarpal (StW 63).

StW 330 is an excellently-preserved left fourth metacarpal (figure 4.2.6). It preserves the base and entire shaft distal to the base of the head. Determination on sexual maturity is not possible given the absence of the head, however its size and well-developed carpometacarpal facets indicate that StW 33 derives from an individual near or at adulthood (Kivell *et al*., 2020).

Figure 4.2.6 (a): The StW 330 *Australopithecus africanus* fourth left proximal metacarpal, showing from left to right, palmar, dorsal, radial, and proximal view. From Kivell *et al*., 2020.

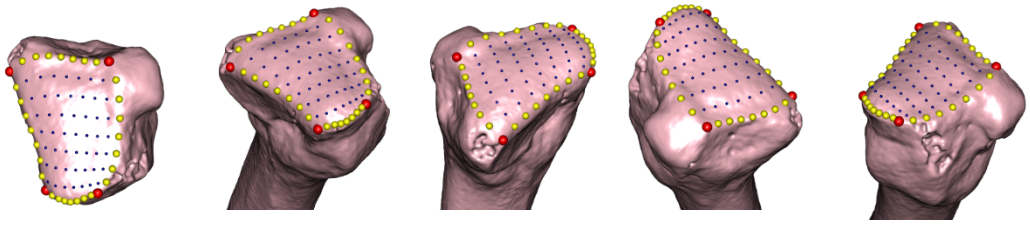

Figure 4.2.6 (b): Surface mesh rendering of the StW 330 *Australopithecus africanus* left fourth metacarpal, with landmarks used to represent the specimen. Viewed from, left to right: distal, mediopalmar, mediodorsal, laterodorsal, and lateropalmar views. Red spheres denote fixed landmarks, yellow spheres denote curve sliding semilandmarks, and blue spheres denote surface sliding semilandmarks.

StW 65 is the robust right fourth metacarpal of an adult individual (figure 4.2.7). It is broken at the point where the shaft expands at the base of the head, and its distal end is missing. However, the proximal joint surfaces are present and well preserved (Kivell *et al*., 2020).

Figure 4.2.7 (a): The StW 65 fourth right *Australopithecus africanus* metacarpal, showing from left to right, palmar, dorsal, ulnar, and radial view, with a proximal view below. From Kivell *et al*., 2020.

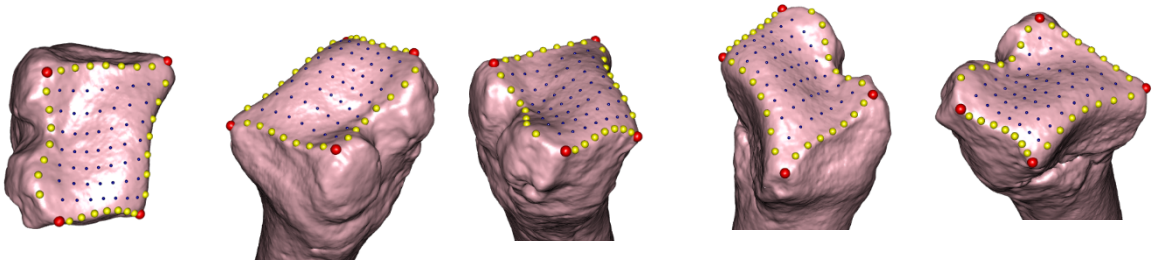

Figure 4.2.7 (b): Surface mesh rendering of the StW 65 *Australopithecus africanus* right fourth metacarpal, with landmarks used to represent the specimen. Viewed from, left to right: distal, laterodorsal, lateropalmar, mediodorsal, and mediopalmar views. Red spheres denote fixed landmarks, yellow spheres denote curve sliding semilandmarks, and blue spheres denote surface sliding semilandmarks.

StW 63 is the left fifth metacarpal of an adult individual (figure 4.2.8). It was recovered in two pieces, broken at two-thirds of its length from the proximal base, and is missing the dorsal half of the distal end, but is otherwise intact and exhibits very good surface preservation (Kivell *et al.,* 2020).

Figure 4.2.8(a): The StW 63 *Australopithecus africanus* fifth left metacarpal, shown from left to right, medial, lateral, dorsal, and palmar views. From Kivell *et al*., 2020.

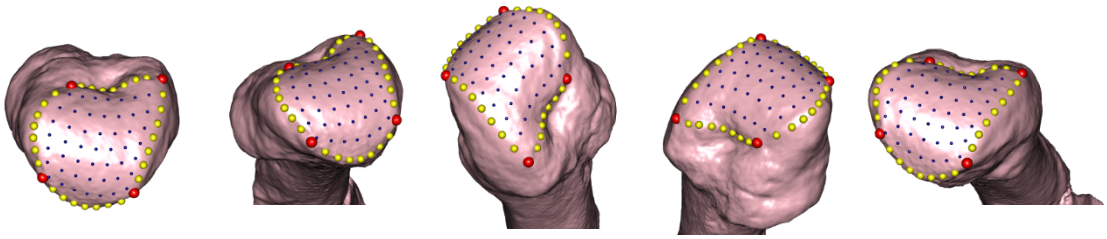

Figure 4.2.8(b): Surface mesh rendering of the StW 63 *Australopithecus africanus* left fifth metacarpal, with landmarks used to represent the specimen. Viewed from, left to right: distal, mediopalmar, laterodorsal, mediodorsal, and lateropalmar views. Red spheres denote fixed landmarks, yellow spheres denote curve sliding semilandmarks, and blue spheres denote surface sliding semilandmarks.

Australopithecus sediba

The *Australopithecus sediba* material used in this project consist of a right hamate (U.W. 88-95), a left fourth metacarpal (U.W. 88-117), and a right fifth metacarpal (U.W. 88-118). All derive from the MH2 skeleton, which was discovered in 2008 at Malapa, South Africa. MH2 is an adult, likely female skeleton, dated to 1.98 Ma (Berger *et al.,* 2010; Pickering *et al.,* 2011).

Both the left (**U.W. 88-106**), and right (**U.W. 88-95**) hamates of MH2 are relatively complete and undistorted (Kivell *et al*., 2018). U.W. 88-106 (figure 4.2.9) is perfectly preserved and complete except for a pit at the distal edge of the dorsal surface. U.W. 88-95 (figure 4.2.9) is

also complete apart for a small fragment of the distopalmar tip of the hamulus. The morphology of both the left and right hamates of MH2 are identical and comparable to each other, however the overall size of U.W. 88-95 (right) and its facets are generally slightly smaller than that of U.W. 88-106 (left), which is consistent with patterns of bilateral symmetry seen within individuals (Kivell *et al*., 2018). Given the identical morphology of the two MH2 hamates, and that U.W. 88-106 exhibits slight taphonomic damage at or near the bone's articulation with the metacarpals, only the right hamate (U.W. 88-95) was included in this project.

Figure 4.2.9(a): The left (U.W. 88-106) and right (U.W. 88-95) hamates of *Australopithecus sediba* MH2 hand, shown in dorsal view, with proximal towards the top (above); medial view (middle); and lateral view, with palmar towards the top (bottom). From Kivell *et al*., 2018.

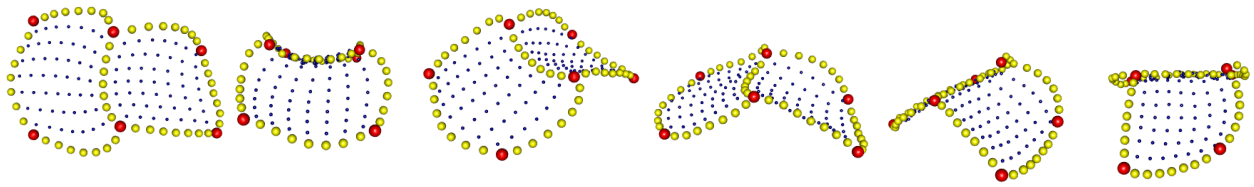

Figure 4.2.9(b): Landmark representation of the U.W. 88-95 *Australopithecus sediba* right hamate, viewed from, left to right: distal, lateral, laterodorsal, dorsal, mediodorsal, and medial views. Red spheres denote fixed landmarks, yellow spheres denote curve sliding semilandmarks, and blue spheres denote surface sliding semilandmarks.

U.W. 88-117 (figure 4.2.10) is a complete and perfectly preserved right fourth metacarpal, with the exception of a small fragment missing from the lateral epicondyle and a thin fracture running the circumference of the shaft proximal to the midshaft (Kivell *et al*., 2018). However, the proximal base is slightly abraded, so that that the lateral and dorsal borders of the hamate facet blend with the non-articular area and lack a definitive outline. The base of U.W. 88-117 is mediolaterally broad relative to its shaft and is dominated by its articular surface for the hamate.

Figure 4.2.10(a): The *Australopithecus sediba* MH2 right fourth metacarpal U.W. 88-117 shown, from left to right, palmar, medial, lateral, and dorsal views. From Kivell *et al*., 2018.

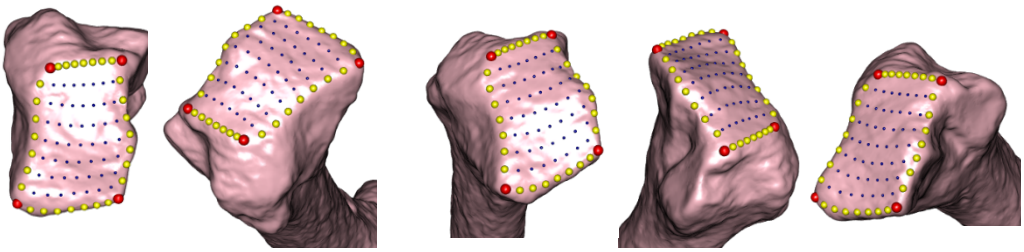

Figure 4.2.10(b): Surface mesh rendering of the U.W. 88-117 *Australopithecus sediba* right fourth metacarpal, with landmarks used to represent the specimen. Viewed from, left to right: distal, laterodorsal, lateropalmar, mediodorsal, and mediopalmar views. Red spheres denote fixed landmarks, yellow spheres denote curve sliding semilandmarks, and blue spheres denote surface sliding semilandmarks.

U.W. 88-118 is a right fifth metacarpal of the *Australopithecus sediba* MH 2 skeleton (figure 4.2.11). It is complete except for a missing fragment of the ridge for the *opponens digiti minimi* muscle tendon attachment on the medial surface of the midshaft, and a small fragment of the palmar shaft, proximal to the midshaft. There is also a fracture that runs the circumference of the shaft just proximal to the head (Kivell *et al*., 2018). The base of U.W. 88-118 is

distoproximally tall and mediolaterally broad relative to its shaft. The medial portion of the base flares strongly with a robust protuberance for the attachment of the *extensor carpi ulnaris* muscle dorsally, and the pisohamate ligament palmarly (Kivell *et al*., 2018). The dorsal surface of the base has a prominent tubercle on the lateral side for the attachment of the dorsal metacarpal ligament. The hamate facet dominates the proximal end of U.W. 88-118.

Figure 4.2.11(a): The *Australopithecus sediba* MH2 right fifth metacarpal U.W. 88-118 shown in, from left to right, palmar, medial lateral, dorsal, distal (far right, above), and proximal (far right, below) views. From Kivell *et al*., 2018.

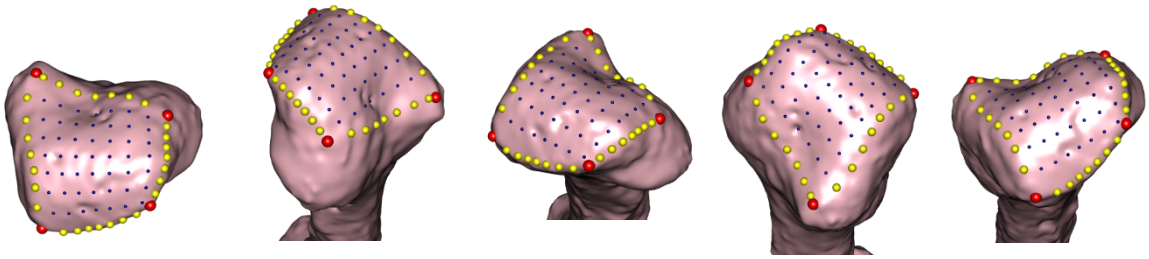

Figure 4.2.11 (b): Surface mesh rendering of the U.W.88-118 *Australopithecus sediba* right fifth metacarpal, with landmarks used to represent the specimen. Viewed from, left to right: distal, mediodorsal, mediopalmar, laterodorsal, and lateropalmar views. Red spheres denote fixed landmarks, yellow spheres denote curve sliding semilandmarks, and blue spheres denote surface sliding semilandmarks.

Paranthropus robustus / early *Homo*

SKW 2954 (figure 4.2.12) is a complete right fourth metacarpal, recovered from Member 2 Swartkrans, which is aged to between 1.36 and 1.1 Ma (Balter *et al.,* 2008; Gibbon *et al.,* 2014; Herries *et al.,* 2009). Both *Paranthropus* and early *Homo* fossils have been recovered from Member 2 (Pickering *et al.,* 2012; Susman, 1989), and Susman (1989) did not specifically assign SKW 2954 to either of these taxa. Nevertheless, the SKW 2954 fourth metacarpal is essentially human-like in its morphology and is comparable in size and articulates well with the SKW 3646 third metacarpal (Susman, 1989).

Figure 4.2.12 (a): The *Paranthropus robustus /* early *Homo* SKW-2954 right fourth metacarpal, from left: palmar, dorsal, medial, and lateral view. From Susman, 1989.

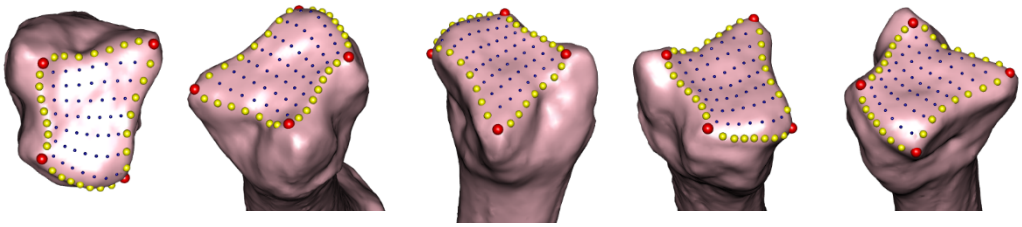

Figure 4.2.12 (b): Surface mesh rendering of the SkW-2954 *Paranthropus robustus /* early *Homo* right fourth metacarpal, with landmarks used to represent the specimen. Viewed from, left to right: distal, laterodorsal, mediodorsal, lateropalmar, and mediopalmar views. Red spheres denote fixed landmarks, yellow spheres denote curve sliding semilandmarks, and blue spheres denote surface sliding semilandmarks.

Homo

Homo naledi

U.W. 101-1729, U.W. 101-1318, and U.W. 101-1309 are all elements of the adult Hand 1 *Homo naledi* paratype (Kivell *et al*., 2015). Hand 1 is a complete (other than a missing pisiform) right hand of an adult hominin which was recovered from the Dinaledi Chamber of the Rising Star cave system in South Africa. Overall, Hand 1 is small, similar in size to the *Australopithecus sediba* MH2 female hand.

U.W. 101-1729 is a right hamate (figure 4.2.13). It is generally complete and well-preserved, although trabeculae are exposed on the dorsal edge of the MC-V facet.

Figure 4.2.13(a): The *Homo naledi* U.W. 101-1729 right hamate, from a distal, proximal, medial, lateral, palmar, and dorsal view. From Kivell *et al*., 2015.

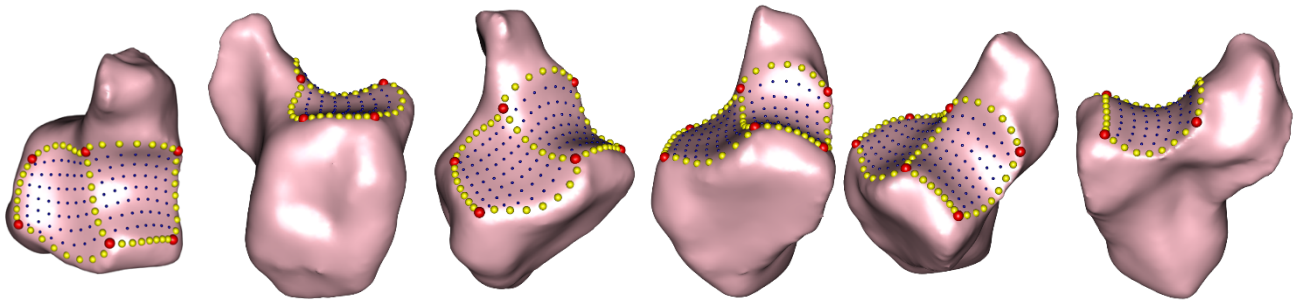

Figure 4.2.13(b): Surface mesh rendering of the U.W. 101-1729 *Homo naledi* right hamate, with landmarks used to represent the specimen. Viewed from, left to right: distal, lateral, laterodorsal, dorsal, medioodorsal, and medial views. Red spheres denote fixed landmarks, yellow spheres denote curve sliding semilandmarks, and blue spheres denote surface sliding semilandmarks.

U.W. 101-1318, a right fourth metacarpal, is complete apart from a large portion of the lateral and dorsal portions of the distal epiphysis (figure 4.2.14). While the full extent of the bone's articular surface with the hamate is retained, the cortex of the lateral border of the hamate is eroded (Kivell *et al.*, 2015). The hamate facet dominates the small, square-shaped base of the bone.

Figure 4.2.14(a): The *Homo naledi* U.W. 101-1318 right fourth metacarpal, from a medial, lateral, palmar, and dorsal view. From Kivell *et al.*, 2015.

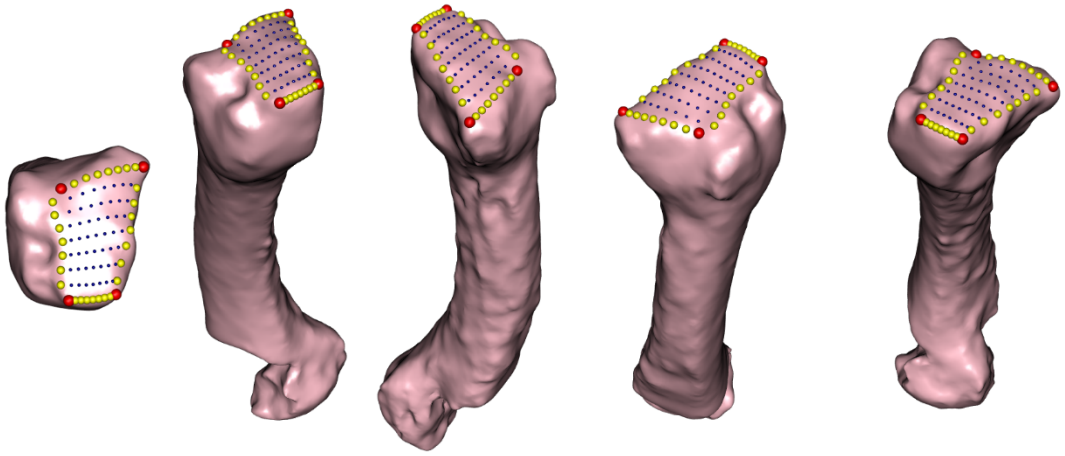

Figure 4.2.14 (b): Surface mesh rendering of the U.W. 101-1318 *Homo naledi* right fourth metacarpal, with landmarks used to represent the specimen. Viewed from, left to right: distal, lateropalmar, mediodorsal, laterodorsal, and mediopalmar views. Red spheres denote fixed landmarks, yellow spheres denote curve sliding semilandmarks, and blue spheres denote surface sliding semilandmarks.

U.W. 101-1309 is a complete and well-preserved right fifth metacarpal (figure 4.2.15). The narrow hamate facet extends onto the palmar surface of the base. The MC-IV facet is roughly

rectangular in shape and is mildly dorsopalmarly curved and oriented equally laterally and dorsally, and slightly proximally (Kivell *et al.,* 2015).

Figure 4.2.15(a): The *Homo naledi* U.W. 101-1309 right fifth metacarpal, from a palmar, dorsal medial, and lateral view. From Kivell *et al.,* 2015.

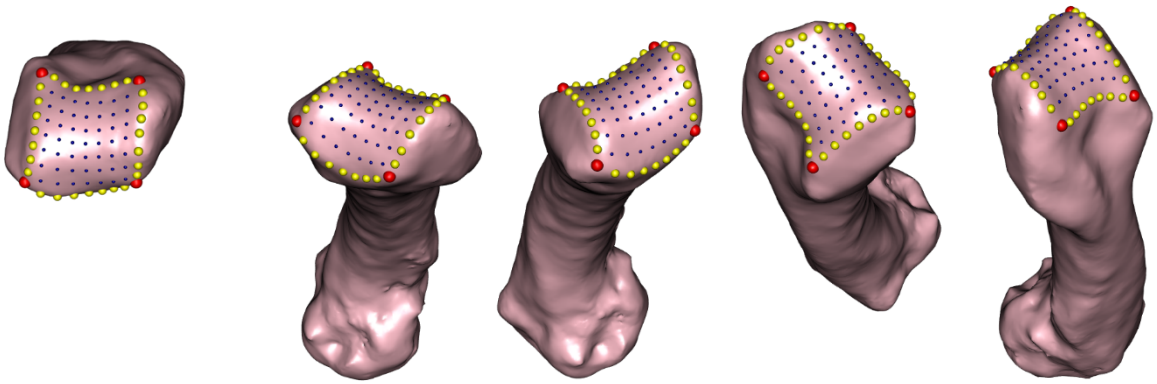

Figure 4.2.15(b): Surface mesh rendering of the U.W. 101-1309 *Homo naledi* right fourth metacarpal, with landmarks used to represent the specimen. Viewed from, left to right: distal, lateropalmar, medio, lateropalmar, and lateropalmar views. Red spheres denote fixed landmarks, yellow spheres denote curve sliding semilandmarks, and blue spheres denote surface sliding semilandmarks.

The **U.W. 102a-028** right fourth metacarpal (figure 4.2.16) has a small base and a relatively radioulnarly broad head. The metacarpal shaft is substantially curved and is relatively robust for its length (Hawks *et al.,* 2017).

Figure 4.2.16(a): The *Homo naledi* U.W. 102a-028 right fourth metacarpal. From left: dorsal, ulnar, palmar, and radial views. Right, from top: distal and proximal views (scale bar = 1cm). From Hawks *et al.,* 2017.

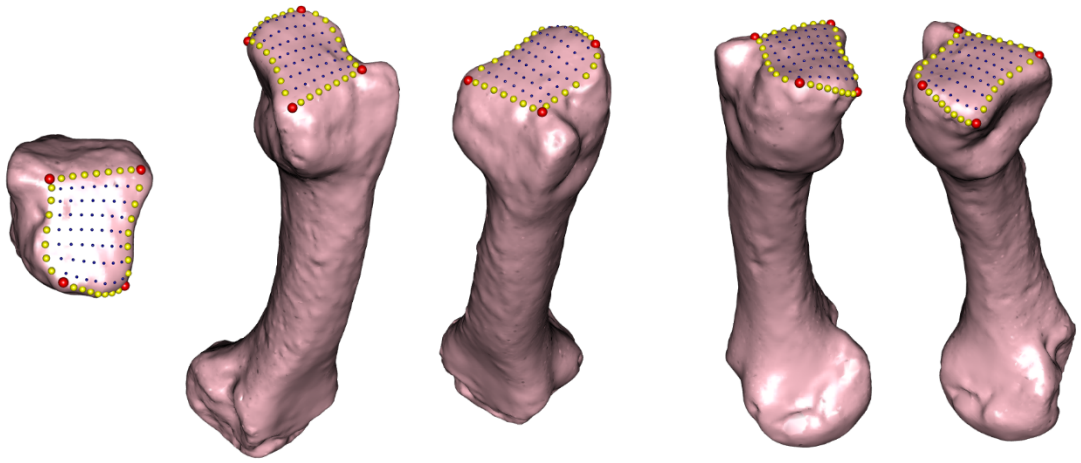

Figure 4.2.16 (b): Surface mesh rendering of the U.W. 102a-028 *Homo naledi* right fourth metacarpal, with landmarks used to represent the specimen. Viewed from, left to right: distal, mediodorsal, laterodorsal, lateropalmar, and mediopalmar views. Red spheres denote fixed landmarks, yellow spheres denote curve sliding semilandmarks, and blue spheres denote surface sliding semilandmarks.

Homo floresiensis

The Homo floresiensis material used in this project is a composite mesh of a hamate produced from two partial hamates excavated in 2004 – LB21, a left partial hamate, and LB22, a right partial hamate, both of which originate from a single individual (Orr *et al*., 2013). LB21 consists of a well-preserved body. However, the MC-V articular surface of this hamate is missing, owing to the distoulnar corner of the bone being missing. The hamulus of LB21 is broken off at its root with the hamate body and is missing almost entirely. Much of the body and hamulus of LB22, the corresponding right hamate, is preserved, although cortical bone on the dorsal aspect of its body is absent, and the distoradial edge of the hamulus has been abraded. The stout hamulus of LB22 is relatively long and inclines somewhat distally (Orr *et al*., 2013), and the palmarly-preserved portion of the LB22 hamate-MCV surface extends out to approximately halfway along the length of the hamulus. Approximately 50% of the carpometacarpal surface of the LB22 hamate is absent (Orr *et al*., 2013), and the dorsal portion of the hamate-MCV articular surface is damaged.

Although both LB21 and LB22 are incomplete, both are similar in the anatomy for which they overlap, and each preserve the corresponding morphology in the portions where the other is missing or damaged. Orr *et al*. (2013) produced a composite *Homo floresiensis* hamate by reflecting the left LB21 hamate across the axis of symmetry, and aligning it with the right LB22 hamate, and subsequently merging both hamates, resulting in a complete composite right hamate. It is this composite hamate model that is used in this project (figure 4.2.17).

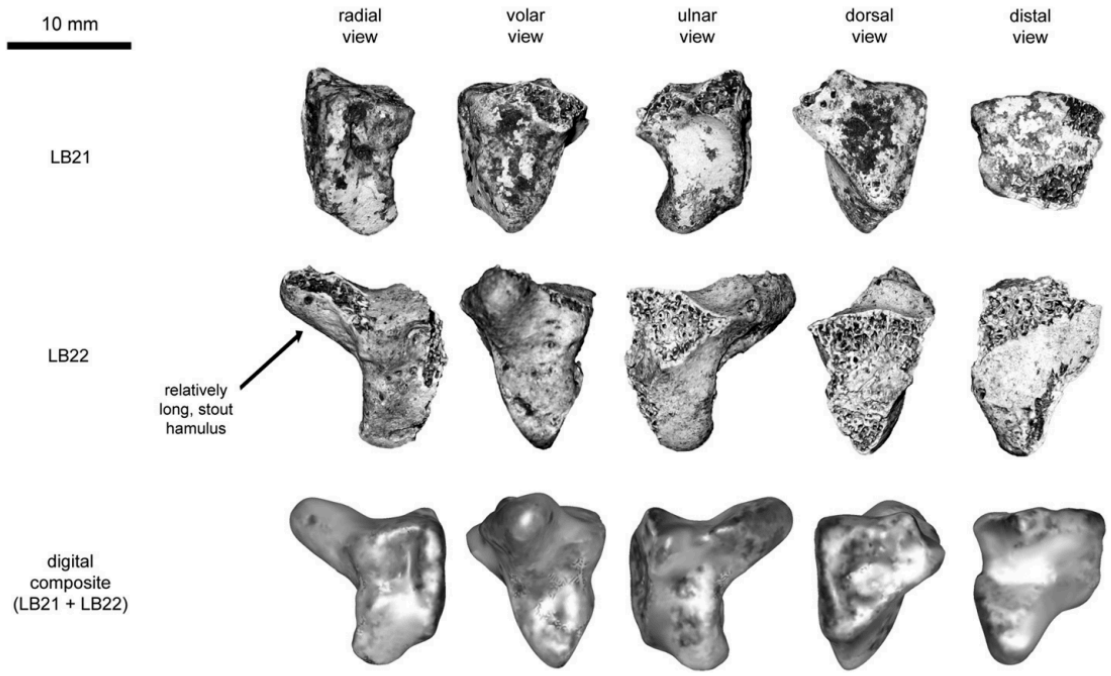

Figure 4.2.17(a): Images of the LB21 and LB22 *Homo floresiensis* hamates, along with the digital composite used in this study, taken from a lateral (radial), palmar (volar), medial (ulnar), dorsal and distal view. From Orr *et al*., 2013.

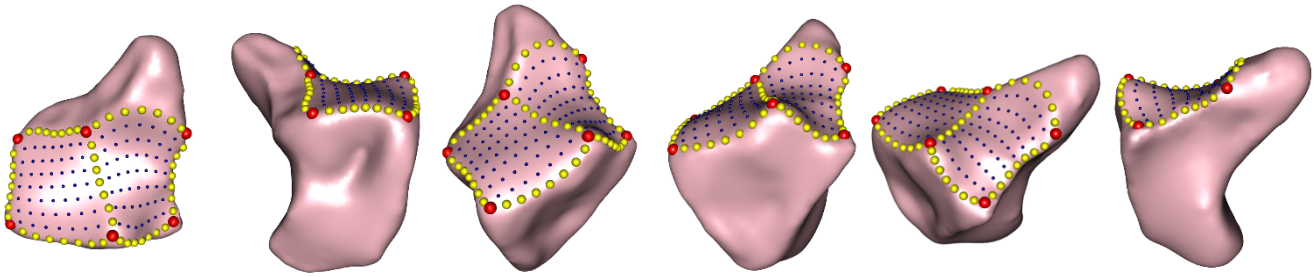

Figure 4.2.17(b): Surface mesh rendering of the Liang Bua-21/22 *Homo floresiensis* right hamate, with landmarks used to represent the specimen. Viewed from, left to right: distal, lateral, laterodorsal, dorsal, medioodorsal, and medial views. Red spheres denote fixed landmarks, yellow spheres denote curve sliding semilandmarks, and blue spheres denote surface sliding semilandmarks.

Homo neanderthalensis

Kebara-2 (KMH2) is a 61-59 KA adult male Neanderthal left hamate. Discovered by Arensburg *et al.* (1983) in a Mousterian layer of the Kebara Cave, Israel, Kebara-2 represents the most complete Neanderthal postcranial skeleton discovered to date.

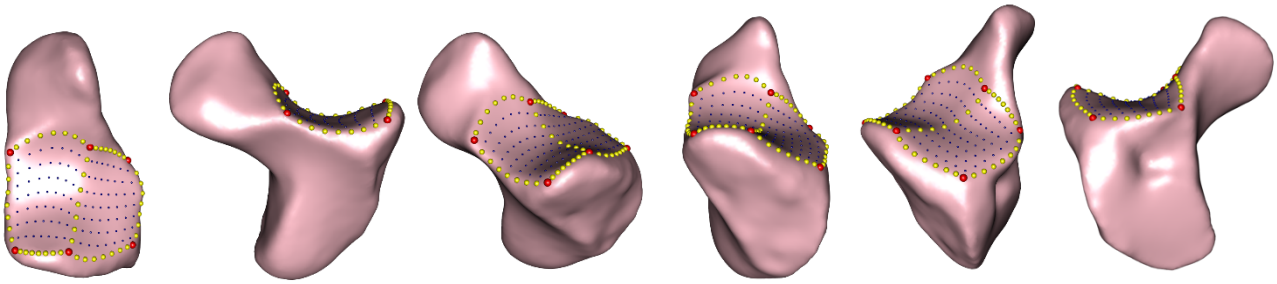

Figure 4.2.18: Surface mesh rendering of the Kebara-2 *Homo neanderthalensis* right hamate, with landmarks used to represent the specimen. Viewed from, left to right: distal, lateral, laterodorsal, dorsal, medioodorsal, and medial views. Red spheres denote fixed landmarks, yellow spheres denote curve sliding semilandmarks, and blue spheres denote surface sliding semilandmarks.

Shanidar-4 is the most complete hand skeleton associated with Neanderthals. This left hand of an adult male aged 30 to 45 years (figure 4.2.19), discovered in the Shanidar Cave in Kurdistan in 1960 (Solecki, 1975), is dated to between 75-100 ka (Trinkaus, 1983). The hand lacks only the lunate (the corresponding right lunate is recovered), and one distal non-pollical distal phalanx (Trinkaus, 1983). The Shanidar-4 hamate is complete, with a maximum length of 20.5 mm. The primary feature of note of the Shanidar-4 hamate is hypertrophy of the hamulus, which is exceptionally large, with its palmar end being round and bulbous (Trinkaus, 1983).

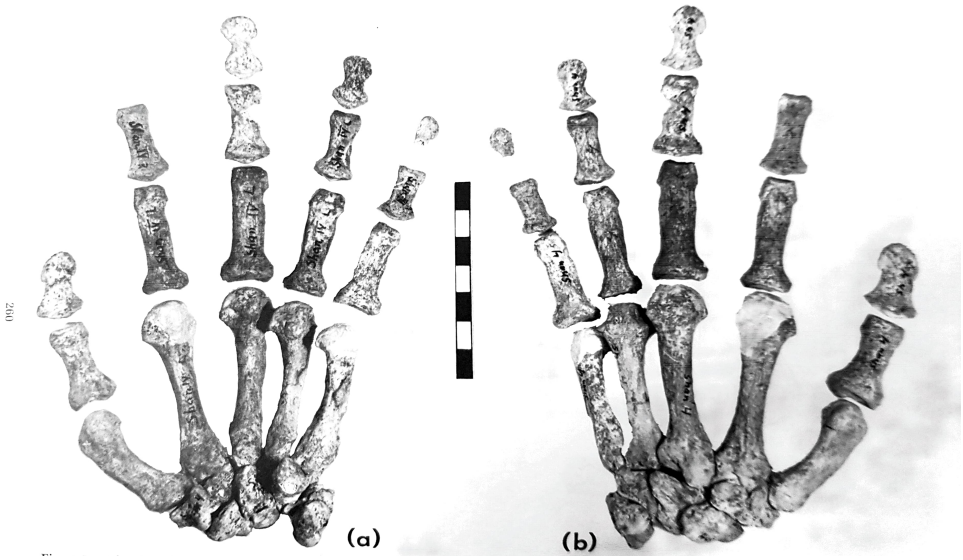

Figure 4.2.19(a): The Shanidar 4 *Homo neanderthalensis* left hand remains from a palmar (a) and dorsal (b) view. From Trinkaus, 1983.

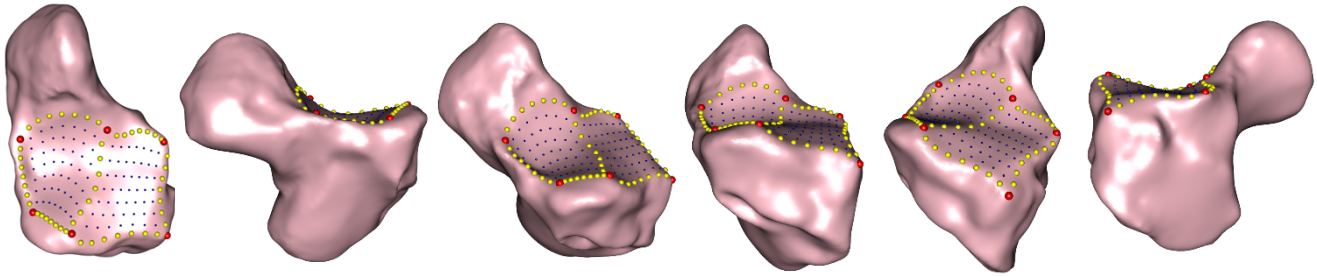

Figure 4.2.19 (b): Surface mesh rendering of the Shanidar-4 *Homo neanderthalensis* right hamate, with landmarks used to represent the specimen. Viewed from, left to right: distal, lateral, laterodorsal, dorsal, medioodorsal, and medial views. Red spheres denote fixed landmarks, yellow spheres denote curve sliding semilandmarks, and blue spheres denote surface sliding semilandmarks.

The **Tabun 1** hamate is from the left hand of an adult female Neanderthal. Discovered at Mount Carmel, Israel, it is dated from between 122-50 Ka, and is associated with Mousterian assemblages (Garrod and Bate, 1937).

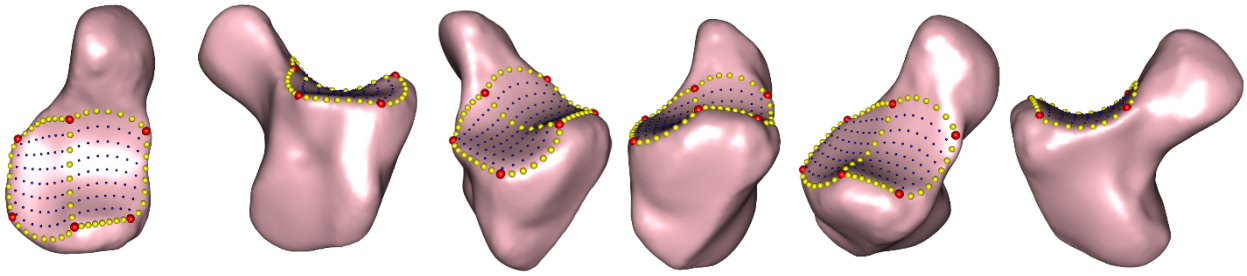

Figure 4.2.20: Surface mesh rendering of the Tabun-1 *Homo neanderthalensis* right hamate, with landmarks used to represent the specimen. Viewed from, left to right: distal, lateral, laterodorsal, dorsal, medioodorsal, and medial views. Red spheres denote fixed landmarks, yellow spheres denote curve sliding semilandmarks, and blue spheres denote surface sliding semilandmarks.

Regourdou-1 was discovered in 1957 near Lascaux in the Dordogne of southwestern France. Dated to ~70 Ka (Vandermeersch, 1963), Regourdou 1 was probably between 23-30 years old at death (Volpato *et al*., 2012), and while sex is generally considered 'indeterminate' based on the small size of the long bones (Meyer *et al.,* 2011; Vandermeersch and Trinkaus, 1995), the anatomical proportions of the body and alae in the superior sacrum suggest it was a male (Volpato *et al.,* 2012). The right hamate of Regourdou-1 was used in this project.

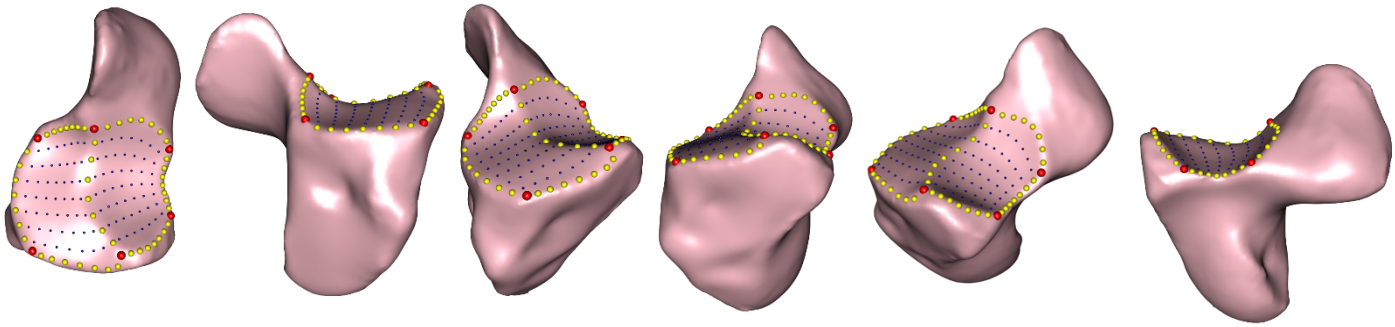

Figure 4.2.21: Surface mesh rendering of the Regourdou-1 *Homo neanderthalensis* right hamate, with landmarks used to represent the specimen. Viewed from, left to right: distal, lateral, laterodorsal, dorsal, medioodorsal, and medial views. Red spheres denote fixed landmarks, yellow spheres denote curve sliding semilandmarks, and blue spheres denote surface sliding semilandmarks.

Early *Homo sapiens*

Qafzeh-9 has been reported by Vandermeersch (1981) to be a late adolescent, skeletally mature (with fused metacarpal epiphyses) female, while others (Rak, 1990; Rosenberg, 1988; Wolpoff, 1999) believe Qafzeh-9 to be male. Qafzeh-9 dates from 100-80 Ka (Grun and Stringer, 1991; Valladas *et al*., 1987) from Israel. The Skhul/Qafzeh early modern humans are associated with Mousterian lithic technologies.

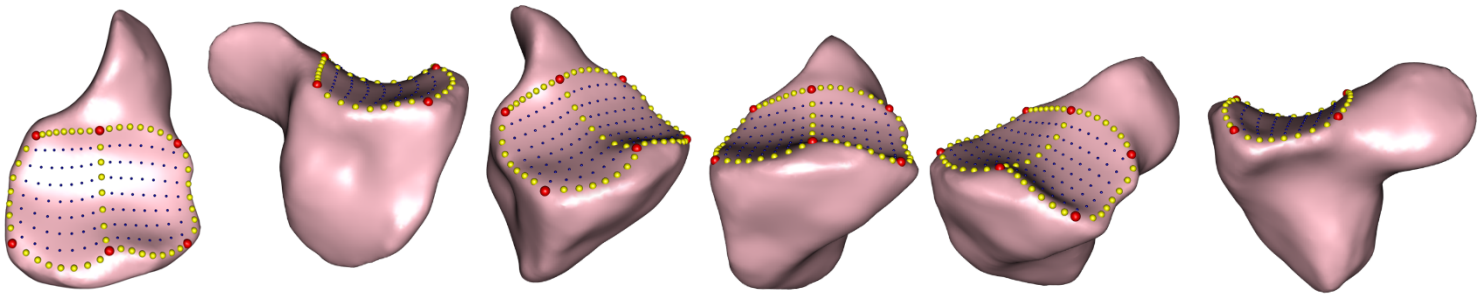

Figure 4.2.22: Surface mesh rendering of the Qafzeh-9 early *Homo sapiens* right hamate, with landmarks used to represent the specimen. Viewed from, left to right: distal, lateral, laterodorsal, dorsal, medioodorsal, and medial views. Red spheres denote fixed landmarks, yellow spheres denote curve sliding semilandmarks, and blue spheres denote surface sliding semilandmarks.

The **Tianyuan** early modern *Homo sapiens* skeleton was found in Tianyuan Cave, Zhoukoudian, China, in 2003. It is a skeleton of an adult male estimated to have died in his 40s or 50s, and was dated to 42-39 Ka (Shang *et al*., 2007). The hamate has a large hamulus length and

has the reduced palmar projection of early modern humans, but its relative proximodistal length is similar to that of Neanderthals (Shang *et al*., 2007).

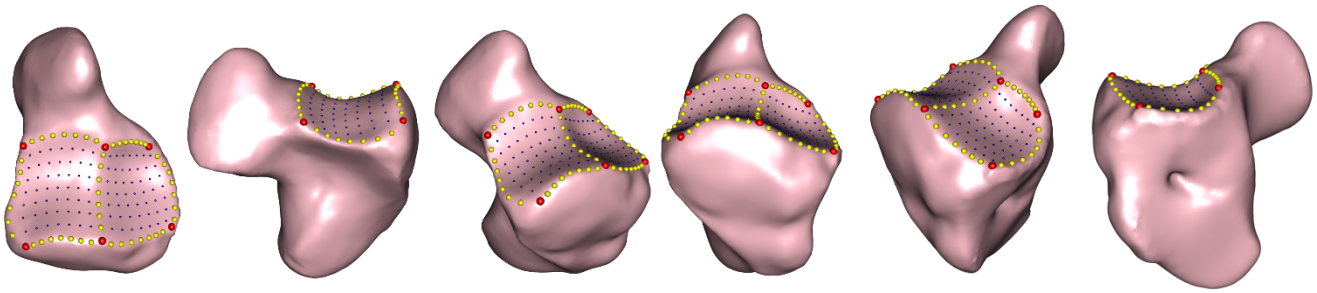

Figure 4.2.23: Surface mesh rendering of the Tianyuan early *Homo sapiens*right hamate, with landmarks used to represent the specimen. Viewed from, left to right: distal, lateral, laterodorsal, dorsal, medioodorsal, and medial views. Red spheres denote fixed landmarks, yellow spheres denote curve sliding semilandmarks, and blue spheres denote surface sliding semilandmarks.

Section III: Results

5 The hamate-metacarpal articular surface

5.1 Hamate-metacarpal surface average shapes

Homo sapiens

The average hamate-metacarpal shape of the *Homo sapiens* population is shown in figure 5.1.1. The human hamate's metacarpal articulation displays a very moderate palmodorsal concave curvature, and a palmar border that is not distally projecting as a result. The mean shape of the hamate-metacarpal surface in modern humans, particularly that of the fifth metacarpal's articulation, is squat in the palmodorsal plane, resulting in a mediolateral length of the surface which is longer than the palmodorsal length. The articulation for the fourth metacarpal is relatively smooth and lacks the prominent distal ballooning in the central-lateral area of its surface that is seen in other taxa (see below). The most notable characteristics of the mean shape of the *Homo sapiens* population relate to the surface for the fifth metacarpal, which is enlarged in absolute terms relative to the surface for the fourth metacarpal, largely due to its elongation in the mediolateral plane. The two surfaces are also notably stepped, with a fifth metacarpal surface that is not only angled medially relative to a distally-facing fourth metacarpal surface, but which is also mildly mediolaterally convex, resulting in a saddle-shaped morphology of the joint surface that is increasingly medially-facing and proximally projecting as it moves medially.

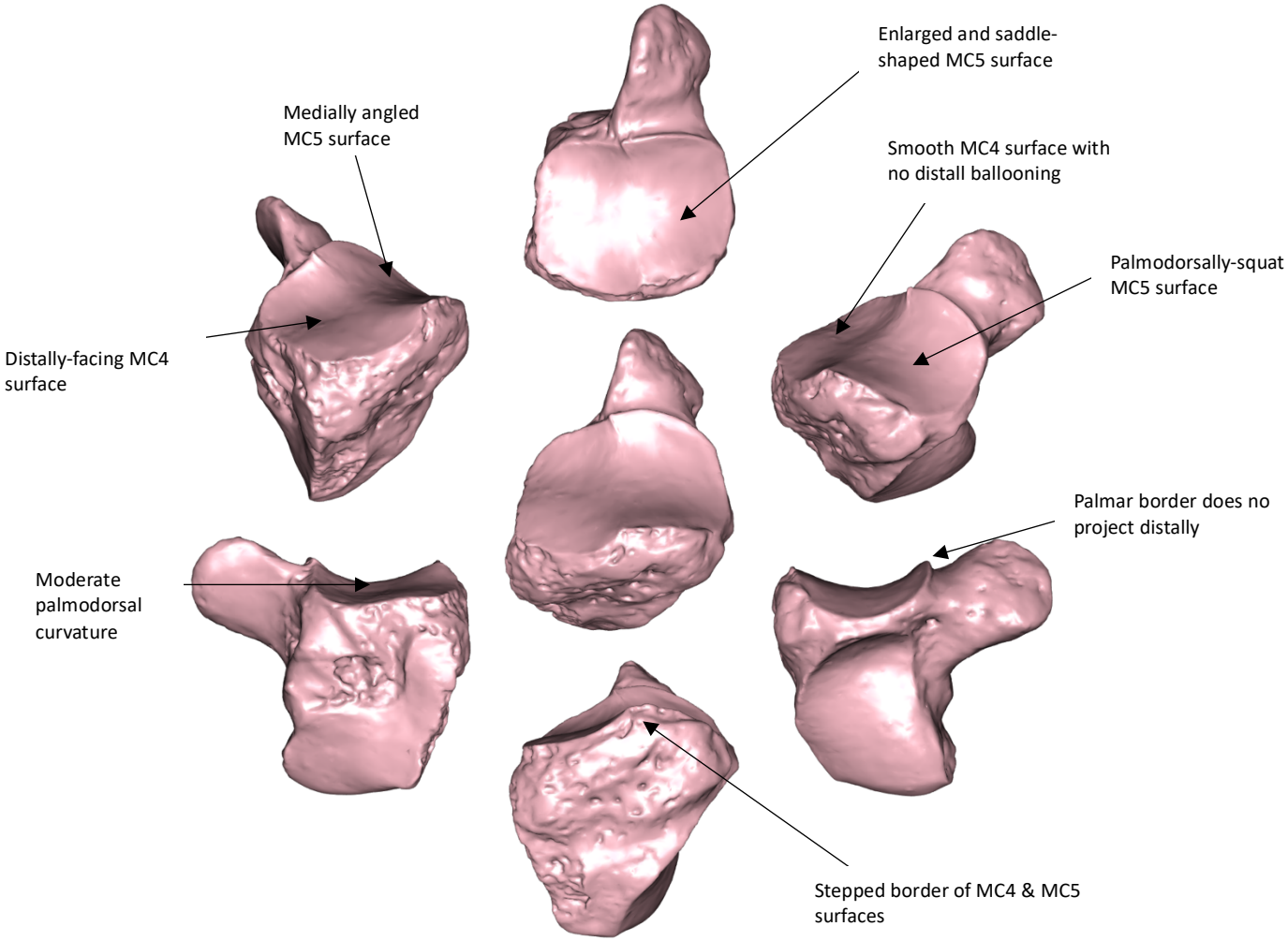

Figure 5.1.1: The mean shape of the hamate's articular surface for the fourth and fifth metacarpals for the *Homo sapiens* population, represented by the specimen closest to the group's mean shape warped to the mean landmark coordinates of the group. The central figure is from the distodorsal view; Clockwise from top: distal, mediodorsal, medial, dorsal, lateral, and laterodorsal views.

Gorilla

The average shape of the hamate-metacarpal articular surface of *Gorilla* is shown in figure 5.1.2. The *Gorilla* mean shape exhibits a notably strong palmodorsal concave curvature, particularly on the surface for the fifth metacarpal, which has a palmar portion that projects strongly distally, resulting in an acute apex of the palmodorsal curvature. The surface for the fifth metacarpal is mediolaterally narrow, and has a strong mediolateral convex curvature concentrated on its dorsal portion. The surface for the fourth metacarpal in *Gorilla* shares a strong palmodorsal curvature, though its palmar edge does not project distally to the same extent. There is a prominent ballooning of the fourth metacarpal surface on the dorsolateral

portion of the surface, resulting in an uneven surface. From a distal viewpoint the mean shape of *Gorilla* is notable in that the articulation for the fourth metacarpal is greater in mediolateral width than the corresponding width of the fifth metacarpal's articulation, with this trend reversing towards the palmar half, where the fifth metacarpal portion of the surface is marginally wider, and, with the strong palmodorsal curvature considered, the surface as a whole is longer palmodorsally than mediolaterally. Lastly, both surfaces face towards a distal direction, and do not display a divergence of direction as is seen in humans.

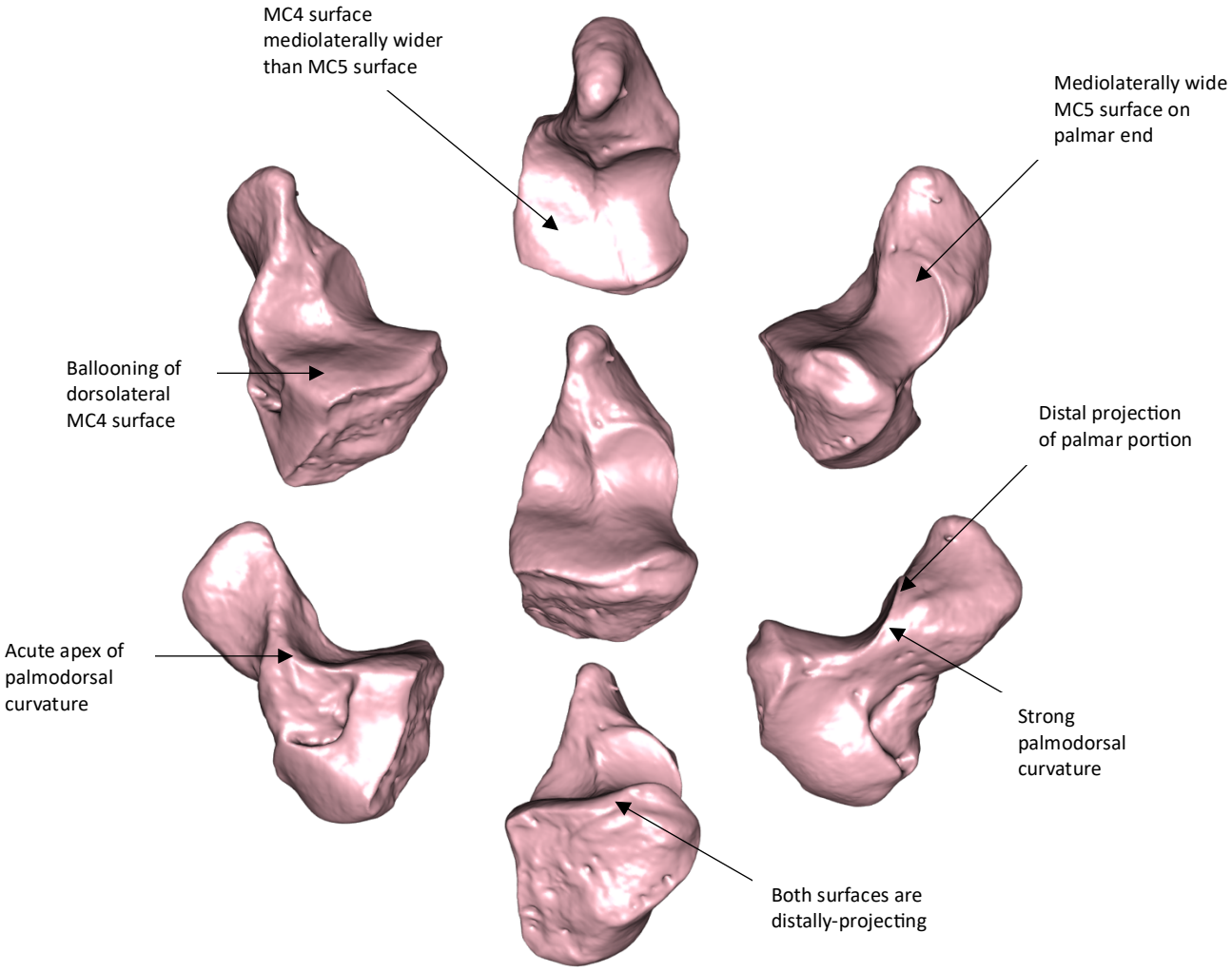

Figure 5.1.2: The mean shape of the hamate's articular surface for the fourth and fifth metacarpals for the *Gorilla* population, represented by the specimen closest to the group's mean shape warped to the average landmark coordinates of the group. The central figure is from the distodorsal view; Clockwise from top: distal, mediodorsal, medial, dorsal, lateral, and laterodorsal views.

Pan troglodytes

The average shape of the *Pan troglodytes* population is shown in figure 5.1.3. In chimpanzees, the articular surface for the fourth metacarpal is notably larger than that of the fifth metacarpal, primarily as a result of an increased mediolateral width of the fourth metacarpal surface at the expense of the fifth. There is a prominent step between the two surfaces, especially on the dorsal edge, with the fifth metacarpal surface situated distal to the fourth. The distally-projecting ballooning of the dorsolateral surface of the fourth metacarpal surface that is characteristic of non-human taxa is extremely prominent in *Pan troglodytes*, resulting in an erratic and irregular surface of the hamate-MC4 surface, which has a palmar half that is strongly concave and scooped, and a dorsal portion that slopes towards the laterodorsal corner of the surface.

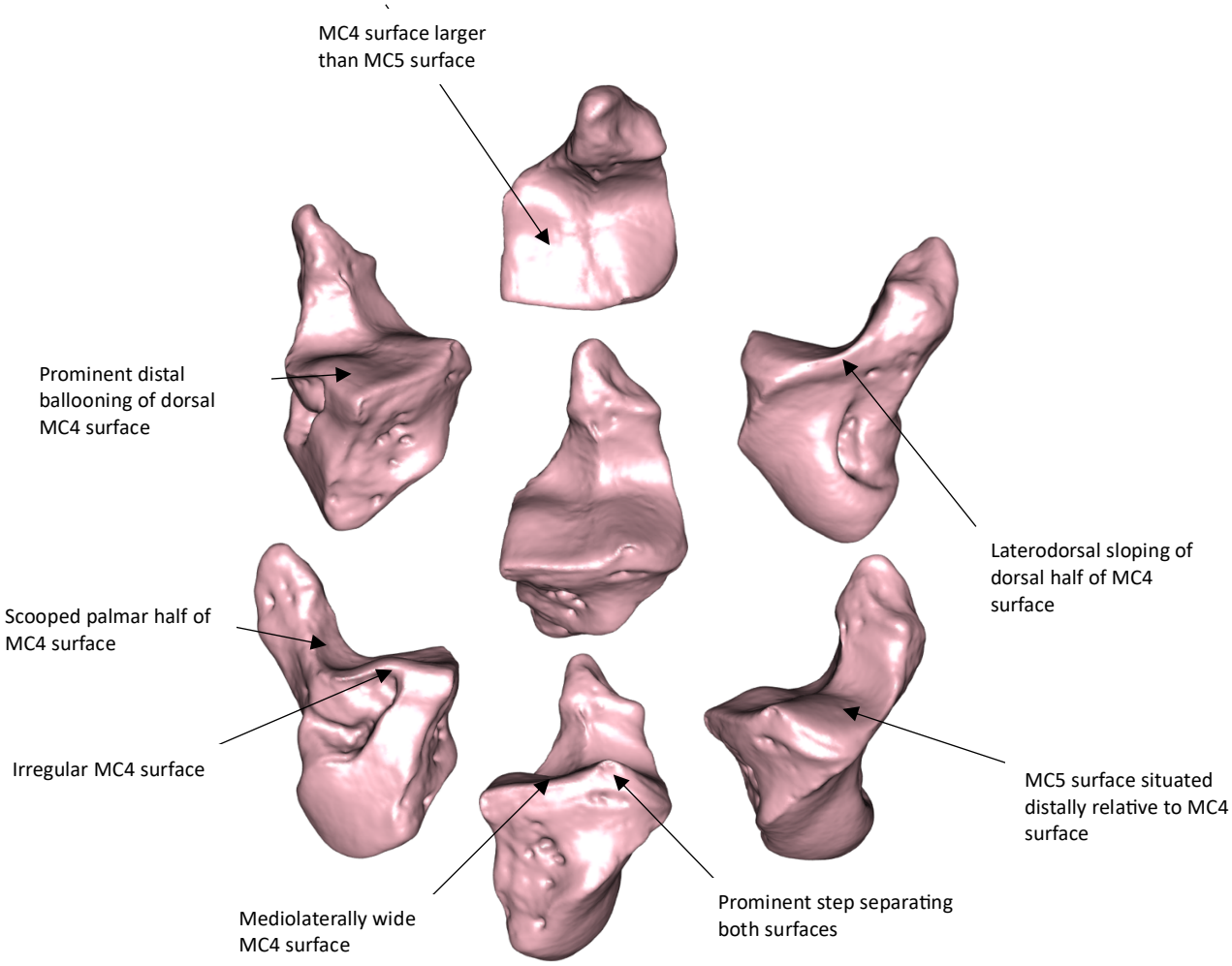

Figure 5.1.3: The mean shape of the hamate's articular surface for the fourth and fifth metacarpals for the *Pan troglodytes* population, represented by the specimen closest to the group's mean shape warped to the group's average landmark coordinates. The central figure is from the distodorsal view; Clockwise from top: distal, mediodorsal, medial, dorsal, lateral, and laterodorsal views.

Pongo

Of all the extant taxa, the average shape of the *Pongo* population, shown in figure 5.1.4, exhibits the greatest continuity between the articulations for the fourth and fifth metacarpals, with no obvious staggering or divergence at the border separating the two. The surface for the fifth metacarpal in *Pongo* is mediolaterally narrow and palmodorsally long, with curved mediopalmar and mediodorsal corners and a strong palmodorsal curvature, resulting in a palmar edge that projects strongly distally. The surface of both metacarpal surfaces bulge distally before sloping proximally towards the dorsal edge. The lateral bulge on the articular surface for the fourth metacarpal is pronounced, and the laterodorsal corner of the surface is strongly sloping, projecting proximolaterally.

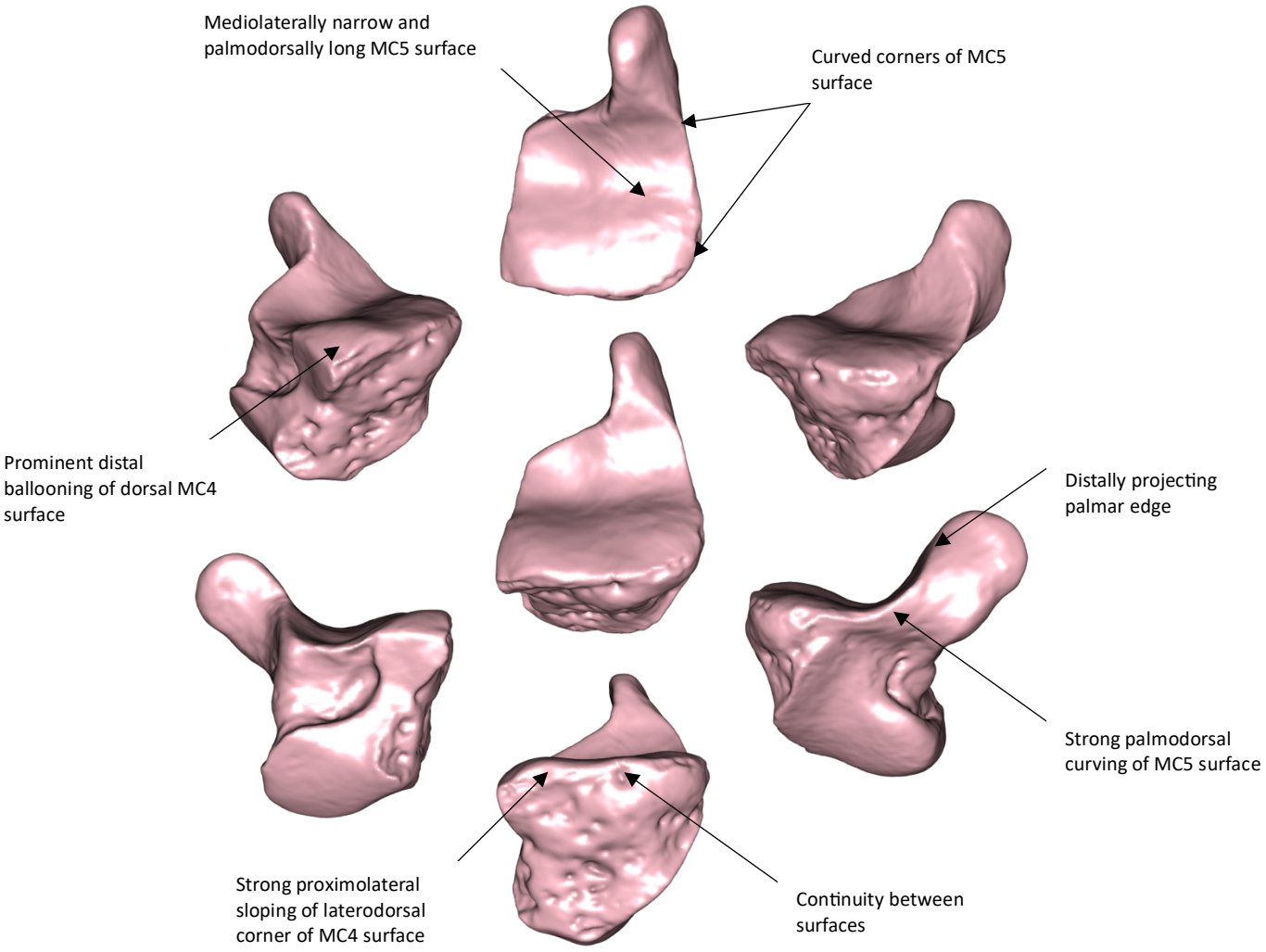

Figure 5.1.4: The mean shape of the hamate's articular surface for the fourth and fifth metacarpals for the *Pongo* population, represented by the specimen closest to the group's mean shape warped to the average landmark coordinates of the population. The central figure is from the distodorsal view; Clockwise from top: distal, mediodorsal, medial, dorsal, lateral, and laterodorsal views.

Table 5.1: Comparison of the mean hamate shape of each extant taxa							
Hamate	Distal	Mediodorsal	Distodorsal	Laterodorsal	Lateral	Dorsal	Medial
Homo sapiens	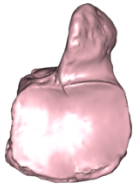	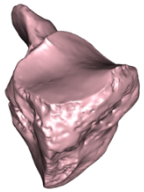	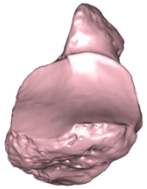	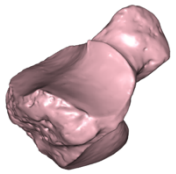	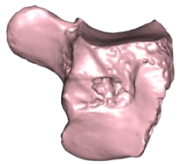	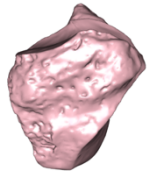	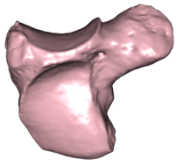
Gorilla	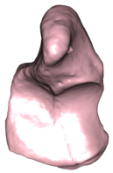	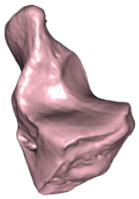	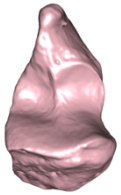	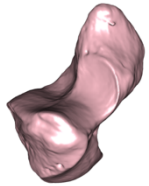	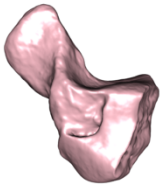	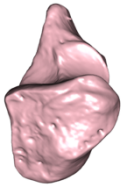	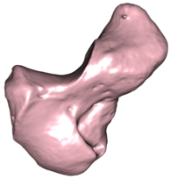
Pan troglodytes	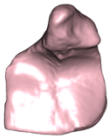	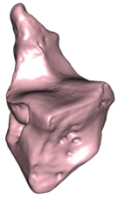	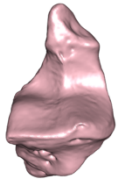	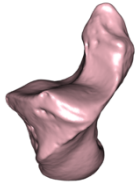		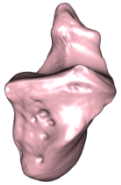	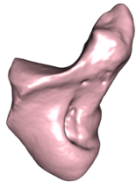
Pongo		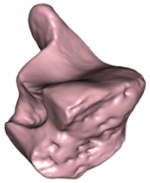		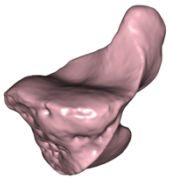	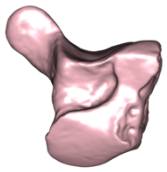	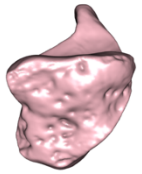	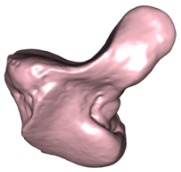

5.2 Principal components analysis of the hamate-metacarpal surface

The first four principal components, which each accounted for more than 5% of the cumulative variance, were considered meaningful according to Bookstein's (2014) criterion, and cumulatively accounted for 61.8% of the total variance. The first principal component accounted for 30.8% of the variation, with PC 2 accounting for 14.2%. PC 3 and 4 accounting for 10.3% and 6.5% of the total variance, respectively. Principal component five, and each subsequent principal component, accounted for less than 5% of the total cumulative variation (figure 5.2.1). The first 15 principal components accounted for more than 90.4% of the total variation, with the 15th principal component accounting for 1.07% of the total variation.

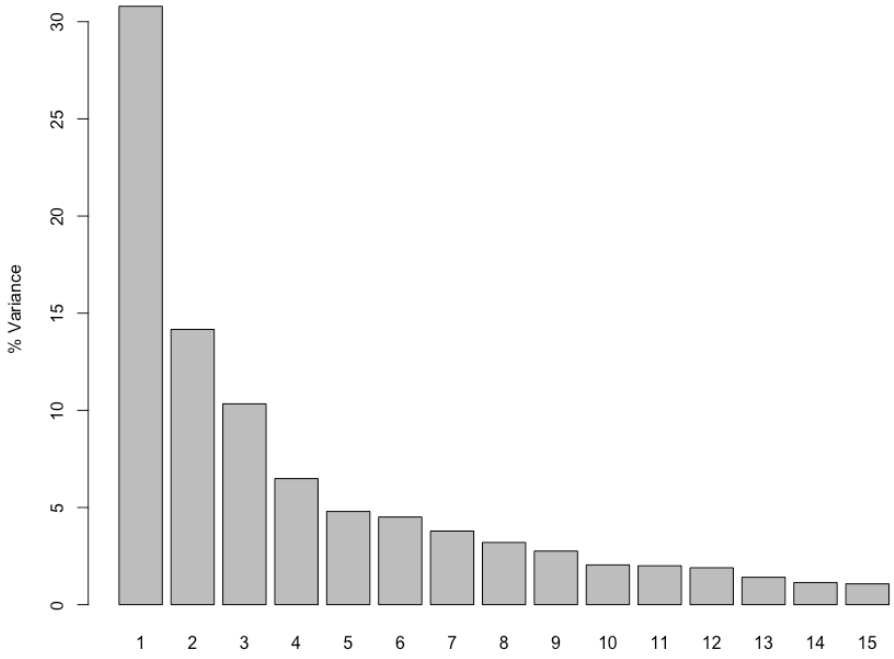

Figure 5.2.1: Graph showing the percentage of variance accountable to the first 15 principal components of the principal component analysis of the hamate's articular surface for the fourth and fifth metacarpals. The first four principal components account for approximately 61.8% of the variation in shape. Principal component 5 and each subsequent PC accounted for less than 5% of the total variance.

Taxonomic differences between groups

The Hotelling's T^2 tests to assess variation between the two constituent species of *Gorilla* and *Pongo* did not reveal significant differences between the means of *Gorilla gorilla* and *Gorilla beringei* along the first four principal components (T^2 = 1.9694, df = 4, 34; p = 0.1215), nor between the two species of *Pongo* (*Pongo abelii* and *Pongo pygmaeus*) (T^2 = 1.7006, df = 4, 12; p = 0.2143). As such, species of both genera were pooled into their respective genera. A multiple analysis of variance (MANOVA) conducted on the scores of the first four principal components of the *Pan troglodytes* sample did not return significant differences in the principal component scores between sub-species of *Pan troglodytes* [F (3, 24) = 1.570, p = 0.128, Wilk's Λ = 0.464]. The *Pan troglodytes* sample was therefore not divided into its constituent sub-species during analysis of the hamate's distal articular surface.

Analysis of Variance (ANOVA)

Results of the analysis of variance of each group along scores of the first four principal components are shown in table 5.2.1. Significant differences ($p \leq 0.05$) between taxa were returned along the first three principal components ($p < 0.001$). No statistically significant differences between the mean scores of the extant taxa was observed along the fourth principal component (p = 0.991), and assessment of a box-and-whisker plot of PC scores along this axis, and bivariate scatterplots involving PC 4 scores, showed that the fourth principal component was not informative in distinguishing between extant taxa or in relating them to fossil specimens.

Table 5.2.1: Results of analysis of variance on principal component scores one through four on extant groups for the hamate-metacarpal surface.

Principal Component	DF	Sum of Squares	Mean Squares	*F* Value	*p*
PC 1	3	0.7599	0.25329	137.2	**<0.001**
PC 2	3	0.3511	0.11703	125.5	**<0.001**
PC 3	3	0.25551	0.08517	124.5	**<0.001**
PC 4	3	0.00016	0.00005	0.036	0.991

The mean and standard deviation of the scores of the first three principal components for each extant group is shown in table 5.2.2, with the principal component values of each fossil for each principal component also shown. Subscripts next to the principal component scores of fossil specimens indicate extant taxa groups to which that particular fossil specimen deviates at least one standard deviation from the mean value of the extant group. AL 333-50 (*Australopithecus afarensis*) was more than one standard deviation from the mean shape of all groups along all three principal components, while KNM-WT-22944-I (*Australopithecus cf. Australopithecus afarensis*) was within 1 SD of the *Homo sapiens* group mean along PC 1 only. Liang Bua 21/22 (*Homo floresiensis*) and UW-101-1729 (*Homo naledi*) were within 1 SD of *Homo sapiens* along the first and third principal component. The only average value that UW-88-1729 (*Australopithecus sediba*) was within one standard deviation of was the third PC mean value of the *Pan troglodytes* group.

Table 5.2.2: Mean and standard deviation (in parentheses) of principal component (PC) scores for *Homo sapiens, Gorilla, Pan troglodytes,* and *Pongo* compared with PC scores of fossil specimens AL333-14 (*Australopithecus afarensis*), Kebara-2 (*Homo neanderthalensis*), KNM-WT-22944 (cf. Australopithecus afarensis), Liang Bua-21/22 (*Homo floresiensis*), Qafzeh-9 (early *Homo sapiens*), and Regourdou-1 (*Homo neanderthalensis*).

Group	*Homo sapiens* (*n* = 54)	*Gorilla* (*n* = 36)	*Pan troglodytes* (*n* = 40)	*Pongo* (*n* =20)	AL 333-50	Kebara-2	KNM-WT 22944	Liang Bua-21/22	Qafzeh-9	Regourdou-1
PC 1	0.0900 (0.0523)	-0.0278 (0.0390)	-0.0606 (0.0364)	-0.0996 (0.0330)	$0.0169_{Hs,G,Pt,Po}$	$0.0168_{Hs,G,Pt,Po}$	$0.0659_{G,Pt,Po}$	$0.0594_{G,Pt,Po}$	$0.0554_{G,Pt,Po}$	$0.00266_{Hs,Pt,Po}$
PC 2	0.0328 (0.0310)	-0.0747 (0.0257)	0.00511 (0.0332)	0.0676 (0.0324)	$-0.0314_{Hs,G,Pt,Po}$	$0.00784_{G,Po}$	$-0.0410_{Hs,G,Pt,Po}$	$-0.0566_{Hs,Pt,Po}$	$0.0342_{G,Po}$	$0.0234_{G,Po}$
PC 3	0.00549 (0.0245)	0.0306 (0.0242)	-0.0615 (0.0305)	0.0605 (0.0238)	$-0.0192_{Hs,G,Pt,Po}$	$0.0422_{Hs,Pt}$	$-0.0241_{Hs,G,Pt,Po}$	$0.0197_{Pt,Po}$	$0.0103_{Pt,Po}$	$-0.0245_{Hs,G,Pt,Po}$

[a] Subscripts indicate a group that the fossil specimen differs at least 1 standard deviation from. Hs = *Homo sapiens*; G = *Gorilla*; Pt = *Pan troglodytes*; Po = *Pongo.*

Table 5.2.2 (*cont.*): Mean and standard deviation (in parentheses) of principal component (PC) scores for *Homo sapiens, Gorilla, Pan troglodytes,* and *Pongo* compared with PC scores of fossil specimens Shanidar-4 (*Homo neanderthalensis*), Tabun-1 (*Homo neanderthalensis*), Tianyuan (early *Homo sapiens*), UW-101-1729 (*Homo naledi*), and UW-88-95 (*Australopithecus sediba*).

Group	*Homo sapiens* (*n* = 54)	*Gorilla* (*n* = 36)	*Pan troglodytes* (*n* = 40)	*Pongo* (*n* =20)	Shanidar-4	Tabun-1	Tianyuan	UW-101-1729	UW-88-1729
PC 1	0.0900 (0.0523)	-0.0278 (0.0390)	-0.0606 (0.0364)	-0.0996 (0.0330)	$0.0386_{G,Pt,Po}$	$0.0315_{Hs,G,Pt,Po}$	$0.113_{G,Pt,Po}$	$0.107_{G,Pt,Po}$	$0.166_{Hs,G,Pt,Po}$
PC 2	0.0328 (0.0310)	-0.0747 (0.0257)	0.00511 (0.0332)	0.0676 (0.0324)	$0.00181_{G,Po}$	$0.0646_{Hs,G,Pt}$	$-0.0148_{Hs,G,Po}$	$-0.0688_{Hs,Pt,Po}$	$-0.0344_{Hs,G,Pt,Po}$
PC 3	0.00549 (0.0245)	0.0306 (0.0242)	-0.0615 (0.0305)	0.0605 (0.0238)	$0.0554_{Hs,G,Pt}$	$0.0382_{Hs,Pt}$	$0.00630_{G,Pt,Po}$	$-0.0176_{G,Pt,Po}$	$-0.0678_{Hs,G,Po}$

[a] Subscripts indicate a group that the fossil specimen differs at least 1 standard deviation from. Hs = *Homo sapiens*; G = *Gorilla*; Pt = *Pan troglodytes*; Po = *Pongo.*

Principal Component 1 shape and groupings

Shape variation along the first principal component (30.8%) was primarily dictated by the relative size and shape of the hamate-MCV articulation compared to that of the hamate-MCIV articulation. The shape differences described by the first principal component were most informative in distinguishing *Homo sapiens* from the non-human great ape groups.

The negative aspect of the first principal component represents a hamate-metacarpal articular shape dominated by the articular surface for the fourth metacarpal, being proportionally greater in absolute size than the hamate-MCV surface. This disparity of size is largely a result of their mediolateral widths. The fifth metacarpal surface is mediolaterally narrow and elongated in the palmodorsal direction. It is also prominently distally-projecting palmarly, resulting in an acute curvature in which the palmar and dorsal portions of the surface are flat and separated by an acute apex. The surface of the hamate's MC-IV articulation, which is in a continuous plane to the fifth metacarpal surface, with both facing distally, and no notable discrepancy or directional change from one to the other, is also strongly palmodorsally concave, but has a prominent distally-projecting ballooning of its laterodorsal surface that is characteristic of the non-human taxa. These features result in an irregularly-shaped hamate-MCIV surface which undulates both in the mediolateral and palmodorsal planes.

The positive aspect of the first principal component is representative of a hamate-metacarpal articular surface that is dominated by a mediolaterally expanded and mildly convex fifth metacarpal surface, and a correspondingly diminished fourth metacarpal articular surface (figure 5.2.2). Palmodorsally the entire surface is compressed compared to the negative shape and does not exhibit the strong palmodorsal curvature, but rather is gentle and oblique in its palmodorsal curvature. There is also an obvious disparity in the orientation of the two surfaces, with the surface for the fifth metacarpal angled medially and sloping proximally relative to the distally-facing fourth metacarpal surface. The medial projection of the surface is magnified by the mediolaterally convex nature of the surface, with the proximomedial inclination expanding towards the mediodorsal edge. The border separating the two metacarpal surfaces projects distally relative to the fourth metacarpal surface and is positioned more laterally so as to accommodate the increased size of the MC-V surface relative to that of MC-IV. The gentle

mediolateral convex curvature of the surface, coupled with a mild palmodorsal concave curvature, results in a saddle-shaped morphology of the hamate-MCV articular surface. In contrast, the smaller hamate-MCIV articular surface is only slightly concave in the palmodorsal plane, and the distally-projecting bulge prominent in non-human taxa is absent, resulting in a more regular and smooth surface.

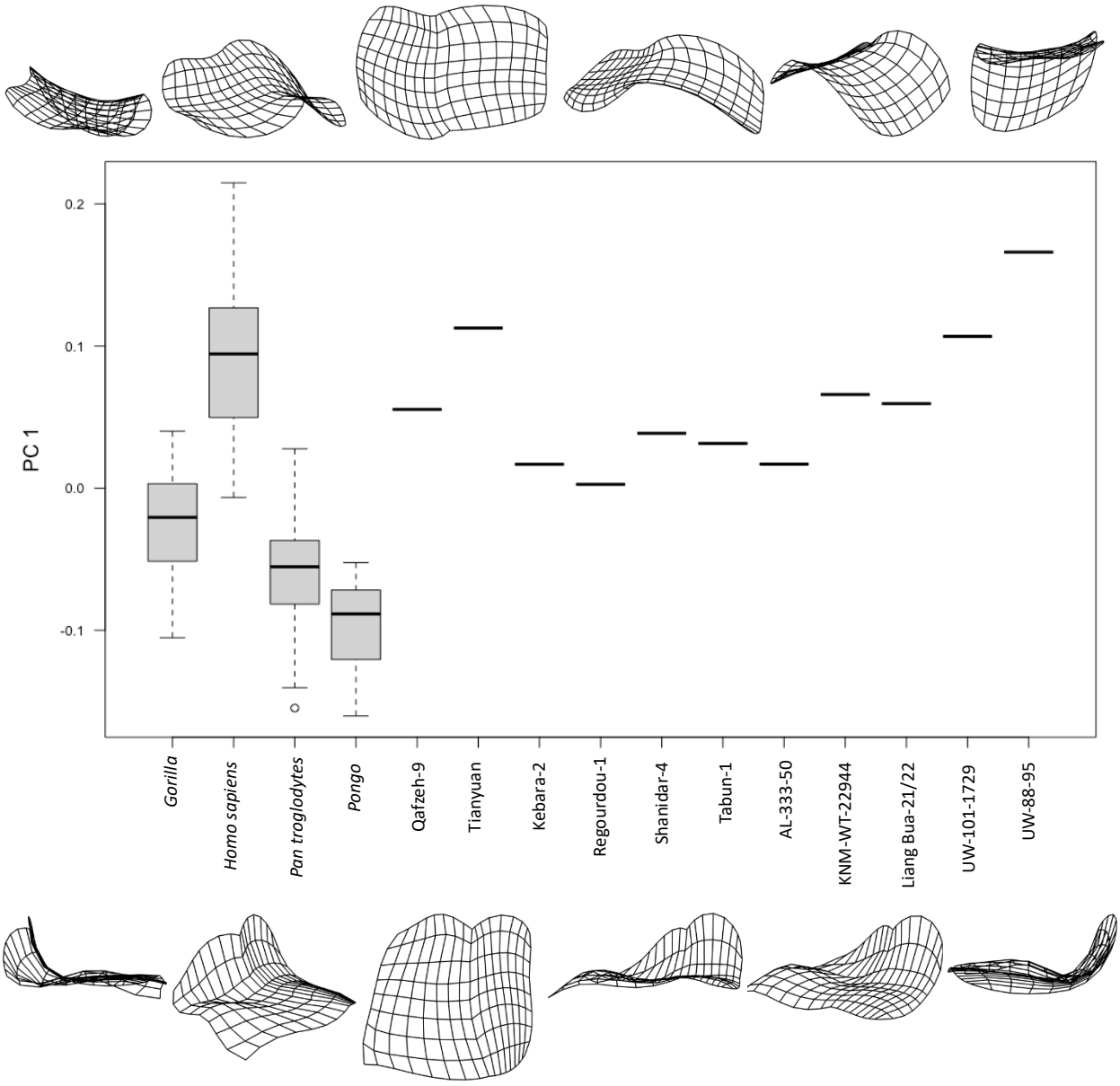

Figure 5.2.2: Boxplot of the first principal component score of the hamate's metacarpal articular surface for *Gorilla, Homo sapiens, Pan troglodytes,* and *Pongo* compared with fossil specimens Qafzeh-9, Tianyuan (early *Homo sapiens*); Kebara-2, Regourdou-1, Shanidar-4, Tabun-1 (*Homo neanderthalensis*); AL-333-50 (*Australopithecus afarensis*); KNM-WT-22944 (cf. Australopithecus afarensis) ; Liang Bua (*Homo floresiensis*); UW-101-1729 (*Homo naledi*); and UW-88-95 (*Australopithecus sediba*). Black lines represent the median of the group, boxes are interquartile ranges, and whiskers are the non-outlier ranges, while white circles are outliers.

Table 5.2.3: Tukey honestly significant difference (HSD) *post-hoc* test results on PC 1 scores among *Homo, Pan, Gorilla, and Pongo.* Significant results ($p < 0.05$) were highlighted in bold.

Group		Mean difference	*p*	95% confidence interval	
				Lower bound	Upper bound
Homo	*Gorilla*	0.118	**<0.001**	0.094	0.142
	Pan troglodytes	0.151	**<0.001**	0.127	0.174
	Pongo	0.190	**<0.001**	0.158	0.221
Gorilla	*Homo*	-0.118	**<0.001**	-0.142	-0.094
	Pan troglodytes	0.033	**0.005**	0.008	0.058
	Pongo	0.072	**<0.001**	0.039	0.104
Pan troglodytes	*Homo*	-0.151	**<0.001**	-0.174	-0.127
	Gorilla	-0.033	**0.005**	-0.058	-0.008
	Pongo	0.039	**0.011**	0.007	0.071
Pongo	*Homo*	-0.190	**<0.001**	-0.221	-0.158
	Gorilla	-0.072	**<0.001**	-0.104	-0.039
	Pan troglodytes	-0.039	**0.011**	-0.071	-0.007

Results of Tukey's Honest Significant Difference test on the scores of the first principal component show that all groups were significantly different from one another (table 5.2.3), with assessment of the box-and-whisker plot (figure 5.2.2) showing a clear distinction between *Homo sapiens*, which dominated, and was almost entirely in the positive aspect of PC 1, and the non-human great ape groups, which were predominantly in the negative aspect. Each of the non-human groups overlapped to a degree with one another, and while the upper quartiles of *Gorilla* and *Pan troglodytes* overlapped with the lower quartile of *Homo sapiens*, the *Pongo* sample did not overlap with *Homo sapiens.*

All the fossil specimens were within the range of the *Homo sapiens* sample, with the two early-*Homo sapiens* specimens (Qafzeh-9 and Tianyuan) within the interquartile range of the group. All four *Homo neanderthalensis* specimens were found in the 1st quartile of *Homo sapiens* and in the 4th quartiles of the African great apes, with Regordou-1 having the lowest PC 1 score of all the fossils specimens. AL-333-50 (*Australopithecus afarensis*) was also found in the vicinity where *Homo sapiens* overlapped with *Gorilla* and *Pan troglodytes.* KNM-WT-22944-I (cf. *Australopithecus afarensis*) and Liang Bua 21/22 (*Homo floresiensis*) were within the lower interquartile range of *Homo sapiens*, and outside the ranges of the other taxa. UW-101-1729 (*Homo naledi*) was in the upper interquartile range of *Homo sapiens,* while UW-88-95 (*Australopithecus sediba*), which had the highest PC-1 score of all the fossil specimens, was in the 4th quartile of the *Homo sapiens* sample.

Principal Component 2 shape and groupings

As with the first principal component, shape change along the second principal component (14.2% of the total shape variation) was dictated by the hamate's articulation for the fifth metacarpal. This axis primarily concerned the strength of palmodorsal concave curvature, and mediolateral flatness and narrowness of the hamate's surface for the fifth metacarpal, and any shape changes in the articular surface of the fourth metacarpal along the second principal component appears to have been dictated by shape variation of the fifth metacarpal articular surface. The second principal component was most informative in separating *Gorilla* from *Homo sapiens* and especially *Pongo.*

The negative aspect of PC2 represents an MC-V surface which is strongly palmodorsally concave, caused by the palmar border of the MC-V surface protruding distally, causing the surface to curve to an almost a 90° angle. The negative PC 2 shape is also more mediolaterally narrow at the waist, and its dorsal portion, which exhibits a slight convex curvature laterally, slopes toward its medial edge. The palmar portion is mediolaterally flat and expanded. The positive aspect of PC 2 represents a hamate-metacarpal surface in which the mediolateral and palmodorsal curvature of the fifth metacarpal articulation is less extreme. The palmar portion of the hamate-MCV surface is not as distally-projecting, nor is it as mediolaterally expanded as in the maximum shape. As a result, there is no convex curving of the dorsal border, and the surface is mediolaterally widest at the central portion.

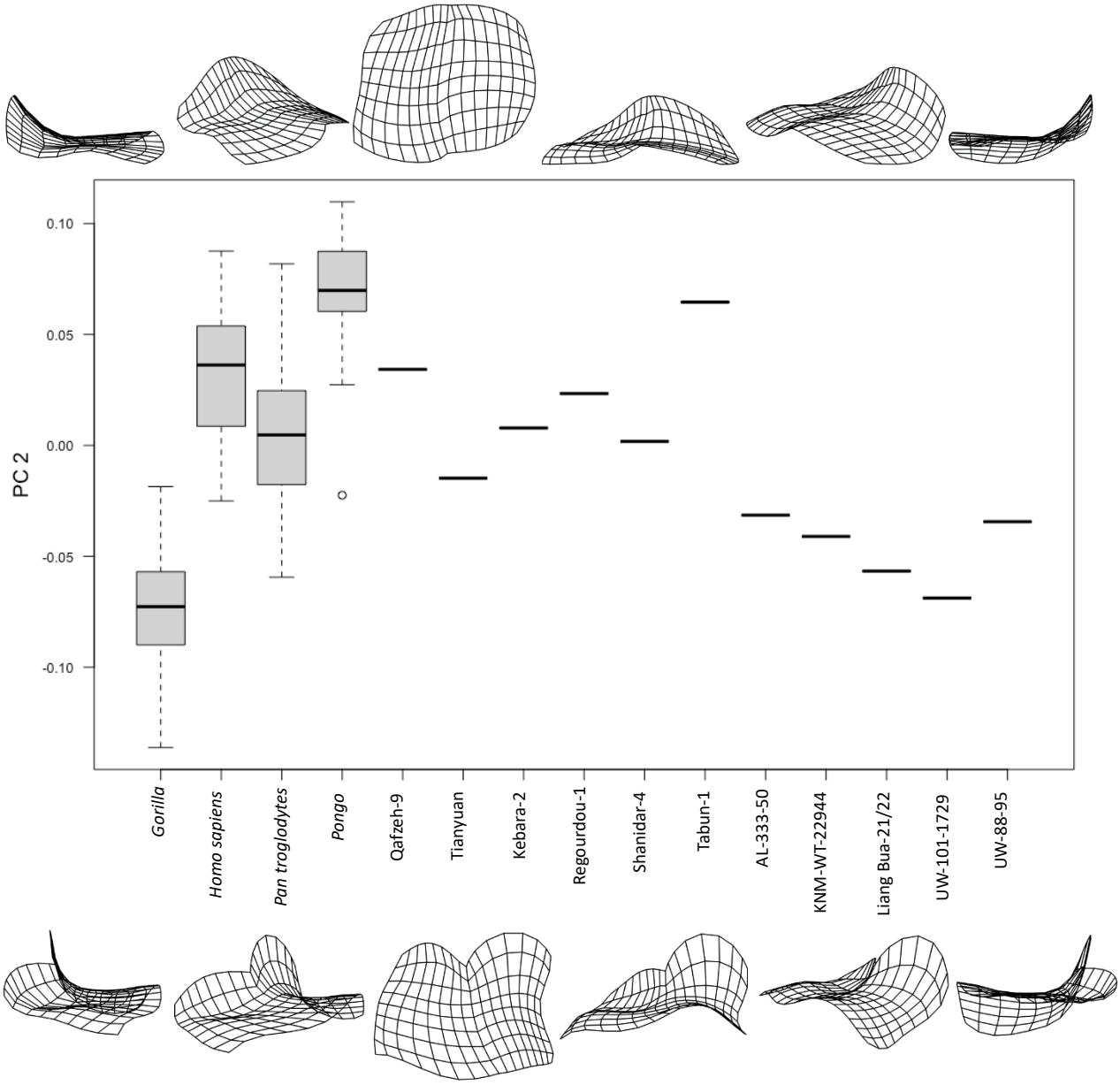

Figure 5.2.3: Boxplot of the second principal component score of the hamate's metacarpal articular surface for *Gorilla, Homo sapiens, Pan troglodytes,* and *Pongo* compared with fossil specimens Qafzeh-9, Tianyuan (early *Homo sapiens*); Kebara-2, Regourdou-1, Shanidar-4, Tabun-1 (*Homo neanderthalensis*); AL-333-50 (*Australopithecus afarensis*); KNM-WT-22944 (cf. Australopithecus afarensis); Liang Bua (*Homo floresiensis*); UW-101-1729 (*Homo naledi*); and UW-88-95 (*Australopithecus sediba*). Black lines represent the median of the group, boxes are interquartile ranges, and whiskers are the non-outlier ranges.

Table 5.2.4: Tukey honestly significant difference (HSD) *post-hoc* test results on PC 2 scores among *Homo, Pan, Gorilla, and Pongo.* Significant results ($p < 0.05$) were highlighted in bold.

Group		Mean difference	*p*	95% confidence interval	
				Lower bound	Upper bound
Homo sapiens	*Gorilla*	0.107	**<0.001**	0.091	0.124
	Pan troglodytes	0.028	**<0.001**	0.011	0.044
	Pongo	-0.035	**<0.001**	-0.057	-0.013
Gorilla	*Homo sapiens*	-0.107	**<0.001**	-0.124	-0.091
	Pan troglodytes	-0.080	**<0.001**	-0.098	-0.062
	Pongo	-0.142	**<0.001**	-0.165	-0.119
Pan troglodytes	*Homo sapiens*	-0.028	**<0.001**	-0.044	-0.011
	Gorilla	0.080	**<0.001**	0.062	0.098
	Pongo	-0.062	**<0.001**	-0.085	-0.040
Pongo	*Homo sapiens*	0.035	**<0.001**	0.013	0.057
	Gorilla	0.142	**<0.001**	0.119	0.165
	Pan troglodytes	0.062	**<0.001**	0.040	0.085

Results of Tukey's Honest Significant Difference test on the second principal component scores showed that, as with the first principal component, all groups were significantly different from each other (table 5.2.4). Analysis of the box-and-whisker representation (figure 5.2.3) show that *Gorilla* and *Pongo* were the two groups that differentiated most from each other, with *Gorilla* being entirely in the negative aspect of PC 2, and *Pongo* entirely in the positive aspect. *Pan troglodytes,* which had a mean value approximating neutrality, was distributed fairly evenly between the negative and positive halves, and overlapped considerably with every other group. The *Homo sapiens* sample also overlapped considerably with *Pan troglodytes* and *Pongo*, but only marginally with *Gorilla*, being predominantly in the positive half of PC 2.

The fossil specimens were distributed widely across PC 2, and scores of the second principal component were of less utility in assessing shape affinities of the fossil specimens compared with the first principal component. All the early *Homo sapiens* and *Homo neanderthalensis* specimens were within the ranges of *Homo sapiens* and *Pan troglodytes*, with Qafzeh-9 and Tabun-1 also in the *Pongo* range. All earlier fossil specimens were concentrated in the negative half of the PC. AL-333-50 (*Australopithecus afarensis*), KNM-WT-22944-I (*Australopithecus cf. Australopithecus afarensis*), Liang Bua-21/22 (*Homo floresiensis*) and UW-88-95 (*Australopithecus sediba*) all had PC 2 scores lower than the range of *Homo sapiens*, but within the ranges of *Gorilla* and *Pan troglodytes.* UW-101-1729 (*Homo naledi*) was the only fossil specimen within the range of a solitary extant group, having the lowest PC 2 score of all fossil

specimens and residing within the interquartile range of *Gorilla*, near the mean value of that group.

Principal Component 3 shape and groupings

Shape variation along the third principal component accounted for 10.3% of the total shape variation and was dictated primarily by the strength of palmodorsal concave curvature of the central aspect of the surface. The third principal component was most informative in distinguishing between *Pan troglodytes* and *Pongo.*

The negative aspect of PC3 represents a hamate-metacarpal surface in which the palmodorsal midline is highly curved and elevated distally. This is accompanied by mediopalmar and lateropalmar corners which are more proximal than the central palmar apex. The distal projection of the central ridge, which is particularly pronounced at the proximal and dorsal convergence of the two surfaces, resulted not only in the two surfaces being highly concaved at their shared border, but also a hamate-metacarpal surface that is highly stepped, with the two surfaces being incongruent. The hamate-MCV surface slopes towards its medial edge in a relatively uniform manner. However, the hamate-MCIV surface is more irregular, exhibiting a strong concaved dorsal edge which develops palmarly into the distally-projecting bulge characteristic of the non-human groups (figure 5.2.4).

The central border in the shape representative of the PC 3 maxima displays a much gentler and more oblique proximodistally-concave curvature, resulting in a relatively mediolaterally flat hamate-metacarpal surface where the transition from the MC-IV surface to the MC-V surface is smooth and uniform, with both metacarpal surfaces in the same plane, facing squarely distally. Furthermore, the palmar corners of the hamate-metacarpal surfaces both project further out and palmar-wards relative to the minimum shape. These aspects result in a smoother overall shape of the hamate-metacarpal surface, and a less prominent distally-projecting bulge on the MC4 surface amplified this trend.

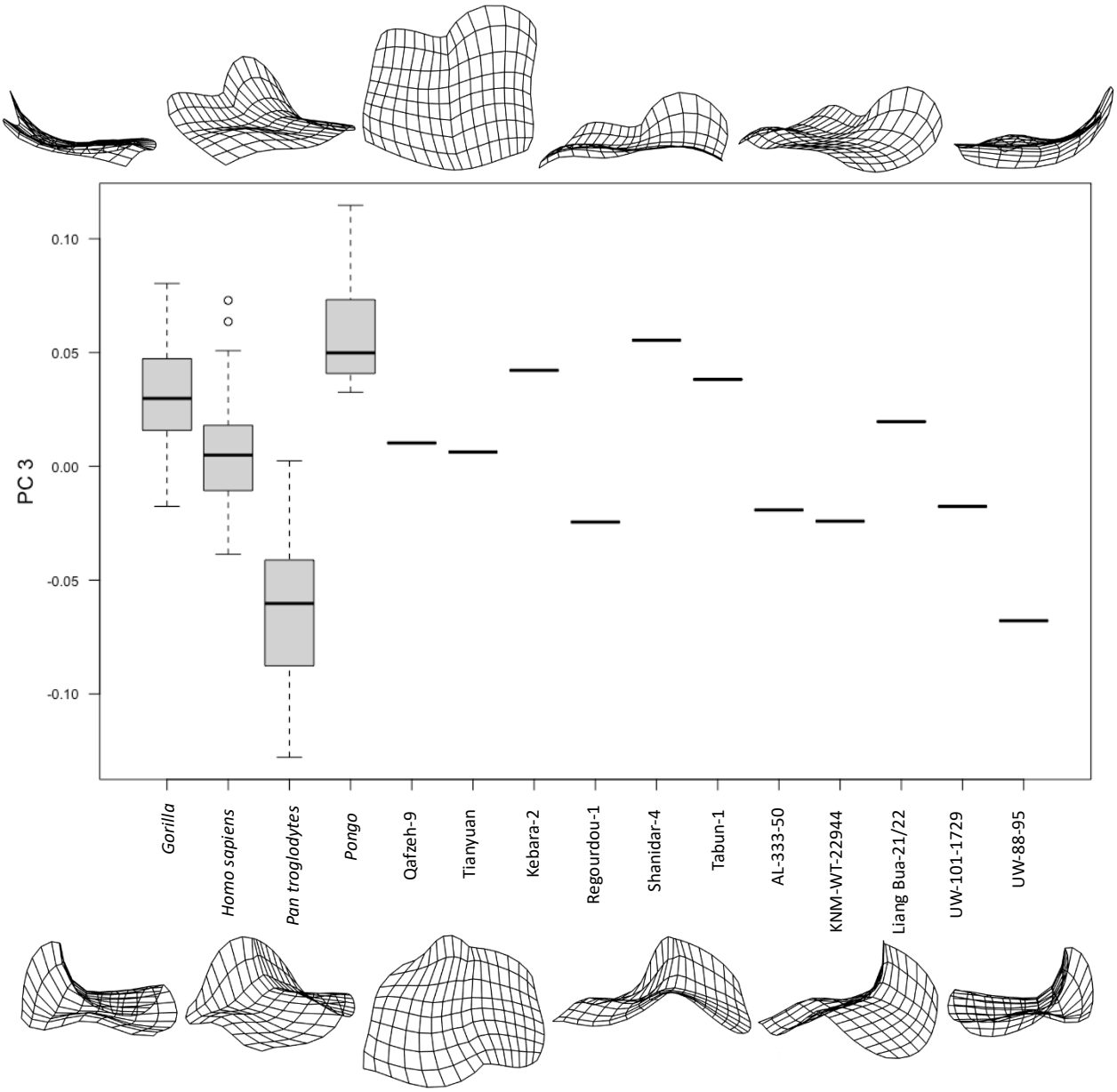

Figure 5.2.4: Boxplot of the third principal component score of the hamate's metacarpal articular surface for *Gorilla, Homo sapiens, Pan troglodytes,* and *Pongo* compared with fossil specimens Qafzeh-9, Tianyuan (early *Homo sapiens*); Kebara-2,Regourdou-1, Shanidar-4, Tabun-1 (*Homo neanderthalensis*); AL-333-50 (*Australopithecus afarensis*); KNM-WT-22944 (cf. Australopithecus afarensis) ; Liang Bua (*Homo floresiensis*); UW-101-1729 (*Homo naledi*); and UW-88-95 (*Australopithecus sediba*). Black lines represent the median of the group, boxes are interquartile ranges, and whiskers are the non-outlier ranges.

Table 5.2.5: Tukey honestly significant difference (HSD) *post-hoc* test results on PC 3 scores among *Homo, Pan, Gorilla, and Pongo.* Significant results ($p < 0.05$) were highlighted in bold.

Group		Mean difference	*p*	95% confidence interval	
				Lower bound	Upper bound
Homo sapiens	*Gorilla*	-0.025	**<0.001**	-0.040	-0.011
	Pan troglodytes	0.067	**<0.001**	0.053	0.081
	Pongo	-0.055	**<0.001**	-0.074	-0.036
Gorilla	*Homo sapiens*	0.025	**<0.001**	0.011	0.040
	Pan troglodytes	0.092	**<0.001**	0.077	0.107
	Pongo	-0.030	**0.001**	-0.050	-0.010
Pan troglodytes	*Homo sapiens*	-0.067	**<0.001**	-0.081	-0.053
	Gorilla	-0.092	**<0.001**	-0.107	-0.077
	Pongo	-0.122	**<0.001**	-0.142	-0.102
Pongo	*Homo sapiens*	0.055	**<0.001**	0.036	0.074
	Gorilla	0.030	**0.001**	0.010	0.050
	Pan troglodytes	0.122	**<0.001**	0.102	0.142

Results of Tukey's Honest Significant Difference test on the third principal component scores are reported in table 5.2.5. As with the previous two principal components, the results showed that all groups were significantly different from each other. Investigation of the box and whisker plot show that the third principal component was most informative in separating *Pan troglodytes* and *Pongo* from one another (figure 5.2.4), with *Pan troglodytes* occupying the negative aspect of PC 3, and *Pongo* exclusively within the positive aspect. The *Homo sapiens* group, whose median value was close to neutral, was distributed evenly between the negative and positive halves and overlapped considerably with all three non-human groups. The interquartile range of *Gorilla* was entirely within the positive half, with much of its range overlapping with *Pongo*, and only a portion of its 1st quartile being in the negative aspect, overlapping with the higher scores of *Pan troglodytes*.

Both the early *Homo sapiens* specimens (Qafzeh-9 and Tianyuan) had PC 3 scores that were very close to the median value of the extant *Homo sapiens* sample. Of the four *Homo neanderthalensis* specimens, three (Kebara-2, Shanidar-4, and Tabun-1) had positive PC 3 scores and were within the ranges of *Gorilla, Pongo,* and *Homo sapiens*, while Regourdou-1 had a negative PC 3 score and was within the range of *Homo sapiens* and *Pan troglodytes.* AL-333-50 (*Australopithecus afarensis*), KNM-WT-22944-I (*Australopithecus cf. Australopithecus afarensis*), and UW-1729 (*Homo naledi*) were also found within the ranges of *Homo sapiens* and *Pan troglodytes*, while Liang Bua-21/22 (*Homo floresiensis*) was in the positive aspect, within the

ranges of *Homo sapiens* and *Gorilla*. Among fossil specimens, only UW-88-95 (*Australopithecus sediba*) was clearly outside the *Homo sapiens* range, and, having the most negative PC score of all fossil samples, was in the 2nd quartile of the *Pan troglodytes* group.

Bivariate Scatterplots of Principal Component Scores

PC 1 v PC 2

A bivariate scatterplot of PC 1 against PC 2 (figure 5.2.5) effectively separated *Homo sapiens*, situated primarily in the upper right quadrant, from all other taxa, with no overlap with any other taxon. The non-human taxa were positioned mostly in the left half of the scatterplot. *Pongo* was almost entirely in the upper left, and *Gorilla* was predominantly in the lower left quadrant, with a third of its sample in the lower right quadrant. While there was no overlap in the morphospaces of *Gorilla* and *Pongo*, the *Pan troglodytes* sample, being distributed across both the upper and lower left quadrants, overlapped with both the *Gorilla* and *Pongo* samples.

Both the early *Homo sapiens* fossil specimens (Tianyuan and Qafzeh-9) were found within the *Homo sapiens* morphospace, as was Tabun-1 (*Homo neanderthalensis*). However, the other three Neanderthal specimens were either on the border of the *Homo sapiens* morphospace (Shanidar-4), or outside it, in the area between *Pan troglodytes* and *Homo sapiens*, albeit remaining in the upper right quadrant (Kebara-2 and Regourdou-1). AL-333-50 (*Australopithecus afarensis*) was in the vicinity of the *Pan troglodytes* morphospace and was the sole fossil specimen which was unambiguously nearer to the great ape groups than to modern humans. The remaining four fossil specimens (Liang Bua (*Homo floresiensis*); KNM-WT-22944-I (*Australopithecus cf. Australopithecus afarensis*); UW-101-1729 (*Homo naledi*); UW-88-95 (*Australopithecus sediba*) were all in the lower right quadrant, below the *Homo sapiens* morphospace.

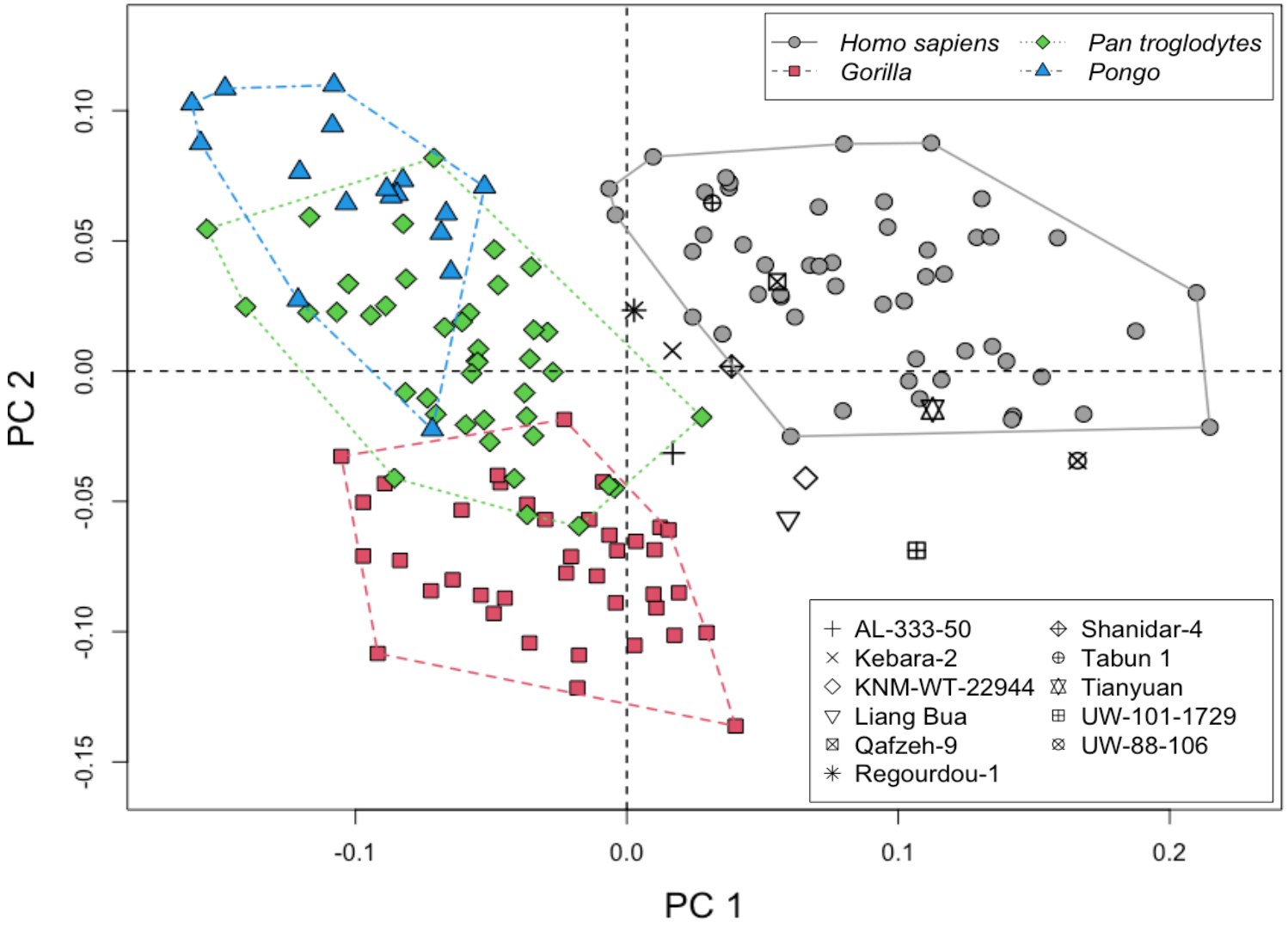

Figure 5.2.5: Scatterplot of the first vs. second principal component (PC 1 (30.8%) vs. PC 2 (14.2%)) scores of extant samples (*Homo sapiens*, Gorilla, Pan *troglodytes,* and *Pongo*) and fossil specimens. The *Homo sapiens* sample dominates the upper-right section of the plot, with non-human taxa concentrated to the left, as are all the fossil specimens.

PC 1 v PC 3

The bivariate scatterplot of PC 1 against PC 3 was most informative in separating *Pan troglodytes* from all other groups, though there was clear separation between all four taxa (figure 5.2.6). The lower left quadrant is dominated by *Pan troglodytes*, while the *Pongo* sample is entirely within the upper right quadrant. *Gorilla* is also predominantly in the upper left quadrant, although the *Gorilla* morphospace does encroach on the two right quadrants. *Homo sapiens* is again predominantly within the right half of the morphospace. The only taxa to overlap with any other taxa is *Gorilla,* which is situated between *Pongo* and *Homo sapiens*, and shares morphospace with both. *Pan troglodytes* does not overlap with any other group.

All but four of the fossil specimens are situated solely within the *Homo sapiens* morphospace, with three fossil specimens not located in the *Homo sapiens* morphospace. Kebara-2 (*Homo neanderthalensis*) is located at the intersection of *Homo sapiens* and *Gorilla*, while UW-88-95 (*Australopithecus sediba*) is located to the far right of the boxplot, below *Homo sapiens*. AL-333-50 (*Australopithecus afarensis*) is between the *Pan troglodytes* and *Homo sapiens* morphospace*,* and just below that of *Gorilla*. Interestingly, Regourdou-1 (*Homo neanderthalensis*) lies within the *Pan troglodytes* morphospace for this scatterplot and is the only *Homo* fossil which is not in the *Homo sapiens* morphospace.

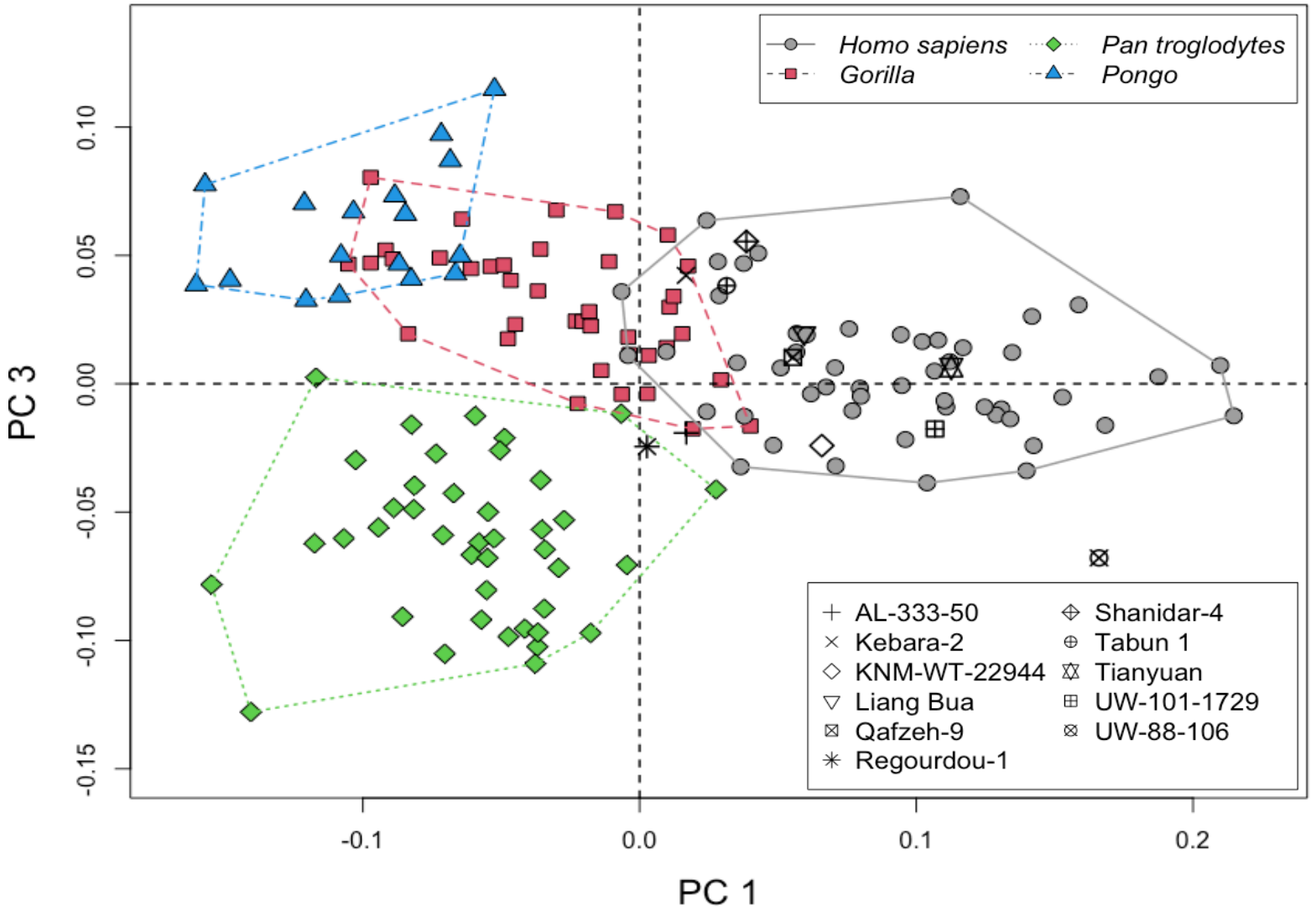

Figure 5.2.6: Scatterplot of the first vs. third principal component (PC 1 (30.8%) vs. PC 3 (10.3%)) scores of extant samples (*Homo sapiens*, Gorilla, Pan *troglodytes,* and *Pongo*) and fossil specimens. *Homo sapiens* dominates the right half of the plot, with non-human taxa to the left. *Pan troglodytes* dominates the lower half.

PC 2 v PC 3

A bivariate scatterplot of PC2 against PC3 was successful in separating the non-human groups from each other with no overlap (figure 5.2.7). The *Homo sapiens* morphospace is relatively central, spanning all four quadrants, and overlaps with all three non-human groups to varying extents. *Pongo* occupies the upper right quadrant (with the exception of a solitary datapoint in the upper left); *Gorilla* is predominantly in the upper left quadrant, while the morphospace of *Pan troglodytes* is almost entirely in the lower half of the scatterplot. There is considerable overlap between the morphospaces of *Homo sapiens* and *Pan troglodytes,* while a solitary *Gorilla* specimen encroached on the *Homo sapiens* morphospace. The *Homo sapiens* and *Pongo* samples slightly overlap each other in the upper right quadrant.

All the Neanderthal and early *Homo sapiens* fossil specimens (early *Homo sapiens*: Tianyuan; Qafzeh-9. *Homo neanderthalensis*: Kebara-2; Shanidar-4; Tabun-1; Regourdou-1) are within the *Homo sapiens* morphospace (Regourdou-1 was in the space where *Pan troglodytes* and *Homo sapiens* overlap, while Tabun-1 is on the border of *Pongo*'s morphospace). All the Australopithecine specimens (AL-333-50 (*Australopithecus afarensis*), KN-WT-22944-I (*Australopithecus cf. Australopithecus afarensis*) and UW-88-95 (*Australopithecus sediba*) are located solely within the *Pan troglodytes* morphospace in the lower left quadrant. UW-101-1729 (*Homo naledi*) is also in the lower-left quadrant, but in the space between *Gorilla* and *Pan troglodytes*, while Liang Bua-21/22 (*Homo floresiensis*) is the sole fossil specimen to fall within the *Gorilla* morphospace (figure 5.2.7).

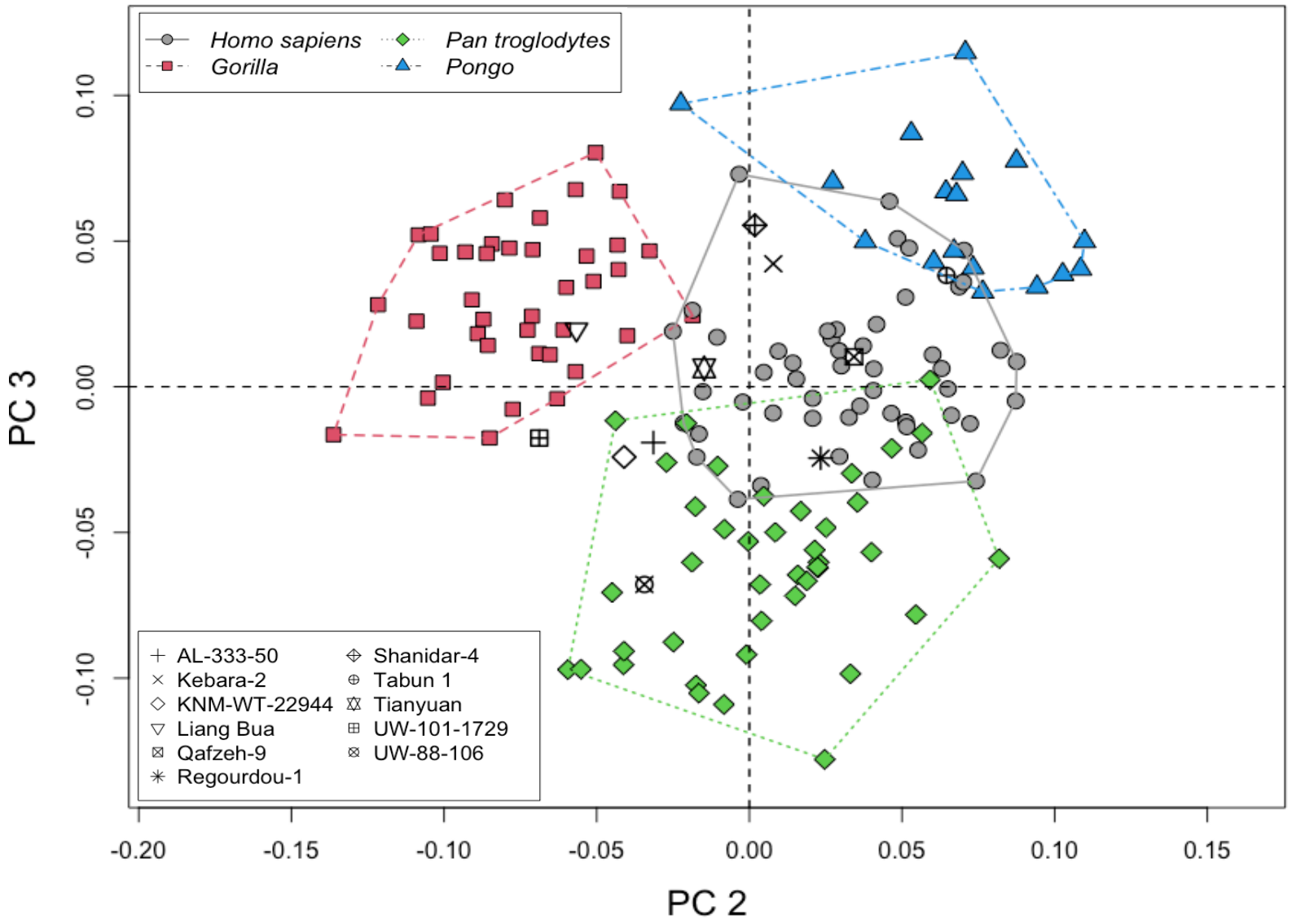

Figure 5.2.7: Scatterplot of the second vs. third principal component (PC 2 (14.2%) vs. PC 3 (10.3%)) scores of extant samples (*Homo sapiens*, Gorilla, Pan *troglodytes,* and *Pongo*) and fossil specimens. This plot separates the non-human great ape samples from each other.

5.3 Canonical variate analysis of the hamate-metacarpal surface

The first 15 principal components, which accounted for 90.4% of the total variance, were used to conduct a canonical variate analysis (CVA) of the hamate's metacarpal articular surface. The CVA had an accuracy of 99% in categorizing extant cases into their *a priori* taxon group (k = 0.99) (table 5.3.1), with a 100% success-rate for the *Homo sapiens, Gorilla*, and *Pongo* samples, and a 97.5% success rate for the *Pan troglodytes* sample, with one *Pan troglodytes* specimen misclassified as *Gorilla*. The first CV axis accounted for 50.0% of the variance of shape between groups, while the second and third CV axes contributed to 29.0% and 21.9% of the variance, respectively.

Table 5.3.1: Cross-validation counts for a CVA of the first 15 PCs of the hamate's metacarpal articulation.

	Gorilla	*Homo sapiens*	*Pan troglodytes*	*Pongo*	*N*
Gorilla	39 (100%)	0	0	0	39
Homo sapiens	0	51 (100%)	0	0	51
Pan troglodytes	1	0	40 (97.6%)	0	41
Pongo	0	0	0	17 (100%)	17

MANOVA along the canonical variates axes returned significant results between extant groups ($F(3, 144) = 364.91$, $p < 0.001$, Wilks' $\Lambda = 0.003$). One-way analysis of variance tests performed on the three CV scores of the extant sample, with the sample divided by groups, indicated that at least one pairwise comparison of means between two of the groups were significant along all three CV axes (table 5.3.2). Results of the Hotelling's HSD tests along the scores of the first canonical variate axis showed that the mean values of all groups were significantly different from each other, with the exception of the pairwise comparison between *Pan troglodytes* and *Pongo* (p = 0.115, 95% C.I. = -0.101, 1.398) (table 5.3.3). This pattern was repeated along the second canonical variate axis, with the mean values of for *Pan troglodytes* and *Pongo* not differing significantly (p = 0.917, 95% C.I. = -0.936, 0.564). Along the third canonical variate there was no significant difference between the mean values of *Homo sapiens* and *Gorilla* (p = 0.667, 95% C.I. = -0.795, 0.311), however all other pairwise comparisons were statistically significant (table 5.3.3).

Table 5.3.2: Results of analysis of variance on canonical variate scores on extant groups.

Canonical Variate	DF	Sum of Squares	Mean Squares	*F* Value	*p*
CV 1	3, 144	1278	426	426	**<0.001**
CV 2	3, 144	755.8	251.9	251.9	**<0.001**
CV 3	3, 144	569.3	189.8	189.8	**<0.001**

Table 5.3.3: *P*-values for Tukey's HSD pairwise comparisons of canonical variate scores along three CV axes for the hamate-metacarpal surface.

	Homo sapiens	Gorilla	Pan troglodytes	Pongo
Canonical Variate 1 (49.1%)				
Homo sapiens	-	**<0.001**	**<0.001**	**<0.001**
Gorilla		-	**<0.001**	**<0.001**
Pan troglodytes			-	0.115
Pongo				-
Canonical Variate 2 (29.0%)				
Homo sapiens	-	**<0.001**	**<0.001**	**<0.001**
Gorilla		-	**<0.001**	**<0.001**
Pan troglodytes			-	0.917
Pongo				-
Canonical Variate 3 (21.9%)				
Homo sapiens	-	0.667	**<0.001**	**<0.001**
Gorilla		-	**<0.001**	**<0.001**
Pan troglodytes			-	**<0.001**
Pongo				-

The CVA of the first 15 principal component scores on the hamate-metacarpal articular surface classified all fossil specimens as belonging to the *Homo sapiens* group, with all but two assigned to *Homo sapiens* with a confidence of at least 99.9% (table 5.3.4). AL-333-50 (*Australopithecus afarensis*) was classified as *Homo sapiens* with a likelihood of 66.8%, and a 33.2% likelihood of belonging to *Pan troglodytes.* Similarly, Liang Bua-21/22 (*Homo floresiensis*) had a likelihood of 54.3% of belonging to the human group, and a 45.4% likelihood of belonging to *Pan troglodytes* (table 5.3.4).

Table 5.3.4: Canonical variate analysis (CVA) classification results of fossil specimens based on scores of the first 15 principal components. The column to the right shows the group to which each fossil specimen was classified by the linear discriminant analysis. Results are in percentage.

	Homo sapiens	*Gorilla*	*Pan troglodytes*	*Pongo*	Classification
AL-333-50	66.8	0.0	33.2	0.0	*Homo sapiens*
Kebara-2	100.0	0.0	0.0	0.0	*Homo sapiens*
KNM-WT-22944	100.0	0.0	0.0	0.0	*Homo sapiens*
Liang Bua-21/22	54.3	0.1	45.4	0.3	*Homo sapiens*
Qafzeh-9	100.0	0.0	0.0	0.0	*Homo sapiens*
Regourdou-1	100.0	0.0	0.0	0.0	*Homo sapiens*
Shanidar-4	100.0	0.0	0.0	0.0	*Homo sapiens*
Tabun-1	100.0	0.0	0.0	0.0	*Homo sapiens*
Tianyuan	100.0	0.0	0.0	0.0	*Homo sapiens*
UW-101-1729	99.9	0.1	0.0	0.0	*Homo sapiens*
UW-88-95	100.0	0.0	0.0	0.0	*Homo sapiens*

First Canonical Variate Axis

Shape change along the first canonical variate axis, which accounted for 50.0% of the variance in shape between groups, corresponds to the shape change along the first principal component (described in section 5.2 and represented visually in figure 5.2.2), in which the minima represents a shape dominated by a mediolaterally elongated hamate-MCIV surface which is acutely curved in the palmodorsal plane with a prominent laterodorsal ballooning, and an overall surface that is acutely palmodorsally hooked. The maxima of CV 1 represents a surface dominated by a mediolaterally expanded surface for the fifth metacarpal which is mildly concaved palmodorsally and convex mediolaterally, resulting in a saddle-shaped hamate-MCV articulation. The hamate-metacarpal surface is stepped along the border of the two articulations, with the surface for the fifth metacarpal angled medially. Wireframe representations of the minimum and maximum shapes are shown in figure 5.3.1. CV 1 separates *Homo sapiens*, which is exclusively in the positive range of the axis, from the other extant taxa groups, which are primarily in the negative range (figure 5.3.1). While there is considerable overlap in the range of CV 1 scores of the extant non-human taxa (especially between *Pan troglodytes* and *Pongo*), the range of *Homo sapiens* does not overlap with the ranges of any other extant group.

All fossil specimens are found within the positive aspect of the first canonical variate axis, with all but three fossil specimens residing in the range of *Homo sapiens* (figure 5.3.1). Qafzeh-9 (early *Homo sapiens*), Tabun-1 (*Homo neanderthalensis*), and UW-88-95 (*Australopithecus sediba*) – which has the highest CV 1 score of all fossil specimens – are all within the interquartile range of *Homo sapiens*, while Tianyuan (early *Homo sapiens*), Kebara-2, Regourdou-1, Shanidar-4 (*Homo neanderthalensis*), and KNM-WT-22944-I (*Australopithecus cf. Australopithecus afarensis*) are all within the 1st quartile of the extant *Homo sapiens* sample. AL-333-50 (*Australopithecus afarensis*), UW-101-1729 (*Homo naledi*), and Liang Bua-21/22 (*Homo floresiensis*) have CV 1 scores lower than the *Homo sapiens* minimum value. However, of all the fossil specimens, it is only Liang Bua-21/22 that has a CV 1 score within the range of a non-human extant taxon, being in the highest echelons of the 4th quartile range of *Pongo* (figure 5.3.1).

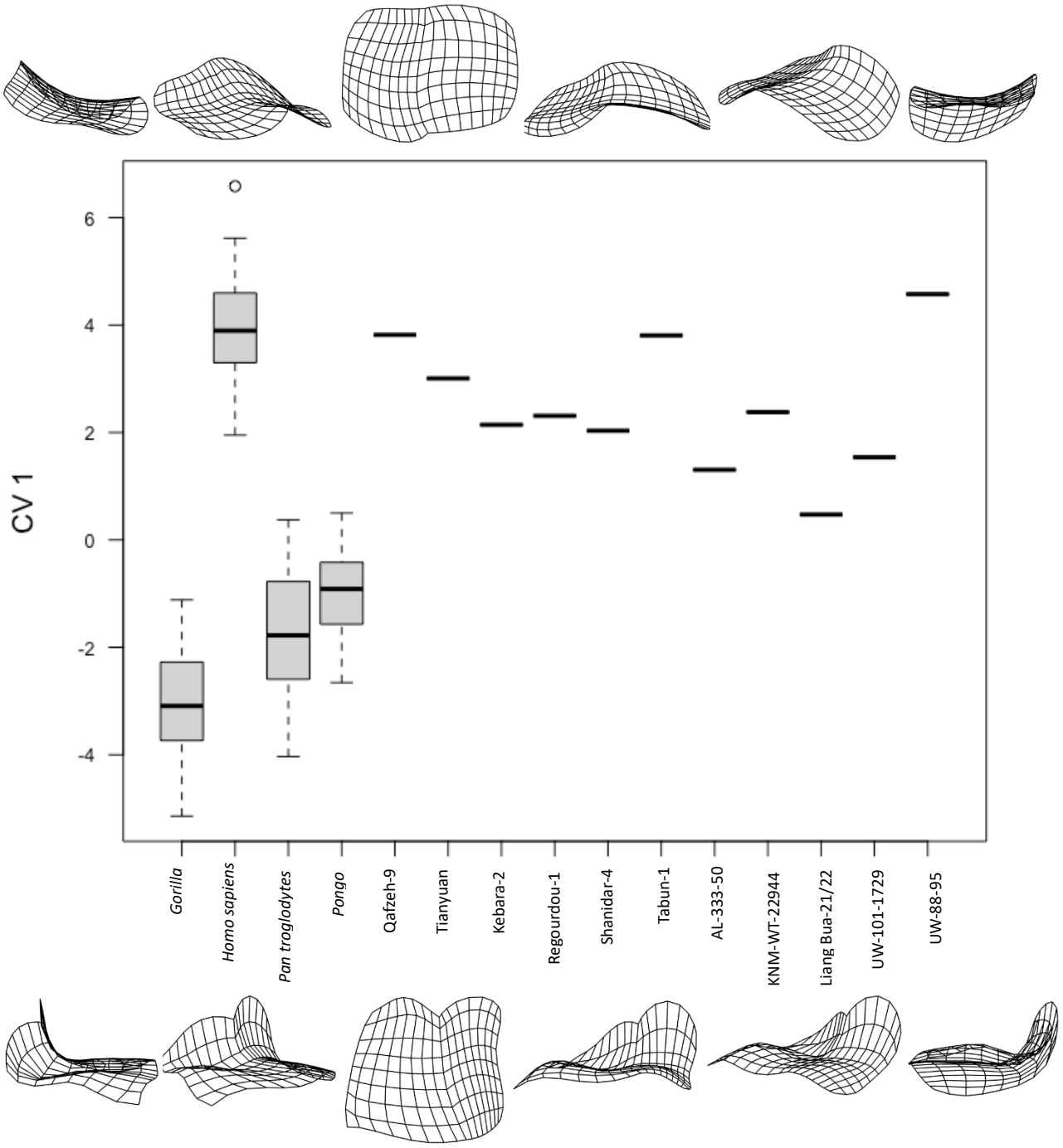

Figure 5.3.1: Boxplot of the scores of the first Canonical Variate axis of the hamate's metacarpal articular surface for *Gorilla, Homo sapiens, Pan troglodytes,* and *Pongo* compared with fossil specimens Qafzeh-9, Tianyuan (early *Homo sapiens*); Kebara-2,Regourdou-1, Shanidar-4, Tabun-1 (*Homo neanderthalensis*); AL-333-50 (*Australopithecus afarensis*); KNM-WT-22944 (cf. Australopithecus afarensis) ; Liang Bua (*Homo floresiensis*); UW-101-1729 (*Homo naledi*); and UW-88-95 (*Australopithecus sediba*). Black lines represent the median of the group, boxes are interquartile ranges, and whiskers are the non-outlier ranges. White circles represent outliers.

Second Canonical Variate Axis

Shape change along the second canonical variate axis, which accounts for 29.0% of the total variance, corresponds to the shape change along the second principal component (described in section 5.2 and represented visually in figure 5.2.3). The second canonical variate axis concerns differences in shape of the *Gorilla* population relative to the other extant non-human taxa (*Pan troglodytes* and *Pongo*) (figure 5.3.2). The range of the *Homo sapiens* sample overlaps with all three non-human groups to varying extents, with the 1st quartile of *Homo sapiens* overlapping with the fourth quartile of *Gorilla*, its uppermost extreme overlapping with the very lowest scores of *Pan troglodytes*, and the upper half of *Homo sapiens* overlapping with the 1st quartile of *Pongo*. The second CV axis does not appear to be primarily concerned with shape differences between *Homo sapiens* and other taxa. The *Gorilla* sample occupies the most negative aspect of CV 2, which represents a hamate-metacarpal articulation in which the surface for the fifth metacarpal is elevated distally relative to the fourth, and which displays a strong mediolateral convex curvature on its dorsal portion, though is mediolaterally straight on its distally-projected palmar portion. While the *Gorilla* sample is entirely in the negative aspect, the *Pan troglodytes* sample is entirely within the positive range of CV 2 axis and represent the highest CV 2 scores. The CV 2 maxima represents a shape in which the palmodorsal midline is highly curved and elevated distally, resulting in a distally-elevated MCV surface and an MC-IV surface that has a palmodorsally elongated medial half relative to a correspondingly shortened lateral half. Almost the entirety of the *Pan troglodytes* sample overlaps with the range of *Pongo.* While the lower aspect of the *Pongo* range is found in the negative aspect of the CV axis, the sample does not overlap with the 4th quartile of *Gorilla.*

All but one of the fossil specimens are within the range of *Homo sapiens,* with Kebara-2 (*Homo neanderthalensis*) being marginally below the range of modern humans. There is substantial overlap between the range of *Homo sapiens* with the 4th quartile of *Gorilla* and the 1st quartile of *Pongo,* and only three fossil specimens fall exclusively within the range of *Homo* sapiens: Tianyuan (early *Homo sapiens*) Regourdou-1 (*Homo neanderthalensis*), and UW-88-95 (*Australopithecus sediba*).

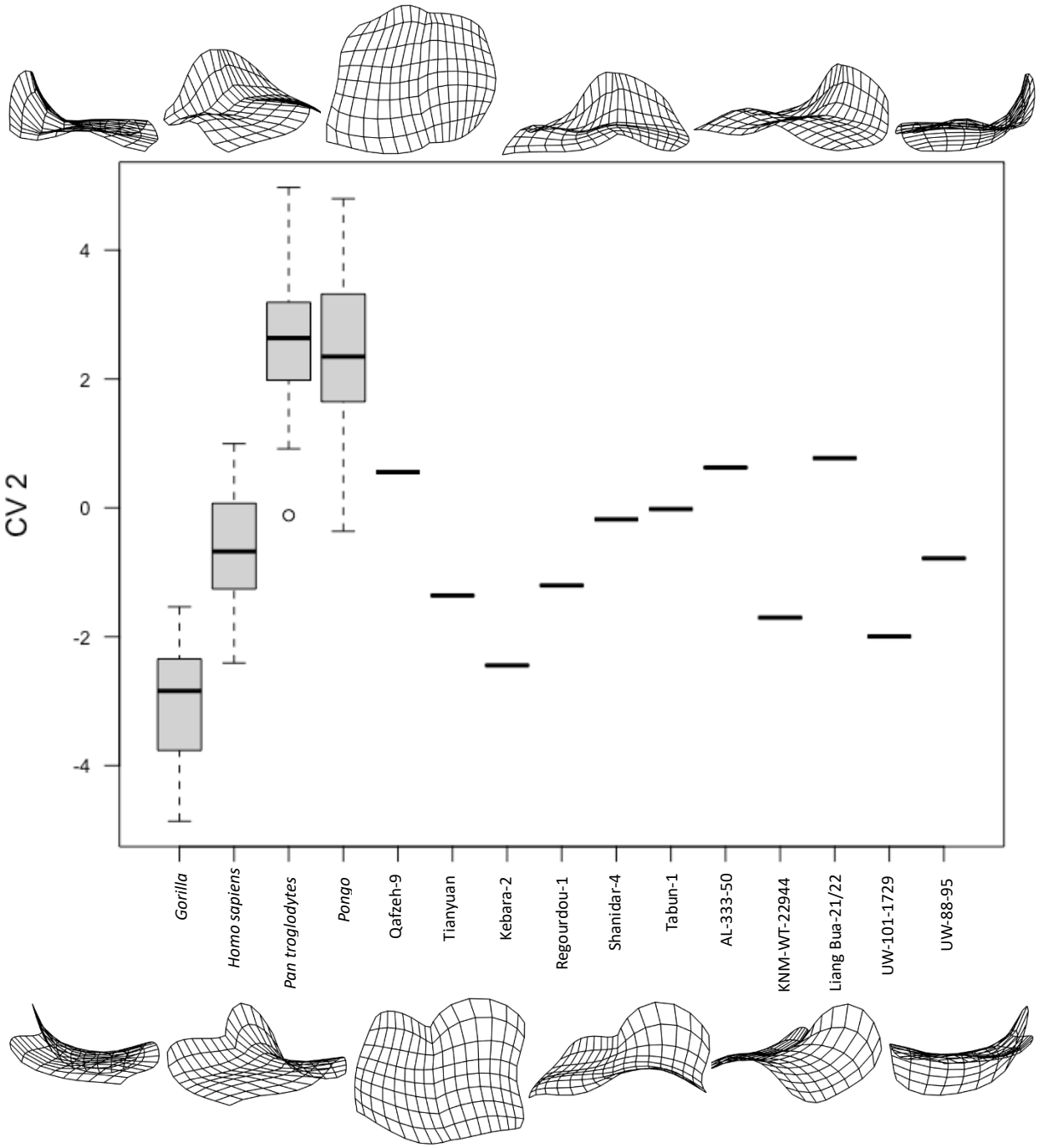

Figure 5.3.2: Boxplot of the scores of the second Canonical Variate axis of the hamate's metacarpal articular surface for *Gorilla, Homo sapiens, Pan troglodytes,* and *Pongo* compared with fossil specimens Qafzeh-9, Tianyuan (early *Homo sapiens*); Kebara-2,Regourdou-1, Shanidar-4, Tabun-1 (*Homo neanderthalensis*); AL-333-50 (*Australopithecus afarensis*); KNM-WT-22944 (cf. Australopithecus afarensis) ; Liang Bua (*Homo floresiensis*); UW-101-1729 (*Homo naledi*); and UW-88-95 (*Australopithecus sediba*). Black lines represent the median of the group, boxes are interquartile ranges, and whiskers are the non-outlier ranges. White circles represent outliers.

Third Canonical Variate Axis

The third canonical variate axis accounts for 20% of the total shape variation between groups. Shape change along the third CV axis corresponds to shape change along the third principal component (described in section 5.2 and represented visually in figure 5.2.4), and is broadly similar to the change in shape along the second canonical variate axis, with the maximal shape of CV 2 being comparable with the minimal shape of CV 3. The third canonical variate axis seperates the *Pongo* sample, which is entirely in the positive aspect, from the three other extant taxa (figure 5.3.3). Again, the *Homo sapiens* sample is distributed evenly at the neutral value of the axis, with its mean value approximating zero. The third canonical variate axis does not appear to be dictated by the shape of the human sample. Likewise, the *Gorilla* sample is distributed fairly eveny between the positive and negative aspects, although skewed slightly to the negative. *Pan troglodytes* is predomanly in the negative aspect of CV 3, with only its higher values of the 4th quartile having positive scores.

The fossil specimens are distributed widely across the axis, though are weighted to the negative aspect, with no fossil specimens found in the range of *Pongo.* The majoirty of the fossils span the values of all three extant African great ape taxa. Shanidar-4 (*Homo neanderthalensis*) is the only fossil specimen that has a higher CV 3 score than the *Homo sapiens* range, while it is only WU-88-95 (*Australopithecus sediba*) that has a lower CV 3 score than the *Homo sapiens* range, residing in the range of the 1st quartile of *Pan troglodytes* (figure 5.3.3). All other fossil samples are within the *Homo sapiens* range, as well as one or both of the African great apes.

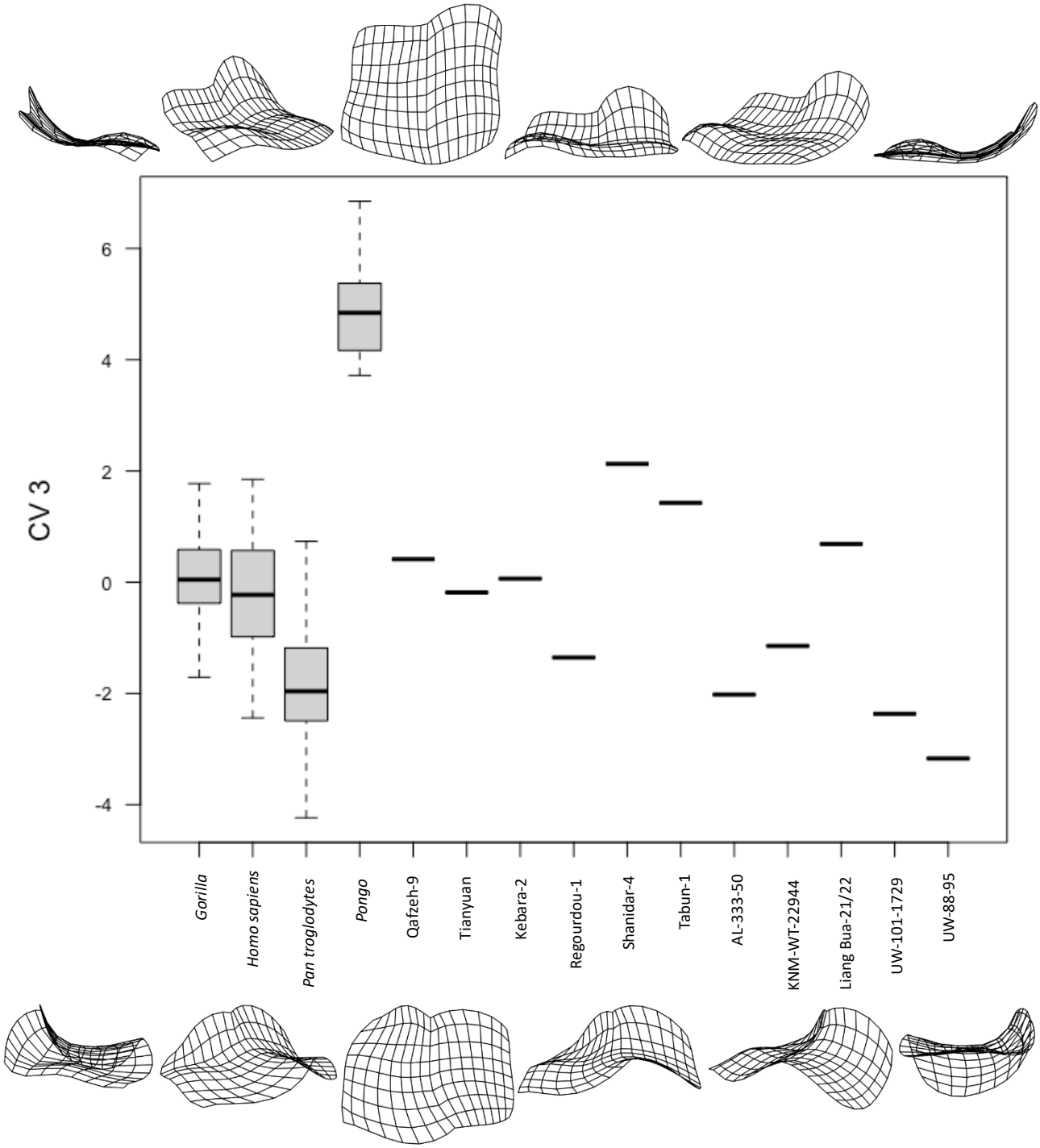

Figure 5.3.3: Boxplot of the scores of the third Canonical Variate axis of the hamate's metacarpal articular surface for *Gorilla, Homo sapiens, Pan troglodytes,* and *Pongo* compared with fossil specimens Qafzeh-9, Tianyuan (early *Homo sapiens*); Kebara-2,Regourdou-1, Shanidar-4, Tabun-1 (*Homo neanderthalensis*); AL-333-50 (*Australopithecus afarensis*); KNM-WT-22944 (cf. Australopithecus afarensis) ; Liang Bua (*Homo floresiensis*); UW-101-1729 (*Homo naledi*); and UW-88-95 (*Australopithecus sediba*). Black lines represent the median of the group, boxes are interquartile ranges, and whiskers are the non-outlier ranges.

CVA Scatterplots

CV 1 v CV 2

A scatterplot of the scores of the first canonical variate axis against those of the second canonical variate axis, with 95% confidence intervals, is shown in figure 5.3.4. This scatterplot distributed the taxa into three clusters, with *Gorilla* dominating the lower left quadrant, *Homo sapiens* found exclusively in the right half and occupying a relatively confined and localized area compared to the other extant groups, and the *Pan troglodytes* and *Pongo* samples clustered together in the upper left quadrant and showing no distinction between their samples.

The majority of the fossil specimens are found within the 95% confidence ellipse of *Homo sapiens*, with two (Kebara-2, *Homo neanderthalensis*; UW-101-1729, *Homo naledi*) being just outside the 95% confidence ellipse, but within the vicinity of the *Homo sapiens* sample. Liang Bua-21/22 (*Homo floresiensis*) and AL-333-50 (*Australopithecus afarensis*) are well outside the vicinity of the *Homo sapiens* sample, with both being within the 95% confidence ellipse of *Pongo*. AL-333-50 is intermediate between the 95% confidence ellipses of *Homo sapiens* and *Pan troglodytes,* while Liang Bua-21/22 is within the *Pan troglodytes* 95% confidence ellipse (figure 5.3.4).

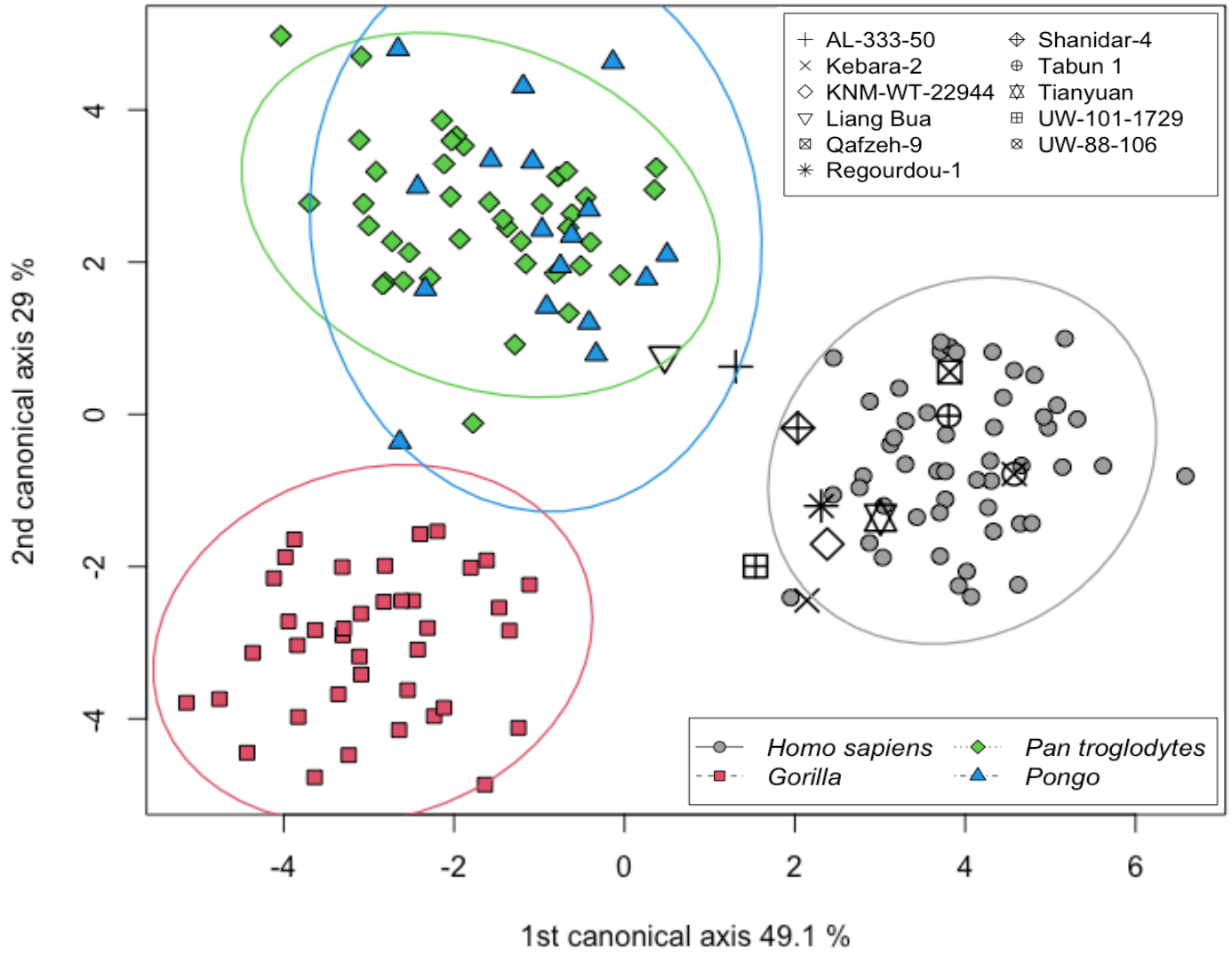

Figure 5.3.4: Scatterplot of the first vs. second canonical variates axis (CV 1 (49.1%) vs. CV 2 (29.0%)) scores of extant samples (*Homo sapiens*, Gorilla, Pan *troglodytes,* and *Pongo*) and fossil specimens. *Homo sapiens* and *Gorilla* samples are separated from a *Pan troglodytes* and *Pongo* cluster, with the majority of fossils in the *Homo sapiens* sample. Liang Bua -21/23 (*Homo floresiensis*) and AL 333-50 (*Australopithecus afarensis*) are in the *Pan troglodytes-Pongo* cluster.

CV 1 v CV 3

A scatterplot of the first against third canonical variate axis is shown in figure 5.3.5. As with the scatterplot of CV 1 against CV 2, this scatterplot separated the four extant taxa into three clusters. However, rather than being clustered with *Pongo* as before, here *Pan troglodytes* is clustered with *Gorilla* in the lower-left quadrant, while the *Pongo* sample is more concentrated in the upper-left quadrant. Again, the *Homo sapiens* sample is localized in the right half of the plot.

Half of the fossil specimens are found within the 95% confidence ellipse of the *Homo sapiens* sample, including both early *Homo sapiens* specimens (Qafzeh-9 & Tianyuan), three of the four *Homo neanderthal* specimens (Regourdou-1, Kebara-2, Tabun-1), and KNM-WT-22944-I (*Australopithecus cf. Australopithecus afarensis*). The remaining *Homo neanderthalensis* specimen (Shanidar-4) is located between the 95% confidence ellipses of *Pongo* and *Homo sapiens* (figure 5.3.5). Liang Bua-21/22 (*Homo floresiensis*), UW-101-1729 (*Homo naledi*), and AL-333-50 (*Australopithecus afarensis*) are closer to the *Pan troglodytes* sample than to the *Homo sapiens* sample, while, although outside the 95% confidence ellipse of *Homo sapiens*, UW-88-95 (*Australopithecus sediba*) is clearly within the vicinity of the *Homo sapiens* sample.

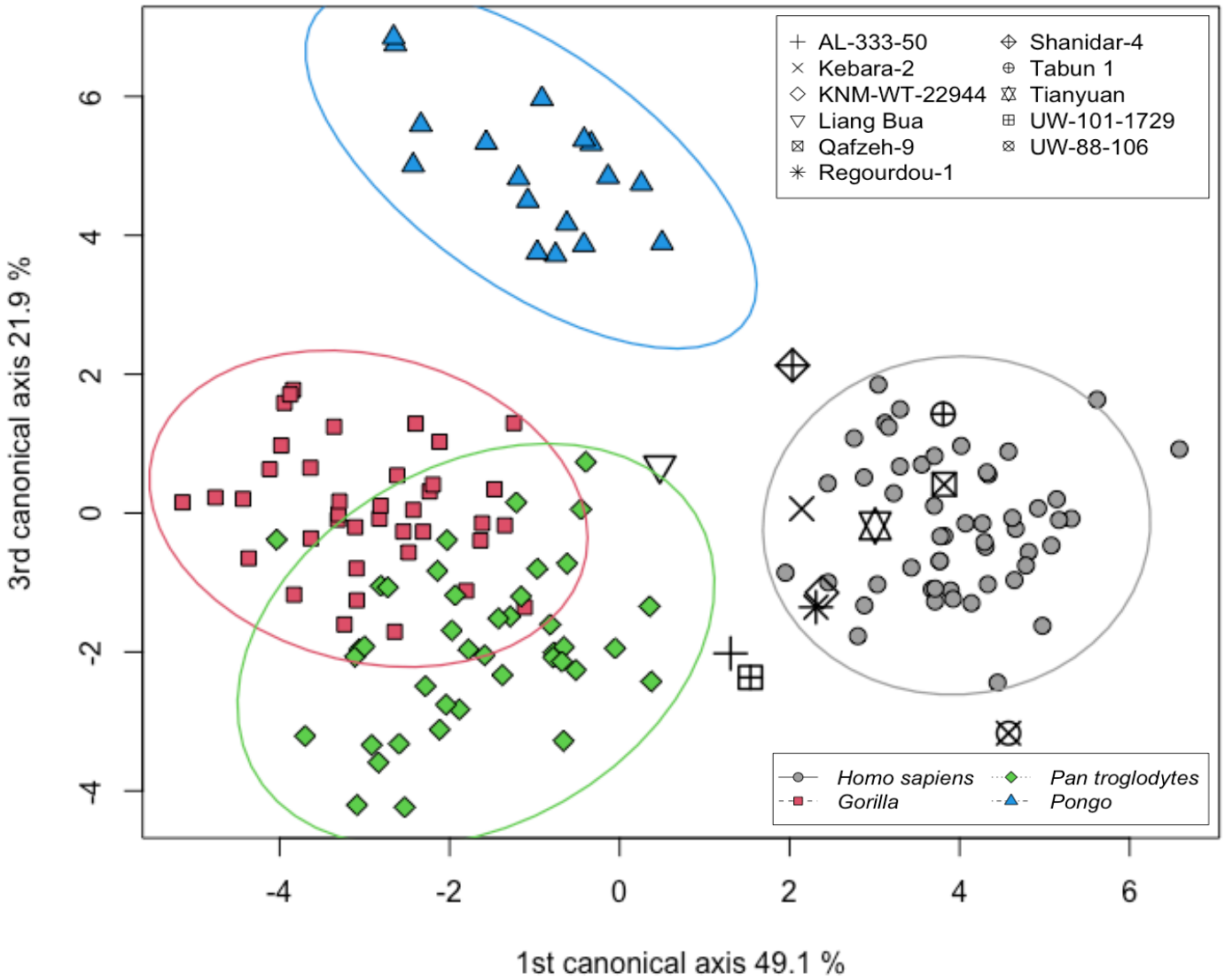

Figure 5.3.5: Scatterplot of the first vs. third canonical variates axis (CV 1 (49.1%) vs. CV 3 (21.9%)) scores of extant samples (*Homo sapiens*, Gorilla, Pan *troglodytes,* and *Pongo*) and fossil specimens. The *Homo sapiens* and *Pongo* samples are separate from a cluster of non-human African great-ape specimens. The *Homo sapiens* and *Pongo* samples are separate from a cluster of non-human African great-ape specimens.

CV 2 v CV 3

The scatterplot of the scores of the second against third canonical variate, shown in figure 5.3.6, is most effective in separating the *Pongo* sample from other extant taxa. The *Pongo* sample is found in the extreme upper half of the plot, and predominantly in the upper-right quadrant, and does not overlap with the sample of any other extant taxon, or with any fossil specimens. The samples of *Pan troglodytes* and *Gorilla* do not overlap with each other, though both overlap considerably with the *Homo sapiens* sample, which is distributed across all four quadrants, being centred at the intersection of the plot axes. The *Gorilla* sample is found exclusively in the left half of the plot, and the *Pan troglodytes* sample is exclusively in the right half, being predominantly in the lower-right quadrant.

All fossil specimens are distributed around the interjection of the axes, and are within, or close to the vicinity of, the *Homo sapiens* sample (figure 5.3.6). While UW-101-1729 (*Homo naledi*) and UW-88-95 (*Australopithecus sediba*) are situated outside the 95% confidence ellipse of *Homo sapiens*, they are both closer to the *Homo sapiens* sample than to *Gorilla* or *Pan troglodytes.* Three of the four *Homo neanderthalensis* specimens (Regourdou-1, Tabun-1, and Shanidar-4) as well as Qafzeh-9 (early *Homo sapiens*) and Liang Bua-21/22 (*Homo floresiensis*) are within the 95% confidence ellipse of *Homo sapiens* alone, while Tianyuan (early *Homo sapiens*), Kebara-2 (*Homo neanderthalensis*) and KNM-WT-22944-I (*Australopithecus cf. Australopithecus afarensis*) are within the intersection of *Homo sapiens* and *Gorilla*. AL-333-50 (*Australopithecus afarensis*) is the sole fossil specimen situated within the 95% confidence ellipse of *Pan troglodytes*, also being within the 95% confidence ellipse of *Homo sapiens.*

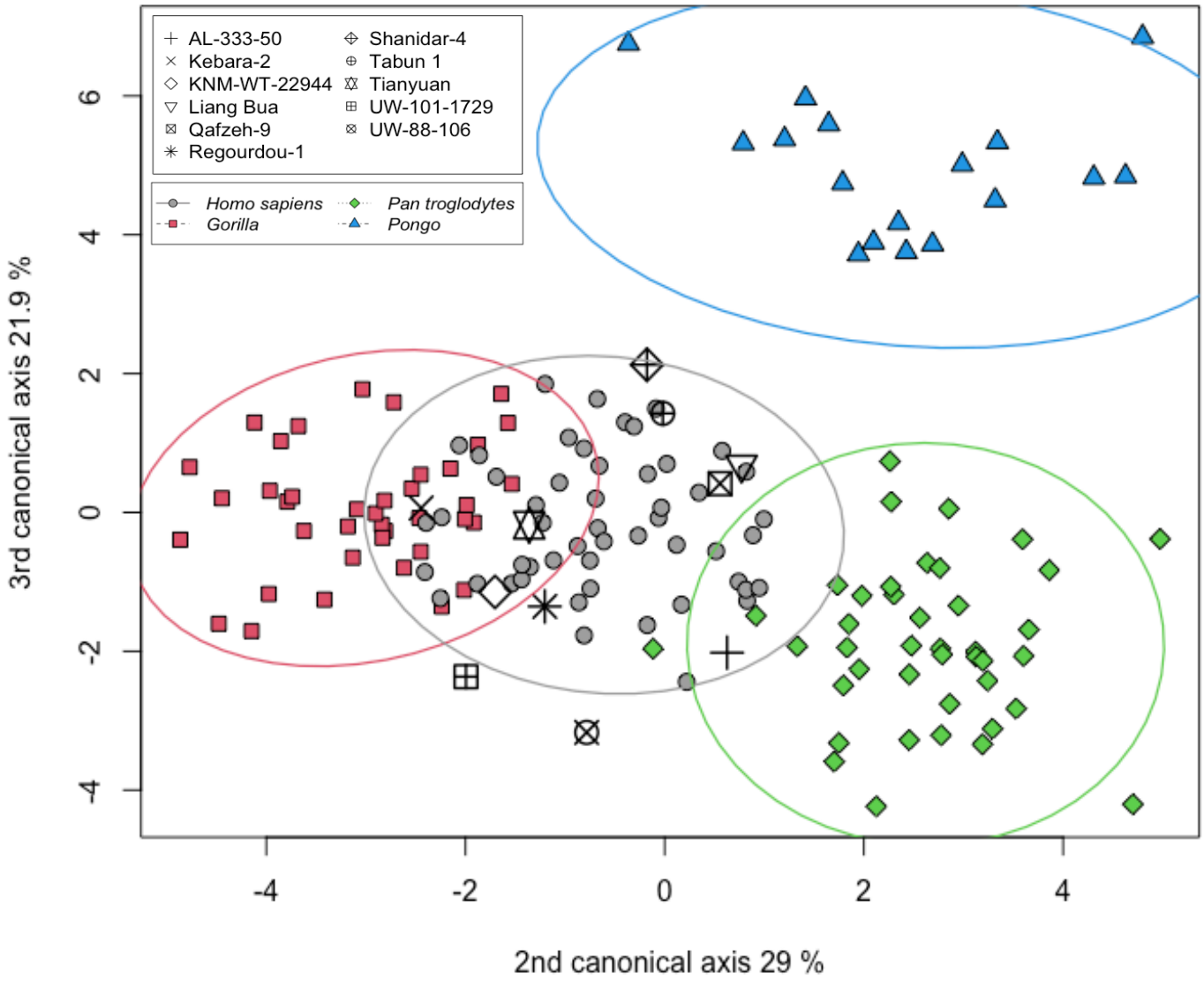

Figure 5.3.6: Scatterplot of the second vs. third canonical variates axis (CV 1 (49.1%) vs. CV 2 (29.0%)) scores of extant samples (*Homo sapiens*, Gorilla, Pan *troglodytes,* and *Pongo*) and fossil specimens. This plot separates *Pongo*, in the upper half of the plot, from taxa of African origin, in the lower half. All fossil specimens are centred around the *Homo* sapiens *sample.*

5.4 Hamate-metacarpal Procrustes distances

The Procrustes distance of the mean shape of each sample from each other is shown in table 5.4.1, with the Procrustes distances of the fossil specimens from the mean shape of each extant taxon sample shown in table 5.4.2. Of the extant group mean shapes, *Gorilla* and *Pan troglodytes* were closest to each other, followed by *Pan troglodytes* and *Pongo*. The greatest distances were between *Pongo* and *Homo sapiens*, with *Homo sapiens* also being a considerable distance from *Pan troglodytes*, and *Pongo* from *Gorilla. Homo sapiens* was closest to *Gorilla* of the non-human taxa. Fossil specimens were consistently closer to the *Homo sapiens* mean shape than to any other group, with the exception of AL-333-50 (*Australopithecus afarensis*), which was marginally closer to non-human African great apes than to modern humans. Qafzeh-9 (early *Homo sapiens*) is the fossil specimen with the smallest Procrustes distance from the mean shape of modern humans.

Table 5.4.1: Procrustes distances between the average shapes of the extant groups.

	Homo sapiens	*Gorilla*	*Pan troglodytes*	*Pongo*
Homo sapiens	-	0.162	0.168	0.207
Gorilla		-	0.129	0.170
Pan troglodytes			-	0.149
Pongo				-

Table 5.4.2: The Procrustes distance of each fossil from the mean shape of each extant taxon group.

	Homo sapiens	*Gorilla*	*Pan troglodytes*	*Pongo*
AL-333-50	0.156	0.150	0.152	0.215
Kebara-2	0.133	0.139	0.167	0.181
KNM-WT-22944	0.130	0.152	0.175	0.238
Liang Bua-21/22	0.189	0.191	0.220	0.253
Qafzeh-9	0.085	0.161	0.160	0.187
Regourdou-1	0.152	0.166	0.148	0.197
Shanidar-4	0.159	0.177	0.203	0.207
Tabun-1	0.108	0.171	0.167	0.162
Tianyuan	0.119	0.188	0.215	0.256
UW-101-1729	0.145	0.176	0.210	0.276
UW-88-95	0.188	0.262	0.268	0.339

Results of the Shapiro-Wilk tests for normality along the linear distances of extant species from the mean value of their respective group are shown in table 5.4.2. The Shapiro-Wilks test for normality showed that the Procrustes distances of each taxon group from their respective mean shape were normally distributed for all four extant taxa group.

Table 5.4.3: Results of the Shapiro-Wilk tests for normality tests performed on the Procrustes distances of each sample from their respective average group shapes.

	Homo sapiens	*Gorilla*	*Pan troglodytes*	*Pongo*
p	0.142	0.080	0.709	0.290

The Procrustes distance of each fossil specimen from the mean shape of each extant group (in standard deviations) is shown in table 5.4.4. The two early *Homo sapiens* specimens were closer to the mean of the *Homo sapiens* group than 88.41% (Qafzeh-9) and 33.12% (Tianyuan) of the modern human specimens. Of the four *Homo neanderthalensis* specimens, Tabun-1 was the closest to the *Homo sapiens* mean shape, being closer than 54.28% of the modern human sample, followed by Kebara-2, which was closer than 13.66% of the human sample to their mean shape. Shanidar-4 was closer to the *Homo sapiens* mean shape than less than 1% of the sample, though was still closer to the mean shape of *Homo sapiens* than to any other group, while Regourdou-1 was closer than 2.28% of the human sample to the mean of that group, while being closer than 13.33% of chimpanzees to that group's mean shape. UW-101-1729 (*Homo naledi*) and KNM-WT-22944-I (*Australopithecus cf. Australopithecus afarensis*) were closer to the mean shape of *Homo sapiens* than to any other group, with KNM-WT-22944-I being closer to the human mean shape than 16.77% of the human sample, and UW-101-1729 being closer than less than 5%. AL-333-50 (*Australopithecus afarensis*), while being categorized as *Homo sapiens* by the CVA (table 5.4.4), was relatively closer to the mean shapes of *Pan troglodytes* (10.01%) and *Gorilla* (3.12%) than it was to the mean shape of *Homo sapiens* (1.34%). The remaining two fossil specimens, UW-88-95 (*Australopithecus sediba*) and Liang Bua-21/22 (*Homo floresiensis*) were approximately equidistant from the mean shapes of all four extant taxa, being further away from the mean shapes of all taxa than 99.99% to 100% of each taxa's sample.

Table 5.4.4: Distances in standard deviations of each fossil from the mean of the distance of each individual of the extant group from the group mean. Calculations were conducted on Procrustes distances. In parentheses, the value of the upper-tail cumulative distribution function multiplied by 100.

	Homo	Gorilla	Pan	Pongo
AL-333-50	2.21 (1.34%)	1.86 (3.12%)	1.28 (10.01%)	4.83 (0.00%)
Kebara-2	1.10 (13.66%)	1.38 (8.34%)	1.85 (3.20%)	3.39 (0.03%)
KNM-WT-22944	0.96 (16.77%)	1.95 (2.57%)	2.17 (1.50%)	5.83 (0.00%)
Liang Bua-21/22	3.81 (0.01%)	3.65 (0.01%)	3.91 (0.00%)	6.50 (0.00%)
Qafzeh-9	-1.20 (88.41%)	2.36 (0.91%)	1.60 (5.46%)	3.64 (0.01%)
Regourdou-1	2.00 (2.28%)	2.55 (0.54%)	1.11 (13.33%)	4.10 (0.00%)
Shanidar-4	2.36 (0.92%)	3.04 (0.12%)	3.24 (0.06%)	4.51 (0.00%)
Tabun-1	-0.11 (54.28%)	2.77 (0.28%)	1.87 (3.09%)	2.59 (0.49%)
Tianyuan	0.44 (33.12%)	3.53 (0.02%)	3.70 (0.01%)	6.62 (0.00%)
UW-101-1729	1.68 (4.66%)	3.00 (0.14%)	3.51 (0.02%)	7.44 (0.00%)
UW-88-95	3.77 (0.01%)	6.77 (0.00%)	5.77 (0.00%)	10.16 (0.00%)

6 The hamate-metacarpal 4 articular surface

6.1. Hamate-metacarpal-4 surface average shapes

Homo sapiens

The average shape of the hamate's articular surface for the fourth metacarpal in *Homo sapiens* is shown in figure 6.1.1. It is longer in its palmodorsal plane relative to its mediolateral plane, and the palmar end of the surface curves gently distally, especially at its mediopalmar corner, resulting in a moderate bevelling of the surface, and a gentle palmodorsal concavity. The surface is also mildly concave in the mediolateral plane, and the laterodorsal portion of the surface protrudes slightly dorsally resulting in a slight protrusion in that area. The medial border is longer than the lateral, with the mediopalmar and mediodorsal corners protruding further distally than the corresponding lateral corners.

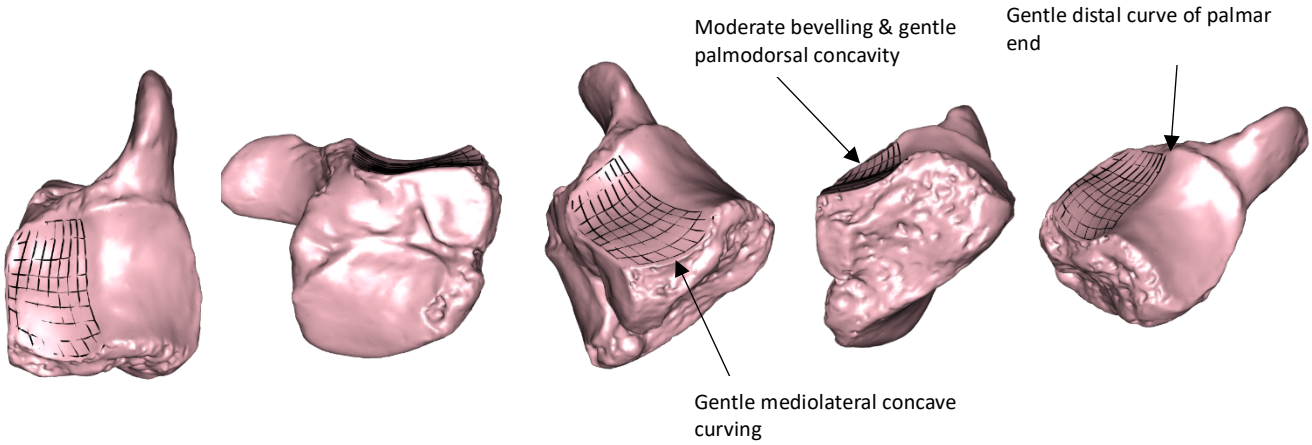

Figure 6.1.1: The mean shape of the hamate's articular surface for the fourth metacarpals for the *Homo sapiens* population, represented by the specimen closest to the group's mean shape warped to the average landmark coordinates of the population, superimposed with wireframe representation of the surface. From left to right: distal, lateral, laterodorsal, dorsal, mediodorsal, and medial views.

Gorilla

Wireframe representations of the average shape of the hamate-MC4 articular surface in *Gorilla* is shown in figure 6.1.2. As with *Homo sapiens,* the mean shape of *Gorilla* is generally rectangular from a distal view, with a medial border that is longer than its lateral counterpart,

and a shorter palmar border relative to the dorsal border. The mediodorsal corner strongly protrudes distomedially, resulting in a curved medial border. The medial and palmar portions of the surface are strongly concave, resulting in a basin-like bevelled morphology, further facilitated by the mediolaterally concave palmar border. The dorsal half of the surface is undulating, resulting from a pronounced distal ballooning of the surface towards the laterodorsal area of the surface.

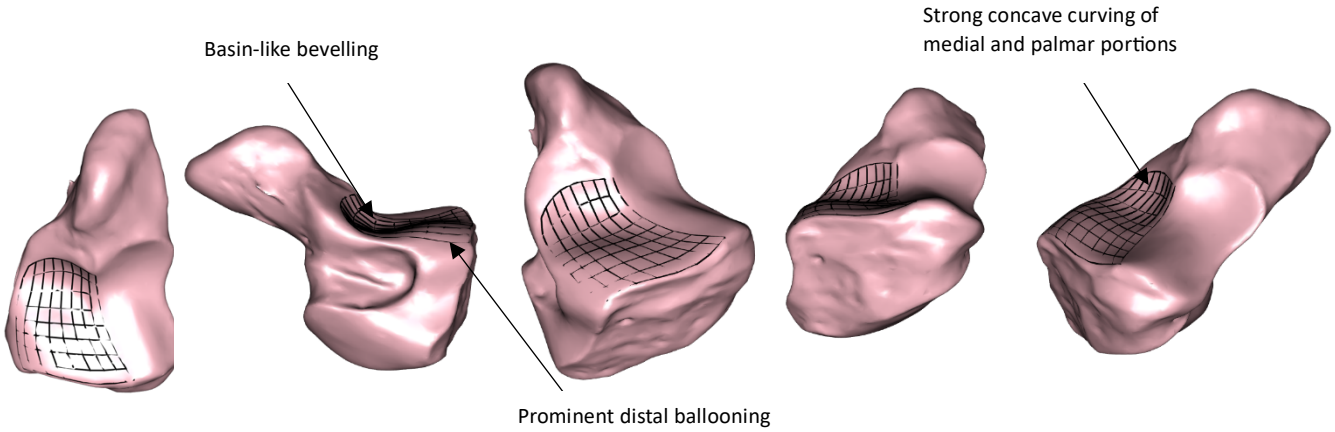

Figure 6.1.2: The mean shape of the hamate's articular surface for the fourth metacarpals for the *Gorilla* population, represented by the specimen closest to the group's mean shape warped to the average landmark coordinates of the population, superimposed with wireframe representation of the surface. From left to right: distal, lateral, laterodorsal, dorsal, mediodorsal, and medial views.

Pan troglodytes

Perhaps the most notable feature of the mean shape of the *Pan troglodytes* articular surface, shown in figure 6.1.3, is its strongly distally-projecting mediopalmar corner, which results in a palmar edge that slopes proximally from medial to lateral, and a very strong scooping bevelled morphology of the mediopalmar quadrant. The *Pan troglodytes* mean shape also has a very notably-pronounced distally-protruding elevation on the lateral portion of its surface, which dominates the lateral half of the surface, and is situated in a more palmar location relative to the average shape of the other taxa, continuing onto the lateral edge of the surface, resulting in a strongly palmodorsally undulating lateral edge. The medial border is strongly concave not only in the proximal direction, but also laterally, due to the dorsomedial projection of the corner, resulting in a medial edge that is palmodorsally longer relative to the lateral edge.

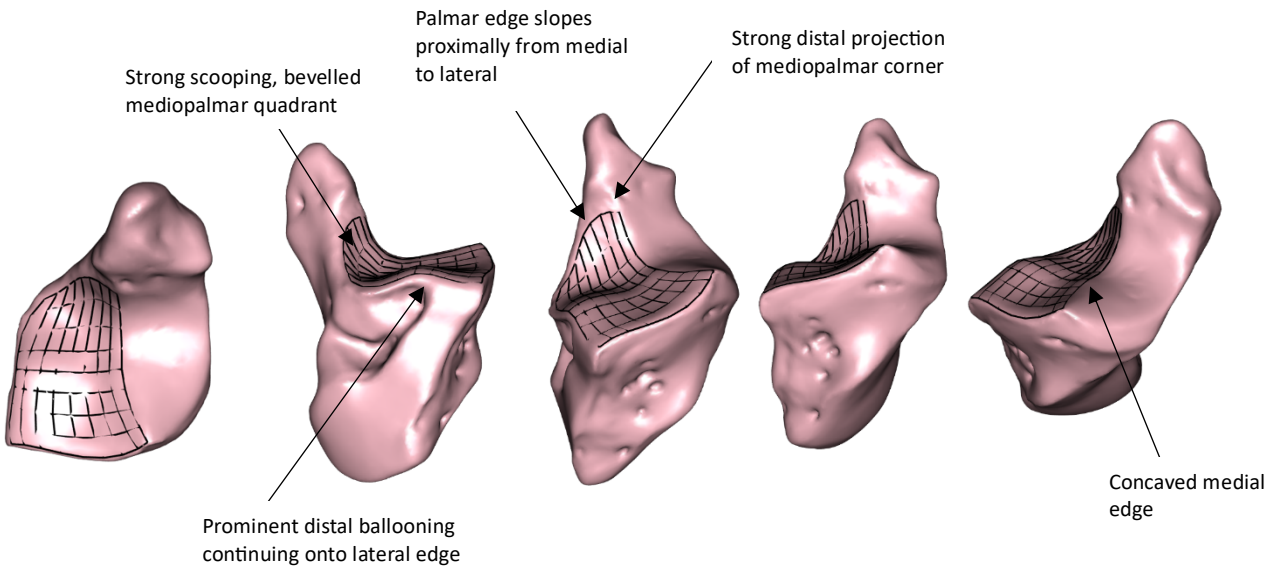

Figure 6.1.3: The mean shape of the hamate's articular surface for the fourth metacarpals for the *Pan troglodytes* population, represented by the specimen closest to the group's mean shape warped to the average landmark coordinates of the population, superimposed with wireframe representation of the surface. From left to right: distal, lateral, laterodorsal, dorsal, mediodorsal, and medial views.

Pongo

The average shape of the *Pongo* population, shown in figure 6.1.4, is, when viewed from a distal viewpoint, of a relatively rectangular shape, with a straight medial edge and a lateral edge that bulges laterally palmarly and dorsally, resulting in a constricted waist. The palmar edge is straight and sloped slightly towards the lateral corner. The palmar half of the *Pongo* surface is gently concave and mostly uniform in the mediolateral plane. However, the laterodorsal quadrant is notably more elevated than the mediodorsal quadrant, though the dorsal portion as a whole slopes strongly proximally towards the dorsal edge.

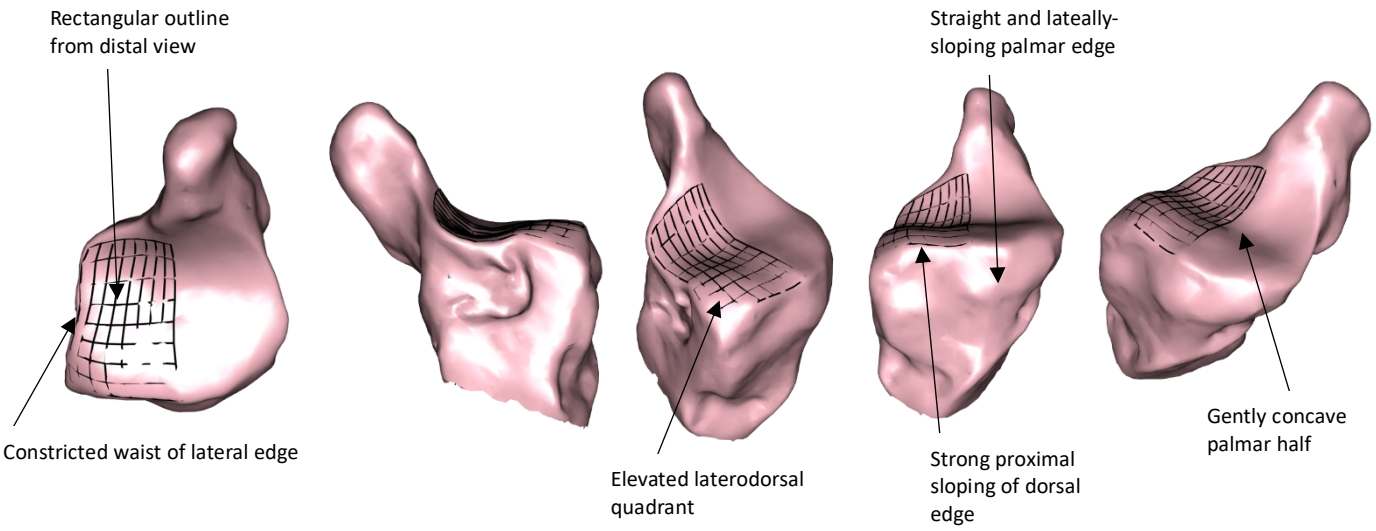

Figure 6.1.4: The mean shape of the hamate's articular surface for the fourth metacarpals for the *Pongo* population, represented by the specimen closest to the group's mean shape warped to the average landmark coordinates of the population, superimposed with wireframe representation of the surface. From left to right: distal, lateral, laterodorsal, dorsal, mediodorsal, and medial views.

Table 6.1: Comparison of the mean hamate-metacarpal 4 shape of each extant taxa

Ham-MC4	Distal	Lateral	Laterodorsal	Dorsal	Mediodorsal
Homo sapiens	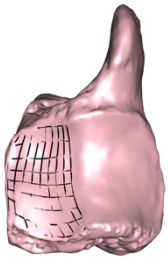	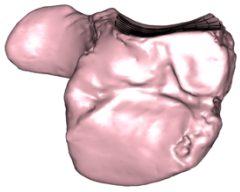	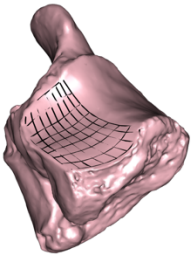	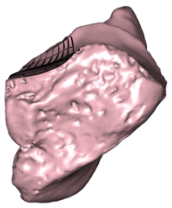	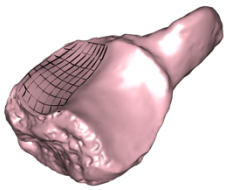
Gorilla	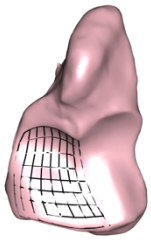	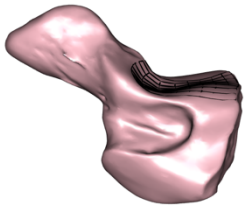	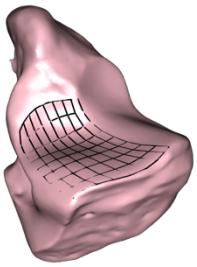	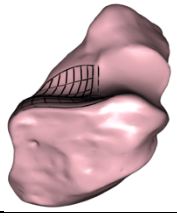	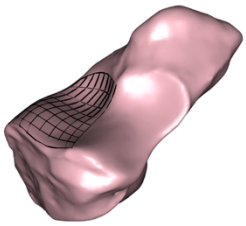
Pan troglodytes	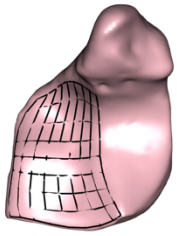	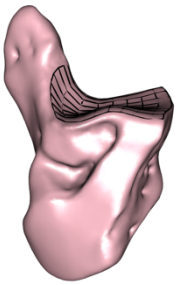	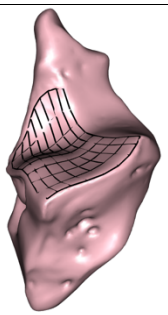	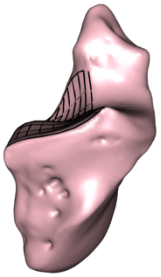	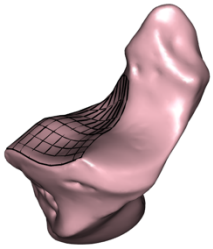
Pongo	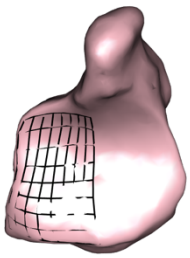		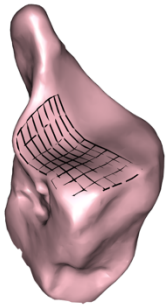	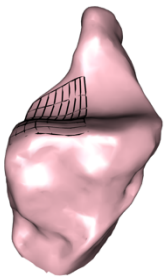	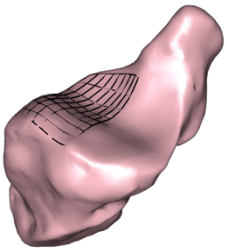

6.2 Hamate-MC4 Principal Components Analysis

The first three principal components were considered meaningful in accordance with Bookstein's (2014) definition, and accounted for 52.9% of the total variation, with PC 1 accounting for 26.5% of total variance, PC 2 accounting for 15.8%, and PC 3 10.6% (figure 6.2.1). The first six principal components represented more than 5% of the cumulative shape variance of the hamate's articular surface for the fourth metacarpal, and cumulatively accounted for 73.4% of the total variance. PC 4 and PC 5 represented 8.0% and 6.7% of the total variance respectively, while PC 6 accounted for 5.8%. Principal component seven and all other principal components thereafter accounted for less than 5% of the total cumulative variation. 90.7% of the total variation was represented by the first 12 principal components, with the 12th principal component accounting for 1.4% of the total variation.

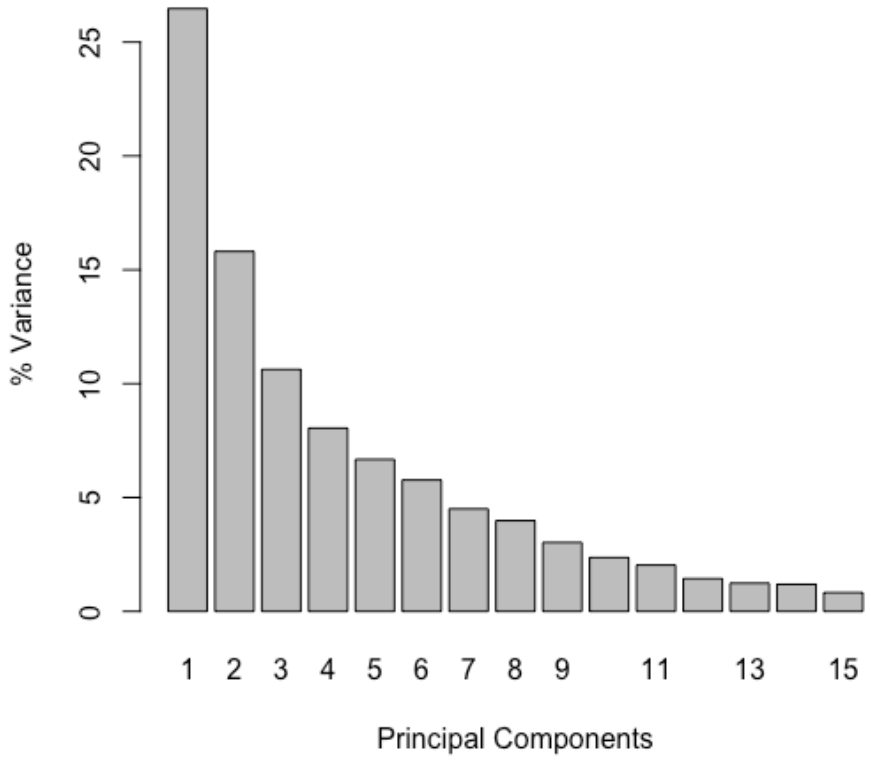

Figure 6.2.1: Graph showing the percentage of variance accountable to the first 15 principal components of the principal component analysis of the hamate's articulation for the fourth metacarpal. The first six principal components accounted for approximately 73.4% of the variation in shape.

Taxonomic differences between groups

The Hotelling's T^2 test conducted on the first six principal components showed there was no statistically significant difference between the samples of *Gorilla gorilla* and *Gorilla beringei* along the values of the first six principal components (T^2 = 1.9087, df = 6, 32; p = 0.1098), nor between the two species of *Pongo* (*Pongo abelii* and *Pongo pygmaeus*) (T^2 = 0.37582, df = 6, 10; p = 0.8784). As such, the two species of *Gorilla* and the two species of *Pongo* were pooled at the genus level. A multiple analysis of variance conducted on the values of the first six principal components of the *Pan troglodytes* sample also returned no statistically significant differences in the values of the principal component scores based on sub-species of *Pan troglodytes* [F (3, 15) = 1.1336, p = 0.3457, Wilks Λ = 0.4037], and the *Pan troglodytes* sample was not partitioned into its constituent sub-species.

Analysis of Variance (ANOVA)

Results for the analysis of variance (ANOVA) of the scores of the first six principal components divided by taxon are shown in table 6.2.1. Significant results ($p \leq 0.05$) were seen in the first five principal components, with no significant result along the sixth principal component (p = 0.944). The mean and standard deviation of the scores of the first five principal components for each extant taxon sample is shown in table 6.2.2, with the principal component values of each fossil also shown. Subscripts next to the principal component scores of fossil specimens indicate extant taxa groups for which that particular fossil specimen deviates at least one standard deviation from.

Table 6.2.1: Results of analysis of variance on principal component scores one through six on extant groups.

Principal Component	DF	Sum of Squares	Mean Squares	*F* Value	*p*
PC 1	3, 144	0.5711	0.19037	85.88	**<0.001**
PC 2	3, 144	0.3283	0.10943	74.28	**<0.001**
PC 3	3, 144	0.1140	0.03799	22.82	**<0.001**
PC 4	3, 144	0.0647	0.02157	16.22	**<0.001**
PC 5	3, 144	0.0851	0.028366	34.35	**<0.001**
PC 6	3, 144	0.0005	0.0001617	0.13	0.944

Table 6.2.2: Mean and standard deviation (in parentheses) of principal component scores 1-5 for *Homo sapiens, Gorilla, Pan troglodytes,* and *Pongo* compared with PC scores of fossil specimens AL333-14 (*Australopithecus afarensis*), Kebara-2 (*Homo neanderthalensis*), KNM-WT-22944 (cf. Australopithecus afarensis), Liang Bua-21/22 (*Homo floresiensis*), Qafzeh-9 (early *Homo sapiens*), and Regourdou-1 (*Homo neanderthalensis*).

Group	*Homo sapiens* (*n* = 54)	*Gorilla* (*n* = 36)	*Pan troglodytes* (*n* = 40)	*Pongo* (*n* =20)	AL333-50	Kebara-2	KNM-WT-22944	Liang Bua-21/22	Qafzeh-9	Regourdou-1
PC 1	-0.009 (0.051)	-0.083 (0.04)	0.066 (0.046)	0.086 (0.051)	$-0.04_{G,Pt,Po}$	$-0.028_{G,Pt,Po}$	$-0.072_{Hs,Pt,Po}$	$-0.106_{Hs,Pt,Po}$	$-0.005_{G,Pt,Po}$	0.035_{G}
PC 2	-0.059 (0.036)	0.024 (0.039)	0.055 (0.039)	-0.001 (0.042)	$0.01_{Hs,Pt}$	$-0.057_{G,Pt,Po}$	$-0.012_{Hs,Pt}$	$0.013_{Hs,Pt}$	$-0.025_{G,Pt}$	$-0.066_{G,Pt,Po}$
PC 3	0.002 (0.04)	-0.011 (0.04)	0.033 (0.037)	-0.062 (0.052)	0.012_{Po}	-0.013_{Pt}	$-0.072_{Hs,G,Pt}$	$0.101_{Hs,G,Pt,Po}$	$-0.04_{Hs,Pt}$	0.005_{Po}
PC 4	-0.001 (0.034)	0.015 (0.035)	0.016 (0.044)	-0.052 (0.024)	0.017_{Po}	0.007_{Po}	0.009_{Po}	$0.105_{Hs,G,Pt,Po}$	$-0.021_{G,Po}$	0.032_{Po}
PC5	0.023 (0.024)	-0.03 (0.037)	0.006 (0.026)	-0.038 (0.027)	$0.041_{G,Pt,Po}$	0.006_{Po}	$0.077_{Hs,G,Pt,Po}$	$-0.006_{Hs,Po}$	$0.027_{G,Po}$	$0.023_{G,Po}$

[a] Subscripts indicate a group that the fossil specimen differs at least 1 standard deviation from the mean of: Hs = *Homo sapiens*; G = *Gorilla*; Pt = *Pan troglodytes*; Po = *Pongo.*

Table 6.2.2 (*cont.*): Mean and standard deviation (in parentheses) of principal component scores 1-5 for *Homo sapiens, Gorilla, Pan troglodytes,* and *Pongo* compared with PC scores of fossil specimens Shanidar-4 (*Homo neanderthalensis*), Tabun-1 (*Homo neanderthalensis*), Tianyuan (early *Homo sapiens*), UW-101-1729 (*Homo naledi*), and UW-88-95 (*Australopithecus sediba*).

Group	*Homo sapiens* (*n* = 54)	*Gorilla* (*n* = 36)	*Pan troglodytes* (*n* = 40)	*Pongo* (*n* =20)	Shanidar-4	Tabun-1	Tianyuan	UW-101-1729	UW-88-95
PC 1	-0.009 (0.051)	-0.083 (0.04)	0.066 (0.046)	0.086 (0.051)	$-0.042_{G,Pt,Po}$	0.039_{G}	$-0.065_{Hs,Pt,Po}$	$-0.144_{Hs,G,Pt,Po}$	$-0.028_{G,Pt,Po}$
PC 2	-0.059 (0.036)	0.024 (0.039)	0.055 (0.039)	-0.001 (0.042)	$0.049_{G,Pt,Po}$	$-0.085_{G,Pt,Po}$	0.036_{Hs}	0.036_{Hs}	$0.013_{Hs,Pt}$
PC 3	0.002 (0.04)	-0.011 (0.04)	0.033 (0.037)	-0.062 (0.052)	$0.037_{G,Po}$	-0.023_{Pt}	$-0.048_{Hs,Pt}$	$0.048_{Hs,G,Po}$	0.012_{Po}
PC 4	-0.001 (0.034)	0.015 (0.035)	0.016 (0.044)	-0.052 (0.024)	$0.047_{Hs,G,Pt}$	$-0.043_{Hs,G,Pt}$	$-0.025_{G,Po}$	$-0.071_{Hs,G,Pt}$	$-0.08_{Hs,G,Pt,Po}$
PC 5	0.023 (0.024)	-0.03 (0.037)	0.006 (0.026)	-0.038 (0.027)	$-0.047_{Hs,Pt}$	$0.028_{G,Po}$	$0.047_{G,Pt,Po}$	$0.08_{Hs,G,Pt,Po}$	$0.109_{Hs,G,Pt,Po}$

[a] Subscripts indicate a group that the fossil specimen differs at least 1 standard deviation from the mean of: Hs = *Homo sapiens*; G = *Gorilla*; Pt = *Pan troglodytes*; Po = *Pongo.*

Principal Component 1 shape and groupings

Shape change along the first principal component accounted for 26.5% of the total variation. The first principal component was most informative in distinguishing *Gorilla* from the other great ape groups and was not of great relevance for interpreting differences between *Homo sapiens* and non-human great apes (figure 6.2.2). Shape change along the first principal component related primarily with strength of the distal projection of the mediopalmar edge and the ballooning protrusion of the laterodorsal surface, and consequent irregularity of the shape of the surface (figure 6.2.2).

The shape representing the maxima of the first principal component is palmodorsally elongated and displays a prominent distal projection of the mediopalmar corner and a very pronounced ballooning projection of the surface along the lateral section. These features result in a highly irregular and complex surface, owing largely to the distal ballooning of the laterodorsal surface, as well as an irregular palmar border in which the medial side is strongly bevelled, while the lateral side is less so. The shape representing the maxima of PC 1 is very similar to the mean shape of the *Pan troglodytes* sample (figure 6.1.3). The shape representing the minima of PC 1 is much more regular and less complex, lacking the distinctive dorsolateral distal ballooning of the surface. Compared with the maximum shape, the palmar edge is less bevelled, with the lateropalmar and mediopalmar portions projecting palmar-wards to roughly the same extent. The lateral edge of the surface is slightly expanded at its midsection, and overall, the surface is less mediopalmarly narrow. The ballooning of the lateral surface is far less prominent, and the surface is more featureless.

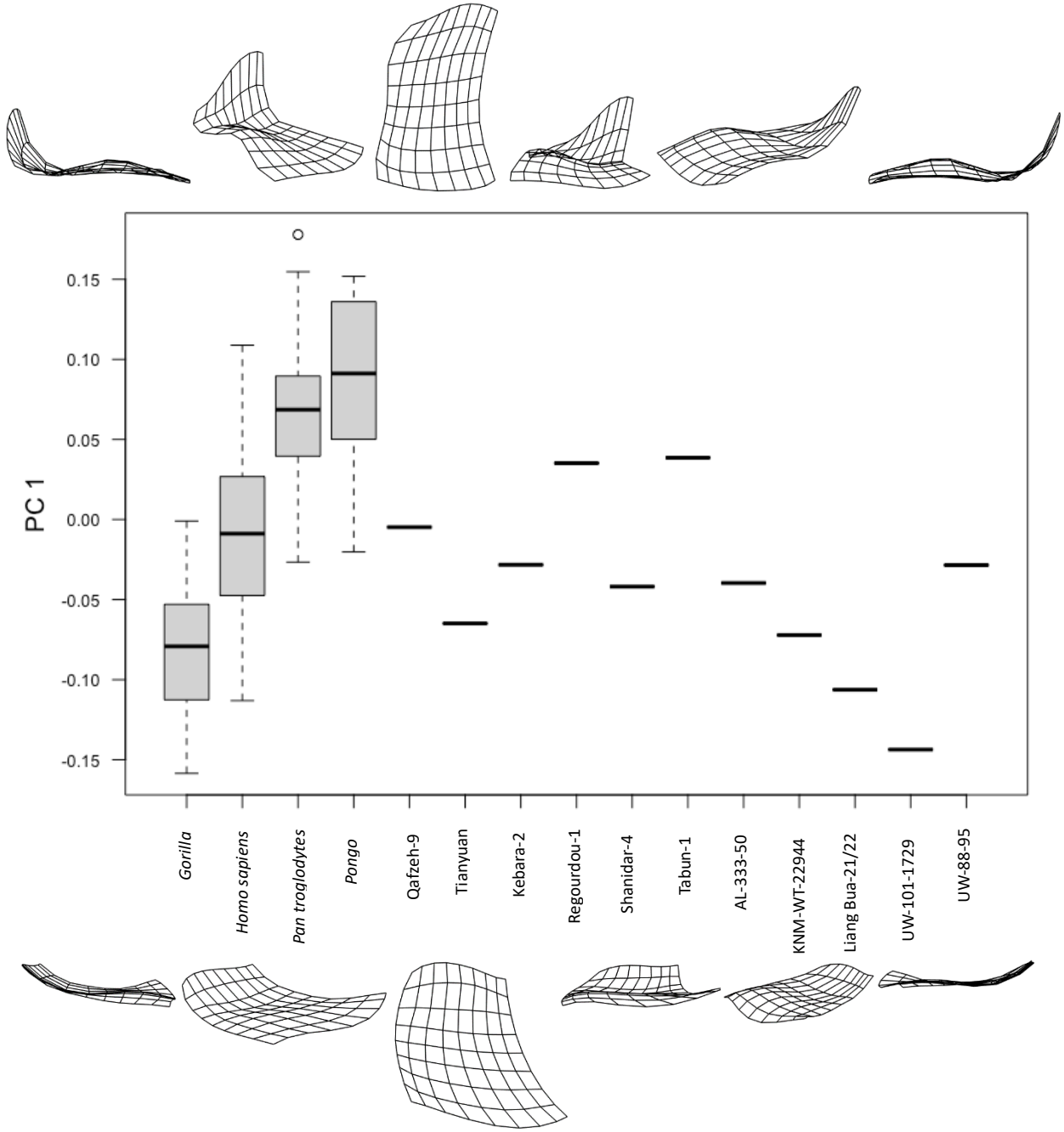

Figure 6.2.2: Boxplot of the first principal component scores for *Gorilla*, *Homo sapiens*, *Pan troglodytes*, and *Pongo* compared to fossil specimens Qafze-9 and Tianyuan (early *Homo sapiens*); Kebara-2, Regourdou-1, Shanidar-4, and Tabun-1 (*Homo neanderthalensis*); AL-333-50 (*Australopithecus afarensis*); KNM-WT-22944 (cf. Australopithecus afarensis) ; Liang Bua 21/22 (*Homo floresiensis*); UW-101-1729 (*Homo naledi*); and UW-88-95 (*Australopithecus sediba*). Black horizontal lines represent the median values of extant groups, and PC scores of fossil specimens, boxes are the interquartile range, whiskers are the non-outlier ranges, and empty circles are outliers.

Table 6.2.3: Tukey honestly significant difference (HSD) *post-hoc* test results on PC 1 scores among *Homo, Pan, Gorilla, and Pongo.* Significant results ($p < 0.05$) were highlighted in bold.

Group		Mean difference	*p*	95% confidence interval	
				Lower bound	Upper bound
Homo	*Gorilla*	0.073	**<0.001**	0.047	0.099
	Pan	-0.075	**<0.001**	-0.101	-0.049
	Pongo	-0.095	**<0.001**	-0.130	-0.061
Gorilla	*Homo*	-0.073	**<0.001**	-0.099	-0.047
	Pan	-0.148	**<0.001**	-0.176	-0.121
	Pongo	-0.168	**<0.001**	-0.204	-0.133
Pan	*Homo*	0.075	**<0.001**	0.049	0.101
	Gorilla	0.148	**<0.001**	0.121	0.176
	Pongo	-0.020	0.445	-0.056	0.015
Pongo	*Homo*	0.095	**<0.001**	0.061	0.130
	Gorilla	0.168	**<0.001**	0.133	0.204
	Pan	0.020	0.445	-0.015	0.056

Along the first principal component, Tukey's Honestly Significant Difference test indicated that there is a significant difference between the means of all extant groups, except for between *Pan troglodytes* and *Pongo* (table 6.2.3). *Gorilla* specimens are situated exclusively in the negative aspect of PC 1, while *Pan troglodytes* and *Pongo* are predominantly in the positive aspect, having a similar range. While the median of the *Homo sapiens* group is in the negative aspect of PC 1, the group's range is distributed fairly evenly and broadly between the negative and positive aspects, indicating that shape change along the first principal component is not directly pertinent to *Homo sapiens.*

All but two of the fossil specimens are in the negative range of the first principal component, and within the range of *Gorilla* (figure 6.2.2). Regourdou-1 and Tabun-1, both *Homo neanderthalensis* specimens, have a positive PC 1 score, but are within one standard deviation of the mean of *Pan troglodytes, Pongo,* and *Homo sapiens* (table 6.2.2). Regourdou-1 and Tabun-1, along with the modern *Homo sapiens* specimen Qafzeh-9, are the only three fossil specimens within the range of all three African great apes (including *Homo sapiens*). Other than Regourdou-1 and Tabun-1, all fossil specimens are negatively-scored along PC 1. UW-101-1729 (*Homo naledi*) is the only fossil specimen outside the range of *Homo sapiens*, and though it is within the *Gorilla* range, it is more than one standard deviation from the mean of every extant group. UW-101-1729, along with the three other most negatively-scored fossil specimens, Tianyuan-1 (early *Homo sapiens*), KNM-WT-22944-I (*Australopithecus cf. Australopithecus afarensis*), and Liang Bua

21/22 (*Homo floresiensis*) are the only four fossil specimens whose PC 1 score was more than one standard deviation from the mean of the *Homo sapiens* group.

Principal Component 2 shape and groupings

The second principal component accounted for 15.8% of the total variation. Shape change along the second principal component relates primarily to the acuteness of curvature in the palmodorsal plane, especially along the medial border of the surface, and, as with PC 1, the smoothness of the surface as a whole (figure 6.2.3). The second principal component is most effective in distinguishing *Homo sapiens* from *Pan troglodytes*.

The shape representative of the negative extreme of PC 2 is relatively flat in both the palmodorsal and mediolateral planes, and overall, quite featureless. It is palmodorsally long and mediolaterally narrow. Both the mediopalmar and mediodorsal corners are slightly distally-projecting relative to their corresponding lateral corners, resulting in a mild palmodorsal concave curvature of the medial edge. The dorsal edge curves proximally, resulting in a slight wavy profile of the surface, becoming more pronounced towards the lateral edge (figure 6.2.3). The minimum shape of PC 2 closely resembles the mean shape of the *Homo sapiens* sample (figure 6.1.1).

The shape representative of the maxima of the second principal component is mediolaterally wider than the corresponding minimum shape (figure 6.2.3). However, the most striking features of this shape are the acute concavity of the medial edge, caused by the distodorsal projection of the mediopalmar corner, and the prominent distal ballooning of the lateral part of the surface. In conjunction, this results in a strong, scooped, and highly bevelled mediopalmar portion, and while the medial half of the surface is curved in a smooth and regular manner, the lateral section is highly erratic, with the distal bulging feature causing the lateral border to be elevated relative to the medial, resulting in a highly complex surface. This surface morphology is reminiscent of the shape representative of the PC 1 maxima (figure 6.2.2), but with a wider mediolateral profile and exaggerated features.

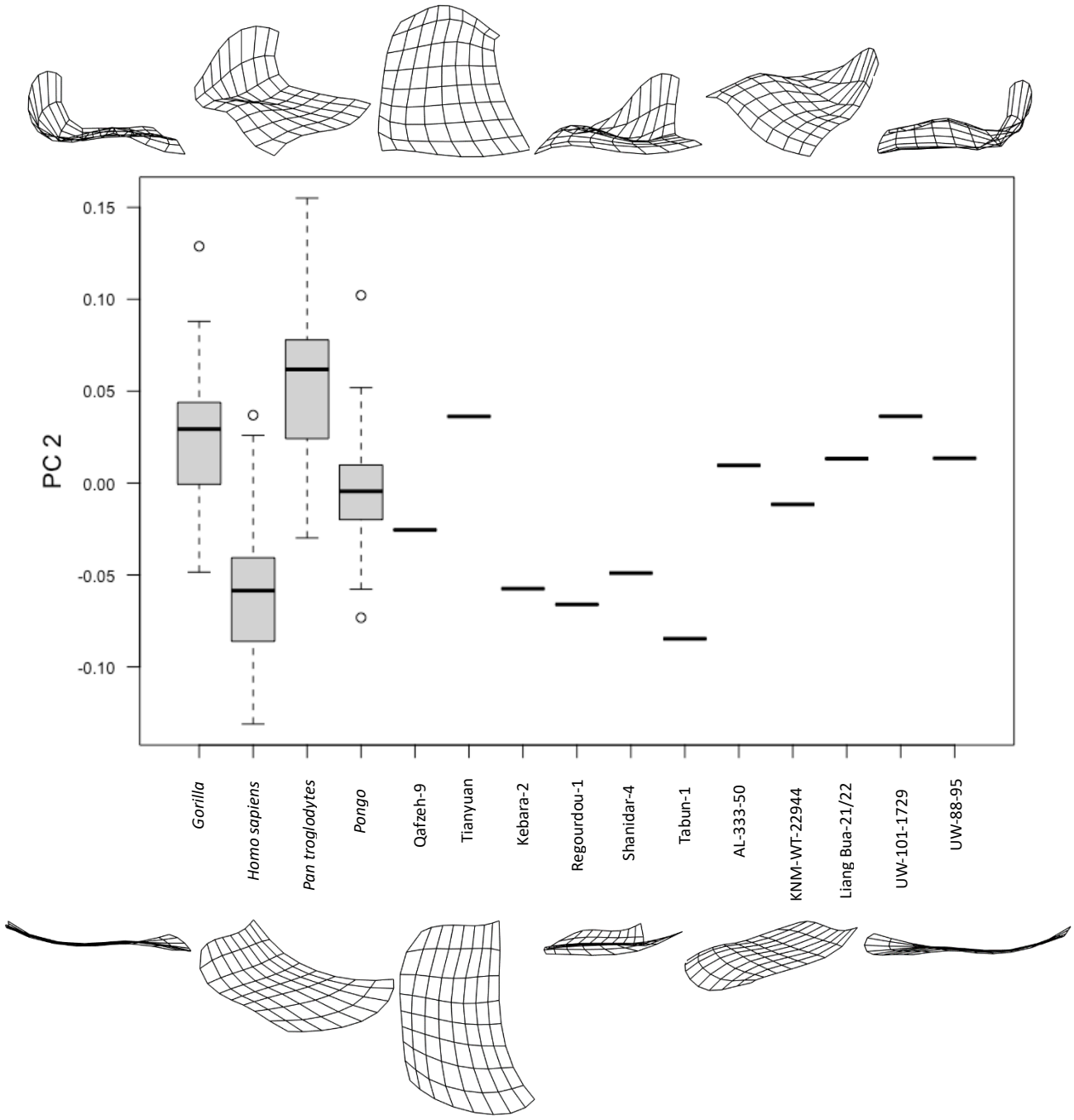

Figure 6.2.3: Boxplot of the second principal component scores for *Gorilla*, *Homo sapiens*, *Pan troglodytes*, and *Pongo* compared to fossil specimens Qafze-9 and Tianyuan (early *Homo sapiens*); Kebara-2, Regourdou-1, Shanidar-4, and Tabun-1 (*Homo neanderthalensis*); AL-333-50 (*Australopithecus afarensis*); KNM-WT-22944 (cf. Australopithecus afarensis) ; Liang Bua 21/22 (*Homo floresiensis*); UW-101-1729 (*Homo naledi*); and UW-88-95 (*Australopithecus sediba*). Black horizontal lines represent the median values of extant groups, and PC scores of fossil specimens, boxes represent the interquartile range, whiskers are the non-outlier ranges, and empty circles are outliers.

Table 6.2.4: Tukey honestly significant difference (HSD) *post-hoc* test results on PC 2 scores among *Homo, Pan, Gorilla, and Pongo.* Significant results ($p < 0.05$) were highlighted in bold.

Group		Mean difference	*p*	95% confidence interval	
				Lower bound	Upper bound
Homo	*Gorilla*	-0.084	**<0.001**	-0.105	-0.062
	Pan	-0.115	**<0.001**	-0.136	-0.094
	Pongo	-0.058	**<0.001**	-0.086	-0.030
Gorilla	*Homo*	0.084	**<0.001**	0.062	0.105
	Pan	-0.031	**0.002**	-0.053	-0.009
	Pongo	0.026	0.097	-0.003	0.055
Pan	*Homo*	0.115	**<0.001**	0.094	0.136
	Gorilla	0.031	**0.002**	0.009	0.053
	Pongo	0.057	**<0.001**	0.028	0.086
Pongo	*Homo*	0.058	**<0.001**	0.030	0.086
	Gorilla	-0.026	0.097	-0.055	0.003
	Pan	-0.057	**<0.001**	-0.086	-0.028

Tukey's HSD text for the second principal component showed that all groups have means that arere statistically significantly different from each other, with the exception of *Gorilla* and *Pongo*, whose means do not differ significantly (table 6.2.4). The second principal component is most informative in separating *Homo sapiens* from *Pan troglodytes* and *Gorilla*, though there is considerable overlap between the ranges of all the extant taxa. The *Homo sapiens* sample is strongly skewed towards the negative portion of the second principal component. In contrast, the interquartile ranges of both *Gorilla* and *Pan troglodytes* are positive, with the upper quartile of *Pan troglodytes* extending to the positive extreme of PC 2. The range of *Pongo* is spread evenly between negative and positive scores, with its median approximating the midpoint of the second principal component (figure 6.2.3).

The fossil specimens are distributed widely across the second principal component (figure 6.2.3), and as such the second principal component is of very limited utility in assessing the placement of fossil hominin taxa with relation to extant taxa, will many specimens having a PC 2 value within the ranges of all four studied extant taxa. The two early modern *Homo sapiens* specimens (Qafzeh-9 and Tianyuan) are both outside the interquartile range of the *Homo sapiens* sample. Qafze-9 has a negative PC 2 score and is within the group's upper quartile. However, Tianyuan, which has a positive PC 2 score, is marginally outside the human range and is more than one standard deviation from the group mean (table 6.2.2), although it has a PC 2 score comparable to an extremal *Homo sapiens* specimen (figure 6.2.3). The four *Homo*

neanderthalensis specimens (Kebara-2; Regourdou-1; Shanidar-4; Tabun-1) are the only fossil specimens within the interquartile range of *Homo sapiens* and are the only specimens not within the range of all three non-human taxa. All four neanderthal specimens are within one standard deviation of the mean of *Homo sapiens* and are more than one standard deviation from the mean of the non-human groups (table 6.2.2; figure 6.2.3). UW-101-1729 (*Homo naledi*) is the only other fossil specimen outside the range of *Homo sapiens*, and has a similar PC 2 score to Tianyuan. The remaining fossil specimens (AL-333-50, *Australopithecus* afarensis; KNM-WT-22944-I, *Australopithecus cf. Australopithecus afarensis*; Liang Bua 21/22, *Homo floresiensis*; UW-88-95, *Australopithecus sediba*), are within the range of all four extant taxa, and within the upper quartile of *Homo sapiens*, but more than one standard deviation from the group mean. AL-333-50, Liang Bua-21/22, and UW-88-95 are all within the interquartile range of *Gorilla*, while KNM-WT-22944-I is close the median value of *Pongo.*

Principal Component 3 shape and groupings

The third principal component, which accounts for 10.6% of the total variation, is of limited effectiveness in distinguishing between extant groups, though the greatest separation is between the *Pan troglodytes* and *Pongo* samples (figure 6.2.4). Shape change along this principal component is most concerned with the lateral half of the articular surface. The shape of the negative aspect of the third principal component exhibits a highly palmodorsally-concave curvature that is mediolaterally uniform across the surface (figure 6.2.4). The negative shape is scooped in a palmodorsal profile, with the lateropalmar and mediopalmar corners projecting distally to approximately the same extent. While there is a ballooning of the surface characteristic of non-human taxa, it is subtle and migrated more centrally and distally, resulting in a distal edge that slopes proximally.

The shape representative of the PC 3 maxima displays less bevelling of the palmar edge than the minimum shape, with only the mediopalmar corner projecting distally, resulting in an erratic and laterally-sloping palmar edge. The distal ballooning feature is much more prominent and is located in a more lateral and palmar location. As with the maxima of PCs 1 and 2, the maximal shape of PC 3 is most reminiscent of the *Pan troglodytes* sample mean shape (figure 6.1.3).

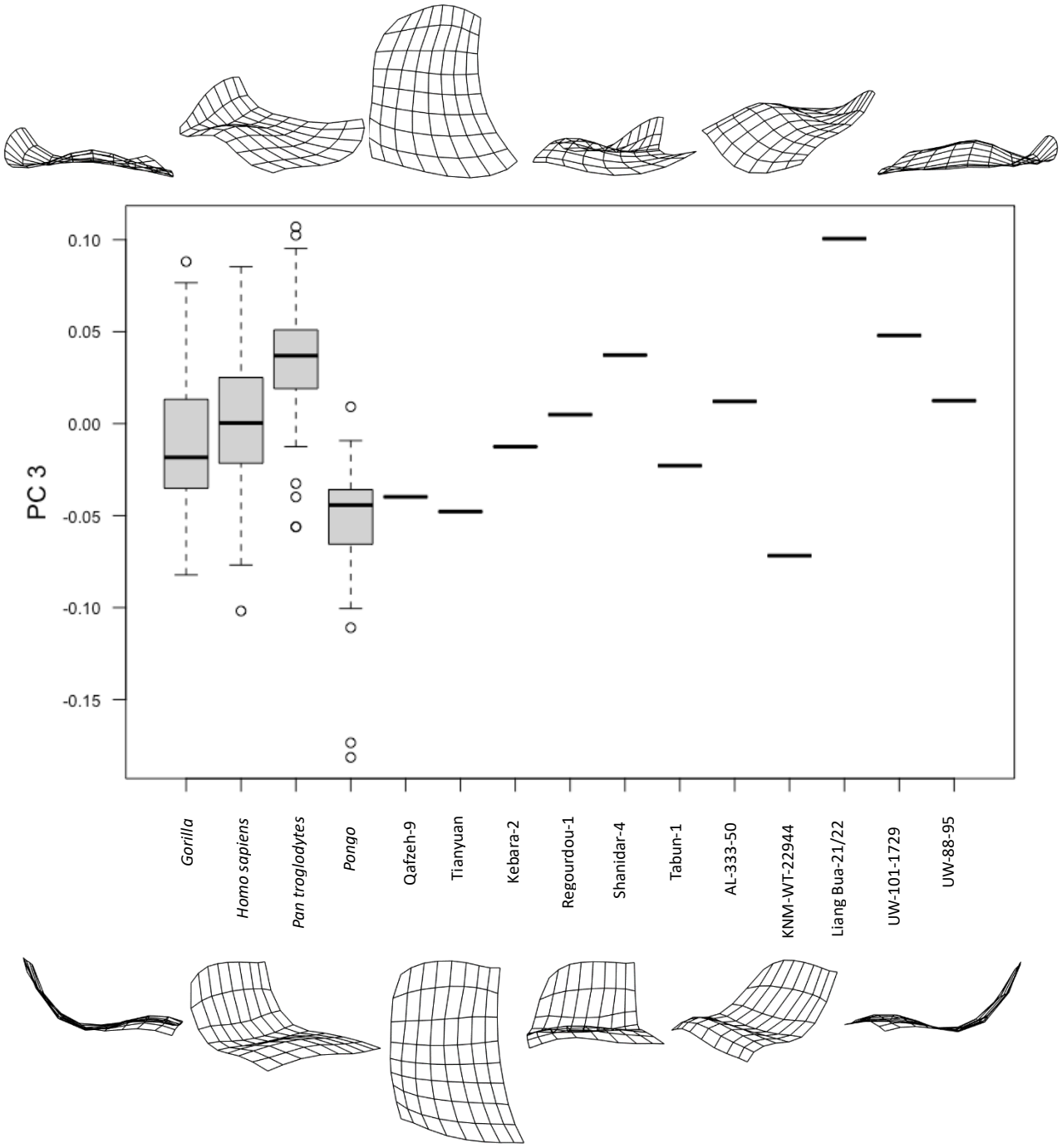

Figure 6.2.4: Boxplot of the third principal component scores for *Gorilla*, *Homo sapiens*, *Pan troglodytes*, and *Pongo* compared to fossil specimens Qafze-9 and Tianyuan (early *Homo sapiens*); Kebara-2, Regourdou-1, Shanidar-4, and Tabun-1 (*Homo neanderthalensis*); AL-333-50 (*Australopithecus afarensis*); KNM-WT-22944 (*Australopithecus cf. Australopithecus afarensis*); Liang Bua 21/22 (*Homo floresiensis*); UW-101-1729 (*Homo naledi*); and UW-88-95 (*Australopithecus sediba*). Black horizontal lines represent the median values of extant groups, and PC scores of fossil specimens, boxes are the interquartile range, whiskers are the non-outlier ranges, and empty circles are outliers.

Table 6.2.5: Tukey honestly significant difference (HSD) *post-hoc* test results on PC 3 scores among *Homo, Pan, Gorilla, and Pongo.* Significant results ($p < 0.05$) were highlighted in bold.

Group		Mean difference	*p*	95% confidence interval	
				Lower bound	Upper bound
Homo	*Gorilla*	0.013	0.469	-0.010	0.035
	Pan	-0.031	**0.003**	-0.053	-0.008
	Pongo	0.064	**<0.001**	0.034	0.094
Gorilla	*Homo*	-0.013	0.469	-0.035	0.010
	Pan	-0.043	**<0.001**	-0.067	-0.020
	Pongo	0.052	**<0.001**	0.021	0.082
Pan	*Homo*	0.031	**0.003**	0.008	0.053
	Gorilla	0.043	**<0.001**	0.020	0.067
	Pongo	0.095	**<0.001**	0.064	0.125
Pongo	*Homo*	-0.064	**<0.001**	-0.094	-0.034
	Gorilla	-0.052	**<0.001**	-0.082	-0.021
	Pan	-0.095	**<0.001**	-0.125	-0.064

Along the third principal component, the means of *Homo sapiens* and *Gorilla* were not significantly different from one another, and the boxplot of the third principal component shows no great distinction between the samples of *Gorilla* and *Homo sapiens* along this axis (table 6.2.5; figure 6.2.4). All other groups significantly differed from each other, though the ranges of both *Pan troglodytes* and *Pongo* overlapped considerably with those of *Homo sapiens* and *Pongo* (figure 6.2.4). The third principal component is most informative in separating *Pan troglodytes* and *Pongo*, which, but for some extremal points, do not overlap. However, there is considerable overlap in the samples of all other pairings along the third principal component.

The fossil specimens exhibit a broad range of values across the third principal component, distributed approximately evenly between the negative and positive halves. Liang Bua-21/22 (*Homo floresiensis*) is strongly positive and outside the range of all extant groups, and more than one standard deviation from their means, although it shares a similar PC 3 value to extremal *Pan troglodytes* specimens (table 6.2.2; figure 6.2.4). Both early modern *Homo sapiens* specimens (Qafzeh-9; Tianyuan) are within the interquartile range of *Pongo,* and while both are within the lower quartile range of *Homo sapiens*, Tianyuan is more than one standard deviation from the *Homo sapiens* mean value (table 6.2.2). KNM-WT-22944-I (*Australopithecus cf. Australopithecus afarensis*) has the most negative score of all fossil specimens, being in the lower quartile of *Pongo*, and more than one standard deviation from the means of all other groups. Kebara-2 (*Homo neanderthalensis*) is the only fossil within the range of all four extant groups, though it is

at least one standard deviation from the *Pan troglodytes* mean value. Tabun-1 (*Homo neanderthalensis*) is within the ranges of *Pongo*, *Homo sapiens*, and *Gorilla*, while the remaining fossil specimens (Regourdou-1, Shanidar-4 (*Homo neanderthalensis*); AL-333-50 (*Australopithecus afarensis*); UW-101-1729 (*Homo naledi*); UW-88-95 (*Australopithecus sediba*)) are within the ranges of *Homo sapiens*, *Gorilla*, and *Pan troglodytes*, though only Regourdou-1 and Shanidar-4 are within one standard deviation of the mean of *Homo sapiens* (table 6.2.2).

Principal Component 4 shape and groupings

While the fourth principal component, which accounts for 8.0% variation, is most effective in separating *Pongo* from the other three taxa, there is considerable overlap between the samples of the four extant taxa, and the fossil specimens are widely dispersed across the principal component. The most prominent shape changes between the shapes representing the minima and maxima of the fourth principal component are found at the mediopalmar and laterodorsal corners, and resultant changes at the palmar and dorsal edges.

The negative aspect of PC 4 (figure 6.2.5) is characterised by a shape that is proximodistally flatter than the positive-most shape, predominantly as a result of the mediopalmar and mediodorsal corners not greatly protruding distally relative to the rest of the surface. In the shape representing the PC 4 maxima, the mediopalmar and mediodorsal corners project more distally and less palmarly, resulting in a more acute curvature of the surface towards the mediopalmar corner in the maximum shape, and a higher and more arched palmar edge.

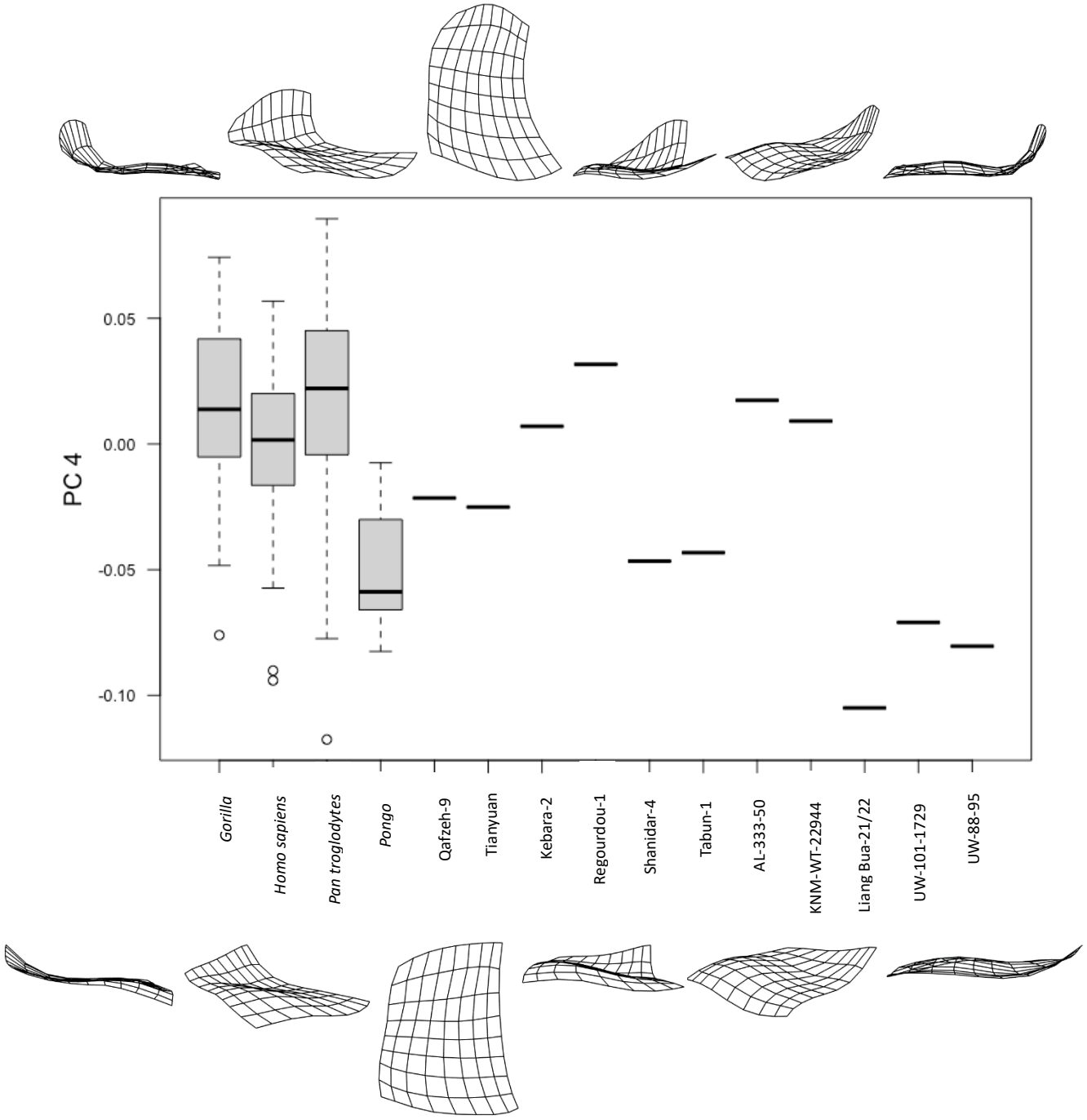

Figure 6.2.5: Boxplot of the fourth principal component scores for *Gorilla*, *Homo sapiens*, *Pan troglodytes*, and *Pongo* compared to fossil specimens Qafze-9 and Tianyuan (early *Homo sapiens*); Kebara-2, Regourdou-1, Shanidar-4, and Tabun-1 (*Homo neanderthalensis*); AL-333-50 (*Australopithecus afarensis*); KNM-WT-22944 (*cf. Australopithecus afarensis*) ; Liang Bua 21/22 (*Homo floresiensis*); UW-101-1729 (*Homo naledi*); and UW-88-95 (*Australopithecus sediba*). Black horizontal lines represent the median values of extant groups, and PC scores of fossil specimens, boxes are the interquartile range, whiskers are the non-outlier ranges, and empty circles are outliers.

Table 6.2.6: Tukey honestly significant difference (HSD) *post-hoc* test results on PC 4 scores among *Homo, Pan, Gorilla, and Pongo.* Significant results ($p < 0.05$) were highlighted in bold.

Group		Mean difference	*p*	95% confidence interval	
				Lower bound	Upper bound
Homo	*Gorilla*	-0.016	0.180	-0.036	0.004
	Pan	-0.017	0.110	-0.037	0.003
	Pongo	0.051	**<0.001**	0.024	0.077
Gorilla	*Homo*	0.016	0.180	-0.004	0.036
	Pan	-0.002	0.997	-0.023	0.020
	Pongo	0.067	**<0.001**	0.039	0.094
Pan	*Homo*	0.017	0.110	-0.003	0.037
	Gorilla	0.002	0.997	-0.020	0.023
	Pongo	0.068	**<0.001**	0.041	0.096
Pongo	*Homo*	-0.051	**<0.001**	-0.077	-0.024
	Gorilla	-0.067	**<0.001**	-0.094	-0.039
	Pan	-0.068	**<0.001**	-0.096	-0.041

The only significant results returned from the Tukey's HSD test was between *Pongo* and the other groups, with no significant difference between the scores of *Homo sapiens, Gorilla,* and *Pan troglodytes* (table 6.2.6). While the values of *Gorilla, Homo sapiens,* and *Pan troglodytes* are spread across both the positive and negative aspects of the fourth principal component, the values of *Pongo* specimens are exclusively negative (figure 6.2.5). The *Homo sapiens* sample is distributed fairly evenly between the negative and positive halves, with a mean value very near to neutral, while both *Gorilla* and *Pan troglodytes* are skewed towards the positive half.

The majority of the fossil specimens are within the ranges of *Homo sapiens, Pan troglodytes,* and *Gorilla* (figure 6.2.5). Liang Bua 21/22 (*Homo floresiensis*) has the most negative PC 4 value of all fossils, and is outside the ranges, and more than one standard deviation from, the means of all four extant groups (table 5.2.2; figure 6.2.5). UW-101-1729 (*Homo naledi*) and UW-88-95 (*Australopithecus sediba*) are both outside the *Homo sapiens range,* and while all other fossil specimens are within the range of *Homo sapiens*, Shanidar-4 and Tabun-1 (*Homo neanderthalensis*) are more than one standard deviation from the mean value of the *Homo sapiens* sample (table 6.2.2). Qafzeh-9 and Tianyuan (early *Homo sapiens*) fall within the ranges of all four groups, and into the lower quartile of *Homo sapiens*, while Kebara-2 (*Homo neanderthalensis*), AL-333-50 (*Australopithecus afarensis*), and KNM-WT-22944-I (*Australopithecus cf. Australopithecus afarensis*) are in the interquartile ranges of all African great apes (*Homo sapiens, Gorilla,* and *Pan troglodytes*). Regourdou-1, which has the most positive PC

4 value of all fossil taxa, is in the interquartile range of *Pan troglodytes* and *Gorilla*, and in the upper quartile of *Homo sapiens* (figure 6.2.5). Given the considerable overlap between the samples of the four extant taxa, and the wide dispersal of the fossils, the fourth principal component, as with the third, is of very limited utility in distinguishing between groups or in assessing fossil affinities to the extant samples.

Principal Component 5 shapes and groupings

The main shape changes along the fifth principal component, which accounted for 6.7% of the variation, concerns the prominence of the distal ballooning of the laterodorsal surface characteristic of non-human taxa, and resultant degree of both palmodorsal and mediolateral convex/concave curvature of the surface, especially its dorsal portion. Again, there is considerable overlap in the samples of the extant taxa, and fossil specimens were widely dispersed across the principal component.

The laterodorsal quadrant of the shape representing the negative aspect of the fifth principal component displayed such a prominent distal protrusion that the entire dorsal portion of the surface resembled a spherical surface, though skewed to the lateral edge, and with a dorsolateral corner sloping strongly proximally (figure 6.2.6). In contrast, the maximum shape of the fifth principal component is completely absent of any such ballooning of its surface. As such, the entire surface is concave in both its mediolateral and dorsopalmar planes. A secondary, more subtle difference concerned the palmar edge, with the palmar edge of the maxima appearing concaved and sloping laterally when viewed from a dorsal vantage, while the palmar border of the minimum shape is arched, with its central part extending distally past the palmar corners.

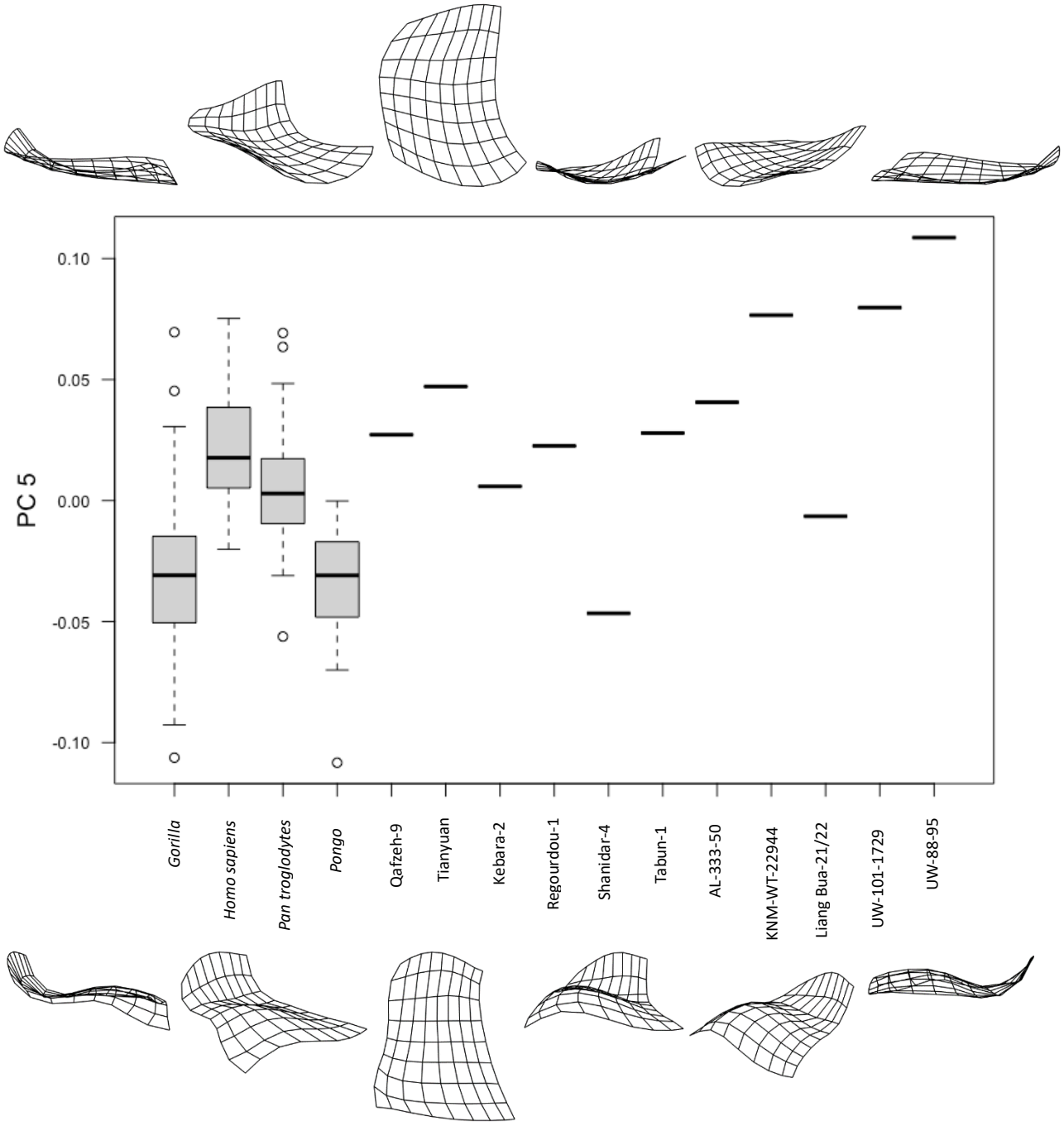

Figure 6.2.6: Boxplot of the fifth principal component scores for *Gorilla*, *Homo sapiens*, *Pan troglodytes*, and *Pongo* compared to fossil specimens Qafze-9 and Tianyuan (early *Homo sapiens*); Kebara-2, Regourdou-1, Shanidar-4, and Tabun-1 (*Homo neanderthalensis*); AL-333-50 (*Australopithecus afarensis*); KNM-WT-22944 (cf. *Australopithecus afarensis*) ; Liang Bua 21/22 (*Homo floresiensis*); UW-101-1729 (*Homo naledi*); and UW-88-95 (*Australopithecus sediba*). Black horizontal lines represent the median values of extant groups, and PC scores of fossil specimens, boxes are the interquartile range, whiskers are the non-outlier ranges, and empty circles are outliers.

Table 6.2.7: Tukey honestly significant difference (HSD) *post-hoc* test results on PC 5 scores among *Homo, Pan, Gorilla, and Pongo.* Significant results ($p < 0.05$) were highlighted in bold.

Group		Mean difference	*p*	95% confidence interval	
				Lower bound	Upper bound
Homo	*Gorilla*	0.052	**<0.001**	0.036	0.068
	Pan	0.017	**0.031**	0.001	0.032
	Pongo	0.060	**<0.001**	0.039	0.081
Gorilla	*Homo*	-0.052	**<0.001**	-0.068	-0.036
	Pan	-0.036	**<0.001**	-0.052	-0.019
	Pongo	0.008	0.777	-0.014	0.030
Pan	*Homo*	-0.017	**0.031**	-0.032	-0.001
	Gorilla	0.036	**<0.001**	0.019	0.052
	Pongo	0.044	**<0.001**	0.022	0.065
Pongo	*Homo*	-0.060	**<0.001**	-0.081	-0.039
	Gorilla	-0.008	0.777	-0.030	0.014
	Pan	-0.044	**<0.001**	-0.065	-0.022

With the exception of *Gorilla* and *Pongo*, the means of the fifth principal component of all the groups are significantly different from one another (table 6.2.7). The interquartile ranges of both *Gorilla* and *Pongo* are in the negative half of PC 5, while the interquartile range of *Homo sapiens* is exclusively positive, though its lower quartile range does encroach into the negative aspect (figure 6.2.6). The median of *Pan troglodytes* is near to zero, and the sample is dispersed fairly evenly between negative and positive values. Though the *Homo sapiens* sample has the most positive value, several extremal *Pan troglodytes* and *Gorilla* specimens have a similarly high value. Again, there is considerable overlap between extant groups along the fifth principal component, and fossil specimens are widely dispersed, though skewed to the positive aspect of the principal component.

Shanidar-4 (*Homo neanderthalensis*) has the most negative PC 5 score of all fossil specimens and is the only fossil specimen to fall below the ranges of *Homo sapiens* and *Pan troglodytes.* It is within the interquartile ranges of *Gorilla* and *Pongo*, and more than one standard deviation from the mean of both the latter taxa (figure 6.2.6; table 6.2.2). Three fossil specimens have PC 5 values higher than the maximum of all extant taxa groups. KNM-WT-22944-I (*Australopithecus cf. Australopithecus afarensis*) and UW-101-1729 (*Homo naledi*) are both marginally higher than the range of *Homo sapiens*, while UW-88-95 (*Australopithecus sediba*) has an extremely high PC 5 score (figure 6.2.6). All three of these specimens are more than one standard deviation from the means of all extant groups (table 6.2.2). All other fossil specimens,

which include the two early modern *Homo sapiens* specimens (Qafzeh-9; Tianyuan), three of the four *Homo neanderthalensis* specimens (Kebara-2; Regourdou-1; Tabun-1), and AL-333-50 (*Australopithecus afarensis*) are within the ranges of both *Homo sapiens* and *Pan troglodytes* (figure 6.2.6).

Bivariate Scatterplots

PC 1 v PC 2

Bivariate scatterplots of the first three principal components are shown in figures 6.2.7 to 6.2.9. The bivariate scatterplot of the first principal component against the second separated the four extant taxa into two distinct clusters (figure 6.2.7). In the lower-left section of the scatterplot are *Gorilla* and *Homo sapiens*, while *Pan troglodytes* and *Pongo* occupy the upper-right section. Within these two clusters, there is considerable overlap between the two constituent taxa, but very little interaction between the two clusters. *Gorilla* is exclusively in the left half of the boxplot, while the morphospace of *Homo sapiens* is spread predominantly across the lower two quadrants, with a small area in the upper left quadrant. *Pan troglodytes* is situated mainly in the upper right quadrant, while *Pongo* is distributed across both quadrants of the right half of the scatterplot, with both taxa sharing a considerable amount of morphospace.

All the fossil specimens are located within the *Gorilla-Homo sapiens* cluster, with all but two resting within the *Homo sapiens* morphospace (figure 6.2.7). Tianyuan (*Homo sapiens*) is solely within the *Gorilla* morphospace, but in the vicinity of *Homo sapiens*, while UW-101-1729 (*Homo naledi*) is found further out from the *Homo sapiens* morphospace, having a PC 1 score below the range of that group. Liang Bua-21/22 (*Homo floresiensis*), AL-333-50 (*Australopithecus afarensis*), KNM-WT-22944-I (*Australopithecus cf. Australopithecus afarensis*), and UW-88-95 (*Australopithecus sediba*) are all situated in the shared *Gorilla-Homo sapiens* morphospace, while all *Homo neanderthalensis* specimens (Kebara-2, Shanidar-4, Tabun-1, Regourdou-1) and Qafzeh-9 (early *Homo sapiens*) are within the *Homo sapiens* morphospace alone.

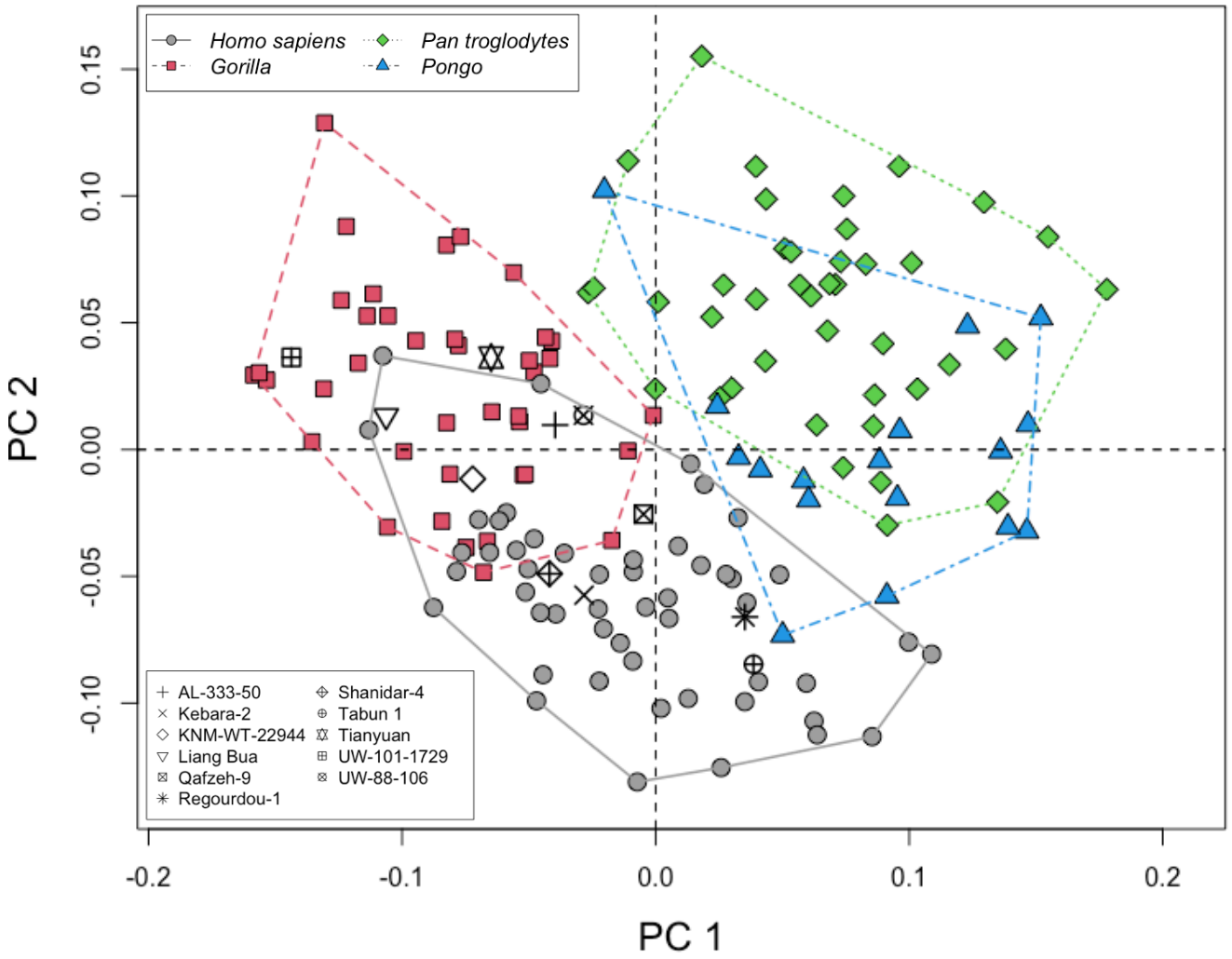

Figure 6.2.7: Scatterplot of the first vs. second principal component scores of extant samples (*Homo sapiens, Gorilla, Pan troglodytes* and *Pongo*) and fossil specimens AL-333-50 (*Australopithecus afarensis*), KNM-WT-22944 (cf. Australopithecus afarensis) , Liang Bua-21/22 (*Homo floresiensis*), UW-101-13729 (*Homo naledi*), and UW-88-95 (*Australopithecus sediba*), Kebara-2, Regourdou-1, Shanidar-4, Tabun-1 (*Homo neanderthalensis*), and Qafzeh-9 and Tianyuan (early *Homo sapiens*. The first principal component accounted for 26.5% of the variation, while the second principal component accounted for 15.8%. The scatterplot of PC 1 vs PC 2 separates the extant taxa into two clusters, with the fossil specimens concentrated in the *Homo sapiens – Gorilla* cluster.

PC 1 v PC 3

The bivariate scatterplot of the first against the third principal component is shown in figure 6.2.8. The *Homo sapiens* morphospace is centred at the midpoint of the scatterplot and is distributed evenly across all four quadrants. *Gorilla* is exclusively in the negative half of the plot, across both the upper and lower left quadrants, while *Pan troglodytes* is concentrated primarily in the upper left quadrant, with considerable encroachment into the upper-left and lower-right quadrants, and minimally into the lower-left. Both *Gorilla* and *Pan troglodytes* overlap considerably with the morphospace of *Homo sapiens* and have a small area of interaction with each other in the left half of the plot. The bivariate scatterplot of PC 1 against PC 3 is most effective in distinguishing the *Pongo* morphospace, which is located mostly in the lower-right quadrant, and while *Pongo* overlaps with *Homo sapiens* and *Pan troglodytes,* there is no interaction between *Pongo* and *Gorilla*.

The fossil specimens are distributed across the cluster of African Great Ape taxa (*Gorilla*, *Pan troglodytes*, and *Homo sapiens*), with all but three within the *Homo sapiens* morphospace. Liang Bua-21/22 (*Homo floresiensis*), the only fossil specimen not within an extant taxon's morphospace, is slightly above the area of *Gorilla*, while UW-101-1729 (*Homo naledi*) and KNM-WT-22944-I (*Australopithecus cf. Australopithecus afarensis*) is solely within the *Gorilla* morphospace. All other fossil specimens are within the morphospace of *Homo sapiens*, with Shanidar-4, Kebara-2 (*Homo neanderthalensis*), Tianyuan (early *Homo sapiens*), AL-333-50 (*Australopithecus afarensis*), and UW-88-95 (*Australopithecus sediba*) located in the vicinity shared by *Homo sapiens* and *Gorilla*, Regourdou-1 (*Homo neanderthalensis*) within the *Homo sapiens-Pan troglodytes* morphospace, and Tabun-1 (*Homo neanderthalensis*) within the morphospace of *Homo sapiens, Pan troglodytes,* and *Pongo.* Qafzeh-9 (early *Homo sapiens*) is the only fossil specimen solely within the morphospace of *Homo sapiens.*

The bivariate scatterplots of PCs 2v3, 2v4, 3v4, 3v5, and 4v5 are not informative in distinguishing between extant groups nor in interpreting the relationship of fossil hominin specimens to extant taxa. As such, they are not discussed in the main body of the text, though they are available for reference in Appendix I.

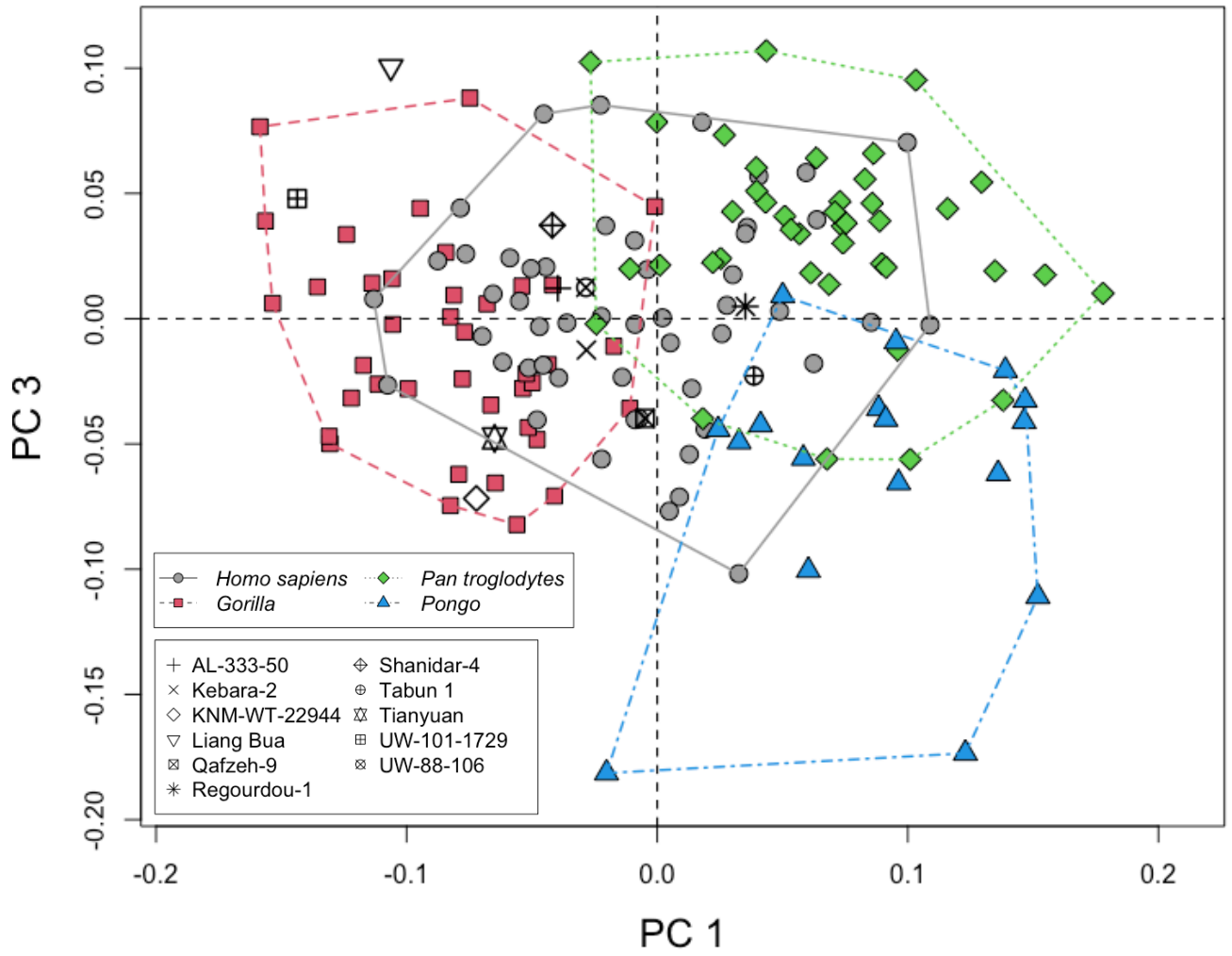

Figure 6.2.8: Scatterplot of the first vs. third principal component scores of extant samples (*Homo sapiens, Gorilla, Pan troglodytes* and *Pongo*) and the fossil specimens. The first principal component accounted for 26.5% of the variation, while the third principal component accounted for 10.6%. The scatterplot of PC 1 vs PC 3 is most effective in separating *Pongo* from the other extant taxa, with the fossil specimens being distributed across the African apes and *Homo sapiens* morphospaces.

PC 2 v PC 5

Of all the bivariate scatterplots concerning the principal components of the hamate's articular surface for the fourth metacarpal, the bivariate scatterplot of the second against fifth principal component was the most effective in separating *Homo sapiens* from the other taxonomical groups (figure 6.2.9). The morphospace of *Homo sapiens* is concentrated in the upper-left quadrant along a bottom-left-to-upper-right axis, at the negative PC 2 scores and positive PC 5 scores, with small sections of the morphospace expanding into the lower-left and upper-right quadrants. All the non-human groups, in contrast, are distributed in a cluster across the lower-left, upper-right, and lower-left quadrants, along a similar axis. There is considerable overlap of the morphospaces of the non-human groups in this scatterplot, though no interaction between the morphospaces of the *Homo sapiens* sample and the cluster of non-human taxa.

Despite the clear distinction of the *Homo sapiens* morphospace from those of the other extant taxa, the fossil specimens do not all fall neatly into the morphospace of *Homo sapiens.* Interestingly, Tianyuan, which is an early *Homo sapiens* specimen, lies within the *Pan troglodytes* zone, although it is within the upper *Homo sapiens* range for both PC 2 and PC 5. Liang Bua-21/22 (*Homo floresiensis*) is within the morphospace shared between all non-human taxa, while Shanidar-4 (*Homo neanderthalensis*), which has a PC 5 value below the modern human range, is exclusively within the *Pongo* morphospace. Five fossil specimens are to be found within the morphospace of modern humans, including Qafzeh-9 (early *Homo sapiens*), Regourdou-1, Kebara-2, Tabun-1 (*Homo neanderthalensis*), and Al-333-50 (*Australopithecus afarensis*). The remaining three fossil specimens (UW-88-95, *Australopithecus sediba*; KNM-WT-22944-I, *Australopithecus cf. Australopithecus afarensis*; UW-101-1729, *Homo naledi*), while outside the *Homo sapiens* morphospace, appear to follow the axis of the human morphospace, being above the human sample.

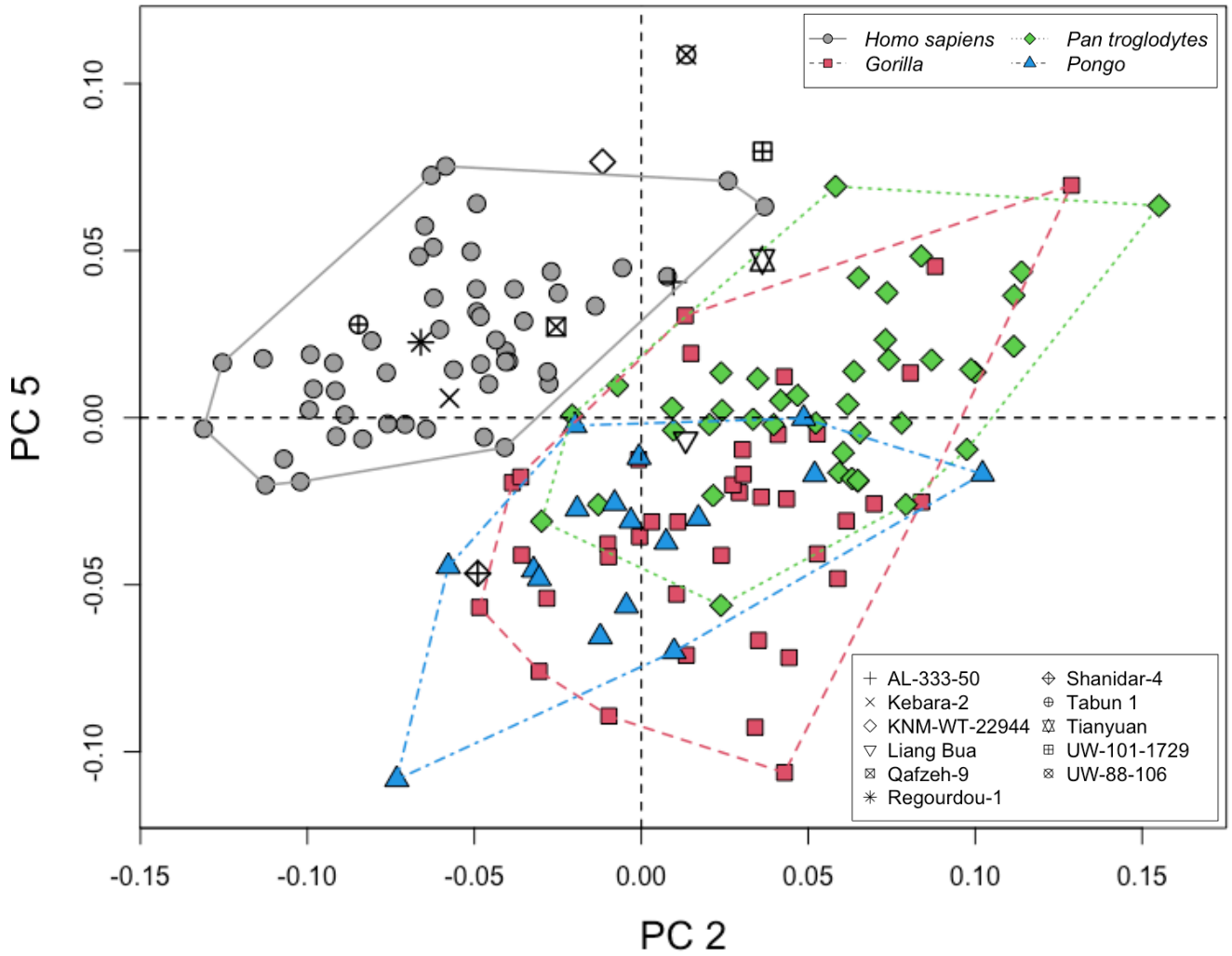

Figure 6.2.9: Scatterplot of the second vs. fifth principal component scores of extant samples (*Homo sapiens, Gorilla, Pan troglodytes* and *Pongo*) and the fossil specimens. The fifth principal component accounts for only 6.7% of the total variation, however the scatterplot of PC 2 vs PC 5 is the most effective in separating *Homo sapiens* from other taxa. Most fossil specimens were within or near the vicinity of the *Homo sapiens* morphospace, while several, most notably Tianyuan (early *Homo sapiens*), were in the morphospace of non-human taxa.

6.3 Hamate-MC 4 Canonical Variate Analysis

The first 12 principal components accounted for 90.73% of the variance for the principal components analysis of the hamate-fourth metacarpal articular surface. Results of the canonical variate analysis that was carried out using these first 12 principal components are shown in table 6.3.1 and 6.3.2. The first canonical variate accounted for 55.6% of the variation between groups, with the second accounting for 24.9%. The third canonical variate accounted for 19.5% of the variation in shape between groups. The canonical variate analysis was successful in classifying extant specimens into their *a priori* groups with an accuracy of 97.30% (k = 0.96). All specimens of *Homo sapiens* and *Pongo* were correctly categorized into their respective groups, while two specimens of *Pan troglodytes* were misclassified as belonging to *Gorilla*, and one as *Homo sapiens,* resulting in *Pan troglodytes* being correctly classified in 92.68% of cases. The *Gorilla* sample was correctly classified with an accuracy of 97.4%, with one specimen being misassigned as *Pongo*.

Table 6.3.1: Table of predicted taxa against actual taxa. *A priori* classification is along the horizontal, with group classification through linear discriminant analysis is along the vertical.

	Gorilla	*Homo sapiens*	*Pan troglodytes*	*Pongo*	*N*
Gorilla	38 (97.4%)	0	0	1	39
Homo sapiens	0	51 (100%)	0	0	51
Pan troglodytes	2	1	38 (92.68%)	0	41
Pongo	0	0	0	17 (100%)	17

MANOVA along the three canonical variates axes returned significant results between all extant groups ($F(3, 144) = 221.59$, $p < 0.001$, Wilks' $\Lambda = 0.0095$). Results of the one-way analysis of variance along each CV, shown in table 6.3.3, revealed a statistically significant difference in CV score between at least two groups along all three CV axes. Results of the pairwise Tukey's HSD test for the means comparisons of taxonomic groups along each canonical variate axis is shown in table 6.3.4. Results of the Tukey HSD tests along the scores of the first and second canonical variate axes showed that the mean values of all groups were significantly different from each other. Along the third canonical variate there was no significant difference between the mean value of *Homo sapiens* and *Gorilla* (p = 0.125, 95% C.I. = -1.023, 0.083) or between *Homo sapiens*

and *Pan troglodytes* (*p* = 0.296, 95% C.I. = -0.915, 0.176), while all other pairwise comparisons were statistically significant (table 6.3.3).

Table 6.3.2: Results of analysis of variance on canonical variate scores on extant groups.

Canonical Variate	DF	Sum of Squares	Mean Squares	*F* Value	*p*
CV 1	3, 144	971.5	323.8	323.8	**<0.001**
CV 2	3, 144	435.6	145.2	145.2	**<0.001**
CV 3	3, 144	340.9	113.6	113.6	**<0.001**

Table 6.3.3: *P*-values for Tukey's HSD pairwise comparisons of canonical variate scores.

	Homo sapiens	Gorilla	Pan troglodytes	Pongo
Canonical Variate 1 (55.6%)				
Homo sapiens	-	**<0.001**	**<0.001**	**<0.001**
Gorilla		-	**<0.001**	**<0.001**
Pan troglodytes			-	**<0.001**
Pongo				-
Canonical Variate 2 (24.9%)				
Homo sapiens	-	**<0.001**	**<0.001**	**<0.001**
Gorilla		-	**<0.001**	**<0.001**
Pan troglodytes			-	**<0.001**
Pongo				-
Canonical Variate 3 (19.5%)				
Homo sapiens	-	0.125	0.296	**<0.001**
Gorilla		-	**0.001**	**<0.001**
Pan troglodytes			-	**<0.001**
Pongo				-

Results of the canonical variant analysis for the hamate's fourth metacarpal articulation using the values of the first 12 principal components classified all but one fossil specimen as belonging to the *Homo sapiens* group. AL-333-50 (*Australopithecus afarensis*) was classified as *Gorilla* with a confidence of 65.9%, and a probability of 31.8% of belonging to the *Homo sapiens* sample. Eight of the fossil specimens were classified as *Homo sapiens* with a confidence of above 99%. Liang Bua-21/22 (*Homo floresiensis*) was categorized as *Homo sapiens* with a confidence 92.9% and a probability of 7.1% as belonging to *Gorilla.* Shanidar-4 (*Homo neanderthalensis*) was categorized as *Homo sapiens* with a confidence of 85.0%, and a 13.9% likelihood of belonging to the *Gorilla* group (table 6.3.4).

Table 6.3.4: Canonical variate analysis (CVA) classification results of fossil specimens. Results were in percentage.

	Homo sapiens	*Gorilla*	*Pan troglodytes*	*Pongo*	Classification
AL-333-50	31.8	65.9	2.2	0.0	*Gorilla*
Kebara-2	99.8	0.2	0.0	0.0	*Homo sapiens*
KNM-WT-22944	100.0	0.0	0.0	0.0	*Homo sapiens*
Liang Bua-21/22	92.9	7.1	0.0	0.0	*Homo sapiens*
Qafzeh-9	100.0	0.0	0.0	0.0	*Homo sapiens*
Regourdou-1	100.0	0.0	0.0	0.0	*Homo sapiens*
Shanidar-4	85.0	13.9	0.1	1.1	*Homo sapiens*
Tabun-1	100.0	0.0	0.0	0.0	*Homo sapiens*
Tianyuan	100.0	0.0	0.0	0.0	*Homo sapiens*
UW-101-1729	100.0	0.0	0.0	0.0	*Homo sapiens*
UW-88-95	100.0	0.0	0.0	0.0	*Homo sapiens*

First Canonical Variate Axis

The means of each taxonomic group was significantly different from each other along CV 1, except for between *Pongo* and *Gorilla* (table 6.3.3). The first canonical variate axis was most effective in separating *Homo sapiens,* which occupied the extreme negative end, from non-human taxa, particularly *Pan troglodytes*, which was only found in the positive aspect of CV 1. Both *Gorilla* and *Pongo* were distributed across the negative and positive halves, though both were weighted slightly to the positive aspect, and but for extremal *Homo sapiens* outliers, did not overlap to any great degree with the human sample.

The negative aspect of the first canonical variate axis resembles the *Homo sapiens* mean shape (figure 6.1.1), being mediolaterally narrow and palmodorsally long, with only a mild and obtuse palmodorsal concavity and a dorsal edge that sloped proximally. The surface is simple and relatively flat, with no distal ballooning of the laterodorsal surface evident. In contrast, the shape representative of the maxima of CV 1 is highly complex and irregular. It is characterised by a strongly distally-projecting mediopalmar corner and a very prominent distally-ballooning projection in the laterodorsal area. The strong distal projection of the mediopalmar corner results in a strongly palmodorsal concave curvature of the medial border, and when coupled with the prominent distal protrusion, results in a complex articular surface. The surface is mediolaterally wide, especially in its dorsal aspect, and is not as palmodorsally long as the minimal shape.

All fossil specimens are in the negative aspect of CV 1, and while several are outside the range of *Homo sapiens*, those that are have a comparable CV 1 score to extremal, outlying *Homo sapiens* specimens. For example, Qafzeh-9 and Regourdou-1, the two positive-most fossil specimens, are within the 1st quartile range of *Gorilla* and *Pongo*, though have equivalent scores to *Homo sapiens* outlier points.

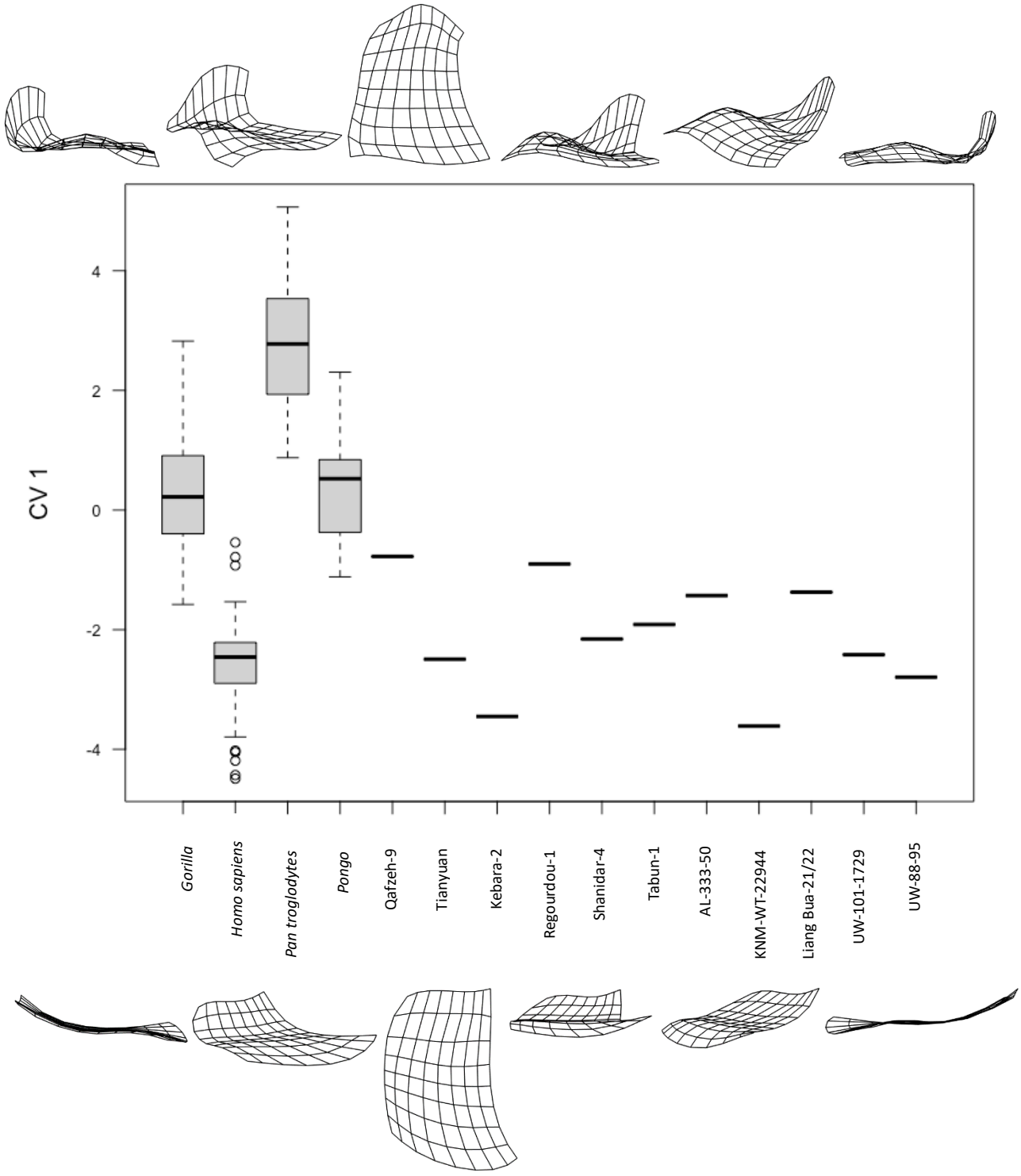

Figure 6.3.1: Boxplot of the first canonical variate scores for *Gorilla*, *Homo sapiens*, *Pan troglodytes*, and *Pongo* compared to fossil specimens Qafze-9 and Tianyuan (early *Homo sapiens*); Kebara-2, Regourdou-1, Shanidar-4, and Tabun-1 (*Homo neanderthalensis*); AL-333-50 (*Australopithecus afarensis*); KNM-WT-22944 (cf. Australopithecus afarensis) ; Liang Bua 21/22 (*Homo floresiensis*); UW-101-1729 (*Homo naledi*); and UW-88-95 (*Australopithecus sediba*). Black horizontal lines represent the median values of extant groups, and PC scores of fossil specimens, boxes are the interquartile range, whiskers are the non-outlier ranges, and empty circles are outliers.

Second Canonical Variate Axis

With the exception of *Homo sapiens* and *Pan troglodytes,* the mean values of CV 2 scores for each taxon were statistically significantly different from one another (table 6.3.3). CV 2 is most effective in separating the *Gorilla* sample, which has exclusively negative CV 2 values, from the other extant groups, in particular *Homo sapiens* and *Pan troglodytes*.

Shape change along the second canonical variate axis is primarily concerned with the nature of the bevelling of the palmar surface. The positive aspect of the axis corresponds to a surface in which distal bevelling of the palmar edge is strongly concentrated at the mediopalmar corner, with very little bevelling at the lateropalmar corner, resulting in a very asymmetrical palmar edge. In this respect, the positive aspect corresponds closely to the *Pan troglodytes* shape. The negative end of the axis corresponds more closely with the *Gorilla* mean shape, in which the distal bevelling of the surface is more uniform, though concentrated slightly towards the lateropalmar corner. Both shapes have a prominent distal ballooning of the laterodorsal surface, though this feature is concentrated more laterally and palmarly in the positive shape, resulting in a mediodorsal corner that appears to project slightly more distally relative to the minimum shape.

There is no overlap between the scores of *Gorilla* and *Homo sapiens* along CV 2, and minimal overlap with *Pan troglodytes*, though the upper quartile of *Gorilla* does overlap with the lower quartile of *Pongo*. The fossil specimens are concentrated around the midpoint of CV 2, though slightly skewed to the positive aspect. While most are within the range of *Homo sapiens*, UW-88-95 (*Australopithecus sediba*) has a CV 2 score that is above the range of *Homo sapiens* and within that of *Pan troglodytes*, while the CV 2 score of AL-333-50 (*Australopithecus afarensis*) is below the range of the *Homo sapiens* sample, within the area of overlap between *Pongo* and *Gorilla* (figure 6.3.2).

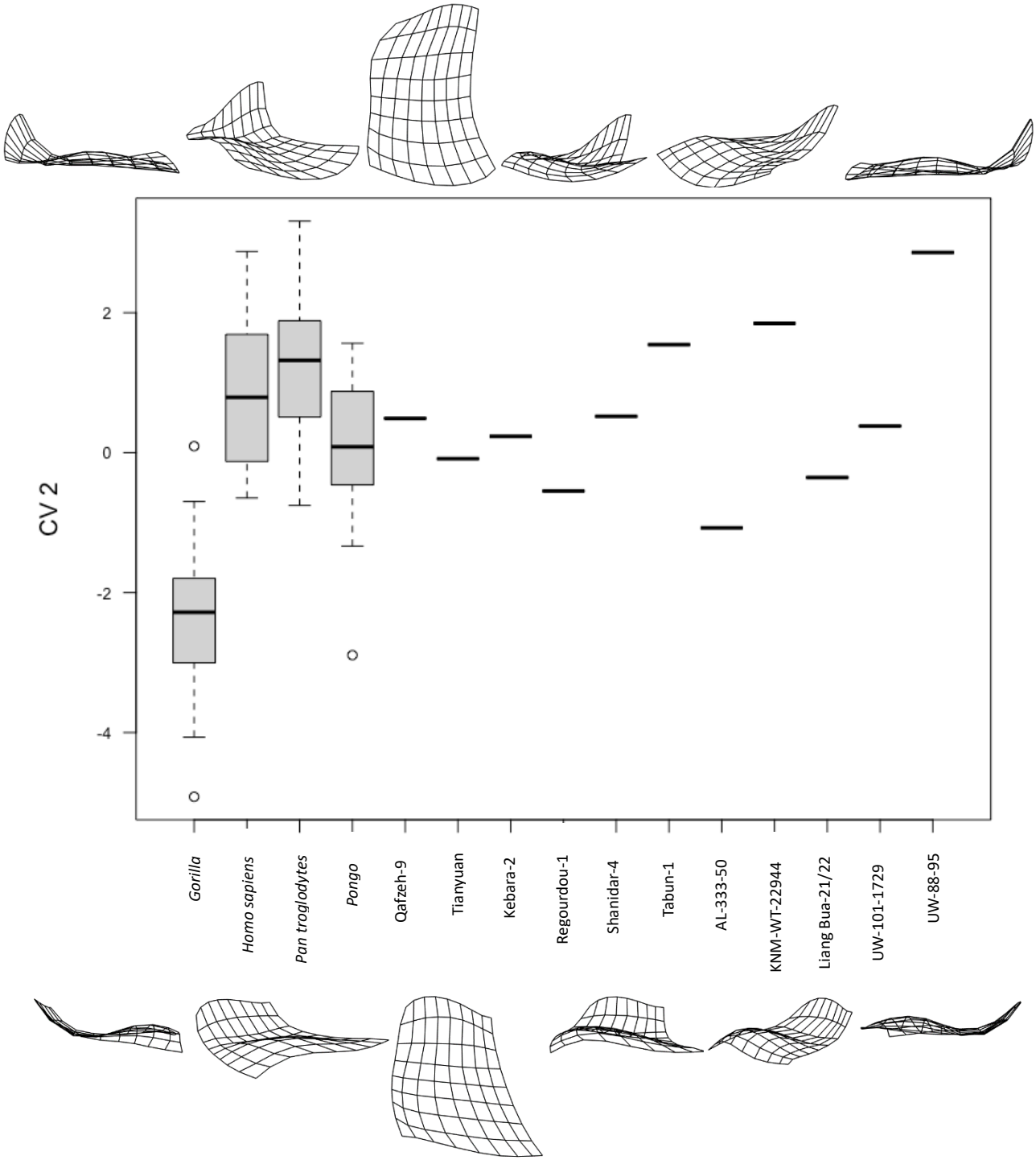

Figure 6.3.2: Boxplot of the second canonical variate scores for *Gorilla*, *Homo sapiens*, *Pan troglodytes*, and *Pongo* compared to fossil specimens Qafze-9 and Tianyuan (early *Homo sapiens*); Kebara-2, Regourdou-1, Shanidar-4, and Tabun-1 (*Homo neanderthalensis*); AL-333-50 (*Australopithecus afarensis*); KNM-WT-22944 (cf. Australopithecus afarensis) ; Liang Bua 21/22 (*Homo floresiensis*); UW-101-1729 (*Homo naledi*); and UW-88-95 (*Australopithecus sediba*). Black horizontal lines represent the median values of extant groups, and PC scores of fossil specimens, boxes are the interquartile range, whiskers are the non-outlier ranges, and empty circles are outliers.

Third Canonical Variate Axis

There is no significant difference in between the mean values of the CV 3 scores of *Homo sapiens, Pan troglodytes*, and *Gorilla*, though the mean value of the *Pongo* sample is significantly different from that of all other extant groups (table 6.3.3). Accordingly, the third Canonical Variate axis separates *Pongo*, in the extreme positive end of the axis, from all other taxa, which are distributed broadly evenly between negative and positive scores, with no overlap. The positive aspect of the axis represents an articular surface in which the distal ballooning of the surface is prominent and concentrated laterally, thereby expanding the waist of the surface laterally. The morphology of the surface representative of the negative-most value lacks a prominent lateral ballooning, but rather has a uniform proximal sloping of the dorsal edge, with a resultant mediolateral constriction of the waist and a straighter medial edge.

All of the fossil specimens are in the lower range of the axis, with all but two within the range of *Homo sapiens, Pan troglodytes*, and *Gorilla*. KNM-WT-22944-I (*Australopithecus cf. Australopithecus afarensis*) has the most positive CV 3 value and is within the 4th quartile of *Homo sapiens* and *Gorilla.* UW-101-1729 (*Australopithecus sediba*) has the most negative value of all fossil specimens and is the only specimen outside the range of *Homo sapiens*, being in the first quartile of *Pan troglodytes* and *Gorilla.*

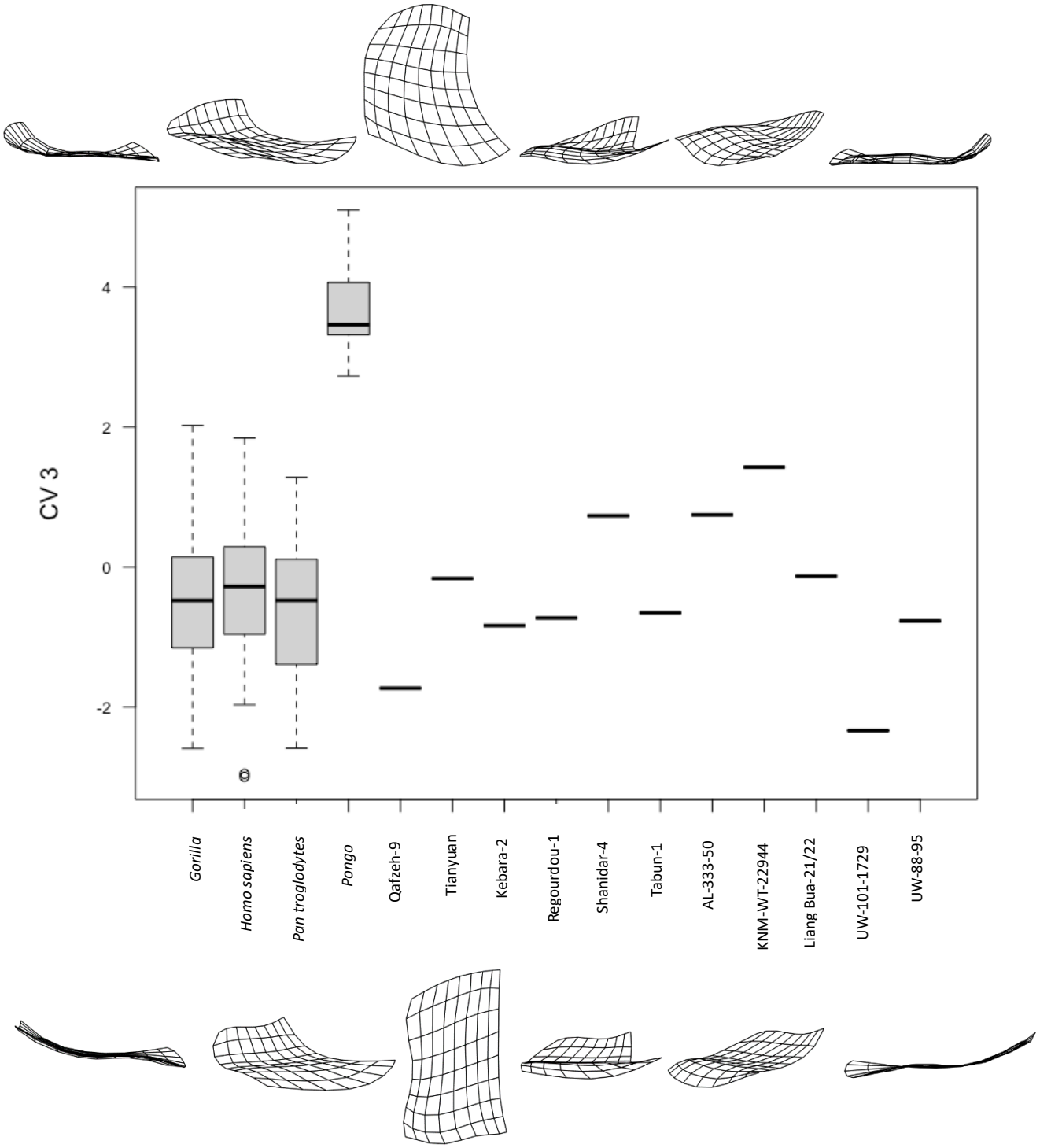

Figure 6.3.3: Boxplot of the third canonical variate scores for *Gorilla*, *Homo sapiens*, *Pan troglodytes*, and *Pongo* compared to fossil specimens Qafze-9 and Tianyuan (early *Homo sapiens*); Kebara-2, Regourdou-1, Shanidar-4, and Tabun-1 (*Homo neanderthalensis*); AL-333-50 (*Australopithecus afarensis*); KNM-WT-22944 (cf. Australopithecus afarensis) ; Liang Bua 21/22 (*Homo floresiensis*); UW-101-1729 (*Homo naledi*); and UW-88-95 (*Australopithecus sediba*). Black horizontal lines represent the median values of extant groups, and PC scores of fossil specimens, boxes are the interquartile range, whiskers are the non-outlier ranges, and empty circles are outliers.

CVA Scatterplots

CV 1 v CV 2

A scatterplot of the scores of the first canonical variate against the second is shown in figure 6.3.4, and successfully separates the African great apes and *Homo sapiens* from each other, while *Pongo* is distributed widely across the centre of the plot. The *Homo sapiens* sample is concentrated in the upper-left quadrant, *Pan troglodytes* in the upper-right, and *Gorilla* centrally in the lower half. All of the fossil specimens are within or, in the case of Liang-Bua 21/22 (*Homo floresiensis*), very near the vicinity of, the 95% confidence ellipse of *Homo sapiens*. Three fossil hominins ((early *Homo* sapiens), Liang Bua-21/22 (*Homo floresiensis*), and Shanidar-4 (*Homo neanderthalensis*)) that are within the *Gorilla* 95% confidence ellipse belong to confirmed tool-using species. AL-333-50 (*Australopithecus afarensis*) is the only specimen within the 95% confidence ellipse of *Homo sapiens* and *Pongo.*

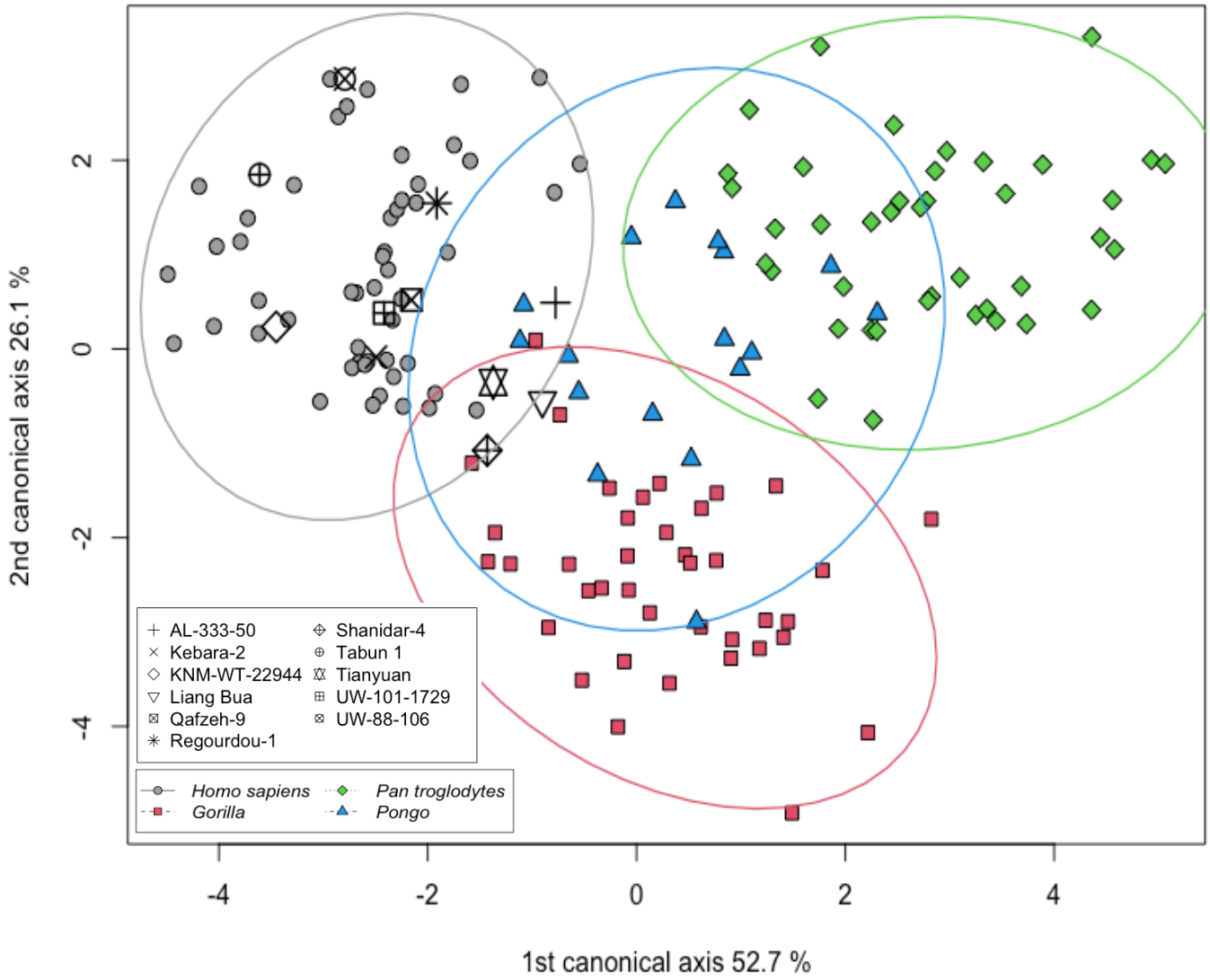

Figure 6.3.4: Scatterplot of the first vs. second canonical variates axis (CV 1 (57.2%) vs. CV 2 (26.1%)) scores of extant samples (*Homo sapiens*, Gorilla, Pan *troglodytes,* and *Pongo*), with 95% confidence ellipses, and fossil specimens. The plot separates African taxa from each other, with *Pongo* distributed centrally.

CV 1 v CV 3

A scatterplot of CV 1 against CV 3 (figure 6.3.5) separates the *Pongo* sample, in the upper half of the plot, from the African taxa, which are concentrated in the lower half. The *Homo sapiens* and *Pan troglodytes* samples are also separate, with *Homo sapiens* to the lower left, while *Pan troglodytes* are in the lower right of the plot. The *Gorilla* sample is positioned centrally at the lower portion of the scatterplot and overlaps considerably with both the *Homo sapiens* and *Pan troglodytes* samples. The 95% ellipse of *Pongo* does not overlap with that of any other taxon. All the fossil specimens are again situated within the *Homo sapiens* 95% confidence ellipse, with several occupying the area where *Homo sapiens* and *Gorilla* overlap.

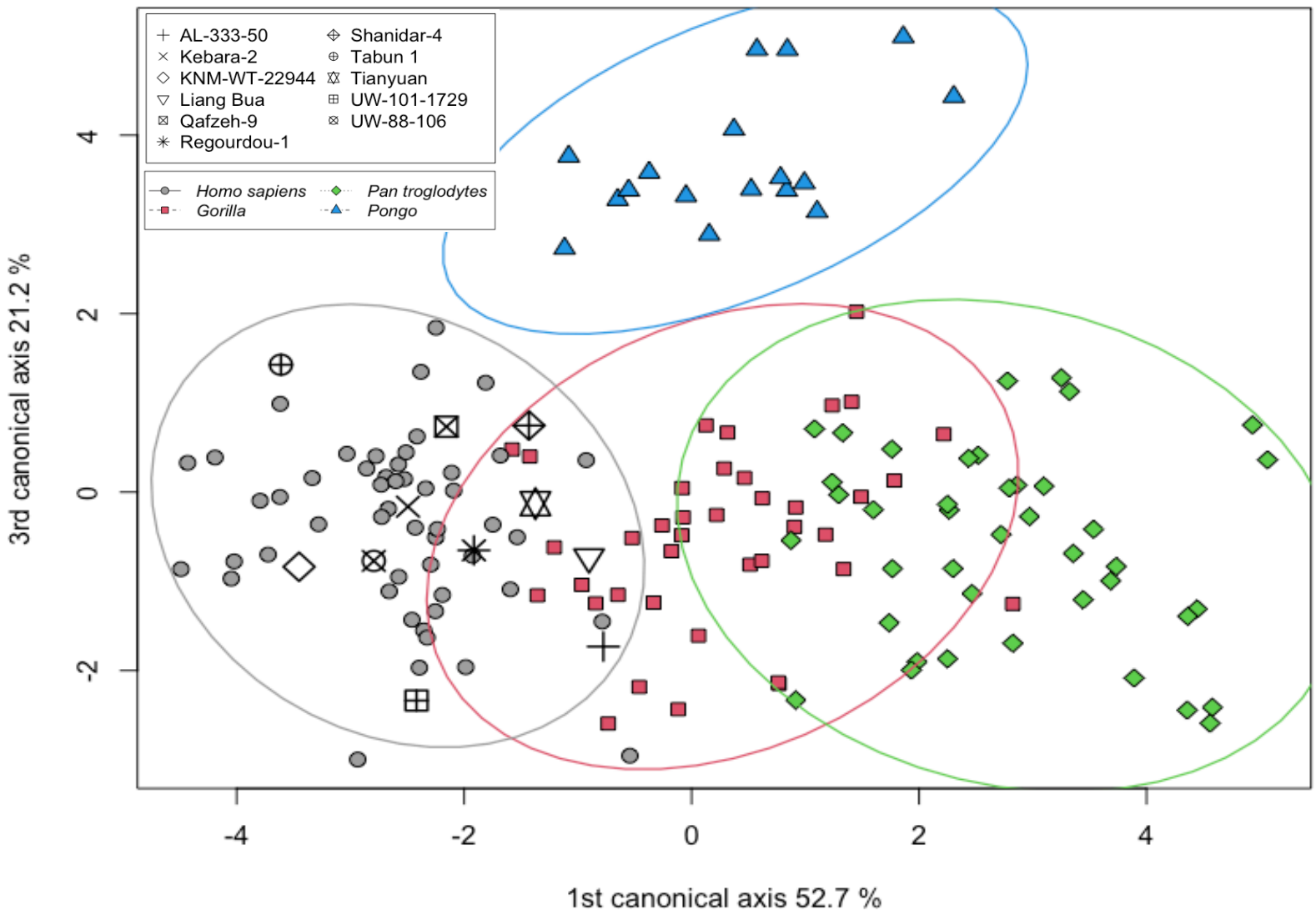

Figure 6.3.5: Scatterplot of the first vs. third canonical variates axis (CV 1 (52.7%) vs. CV 3 (21.2%)) scores of extant samples (*Homo sapiens*, Gorilla, Pan *troglodytes,* and *Pongo*), with 95% confidence ellipses, and fossil specimens. African taxa are concentrated in the lower half of the plot, with *Pongo* in the upper half. All fossil specimens are within the 95% confidence ellipse of *Homo sapiens.*

CV 2 v CV 3

The scatterplot of CV 2 against CV 3 again separates *Pongo*, in the upper half of the plot, from the African taxa, which are concentrated in the lower half. However, in this plot, there is no discrepancy between the samples of *Homo sapiens* and *Pan troglodytes*, which are both to the right of the plot and almost completely overlap each other. *Gorilla* is concentrated in the lower left section of the plot, though its 95% confidence ellipse overlaps with those of *Homo sapiens* and *Pan troglodytes* (figure 6.3.6). Again, all fossil specimens are within the 95% confidence ellipse of *Homo sapiens*, though none exclusively.

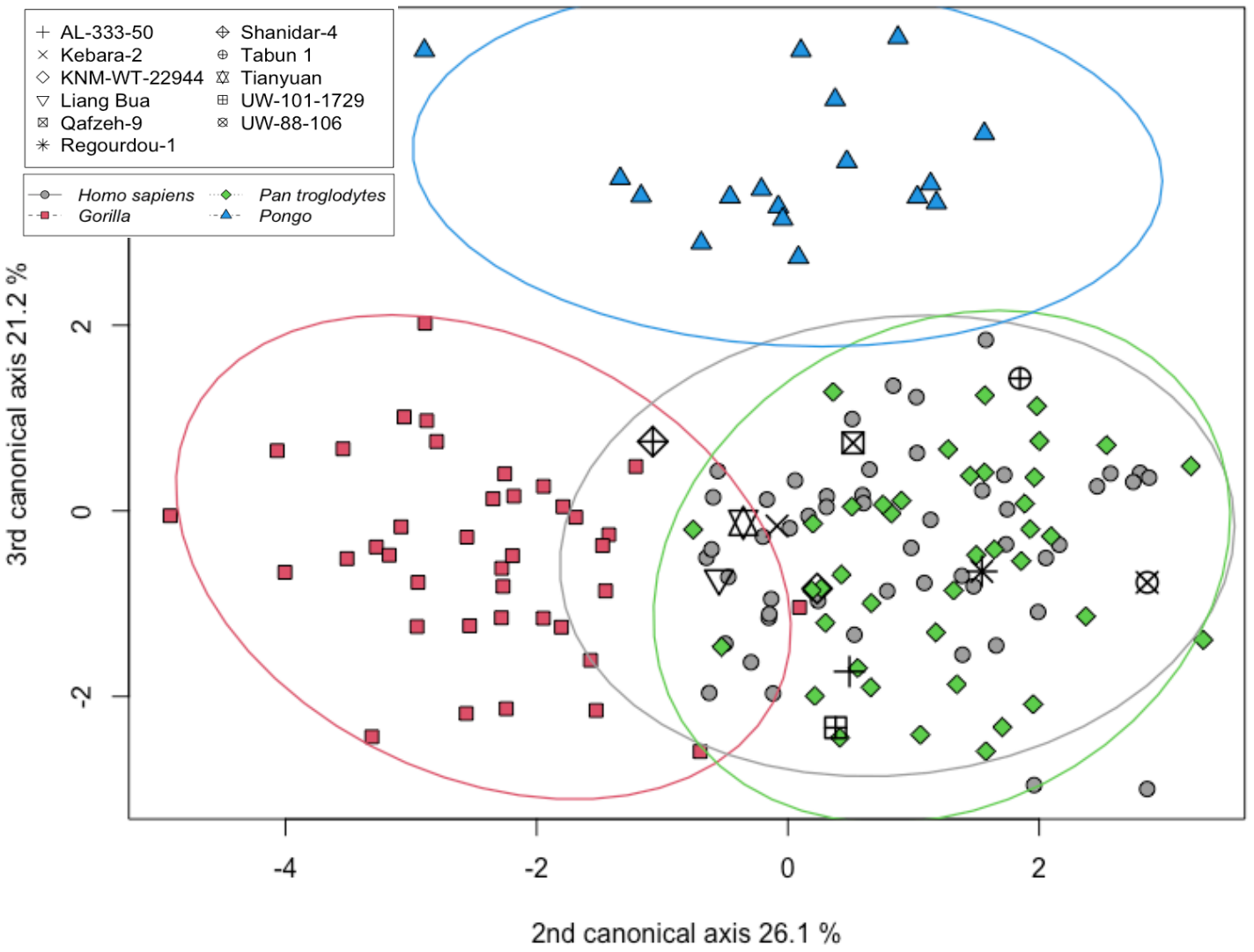

Figure 6.3.6: Scatterplot of the second vs. third canonical variates axis (CV 2 (26.1%) vs. CV 3 (21.2%)) scores of extant samples (*Homo sapiens*, Gorilla, Pan *troglodytes,* and *Pongo*), with 95% confidence ellipses, and fossil specimens. Again, the African taxa are concentrated in the lower half of the plot, though *Homo sapiens* and *Pan troglodytes* are clustered together in the lower-right quadrant.

6.4 Hamate-MC4 Procrustes distances

The Procrustes distances of the extant group means from each other are shown in table 6.4.1. *Homo sapiens* and *Gorilla* are the two mean shapes closest to each other, while *Pongo* and *Gorilla* have the greatest pairwise distance, followed by *Gorilla* and *Pan troglodytes*. The Procrustes distances of each fossil specimen from the average shape of each extant taxon group is shown in table 6.4.2. All the fossil specimens are consistently closer to the mean shapes of *Homo sapiens* and *Gorilla* than they are to *Pan troglodytes* and *Pongo*, and several fossil specimens, including AL-333-50 (*Australopithecus afarensis*), Liang Bua-21/22 (*Homo floresiensis*), Tianyuan (early *Homo sapiens*), and UW-101-1729 (*Homo naledi*) are a greater Procrustes distance from the *Homo sapiens* mean shape than they are from the *Gorilla* mean shape.

Table 6.4.1: Procrustes distances between the average shapes of the extant groups for the hamate's articular surface for the fourth metacarpal.

	Homo sapiens	*Gorilla*	*Pan troglodytes*	*Pongo*
Homo sapiens	-	0.127	0.143	0.153
Gorilla		-	0.162	0.192
Pan troglodytes			-	0.142
Pongo				-

Table 6.4.2: The Procrustes distance of each fossil from the mean shape of each extant taxon group.

	Homo sapiens	*Gorilla*	*Pan troglodytes*	*Pongo*
AL-333-50	0.144	0.140	0.168	0.211
Kebara-2	0.074	0.123	0.166	0.174
KNM-WT-22944	0.154	0.157	0.218	0.225
Liang Bua-21/22	0.211	0.192	0.243	0.274
Qafzeh-9	0.098	0.149	0.161	0.152
Regourdou-1	0.110	0.179	0.159	0.174
Shanidar-4	0.136	0.152	0.194	0.196
Tabun-1	0.103	0.196	0.178	0.148
Tianyuan	0.167	0.152	0.201	0.214
UW-101-1729	0.209	0.182	0.251	0.295
UW-88-95	0.207	0.227	0.231	0.250

Results of the Shapiro-Wilks tests for normality on the Procrustes distances of samples from the mean shape of that group are shown in table 6.4.3. Results showed that the distributions of *Homo sapiens* and *Gorilla* were not normally distributed. Each group was therefore transformed to a normal distribution using a natural log transformation, and the log-transformed data was used to calculate absolute distances.

Table 6.4.3: Results of the Shapiro-Wilk normality tests performed on the individual distances distribution from their respective group mean shapes (top row), and the corresponding square-root-transformed data.

	Homo sapiens	*Gorilla*	*Pan troglodytes*	*Pongo*
p	**0.0481**	**0.006**	0.943	0.074
p (log-transformed)	0.881	0.248	0.922	0.794

The Procrustes distance of each fossil specimen from the mean shape of each extant group (in standard deviations) is shown in table 6.4.4, with the upper tail cumulative distribution, represented as a percentage, shown in parentheses. All the Neanderthal specimens are closer to the mean shape of modern humans than to the mean shape of *Gorilla* with respect to their respective samples, as is Qafzeh-9, an early *Homo sapiens*. Interestingly, Tianyuan (early *Homo sapiens*) is closer to a greater percentage of the gorilla sample to the group's mean shape (7.20%) than it is to the mean shape of *Homo sapiens* relative to that group's sample (2.49%), as are Liang Bua-21/22 (*Homo floresiensis*), A.L. 333-50 (*Australopithecus afarensis*), and U.W. 101-1729 (*Homo naledi*). U.W. 88-95 (*Australopithecus sediba*) is closer to the mean shapes of *Pan troglodytes* and *Pongo* than to *Homo sapiens* and *Gorilla* with respect to the distances of the group samples, though in each case, this specimen is closer to the mean shape of each group than less than 1% of each group's sample.

Table 6.4.4: Distances (in standard deviations) of each fossil from the mean of the distance of each individual of the extant group from the group mean. Calculations were conducted on Procrustes distances. In parentheses, the value of the upper-tail cumulative distribution function multiplied by 100.

	Homo sapiens	*Gorilla*	*Pan troglodytes*	*Pongo*
AL-333-50	1.27 (10.28%)	1.1 (13.50%)	1.43 (7.57%)	2.15 (1.59%)
Kebara-2	-1.94 (97.38%)	0.51 (30.50%)	1.37 (8.51%)	1.48 (6.92%)
KNM-WT-22944	1.58 (5.69%)	1.59 (5.56%)	2.51 (0.60%)	2.35 (0.93%)
Liang Bua-21/22	3.08 (0.10%)	2.48 (0.65%)	2.97 (0.15%)	3.03 (0.12%)
Qafzeh-9	-0.59 (72.08%)	1.36 (8.74%)	1.25 (10.64%)	1.04 (15.01%)
Regourdou-1	-0.04 (51.61%)	2.19 (1.44%)	1.21 (11.34%)	1.49 (6.76%)
Shanidar-4	0.99 (16.00%)	1.46 (7.22%)	2.03 (2.11%)	1.88 (2.99%)
Tabun-1	-0.32 (62.72%)	2.59 (0.48%)	1.68 (4.69%)	0.94 (17.34%)
Tianyuan	1.96 (2.49%)	1.46 (7.20%)	2.18 (1.47%)	2.19 (1.43%)
UW-101-1729	3.03 (0.12%)	2.25 (1.23%)	3.11 (0.09%)	3.27 (0.05%)
UW-88-95	2.99 (0.14%)	3.24 (0.06%)	2.76 (0.29%)	2.71 (0.34%)

7 The hamate-metacarpal 5 articular surface

7.1 Hamate-metacarpal 5 surface average shapes

Homo sapiens

The average shape of the hamate's articular surface for the fifth metacarpal in *Homo sapiens* is shown in figure 7.1.1. The mean shape of *Homo sapiens* is gently concavely curved in the palmodorsal plane, and convexly in the mediolateral plane, which results in a saddle-shaped morphology characteristic of the species. The lateral border is of slightly greater palmodorsal length than the more proximally-positioned medial border, which bulges medially, while the lateropalmar corner is positioned slightly more palmar-wards than the mediopalmar corner. Overall, it is a square-to-rectangular shape when viewed from a distal vantage.

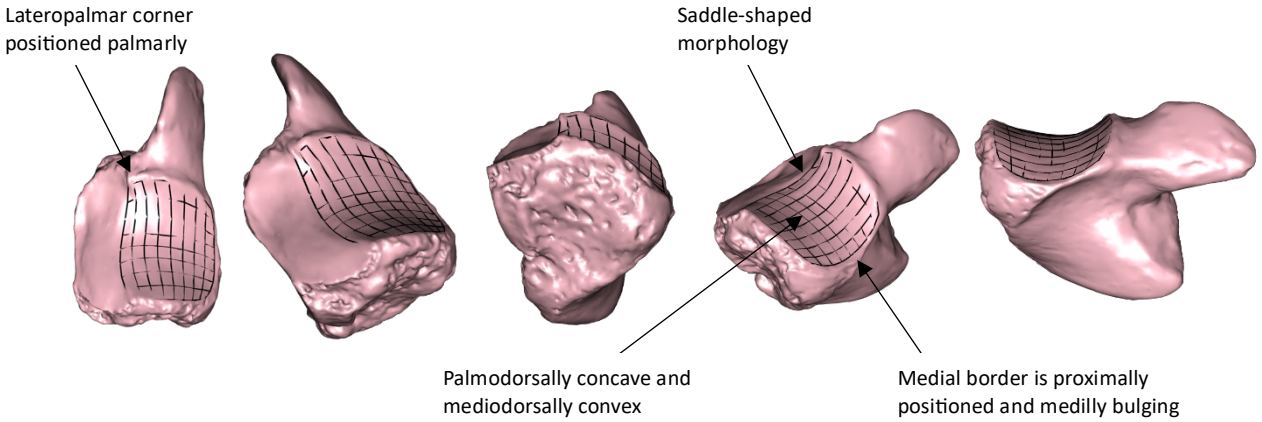

Figure 7.1.1: The mean shape of the hamate's articular surface for the fifth metacarpals for the *Homo sapiens* population, represented by the specimen closest to the group's mean shape warped to the average landmark coordinates of the population, superimposed with wireframe representation of the surface. From left to right: distal, lateral, laterodorsal, dorsal, mediodorsal, and medial views.

Gorilla

The mean shape of *Gorilla*, shown in figure 7.1.2, is narrow mediolaterally and highly elongated palmodorsally. There is a marked differentiation in shape between the palmar and dorsal halves of this articular surface. The dorsal half is strongly mediolaterally arched, with mediodorsal and laterodorsal corners that are more proximally-positioned than the centre, while

the palmar portion of the surface is mediolaterally flat to very slightly concave with mediopalmar and lateropalmar corners that are positioned proximally relative to the distally-projecting centre of the palmar border. The palmar and dorsal halves of the surface are separated by an almost 90° apex, resulting in an extremely strong bevelling of the surface. This strong angulation of the surface is accompanied by a mild mediolateral constriction at the apex, resulting in a constricted waist of the surface when viewed from a distal vantage.

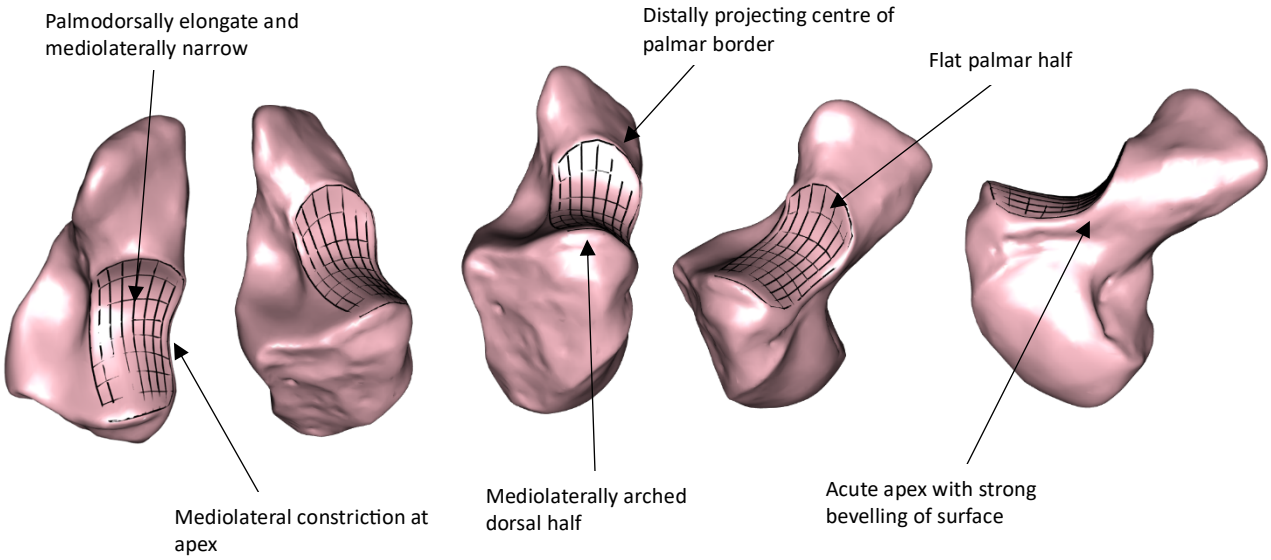

Figure 7.1.2: The mean shape of the hamate's articular surface for the fifth metacarpals for the *Gorilla* population, represented by the specimen closest to the group's mean shape warped to the average landmark coordinates of the population, superimposed with wireframe representation of the surface. From left to right: distal, lateral, laterodorsal, dorsal, mediodorsal, and medial views.

Pan troglodytes

The mean shape of the *Pan troglodytes* population is shown in figure 7.1.3. The *Pan troglodytes* mean shape appears somewhat intermediate between those of *Homo sapiens* and *Gorilla.* The dorsal portion of the surface, as with *Homo sapiens*, displays a mild mediolateral convex curvature, resulting in a surface that slopes proximally towards its medial edge. However, as with *Gorilla*, the palmar and dorsal halves of the surface are separated by a strong right-angled apex, although the dorsal section is proportionally longer than its palmar counterpart. The palmar section is mediolaterally flat, with a lateropalmar corner that projects more distally than the mediopalmar, and the palmodorsal profile of the surface is strongly bevelled.

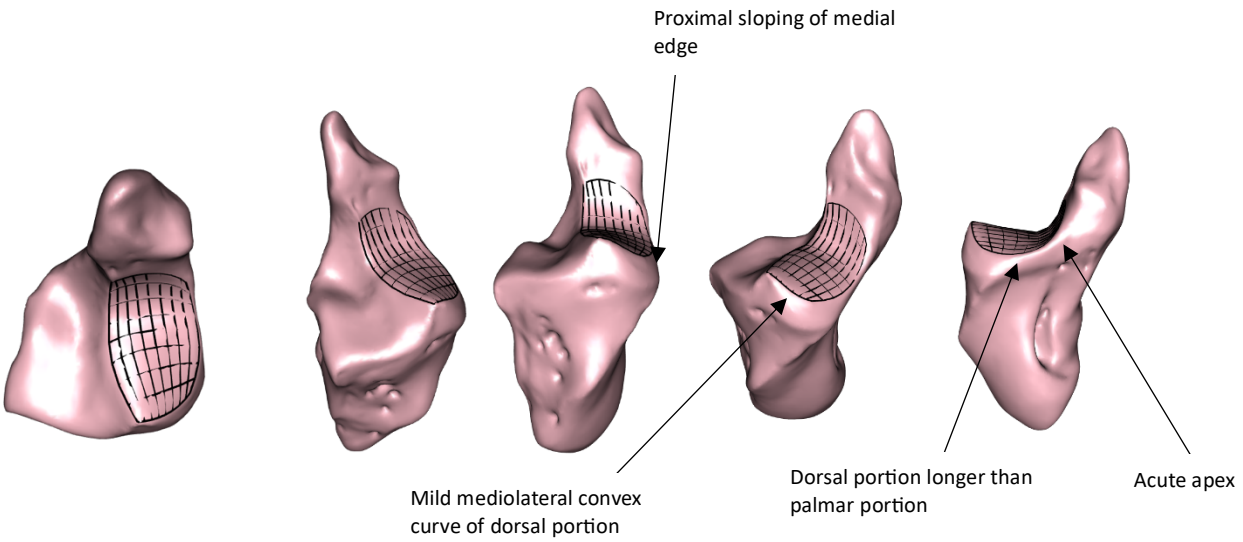

Figure 7.1.3: The mean shape of the hamate's articular surface for the fifth metacarpals for the *Pan troglodytes* population, represented by the specimen closest to the group's mean shape warped to the average landmark coordinates of the population, superimposed with wireframe representation of the surface. From left to right: distal, lateral, laterodorsal, dorsal, mediodorsal, and medial views.

Pongo

As with *Pan troglodytes* and *Gorilla*, the average shape of the hamate-MC5 articular surface in *Pongo*, shown in figure 7.1.4, is palmodorsally long and mediolaterally narrow, and is strongly bevelled with dorsal and palmar portions separated by a strong axis. The palmar edge of the surface is gently arched, and the surface is split fairly evenly into a mediolaterally-flat dorsal surface and a uniformly-curving palmar surface. The dorsal portion of the hamate-MC5 articular surface in *Pongo* is notable in having a medial edge that slopes proximally from an otherwise mediolaterally-horizontal surface, and a more gradual but equally strong slope towards the dorsal edge. The laterodorsal corner of the surface is more distally-projecting than the corresponding mediodorsal corner, resulting in a curving dorsal edge when viewed from a distal viewpoint, and a lateral border which is somewhat greater in length than the medial edge.

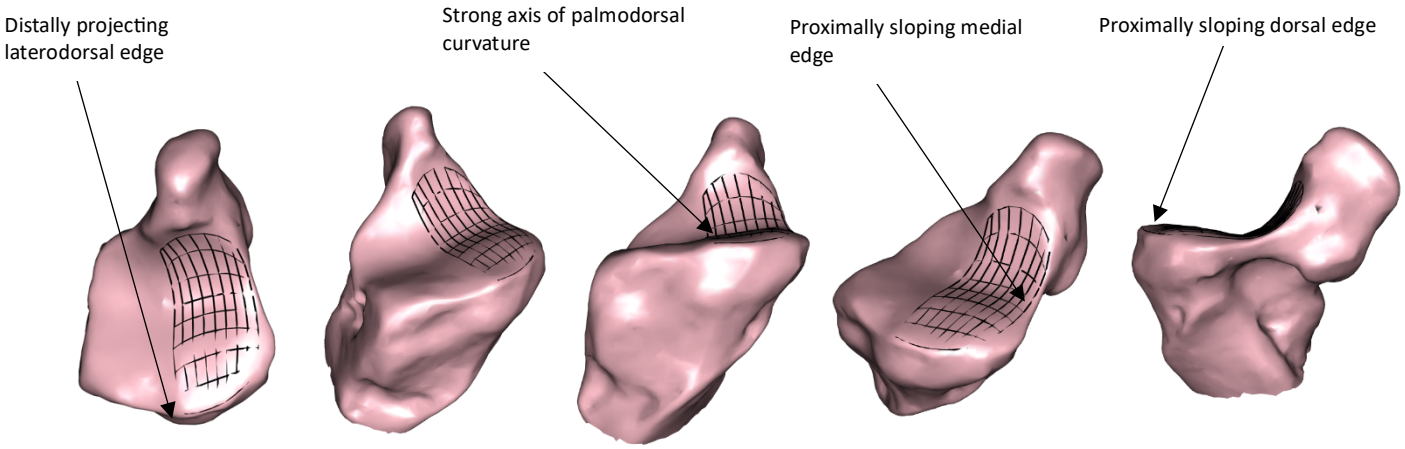

Figure 7.1.4: The mean shape of the hamate's articular surface for the fifth metacarpals for the *Pongo* population, represented by the specimen closest to the group's mean shape warped to the average landmark coordinates of the population, superimposed with wireframe representation of the surface. From left to right: distal, lateral, laterodorsal, dorsal, mediodorsal, and medial views.

Table 7.1: Comparison of the mean hamate-metacarpal 5 shape of each extant taxa					
Ham-MC5	Distal	Laterodorsal	Dorsal	Mediodorsal	Medial
Homo sapiens	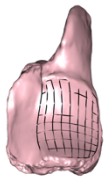	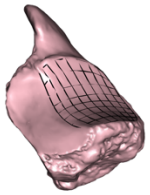	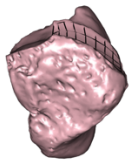	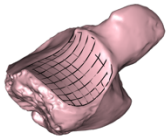	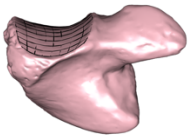
Gorilla	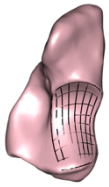	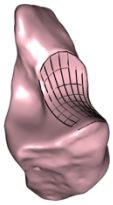		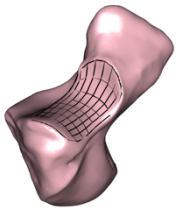	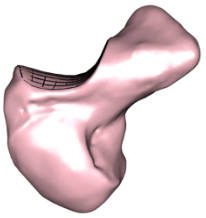
Pan troglodytes	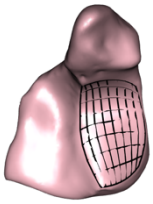	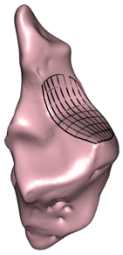	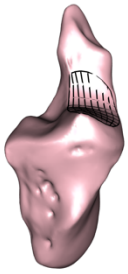	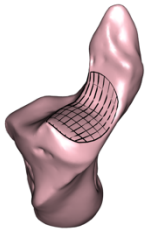	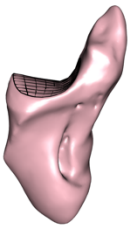
Pongo	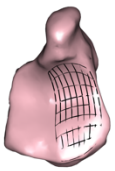	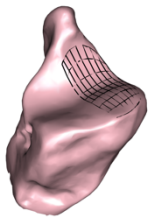	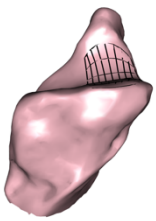	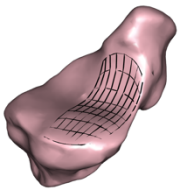	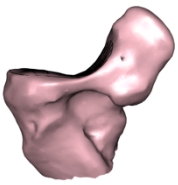

7.2 Hamate-MC5 principal components analysis

The first two principal components, which cumulatively accounted for 58.3% of the total variance, were regarded as meaningful by Bookstein's (2014) criterion. The first principal component contributed to 40.4% of the total variance, and the second principal component accounted for 17.9%. The first five principal components each accounted for more than 5% of the total variance, with the third, fourth, and fifth principal components accounting for 8.5%, 6.7%, and 5.1%, respectively (figure 7.2.1). While only the first two principal components were considered meaningful according to Bookstein's criterion, the first five principal components were also investigated in case any important shape variations were explained by these axes. The first nine principal components accounted for more than 90% of the total variance, with the ninth principal component accounting for 1.9% of the total variance in shape of the hamate-MC5 articulation.

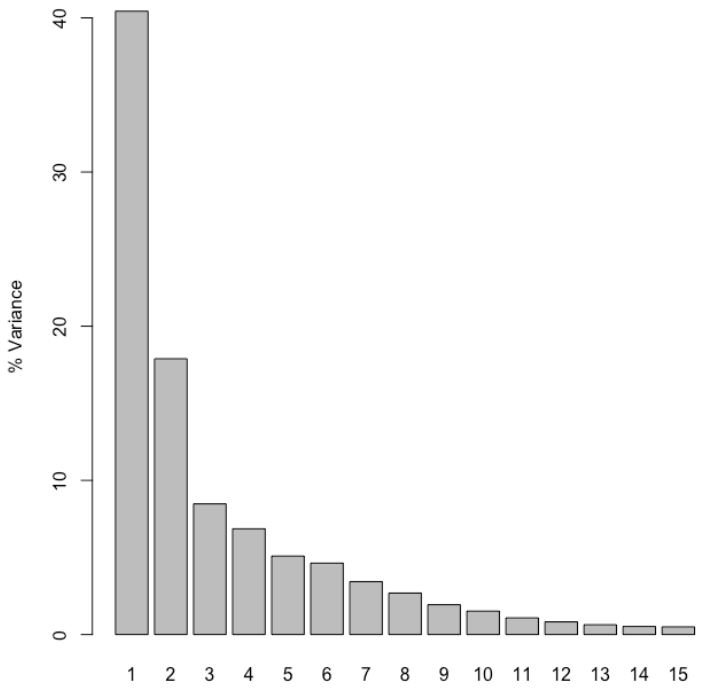

Figure 7.2.1: Graph showing the percentage of variance each of the first 15 principal components of the PCA of the hamate's articulation with the fifth metacarpal were accountable for. The first five principal components each account for more than 5% of the total variation, and the first nine principal components cumulatively account for 91.4% of the total variation.

Taxonomic differences between groups

The Hotelling's T^2 tests did not reveal significant differences between the means of the *Gorilla gorilla* and *Gorilla beringei* sample along the first five principal components (T^2 = 2.1914, df = 5, 33; p = 0.0789), nor between the two species of *Pongo* (*Pongo abelii* and *Pongo pygmaeus*) (T^2 = 1.2204, df = 5, 12; p = 0.2672). Species of both genera were therefore pooled at the genus level. A multiple analysis of variance conducted on the first five principal component scores of *Pan troglodytes*, with specimens divided by sub-species, also did not reveal significant variation between sub-species [F (3, 24) = 1.057, p = 0.4126, Λ = 0.582]. The *Pan troglodytes* sub-species samples were therefore pooled at the species level.

ANOVA and *Tukey HSD tests*

Results for the analysis of variance (ANOVA) of the scores of the first five principal components divided by taxon are shown in table 7.2.1. Significant results ($p \leq 0.05$) were seen in the first four principal components, with no statistically significant difference in the scores of the fifth principal component between taxa (p = 0.759). While there was a significant result from the ANOVA of PC 4 (p = 0.013), a *post-hoc* Tukey HSD test of this PC revealed that the only pairwise test to return a significant result was between *Homo sapiens* and *Gorilla*, at p = 0.050. Visual assessment of the box-and-whisker plot of this PC axis, and bivariate scatterplots involving PC 4 showed that the fourth principal component was not informative in distinguishing between extant groups, nor in informing the affinities of fossil specimens relative to the extant groups. As such, shape change and extant groups and fossil specimen relationships were explored along the first three principal components only.

Table 7.2.1: Results of analysis of variance on principal component scores one through five on extant groups.

Principal Component	DF	Sum of Squares	Mean Squares	*F* Value	*p*
PC 1	3, 144	1.4948	0.4983	119.5	**<0.001**
PC 2	3, 144	0.4718	0.1573	47.12	**<0.001**
PC 3	3, 144	0.1069	0.03564	14.73	**<0.001**
PC 4	3, 144	0.026	0.00234	3.714	**0.013**
PC 5	3, 144	0.251	0.00174	0.391	0.759

The means and standard deviations of each extant taxon group along the first three principal components are shown in table 7.2.2, along with the principal component scores of each fossil along the first three principal components. Subscripts next to the principal component scores of fossil specimens indicate extant groups for which that particular fossil specimen is at least one standard deviation from the group's mean value. AL 333-50 (*Australopithecus afarensis*) and UW 88-95 (*Australopithecus sediba*) were both more than one SD from the average PC1 value of all extant taxa along the first principal component, while KNM-WT-22944-I (*Australopithecus cf. Australopithecus afarensis*), Lang Bua 21/22 (*Homo floresiensis*), and UW 101-1729 (*Homo naledi*) were within 1 SD of the *Homo sapiens* mean PC1 value. Regourdou-1 and Tabun-1 (*Homo neanderthalensis*) were both more than one SD from the mean value of the *Homo sapiens* sample along the first principal component.

Table 7.2.2: Mean and standard deviation (in parentheses) of the first three principal component scores for *Homo sapiens, Gorilla, Pan troglodytes,* and *Pongo* compared with PC scores of fossil specimens AL333-14 (*Australopithecus afarensis*), Kebara-2 (*Homo neanderthalensis*), KNM-WT-22944 (cf. Australopithecus afarensis) , Liang Bua-21/22 (*Homo floresiensis*), Qafzeh-9 (early *Homo sapiens*), and Regourdou-1 (*Homo neanderthalensis*).

Group	*Homo sapiens* (*n* = 54)	*Gorilla* (*n* = 36)	*Pan troglodytes* (*n* = 40)	*Pongo* (*n* =20)	AL333-50	Kebara-2	KNM-WT-22944	Liang Bua-21/22	Qafzeh-9	Regourdou-1
PC 1	-0.129 (0.078)	0.0722 (0.0669)	0.0586 (0.0502)	0.135 (0.0386)	$-0.476_{Hs,G,Pt,Po}$	$0.0144_{Hs,Po}$	$-0.0921_{G,Pt,Po}$	$-0.0553_{G,Pt,Po}$	$-0.0759_{G,Pt,Po}$	$-0.0194_{Hs,G,Pt,Po}$
PC 2	0.0169 (0.0618)	-0.0870 (0.0531)	0.0617 (0.0629)	0.0197 (0.0389)	0.0363_{G}	$-0.0345_{Pt,Po}$	$-0.0317_{G,Pt,Po}$	$-0.0653_{Hs,Pt,Po}$	$0.0599_{G,Po}$	$-0.0049_{G,Pt}$
PC 3	-0.0121 (0.0375)	0.0147 (0.0417)	0.00859 (0.0695)	-0.0205 (0.0341)	$0.0397_{Hs,Po}$	-0.0302_{G}	0.0286_{Po}	0.0016	-0.0097	$0.0822_{Hs,G,Pt,Po}$

[a] Subscripts indicate a group that the fossil specimen differs at least 1 standard deviation from the mean of: Hs = *Homo sapiens*; G = *Gorilla*; Pt = *Pan troglodytes*; Po = *Pongo.*

Table 7.2.2 (*cont.*): Mean and standard deviation (in parentheses) of the first three principal component scores for *Homo sapiens, Gorilla, Pan troglodytes,* and *Pongo* compared with PC scores of fossil specimens Shanidar-4 (*Homo neanderthalensis*), Tabun-1 (*Homo neanderthalensis*), Tianyuan (early *Homo sapiens*), UW-101-1729 (*Homo naledi*), and UW-88-95 (*Australopithecus sediba*).

Group	*Homo sapiens* (*n* = 54)	*Gorilla* (*n* = 36)	*Pan troglodytes* (*n* = 40)	*Pongo* (*n* =20)	Shanidar-4	Tabun-1	Tianyuan	UW-101-1729	UW-88-95
PC 1	-0.129 (0.078)	0.0722 (0.0669)	0.0586 (0.0502)	0.135 (0.0386)	$-0.0547_{G,Pt,Po}$	$-0.0377_{Hs,G,Pt,Po}$	$-0.1339_{G,Pt,Po}$	$-0.1414_{G,Pt,Po}$	$-0.289_{Hs,G,Pt,Po}$
PC 2	0.0169 (0.0618)	-0.0870 (0.0531)	0.0617 (0.0629)	0.0197 (0.0389)	$-0.1258_{Hs,Pt,Po}$	$-0.0411_{Pt,Po}$	$-0.0543_{Hs,Pt,Po}$	$-0.0950_{Hs,Pt,Po}$	0.0229_{G}
PC 3	-0.0138 (0.0375)	-0.00767 (0.0417)	0.0395 (0.0695)	-0.0426 (0.0341)	$0.0262_{Hs,Po}$	-0.0026_{Po}	$0.0379_{Hs,G,Po}$	$0.0672_{Hs,G,Po}$	$0.0548_{Hs,G,Po}$

[a] Subscripts indicate a group that the fossil specimen differs at least 1 standard deviation from the mean of: Hs = *Homo sapiens*; G = *Gorilla*; Pt = *Pan troglodytes*; Po = *Pongo.*

Principal Component 1 shape and groupings

The first principal component, which accounted for 40.4% of the total variation in the shape of the hamate-MCV surface, most clearly distinguished *Homo sapiens* from the non-human extant groups. The first principal component represents a transition in shape from a mediolaterally wide and convex, and palmodorsally short and gently concave surface, to a narrow and palmodorsally long surface with a strong concavity (figure 7.2.2).

The shape representative of the most negative value of PC 1 has a mediolateral width approximate to its palmodorsal length, resulting in an approximately square surface when viewed distally (figure 7.2.2). Its palmodorsally concave curvature is highly oblique and gentle, with a gradual apex of the curvature near the dorsum of the surface. Mediolaterally, the surface is convex and bulges medially, leading to a distinctively mild, wide saddle-shaped morphology. The positive aspect of the first principal component is, in contrast, defined by a long and narrow surface with an acute apex closer to the palmar edge than to the dorsal, resulting in a morphology in which the palmar portion of the surface approaches a 90° angle to its proportionally longer dorsal surface. While the dorsal portion of the surface retains some mediolateral convexity, the palmar portion is flat, or even slightly concave, and rather than the gentle saddle-shaped characteristic of the minimum shape, the maximum shape is highly bevelled at its palmar end (figure 7.2.2). Comparison of the minimum and maximum shapes of PC 1 with the mean shapes of the extant groups reveal that the negative portion of PC 1 is characterised by a shape corresponding closely to the mean of *Homo sapiens* (figure 7.1.1), which is mediolaterally wide relative to its palmodorsally squat length, with a characteristic saddle-shaped morphology. In contrast, the more generic morphologies of the non-human groups are characterized by a long, narrow, and strongly bevelled morphology which do not display the saddle-shaped morphology characteristic of the modern human hamate articular surface for the fifth metacarpal. The extant group mean shape which most closely resembles the positive extreme is that of *Pongo* (figure 7.1.4).

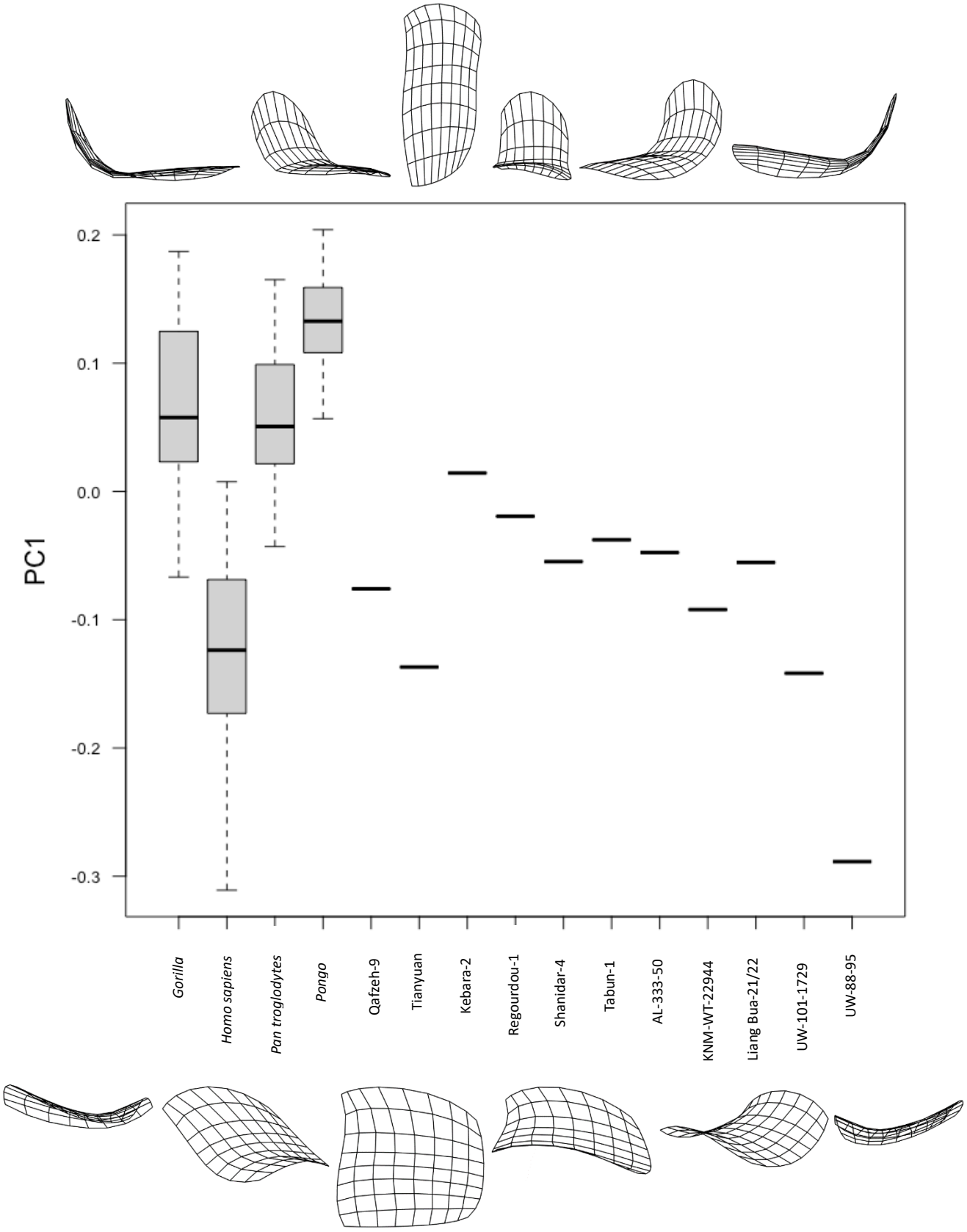

Figure 7.2.2: Boxplot of the first principal component score of the hamate's metacarpal 5 articular surface for *Gorilla, Homo sapiens, Pan troglodytes,* and *Pongo* compared with fossil specimens Qafzeh-9, Tianyuan (early *Homo sapiens*); Kebara-2, Regourdou-1, Shanidar-4, Tabun-1 (*Homo neanderthalensis*); AL-333-50 (*Australopithecus afarensis*); KNM-WT-22944 (cf. Australopithecus afarensis) ; Liang Bua (*Homo floresiensis*); UW-101-1729 (*Homo naledi*); and UW-88-95 (*Australopithecus sediba*). Black lines represent the median of the group, boxes are interquartile ranges, and whiskers are the non-outlier ranges.

Table 7.2.3: Tukey honestly significant difference (HSD) *post-hoc* test results on PC 1 scores among *Homo, Pan, Gorilla, and Pongo.* Significant results ($p < 0.05$) were highlighted in bold.

Group		Mean difference	*p*	95% confidence interval	
				Lower bound	Upper bound
Homo	*Gorilla*	0.201	**<0.001**	0.165	0.237
	Pan	0.188	**<0.001**	0.152	0.223
	Pongo	0.264	**<0.001**	0.217	0.311
Gorilla	*Homo*	-0.201	**<0.001**	-0.237	-0.165
	Pan	-0.014	0.784	-0.051	0.024
	Pongo	0.063	**0.006**	0.014	0.111
Pan	*Homo*	-0.188	**<0.001**	-0.223	-0.152
	Gorilla	0.014	0.784	-0.024	0.051
	Pongo	0.076	**<0.001**	0.028	0.125
Pongo	*Homo*	-0.264	**<0.001**	-0.311	-0.217
	Gorilla	-0.063	**0.006**	-0.111	-0.014
	Pan	-0.076	**<0.001**	-0.125	-0.028

Results of Tukey's Honestly Significantly Different *post-hoc* test showed that all the extant taxa differ significantly from each other along the first principal component, with the exception of *Gorilla* and *Pan troglodytes* ($p = 0.784$) (table 7.2.3, figure 7.2.2). Assessment of the box-and-whisker plot for PC 1 shows that *Homo sapiens* is most distinct from all other extant taxa, with its range being almost entirely in the negative half of PC 1. In contrast, the non-human groups are predominantly in the positive half, with *Pongo* having the most positive range of values, and is entirely within the positive half of PC 1. While there is a degree of overlap between the 4th quartile of *Homo sapiens* and the 1st quartiles of the African apes, no overlap is seen between the ranges of *Homo sapiens* and *Pongo.*

All but one of the fossil specimens are within the range of *Homo sapiens* – Kebara-2 is very marginally outside the upper range of modern humans. The two early modern human specimens (Qafzeh-9 and Tianyuan) are within the interquartile range of *Homo sapiens,* while all the Neanderthal specimens (Kebara-2; Regourdou-1; Shanidar-4; Tabun-1) are within (or on the border of, in the case of Kebara-2) the 4th quartile*,* and within the 1st quartile of *Gorilla* and variably *Pan troglodytes*. AL-333-50 (*Australopithecus afarensis*) and Liang Bua-21/22 (*Homo floresiensis*) are also in the upper quartile of *Homo sapiens* and the lower quartile of African great apes, while KNM-WT-22944-I (*Australopithecus afarensis cf. Australopithecus*), and UW-101-1729 (*Homo naledi*) are within the interquartile range of *Homo sapiens*, with UW-101-1729 being near the group's mean. UW-88-95 (*Australopithecus sediba*) is located at the extreme negative

end of PC 1 and is the only fossil specimen within the 1st quartile of *Homo sapiens.* None of the fossil specimen's PC 1 scores are within one standard deviation (SD) of the mean of *Pongo,* and only Kebara-1 is within one SD of the means of both *Pan troglodytes* and *Gorilla* (table.7.2.2). The PC 1 values of Kebara-2, AL-33-50, Regourdou-1, Tabun-1, and AL-101-1729 are all more than one standard deviation away from the mean of *Homo sapiens*.

Principal Component 2 shape and groupings

The second principal component, which accounts for 17.9% of the total variance, distinguishes the shape of the hamate-fifth metacarpal articular surface of *Gorilla* from the other extant groups, though considerable overlap is observed between all taxa. The second principal component differentiates between an articular surface with a flared palmar border and strong but consistent palmodistal concave curvature of the negative shape, and a pear-shaped morphology of the positive shape, in which the middle of the surface is mediolaterally expanded relative to its palmar and dorsal ends.

The negative portion of the second principal component describes a shape that is notable in its mediolaterally-flared palmar border relative to its narrow dorsal border, its strong and fairly regular palmodorsal concave curvature, and the obvious mediolateral convex curvature of its dorsal portion (figure 7.2.3). This shape corresponds closely to the average shape of the hamate-MCV surface of the *Gorilla* sample (figure 7.1.2). The shape representative of the maxima of the second principal component, by contrast, has a mediolaterally narrowed palmar border, which is pinched and elongated at the lateropalmar corner, expanding into a bulbous middle (figure 7.2.3). The dorsal two-thirds of the PC 2 positive shape is flat but for a subtle proximal sloping of the surface towards its mediodorsal corner, with a concentrated distal bevelling of the surface at its palmar third, contrasting with the smooth and constant curving of the negative shape. The maximum shape of PC 2 does not resemble the mean shape of any of the extant groups in particular, but rather appears to be an amalgamation, with a dorsal half resembling the corresponding *Pan troglodytes* portion, and a palmar portion akin to a *Homo sapiens-Pan troglodytes* hybrid.

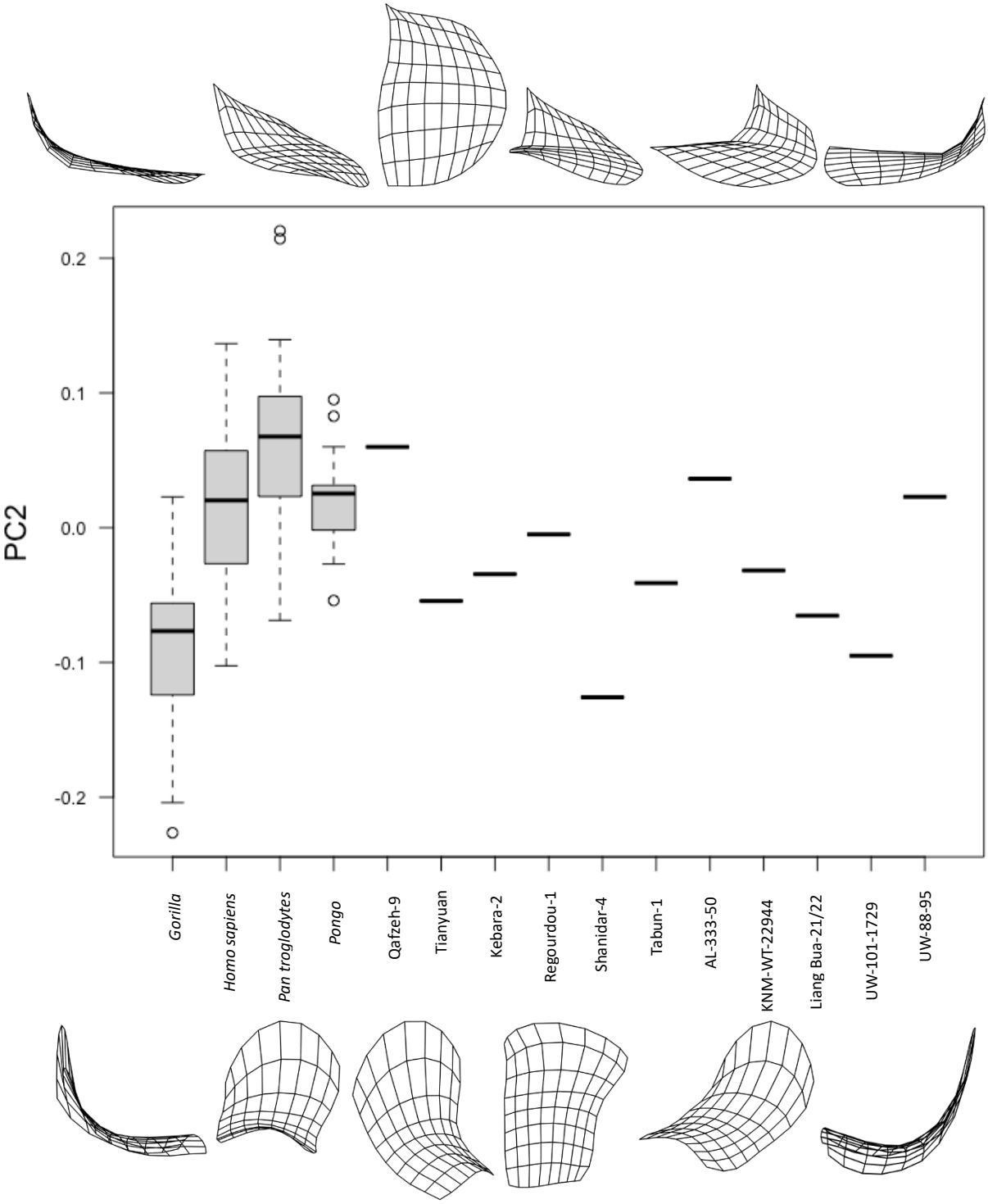

Figure 7.2.3: Boxplot of the second principal component score of the hamate's metacarpal articular surface for *Gorilla, Homo sapiens, Pan troglodytes,* and *Pongo* compared with fossil specimens Qafzeh-9, Tianyuan (early *Homo sapiens*); Kebara-2, Regourdou-1, Shanidar-4, Tabun-1 (*Homo neanderthalensis*); AL-333-50 (*Australopithecus afarensis*); KNM-WT-22944 (cf. Australopithecus afarensis); Liang Bua (*Homo floresiensis*); UW-101-1729 (*Homo naledi*); and UW-88-95 (*Australopithecus sediba*). Black lines represent the median of the group, boxes are interquartile ranges, and whiskers are the non-outlier ranges.

Table 7.2.4: Tukey honestly significant difference (HSD) *post-hoc* test results on PC 2 scores among *Homo, Pan, Gorilla, and Pongo.* Significant results ($p < 0.05$) were highlighted in bold.

Group		Mean difference	*p*	95% confidence interval	
				Lower bound	Upper bound
Homo sapiens	*Gorilla*	0.104	**<0.001**	0.072	0.136
	Pan troglodytes	-0.045	**0.002**	-0.076	-0.013
	Pongo	-0.003	0.998	-0.045	0.039
Gorilla	*Homo sapiens*	-0.104	**<0.001**	-0.136	-0.072
	Pan troglodytes	-0.149	**<0.001**	-0.182	-0.115
	Pongo	-0.107	**<0.001**	-0.150	-0.063
Pan troglodytes	*Homo sapiens*	0.045	**0.002**	0.013	0.076
	Gorilla	0.149	**<0.001**	0.115	0.182
	Pongo	0.042	0.061	-0.001	0.085
Pongo	*Homo sapiens*	0.003	0.998	-0.039	0.045
	Gorilla	0.107	**<0.001**	0.063	0.150
	Pan troglodytes	-0.042	0.061	-0.085	0.001

There is no significant difference between *Pongo* and *Homo sapiens* along the second principal component ($p = 0.998$), nor between *Pongo* and *Pan troglodytes* ($p = 0.061$), although significant differences were observed between all other pairings (table 7.2.4). Among the extant groups, *Gorilla* is the most distinct of the extant great ape groups along the second principal component (figure 7.2.3). The median and interquartile range of *Gorilla* is entirely within the negative aspect of PC 2, and its 4th quartile is almost entirely in the negative range. In contrast, the interquartile range and median of *Pan troglodytes* is entirely within the positive half, although a substantial portion of its 1st quartile is in the negative range. The median values of both *Homo sapiens* and *Pongo* are positive, although both are near to the centre of the PC. The interquartile ranges of both groups span both the negative and positive aspects, while inclining towards the positive, especially in *Pongo*. The ranges of both *Pan troglodytes* and *Pongo*, but for a number of outliers, are situated within the greater range of *Homo sapiens*, and while *Pongo* and *Homo sapiens* have a similar median, the median of *Pan troglodytes* is the most positive of all groups.

While both early *Homo sapiens* fossil specimens are within the range of *Homo sapiens* – Qafzeh-9 in the 4th quartile, and Tianyuan in the 1st quartile, Tianyuan is more than one standard deviation from the mean of *Homo sapiens*. Tianyuan is also more than one SD from *Pan troglodytes* and *Pongo,* while Qafzeh-9 is one standard deviation from all non-human group means (table 7.2.4). All four Neanderthal specimens were in the negative aspect of PC 2, with Shanidar-4 being the most negatively-scored of all fossils and exclusively within the *Gorilla* range, and more than one standard deviation from the mean of all groups, with the exception of *Gorilla*

(table 7.2.2). The other three neanderthal specimens (Kebara-2, Regourdou-1, and Tabun-1) are within the ranges of all three great apes (Regourdou-1 is within the range of all extant groups), although Shanidar-4 is also more than one standard deviation from *Homo sapiens*, as is Liang Bua-21/22 and UW-101-1729. Liang Bua-21/22 (*Homo floresiensis*) and UW-101-1729 (*Homo naledi*) both have negative PC 2 scores and are within the ranges of *Gorilla* and *Homo sapiens*, with Liang Bua-21/22 also resting within the range of *Pan troglodytes* while being more than one SD from its mean. KNM-WT-2294-I (*Australopithecus cf. Australopithecus afarensis*) is within the range of all groups except for *Pongo* and is within one SD of the mean of *Homo sapiens.* Both AL-33-50 (*Australopithecus afarensis*) and UW-88-95 (*Australopithecus sediba*) have positive PC 2 scores, being within the interquartile ranges of *Pan troglodytes* and *Homo sapiens* and the upper quartile of *Pongo*, and within one standard deviation of the mean of all groups except for *Gorilla.*

Principal Component 3 shape and groupings

The third principal component, which accounted for 8.5% of the total variance, represents shape change that is dictated by a palmodorsal pinching or expansion of the lateral border, and associated, secondary changes relating to this shape change. Both the shapes representing the minima and maxima of this axis are radioulnarly narrow and palmodorsally long. While the upper third of this axis is almost exclusively occupied by *Pan troglodytes* specimens and is most effective in distinguishing *Pan troglodytes* from other taxa, the chimpanzee sample spans the entirety of the axis, with all other observations concentrated in the lower two thirds (figure 7.2.4). There does not therefore appear to be a clear distinguishing signal between taxa along the third principal component, and all fossil taxa overlap with at least two, if not all, extant groups.

The negative portion of the third principal component represents an articular surface in which the dorsal two thirds of the surface is relatively flat in the palmodorsal plane, with a mild distally-directed bevelling at its palmar third and a consistent and subtle mediolateral convexity caused by medial and lateral borders that are subtly proximally depressed in equal measure (figure 7.2.4). This results in a very gentle saddle-shaped morphology, though much narrower and longer than that characteristic of *Homo sapiens* seen at the minima of the first principal component (figure 7.2.2). Among the extant taxa, the PC3 minimum shape most closely resembles the mean of *Pongo* (figure 7.1.4), albeit with a more pronounced convex mediolateral curvature, especially in its palmar portion.

The shape representative of the positive aspect of the third principal component is strongly concave in the palmodorsal plane and has a lateral border that is positioned more distally relative to its corresponding medial border, resulting from laterodorsal and lateropalmar corners that are more distally projecting than their medial counterparts, and pinched to the palmodorsal midline of the surface, resulting in a constricted lateral border (figure 7.2.4). The dorsal half of the surface is sloped strongly proximally from the lateral to the medial border, especially towards the mediodorsal corner. Overall, the positive shape of PC 3 resembles the mean shape of *Pan troglodytes* (figure 7.1.3), albeit with a more pronounced pinching of the lateral border, resulting in a strong palmodorsal concave curving of its lateral border.

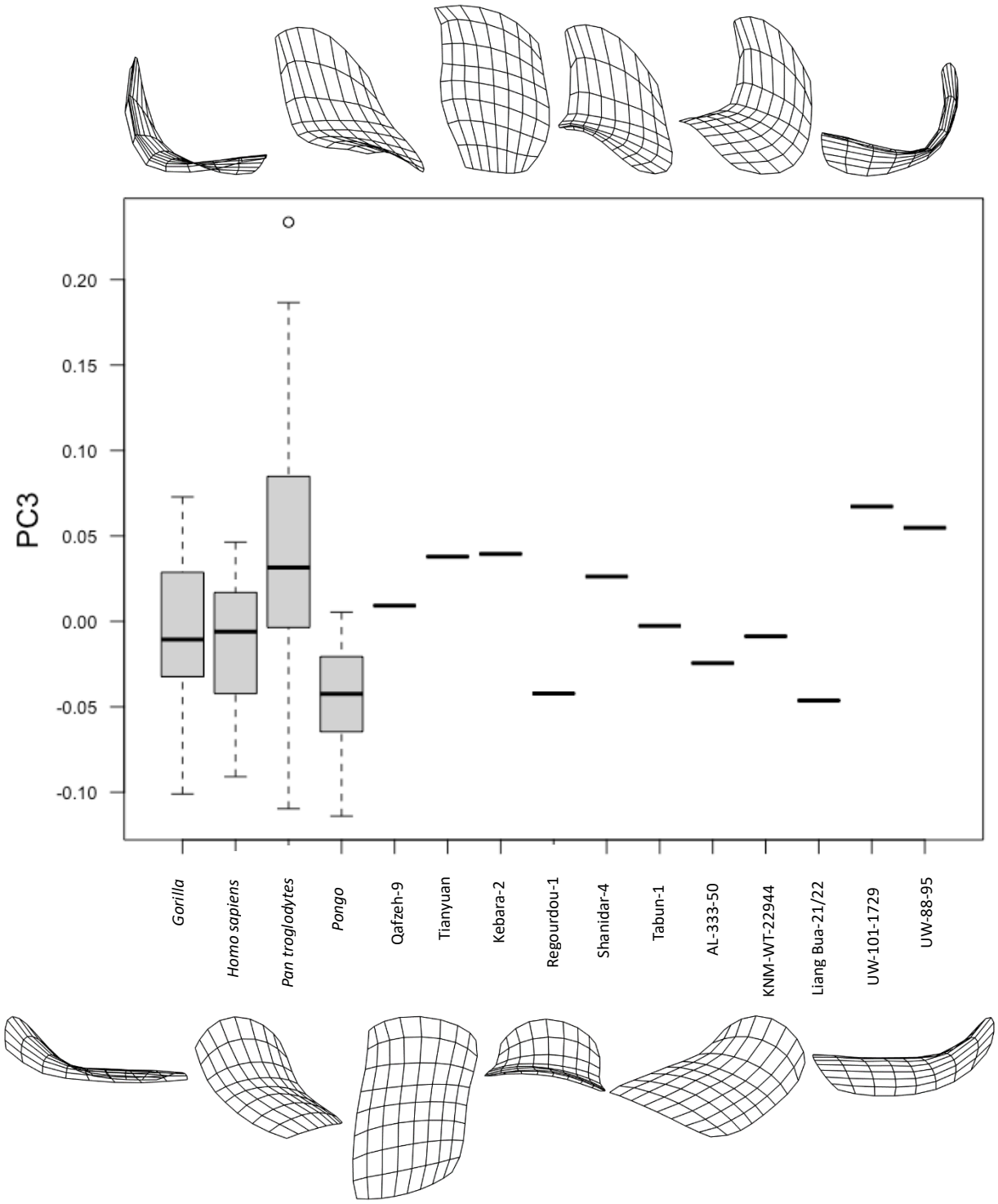

Figure 7.2.4: Boxplot of the third principal component score of the hamate's metacarpal articular surface for *Gorilla, Homo sapiens, Pan troglodytes,* and *Pongo* compared with fossil specimens Qafzeh-9, Tianyuan (early *Homo sapiens*); Kebara-2, Regourdou-1, Shanidar-4, Tabun-1 (*Homo neanderthalensis*); AL-333-50 (*Australopithecus afarensis*); KNM-WT-22944 (cf. Australopithecus afarensis); Liang Bua (*Homo floresiensis*); UW-101-1729 (*Homo naledi*); and UW-88-95 (*Australopithecus sediba*). Black lines represent the median of the group, boxes are interquartile ranges, and whiskers are the non-outlier ranges.

Table 7.2.5: Tukey honestly significant difference (HSD) *post-hoc* test results on PC 3 scores among *Homo, Pan, Gorilla, and Pongo.* Significant results ($p < 0.05$) were highlighted in bold.

Group		Mean difference	*p*	95% confidence interval	
				Lower bound	Upper bound
Homo	*Gorilla*	-0.006	0.935	-0.033	0.021
	Pan	-0.053	**<0.001**	-0.080	-0.027
	Pongo	0.029	0.161	-0.007	0.065
Gorilla	*Homo*	0.006	0.935	-0.021	0.033
	Pan	-0.047	**<0.001**	-0.076	-0.019
	Pongo	0.035	0.073	-0.002	0.072
Pan	*Homo*	0.053	**<0.001**	0.027	0.080
	Gorilla	0.047	**<0.001**	0.019	0.076
	Pongo	0.082	**<0.001**	0.045	0.119
Pongo	*Homo*	-0.029	0.161	-0.065	0.007
	Gorilla	-0.035	0.073	-0.072	0.002
	Pan	-0.082	**<0.001**	-0.119	-0.045

Along the third principal component, values of the *Pan troglodytes* sample are significantly distinct from all other groups, while there is no significant difference between the principal component scores of *Homo sapiens, Gorilla,* and *Pongo* (table 7.2.5). However, overlap between groups along scores of the third principal component are ubiquitous compared with the first two principal components, and the significant result obtained for *Pan troglodytes* is due to that groups incursion to the maxima of the axis (figure 7.2.4). The range of the *Pan troglodytes* sample spans the entirety of PC 3 and is the only group that displays strong positive values. It also envelopes the ranges of all the other extant groups, which all trend more towards the negative aspect of PC 3, with the range of *Pongo* almost entirely in the negative half. The *Gorilla* and *Homo sapiens* samples are distributed more evenly across the negative and positive halves, with the range of *Homo sapiens* enveloped entirely by that of *Gorilla.*

Given the high overlap in PC 3 scores between the taxa, interpretation of shape along the third principal component is challenging and of limited value, as all four extant taxa exhibit strong negative scores, with *Gorilla* and *Homo sapiens* being neutrally centred. However, it is only specimens of *Pan troglodytes* that have the strongest positive PC 3 scores, and the maxima of the third principal component is most indicative of the morphology of the *Pan troglodytes* surface (figure 7.1.3), which slopes from a pinched and highly angled lateral border to a proximodistally-drooping medial border.

With the exception of UW-101-1729 (*Homo* naledi) and UW-88-95 (*Australopithecus sediba*), all fossil specimens fall within the ranges of *Homo sapiens*, *Pan troglodytes*, and *Gorilla* (figure 7.2.5). UW-101-1729 and UW-88-95 have the most positive PC 3 scores among fossils, and along with Kebara-2 (*Homo neanderthalensis*) and Tianyuan (early *Homo sapiens*), are within one standard deviation of *Pan troglodytes* alone, while Shanidar-4 (*Homo neanderthalensis*) is more than one standard deviation from the mean of *Homo sapiens* and *Pongo*. Regourdou-1 (*Homo neanderthalensis*), Liang Bua-21/22 (*Homo floresiensis*) and Tabun-1 (*Homo neanderthalensis*) are the only fossil specimens whose PC 3 scores are more than one standard deviation from the mean of *Pan troglodytes,* and have a strong negative score comparable to the mean of *Pongo*, despite falling within the range of all four taxa. AL-33-50 (*Australopithecus afarensis*), KNM-WT-22944-I (*Australopithecus cf. Australopithecus afarensis*), Tabun-1 (*Homo neanderthalensis*) and Qafzeh-9 (early *Homo sapiens*) all have relatively neutral PC 3 scores and are within one standard deviation of the mean of *Homo sapiens, Gorilla,* and *Pan troglodytes.*

PCA Bivariate Scatterplots

PC 1 vs. PC 2 Scatterplot

A scatterplot of PC1 against PC2 for the hamate's articular surface for the fifth metacarpal is shown in figure 7.2.5. This scatterplot is most effective in separating the *Homo sapiens, Pan troglodytes*, and *Gorilla* groups from each other. *Homo sapiens* is the most distinct group and is almost entirely contained within the left half of the scatterplot, more or less equally distributed between the upper and lower quadrants of the left half. But for a narrow portion of the upper left quadrant where it interacts with *Pan troglodytes*, the morphospace of *Homo sapiens* does not overlap with any other group. The non-human groups are located predominantly within the right half of the scatterplot, with *Pan troglodytes* mostly in the upper right quadrant, *Gorilla* in the lower right, and *Pongo* occupying a concentrated area furthest right and straddling both quadrants. The morphospaces of *Gorilla* and *Pan troglodytes* slightly overlap, while *Pongo* overlaps with both non-human African great ape taxa. There is a small area in the right half of the scatterplot where all three of the non-human great ape groups overlap.

The majority of the fossil specimens are within the vicinity of the *Homo sapiens* morphospace. UW-88-95 (*Australopithecus sediba*) is to the far-left side of the scatterplot and is amongst the observations farthest away from the non-human groups. Likewise, UW-101-1729 (*Homo naledi*), KNM-WT-22944-I (*Australopithecus cf. Australopithecus afarensis*), Tianyuan and Qafzeh-9 (early *Homo sapiens*) are all squarely within the *Homo sapiens* convex hull, as is AL-333-50 (*Australopithecus afarensis*), albeit closer to the border of *Pan troglodytes.* Liang Bua-21/22 (*Homo floresiensis*) and Tabun-1 (*Homo neanderthalensis*) are marginally outside the *Homo sapiens* morphospace, falling in the space between modern humans and the African great apes. Two fossil specimens are outside the *Homo sapiens* morphospace and within those of the non-human groups, both being *Homo neanderthalensis* specimens. Kebara-2 is in the vicinity shared between *Pan troglodytes* and *Gorilla*, while Shanidar-4 is on the border of the *Gorilla* morphospace.

A notable trait of the PC 1 vs PC 2 scatterplot is the positioning of archaic hominins relative to more modern specimens. Many of the more archaic species, such as *Australopithecus sediba,*

Australopithecus afarensis, and *Australopithecus afarensis cf. Australopithecus* are squarely within the *Homo sapiens* range. However, all the Neanderthal specimens studied (as well as *Homo floresiensis*) are outside, or just marginally within, the *Homo sapiens* morphospace, near the vicinity of non-human great apes, with three of the four Neanderthal specimens being within non-human morphospaces, and two (Kebara-2 and Shanidar-4) falling within or at the border of the *Gorilla* morphospace, but outside the realm of *Homo sapiens.*

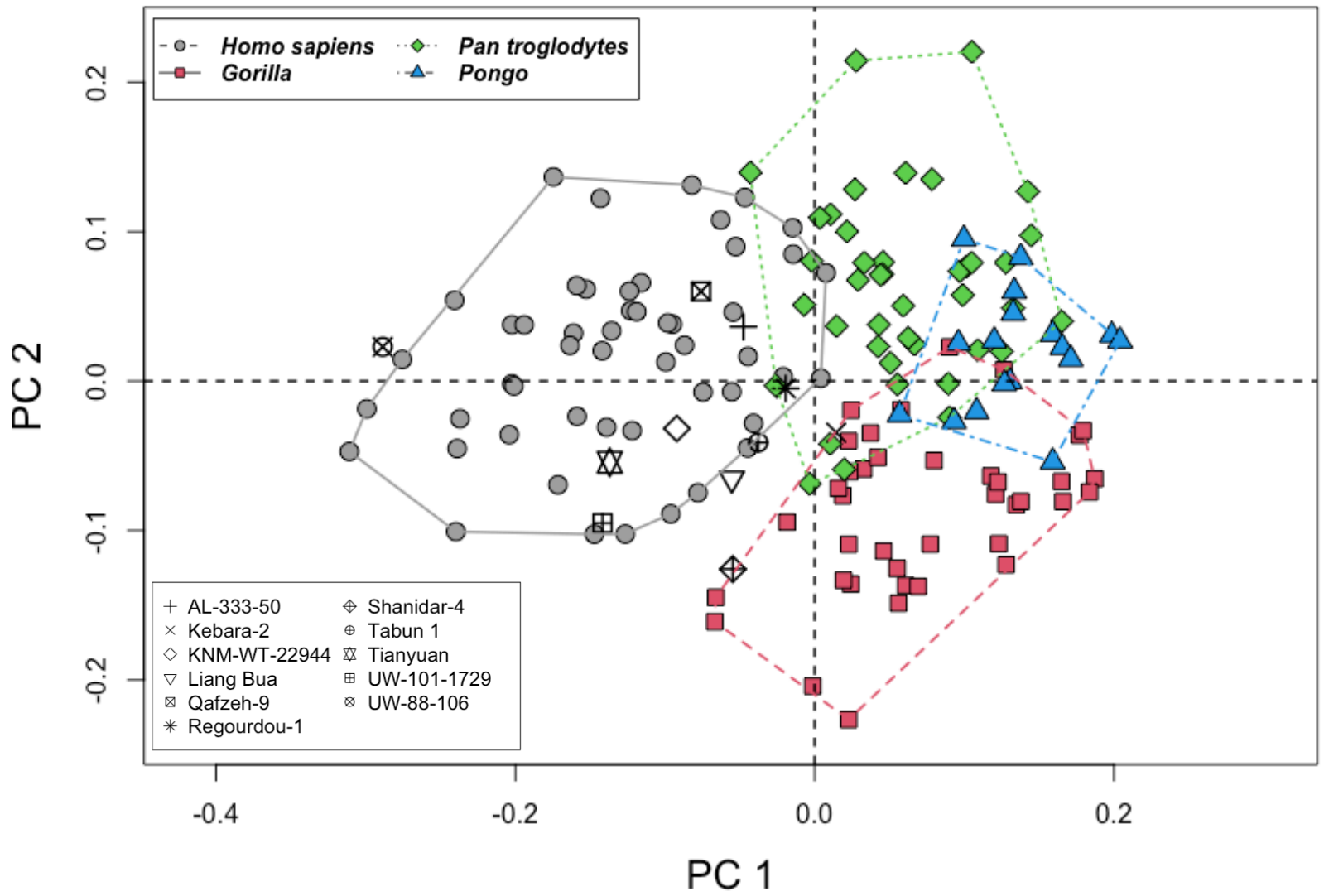

Figure 7.2.5: Scatterplot of the first vs. second principal component scores of extant samples (*Homo sapiens, Gorilla, Pan troglodytes* and *Pongo*) and fossil specimens for the hamate's articular surface for the fifth metacarpal. The *Homo sapiens* sample is clearly separated from non-human taxa, dominating the left half of the plot. All studied fossil specimens, with the exception of Kebara-2 and Shanidar-4 (*Homo neanderthalensis*), are in the vicinity of the *Homo sapiens* morphospace.

PC 1 v PC 3

A scatterplot of the scores of the first principal component against those of the third is shown in figure 7.2.6. Again, the morphospace of *Homo sapiens* is almost entirely within the left half of the scatterplot but has its majority in the lower left quadrant, with the right half of the scatterplot again dominated by the extant non-human groups. There is more overlap between groups in this scatterplot compared with PC 1 vs PC 2. The right quarter of the *Homo sapiens* morphospace overlaps with *Gorilla*, and to a lesser extent with *Pan troglodytes*, and there is significantly more overlap between *Pan troglodytes* and *Gorilla*. Here, *Gorilla* spans all four quadrants, but its morphospace is distributed more within the right half than the left. *Pan troglodytes* is predominantly in the positive aspects of both PC 1 and PC 3, while the morphospace of *Pongo* is almost entirely in the lower right quadrant. Much of *Pongo*'s morphospace is shared with *Gorilla* while being only minimally shared with *Pan troglodytes*.

Many of the fossil specimens lie within the morphospace shared between *Homo sapiens* and *Gorilla*, including the *Homo neanderthalensis* samples Shanidar-4, Tabun-1, and Regourdou-1, which is also within the *Pan troglodytes* morphospace. Kebara-2 (*Homo neanderthalensis*) is the only fossil specimen outside the *Homo sapiens* morphospace but within those of non-human great apes, although it is in close proximity to the morphospace of *Homo sapiens*. Qafzeh-9 and Tianyuan (early *Homo sapiens*) and KNM-WT-22944-I (*Australopithecus afarensis cf. Australopithecus*) are all exclusively within the *Homo sapiens* morphospace, while UW-1010-1729 (*Homo naledi*) and UW-88-95 (*Australopithecus sediba*) are within the group's vicinity, and quite strongly to the left of the scatterplot, and unambiguously closer to *Homo sapiens* than to any other group.

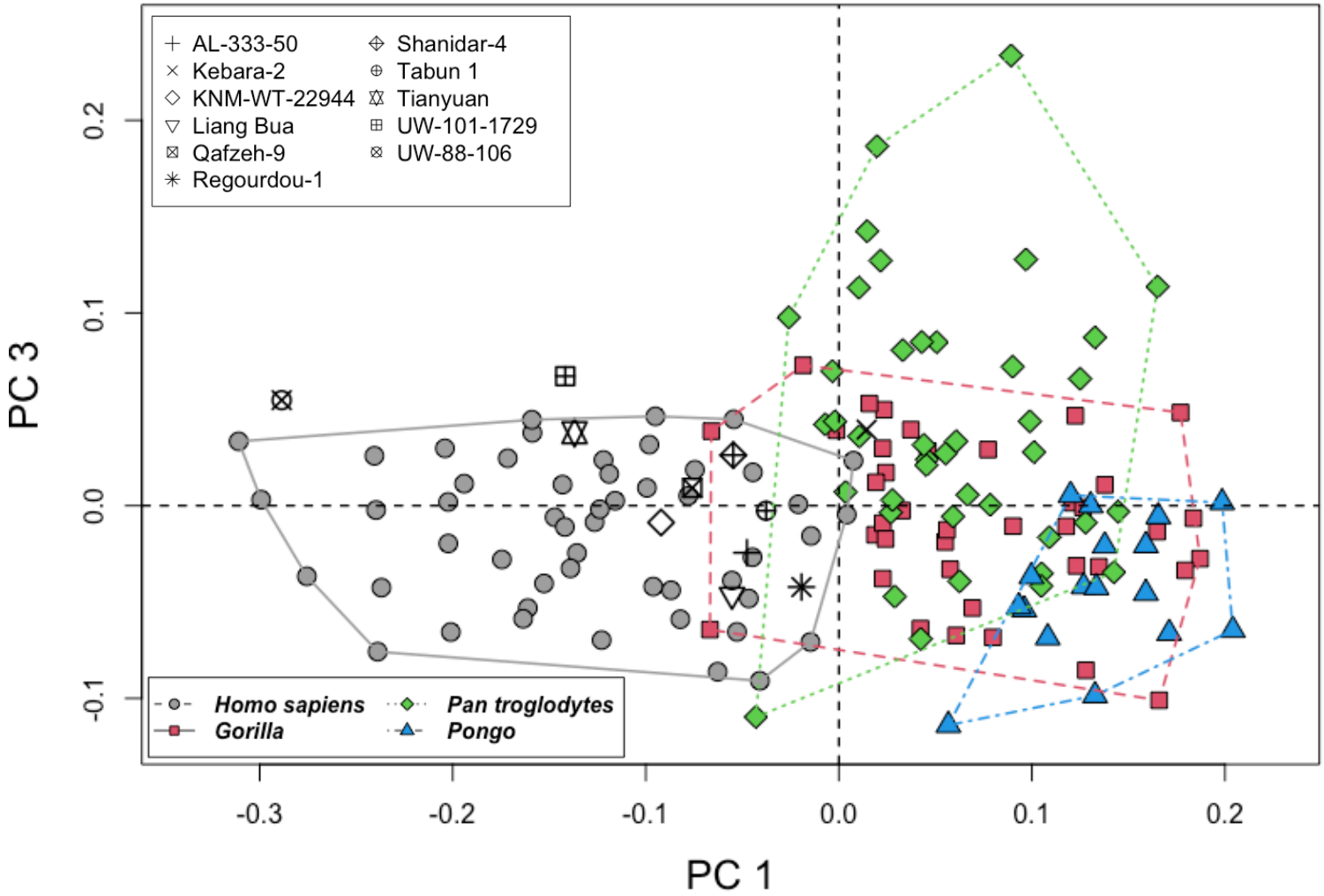

Figure 7.2.6: Scatterplot of the first vs. third principal component scores of extant samples (*Homo sapiens, Gorilla, Pan troglodytes* and *Pongo*) and fossil specimens for the hamate's articular surface for the fifth metacarpal. The *Homo sapiens* morphospace dominates the left half of the plot, with the samples of all non-human taxa predominantly to the left.

PC 2 v PC 3

A scatterplot of the scores of the second principal component against those of the third is displayed in figure 7.2.7. There is considerable overlap between the extant groups in this plot, which is of limited utility in assessing the fossil specimens. The *Homo sapiens* sample is highly concentrated around the centre of the plot and is almost completely intersected by other samples. The scatterplot of PC 2 vs PC 3 is only of real utility in distinguishing between the *Gorilla* and *Pan troglodytes* samples. The *Gorilla* sample is predominantly in the left half of the plot, while the *Pan troglodytes* sample is mostly to the right. As such, these two groups only slightly interact towards the centre of the plot. The *Pan troglodytes* sample is dispersed to a far greater extent than any other group in this plot, largely due to the wide range of PC 3 values in this group compared with others, which are dispersed along the zero of the axis, or in its lower half in the case of *Pongo.*

Given the considerable overlap of the extant groups, and the dispersal of the fossil specimens around the centre of the plot, this scatterplot is also of limited utilization in comparing fossil specimens to the extant sample. Four of the fossil specimens (Tabun-1, Regourdou-1 (*Homo neanderthalensis*); AL-333-50 (*Australopithecus afarensis*); Qafzeh-9 (early *Homo sapiens*)) are within the *Homo sapiens* morphospace, as well as at least one non-human group. The remaining five specimens are outside the range of *Homo sapiens*. Shanidar-4 (*Homo neanderthalensis*), Tianyuan (early *Homo sapiens*), and UW-1010-1729 (*Homo naledi*) are solely within the morphospace of *Gorilla*, while UW-88-95 (*Australopithecus sediba*) is within the *Pan troglodytes* morphospace. Kebara-2 (*Homo neanderthalensis*) is within both *Gorilla* and *Pan troglodytes* morphospaces.

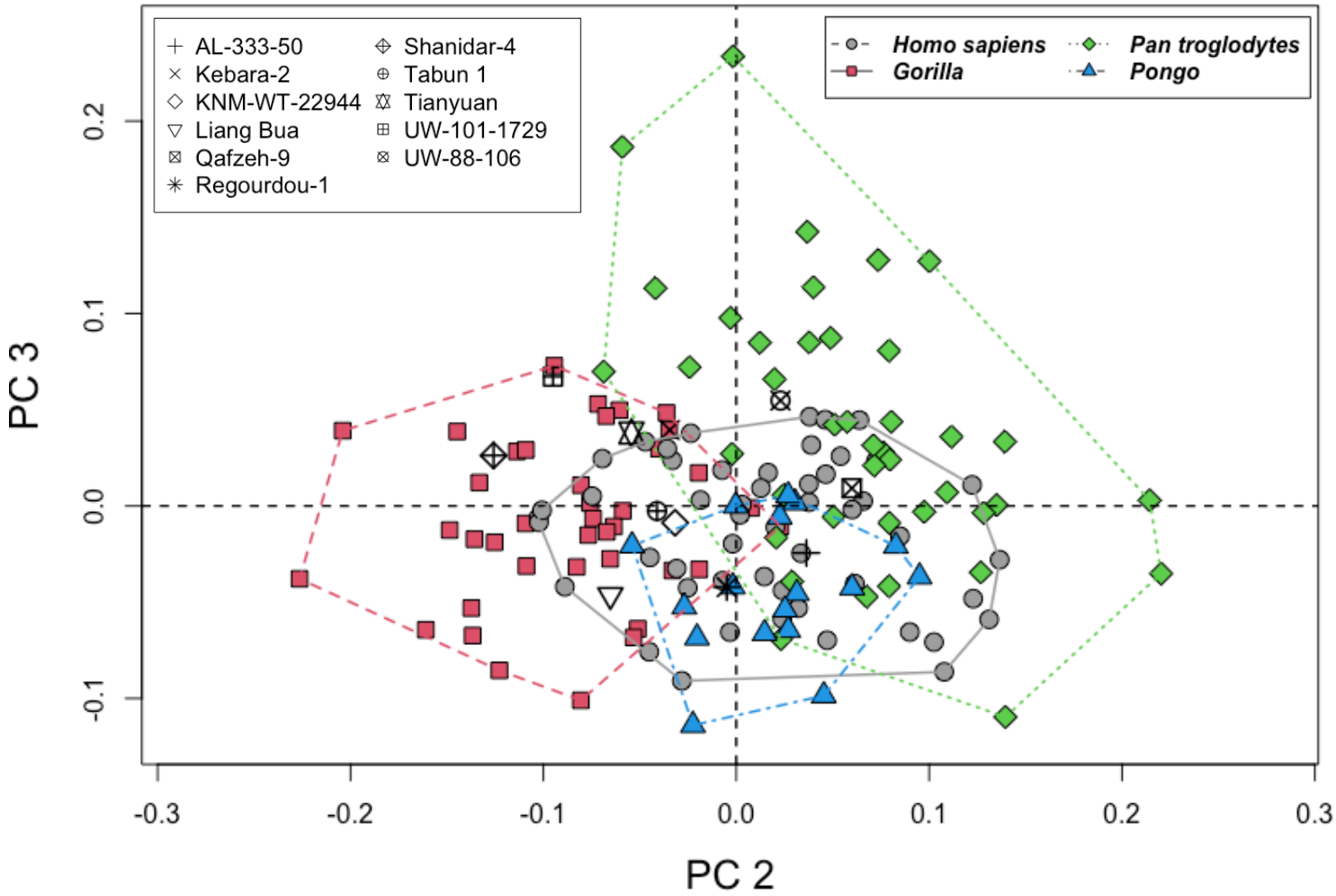

Figure 7.2.7: Scatterplot of the second vs. third principal component scores of extant samples (*Homo sapiens, Gorilla, Pan troglodytes* and *Pongo*) and fossil specimens for the hamate's articular surface for the fifth metacarpal. Due to the high overlap of the extant group morphospaces, this plot is of limited value in interpreting fossil specimen affinities.

7.3 Hamate-MC5 Canonical Variate Analysis

A canonical variate analysis (CVA) with leave-one-out cross-validation was carried out on the extant species sample along first nine principal components, which accounted for 91.44% of the total variance of the PCA, with the extant sample separated by their pre-defined taxonomical groupings. The canonical variate analysis correctly assigned extant specimens to their *a priori* groups in 93.2% of cases ($k = 0.91$) (table 7.3.1). *Homo sapiens* specimens were correctly assigned into their *a priori* group in 96.1% of cases, being mis-assigned as *Pan troglodytes* twice. The *Gorilla* sample was correctly classified in 97.4% of cases, with one specimen misclassified as *Pongo*. *Pan troglodytes*, with a successful classification rate of 87.8%, was mistaken for *Pongo* in three cases, and *Homo sapiens* and *Gorilla* once. *Pongo* was correctly classified with a rate of 88.2%, being misclassified as *Gorilla* in one case and as *Pan troglodytes* once. The first canonical variate axis accounted for 63.45% of the total variance, with the second and third axes accounting for 25.77% and 10.79% of the total variance, respectively.

Table 7.3.1: Table of predicted taxa against actual taxa. *A priori* classification is along the horizontal, with group classification through canonical variants analysis is along the vertical.

	Gorilla	*Homo sapiens*	*Pan troglodytes*	*Pongo*	*N*
Gorilla	38 (97.4%)	0	0	1 (2.5%)	39
Homo sapiens	0	49 (96.1%)	2 (3.9%)	0	51
Pan troglodytes	1 (2.4%)	1 (2.4%)	36 (87.8%)	3 (7.3%)	41
Pongo	1 (5.9%)	0	1 (5.9%)	15 (88.2%)	17

MANOVA along the canonical variates axes returned significant results between extant groups ($F(3, 144) = 133.57$, $p < 0.001$, Wilks' $\Lambda = 0.026$). Results of the one-way analysis of variance tests performed on the CV scores of the extant sample, with the sample divided by *a priori* taxonomic groups, are shown in table 7.3.2. The results of the ANOVA of the scores along each CV axis were significant ($p < 0.05$) for all three CV axes. Results of the Tukey HSD test along the scores of the first canonical variate axis showed that the mean values of all groups were significantly different from each other (table 7.3.3). Along the second and third CV axes, all pairwise comparisons were significant ($P < 0.05$) with the exception of between *Pan troglodytes* and *Pongo* along CV 2 ($p = 0.389$, 95% C.I. = -1.208, 0.292), and *Homo sapiens* and *Gorilla* along CV 3 ($p = 0.289$, 95% C.I. = -0.931, 0.175).

Table 7.3.2: Results of analysis of variance on canonical variate scores on extant groups.

Canonical Variate	DF	Sum of Squares	Mean Squares	*F* Value	*p*
CV 1	3, 144	769.7	256.6	256.6	**<0.001**
CV 2	3, 144	312.6	104.2	104.2	**<0.001**
CV 3	3, 144	130.8	43.62	43.62	**<0.001**

Table 7.3.3: *P*-values for Tukey's HSD pairwise comparisons of canonical variate scores.

	Homo sapiens	Gorilla	Pan troglodytes	Pongo
Canonical Variate 1 (63.45%)				
Homo sapiens	-	**<0.001**	**<0.001**	**<0.001**
Gorilla		-	**<0.001**	**<0.001**
Pan troglodytes			-	**<0.001**
Pongo				-
Canonical Variate 2 (25.77%)				
Homo sapiens	-	**0.006**	**<0.001**	**<0.001**
Gorilla		-	**<0.001**	**<0.001**
Pan troglodytes			-	0.389
Pongo				-
Canonical Variate 3 (10.79%)				
Homo sapiens	-	0.288	**<0.001**	**<0.001**
Gorilla		-	**0.031**	**<0.001**
Pan troglodytes			-	**<0.001**
Pongo				-

All but one fossil specimen was categorized into the *Homo sapiens* group by the CVA. Liang Bua-21/22 (*Homo floresiensis*) was considered, with a likelihood of 72.8%, to be most closely aligned to the *Gorilla* sample, while having a probability of 23.0% of belonging to the *Pan troglodytes* sample, and only a 2.90% likelihood of belonging to *Homo sapiens* (table 7.3.4). All other fossil specimens were assigned as *Homo sapiens*, with AL-333-50 (*Australopithecus afarensis*), KNM-WT-22944-I (*Australopithecus afarensis cf. Australopithecus*), UW-88-95 (*Australopithecus sediba*), both early *Homo sapiens* specimens (Qafzeh-9 & Tianyuan), and three of the four *Homo neanderthalensis* specimens (Regourdou-1, Shanidar-4, Tabun-1) having a probability of >95% as belonging to the *Homo sapiens* sample. Kebara-2 (*Homo neanderthalensis*), while being assigned to the *Homo sapiens* group, only had a probability of 47.5% as belonging to that group, while having a probability of 33.0% and 18.2% as being *Pan troglodytes* and *Gorilla*, respectively.

Table 7.3.4: Canonical variate analysis (CVA) classification results of fossil specimens based on scores of the first nine principal components. The column to the right shows the group to which each fossil specimen was classified by the linear discriminant analysis. Results were in percentage.

	Homo sapiens	*Gorilla*	*Pan troglodytes*	*Pongo*	Classification
AL-333-50	98.90	0.00	1.10	0.00	*Homo sapiens*
Kebara-2	47.50	18.20	33.00	1.30	*Homo sapiens*
KNM-WT-22944	100.00	0.00	0.00	0.00	*Homo sapiens*
Liang Bua-21/22	2.90	72.80	23.00	1.20	*Gorilla*
Qafzeh-9	99.90	0.00	0.10	0.00	*Homo sapiens*
Regourdou-1	98.70	0.10	1.10	0.10	*Homo sapiens*
Shanidar-4	95.80	0.00	3.20	1.00	*Homo sapiens*
Tabun-1	97.80	0.10	1.90	0.20	*Homo sapiens*
Tianyuan	100.00	0.00	0.00	0.00	*Homo sapiens*
UW-101-1729	88.20	10.60	1.20	0.00	*Homo sapiens*
UW-88-95	100.00	0.00	0.00	0.00	*Homo sapiens*

First Canonical Variate Axis

Shape change along the first canonical variate axis corresponds to shape change along the first principal component, which discriminates between a mediolaterally broad surface with a gentle and slight palmodorsal curvature coupled with a mediolateral convex curvature, and a palmodorsally long and mediolaterally narrow surface that is sharply bevelled palmodorsally (figures 7.2.2 & 7.3.1). CV 1 accounts for 63.45% of the total shape variation, and most effectively separates the *Homo sapiens* sample, which is exclusively in the negative aspect of the axis, from *Gorilla* and *Pongo,* which are in the positive (figure 7.3.1). The *Pan troglodytes* sample is distributed fairly evenly between both negative and positive values, with its median value approximating zero, and the fourth quartile of the group overlapping with the first quartile of *Homo sapiens*. There is considerable overlap between the ranges of the three non-human groups, especially between *Pongo* and the two other groups. *Gorilla* and *Pan troglodytes* only overlap their 1st and 4th quartiles, respectively (figure 7.3.1).

The majority of the fossil specimens are in the negative aspect of CV 1, with the exception of Liang Bua-21/22 (*Homo floresiensis*), which has a marginally positive CV 1 score. UW-88-95 (*Australopithecus sediba*) has the most negative CV 1 score of the entire sample, being more negative than the most extremal *Homo sapiens* specimen. The two early *Homo sapiens* specimens (Qafzeh-9 and Tianyuan) are within the *Homo sapiens* range, with Qafzeh-9 being within its interquartile range. Three of the four *Homo neanderthalensis* specimens (Regourdou-1, Shanidar-4, and Tabun-1) are also within the 4th quartile of *Homo sapiens*, as well as in the 1st quartile of *Pan troglodytes*. Kebara-2 (*Homo neanderthalensis*) is outside the *Homo sapiens* range and within the 2nd quartile of *Pan troglodytes*. AL-333-50 (*Australopithecus afarensis*) is within the third quartile of *Homo sapiens*, while KNM-WT-22944-I (*Australopithecus afarensis cf. Australopithecus*) is in its 3rd quartile, and the 1st quartile of *Pan troglodytes.* UW-101-1729 (*Homo naledi*) is marginally outside the range of *Homo sapiens*, and within the 1st quartile of *Pan troglodytes*.

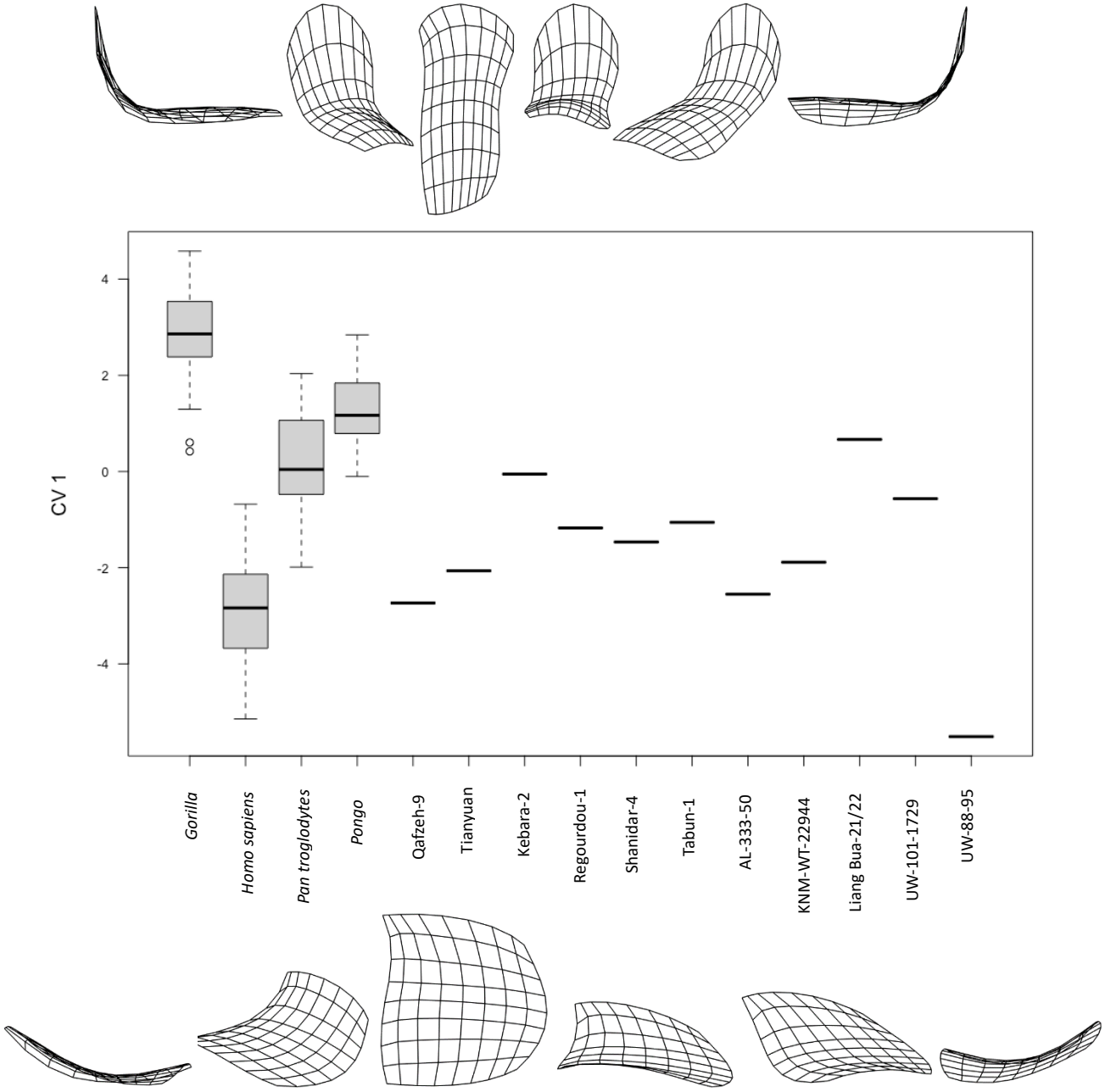

Figure 7.3.1: Boxplot of the scores of the first Canonical Variate axis of the hamate's metacarpal 5 articular surface for *Gorilla, Homo sapiens, Pan troglodytes,* and *Pongo* compared with fossil specimens Qafzeh-9, Tianyuan (early *Homo sapiens*); Kebara-2, Regourdou-1, Shanidar-4, Tabun-1 (*Homo neanderthalensis*); AL-333-50 (*Australopithecus afarensis*); KNM-WT-22944-I (cf. Australopithecus afarensis); Liang Bua (*Homo floresiensis*); UW-101-1729 (*Homo naledi*); and UW-88-95 (*Australopithecus sediba*). Black lines represent the median of the group, boxes are interquartile ranges, and whiskers are the non-outlier ranges.

Second Canonical Variate Axis

The second CV axis broadly corresponds to shape change along the second principal component axis (described in section 7.2 and represented in figure 7.2.3). It accounts for 25.77% of the difference in shape between groups and is most effective in separating *Gorilla* from *Pan troglodytes* and *Pongo*. The maxima of the second Canonical Variate represents a highly bevelled surface with palmar and dorsal parts separated by an approximately 90° apex. The palmar edge is proximally sloping towards the medial side, while the dorsal half is proximally sloping towards its dorsal edge. Overall, the CV 2 maximal shape most closely resembles a *Pan troglodytes* specimen (figure 7.1.3). The minima of CV 2 represents an articular surface that is an amalgamation of the *Gorilla* and *Homo sapiens* samples, with a more gentle, obtuse, and regular palmodorsal curve than the maximal shape, and while the dorsal portion of the surface is highly mediolaterally convex, and the palmar portion is flared and projects distally, it does not exhibit these features to the same extent as the mean shape of *Gorilla* (figure 7.1.2), nor to the shape representative of the minima of PC 2 (figure 7.2.3). The range of the *Gorilla* sample is entirely in the negative portion of CV 2, while the ranges of *Pan troglodytes* and *Pongo* dominate the positive aspect, with very little overlap between *Gorilla* and the other non-human taxa. The range of *Homo sapiens* spans both the negative and positive aspects of CV 2, though is skewed to the negative, with its interquartile range being exclusively in the negative half, although its 4th quartile does overlap with the lower halves of *Pan troglodytes* and *Pongo* (figure 7.3.2).

Every fossil specimen is located within the range of *Homo sapiens,* with all but two (Shanidar-4 (*Homo neanderthalensis*) and AL-333-50 (*Australopithecus afarensis*)) having a negative CV 2 score. These two specimens are the only ones outside the *Gorilla* range. All early *Homo sapiens* and *Homo neanderthalensis* specimens, with the exception of Shanidar-4, as well as Liang Bua-21/22 (*Homo floresiensis*), are within the interquartile range of *Homo sapiens*. Qafzeh-9 (early *Homo sapiens*), Shanidar-4 (*Homo neanderthalensis*), and AL-333-50 (*Australopithecus afarensis*) are also within the 1st quartiles of *Pan troglodytes* and *Pongo* (figure 7.3.2).

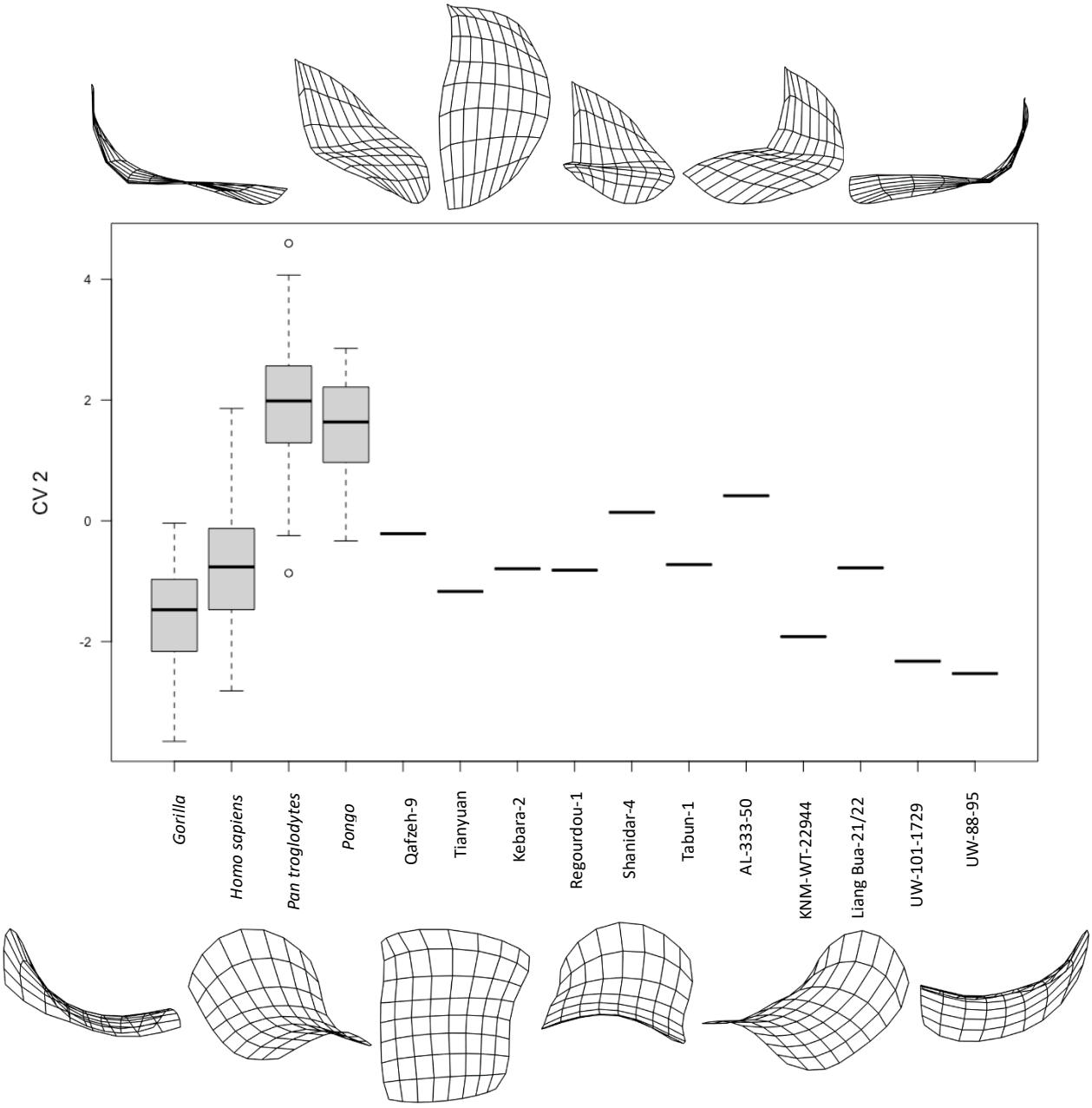

Figure 7.3.2: Boxplot of the scores of the second Canonical Variate axis of the hamate's metacarpal 5 articular surface for *Gorilla, Homo sapiens, Pan troglodytes,* and *Pongo* compared with fossil specimens Qafzeh-9, Tianyuan (early *Homo sapiens*); Kebara-2, Regourdou-1, Shanidar-4, Tabun-1 (*Homo neanderthalensis*); AL-333-50 (*Australopithecus afarensis*); KNM-WT-22944 (cf. Australopithecus afarensis) ; Liang Bua (*Homo floresiensis*); UW-101-1729 (*Homo naledi*); and UW-88-95 (*Australopithecus sediba*). Black lines represent the median of the group, boxes are interquartile ranges, and whiskers are the non-outlier ranges.

Third Canonical Variate Axis

Shape change along the third canonical variance axis, which contributed to 10.79% of the total variance, corresponds to shape change along the third principal component (section 7.2, figure 7.2.4). The maxima of CV 3 is representative of a strongly palmodorsally concave articular surface that slopes proximally from its lateral to its medial edge, with the sloping increasing dorsally, culminating in a proximally-drooping mediodorsal corner. The maximum shape most closely resembles the *Pan troglodytes* sample, while the minimum shape is much more gently palmodorsally concave, with no mediolateral convex curving, but with a proximally-sloping distal edge, as is seen in the mean shape of the *Pongo* sample (figure 7.1.4). The third Canonical Variate axis is most effective in separating *Pongo*, being entirely in the negative aspect of CV 3, from the other groups, especially *Pan troglodytes*, though there is some overlap between the 4th quartile of *Pongo* and the 1st quartile of *Pan troglodytes*, and more considerable overlap between *Pongo* and the two other groups. The interquartile range of *Homo sapiens* is distributed evenly between negative and positive scores, with the sample's median value approximating zero, though its 1st quartile is distributed more broadly than the positive 4th quartile. The range of the *Gorilla* and *Pan troglodytes* samples are also distributed across negative and positive values, though are skewed more towards the positive aspect, especially in *Pan troglodytes*, which has an exclusively positive interquartile range, and displays the most positive scores of the entire sample. There is considerable overlap between the African great apes and *Homo sapiens*, as well as between *Pongo* with *Gorilla* and *Homo sapiens.* The 1st quartile of *Homo sapiens* overlaps with the upper half of *Pongo*, and the 1st quartile of *Gorilla* with *Pongo*'s 4th quartile (figure 7.3.3).

All fossil specimens, with the exception of UW-101-1729 (*Homo naledi*), are found within the ranges of *Gorilla* and *Homo sapiens* and are distributed fairly evenly across the axis. UW-101-1729 has a higher CV 3 score than the most extreme positive *Homo sapiens* specimen. Likewise, all fossil specimens are within the range of the extremal points of *Pan troglodytes*, while four fossil specimens (Tianyuan (early *Homo sapiens*), Shanidar-4, Tabun-1 (*Homo neanderthalensis*), and KNM-WT-22944-I (*Australopithecus afarensis cf. Australopithecus*)) are also in the *Pongo* range (figure 7.3.3).

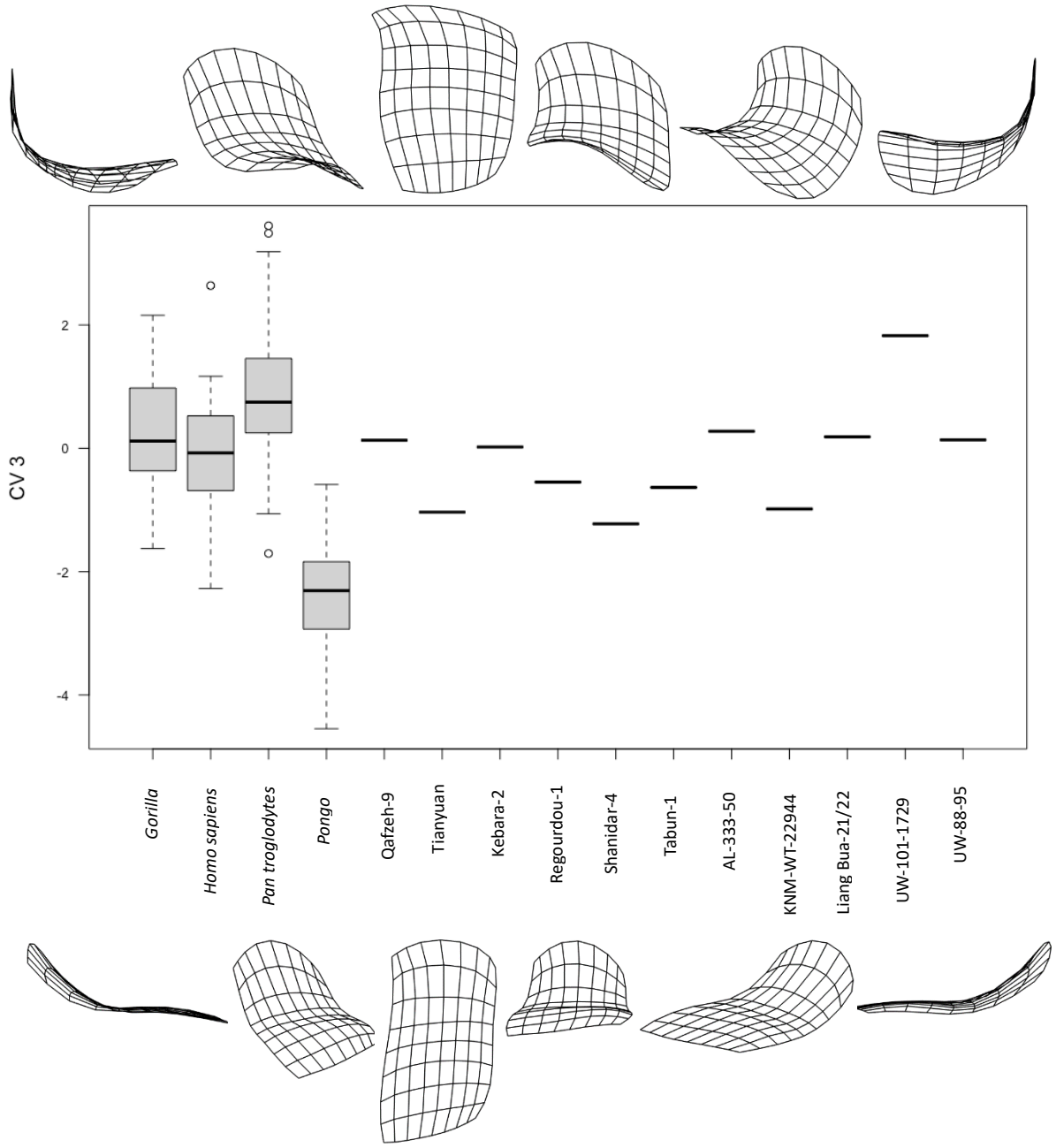

Figure 7.3.3: Boxplot of the scores of the third Canonical Variate axis of the hamate's metacarpal 5 articular surface for *Gorilla, Homo sapiens, Pan troglodytes,* and *Pongo* compared with fossil specimens Qafzeh-9, Tianyuan (early *Homo sapiens*); Kebara-2, Regourdou-1, Shanidar-4, Tabun-1 (*Homo neanderthalensis*); AL-333-50 (*Australopithecus afarensis*); KNM-WT-22944 (cf. Australopithecus afarensis); Liang Bua (*Homo floresiensis*); UW-101-1729 (*Homo naledi*); and UW-88-95 (*Australopithecus sediba*). Black lines represent the median of the group, boxes are interquartile ranges, and whiskers are the non-outlier ranges.

Canonical Varaites Analysis Scatterplots

CV 1 v CV 2

A scatterplot of CV 1 against CV 2, shown in figure 7.3.4, is most effective in seperating the samples of *Homo sapiens*, to the left, from the sample of *Gorilla,* on the right. While there was no overlap in the samples of *Gorilla* and *Homo sapiens*, both groups overlap to some extent with both *Pan troglodytes* and *Pongo*, which are clustered together. The veritcal axis (CV 2) provided seperation of the *Pan troglodytes-Pongo* cluster from the samples of *Gorilla* and *Homo sapiens.*

Most of the fossil specimens are either within or near to the 95% confidence ellipse of *Homo sapiens*. AL-333-50 (*Australopithecus afarensis*) and UW-101-1729 (*Homo naledi*) are marginally outside the *Homo sapiens* 95% confidence ellipse, with AL-333-50 also in the 95% confidence ellipse of *Pan trolgodytes.* UW-88-95 (*Australopithecus sediba*) is in the extreme lower-left quadrant of the scatterplot, having the most negative CV 1 value. Liang Bua-21/22 (*Homo floresiensis*) is the only fossil specimen that is clearly outside the vicinity of the *Homo sapiens* sample, and is positioned at the intersection of the 95% confidence ellipses of all three non-human groups (figure 7.3.4).

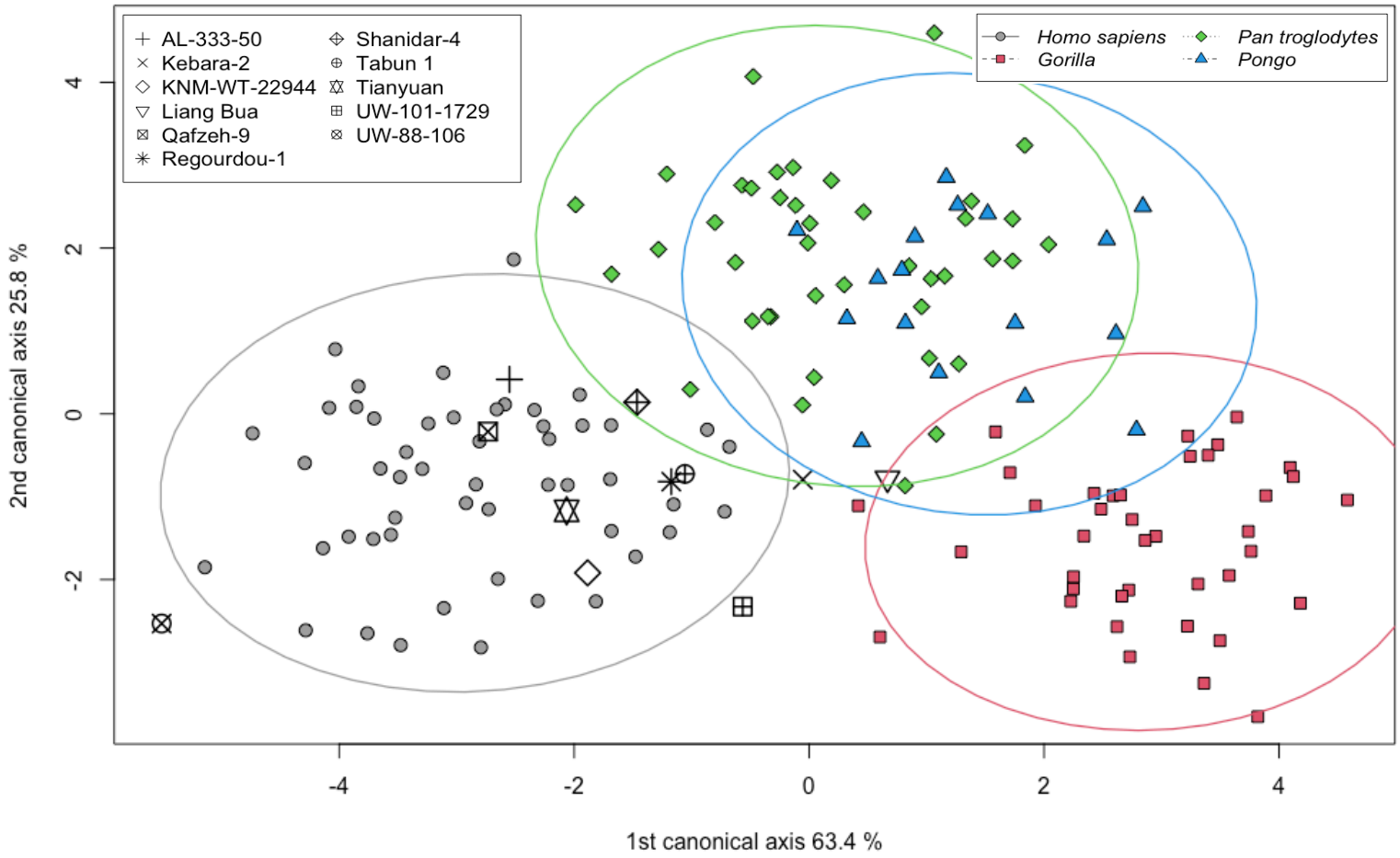

Figure 7.3.4: Scatterplot of the first vs. second canonical variates axis (CV 1 (63.4%) vs. CV 2 (25.8%)) scores of extant samples (*Homo sapiens*, *Gorilla*, Pan *troglodytes,* and *Pongo*) and fossil specimens. The *Homo sapiens* sample is separate from the non-human taxa, being in the lower-left portion of the plot.

CV 1 v CV 3

While the scatterplot of CV 1 against CV 3 (figure 7.3.5) again separates the *Homo sapiens* and *Gorilla* samples along the x axis, with the *Homo sapiens* poulation to the left and the *Gorilla* sample to the right (CV 1), the third canonical variate axis does not distinguish between these two samples. Rather, along the y axis of this plot, which corresponded to CV 3, *Pan troglodytes* occupies the upper half, while *Pongo* is in the lower half, though there remains considerable overlap between the two samples, as well as between each group and *Homo sapiens* and *Gorilla.* The samples of *Homo sapiens* and *Gorilla* do not interact with each other.

Again, the majority of the fossil specimens are found within the 95% confidence ellipse of *Homo sapiens* to the left half of the plot. AL-333-50 (*Australopithecus afarensis*) and UW-101-1729 (*Homo naledi*) are exclusively within the *Pan troglodytes* 95% confidence ellipse, while Liang Bua-21/22 (*Homo floresiensis*) is again the fossil specimen farthest from the *Homo sapiens* sample, being at the intersection of *Pan troglodytes* and *Gorilla.*

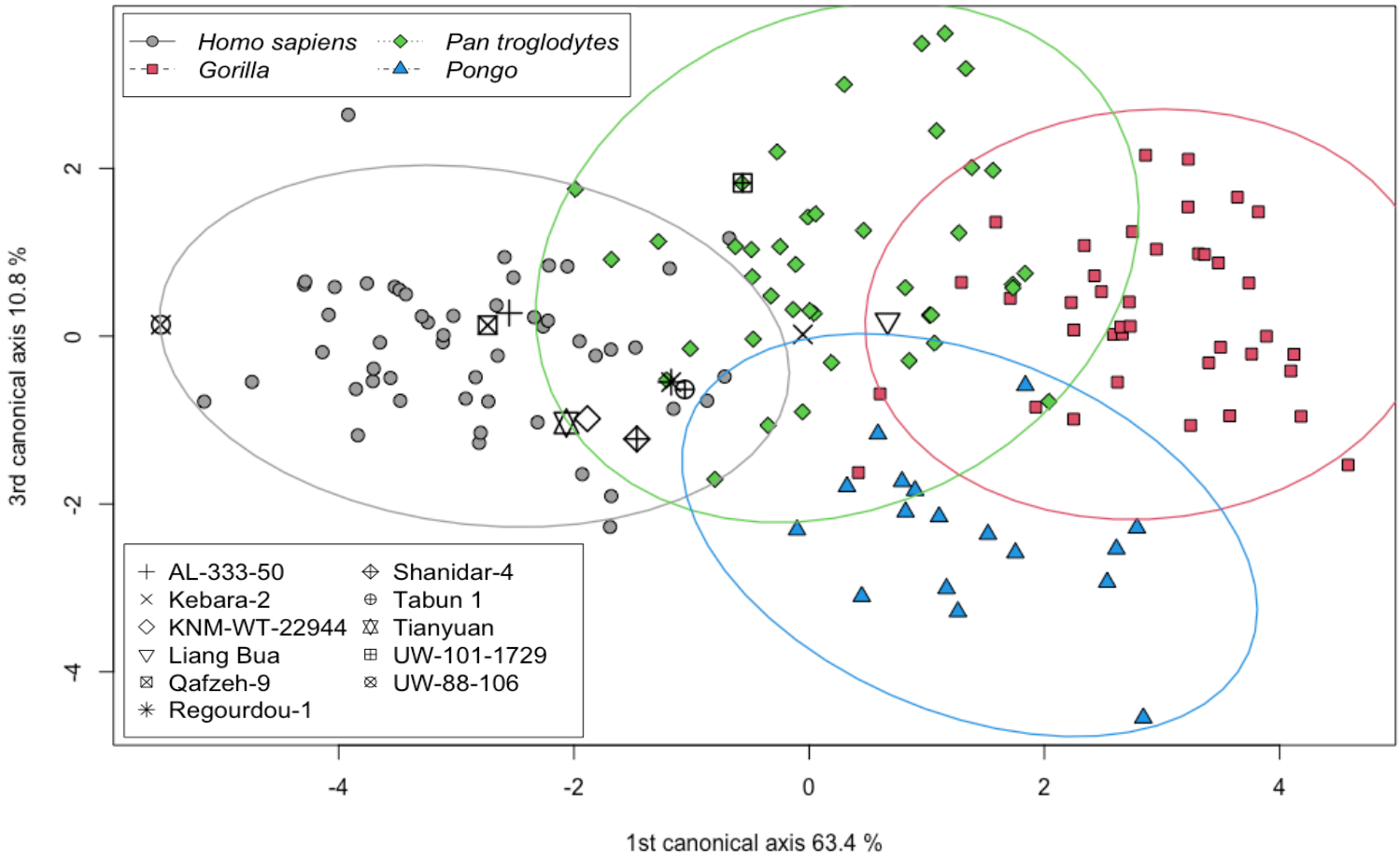

Figure 7.3.5: Scatterplot of the first vs. third canonical variates axis (CV 1 (63.4%) vs. CV 3 (10.8%)) scores of extant samples (*Homo sapiens*, Gorilla, Pan *troglodytes,* and *Pongo*) and fossil specimens. The x axis (CV 1) distinguishes between the African taxa, while the y axis (CV 3) separates African great apes from the *Pongo* sample.

CV 2 v CV 3

The scatterplot of the second against third CV axis is shown in figure 7.3.6. This plot clusters the *Homo sapiens* and *Gorilla* samples to the left, while the *Pan troglodytes* and *Pongo* samples are separated along CV 3 primarily to the right of the plot. There is considerable overlap between the 95% confidence ellipses of all groups, and this plot is of limited value in interpretation of the fossil populaiton, with seven of the fossil specimens residing within the 95% confidence ellipse of at least three extant groups, and three of the remaining four within the realms of *Homo sapiens* and *Gorilla.* It is only UW-101-1729 (*Homo naledi*) that is within the 95% confidence ellipse of a single extant group, being within that of *Gorilla*, and is also the only fossil specimen found outside of the confidence ellipse of *Homo sapiens.*

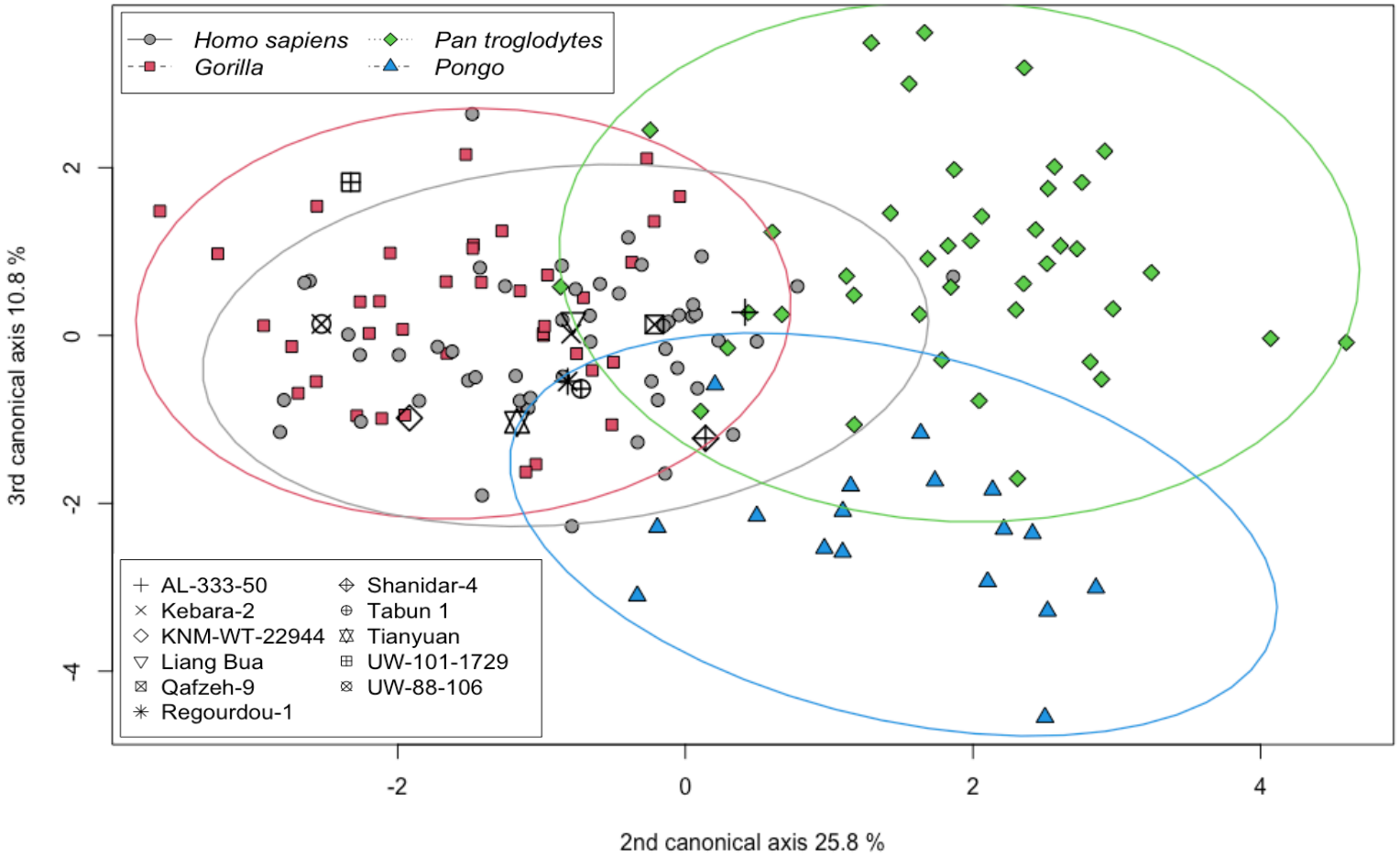

Figure 7.3.6: Scatterplot of the second vs. third canonical variates axis (CV 2 (25.8%) vs. CV 3 (10.8%)) scores of extant samples (*Homo sapiens*, Gorilla, Pan *troglodytes,* and *Pongo*) and fossil specimens. There is high overlap between samples of extant taxa, and all fossil specimens are found in the *Homo sapiens-Gorilla* cluster.

7.4 Hamate-MC-5 Procrustes distances

The Procrustes distance of each fossil specimen from the average shape of each extant taxon group is shown in table 7.4.1, with the Procrustes distance of each fossil specimen from the average shape of each extant taxon group shown in table 7.4.2. The mean shapes of *Pongo, Pan troglodytes* and *Gorilla* were considerably closer to each other than they were to the *Homo sapiens* mean shape. The *Homo sapiens* average shape was closest to that of *Pan troglodytes* followed by *Gorilla*, with *Homo sapiens* and *Pongo* having the greatest pairwise Procrustes distance among the mean shapes of extant taxa.

Fossil specimens are consistently closer to the mean shape of the *Homo sapiens* sample than to the mean shape of any other group, with the exception of Kebara-2 (*Homo neanderthalensis*), which is closer to the mean shape of *Gorilla.* Nevertheless, Kebara-2 is closer to the *Homo sapiens* mean shape than several other fossils, including Liang Bua 21/22 (*Homo floresiensis*), Regourdou-1 (*Homo neanderthalensis*), Shanidar-4 (*Homo neanderthalensis*), and UW-88-95 (*Australopithecus sediba*). UW-88-95 (*Australopithecus sediba*) is the fossil specimen farthest from the *Homo sapiens* mean shape, while Qafzeh-9 (early *Homo sapiens*) is the closest.

Table 7.4.1: Procrustes distances between extant groups.

	Homo sapiens	*Gorilla*	*Pan troglodytes*	*Pongo*
Homo sapiens	-	0.231	0.203	0.272
Gorilla		-	0.161	0.156
Pan troglodytes			-	0.140
Pongo				-

Table 7.4.2: The Procrustes distance of each fossil from the mean shape of each extant taxon group.

	Homo sapiens	*Gorilla*	*Pan troglodytes*	*Pongo*
AL-333-50	0.129	0.204	0.156	0.217
Kebara-2	0.184	0.138	0.149	0.183
KNM-WT-22944	0.117	0.204	0.214	0.257
Liang Bua-21/22	0.224	0.227	0.262	0.283
Qafzeh-9	0.106	0.226	0.166	0.242
Regourdou-1	0.209	0.218	0.218	0.241
Shanidar-4	0.229	0.231	0.274	0.286
Tabun-1	0.120	0.145	0.163	0.198
Tianyuan	0.153	0.258	0.265	0.314
UW-101-1729	0.160	0.236	0.267	0.336
UW-88-95	0.231	0.410	0.383	0.457

Results of the Shapiro-Wilk tests for normality along the linear distances of extant species from the mean value of their respective groups are shown in table 7.4.3. A Shapiro-Wilk test for normality showed that the linear distances of *Gorilla* were not normally distributed. As such, the linear distances of extant species from the mean value of their respective groups were log-transformed. Results of the Shapiro-Wilk test show that the log-transformed data were all normally distributed ($p > 0.05$; table 7.4.3), and the log-transformed values were used in calculating the upper-tail cumulative distribution function.

Table 7.4.3: Results of the Shapiro-Wilk normality tests performed on the individual distances distribution from their respective group mean shapes (top row), and the corresponding square-root-transformed data. Calculations were performed in linear distances considering the first three principal components.

	Homo sapiens	*Gorilla*	*Pan troglodytes*	*Pongo*
p	0.295	**0.011**	0.084	0.258
p (transformed)	0.896	0.319	0.498	0.274

Fossil distances (in standard deviations from the mean of the distance of each individual of the group from the group mean) are shown in table 7.4.4. While Liang Bua-21/22 was the only fossil specimen not categorized as *Homo sapiens* by the CVA, being assigned to *Gorilla*, this specimen was marginally closer to the mean shape of *Homo sapiens* (2.19 SD) than to the mean

shape of *Gorilla* (2.20 SD), although this distance was approximately equal, being closer to the mean shape of *Homo sapiens* than only 1.41% of the human sample, and closer to the *Gorilla* mean shape than only 1.39% of gorillas.

While all other specimens were assigned to the *Homo sapiens* group, in absolute terms, three of the *Homo neanderthalensis* specimens were closer to the mean shapes of *Pan troglodytes* and/or *Gorilla* than to the mean shape of *Homo sapiens.* Kebara-2 was the closest fossil specimen to the *Pan troglodytes* mean shape, with a distance of 0.02 standard deviations, and closer than 49.18% of the group's sample, while also being closer to the *Gorilla* mean shape than 40.56% of that group's sample, and only 8.31% of the *Homo sapiens* sample. Shanidar-4 was closer to the mean shape of *Gorilla* than to *Homo sapiens* and had the second-highest distance from the *Homo sapiens* mean shape among fossils. Regourdou-1 was closer in standard deviations to the mean shape of the *Pan troglodytes* sample, being closer than 7.46% of the chimpanzee sample to the group's mean shape, while being closer than only 2.9% of humans to the *Homo sapiens* mean shape.

Both early *Homo sapiens* specimens (Qafzeh-9 and Tianyuan) were closer to the *Homo sapiens* mean shape than to the mean shape of any other group, with Qafzeh-9 being the closest of all specimens, as it was closer to the group's mean shape than 81.13% of the modern human sample. AL-333-50 (*Australopithecus afarensis*), KNM-WT-22944-I (*Australopithecus afarensis cf. Australopithecus*), and UW-101-1729 (*Homo naledi*) were all closer to the *Homo sapiens* mean shape than to the mean shapes of the other groups, with only Qafzeh-9 being closer than KNM-WT-22944-I. AL-333-50 was also the closest specimen to the mean shape of *Pan troglodytes,* being closer to the mean shape of *Pan troglodytes* than 42.33% of the chimpanzee sample. While UW-88-95 was closer to modern humans than any other group, it was the fossil specimen that bore the least resemblance to the *Homo sapiens* mean shape and was of comparable distance to the mean shapes of all other groups.

Table 7.4.4: Distances (in standard deviations) of each fossil from the mean of the distance of each individual of the extant group from the group mean. Calculations were conducted on Procrustes distances. In parentheses, the value of the upper-tail cumulative distribution function multiplied by 100.

	Homo	*Gorilla*	*Pan troglodytes*	*Pongo*
AL-333-50	-0.07 (52.66%)	1.77 (3.82%)	0.19 (42.33%)	3.44 (0.03%)
Kebara-2	1.38 (8.31%)	0.24 (40.56%)	0.02 (49.18%)	2.66 (0.39%)
KNM-WT-22944	-0.47 (68.11%)	1.78 (3.74%)	1.38 (8.34%)	4.24 (0.00%)
Liang Bua-21/22	2.19 (1.41%)	2.20 (1.39%)	2.15 (1.58%)	4.68 (0.00%)
Qafzeh-9	-0.88 (81.13%)	2.18 (1.47%)	0.41 (34.03%)	3.95 (0. 00%)
Regourdou-1	1.90 (2.90%)	2.03 (2.12%)	1.44 (7.46%)	3.93 (0. 00%)
Shanidar-4	2.28 (1.14%)	2.26 (1.20%)	2.31 (1.04%)	4.73 (0. 00%)
Tabun-1	-0.37 (64.54%)	0.45 (32.56%)	0.35 (36.32%)	3.03 (0.12%)
Tianyuan	0.63 (26.58%)	2.69 (0.36%)	2.18 (1.46%)	5.16 (0. 00%)
UW-101-1729	0.82 (20.62%)	2.35 (0.94%)	2.21 (1.36%)	5.47 (0. 00%)
UW-88-95	2.32 (1.01%)	4.50 (0.00%)	3.58 (0.02%)	6.91 (0. 00%)

8 Metacarpal 4 proximal articulation results

8.1 Metacarpal-4 proximal articulation average shapes

Homo sapiens

The average shape of the proximal articular surface of the fourth metacarpal of *Homo sapiens*, shown in figure 8.1.1, is extremely flat, with a palmar border that curves only slightly distally, and predominantly at the mediopalmar corner. The mediodorsal corner projects more dorsally than the laterodorsal corner, resulting in an angled dorsal border, moving palmarly from the medial corner to the lateral. Relative to the shaft of the fourth metacarpal, the articular surface slopes medially and dorsally

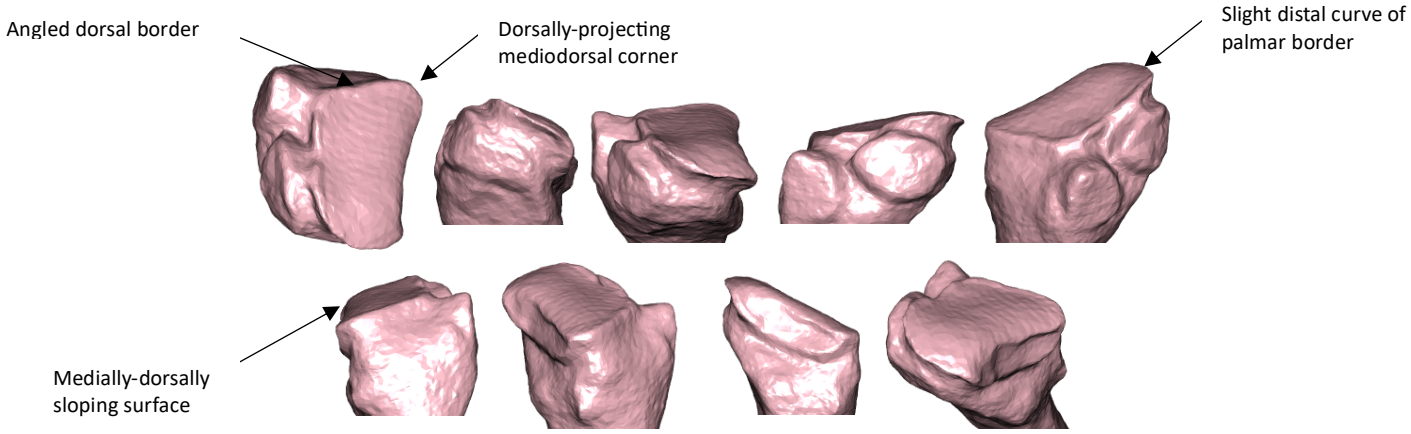

Figure 8.1.1: The average shape of the proximal articular surface of the fourth metacarpal of *Homo sapiens*, produced by warping the mesh of the specimen closest to the group's mean shape to the average shape of the group. The articular surface is shown from eight different viewpoints, from left to right: proximal; palmar; lateropalmar; lateral; laterodorsal; dorsal; mediodorsal; medial; mediopalmar views.

Gorilla

The mean shape of the *Gorilla* fourth metacarpal proximal articular surface is shown in figure 8.1.2. The distal and dorsal projection of the palmar border results in a pronounced bevelled curvature of the surface in the palmar portion. The sloping angle of the surface from the medial to the lateral border is also pronounced, and the dorsal margin lies distally, further exaggerating the angle of bevelling of the palmar portion.

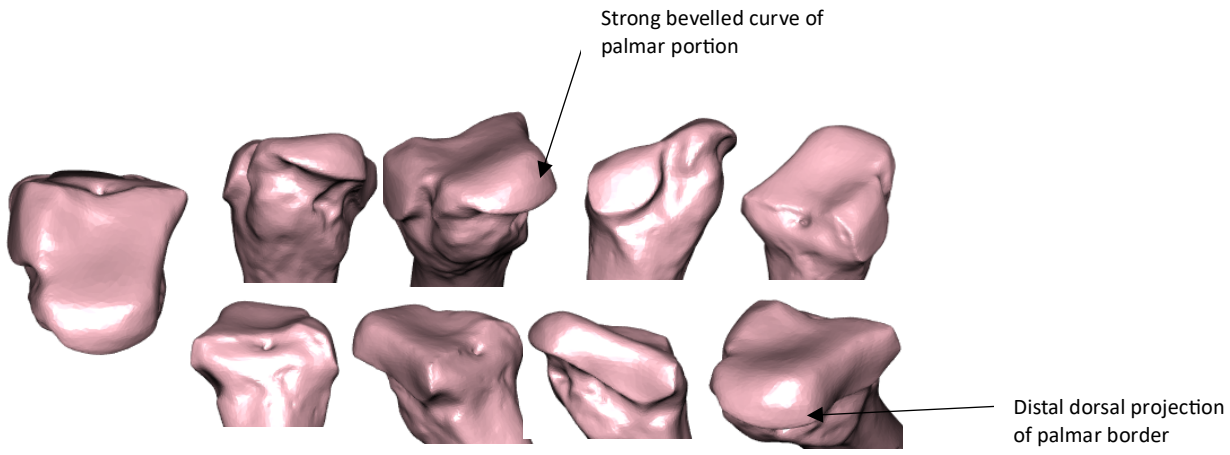

Figure 8.1.2: The average shape of the proximal articular surface of the fourth metacarpal of *Gorilla*, produced by warping the mesh of the specimen closest to the group's mean shape to the average shape of the group. The articular surface is shown from eight different viewpoints, from left to right: proximal; palmar; lateropalmar; lateral; laterodorsal; dorsal; mediodorsal; medial; mediopalmar views.

Pan troglodytes

A notable feature of the mean shape of *Pan troglodytes* (figure 8.1.3) is the prominent divot on the lateral portion of the surface, which continues onto the lateral edge of the surface, and parallels to the ballooning of the dorsolateral surface of the corresponding surface on the *Pan troglodytes* hamate. The mediopalmar corner of the surface is notably medially and distally projected, while the lateropalmar corner remains on a similar plane to the rest of the surface. This results in the bevelling shape of the surface being very acute, although concentrated medially, and becoming absent laterally.

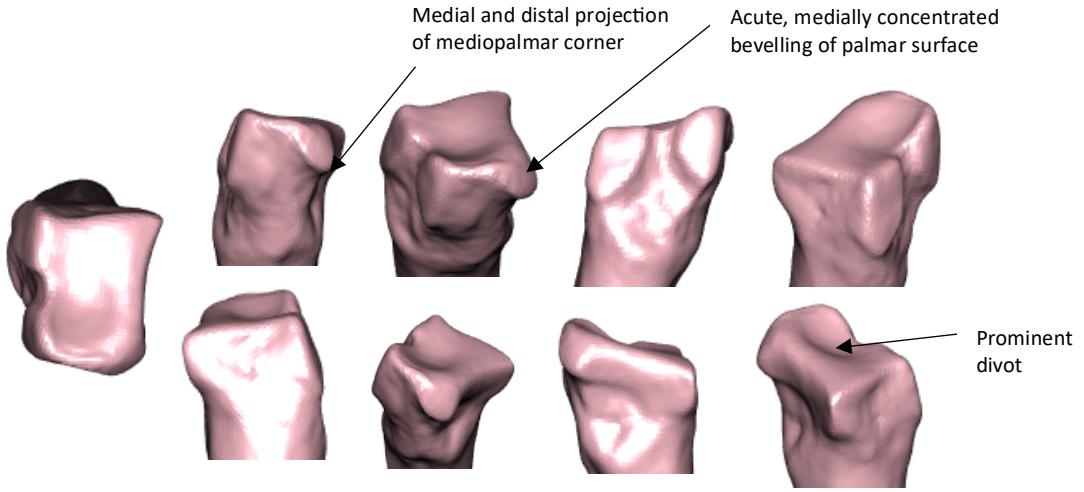

Figure 8.1.3: The average shape of the proximal articular surface of the fourth metacarpal of *Pan troglodytes*, produced by warping the mesh of the specimen closest to the group's mean shape to the average shape of the group. The articular surface is shown from eight different viewpoints, from left to right: proximal; palmar; lateropalmar; lateral; laterodorsal; dorsal; mediodorsal; medial; mediopalmar views.

Pongo

The average shape of the proximal articular surface of the fourth metacarpal in *Pongo* (figure 8.1.4) also displays a strongly bevelled mediopalmar corner relative to a lateropalmar corner that is not projected distally, and results in an asymmetrical bevelling of the palmar edge as in *Pan troglodytes*, albeit less pronounced. There is an obvious distal depression on the dorsal aspect of the surface, though this is positioned more centrally compared to *Pan troglodytes*, although the deepest part is still lateral. If the distal bevelling of the palmar edge is ignored, the surface slopes proximally from its dorsal edge until it reaches the apex of the palmar bevelling.

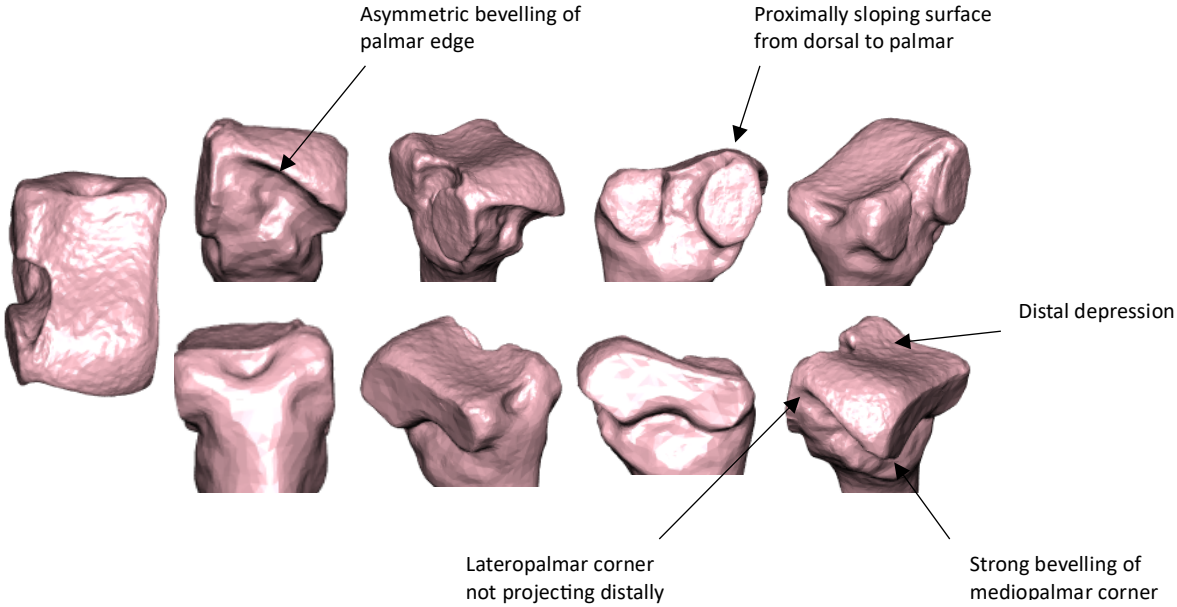

Figure 8.1.4: The average shape of the proximal articular surface of the fourth metacarpal of *Pongo*, produced by warping the mesh of the specimen closest to the group's mean shape to the average shape of the group. The articular surface is shown from eight different viewpoints, from left to right: proximal; palmar; lateropalmar; lateral; laterodorsal; dorsal; mediodorsal; medial; mediopalmar views.

Table 8.1: Comparison of the mean proximal metacarpal 4 shape of each extant taxa							
MC4	Proximal	Lateropalmar	Lateral	Laterodorsal	Mediodorsal	Medial	Mediopalmar
Homo sapiens	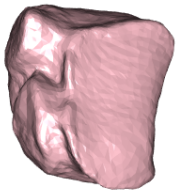	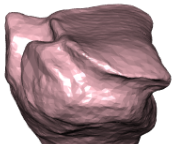	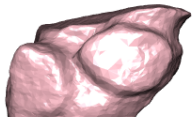	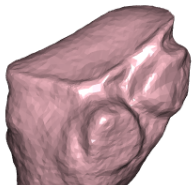	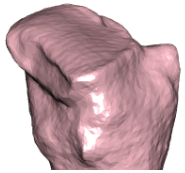	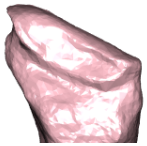	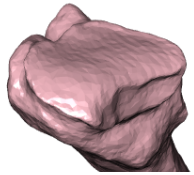
Gorilla	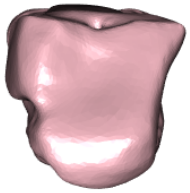	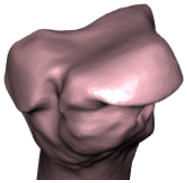		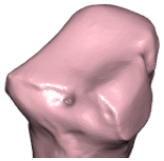	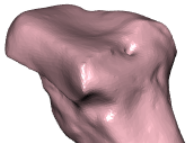		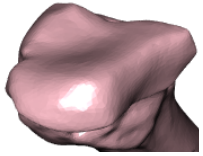
Pan troglodytes				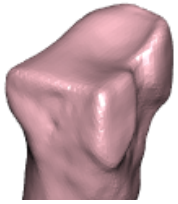			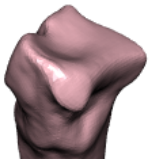
Pongo		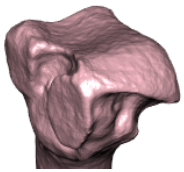		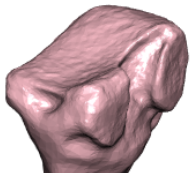	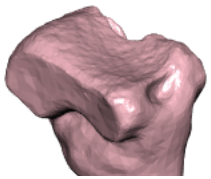		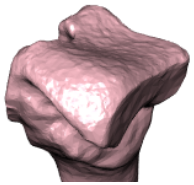

8.2 Metacarpal-4 Principal Components Analysis

The first three principal components were considered meaningful according to Bookstein's (2014) criterion and accounted for 54.7% of the total cumulative variance. PC1 accounted for 22.6% of total variance, with PC2 accounting for 19.2%, and PC3 13.0% (figure 8.2.1). Furthermore, principal components four and five accounted for 9.1% and 6.2% of the total variance, respectively. The first 12 principal components accounted for more than 90% of the total variance, with the 12th PC accounting for 1.5% of the total variance.

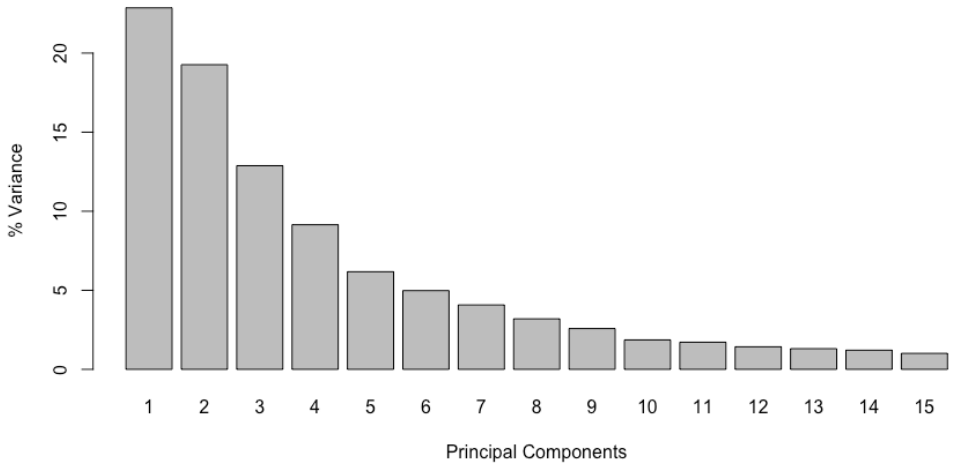

Figure 8.2.1: Graph showing the percentage of variance of the first 15 principal component is accountable for in the principal component analysis of the fourth metacarpal's proximal articular surface.

Taxonomic differences between groups

A Hotelling's T^2 test did not reveal a significant difference between the means of *Gorilla gorilla* and *Gorilla beringei* along first five principal components (T^2 = 0.23805, df = 6, 30; p = 0.9604), nor between the two species of *Pongo* (*Pongo abelii* and *Pongo pygmaeus*) (T^2 = 1.3937, df = 6, 13; p = 0.2884). Species of both genera were therefore pooled into their respective genus. The result of the one-way multiple MANOVA between the sub-species of *Pan troglodytes* on the first five principal component scores did not reveal significant differences in principal component scores based on sup-species [F (3, 23) = 1.1517, p = 0.3372, Wilks = 0.45806]. The *Pan troglodytes*

sample was therefore not divided by its component sub-species during analysis of the fourth metacarpal's proximal articular surface.

Analysis of Variance (ANOVA)

Results of the analysis of variance of each group along scores of the first five principal components are shown in table 8.2.1. Significant differences ($p \leq 0.05$) between taxa were recorded along the first three principal components ($p < 0.001$), with no statistically significant variance in the PC scores of different taxa along the fourth ($p = 0.316$) and fifth ($p = 0.123$) principal components. As such, the fourth and fifth principal components were not analysed further. The mean and standard deviation of the scores of the first three principal components for each extant taxon sample is shown in table 8.2.2, with the principal component values of each fossil for the first three principal components also shown. Subscripts next to the principal component scores of fossil specimens indicate extant taxa groups for which that particular fossil specimen deviates at least one standard deviation from.

Table 8.2.1: Results of analysis of variance on principal component scores one through six on extant groups.

Principal Component	DF	Sum of Squares	Mean Squares	*F* Value	*p*
PC 1	3	0.5962	0.19874	134.1	**<0.001**
PC 2	3	0.4018	0.13394	64.11	**<0.001**
PC 3	3	0.1399	0.04664	22.41	**<0.001**
PC 4	3	0.01655	0.005517	2.624	0.053
PC 5	3	0.00839	0.002797	1.958	0.123

Table 8.2.2: Mean and standard deviation (in parentheses) of principal component (PC) scores for *Homo sapiens, Gorilla, Pan troglodytes,* and *Pongo* compared with PC scores of fossil specimens AL333-14 (*Australopithecus afarensis*), SKW-2954 (*Paranthropus robustus*/early *Homo*), StW330 (Australopithecus africanus), StW65 (*Australopithecus africanus*), UW-101-1318 (*Homo naledi*), UW-102-028 (*Homo naledi*), and UW88-117 (*Australopithecus sediba*).

Group	*H. sapiens* (*n* = 54)	*Gorilla* (*n* = 36)	*P. troglodytes* (*n* = 40)	*Pongo* (*n* =20)	AL333-14	SKW2954	STW-330	STW-65	UW-101-1318	UW-102-028	UW-88-117
PC 1	0.083 (0.037)	-0.032 (0.048)	-0.053 (0.037)	-0.062 (0.046)	$0.018_{Hs,G,Pt,Po}$	$0.029_{Hs,G,Pt,Po}$	$0.078_{G,Pt,Po}$	$0.038_{Hs,G,Pt,Po}$	$0.152_{Hs,G,Pt,Po}$	$0.021_{Hs,G,Pt,Po}$	$0.005_{Hs,Pt,Po}$
PC 2	0.002 (0.041)	0.065 (0.049)	-0.074 (0.051)	0.022 (0.047)	$-0.031_{G,Pt}$	$-0.066_{Hs,G,Po}$	$-0.028_{G,Po}$	$-0.022_{G,Pt}$	$0.000_{G,Pt}$	$-0.068_{Hs,G,Po}$	$-0.041_{Hs,G,Po}$
PC 3	-0.013 (0.046)	0.038 (0.040)	-0.004 (0.053)	-0.060 (0.041)	$0.137_{Hs,G,Pt,Po}$	$0.073_{Hs,Pt,Po}$	$0.076_{Hs,Pt,Po}$	$0.073_{Hs,Pt,Po}$	0.020_{Po}	$0.078_{Hs,Pt,Po}$	0.036_{Po}

[a] Subscripts indicate a group that the fossil specimen differs at least 1 standard deviation from. Hs = *Homo sapiens*; G = *Gorilla*; Pt = *Pan troglodytes*; P = *Pongo.*

Principal Component 1 shape and groupings

The main shape differences along the first principal component, which accounted for 22.6% of the variance, relate to the relative flatness of the surface, and the width of the palmar edge relative to the dorsal. The first principal component separates the *Homo sapiens* sample from the non-human taxa.

The maximal shape of PC1 is extremely flat and featureless, with the dorsal border approximately planar with the palmar border, with the exception of a very slight distalward curvature of the palmar border (figure 8.2.2). The mediodorsal corner is expanded medially and dorsally, resulting in medial and dorsal edges that are longer than their lateral and palmar counterparts, and a surface that appears to constrict palmarly. There is an extremely subtle proximal divot on the laterodorsal surface, but otherwise the surface is extremely flat and featureless. Conversely, the most negative shape along the first principal component exhibits a very strong palmar bevelled shape moving from dorsal to palmar, with the palmar portion angled 90° distally relative to the rest of the surface, especially at the mediopalmar corner. There is an extremely prominent distal depression of the laterodorsal surface which corresponds to the distal ballooning of the corresponding surface on the hamate, and results in the lateral border appearing waisted when viewed from a proximal viewpoint.

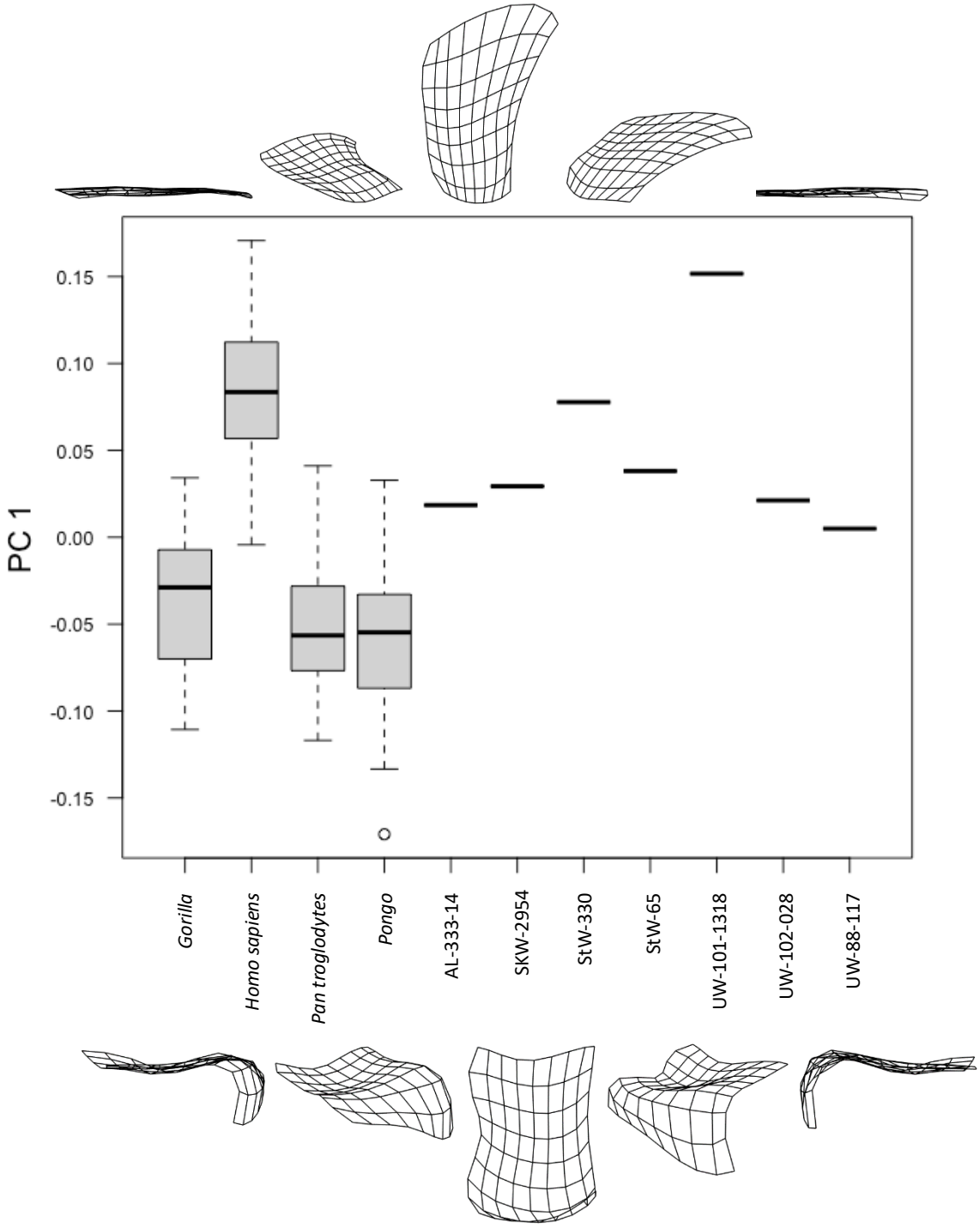

Figure 8.2.2: Boxplot of the first principal component score of the fourth metacarpal's proximal articular surface for *Gorilla, Homo sapiens, Pan troglodytes,* and *Pongo* compared with fossil specimens AL333-14 (*Australopithecus afarensis*), SKW 2954 (*Paranthropus* robustus/early *Homo*), StW 330, StW 65 (*Australopithecus africanus*), UW-101-1318, UW-102-028 (*Homo naledi*) and UW88-117 (*Australopithecus sediba*). Black lines represent the median of the group, boxes are interquartile ranges, and whiskers are the non-outlier ranges.

Table 8.2.3: Tukey honestly significant difference (HSD) *post-hoc* test results on PC 1 scores among *Homo, Pan, Gorilla, and Pongo.* Significant results ($p < 0.05$) were highlighted in bold.

Group		Mean difference	*p*	95% confidence interval	
				Lower bound	Upper bound
Homo	*Gorilla*	0.114	**< 0.001**	0.093	0.135
	Pan	0.142	**< 0.001**	0.121	0.163
	Pongo	0.145	**< 0.001**	0.119	0.171
Gorilla	*Homo*	-0.114	**< 0.001**	-0.135	-0.093
	Pan	0.028	**0.009**	0.005	0.051
	Pongo	0.031	**0.020**	0.003	0.058
Pan	*Homo*	-0.142	**< 0.001**	-0.163	-0.121
	Gorilla	-0.028	**0.009**	-0.051	-0.005
	Pongo	0.003	0.994	-0.025	0.030
Pongo	*Homo*	-0.145	**< 0.001**	-0.171	-0.119
	Gorilla	-0.031	**0.020**	-0.058	-0.003
	Pan	-0.003	0.994	-0.030	0.025

Along the first principal component results of the Tukey Honestly Significantly Different *post-hoc* test show that each taxon is significantly distinct from any other, with the exception of *Pan troglodytes* and *Pongo*, which do not exhibit a significant difference between their means ($p = 0.994$) (table 8.2.3). A box and whisker plot of the scores of the first principal component is shown in figure 8.2.2, and separates the *Homo sapiens* group in the positive range of PC1 from the non-human extant great ape groups, which are all predominantly in the negative range. While the interquartile range of all the non-human samples are negatively scored, their fourth quartiles encroach into the positive half, resulting in the 1st quartile of the *Homo sapiens* sample overlapping with the 4th quartile of all other groups. There is considerable overlap between the samples of all three non-human great ape taxa.

All but one of the fossil specimens are positively scored and within the range of *Homo sapiens*, though it is only StW-330 (*Australopithecus africanus*) which is within the modern human interquartile range. UW-88-117 (*Australopithecus sediba*) is marginally outside the *Homo sapiens* range, and within the ranges of the great apes, while UW-101-1318 (*Homo naledi*) has the most positive score of all fossil specimens and is the only specimen in the 4th quartile of *Homo sapiens.* All other fossil specimens are within the ranges of all groups, at the intersection of the *Homo sapiens* 4th quartile and the 1st quartiles of the non-human groups, except for StW-65 (*Australopithecus africanus*), which is outside the range of *Gorilla* and *Pongo,* but within that of *Pan troglodytes.*

Principal Component 2 shape and groupings

The main shape difference along the second principal component is related to the relative convexity or concavity of the fourth metacarpal's proximal articular surface. The second principal component accounts for 19.2% of the variance, and most effectively separates the *Pan troglodytes* and *Gorilla* samples.

The minima of PC2 describes a shape that exhibits a strong concavity, which is accommodated by the middle third of the surface (in the palmo-lateral plane) projecting distally, while the dorsal and palmar borders (with the exception of the mediopalmar corner) are projected proximally (figure 8.2.3). This results in a PC2 minimum shape that has a particularly pronounced divot along its lateral border, and a palmar border that is strongly sloping distally from its lateral corner to the medial corner, similar to the average shape of the *Pan troglodytes* sample (figure 8.1.3).

The shape of the second principal component's maxima is convex in relation the PC 2 minima. The dorsal border of PC2's maxima is more distally positioned, while its entire palmar border is in a similar plane to the minimum shape's mediopalmar border. However, the middle portion of the surface projects proximally, especially the medial portion, resulting in a convex surface that resembles a characteristic bevelled surface.

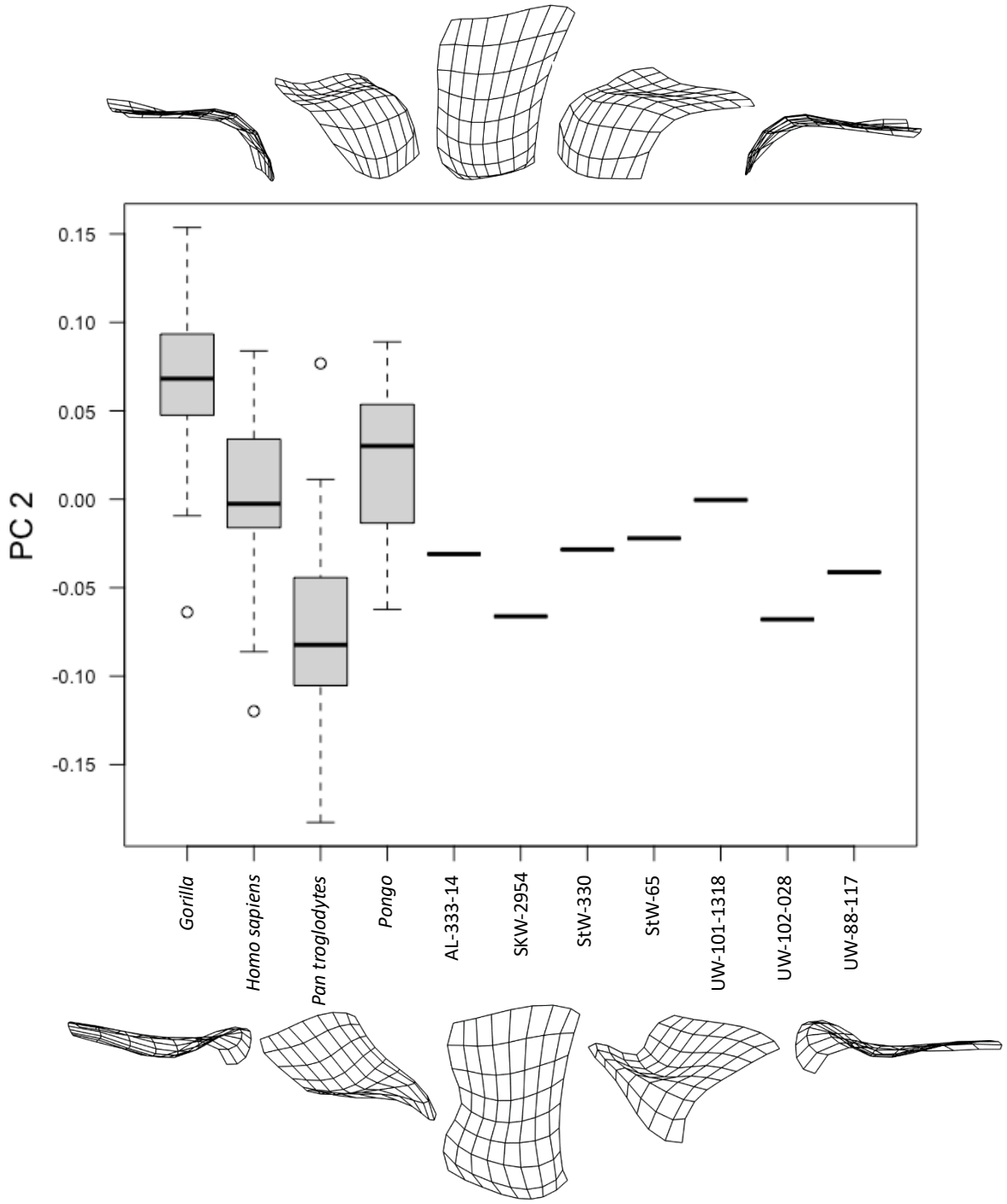

Figure 8.2.3: Boxplot of the second principal component score of the fourth metacarpal's proximal articular surface for *Gorilla, Homo sapiens, Pan troglodytes,* and *Pongo* compared with fossil specimens AL333-14 (*Australopithecus afarensis*), SKW 2954 (*Paranthropus robustus/*early *Homo*), StW 330, StW 65 (*Australopithecus africanus*), UW-101-1318, UW-102-028 (*Homo naledi*) and UW88-117 (*Australopithecus sediba*).Black lines represent the median of the group, boxes are interquartile ranges, and whiskers are the non-outlier ranges.

Table 8.2.4: Tukey honestly significant difference (HSD) *post-hoc* test results on PC 2 scores among *Homo, Pan, Gorilla, and Pongo.* Significant results ($p < 0.05$) were highlighted in bold.

Group		Mean difference	*p*	95% confidence interval	
				Lower bound	Upper bound
Homo	*Gorilla*	-0.081	**< 0.001**	-0.104	-0.057
	Pan	0.073	**< 0.001**	0.049	0.096
	Pongo	-0.027	0.073	-0.056	0.002
Gorilla	*Homo*	0.081	**< 0.001**	0.057	0.104
	Pan	0.153	**< 0.001**	0.128	0.179
	Pongo	0.054	**< 0.001**	0.024	0.084
Pan	*Homo*	-0.073	**< 0.001**	-0.096	-0.049
	Gorilla	-0.153	**< 0.001**	-0.179	-0.128
	Pongo	-0.100	**< 0.001**	-0.130	-0.069
Pongo	*Homo*	0.027	0.073	-0.002	0.056
	Gorilla	-0.054	**< 0.001**	-0.084	-0.024
	Pan	0.100	**< 0.001**	0.069	0.130

Along the second principal component the extant taxa are all significantly different from each other ($p < 0.05$), with the exception of *Homo sapiens* and *Pongo,* whose means do not significantly differ ($p = 0.232$) (table 8.2.4). The second principal component is most informative in separating *Pan troglodytes* in the negative aspect from *Gorilla* in the positive (figure 8.2.3). Neither *Homo sapiens* nor *Pongo* are readily separated from *Pan troglodytes* or *Gorilla* along the second principal component. All fossil specimens appear to be outside the range of *Gorilla,* but within the ranges of the other three extant groups. SKW-2954 (*Paranthropus robustus*/early *Homo*) and UW-102-028 (*Homo naledi*) are closer to the median of *Pan troglodytes* than the other specimens, and both are within the upper interquartile range of *Pan troglodytes*, while all the other fossil specimens are closer to the median of *Homo sapiens*.

Principal Component 3 shape and groupings

Shape variation along the third principal component is described by variation in the relative mediolateral width of the fourth metacarpal's proximal articular surface, especially along its dorsal portion. The third principal component, which informs shape difference between *Gorilla* and *Pongo*, accounts for 13.0% of the total shape variation of the sample.

The minima of PC3 describes a shape that is medio-laterally narrow and proximo-distally elongated and displays a slight contraction of the mid-portion of its lateral border, resulting in a slight 'hourglass' morphology. The maximum shape of PC 3 is represented by a much wider surface in the mediolateral direction (figure 8.2.4). Both the minimum and maximum shapes are complex and irregular, with prominent palmar bevelling and a lateral divot, though these features are more prominent on the minimum shape.

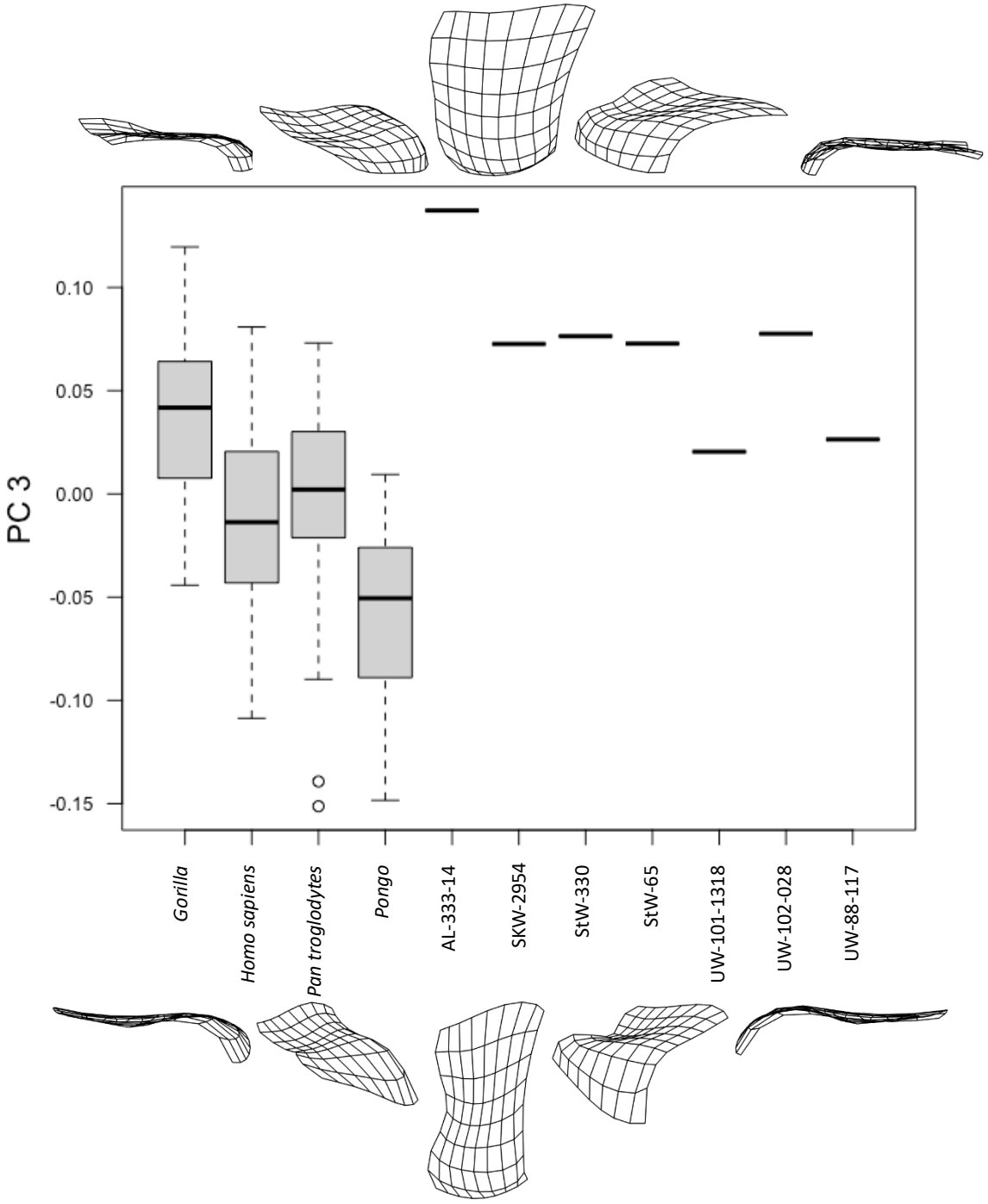

Figure 8.2.4: Boxplot of the third principal component score of the fourth metacarpal's proximal articular surface for *Gorilla, Homo sapiens, Pan troglodytes,* and *Pongo* compared with fossil specimens AL333-14 (*Australopithecus afarensis*), SKW 2954 (*Paranthropus* robustus/early *Homo*), StW 330, StW 65 (*Australopithecus africanus*), UW-101-1318, UW-102-028 (*Homo naledi*) and UW88-117 (*Australopithecus sediba*).Black lines represent the median of the group, boxes are interquartile ranges, and whiskers are the non-outlier ranges.

Table 8.2.5: Tukey honestly significant difference (HSD) *post-hoc* test results on PC 3 scores among *Homo, Pan, Gorilla, and Pongo.* Significant results ($p < 0.05$) were highlighted in bold.

Group		Mean difference	*p*	95% confidence interval	
				Lower bound	Upper bound
Homo	*Gorilla*	-0.048	**< 0.001**	-0.073	-0.023
	Pan	-0.019	0.232	-0.044	0.007
	Pongo	0.051	**< 0.001**	0.020	0.082
Gorilla	*Homo*	0.048	**< 0.001**	0.023	0.073
	Pan	0.029	**0.031**	0.002	0.057
	Pongo	0.098	**< 0.001**	0.066	0.131
Pan	*Homo*	0.019	0.232	-0.007	0.044
	Gorilla	-0.029	**0.031**	-0.057	-0.002
	Pongo	0.069	**< 0.001**	0.036	0.102
Pongo	*Homo*	-0.051	**< 0.001**	-0.082	-0.020
	Gorilla	-0.098	**< 0.001**	-0.131	-0.066
	Pan	-0.069	**< 0.001**	-0.102	-0.036

Along the third principal component, with the exception of *Homo sapiens* and *Pan troglodytes* ($p = 0.232$), the means of each extant taxa are significantly different from each other ($p < 0.05$; table 8.2.5). The main group difference in the third principal component scores is explained by *Pongo* occupying the negative range, and the other non-human groups predominantly occupying the positive portion of the principal component. While there exists a statistically significant difference between *Pan troglodytes* and *Gorilla* along the third principal component, this significance is weak ($p = 0.031$) when compared to the relationship of *Pongo* to other groups ($p < 0.001$), and that of *Homo* and *Gorilla* ($p < 0.001$). Apart from UW-88-117 (*Australopithecus sediba*), which has a PC3 score similar to the mean of Pongo, all fossil specimens lie in the positive portion. AL-333-14 (*Australopithecus afarensis*) is outside the range of all extant groups, while SKW-2954 (*Paranthropus robustus*/early *Homo*), StW-330, StW-65, (*Australopithecus africanus*) and UW-102-028 (*Homo naledi*) are all within the upper ranges of *Gorilla, Homo sapiens,* and *Pan troglodytes.* UW-101-1318 (*Homo naledi*) lies nearer the neutral value of the principal component, and very near to the median value of *Pan troglodytes* and *Homo sapiens* (figure 8.2.4).

Bivariate Scatterplots

PC 1 v PC 2

A bivariate scatterplot of PC1 against PC2 (figure 8.2.5) successfully separates *Homo sapiens* from all great ape groups, though there is slight overlap of the morphospace of modern humans with those of other extant taxa. The *Homo sapiens* sample is almost entirely in the right half of the plot, distributed evenly between the upper and lower halves. The non-human great ape groups, which substantially overlap each other, are predominantly in the left half of the plot. *Gorilla* dominates the upper-left quadrant, *Pan troglodytes* the lower-left, with *Pongo* distributed between both left quadrants more or less evenly, though trending slightly towards the upper left quadrant. But for a solitary extremal datapoint in the lower right quadrant, *Pongo* is almost entirely within the left half of the morphospace and would otherwise not encroach on the morphospace of *Homo sapiens*. The morphology of the *Pongo* (*abelii*) specimen represented by this extremal point is notably flat palmodorsally relative to other *Pongo* specimens and does not exhibit bevelling of the palmar border to the same extent as other specimens within its taxa, explaining its intrusion into the *Homo sapiens* morphospace.

Every fossil specimen is located in the lower-right quadrant of the PC 1 v PC 2 scatterplot, with four situated exclusively within the *Homo sapiens* morphospace. Both *Australopithecus africanus* specimens, one *Homo naledi* specimen (UW-101-1318) and the *Paranthropus robustus*/early *Homo* fossil (SKW-2954) are situated solely within the *Homo sapiens* morphospace, though SKW-2954 lies very near the extremal *Pongo abelii* specimen. AL-333-14 (*Australopithecus afarensis*) is found at the intersection of *Homo sapiens, Pan troglodytes,* and *Pongo*, while the remaining two fossil specimens, while situated very near its border, are outside the *Homo sapiens* morphospace. UW-102-028 (*Homo naledi*) is on the border of the *Homo sapiens, Pan troglodytes,* and *Pongo* morphospaces though exterior to them all, while UW-88-117 (*Australopithecus sediba*) is within the intersectional area of *Pan troglodytes* and *Pongo.* Considering that the two *Homo naledi* specimens analysed each lie at opposing extremal points of the *Homo sapiens* morphospace, this would suggest that this species had a range of variation in the shape of the fourth metacarpal's proximal articular surface similar to that of modern humans.

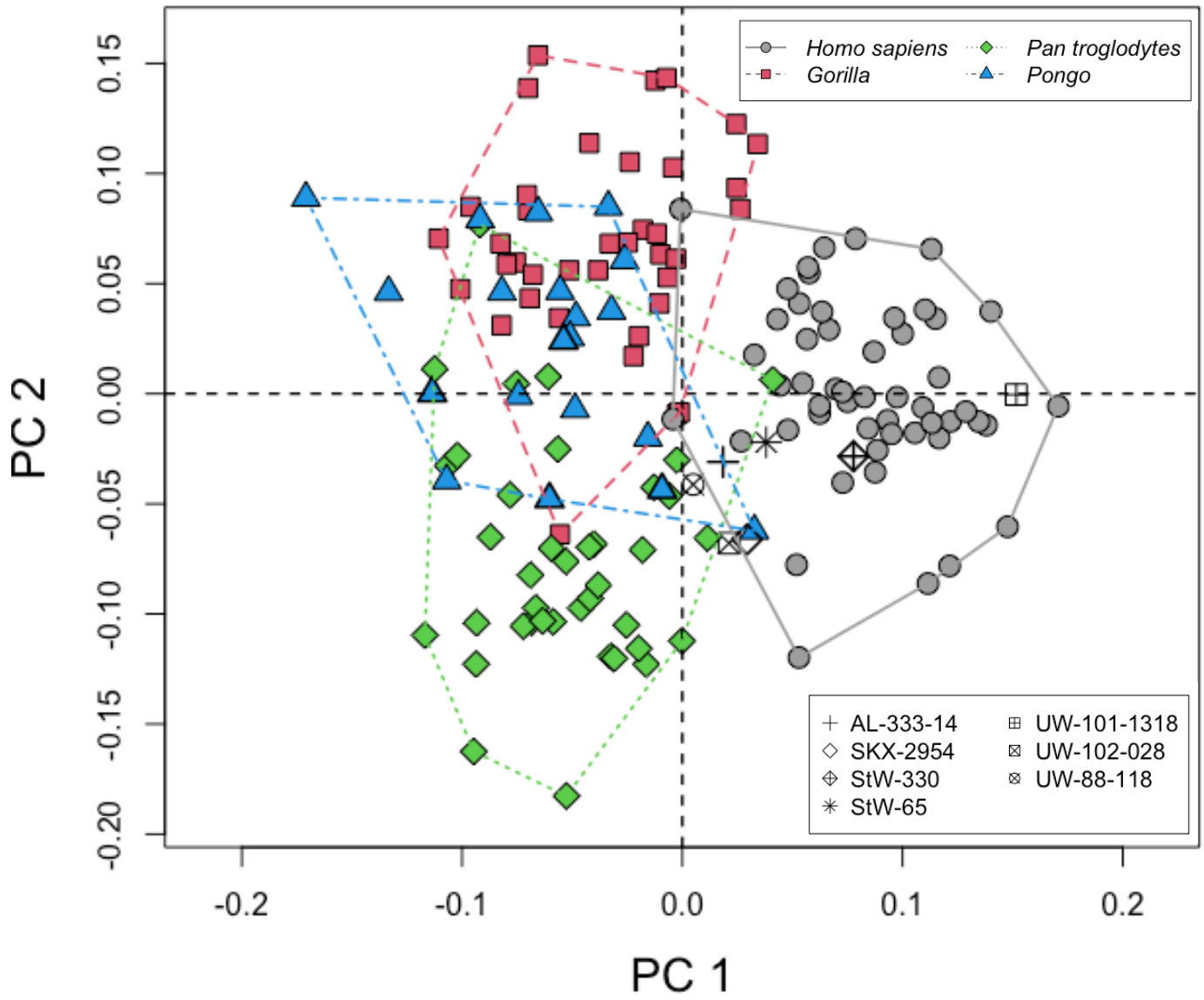

Figure 8.2.5: Scatterplot of the first vs. second principal component scores of extant samples (*Homo sapiens, Gorilla, Pan troglodytes* and *Pongo*) and fossil specimens for the fourth metacarpal's proximal articular surface. The *Homo sapiens* sample is concentrated to the right of the plot.

PC 1 v PC 3

A bivariate scatterplot of PC1 against PC3 is also successful in separating *Homo sapiens* from all great ape groups, with only a slight overlap of the *Homo sapiens* morphospace with each great ape group (figure 8.2.6). As with the PC1 v PC2 bivariate scatterplot, the *Homo sapiens* morphospace is occupied almost exclusively in the right half of the morphospace (equally between the upper and lower quadrants), with the exception of a single datapoint. The left half of the plot is again occupied by the great ape groups, with substantial overlap between the non-human groups. The *Gorilla* sample is again predominantly in the upper left quadrant. The *Pongo* sample is almost entirely within the lower left quadrant, except for a point at the border of the left upper and lower quadrants, resulting in an area of overlap between the *Gorilla* and *Pongo* morphospaces, and an extremal point that encroaches into the *Homo sapiens* morphospace. This is the same specimen as in the previous scatterplot, and other than this point, the morphospaces of *Homo sapiens* and *Pongo* do not overlap with one another. The morphospace of *Pan troglodytes* spans both the upper and lower left quadrants and overlaps much of the *Gorilla* and *Pongo* morphospaces.

In the PC1 v PC3 scatterplot, only three fossil specimens lie within the *Homo sapiens* morphospace, these being UW-101-1318 (*Homo naledi*), UW-88-117 (*Australopithecus sediba*), and STW-330 (*Australopithecus africanus*). UW-88-117 (*Australopithecus sediba*) is also found in the *Gorilla* morphospace. The remaining four fossil specimens, while being in the upper-right quadrant, are outside the morphospaces of any extant group, though are between those of *Homo sapiens* and *Gorilla*, with UW-102-028 (*Homo naledi*) residing on the edge of the *Gorilla* morphospace. AL-333-14 (*Australopithecus afarensis*), having the highest PC 2 score of all extant and fossil specimens, is the fossil specimen farthest from the extant sample.

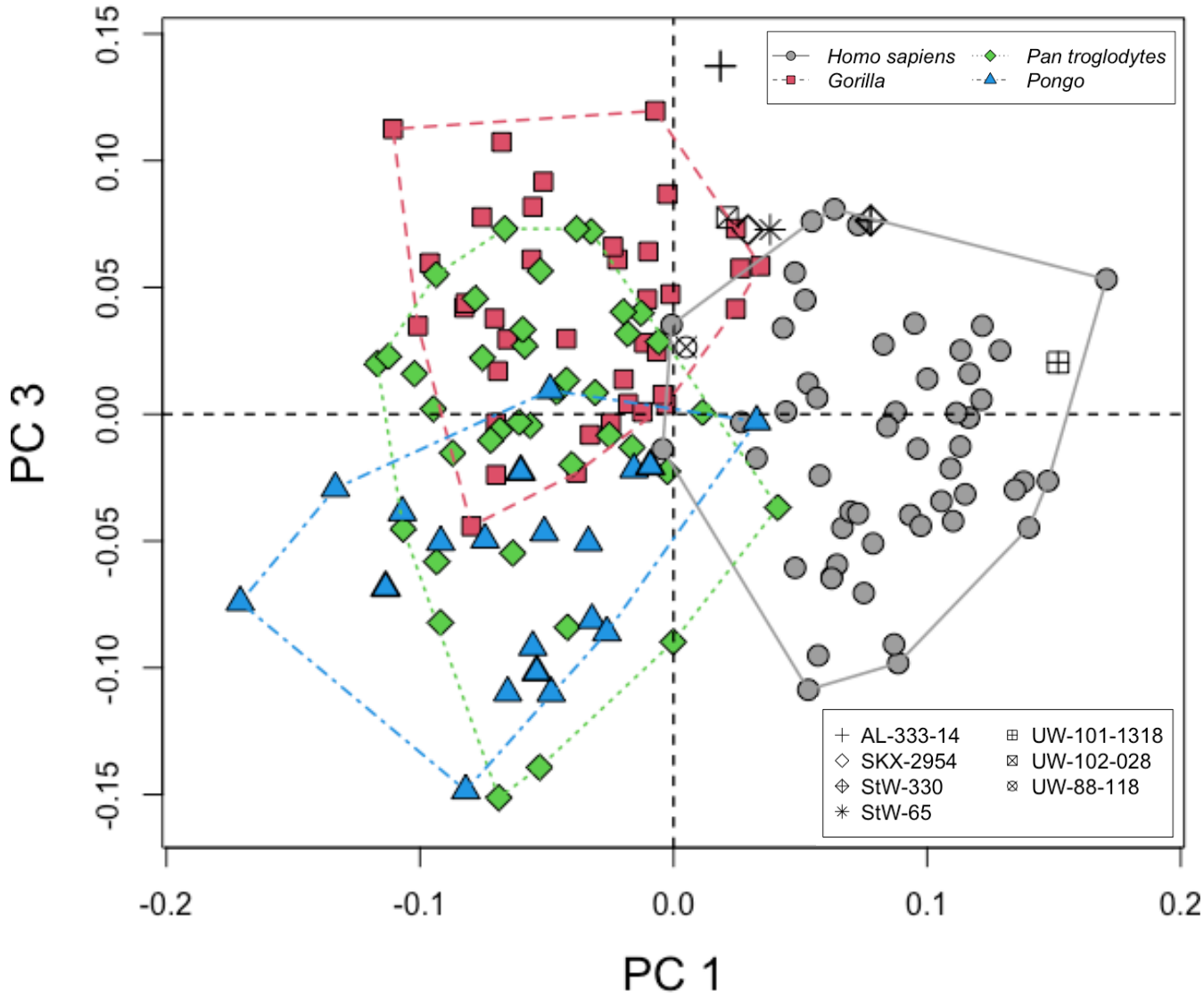

Figure 8.2.6: Scatterplot of the first vs. third principal component scores of extant samples (*Homo sapiens, Gorilla, Pan troglodytes* and *Pongo*) and fossil specimens for the fourth metacarpal's proximal articular surface.

PC 2 v PC 3

There is a high degree of overlap between the groups in the bivariate scatterplot of PC2 against PC3 (figure 8.2.7). This scatterplot is only particularly useful in distinguishing between the non-human African great apes, with *Gorilla* situated predominantly in the upper-right quadrant, and *Pan troglodytes* located predominantly in the left half, with only a very small overlap between the two groups. The morphospace of *Pongo* is almost entirely in the lower half of the scatterplot, and overlaps substantially with *Homo sapiens* and *Pan troglodytes*, and minimally with *Gorilla*. *Homo* straddles all four quadrants equally, with the centre of its morphospace approximating the centre point of the scatterplot.

The PC2 v PC3 bivariate scatterplot is of far less utilization in interpreting fossil specimens compared to the previous two scatterplots. As with the previous plot, AL-333-14 (*Australopithecus afarensis*) is the only fossil specimen that is not near any extant group's morphospace, being the specimen with the positive-most PC 3 score. SKW-2954 (*Paranthropus robustus*/early *Homo*) and UW-102-028 (*Homo naledi*) are between the *Gorilla* and *Pan troglodytes* morphospaces. No fossil specimen is solely within a single extant taxon's morphospace. UW-101-1318 (*Homo naledi*) is at the intersection of the *Homo sapiens*, *Gorilla*, and *Pan troglodytes* morphospaces, while UW-88-117 (*Australopithecus sediba*) is within the intersection of *Homo sapiens* and *Pan troglodytes.* The two *Australopithecus africanus* specimens (StW-330 and StW-65) are in the intersection of *Homo sapiens* and *Gorilla.*

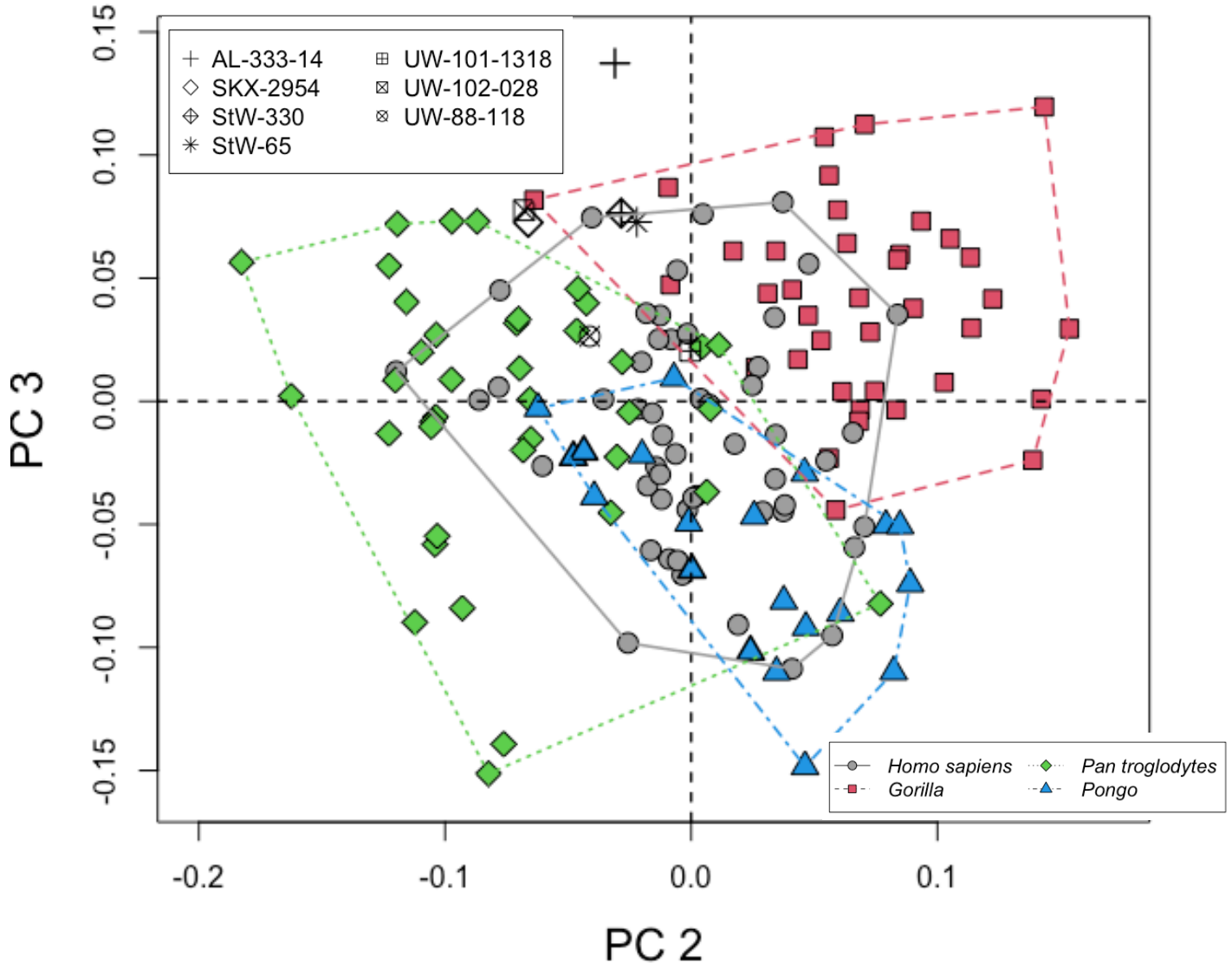

Figure 8.2.7: Scatterplot of the second vs. third principal component scores of extant samples (*Homo sapiens, Gorilla, Pan troglodytes* and *Pongo*) and fossil specimens for the fourth metacarpal's proximal articular surface. There is high overlap in the morphospaces of extant groups.

8.3 Metacarpal 4 canonical variate analysis

The first 12 principal components, which accounted for 90.1% of the total variance, were used to conduct a canonical variate analysis on the fourth metacarpal's proximal articular surface. The canonical variate analysis was successful in categorizing extant specimens into their *a priori* taxonomical group in 98% of cases (k = 0.97), with the only erroneous categorizations being two *Homo sapiens* specimens assigned to *Pongo*, and a *Pan troglodytes* specimen assigned to the *Homo sapiens* sample (table 8.3.1). The first canonical variate axis accounted for 56.8% of the shape difference between groups, while the second and third CV axes accounted for 27.0% and 16.2% respectively.

Table 8.3.1: Table of predicted taxa against actual taxa. *A priori* classification is along the horizontal, with group classification through linear discriminant analysis is along the vertical.

	Gorilla	*Homo sapiens*	*Pan troglodytes*	*Pongo*	*N*
Gorilla	38 (100%)	0	0	0	39
Homo sapiens	0	50 (96.2%)	0	2	51
Pan troglodytes	0	1	38 (97.4%)	0	41
Pongo	0	0	0	20 (100%)	17

MANOVA along the three canonical variates axes returned significant results between extant groups ($F(3, 145) = 216.54$, $p < 0.001$, Wilks' $\Lambda = 0.0101$). One-way analysis of variance tests performed on the CV scores of the extant sample, with the sample divided by *a priori* taxonomy, were significant for all three CV axes (table 8.3.2). Along the first two canonical variate axes, all pairwise comparisons showed significant variation between the means of all extant taxonomic groups. However, along the third axis, statistically significant differences were only observed in pairwise comparisons concerning *Pongo*, with non-significant results returned between the means of *Homo sapiens*, *Gorilla*, and *Pongo* (table 8.3.3).

Table 8.3.2: Results of analysis of variance on canonical variate scores on extant groups.

Canonical Variate	DF	Sum of Squares	Mean Squares	*F* Value	*p*
CV 1	3, 145	993.4	331.1	331.1	**<0.001**
CV 2	3, 145	472	157.3	157.3	**<0.001**
CV 3	3, 145	283.2	94.41	94.41	**<0.001**

Table 8.3.3: *P*-values for Tukey's HSD pairwise comparisons of canonical variate scores.

	Homo sapiens	Gorilla	Pan troglodytes	Pongo
Canonical Variate 1 (56.8%)				
Homo sapiens	-	**<0.001**	**<0.001**	**<0.001**
Gorilla		-	**<0.001**	**<0.001**
Pan troglodytes			-	**<0.001**
Pongo				-
Canonical Variate 2 (27.0%)				
Homo sapiens	-	**<0.001**	**<0.001**	**0.003**
Gorilla		-	**<0.001**	**<0.001**
Pan troglodytes			-	**<0.001**
Pongo				-
Canonical Variate 3 (16.2%)				
Homo sapiens	-	0.199	0.983	**<0.001**
Gorilla		-	0.431	**<0.001**
Pan troglodytes			-	**<0.001**
Pongo				-

A posteriori categorization of fossil specimens into extant groups by the the canonical variate analysis on the first 12 principal components is shown in table 8.3.4. Five of the seven fossil specimens were classified as *Homo sapiens*, with StW-330 (*Australopithecus africanus*), UW-101-1318, UW-102-028 (*Homo naledi*), and UW-88-117 (*Australopithecus sediba*) each being classified with a confidence of 100%, and SKW-2954 (*Paranthropus robustus*/early *Homo*) categorized into the *Homo sapiens* sample with a confidence of 93.7%. The remaining two fossil specimens, AL-333-56 (*Australopithecus afarensis*) and StW-65 (*Australopithecus africanus*) were classified as *Gorilla* with confidence levels of 99.3% and 83.3%, respectively.

Table 8.3.4: Canonical variate analysis (CVA) classification results of fossil specimens. Results were in percentage.

	Homo sapiens	*Gorilla*	*Pan troglodytes*	*Pongo*	Classification
AL-333-56	0.0	99.9	0.1	0.0	*Gorilla*
SKW-2954	93.7	5.2	0.6	0.5	*Homo sapiens*
Stw-330	100.0	0.0	0.0	0.0	*Homo sapiens*
StW-65	3.6	83.3	13.1	0.0	*Gorilla*
WU-101-1318	100.0	0.0	0.0	0.0	*Homo sapiens*
UW-102-028	100.0	0.1	0.0	0.0	*Homo sapiens*
UW-88-117	100.0	0.0	0.0	0.0	*Homo sapiens*

First Canonical Variate Axis

Shape change along the first canonical variate axis (figure 8.3.1) corresponded to shape change along the first principal component, which is described in section 8.2, with graphical representation in figure 8.2.2. The first canonical variate axis contributed to 56.8% of the shape difference between groups and separates *Homo sapiens* from the non-human groups. The modern human sample is exclusively in the positive aspect of CV 1 and does not overlap with the samples of any non-human groups, which are predominantly in the negative. The 4th quartile of both *Gorilla* and *Pongo* is found in the positive half of the axis, while the range of *Pan troglodytes* is entirely in the negative. There is a degree of overlap between all three non-human groups, especially between *Gorilla* and *Pongo,* however only the 4th quartile of *Pan troglodytes* and the 1st of *Pongo* overlap with each other.

The fossil specimens are distributed broadly across CV 1, though only AL-333-56 (*Australopithecus afarensis*) and StW-65 (*Australopithecus africanus*) are in the negative half. AL-333-56, the negative-most fossil, is within the range of the African Great Apes, while StW-65 has a similar value to the *Pongo* median value. SKW-2954 (*Paranthropus robustus*/early *Homo*) is within the 4th quartile range of *Pongo*, while the remaining fossil specimens are above the ranges of the non-human groups. StW-330 (*Australopithecus africanus*) and UW-102-028 (*Homo naledi*) are intermediate between the ranges of *Homo sapiens* and *Pongo,* while UW-88-117 (*Australopithecus sediba*) is the positive-most datapoint. Only UW-1318 (*Homo naledi*) is found within the range of *Homo sapiens*, being near the median value of that group.

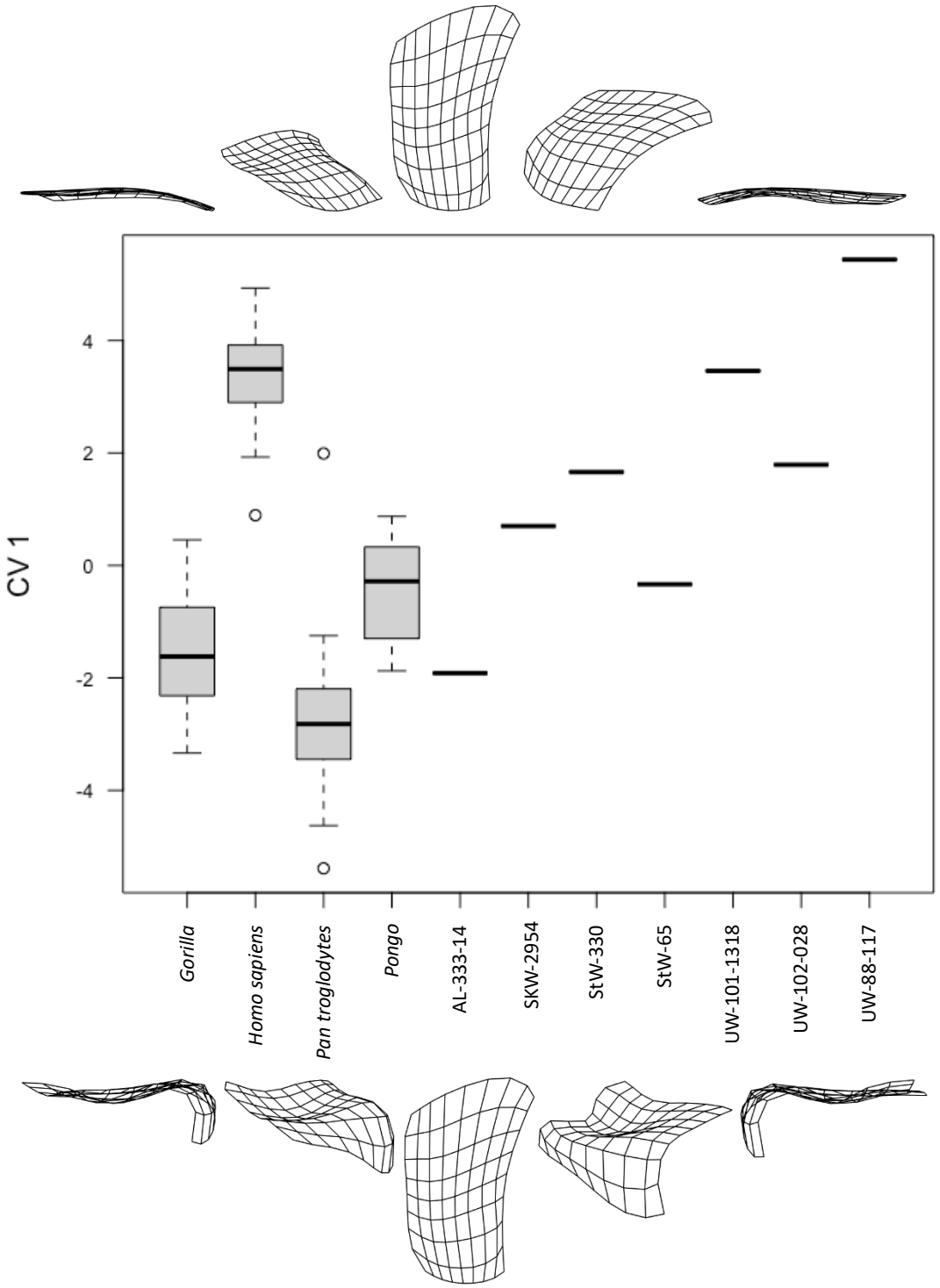

Figure 8.3.1: Boxplot of the scores of the first Canonical Variate axis of the fourth metacarpal's proximal articular surface for *Gorilla, Homo sapiens, Pan troglodytes,* and *Pongo* compared with fossil specimens AL333-14 (*Australopithecus afarensis*), SKW 2954 (*Paranthropus* robustus/early *Homo*), StW 330, StW 65 (*Australopithecus africanus*), UW-101-1318, UW-102-028 (*Homo naledi*) and UW88-117 (*Australopithecus sediba*).Black lines represent the median of the group, boxes are interquartile ranges, and whiskers are the non-outlier ranges.

Second Canonical Variate Axis

The second canonical vitiate axis accounts for 27.0% of the total variation and corresponds to shape change along the second principal component, described in section 8.2 and shown in figure 8.2.3. As with the first CV axis, along the second, *Homo sapiens* have exclusively positive values, *Pan troglodytes* are almost exclusively negative, and *Gorilla* and *Pongo* span both halves, with *Pongo* skewed more positively and *Gorilla* more negatively (figure 8.3.2). While *Homo sapiens* and *Pan troglodytes* do not interact, there is considerable overlap between all other group pairings.

The fossil hominin specimens are concentrated around the neutral value of the second canonical variate axis, with only two fossil specimens diverging notably from the zero value. AL-333-56 (*Australopithecus afarensis*) is the most positive of all fossil specimens and is the only one within the range of *Homo sapiens,* while also being within the *Pongo* and *Gorilla* ranges. UW-102-028 (*Homo naledi*) has the most negative value of fossil hominins and has a similar value to the median value of *Pan troglodytes,* while also being within the *Pongo* range. The remaining five specimens are all within the ranges of all non-human groups.

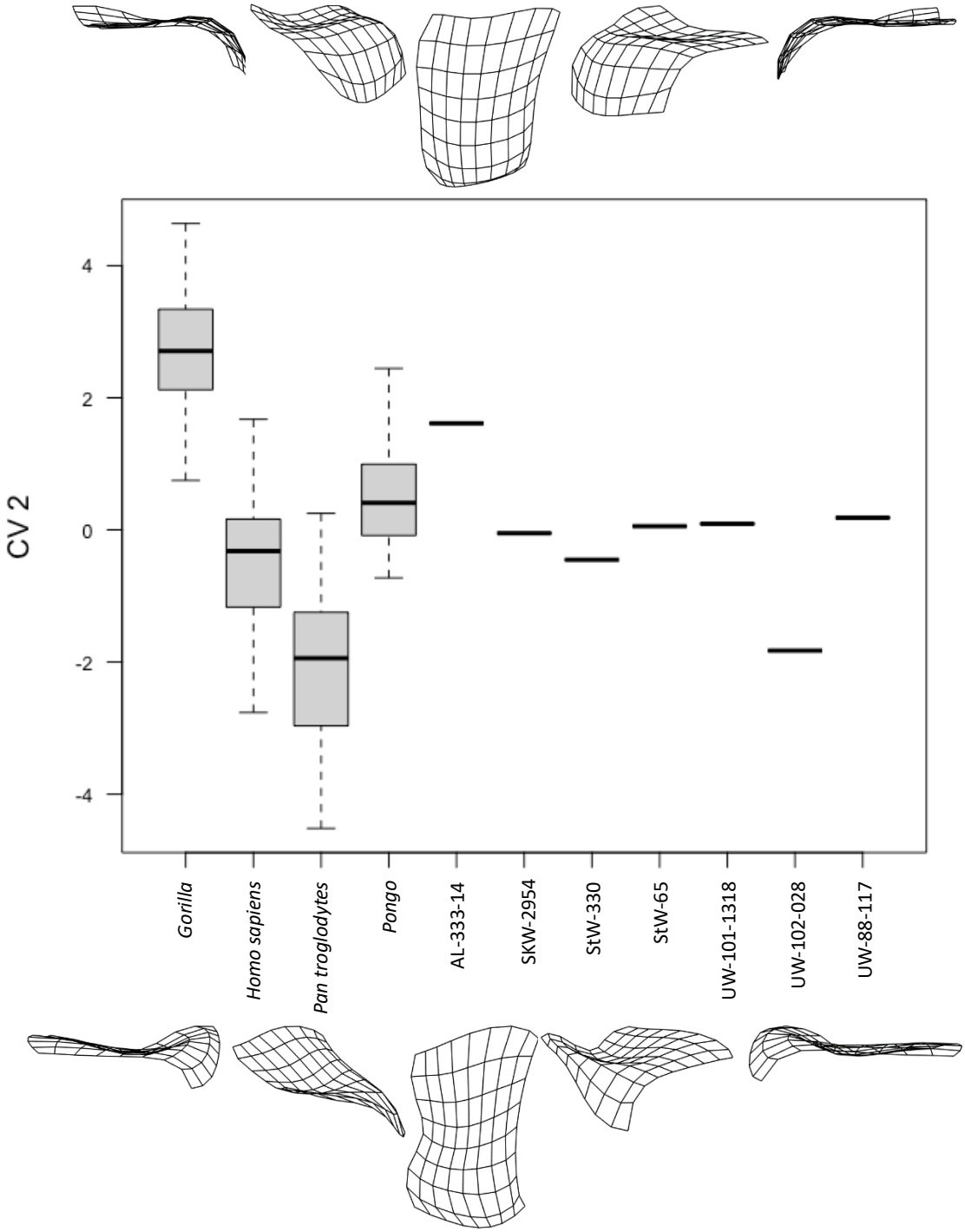

Figure 8.3.2: Boxplot of the scores of the second Canonical Variate axis of the fourth metacarpal's proximal articular surface for *Gorilla, Homo sapiens, Pan troglodytes,* and *Pongo* compared with fossil specimens AL333-14 (*Australopithecus afarensis*), SKW 2954 (*Paranthropus* robustus/early *Homo*), StW 330, StW 65 (*Australopithecus africanus*), UW-101-1318, UW-102-028 (*Homo naledi*) and UW88-117 (*Australopithecus sediba*).Black lines represent the median of the group, boxes are interquartile ranges, and whiskers are the non-outlier ranges.

Third Canonical Variate Axis

Shape change along the third canonical variate (figure 8.3.3) corresponds to the third principal component (shown in figure 8.2.4) and accounts for 16.2% of variation. The third canonical variate axis distinguishes the *Pongo* sample from other groups. The *Pongo* sample is strongly in the negative aspect, with the other three groups distributed across both positive and negative aspects, with no overlap between *Pongo* and all other groups. There is no distinction between the African non-human Great Ape groups and modern humans. Six of the seven fossil hominin specimens are in the positive half and fall within the ranges of the three African Great Ape groups. UW-88-117 (*Australopithecus sediba*) is the sole fossil specimen that has a negative CV 3 value and falls within the 4th quartile of *Pongo.*

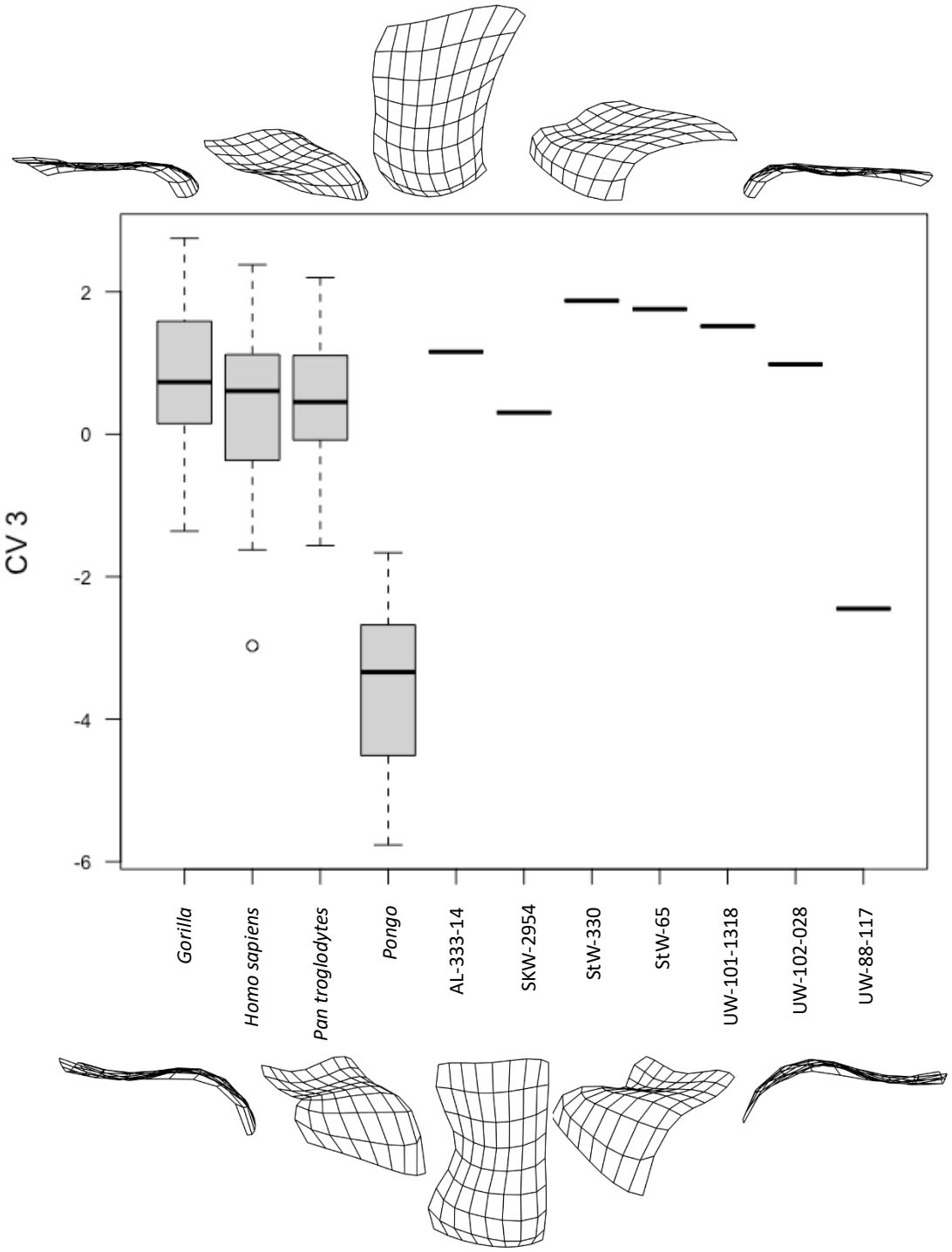

Figure 8.3.3: Boxplot of the scores of the third Canonical Variate axis of the fourth metacarpal's proximal articular surface for *Gorilla, Homo sapiens, Pan troglodytes,* and *Pongo* compared with fossil specimens AL333-14 (*Australopithecus afarensis*), SKW 2954 (*Paranthropus* robustus/early *Homo*), StW 330, StW 65 (*Australopithecus africanus*), UW-101-1318, UW-102-028 (*Homo naledi*) and UW88-117 (*Australopithecus sediba*).Black lines represent the median of the group, boxes are interquartile ranges, and whiskers are the non-outlier ranges.

CVA Scatterplots

CV 1 v CV 2

A scatterplot of CV 1 against CV 2, shown in figure 8.3.4, most effectively seperates *Homo sapiens, Gorilla*, and *Pan troglodytes* from each other, with the *Pongo* sample concentrated at the centre of the plot. The *Homo sapiens* sample dominates the right half of the plot, while the upper-left quadrant is dominated by *Gorilla*, and the lower-left quadrant dominated by *Pan troglodytes.* The 95% confidence ellipse of *Pongo* overlaps slightly with *Homo sapiens*, and considerably with *Gorilla* and *Pan troglodytes*, while there is a small overlap between the two non-human African Great Ape groups.

While there is a concentration of fossil specimens around the *Homo sapiens* sample, the fossils are distributed broadly across the plot. The two *Homo naledi* specimens (UW-101-1318 and UW-101-028), as well as the *Australopithecus sediba* specimen (UW-88-117) and one *Australopithecus africanus* specimen (StW-330) are concentrated among the *Homo sapiens* sample. SKW-2954 (*Paranthropus robustus*/early *Homo*) and StW-65 (*Australopithecus africanus*) are in the centre of the plot, among the *Pongo* sample, while AL-333-56 (*Australopithecus afarensis*) is within the *Pongo* and *Gorilla* 95% confidence ellipses and is the fossil specimen furthest from the modern human sample.

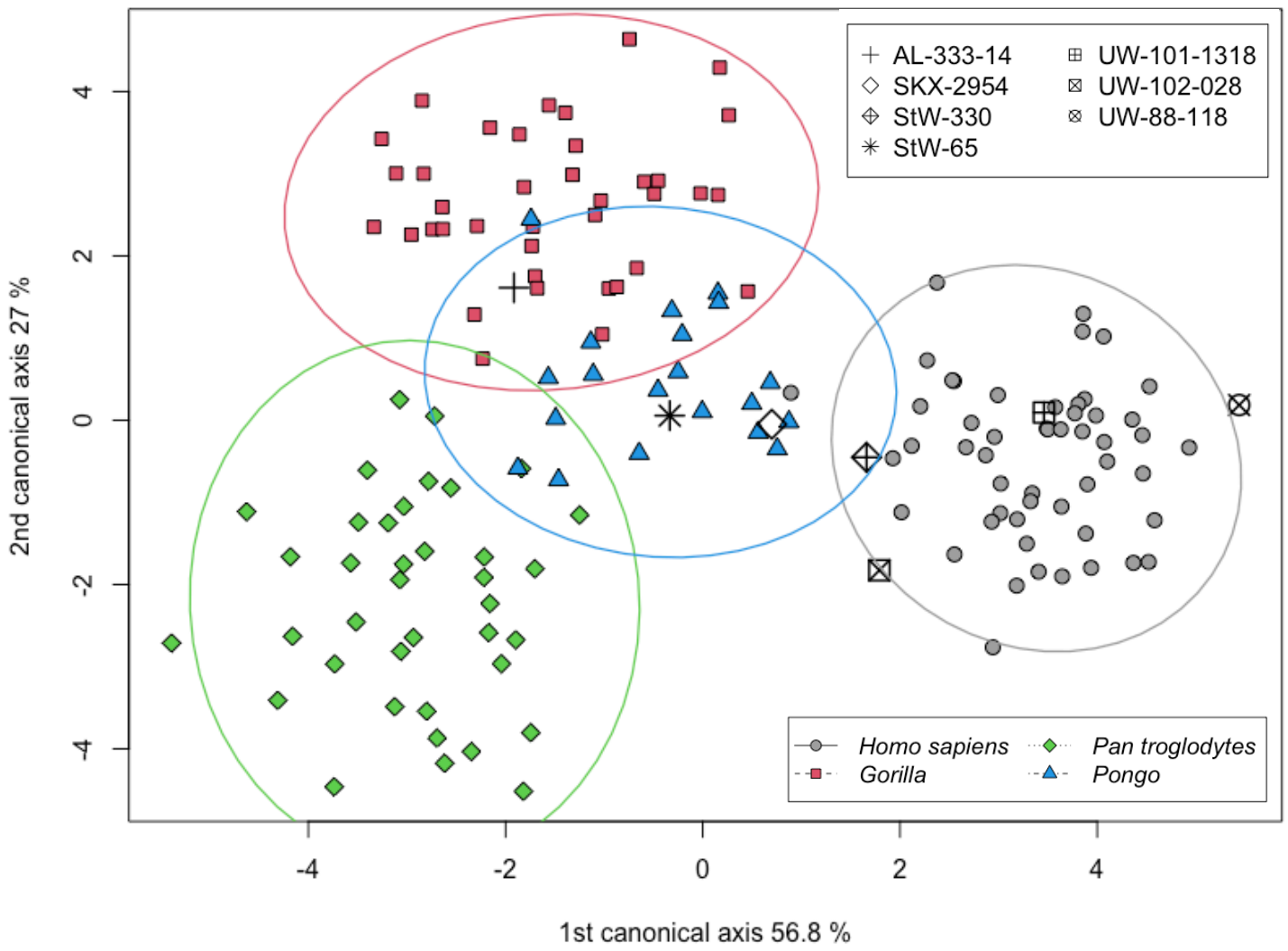

Figure 8.3.4: Scatterplot of the first (56.8%) vs. second (27.0%) canonical variate scores of extant samples (*Homo sapiens, Gorilla, Pan troglodytes* and *Pongo*) and fossil specimens for the fourth metacarpal's proximal articular surface.

CV 1 v CV 3

The scatterplot of CV 1 against CV 3 is shown in figure 8.3.5. This plot is effective in seperating *Homo sapiens* and *Pongo* from *Gorilla* and *Pan troglodytes*, whose samples largely overlap. The lower half of the plot is dominated by *Pongo*, while the African great apes (including *Homo sapiens*) are in the upper half. *Homo sapiens* is in the upper-right quadrant, and the non-human African Great Apes are in the upper-left quadrant. The 95% confidence ellipse of *Homo sapiens* overlaps minimally with that of *Pongo*, while *Pongo* also overlaps to a small extent with *Gorilla*.

Again, the fossil specimens are distributed widely across the plot. UW-101-1318 and UW-102-028 (*Homo naledi*), StW-330 (*Australopithecus africanus*) and UW-88-117 (*Australopithecus sediba*) are within the vicinity of the *Homo sapiens* sample. SKW-2954 (*Paranthropus robustus*/early *Homo*) is located centrally, within the 95% confidence ellipse of *Gorilla*. StW-65 (*Australopithecus africanus*) is also in the confidence ellipse of *Gorilla*, though higher in the plot, while AL-333-56 (*Australopithecus afarensis*) is situated within the *Gorilla* and *Pan troglodytes* samples.

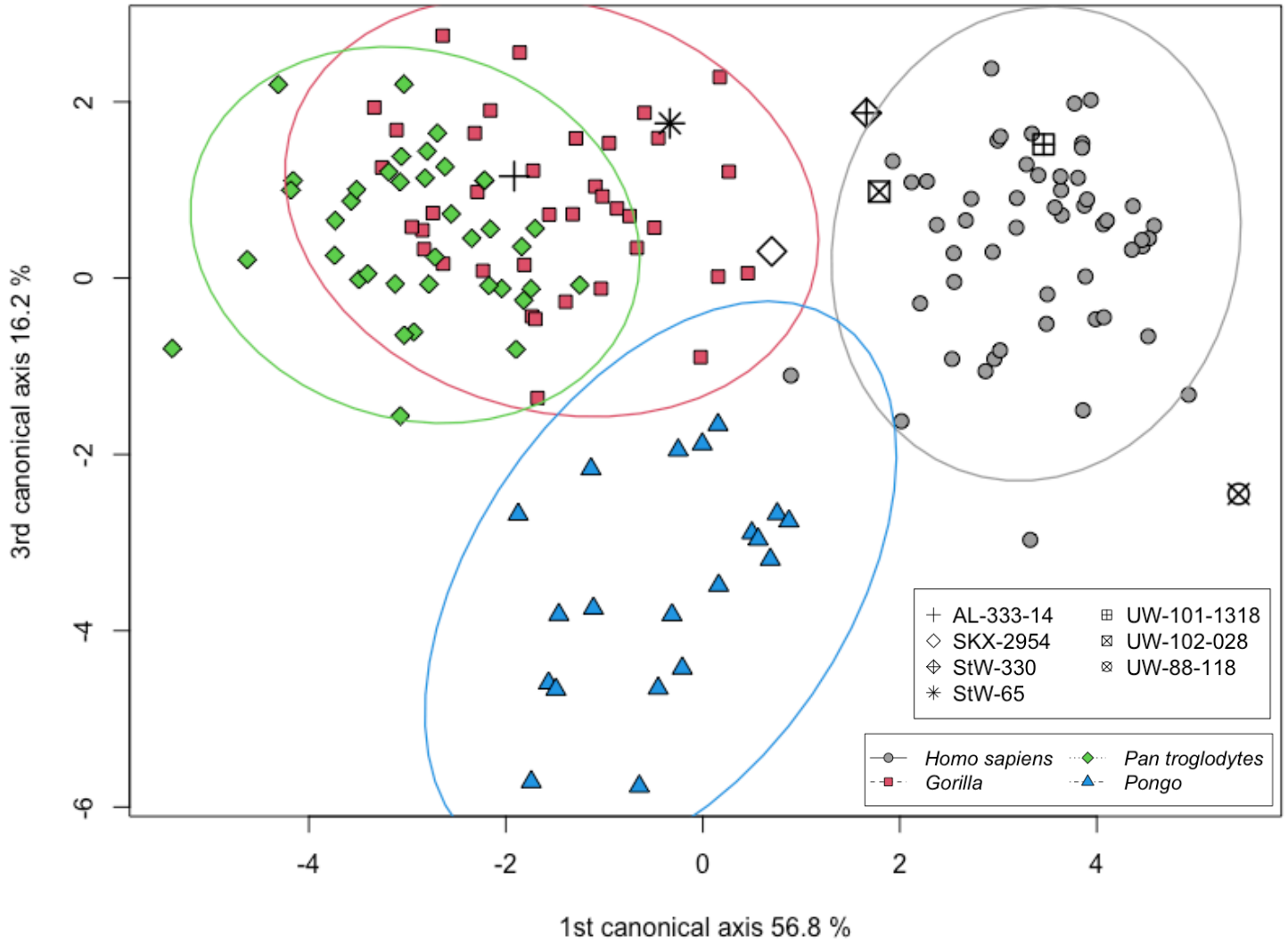

Figure 8.3.5: Scatterplot of the first (56.8%) vs. third (16.2%) canonical variate scores of extant samples (*Homo sapiens, Gorilla, Pan troglodytes* and *Pongo*) and fossil specimens for the fourth metacarpal's proximal articular surface.

CV 2 v CV 3

The scatterplot of CV 2 against CV 3, shown in figure 8.3.6, is most informative in distinguishing between the non-human groups. The *Homo sapiens* sample is concentated in the centre of the plot, and overlaps substantially with all non-human groups, and with *Pan troglodytes* to the greatest extent. *Pongo* is concentrated in the lower-centre of the plot, with *Pan troglodytes* in the upper-left, and *Gorilla* in the upper-right. There is a degree of overlap in the 95% confidence ellipses of all groups with each other.

All the fossil specimens are concentrated around the *Homo sapiens* 95% confidence ellipse, and are also within the 95% confidence of a non-human group. UW-102-028, UW-101-1318 (*Homo naledi*), StW-330, StW-65 (*Australopithecus africanus*), and SKW-2954 (*Paranthropus robustus*/early *Homo*) are all situated in the distributions of *Homo sapiens* and *Pan troglodytes.* AL-333-56 (*Australopithecus afarensis*) is in the sample range of *Homo sapiens* and *Gorilla*. UW-88-117 (*Australopithecus sediba*) is the only fossil specimen not within the 95% confidence ellipse of *Homo sapiens*, though it is near its border, and is situation with the *Pongo* sample.

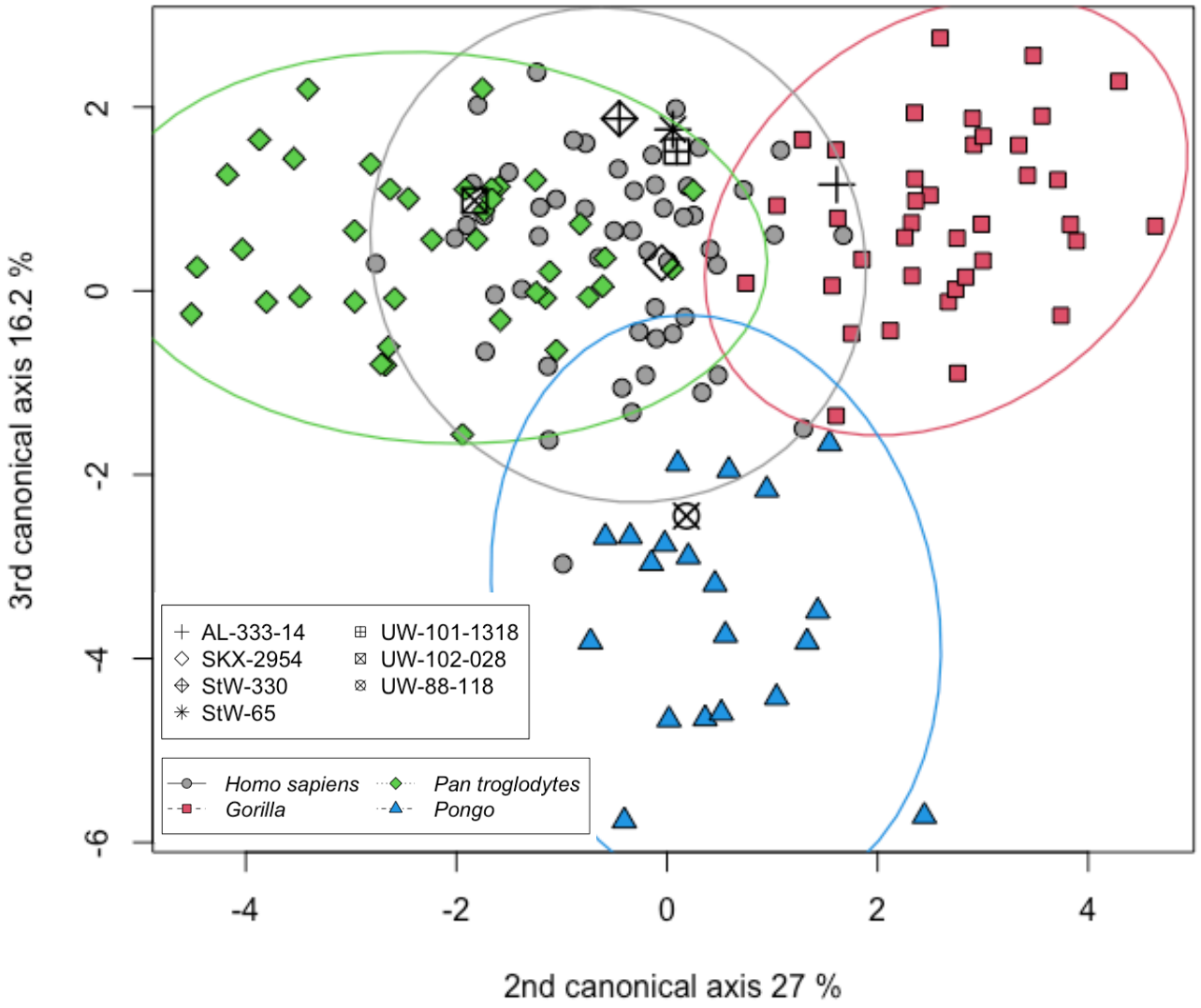

Figure 8.3.6: Scatterplot of the second (27.0%) vs. third (16.2%) canonical variate scores of extant samples (*Homo sapiens, Gorilla, Pan troglodytes* and *Pongo*) and fossil specimens for the fourth metacarpal's proximal articular surface.

8.4 Metacarpal-4 Procrustes distances

The Procrustes distances of the extant group means from each other are shown in table 8.4.1, with the Procrustes distance of each fossil specimen from the average shape of each extant taxon group shown in table 8.4.2. Among the extant sample, the mean shape of *Homo sapiens* is furthest from all other groups, though is considerably closer to the *Gorilla* mean shape than the other two taxa. *Pongo* and *Gorilla* are the mean shapes closest to each other, followed by *Pongo* and *Pan troglodytes.* Among the fossil specimens, StW-330 (*Australopithecus africanus*) is the closest fossil specimen to the *Homo sapiens* mean shape, while AL-333-56 (*Australopithecus afarensis*) is the furthest, being closest to the mean shape of *Gorilla* and equidistant from that of *Homo sapiens* and *Pan troglodytes*. UW-102-028 (*Homo naledi*) is closest to the mean shape of *Pan troglodytes.* All other fossil specimens are closest to the *Homo sapiens* mean shape.

Table 8.4.1: Procrustes distances (below) between extant groups.

	Homo sapiens	*Gorilla*	*Pan troglodytes*	*Pongo*
Homo sapiens	-	0.156	0.222	0.285
Gorilla		-	0.153	0.134
Pan troglodytes			-	0.139
Pongo				-

Table 8.4.2: The Procrustes distance of each fossil from the mean shape of each extant taxon group.

	Homo sapiens	*Gorilla*	*Pan troglodytes*	*Pongo*
AL 333-56	0.227	0.216	0.227	0.259
SKW 2954	0.174	0.201	0.178	0.215
StW 330	0.142	0.186	0.193	0.233
StW 65	0.148	0.165	0.167	0.212
UW-101-1318	0.145	0.231	0.246	0.264
UW-102-028	0.151	0.180	0.145	0.207
UW-88-117	0.198	0.223	0.213	0.211

Results of the Shapiro-Wilk tests for normality along the Procrustes distances of extant species from the mean value of their respective group are shown in table 8.4.3. The Shapiro-Wilks test for normality showed that the Procrustes distances of each taxon group from their mean shape were not normally distributed in the *Gorilla* and *Pan troglodytes* samples. As such,

the Procrustes distances of each taxon group from their respective mean shapes were normalized through a log transformation (table 8.4.3), with the log-transformed data used in subsequent analysis.

Table 8.4.3: Results of the Shapiro-Wilk normality tests performed on the individual distances distribution from their respective group mean shapes (top row), and the corresponding square-root-transformed data. Calculations were performed on Procrustes distances.

	Homo sapiens	*Gorilla*	*Pan troglodytes*	*Pongo*
p	0.140	**0.018**	**0.007**	0.450
P (log-transformed)	0.945	0.147	0.285	0.784

The Procrustes distance of each fossil specimen from the mean shape of each fossil group in standard deviations is shown in table 8.4.4. All fossil specimens, with the exception of UW-102-028 (*Homo naledi*), are closer, with regards to proportion of sample, to the mean shape of *Homo sapiens* than to any other group. UW-102-028 is closer than 21.81% of the *Pan troglodytes* sample to their average shape, compared with 17.91% for the *Homo sapiens* sample. StW 330, StW 65 (*Australopithecus africanus*), and UW-101-1318 (*Homo naledi*) are all closer to the mean shape of *Homo sapiens* than 20% of modern human specimens, while AL-333-14 (*Australopithecus afarensis*) is closer than less than 1% of modern human specimens.

Table 8.4.4: Distances in standard deviations of each fossil in the MC-IV study from the mean of the distance of each individual of each extant group from the mean of its respective group. The value of the upper tail cumulative distribution function multiplied by 100 were in parentheses.

	Homo sapiens	Gorilla	Pan troglodytes	Pongo
AL 333-14	2.442 (0.73%)	3.521 (0.02%)	2.642 (0.41%)	3.321 (0.04%)
SKW 2954	1.443 (7.46%)	3.146 (0.08%)	1.621 (5.25%)	2.569 (0.51%)
StW 330	0.679 (24.87%)	2.719 (0.33%)	1.973 (2.43%)	2.907 (0.18%)
StW 65	0.840 (20.03%)	2.071 (1.92%)	1.358 (8.73%)	2.514 (0.60%)
UW-101-1318	0.766 (22.17%)	3.892 (0.00%)	2.982 (0.14%)	3.403 (0.03%)
UW-102-028	0.919 (17.91%)	2.537 (0.56%)	0.778 (21.81%)	2.429 (0.76%)
UW-88-117	1.931 (2.67%)	3.698 (0.01%)	2.379 (0.87%)	2.506 (0.61%)

9 Metacarpal-5 proximal articulation results

9.1 Metacarpal-5 proximal articulation average shapes

Homo sapiens

The average shape of the proximal articular surface of the fifth metacarpal in *Homo sapiens* (figure 9.1.1) has a mediolaterally wide and palmodorsally contracted surface, resulting in a notably mediolaterally broad and squat articular surface. The surface slopes proximally from the lateral to the medial edge with a concave curvature that is gentle and uniform, while the curvature of the surface is quite strongly palmodorsally convex, resulting in a prominent saddle-shaped morphology of the surface.

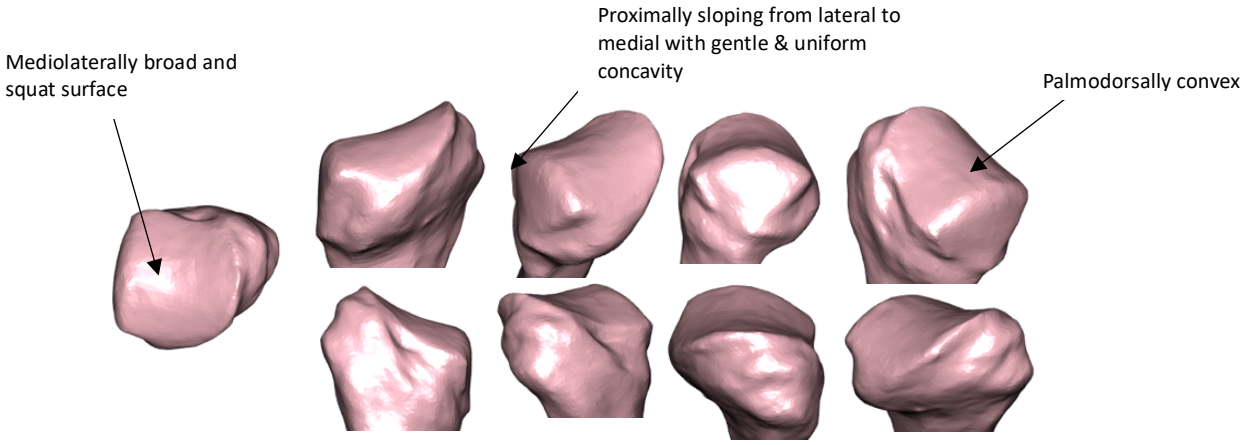

Figure 9.1.1: The average shape of the proximal articular surface of the fifth metacarpal of *Homo sapiens*, produced by warping the mesh of the specimen closest to the group's mean shape. The articular surface is shown from eight different viewpoints. Left: proximal; top row, left to right: palmar; lateropalmar; lateral; laterodorsal; bottom row, left to right: dorsal; mediodorsal; medial; mediopalmar views.

Gorilla

The mean shape of the *Gorilla* fifth metacarpal proximal articular surface is shown in figure 9.1.2. As with the corresponding surface on the hamate, it can be divided into palmar and dorsal portions. The dorsal half is strongly mediolaterally concave and is angled distodorsally, while the palmar surface is slightly convex mediolaterally and faces palmarly. The two portions

of the surface are separated by a strong bevelling, and the surface is both mediolaterally wide and palmodorsally long.

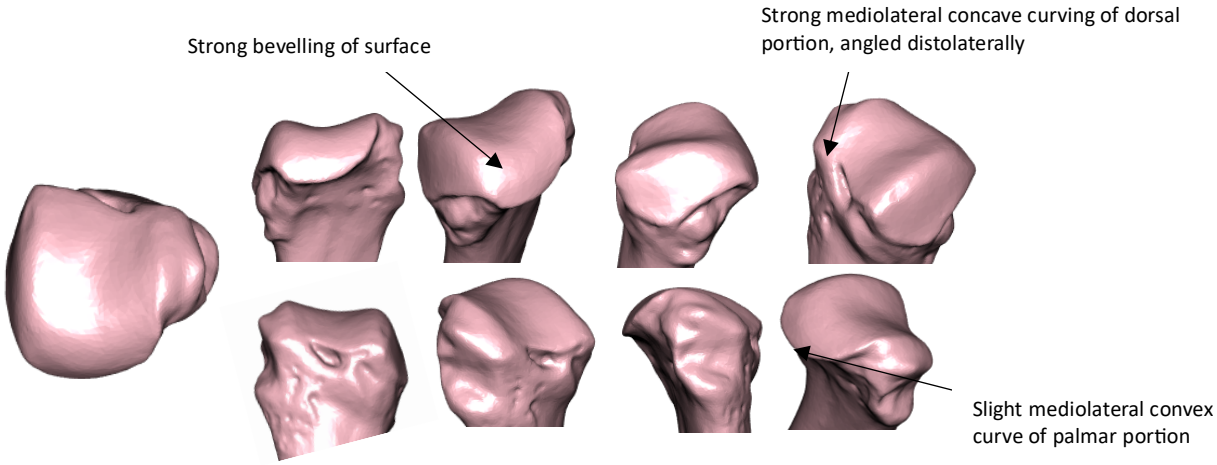

Figure 9.1.2: The average shape of the proximal articular surface of the fifth metacarpal of *Gorilla*, displayed by warping the mesh of the specimen closest to the group's mean shape. The articular surface is shown from eight different viewpoints. Left: proximal; top row, left to right: palmar; lateropalmar; lateral; laterodorsal; bottom row, left to right: dorsal; mediodorsal; medial; mediopalmar views.

Pan troglodytes

The mean shape of *Pan troglodytes*, shown in figure 9.1.3, is mediolaterally narrow, with the dorsal portion of its lateral border shifting medially, and the proximal portion of the medial border shifting laterally. The dorsal portion of the medial border also moves laterally and dorsally, resulting in a particularly narrowed dorsal border of the articular surface. The mediolateral concavity of the articular surface is characteristically asymmetrical, being flatter along the lateral side, and flaring proximally on the medial side. The dorsopalmar convexity of the surface is notably bevelled to resemble a "hockey stick" bevelling in that direction, with the central portion of the surface projecting more palmarly, and the palmar landmarks migrated dorsally relative to the mean shape, resulting in a shallow bulge or inverted cup at the palmar portion.

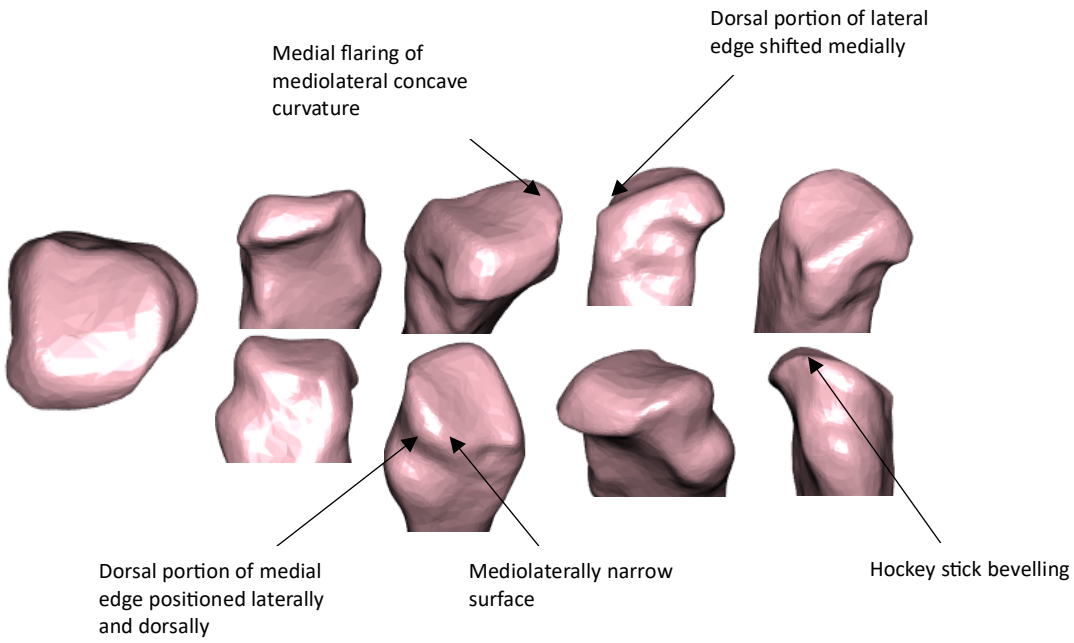

Figure 9.1.3: The average shape of the proximal articular surface of the fifth metacarpal of *Pan troglodytes*, displayed by warping the mesh of the specimen closest to the group's mean shape. The articular surface is shown from eight different viewpoints. Left: proximal; top row, left to right: palmar; lateropalmar; lateral; laterodorsal; bottom row, left to right: dorsal; mediodorsal; medial; mediopalmar views.

Pongo

The trend to a narrower and elongated articular surface observed in *Pan troglodytes* is magnified in *Pongo*, where the dorsal border is extended dorsally, especially more towards the lateral edge, and the palmar border is extended in a palmar direction, again emphasised on the lateral portion. Both the lateral and medial borders are contracted towards the midline, with the medial side also migrating distally. As with *Pan troglodytes,* the more anterior central bulge protrudes more palmarly, resulting in an exaggerated bevelling of the palmodorsal curve, with a particularly long dorsal portion. The mean shape of *Pongo* is shown in figure 9.1.4.

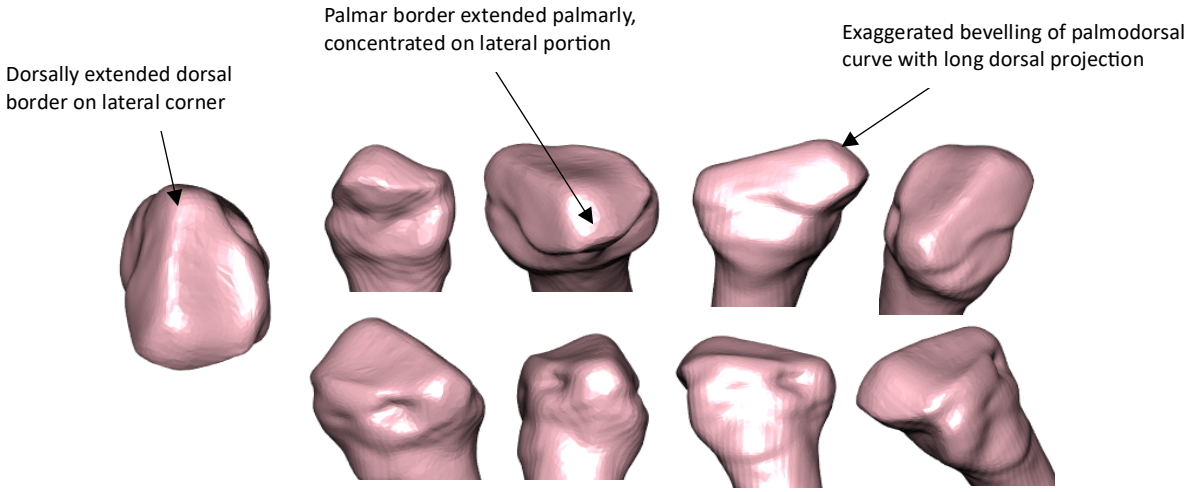

Figure 9.1.4: The average shape of the proximal articular surface of the fifth metacarpal of *Pongo*, displayed by warping the mesh of the specimen closest to the group's mean shape. The articular surface is shown from eight different viewpoints. Left: proximal; top row, left to right: palmar; lateropalmar; lateral; laterodorsal; bottom row, left to right: dorsal; mediodorsal; medial; mediopalmar views.

Table 9.1: Comparison of the mean proximal metacarpal 5 shape of each extant taxa							
MC5	Proximal	Lateropalmar	Lateral	Laterodorsal	Mediodorsal	Medial	Mediopalmar
Homo sapiens	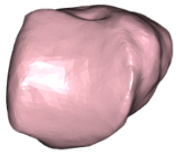		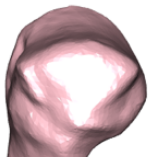	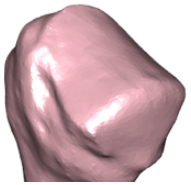	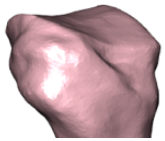	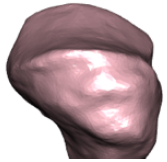	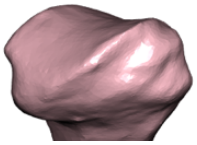
Gorilla	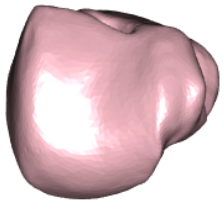		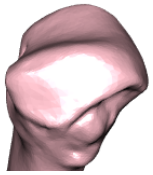	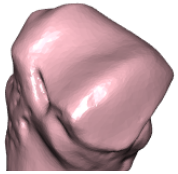	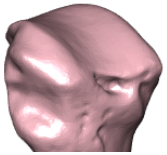	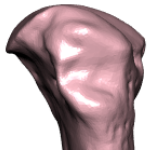	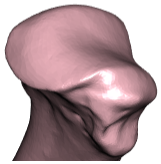
Pan troglodytes							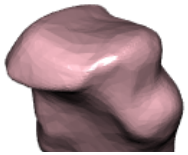
Pongo		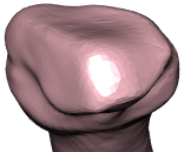		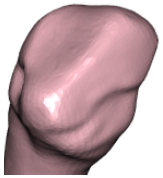	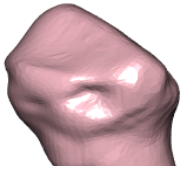		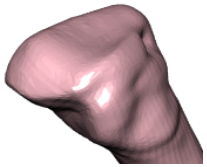

9.2 Metacarpal-5 principal components analysis

The first three principal components, which cumulatively accounted for 63.7% of the total variance, were regarded as meaningful according to Bookstein's (2014) criterion. PC 1 accounted for 42.3% of the total variance, and PC 2 and 3 accounted for 12.0% and 9.3% respectively (figure 9.2.1). While both the fourth and fifth principal components accounted for more than 5% of the total variance (7.1% and 6.8% respectively), analysis of variance tests did not indicate significant differences between extant groups ($p > 0.05$) (table 9.2.1), and investigation of boxplots and scatterplots involving scores of the 4th and 5th PCs showed that they were not informative in distinguishing between groups or in interpreting the relationship of fossil specimens with extant groups. The fourth and fifth principal components were therefore not investigated in detail. The first nine principal components accounted for 90.1% of total variance, with the ninth principal component accounting for 2.4% of the total variance.

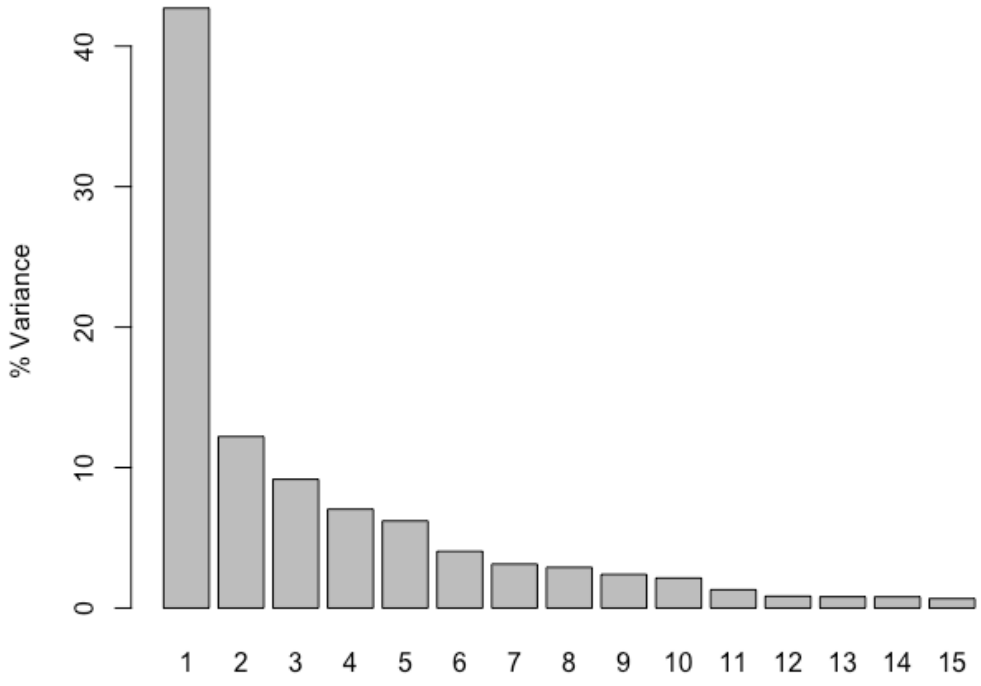

Figure 9.2.1: Graph showing the percentage of variance each principal component is accountable for in the principal component analysis of the fifth metacarpal's proximal articular surface. The first three principal components accounted for approximately 63.7% of the variation in shape, with the first five PCs accounting for 78%.

Taxonomic differences between groups

A Hotelling's T^2 test did not reveal a significant difference between the means of the two species of *Gorilla* (*Gorilla beringei* and *Gorilla gorilla*) along any of the first five principal components (T^2 = 0.517, df = 5, 30; p = 0.762). Similarly, there was no significant difference between the values of the two species of *Pongo* (*Pongo pygmaeus* and *Pongo abelii*) (T^2 = 1.496, df = 5, 15; p = 0.249). The multiple analysis of variance (MANOVA) on the first five principal component scores of the four *Pan troglodytes* species also did not reveal a significant difference in the means of the different sub-species [F (3, 24) = 1.493, p = 0.140, Wilks Λ = 0.393]. As there were no significant differences between the distributions of the principal component scores of the *Gorilla* and *Pongo* samples at the species level, nor of *Pan troglodytes* at the sub-species level, species of *Gorilla* and *Pongo* were pooled into their respective genus, while the sub-species of *Pan troglodytes* were pooled at the species level.

Analysis of Variance (ANOVA)

Results of the analysis of variance of each group along scores of the first five principal components are shown in table 9.2.1. Significant results were reported along the first three principal components. The mean and standard deviation of the scores of the first three principal components for each extant taxon sample is shown in table 9.2.2, with the PC values of each fossil specimen also shown. Subscripts next to the principal component scores of fossil specimens indicate extant groups for which that particular fossil specimen deviates at least one standard deviation from.

Table 9.2.1: Results of analysis of variance on the first five principal component scores on extant groups.

Principal Component	DF	Sum of Squares	Mean Squares	*F* Value	*p*
PC 1	3	1.5576	0.5192	111.4	**<0.001**
PC 2	3	0.3261	0.10869	48.97	**<0.001**
PC 3	3	0.0346	0.011541	3.806	**0.012**
PC 4	3	0.0125	0.004154	1.75	0.159
PC 5	3	0.0052	0.001405	1.233	0.300

Table 9.2.2: Mean and standard deviation (in parentheses) of principal component (PC) scores for *Homo sapiens, Gorilla, Pan troglodytes,* and *Pongo* compared with PC scores of fossil specimens AL333-1, AL333w-89 (*Australopithecus afarensis*), StW63 (*Australopithecus africanus*), UW-101-1309 (*Homo naledi*), and UW88-118 (*Australopithecus sediba*).

Group	*Homo sapiens*	*Gorilla*	*P. troglodytes*	*Pongo*	AL333-14	AL333w-89	StW63	UW-101-1309	UW88-118
	(*n* = 54)	(*n* = 36)	(*n* = 40)	(*n* =21)					
PC1	0.119 (0.062)	-0.014 (0.069)	-0.083 (0.082)	-0.155 (0.051)	0.125 $_{G,Pt,Po}$	0.133 $_{G,Pt,Po}$	0.123 $_{G,Pt,Po}$	0.156 $_{G,Pt,Po}$	0.112 $_{G,Pt,Po}$
PC2	-0.016 (0.046)	-0.001 (0.038)	0.067 (0.058)	-0.080 (0.041)	0.024 $_{Po}$	-0.049 $_{G,Pt}$	-0.037 $_{Pt,Po}$	0.046 $_{G,Pt,Po}$	-0.065 $_{Hs,G,Pt}$
PC3	0.002 (0.045)	-0.024 (0.054)	0.011 (0.068)	0.021 (0.051)	0.045 $_{G}$	-0.099 $_{Hs,G,Pt,Po}$	-0.107 $_{Hs,G,Pt,Po}$	-0.046 $_{Hs,Po}$	0.073 $_{Hs,G,Po}$

[a] Subscripts indicate a group that the fossil specimen differs at least 1 standard deviation from. H = *Homo sapiens*; G = *Gorilla*; P = *Pan troglodytes*; Po = *Pongo*.

Principal Component 1 shape and groupings

The first principal component, which accounted for 42.3% of the total variance, was most effective in separating *Homo sapiens* from the non-human groups, particularly *Pongo*. The first principal component relates to a change in shape from a mediolaterally narrow and a palmodorsally highly-angled bevelled surface, with an abruptly-stepped mediolateral profile at the negative extreme, to a positive shape that is mediolaterally broader than it is palmodorsally long, and displays a mediolaterally gentle and uniform curvature, and a uniform concave curvature mediolaterally.

The negative aspect of the PC1 axis describes a palmodorsally elongated and mediolaterally narrow shape (figure 9.2.2). The surface is strongly bevelled, with an acute 90° apex separating the dorsal portion of the surface from the shorter palmo-proximal portion. The dorsolateral edge of the surface is uniform and in the same plane as the dorsal surface, while the medial edge is more curved and projects more distally, resulting in a sharp angulation of the dorsal portion of the surface in the mediolateral plane, while the palmar portion of the surface is flat. The positive aspect of PC1 represents a mediolaterally broad and palmodorsally squat articular shape, which is gently and uniformly palmodorsally curved (figure 9.2.2). Contrasting with the abruptly-stepped mediolateral profile of the negative shape, the positive shape is uniformly and gently concave mediolaterally. This results in an articular surface with a saddle-shaped morphology.

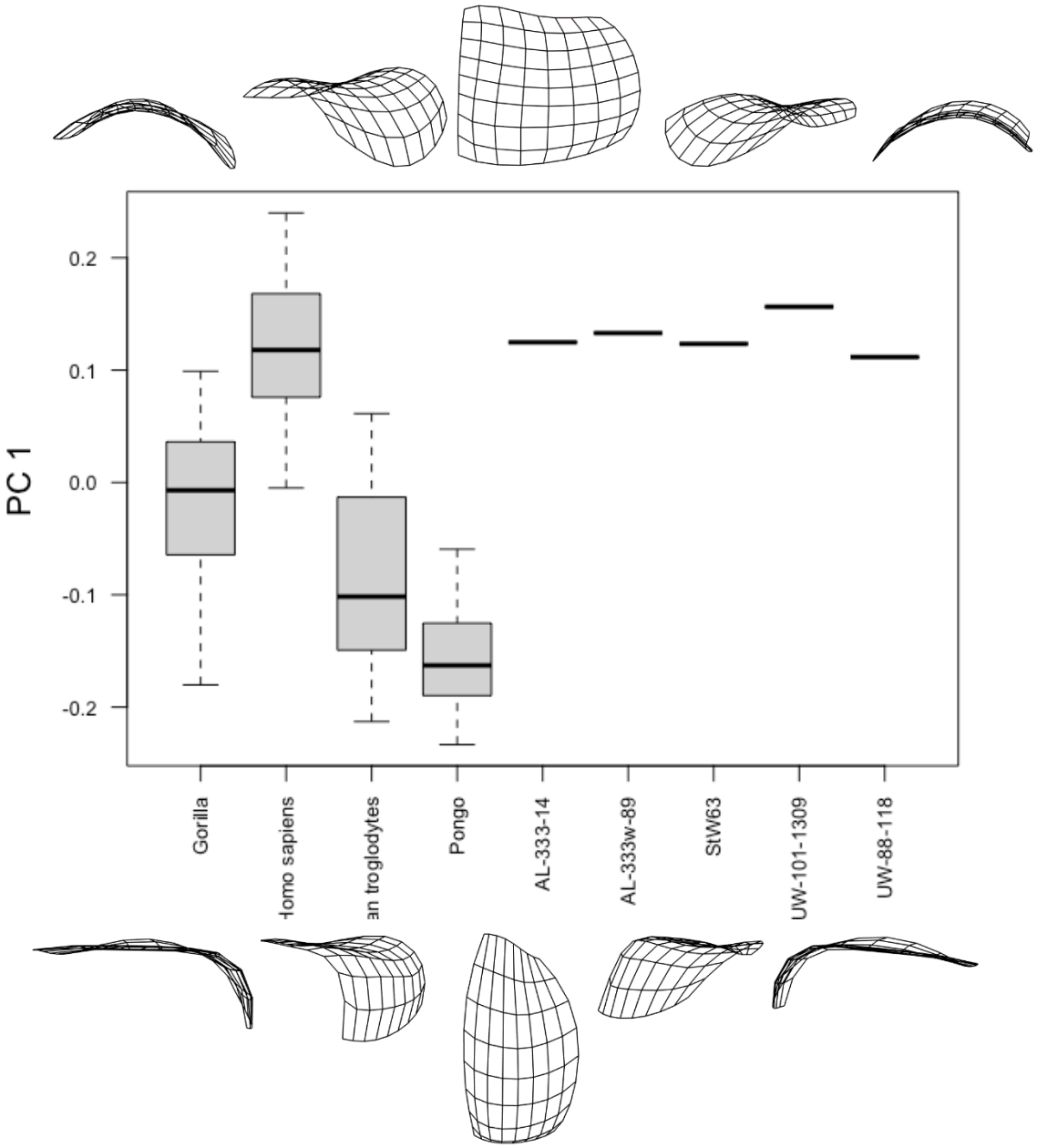

Figure 9.2.2: Boxplot of the first principal component (PC1) scores for *Gorilla, Homo sapiens, Pan troglodytes,* and *Pongo* compared with fossil specimens AL333-14 (*Australopithecus afarensis*), AL333w-89 (*Australopithecus afarensis*), StW63 (*Australopithecus africanus*), UW-101-1309 (*Homo naledi*), and UW88-118 (*Australopithecus sediba*). Black lines represent the median of the group, boxes are interquartile ranges, and whiskers are the non-outlier ranges.

Table 9.2.3: Tukey honestly significant difference (HSD) *post-hoc* test results on PC1 scores among *Homo, Pan, Gorilla, and Pongo.* Significant results ($p < 0.05$) were highlighted in bold.

Group		Mean difference	*p*	95% confidence interval	
				Lower bound	Upper bound
Homo sapiens	*Gorilla*	0.134	**<0.001**	0.096	0.172
	Pan troglodytes	0.203	**<0.001**	0.166	0.240
	Pongo	0.275	**<0.001**	0.229	0.320
Gorilla	*Homo sapiens*	-0.134	**<0.001**	-0.172	-0.096
	Pan troglodytes	0.069	**<0.001**	0.028	0.110
	Pongo	0.141	**<0.001**	0.092	0.190
Pan troglodytes	*Homo sapiens*	-0.203	**<0.001**	-0.240	-0.166
	Gorilla	-0.069	**<0.001**	-0.110	-0.028
	Pongo	0.072	**0.001**	0.024	0.120
Pongo	*Homo sapiens*	-0.275	**<0.001**	-0.320	-0.229
	Gorilla	-0.141	**<0.001**	-0.190	-0.092
	Pan troglodytes	-0.072	**0.001**	-0.120	-0.024

Results of Tukey's Honest Significant Difference test on scores of the first principal component show that all groups were significantly different from each other (table 9.2.3). The box-and-whisker plot of the scores of the first PC shows that this axis is most informative in distinguishing *Homo sapiens* from the non-human great apes, especially *Pongo* and *Pan troglodytes* (figures 9.2.2), with the *Homo sapiens* sample dominating the positive aspect of the axis, being almost entirely in this half. The negative half of PC 1 is occupied almost exclusively by the great apes, with the *Pongo* sample entirely in the negative aspect. While *Gorilla* is distributed across both the positive and negative halves of PC 1 and has a median value approximating zero (although its range is skewed towards the negative), only the 4th quartile of the *Pan troglodytes* sample is in the positive aspect. With the exception of *Homo sapiens* and *Pongo*, which have no overlap in PC 1 values, there is a degree of overlap between all other groups, particularly between the non-human groups. And while the first quartile of *Homo sapiens* overlaps with the fourth quartile of *Pan troglodytes* and the upper half of *Gorilla*, the upper half of the *Homo sapiens* sample occupies its own range in the positive aspect of the first principal component. All the fossil specimens studied are within the interquartile range of *Homo sapiens*, and outside the range of any other extant taxon. Every fossil specimen is also within 1 standard deviation (SD) of the mean PC 1 value of mean *Homo sapiens* (table 9.2.2).

Principal Component 2 shape and groupings

The second principal component accounts for 12.0% of the total variation in the shape of the fifth metacarpal's proximal articular surface. This axis describes changes in the distal projection of the medial edge of the surface relative to the lateral edge, and the strength of curvature in the proximo-distal plane. The second principal component primarily distinguishes between the samples of *Pan troglodytes* and *Pongo*.

The articular shape representative of PC 2's minimum extreme is characterised by a notable distal projection of the surface's medial edge, and a stepped surface with a medial half that is angled distally with a lateral half remaining in a horizontal plane (figure 9.2.3). The surface is strongly curved largely due to a disto-dorsal contraction of the lateropalmar corner. The shape representative of the positive aspect of PC 2 is a surface in which its lateral edge is more distally-projecting than the medial edge, leading to a medial sloping of the surface. However, the discrepancy in the distal heights of the two edges is less extreme than in the PC 2 minimum shape, and overall, the mediolateral profile of the surface is less sloped and stepped than its minimum counterpart. The palmodorsal curvature of the surface is more oblique and less acute, driven largely by a laterodorsal corner that is migrated distally and dorsally, which also results in a dorsal edge that is angled dorsally from the mediodorsal to the laterodorsal corner.

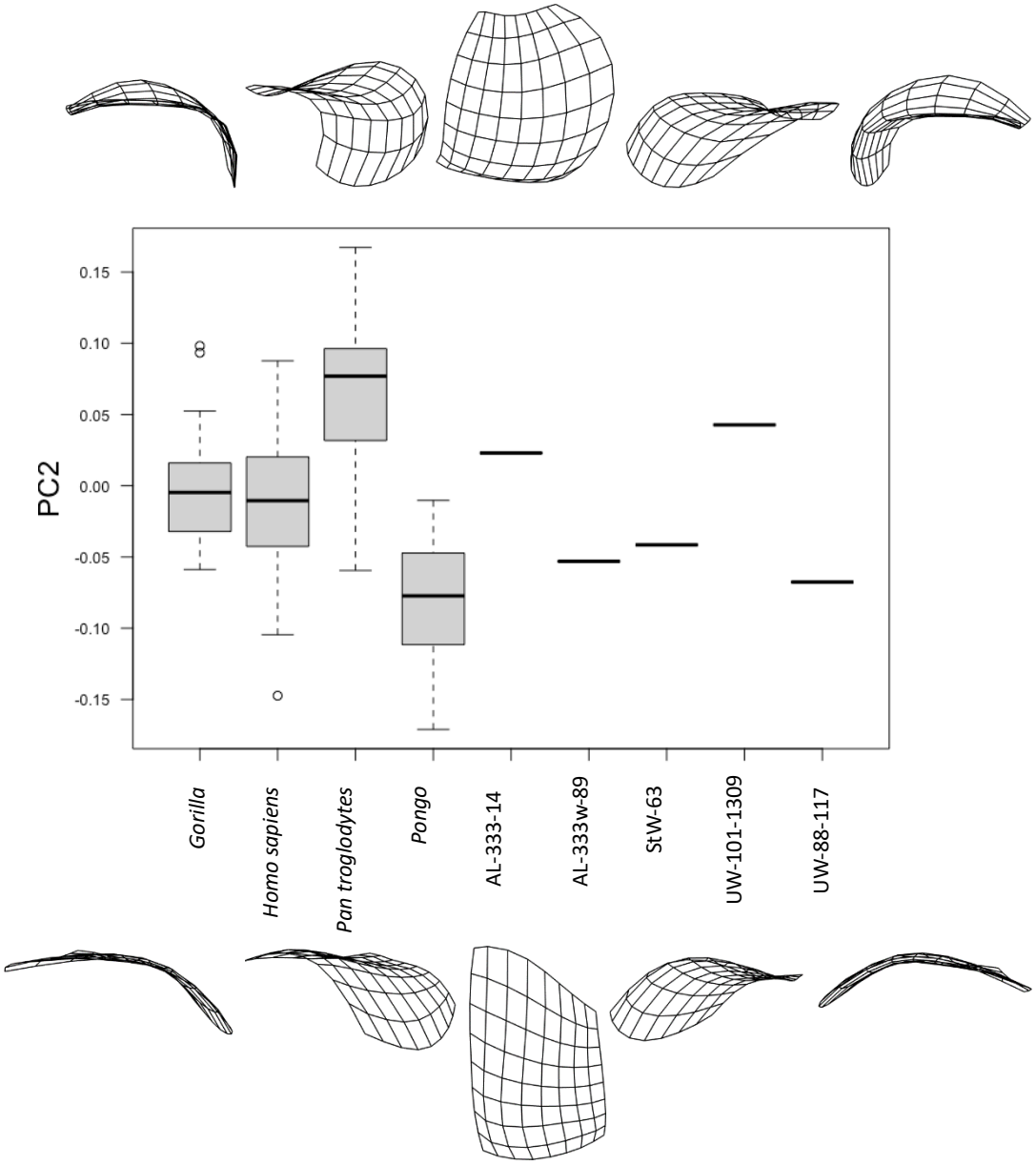

Figure 9.2.3: Boxplot of the second principal component (PC2) scores for *Gorilla, Homo sapiens, Pan troglodytes,* and *Pongo* compared with fossil specimens AL333-14 (*Australopithecus afarensis*), AL333w-89 (*Australopithecus afarensis*), StW63 (*Australopithecus africanus*), UW-101-1309 (*Homo naledi*), and UW88-118 (*Australopithecus sediba*). Black lines represent the median of the group, boxes are interquartile ranges, whiskers are the non-outlier ranges, and empty circles were outliers.

Table 9.2.4: Tukey honestly significant difference (HSD) *post-hoc* test results on PC2 scores among *Homo, Pan, Gorilla, and Pongo.* Significant results ($p < 0.05$) were highlighted in bold.

Group		Mean difference	*p*	95% confidence interval	
				Lower bound	Upper bound
Homo sapiens	*Gorilla*	-0.015	0.459	-0.041	0.011
	Pan troglodytes	-0.083	**<0.001**	-0.108	-0.057
	Pongo	0.064	**<0.001**	0.033	0.096
Gorilla	*Homo sapiens*	0.015	0.459	-0.011	0.041
	Pan troglodytes	-0.068	**<0.001**	-0.096	-0.040
	Pongo	0.079	**<0.001**	0.045	0.113
Pan troglodytes	*Homo sapiens*	0.083	**<0.001**	0.057	0.108
	Gorilla	0.068	**<0.001**	0.040	0.096
	Pongo	0.147	**<0.001**	0.114	0.180
Pongo	*Homo sapiens*	-0.064	**<0.001**	-0.096	-0.033
	Gorilla	-0.079	**<0.001**	-0.113	-0.045
	Pan troglodytes	-0.147	**<0.001**	-0.180	-0.114

Results of Tukey's Honest Significant Difference test on the second principal component revealed that the PC 2 values of the *Homo sapiens* and *Gorilla* samples do not differentiate significantly from each other, with the interquartile range of *Gorilla* resting entirely within the human interquartile range, and *Gorilla*'s entire range, with the exception of extremal points, being within the *Homo sapiens* range (table 9.2.4; figure 9.2.3). The ranges of both *Gorilla* and *Homo sapiens* span both the positive and negative aspects of PC 2, with their median value not deviating greatly from zero (figure 9.2.3), although the *Homo sapiens* sample has a greater range, and is skewed very slightly towards the negative aspect of the axis. Shape variation along the second principal component does not appear to be primarily concerned with these two groups and is most informative in differentiating *Pan troglodytes* from *Pongo.* As with the first principal component, *Pongo* is situated entirely within the negative aspect of the axis, while the interquartile range of *Pan troglodytes* is entirely within the positive half, with only its 1st quartile being in the negative aspect (figure 9.2.3). While both *Homo sapiens* and *Gorilla* have significantly different means from both *Pan troglodytes* and *Pongo,* there is considerable overlap in the ranges of all groups.

The second principal component is less informative than the first with respects to distinguishing the placement of fossil specimens relative to the extant sample. As with the first principal component, all five fossil specimens fall within the range of *Homo sapiens* (figure 9.2.3), although StW-63 (*Australopithecus africanus*) is the only fossil specimen to fall within the interquartile range of *Homo sapiens*, and the PC 2 scores of the fossil specimens span a greater

range than in the first principal component. AL-333-14 (*Australopithecus afarensis*) and UW-101-1309 (*Homo naledi*), having positive PC 2 scores, are within the ranges of *Homo sapiens*, *Pan troglodytes* and *Gorilla,* and are outside the range of *Pongo.* AL-333w-89 (*Australopithecus afarensis*), StW-63 (*Australopithecus africanus*), and UW-88-118 (*Australopithecus sediba*) all have negative values, with AL-333w-89 and StW-63 falling within the range of all four extant groups. UW-88-118 (*Australopithecus sediba*) is within the ranges of *Homo sapiens*, *Gorilla*, and *Pongo*, and is the only fossil specimen outside the *Pan troglodytes* range.

Principal Component 3 shape and groupings

The third principal component, which contributed to 9.3% of the total variation, is explained primarily by changes in the regularity of the palmodorsal convexity of the articular surface, as well as the mediolateral broadness of the central part of the surface. While Hotelling's HSD tests indicated that the values of the *Gorilla* sample varied significantly from those of *Pongo* and *Pan troglodytes*, the range of the *Pan troglodytes* sample span the entire range of values along the third principal component, with the ranges of all other groups falling within that of *Pan troglodytes* (figure 9.2.4). The third principal component is not of great utility in distinguishing between extant groups, nor is it informative in exploring the relationship of fossil specimens relative to extant taxa.

The negative aspect of PC3 is defined by an articular surface that has a uniform palmodorsal curvature in which the apex of the curve is located centrally, being equidistant from the palmar and dorsal edges. The surface is mediolaterally narrow and has a laterodorsal corner that projects dorsally to a greater extent than the mediodorsal corner, resulting in an irregular dorsal edge. Both the mediopalmar and lateropalmar corners are in a similar mediolateral and dorsopalmar plane, and the central part of the palmar edge bulges distally, resulting in a distally-arched palmar edge.

The maxima of the third principal component represents a relatively planar dorsal three-quarters articular surface which transitions sharply to a strongly-bevelled palmar surface, resulting in a morphology that resembles a "hockey-stick" profile. The lateropalmar corner projects more distally than the mediopalmar corner, resulting in a prominent lateropalmar surface that diminishes medially. The surface is concave in the mediolateral plane, with a lateral edge that is higher, projecting more proximally than the corresponding medial edge, with the medial and lateral edges separated by a dorsopalmar groove. The lateral edge is also notably longer than the medial edge, which is uniform in its strong medial curvature, while the lateral edge is straighter but for a slight bulging towards its dorsal portion.

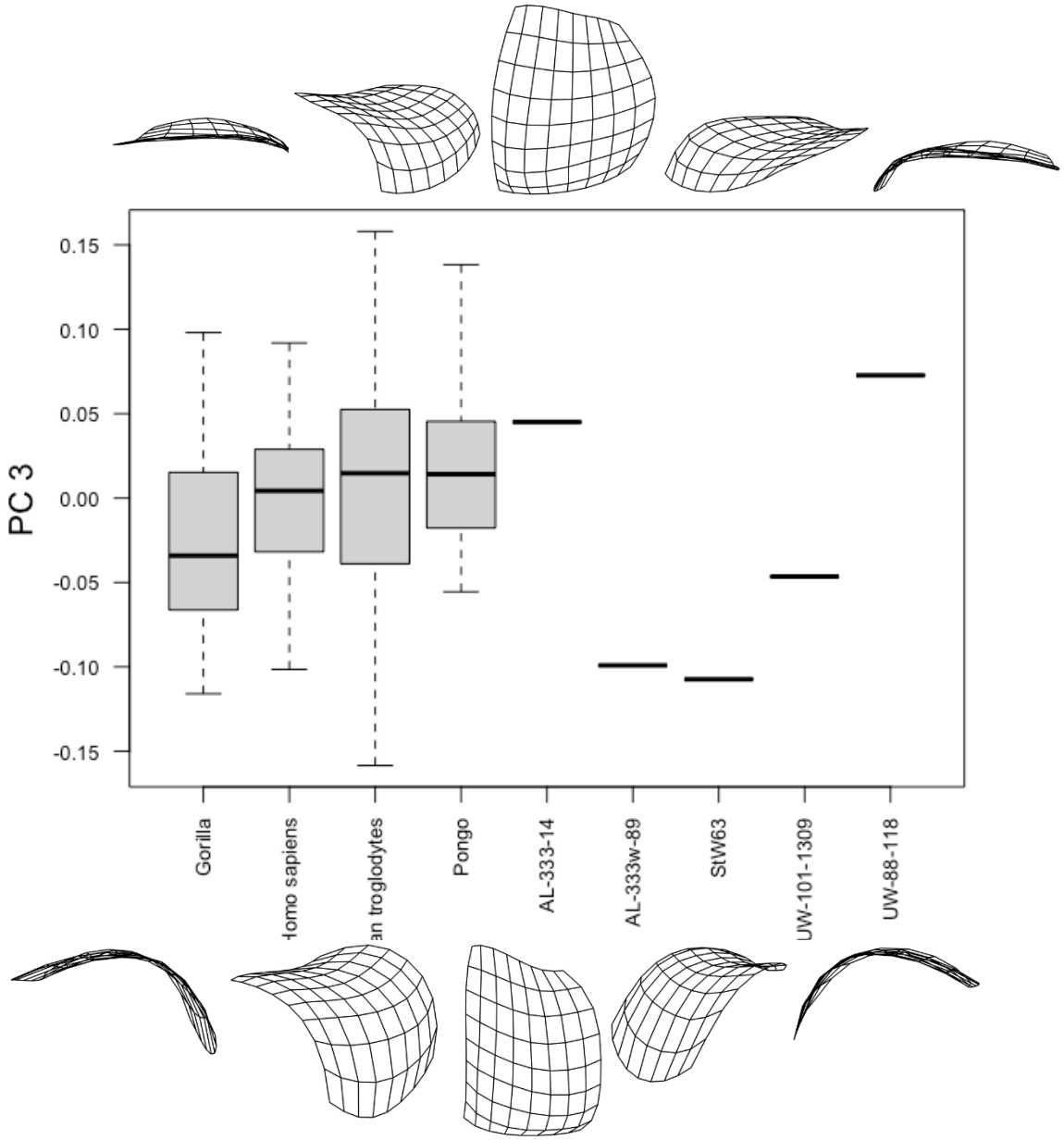

Figure 9.2.4: Boxplot of the third principal component (PC 3) scores for *Gorilla, Homo sapiens, Pan troglodytes,* and *Pongo* compared with fossil specimens AL333-14 (*Australopithecus afarensis*), AL333w-89 (*Australopithecus afarensis*), StW63 (*Australopithecus africanus*), UW-101-1309 (*Homo naledi*), and UW88-118 (*Australopithecus sediba*). Black lines represent the median of the group, boxes are interquartile ranges, whiskers are the non-outlier ranges, and empty circles were outliers.

Table 9.2.5: Tukey honestly significant difference (HSD) *post-hoc* test results on PC 3 scores among *Homo, Pan, Gorilla, and Pongo.* Significant results ($p < 0.05$) were highlighted in bold.

Group		Mean difference	*p*	95% confidence interval	
				Lower bound	Upper bound
Homo sapiens	*Gorilla*	0.025	0.143	-0.005	0.056
	Pan troglodytes	-0.010	0.837	-0.039	0.020
	Pongo	-0.019	0.532	-0.056	0.018
Gorilla	*Homo sapiens*	-0.025	0.143	-0.056	0.005
	Pan troglodytes	-0.035	**0.032**	-0.068	-0.002
	Pongo	-0.045	**0.019**	-0.084	-0.005
Pan troglodytes	*Homo sapiens*	0.010	0.837	-0.020	0.039
	Gorilla	0.035	**0.032**	0.002	0.068
	Pongo	-0.010	0.918	-0.048	0.029
Pongo	*Homo sapiens*	0.019	0.532	-0.018	0.056
	Gorilla	0.045	**0.019**	0.005	0.084
	Pan troglodytes	0.010	0.918	-0.029	0.048

Along the third principal components, the mean value of the *Gorilla* sample differs significantly *Pan troglodytes* and *Pongo*, with no other pairwise comparisons resulting in a significant difference in mean values (table 9.2.5). Assessment of the boxplot representation of PC 3 values shows that the third principal component is of limited value when distinguishing between groups (figure 9.2.4). The range of *Pan troglodytes* spans the entirety of the axis, having both highest and lowest PC 3 scores, and the ranges of all other groups fall within that of *Pan troglodytes*, with the interquartile ranges of *Homo sapiens* and *Pongo*, and the majority of *Gorilla*, falling within the interquartile range of *Pan troglodytes.* The median values of *Homo sapiens*, *Pan troglodytes*, and *Pongo* are very similar to each other (indeed, the medial value of *Pan troglodytes* and *Pongo* are within 0.0006 of each other), with the median value of *Homo sapiens* being slightly above zero. The range of *Gorilla* is also distributed fairly equally across both negative and positive PC 3 values, although its interquartile range is predominantly in the negative aspect, and this sample has the most negative median value of all groups. While the interquartile range of *Pongo* is distributed fairly evenly between the negative and positive halves (skewed slightly to the positive), its 4th quartile has a greater positive range than its corresponding 1st quartile's negative range (figure 9.2.4).

Two of the five fossil specimens have positive PC 3 scores. AL-333-14 (*Australopithecus afarensis*) and UW-88-118 (*Australopithecus sediba*) are within the ranges of all four extant taxa, with AL-333-14 falling within the interquartile ranges of *Pan troglodytes* and *Pongo*. UW-101-1309 (*Homo naledi*) is also in the range of all extant groups, albeit in the negative half. The

remaining two fossil specimens, AL-333w-89 (*Australopithecus afarensis*) and StW-63 (*Australopithecus africanus*), are also found in the negative aspect of PC 3. AL-333w-89 is within the ranges of *Gorilla, Homo sapiens*, and *Pan troglodytes*, while StW-63, which has the most negative PC 3 score, is the only fossil specimen that is not within the *Homo sapiens* range, though it is within the *Gorilla* and *Pan troglodytes* ranges. None of the fossil specimens are found within the interquartile range of *Homo sapiens* along the third principal component.

Bivariate Scatterplots

PC1 vs PC2

A bivariate scatterplot of PC1 against PC2 successfully separates the *Homo sapiens* sample from all non-human great apes, although a slight overlap exists between the morphospaces of the modern human and *Gorilla* samples (figure 9.2.5). The *Homo sapiens* sample is concentrated almost entirely in the right half of the plot, distributed between the upper and lower right quadrants, and weighted slightly to the lower-right quadrant. *Pongo* resides entirely in the lower-left quadrant, while the *Pan troglodytes* morphospace is concentrated in the upper-right, with encroachments into the lower-left and upper-right quadrants. The *Gorilla* sample traverses all four quadrants, though is weighted heavily to the left half of the plot, particularly the upper-left quadrant. While there is some overlap between the *Homo sapiens* and *Gorilla* samples, the other two non-human groups do not overlap with the modern human sample. There is some overlap between all three non-human groups, although *Pongo* overlaps minimally with both, and but for a singular *Gorilla* datapoint, there would be no interaction at all between the two groups. There is considerable overlap between *Pan troglodytes* and *Gorilla*. All the fossils specimens fall within the morphospace occupied exclusively by the *Homo sapiens* sample, owing largely to their strong positive values along PC 1 (figure 9.2.5).

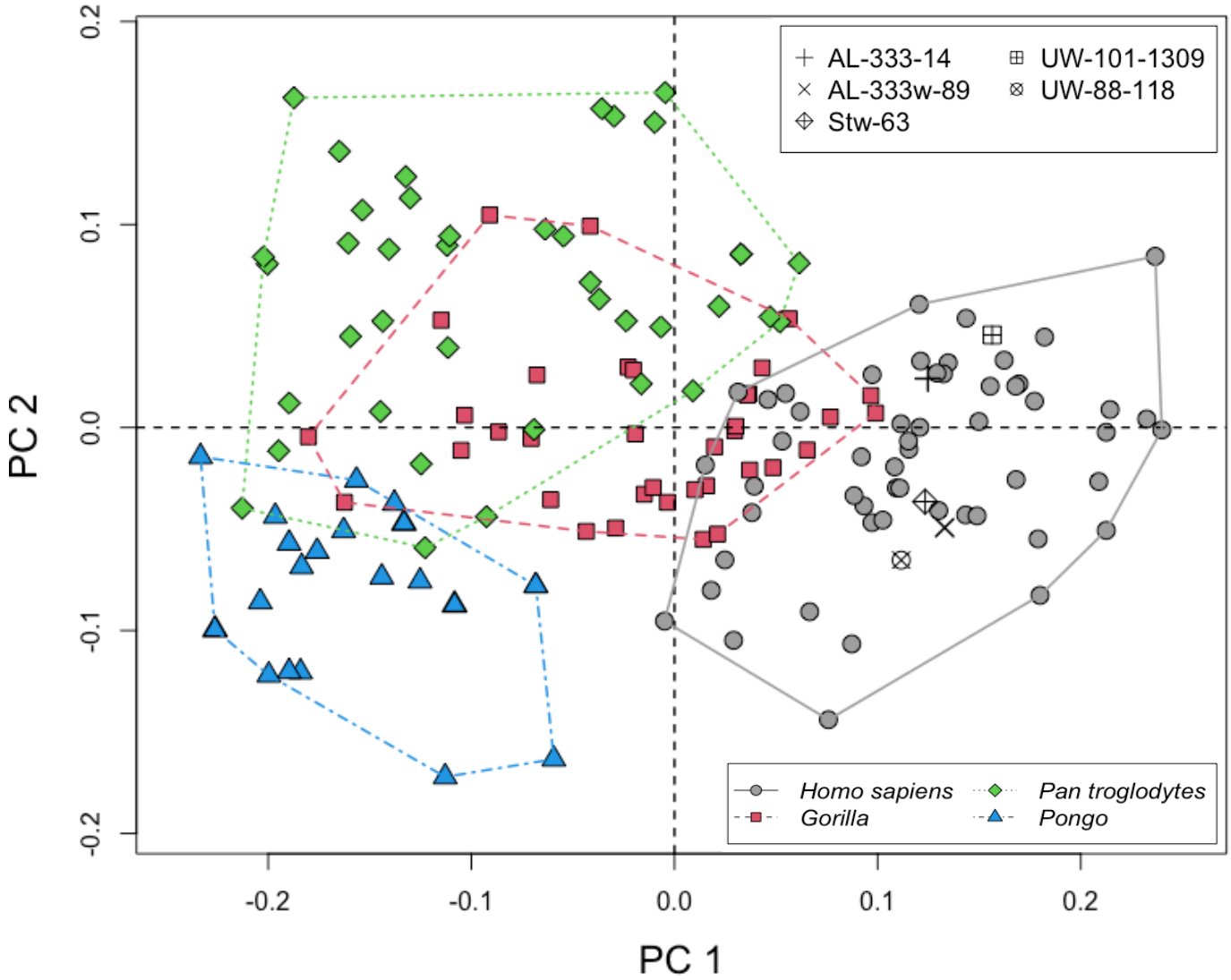

Figure 9.2.5: Scatterplot of the first vs. second principal component (PC 1 (42.3%) vs. PC 2 (12.0%)) scores of extant samples (*Homo sapiens*, Gorilla, Pan *troglodytes,* and *Pongo*) and fossil specimens. The *Homo sapiens* sample is almost completely in the right half of the plot, with the non-human groups dominating the left half. All fossil specimens are found exclusively in the *Homo sapiens* morphospace.

PC1 vs PC3

The bivariate scatterplot of PC 1 against PC 3, shown in figure 9.2.6, shows considerably more overlap between extant groups, which are only clearly separated along the PC 1 axis. There is no discernible separation of the extant taxa along the third PC axis. Again, the morphospace of *Homo sapiens* is distributed evenly between the upper and lower right quadrants. The *Gorilla* sample is distributed across all four quadrants, while being weighted to the lower-left. The *Pan troglodytes* sample is also spread across all four quadrants but is weighted heavily to the left half of the plot. The morphospace of *Pongo* is strongly in the left half of the plot, weighted slightly to the upper-left quadrant. Again, there is some overlap of the morphospaces *Homo sapiens* and *Gorilla* in the right half of the plot, as well as some overlap between the samples of *Homo sapiens* and *Pan troglodytes*, though no interaction between *Pongo* and *Homo sapiens.* The morphospace of *Pan troglodytes* overlaps considerably with those of both *Gorilla* and *Pongo,* and there is also some overlap between the samples of *Gorilla* and *Pongo*. Again, all fossil specimens are located to the right of the plot, and while AL-333-14 (*Australopithecus afarensis*), UW-88-118 (*Australopithecus sediba*), and UW-101-1309 (*Homo naledi*) are within the *Homo sapiens* morphospace, StW-63 (*Australopithecus africanus*) and AL-333w-89 (*Australopithecus afarensis*) are not within the morphospaces of any extant taxa, though they are closet to the vicinity of the *Homo sapiens* sample, being situated to the lower-left of the plot.

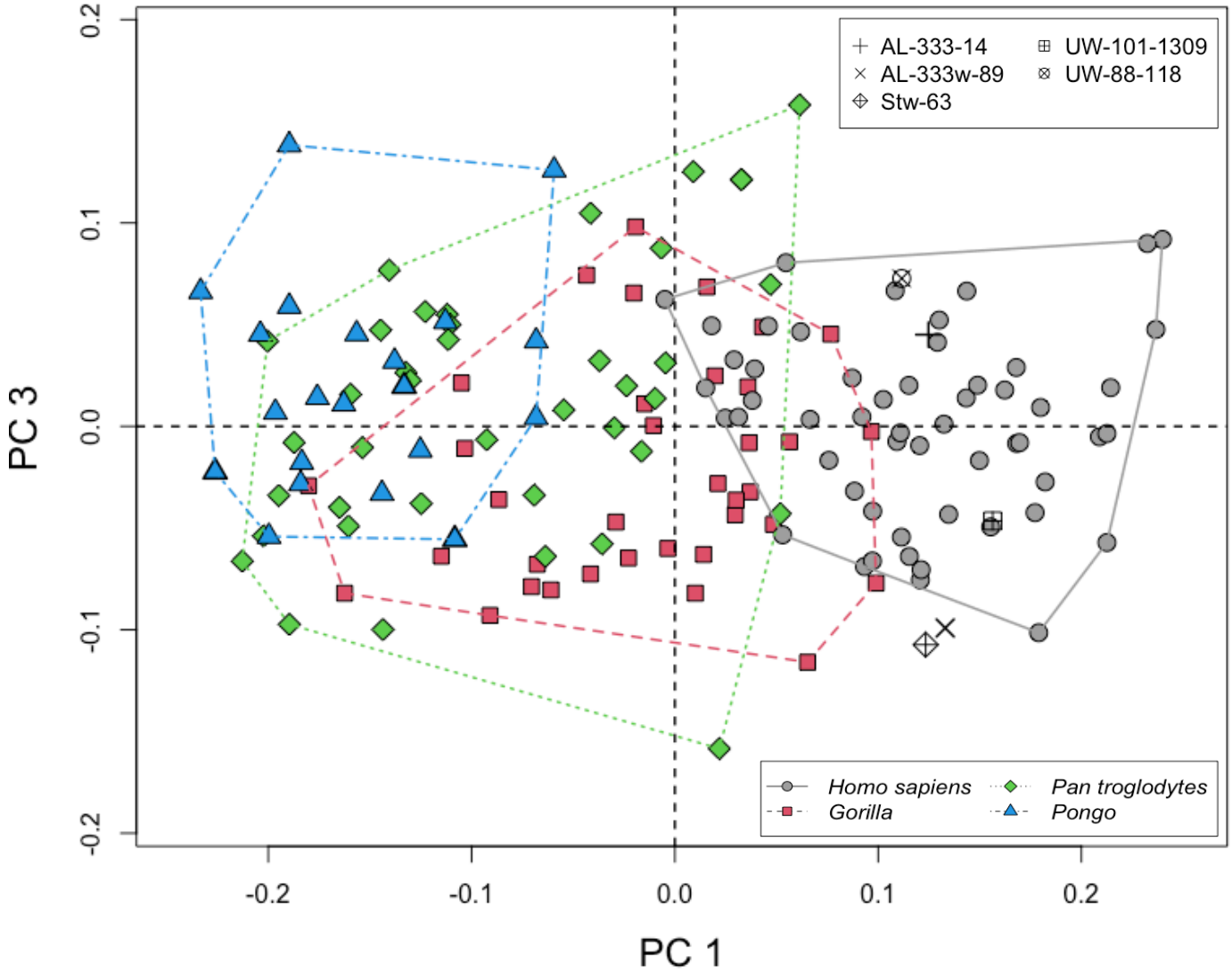

Figure 9.2.6: Scatterplot of the first vs. third principal component (PC 2 (42.3%) vs. PC 3 (9.3%)) scores of extant samples (*Homo sapiens*, Gorilla, Pan *troglodytes,* and *Pongo*) and fossil specimens. Again, the *Homo sapiens* population is almost exclusively in the right half of the plot, with all fossil specimens also in the right half.

PC2 vs PC3

A bivariate scatterplot of PC2 against PC3 is shown in figure 9.2.7. There is considerable overlap between all extant taxa in this plot, with the morphospaces of *Homo sapiens*, *Gorilla*, and *Pan troglodytes* straddling all four quadrants. The *Homo sapiens* sample is weighted slightly to the left half, the *Pan troglodytes* sample weighted slightly to the right half, and the *Gorilla* sample distributed fairly evenly, though weighted slightly to the lower-right quadrant. The *Pongo* sample is concentrated in the upper-left quadrant. The *Homo sapiens* morphospace overlaps considerably with the other groups, with very little of its morphospace independent of any other sample. The *Gorilla* sample is almost completely within the *Pan troglodytes* morphospace, while both African non-human great apes overlap only slightly with *Pongo* in the upper-left quadrant.

The fossil specimens are distributed across all four quadrants, and while they are not all within the *Homo sapiens* morphospace, those that are not fall only marginally outside of it. UW-88-118 (*Australopithecus sediba*) is the only fossil specimen in the upper-left quadrant, being within the *Pongo* morphospace and on the border of the *Homo sapiens* morphospace. AL-333-14 (*Australopithecus afarensis*) is the only fossil specimen found in the upper-right quadrant, and is in the vicinity shared by *Homo sapiens*, *Pan troglodytes*, and *Gorilla*. UW-101-1309 (*Homo naledi*) is in the lower-right quadrant, and on the border of the *Homo sapiens* sample, and within the morphospaces of *Gorilla* and *Pan troglodytes*. AL-333w-89 (*Australopithecus afarensis*) and StW-63 (*Australopithecus africanus*) are in the lower-left quadrant, with AL-333w-89 being the only fossil specimen found exclusively within the *Homo sapiens* morphospace, and StW-63 the only fossil not in any extant group's morphospace. As with the scatterplot of PC 1 against PC 3 (figure 9.2.6), due to the high overlap between extant groups and the wide distribution of fossil specimens, the scatterplot of PC 2 against PC 3 was not informative in distinguishing the affinities of the fossil specimens with the extant taxa, or in distinguishing between extant taxa.

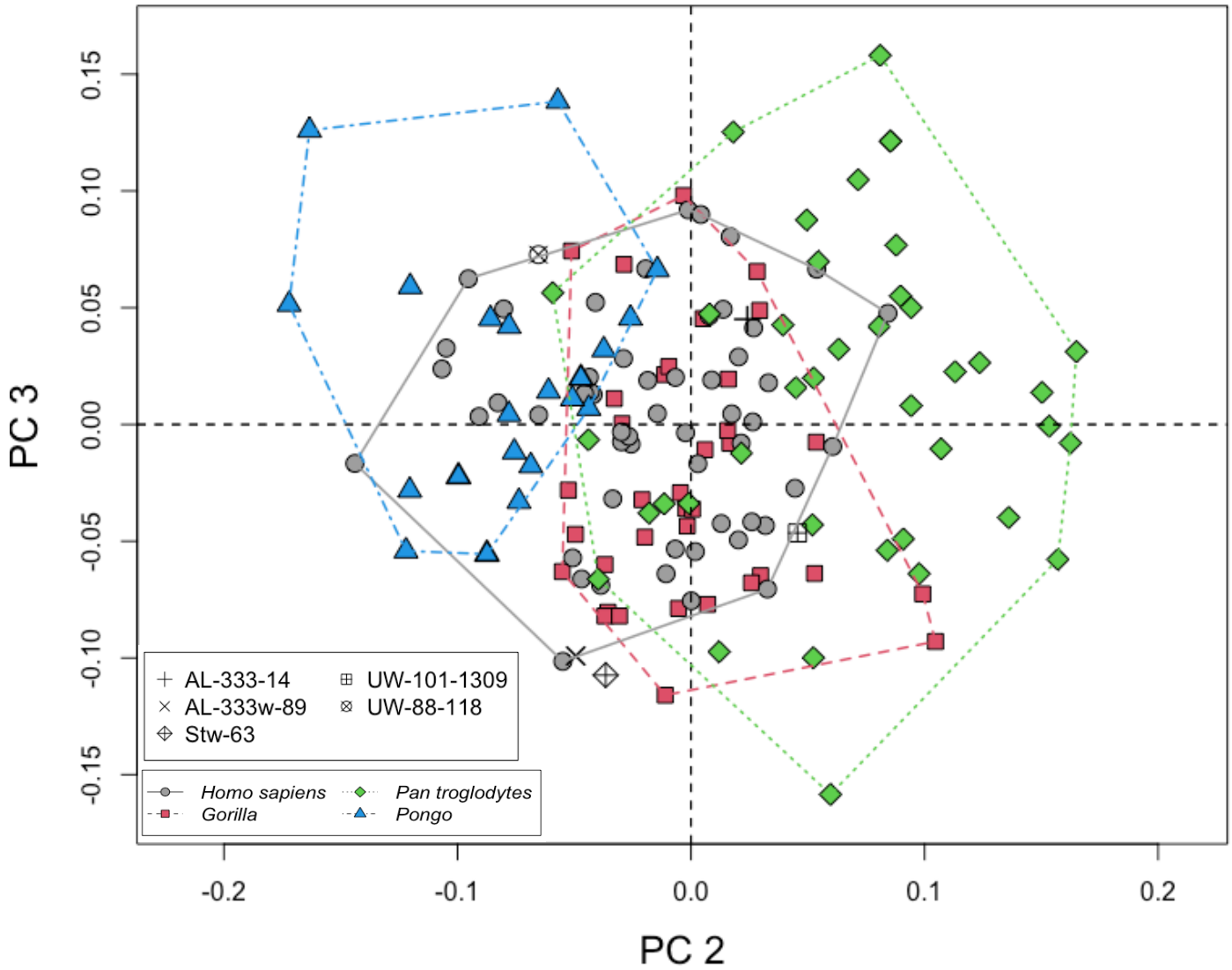

Figure 9.2.7: Scatterplot of the second vs. third principal component (PC 2 (12.3%) vs. PC 3 (9.3%)) scores of extant samples (*Homo sapiens*, Gorilla, Pan *troglodytes,* and *Pongo*) and fossil specimens. There is high overlap between extant groups, and fossil specimens are distributed across the plot.

9.3 Metacarpal-5 canonical variates analysis

A canonical variates analysis (CVA) was carried out on the scores of the first nine principal components, which accounted for 90.05% of the total variance of the PCA, with the extant sample separated by the pre-defined taxonomical groupings. The first canonical variate axis accounted for 58.16% of the total variance, while the second and third CV axes accounted for 25.78% and 16.06% of the total variance, respectively. The overall classification accuracy of the canonical variate analysis on the first nine principal components was 92.7% (*k* = 0.90) (table 9.3.1). *Gorilla* specimens were correctly categorized into their *a priori* sample in 94.4% of cases, with one *Gorilla* specimens being misassigned as *Homo sapiens*, and one as *Pan troglodytes.* Two *Homo sapiens* specimens were erroneously assigned as *Gorilla*, and one as *Pan troglodytes,* resulting in a classification accuracy of 94.4% for the modern human sample. Six of the 40 *Pan troglodytes* specimens were misassigned, leading to an 85.0% classification accuracy for this group, with three specimens each erroneously assigned to *Gorilla* and *Pongo*. All *Pongo* specimens were correctly assigned with a 100% accuracy.

Table 9.3.1: Table of predicted taxa against actual taxa of the canonical variate analysis.

	Gorilla	*Homo sapiens*	*Pan troglodytes*	*Pongo*	*N*
Gorilla	34 (94.4%)	1	1	0	36
Homo sapiens	2	51 (94.4%)	1	0	54
Pan troglodytes	3	0	34 (85.0%)	3	40
Pongo	0	0	0	21 (100.0%)	21

MANOVA along the three canonical variates axes returned significant results between extant groups ($F(3, 147) = 113.24$, $p < 0.001$, Wilks' $\Lambda = 0.037$). Results of the one-way analysis of variance tests performed on the CV scores of the extant sample, with the sample divided by *a priori* taxonomic groups, are shown in table 9.3.2. The ANOVA results were significant ($p < 0.05$) along all three CV axes. Results of the Tukey HSD tests are shown in table 9.3.3. Along the first canonical variate axis, mean values of all groups were significantly different from each other, except for between *Pan troglodytes* and *Pongo* ($p = 0.669$, 95% C.I. = -1.006, 0.395), while the means of all groups were significantly different from each other along the second CV axis. Along the third canonical variate axis, all groups were distinct from each other, except for *Gorilla* and *Pongo* ($p = 0.969$, 95% C.I. = -0.590, 0.838).

Table 9.3.2: Results of analysis of variance on canonical variate scores on extant groups.

Canonical Variate	DF	Sum of Squares	Mean Squares	*F* Value	*p*
CV 1	3, 147	567.5	189.2	189.2	**<0.001**
CV 2	3, 147	251.5	83.85	83.85	**<0.001**
CV 3	3, 147	156.7	52.23	52.23	**<0.001**

Table 9.3.3: *P*-values for Tukey's HSD pairwise comparisons of canonical variate scores.

	Homo sapiens	Gorilla	Pan troglodytes	Pongo
Canonical Variate 1 (63.45%)				
Homo sapiens	-	**<0.001**	**<0.001**	**<0.001**
Gorilla		-	**<0.001**	**<0.001**
Pan troglodytes			-	0.670
Pongo				-
Canonical Variate 2 (25.77%)				
Homo sapiens	-	**<0.001**	**<0.001**	**<0.001**
Gorilla		-	**<0.001**	**<0.001**
Pan troglodytes			-	**<0.001**
Pongo				-
Canonical Variate 3 (10.79%)				
Homo sapiens	-	**<0.001**	**<0.001**	**<0.001**
Gorilla		-	**<0.001**	0.97
Pan troglodytes			-	**<0.001**
Pongo				-

Each of the five fossil specimens were classified as *Homo sapiens* by the CVA*,* four with a confidence of >98% (AL-333-14, AL-333w-89 (*Australopithecus afarensis*); StW-63 (*Australopithecus africanus*); UW-88-118 (*Australopithecus sediba*)). UW-101-1309 (*Homo naledi*) was classified into the *Homo sapiens* group with a lesser certainty of 74.40%, having a likelihood of 25.50% as belonging to the *Gorilla* sample (table 9.3.4).

Table 9.3.4: Canonical variates analysis (CVA) classification results of fossil specimens based on scores of the first nine principal components. The column to the right shows the group to which each fossil specimen was classified by the canonical variate analysis. Results were in percentage.

	Homo sapiens	*Gorilla*	*Pan troglodytes*	*Pongo*	Classification
AL-333-14	99.80	0.20	0.00	0.00	*Homo sapiens*
AL-333w-89	99.90	0.10	0.00	0.00	*Homo sapiens*
StW-63	99.90	0.10	0.00	0.00	*Homo sapiens*
UW-101-1309	74.40	25.50	0.00	0.00	*Homo sapiens*
UW-88-118	98.70	1.30	0.00	0.00	*Homo sapiens*

First Canonical Variate Axis

Shape change along the first canonical variate axis, which accounted for 58.16% of the total variance of shape, corresponded to shape change along the first principal component, described in section 9.2 (figure 9.2.2). The first CV axis distinguishes the *Homo sapiens* sample, which is predominantly in the positive aspect of the axis, from *Pan troglodytes* and *Pongo*, which is in the negative half. The *Gorilla* sample is distributed evenly between the negative and positive aspects, with a median value approximating zero (figure 9.3.1). There is considerable overlap between the CV 1 scores of *Homo sapiens* and *Gorilla*, and the fourth quartile of *Pan troglodytes* overlaps with the first quartile of *Homo sapiens*. However, there is no overlap of the *Homo sapiens* and *Pongo* samples. All three non-human groups overlap considerably in their CV 1 scores, with the range of *Pan troglodytes* overlapping the lower half of *Gorilla* and most of *Pongo.* All of the fossil specimens have positive CV 1 values and are found within the interquartile range of *Homo sapiens*, and outside of the ranges of all non-human taxa.

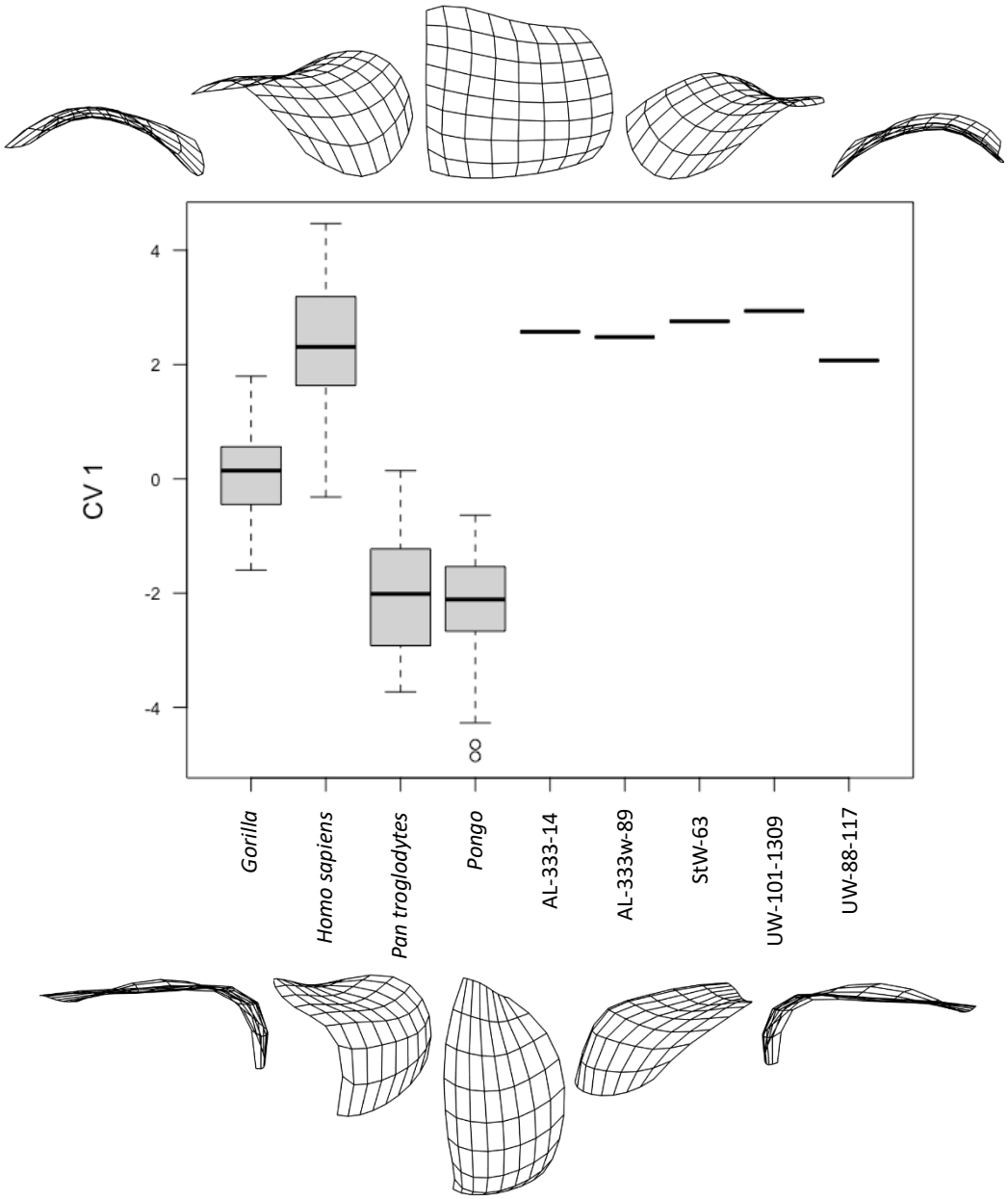

Figure 9.3.1: Boxplot of the scores of the first Canonical Variate axis of the fifth metacarpal's proximal articular surface for *Gorilla, Homo sapiens, Pan troglodytes,* and *Pongo* compared with fossil specimens AL-333-14, AL-333w-89 (*Australopithecus afarensis*); StW-63 (*Australopithecus africanus*); UW-101-1309 (*Homo naledi*); and UW-88-118 (*Australopithecus sediba*). Black lines represent the median of the group, boxes are interquartile ranges, and whiskers are the non-outlier ranges.

Second Canonical Variate Axis

Shape change along the second canonical variate axis, which accounted for 25.78% of the total variation, corresponded to shape change along the second principal component (figure 9.2.3). The second canonical variate axis is effective in separating *Pongo*, being entirely in the negative half of the axis, from the *Gorilla* sample, which is entirely in the positive (figure 9.3.2). *Pan troglodytes* occupies both negative and positive values, though is weighted towards the positive and has the most positive range of all groups. The *Homo sapiens* sample overlaps considerably with all three non-human samples, also having both negative and positive scores, though is weighted to the negative. The range of *Gorilla* is entirely within that of *Pan troglodytes*, while the upper half of *Pongo* is within the first quartile of *Pan troglodytes.*

The fossil specimens are found in both the negative and positive aspects of CV 2, with AL-333w-89 (*Australopithecus afarensis*), StW-63 (*Australopithecus africanus*), and UW-88-118 (*Australopithecus sediba*) having negative CV 2 scores, and AL-333-14 (*Australopithecus afarensis*) and UW-1010-1309 (*Homo naledi*) having positive scores. UW-101-1309, which has the highest score of all fossil specimens, is the only fossil specimen to fall outside the range of *Homo sapiens*, being within the fourth quartiles of *Gorilla* and *Pan troglodytes.* AL-333-14 has a similar value to the median of the *Pan troglodytes* sample and is in the 1st quartile of *Gorilla* and the 4th quartile of *Homo sapiens.* AL-333w-89, StW-63, and UW-88-118 are all within the interquartile range of *Homo sapiens*, as well as being within the 1st quartile of *Pan troglodytes*, and outside the ranges of *Gorilla* and *Pongo*.

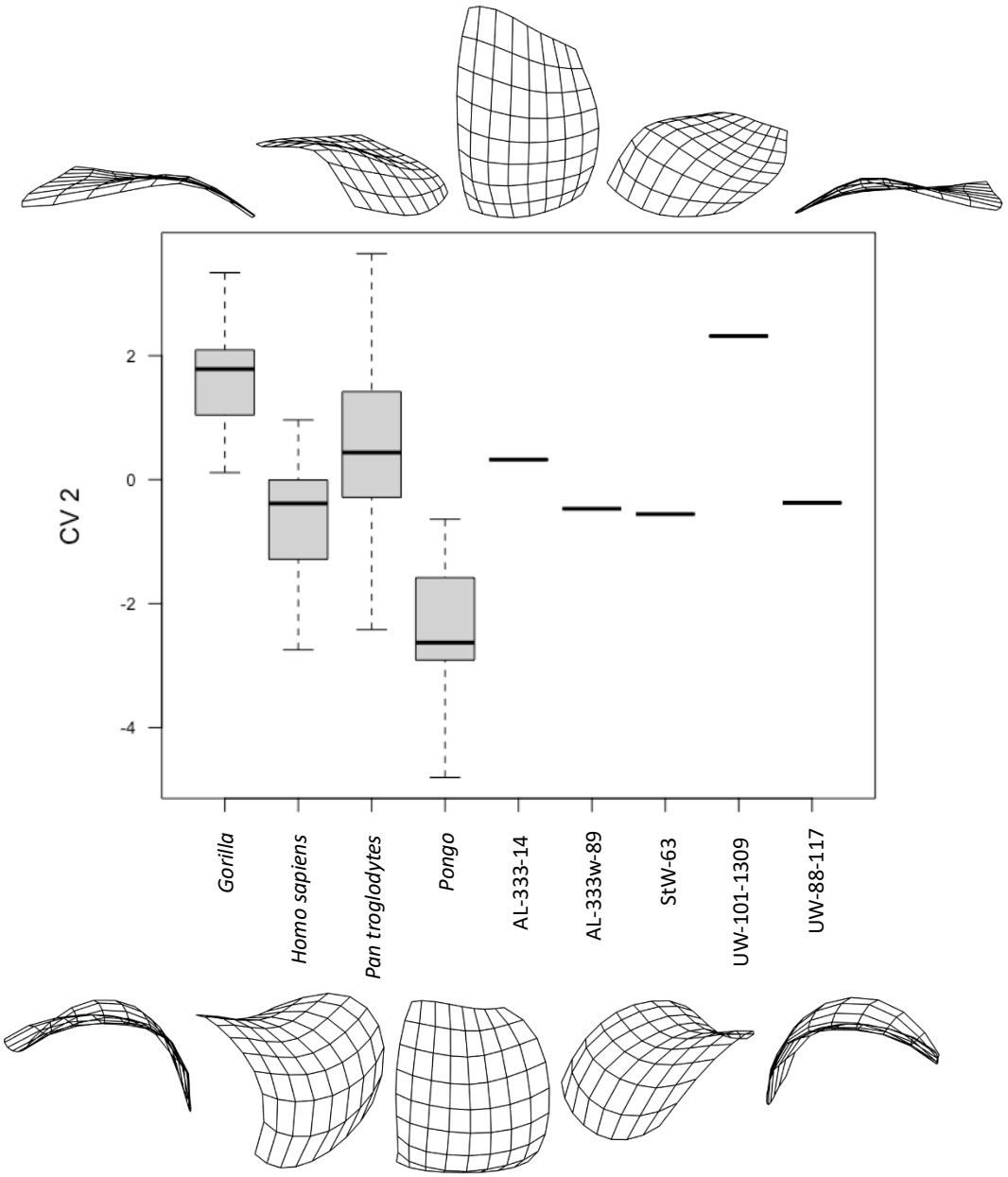

Figure 9.3.2: Boxplot of the scores of the second Canonical Variate axis of the fifth metacarpal's proximal articular surface for *Gorilla, Homo sapiens, Pan troglodytes,* and *Pongo* compared with fossil specimens AL-333-14, AL-333w-89 (*Australopithecus afarensis*); StW-63 (*Australopithecus africanus*); UW-101-1309 (*Homo naledi*); and UW-88-118 (*Australopithecus sediba*). Black lines represent the median of the group, boxes are interquartile ranges, and whiskers are the non-outlier ranges.

Third Canonical Variate Axis

The third canonical variate axis accounts for 16.06% of the total variance in shape, corresponding to the shape change seen in the third principal component, described in section 9.2 (figure 9.2.4). CV 3 best separates *Pan troglodytes* from *Gorilla* and *Pongo*, though there is considerable overlap in the ranges of all groups. Tukey's honestly significant difference test along the values of CV 3 found no significant difference between the values of the *Gorilla* and *Pongo* samples (table 9.3.4), and their ranges are comparable, being primarily in the negative aspect of CV 3 (figure 9.3.3). The *Homo sapiens* and *Pan troglodytes* samples are weighted more to the positive aspect of CV 3, though the range of the *Homo sapiens* sample has a greater negative weighting, with the *Pan troglodytes* range nesting within that of *Homo sapiens.*

The fossil specimens display a range of negative and positive CV 3 scores, though they are not dispersed widely from the midpoint of CV 3. They are all within the interquartile range of *Homo sapiens,* while all but AL-333-14 (*Australopithecus afarensis*) are also within the ranges of all four extant taxa. AL-333-14 has the highest CV 3 value, being higher than the maximum values of *Gorilla* and *Pongo*, though is within the interquartile range of *Pan troglodytes* as well as *Homo sapiens*.

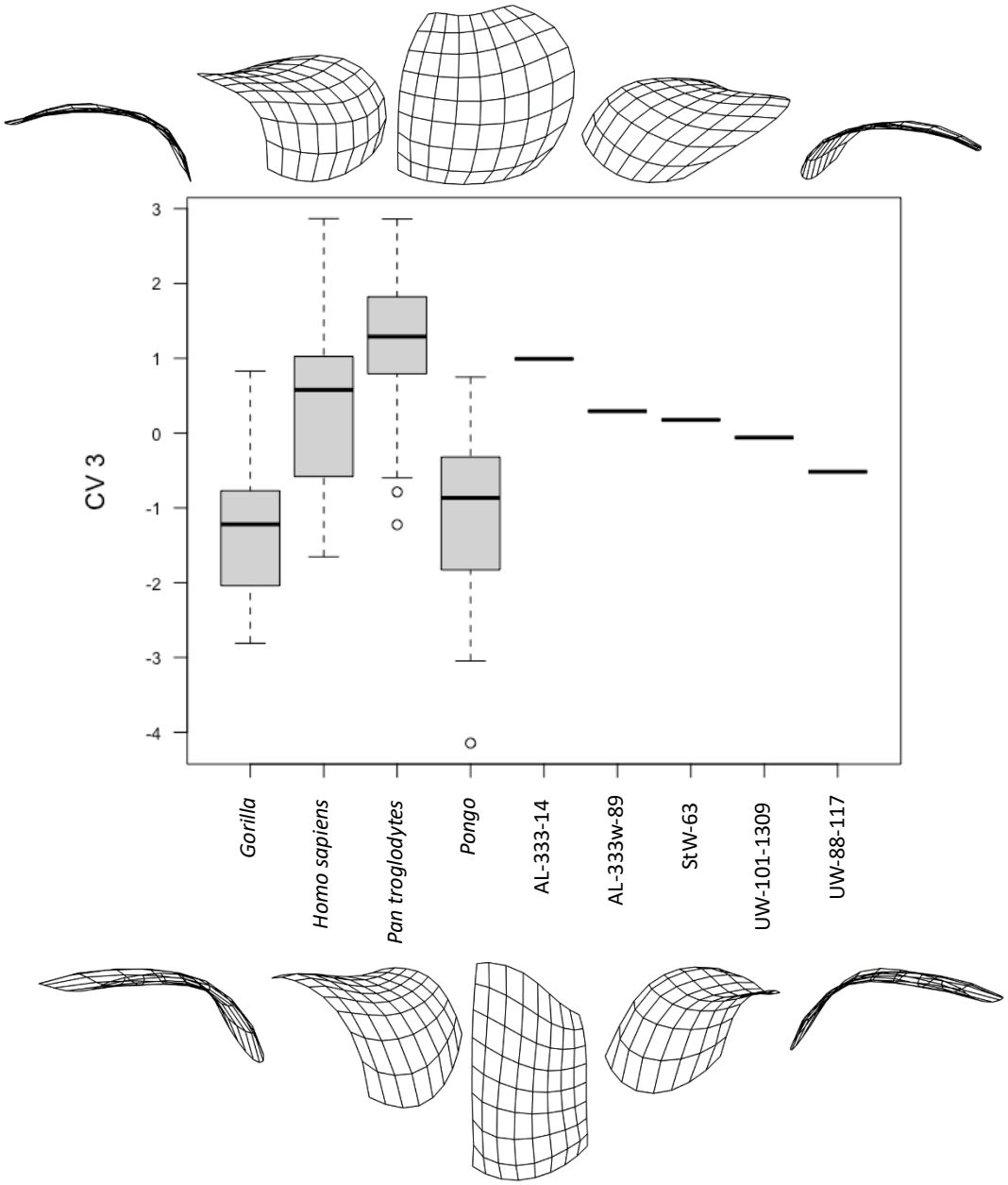

Figure 9.3.3: Boxplot of the scores of the third Canonical Variate axis of the fifth metacarpal's proximal articular surface for *Gorilla, Homo sapiens, Pan troglodytes,* and *Pongo* compared with fossil specimens AL-333-14, AL-333w-89 (*Australopithecus afarensis*); StW-63 (*Australopithecus africanus*); UW-101-1309 (*Homo naledi*); and UW-88-118 (*Australopithecus sediba*). Black lines represent the median of the group, boxes are interquartile ranges, and whiskers are the non-outlier ranges.

Bivariate scatterplots

CV1 vs CV2

A scatterplot of CV 1 against CV 2 is shown in figure 9.3.4. The right half of the plot is domiated by *Homo sapiens*, although *Gorilla* is distributed evenly between the left and right halves. The vertical axis of the plot (CV 2) discriminates between *Gorilla* and *Pongo*, with the *Pan troglodytes* and *Homo sapiens* samples distributed across both the upper and lower halves. While there is a degree of overlap between the 95% confidence ellipses of all groups with each other, there is considerable overlap between the samples of *Gorilla* and *Pan troglodytes*, *Pan troglodytes* and *Pongo*, and some overlap between *Homo sapiens* and *Gorilla*. Every fossil hominin specimen bar one is concentrated tightly within the *Homo sapiens* sample distribution and 95% confidence ellipse. UW-101-1309 (*Homo naledi*) is found above the *Homo sapiens* sample, and is not within the confidence ellipse of any extant group.

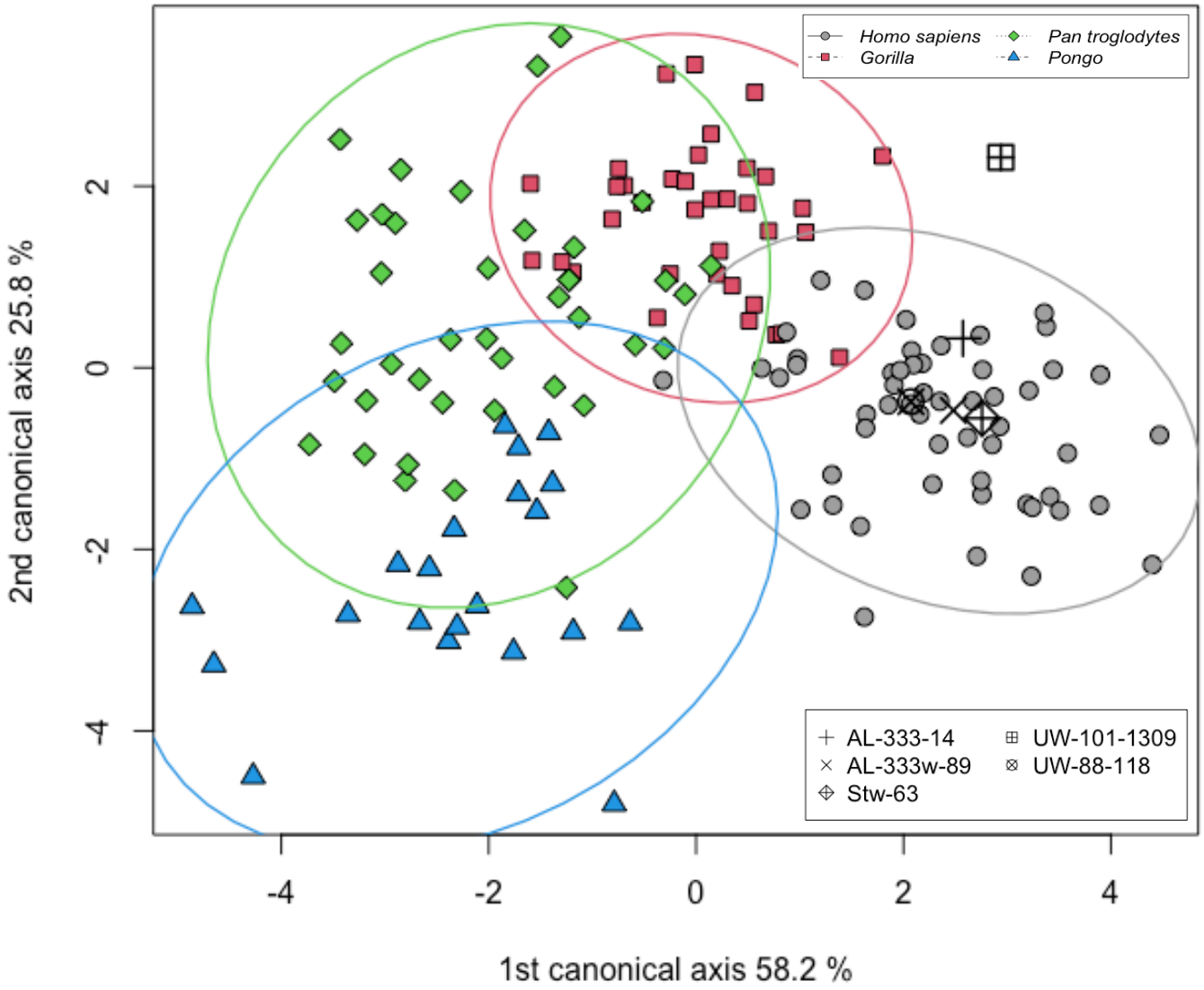

Figure 9.3.4: Scatterplot of the first vs. second canonical variates axis (CV 1 (58.2%) vs. CV 2 (25.8%)) scores of extant samples (*Homo sapiens*, Gorilla, Pan *troglodytes,* and *Pongo*) and fossil specimens. All fossil specimens, with the exception of UW 101-1309 (*Homo naledi*), are within the 95% confidence ellipse of *Homo sapiens.*

CV1 vs CV3

There is overlap in the populaitons of all groups in the bivariate scatterplot of CV 1 against CV 3, which is shown in figure 9.3.5. The *Gorilla* sample is concentrated centrally and overlaps considerably with *Pongo* to the left, *Homo sapiens* to the right, and with *Pan troglodytes* above. While the 95% confidence ellipse of *Homo sapiens* intersects those of the other three groups, there is no actual overlap of the modern human sample with *Pongo* or *Pan troglodytes*, though there is considerable overlap between the samples of all non-human groups. All fossil specimens are found exclusively within the 95% confidence ellipse of the *Homo sapiens* poulation.

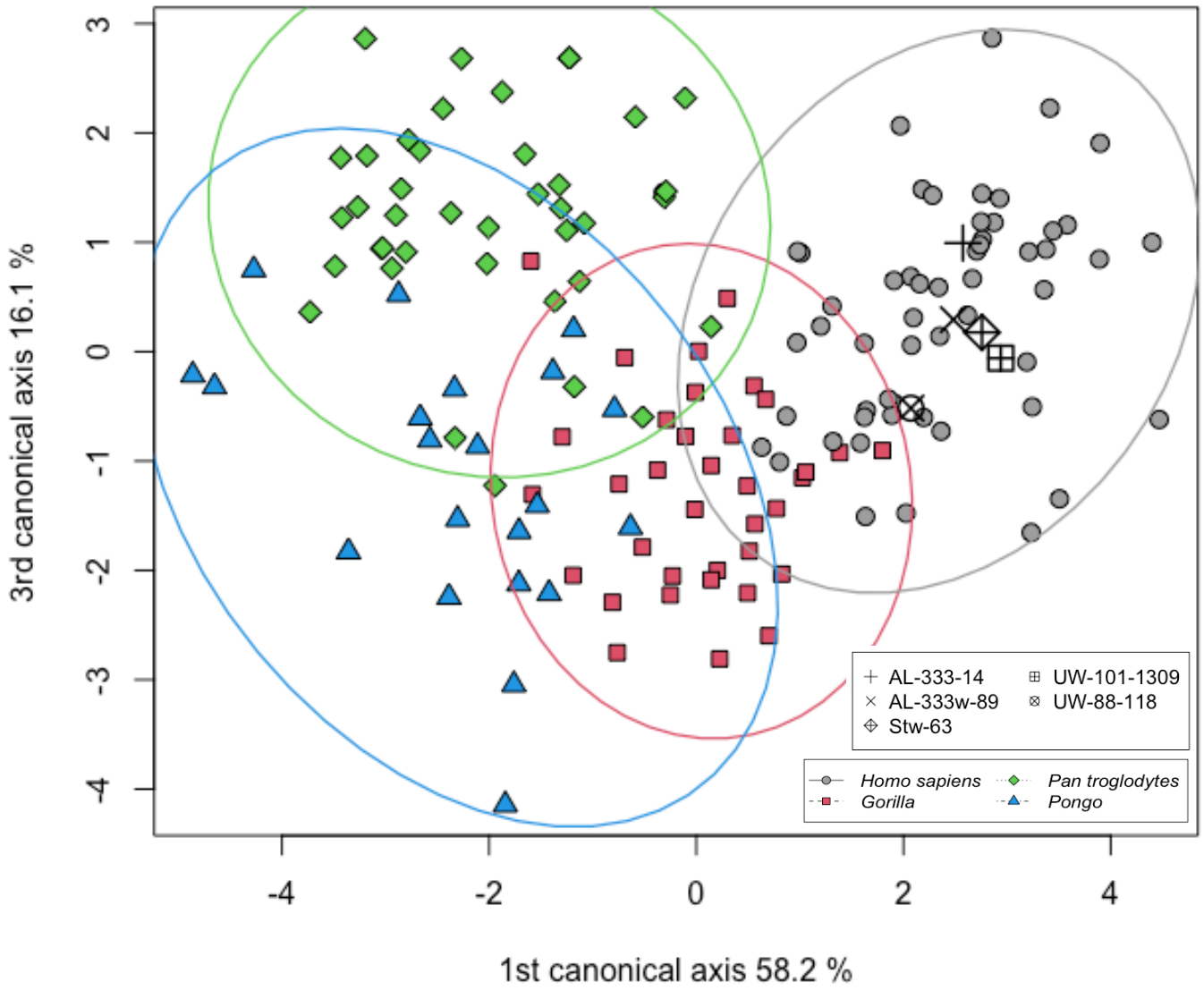

Figure 9.3.5: Scatterplot of the first vs. third canonical variates axis (CV 1 (58.2%) vs. CV 3 (16.1%)) scores of extant samples (*Homo sapiens*, Gorilla, Pan *troglodytes,* and *Pongo*) and fossil specimens. All fossil specimens are found exclusively within the 95% confidence ellipse of the *Homo sapiens* poulation.

CV2 vs CV3

The bivariate scatterplot of CV 2 against CV 3 is shown in figure 9.3.6. The *Homo sapiens* and *Pan troglodytes* samples overlap to a great extent in this plot, which distinguishes mostly between *Gorilla* and *Pongo*, though there is overlap of the 95% confidence ellipses of all groups. The *Pongo* sample is concentrated in the lower-left quadrant, with the *Gorilla* sample in the lower-right. *Homo sapiens* is concentrated centrally, though skewed towards the upper centre of the plot, whlie *Pan troglodytes* is concentrated in the upper-right quadrant though spans all four quadrants. All but one of the fossil specimens are found within the *Pan troglodytes* and *Homo sapiens* confidence ellipses, with UW-101-1309 (*Homo naledi*) found in the confidence ellipses of the non-human African Great Apes. StW-63 (*Australopithecus africanus*) and UW-88-118 (*Australopithecus sediba*) are found in the space where humans, chimpanzees and orangutans interject.

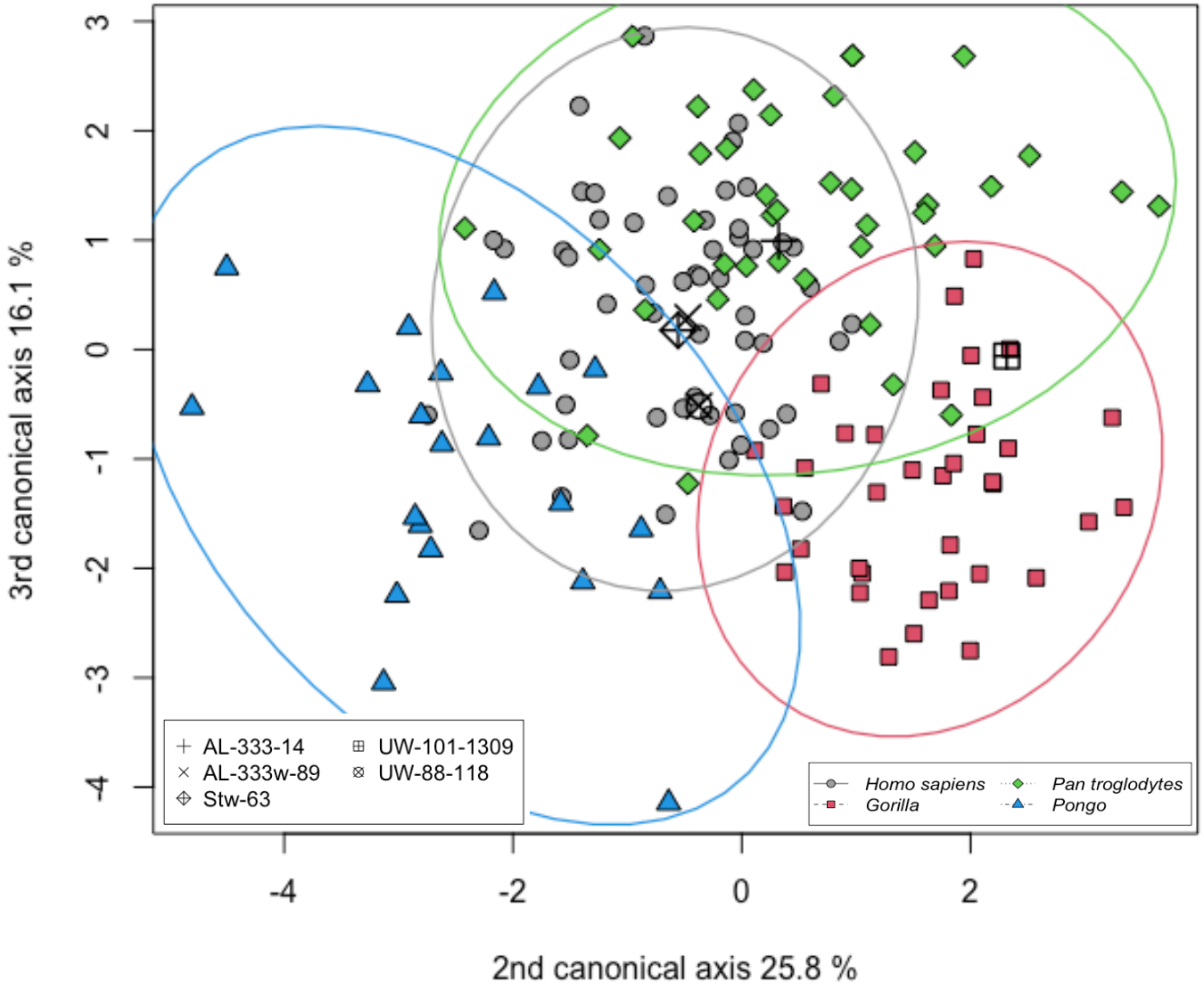

Figure 9.3.6: Scatterplot of the second vs. third canonical variates axis (CV 2 (25.8%) vs. CV 3 (16.1%)) scores of extant samples (*Homo sapiens*, Gorilla, Pan *troglodytes,* and *Pongo*) and fossil specimens.

9.4 Metacarpal-5 Procrustes distances

The Procrustes distances of the extant group mean shapes from each other are shown in table 9.4.1, with the Procrustes distance of each fossil specimen from the average shape of each extant taxon group shown in table 9.4.2. Of the extant groups, the mean shapes of *Gorilla* and *Pan troglodytes* are the most similar to each other, followed by *Homo sapiens* and *Gorilla*. The *Homo sapiens* mean shape is most different from those of *Pan troglodytes* and *Pongo*, while *Pongo* is relatively distinct from all other groups. All five fossil specimens are closer to the mean shape of *Homo sapiens* than to the mean shape of any other group, with UW-88-118 (*Australopithecus sediba*) being the farthest away from the *Homo sapiens* mean shape, though remaining closer to the modern human mean shape than to any other group's mean shape.

Table 9.4.1: Procrustes distances (above the horizontal) between the mean shapes of extant groups.

	Homo sapiens	*Gorilla*	*Pan troglodytes*	*Pongo*
Homo sapiens	-	0.156	0.222	0.285
Gorilla		-	0.121	0.187
Pan troglodytes			-	0.169
Pongo				-

Table 9.4.2: The Procrustes distance of each fossil from the mean shape of each extant taxon group.

	Homo sapiens	*Gorilla*	*Pan troglodytes*	*Pongo*
AL333-14	0.160	0.224	0.265	0.340
AL333w-89	0.156	0.212	0.285	0.333
StW63	0.147	0.200	0.274	0.326
UW-101-1309	0.171	0.227	0.288	0.374
UW-88-118	0.219	0.253	0.311	0.344

Results of the Shapiro-Wilk tests for normality along the linear distances of extant species from the mean value of their respective group are shown in table 9.4.3. The Procrustes distances of the *Homo sapiens* and *Pongo* samples from their respective mean shapes were not normally distributed, therefore the Procrustes distances of the whole sample was transformed by natural log, resulting in a normal distribution for all groups (table 9.4.3).

Table 9.4.3: Results of the Shapiro-Wilk normality tests performed on the individual distances distribution from their respective group mean shapes (top row), and the corresponding square-root-transformed data. Calculations were performed on Procrustes distances.

	Homo sapiens	*Gorilla*	*Pan troglodytes*	*Pongo*
p	**0.026**	0.244	0.262	**0.017**
p (transformed)	0.897	0.406	0.323	0.179

Fossil distances (in standard deviations from the mean of the distance of each individual of the group from the group mean), with the upper-tail cumulative distribution function of each fossil relative to each extant group (in percentage) are shown in table 9.4.4. All fossils were closer to the mean shape of *Homo sapiens* than to the mean shape of any other group, with StW-63 (*Australopithecus africanus*) having the shape closest to the *Homo sapiens* mean shape, being closer than 19.47% of the human sample. UW-88-118 (*Australopithecus sediba*) was least similar to the *Homo sapiens* mean shape, being closer than 0.53% of the human sample, an approximately similar value to its distance from the *Gorilla* and *Pan troglodytes* mean shapes.

Table 9.4.4: Procrustes distances in standard deviations of each fossil in the study from the mean of the distance of each individual of each extant group from the mean of its respective group. The value of the upper tail cumulative distribution function multiplied by 100 were in parentheses.

	Homo sapiens	*Gorilla*	*Pan troglodytes*	*Pongo*
AL333-14	1.239 (10.78%)	2.146 (1.59%)	1.995 (2.30%)	3.250 (0.06%)
AL333w-89	1.133 (12.85%)	1.907 (2.82%)	2.278 (1.14%)	3.176 (0.07%)
StW63	0.861 (19.47%)	1.680 (4.65%)	2.123 (1.69%)	3.110 (0.09%)
UW-101-1309	1.510 (6.56%)	2.215 (1.34%)	2.313 (1.04%)	3.578 (0.02%)
UW-88-118	2.553 (0.53%)	2.663 (0.39%)	2.613 (0.45%)	3.298 (0.05%)

Section IV: Discussion, limitations of the project, and scope for future research

10 Discussion

This project aimed to compare and explore the functional importance of the shape of the fourth and fifth carpometacarpal joints of modern humans, extant non-human great apes, and extinct fossil hominins within the context of early development of hominin lithic technology. These aims were addressed by comparing the morphology of the joint surfaces of modern humans, non-human great apes, and selected fossil hominin specimens using three-dimensional geometric morphometric methods in order to investigate and identify adaptations of the joint surfaces unique to modern humans, and to assess the presence of any such morphologies in fossil hominin taxa so as to inform conclusions on the functionality of the hamate-metacarpal joints of ancestral hominins. Results indicate that several features of the hamate-metacarpal joints of modern humans that confer freedom of movement and force transmission associated with tool-using behaviour are distinct among extant great apes, and these same features are identifiable to varying extents among the fossil hominin specimens analysed. Morphological variations unique to modern humans at the hamate-metacarpal joints appear to be concentrated at the hamate-MC5 joint surface.

10.1 Comparisons between extant taxa

10.1.1 The hamate-metacarpal surface

Results of this project show that the hamate joint surface of modern humans varies significantly from non-human great apes. The hamate-metacarpal joint surface is dominated by the articulation for the fifth metacarpal, which occupies a larger proportion of the hamate's distal articular surface area relative to the corresponding surface for the fourth metacarpal. The overall surface is palmodorsally flatter in humans, and the surfaces of the two joints face divergent directions in modern humans, with the surface for the fourth metacarpal facing distally, and the fifth angled to face a mediodistal direction. These shape differences are reflected in the results

of the first principal component for the hamate-metacarpal surface, which accounts for 30.8% of the shape difference, and distinguished the human sample from all other taxa (figure 5.2.2). In addition to variation in relative size and orientation of the two joint surfaces, the shapes of the fourth and fifth hamate-metacarpal joints of modern humans also exhibit features that distinguish them from non-human taxa. The morphology of the human fifth metacarpal surface itself is notable in having a saddle-shaped morphology, with a gentle palmodorsal concave curvature and a similarly mild mediolateral convex curvature, while the surface for the fourth metacarpal is comparatively flat and featureless, with only a vanishingly mild distal bevelling of its palmar surface, relative to non-human great apes.

The non-human taxa largely lack these features, and generally display a hamate-metacarpal surface in which both articulations face distally and are strongly palmodorsally concave, with the fifth metacarpal surface being more mediolaterally flat and varyingly concave at its dorsal portion only, and the fourth displaying a complex and irregular surface, with both surfaces exhibiting strong distal bevelling of their palmar borders. Perhaps most notably in extant non-human great ape taxa, the fourth carpometacarpal surface occupies a proportionately greater surface area than the fifth, which is narrowed mediolaterally relative to the articulation for the fourth metacarpal. The proportionately larger surface area of the fifth carpometacarpal joint relative to the fourth is indicative of, and likely results from, the increased loads transmitted across this joint during human manipulative behaviours, as suggested by Marzke (1983). Key, Dunmore & Marzke (2019) demonstrated that during Plio-Pleistocene manual behaviours, the fifth finger is frequently and heavily recruited and loaded, alongside the thumb and second digit, with the fifth digit often being located directly beneath or very close to the point of impact when flakes are removed via freehand percussive activities (Key & Dunmore, 2015; Key, Dunmore & Marzke, 2019; Marzke & Shackley, 1986; Marzke *et al.,* 1998). The fifth digit therefore experiences a high proportion of the force incurred on the hand during core reduction due to its positioning in line with the point of impact (Key, Dunmore & Marzke, 2019). These high loads are then transmitted from the finger and across the metacarpal to the carpal complex. A larger surface area of the fifth carpometacarpal joint facilitates the increased load transmission incurred on the joint during Plio-Pleistocene core-reduction activities.

A further notable feature that distinguishes the human hamate-metacarpal articular surface from non-human taxa has received considerably less attention by previous researchers, though the results of this project suggest that it is nonetheless a significant distinguishing feature in the modern human sample, and may facilitate both an increased mobility of the fifth metacarpal, as well as more effective transmission of loads incurred upon the digit. In modern humans, the surfaces for the two metacarpals on the hamate's distal articulation are notably divergent from one another, with the hamate-fifth metacarpal surface facing a more mediodistal direction relative to the distally-facing fourth metacarpal surface (see section 5.2, figure 5.2.2). This arrangement is in stark contrast to the non-human condition, in which both surfaces face distally to largely the same extent. This feature is exaggerated by the two previously-discussed distinguishing features of the fifth carpometacarpal surface, with the medial expansion and convex curvature of the surface amplifying the proximo-medial orientation of the joint surface.

This ulnar deviation of the fifth metacarpal has several outcomes. Firstly, it results in a fifth ray in which its longitudinal axis is also angled mediodistally, with this angle increasing away from the midline of the hand as it progresses distally. This obtuse longitudinal axis of the fifth metacarpal exaggerates the flared radiation of the metacarpal heads and fingers away from the midline of the hand, therefore increasing the width of the transverse arch of the distal metacarpal heads in modern humans and widening the mediolateral width of the palm relative to the wrist. Secondly, a medioproximal orientation of the fifth metacarpal, in combination with the progressively shorter length of the fourth and fifth metacarpals relative to the third (Napier, 1993), augments the oblique orientation of alignment of the metacarpal heads, and the obliquity of the hand when flexed (demonstrated by the oblique direction of the flexure creases of the hand, running from the lower ulnar side of the palm to the upper radial side) (Napier, 1993). This anatomical configuration ensures that when a cylindrical object is held against the palm by the fingers in a power squeeze grip, it is positioned obliquely from the base of the fifth metacarpal to the head of the second (Young, 2003). During hammering movements, the wrist deviates in an ulnar direction just before impact. Combined with the oblique positioning of an object during a power squeeze grip, this aligns the object with the longitudinal axis of the forearm at the moment of strike, thereby increasing the velocity of the tool and providing maximal mechanical advantage (Marzke, Wullstein and Viegas, 1992; Young, 2003).

Thirdly, the axis of flexion and rotation of the fifth metacarpal is reorientated relative to the longitudinal axis of the second-to-fourth metacarpals. It has been noted that flexion of the fifth metacarpal is accompanied by supination. A mediodistal-proximolateral orientation of the axis of flexion results in the fifth metacarpal head migrating not only anteriorly, but also centrally, towards the midline of the hand. Accompanied supination will also enhance the rotation of the metacarpal head around this axis in an arch oblique to the fourth metacarpal head. This movement brings the metacarpal head into more effective opposition of the central palm and the pollex. Taken together, the splaying out of the distal palmar arch, and the oblique axis of flexion and rotation of the fifth metacarpal, not only deepens the cupping posture of the human hand, but will also more effectively wrap the fifth finger firmly around a tool or manipulated object placed obliquely across the palm (for example during a power squeeze grip), and will optimize the positioning of the fifth finger during opposition to the thumb and supination of the fifth digit during precision grips. Furthermore, the mediodistal-lateroproximal divergence of the fifth metacarpal relative to the longitudinal axis of the fourth metacarpal ensures that the positioning of the fourth metacarpal is not obstructive to movement of the fifth. This accentuates the independence of the fifth metacarpal in movements of flexion and conjunct oppositional rotation, and more effectively frees the fifth metacarpal from restrictions in its movements that would otherwise be imposed upon it by the less mobile fourth carpometacarpal joint, further exaggerating abductive and flexile movements of the fifth metacarpal.

The capitate-second metacarpal articulation is oriented somewhat proximally in humans, while in apes it is oriented sagittally (McHenry, 1983; Marzke and Shackley, 1986). Marzke and Shackley (1986) suggested that, in addition to facilitating pronation of the second metacarpal, the proximal orientation of the capitate-MCII articulation allows for the transferral of loads from the second metacarpal to the capitate in axial loading during pad-to-side and three-jaw-chuck grips. The medioproximal orientation of the hamate-MCV articulation, as identified in this study, mirrors the orientation of the capitate-MCII joint, and is likewise likely to transfer the considerable axial loads incurred on the fifth metacarpal, as discussed above, obliquely to the hamate, and thus more economically through the carpal complex towards the forearm. Adaptation of the fifth metacarpal to withstand and transfer such loads is further reflected in its enlarged base and greater general robusticity (Young, 2003).

This divergence in the angle of orientation of the hamate's articular surfaces for the fourth and fifth metacarpals is generally not seen in non-human extant great apes. In *Pongo*, both surfaces are continuous, and it was often challenging to identify the border between the two during landmarking. In the African great apes, the hamate-MC5 surface is situated more distally relative to the hamate-MC 4 surface, and any oblique divergence between the two is minimal and concentrated at the dorsal aspect of the hamate. The more distal positioning of the hamate-MC5 articular surface relative to the fourth in *Gorilla* is likely a consequence of their mode of terrestrial knuckle-walking. In all African apes (including humans), the bones of the fifth ray are the shortest among the non-pollical rays (Susman, 1977). When gorillas knuckle-walk, all four digits touch the ground at roughly the same time, with loads distributed more equally across the four non-pollical rays than in chimpanzees and orangutans (Inoyue, 1992). A distal projection of the fifth carpometacarpal joint relative to the second-to-fourth would mitigate the shorter length of the fifth metacarpal and proximal phalanx relative to the second-to-fourth, though no ulnar deviation of the joint surface accompanies its distal positioning, certainly not to the extent seen in modern humans. As with *Gorilla*, the articulation for the fifth metacarpal in *Pan troglodytes* is situated more distally, resulting in a distal step from the fourth carpometacarpal surface to the fifth. However, the fifth ray is only minimally recruited during chimpanzee knuckle-walking, reflected in the diminished size of the hamate-MC5 joint surfaces.

10.1.2 The hamate-MC5 joint surfaces of extant taxa

When the surfaces of the fifth carpometacarpal joint were assessed in isolation, the saddle-shaped or sellar morphology of the human form was a prominent distinguishing feature, as was the medial expansion of the joint surface. The first principal component of the hamate-MCV surface and of the fifth metacarpal proximal articular surface accounted for 40.4% and 42.3% of the total variation in shape respectively, and distinguished the modern human sample from those of non-human taxa. Results of this study show that the fifth carpometacarpal surface of the human hamate, as mentioned above, is mildly palmodorsally concave, and is accompanied by a gentle mediolateral convexity relative to non-human taxa, while the corresponding surface on the hamate is palmodorsally convex and mediolaterally concave, resulting in a congruent saddle-shaped joint morphology distinctive to humans. Furthermore, both surfaces of the fifth

carpometacarpal joint of modern humans are expanded medially, further enhancing the surface area of the joint and amplifying the sellar morphology of the joint. The diminished and uniform palmodorsal curvature of the joint, which is not bevelled to any extent, enables a high amount of flexibility of the joint.

The features identified as unique to modern humans at the fifth carpometacarpal joint by this study corroborate the qualitative observations of Marzke (1983) and Marzke, Wullstein & Viegas (1992), and can be considered important for the movement and utility of the fifth metacarpal during human dexterous activities, highlighting the important role of the fifth digit in human manual behaviours. The saddle-shaped morphology of the hamate's articular surface for the fifth metacarpal in humans has previously been acknowledged as an important feature of the human hand, as it allows for increased freedom of motion of the fifth metacarpal (Marzke, 1983, 2013; Marzke & Marzke, 2000; Kivell, 2015). As mentioned previously, the fifth metacarpal of modern humans is capable of an extraordinary amount of movement. Not only is the metacarpal capable of abduction and flexion at its proximal articulation, but these movements are accompanied by supination which, in conjunction with asymmetry of the fifth metacarpal head and proximal phalanx (Lewis, 1977; Susman, 1991), rotates the palmar surface of the fifth digit into more effective opposition to the thumb, and augments the cupping posture of the palm. Flexion of the metacarpal is further enabled by the lack of impedance from a palmarly-projecting hamulus, which also enhances the leverage of the *flexor digiti minimi* muscle, augmenting the ray's capacity to resist the considerable extensional forces incurred upon it during stone knapping behaviours, as identified by Key, Dunmore & Marzke (2019).

The adaptation for increased load transmission across the fifth carpometacarpal joint mentioned above may also be a consequence of the strong flexile capacities of the fifth metacarpal, and the pressures incurred on the bone by strong hypothenar musculature during utilization of the distinctly-human power "squeeze" grip, during which cylindrical tools such as hammers are positioned securely at the base of the fifth metacarpal (Marzke, Wullstein & Viegas, 1992). During the power "squeeze" grip, forces are transferred from a cylindrical object to the base of the fifth metacarpal and across the fifth carpometacarpal joint at proportionately greater levels. Strong flexion at the fifth carpometacarpal joint not only buttresses and lodges the base of a tool against the medial base of the palm and directs it towards the thumb, but also holds a

tool securely, preventing it from spinning out of the hand during a down-swing, as well as from being ejected from the hand by the rebounding reaction force of the target. An enlarged fifth carpometacarpal joint enables transmission of the substantial forces incurred on the fifth metacarpal across the joint surface during utilization of the power "squeeze" grip during human tool-related behaviours.

Previous research has demonstrated that the fifth digit is heavily recruited during hard-hammer percussive activities. Further to the conclusions of Key, Dunmore & Marzke (2019), highlighted above, Marzke *et al.* (1998) recorded that ten muscles of the hand were principally involved in hard-hammer percussion. Of these ten muscles that were heavily recruited in both the dominant and non-dominant hand, five were associated with the fifth digit. The fifth metacarpal is the most robust of the non-pollical metacarpals, and the relatively large *opponens digiti minimi* and *abductor digiti minimi* muscles, and prominent muscle markings on the human fifth metacarpal for their insertions, are indicative of powerful hypothenar musculature (Marzke, Wullstein & Viegas, 1992). These features are complemented by a concentration of trabecular bone volume beneath the muscle insertion site for the *opponens digiti minimi* muscle along the ulno-palmar aspect of the fifth metacarpal shaft in humans, which is indicative of frequent recruitment of the muscle, likely during opposition of the fifth finger to the thumb (Stephens *et al.,* 2018). Powerful flexion of the fifth metacarpal, facilitated by an unrestrictive carpometacarpal joint morphology, a palmarly-projecting hamulus, and strong hypothenar musculature, enhances the effectiveness of the functionally important power "squeeze" grip in humans, and the larger articular surfaces of the carpometacarpal joint observed in this study facilitates transmission of the substantial forces acting on the fifth metacarpal.

In contrast to modern humans, the surface morphology of the hamate-MC5 joint surfaces of non-human taxa are more irregular and display features that resist movement and confer stability at the joint. While no quantitative data is available on the mobility of the hamate-MC5 joints of non-human primate taxa, movement of the chimpanzee fifth metacarpal at its carpometacarpal joint is generally considered to be extremely restricted or non-existent (Domalain, Bertin and Daver, 2017). The restrictive nature of the hamate-metacarpal joints is explained by the strong, abrupt, and acute bevelling of the palmar portion of the joint surfaces in non-human great apes, which, in conjunction with a distally-projecting hamulus, as is seen in

Pan troglodytes and *Pongo,* greatly restricts movements of flexion. An acute convex curvature on the dorsum of the joint, and an absence of a sellar morphology of the joint surfaces, further precludes conjunct supination and enhanced oppositional capacity of the digits and protects against mediolateral subluxation of the fifth metacarpal.

The non-human hamate-MC5 joint surfaces are narrow, with a strong distally-projected bevelling of the palmar edge, and in African taxa (especially *Gorilla*), acute convex curvature of the dorsal surface. The narrowness of the fifth carpometacarpal joint and the enlargement of the fourth compared to the human form results in a proportionally lesser surface area relative to the fourth carpometacarpal joint, and reflects the increased loads transmitted across the human fifth carpometacarpal joint during manipulative activities. Marzke, Wullstein & Viegas (1992) suggested that a larger fourth metacarpal joint relative to the fifth is synapomorphic among the *Hominoidea*, as it is a feature shared by all non-human apes. The results of this study appear to corroborate these conclusions and indicate that a radioulnarly enlarged MC5 articulation on the hamate is a derived trait in modern *Homo sapiens.* That the two species of *Pongo* retain a proportionately larger fourth carpometacarpal joint relative to the fifth, despite not engaging in knuckle-walking, and being more adept tool-users than gorillas, reinforces this notion.

In African great apes, the dorsal surface of the fifth hamate-metacarpal surface is strongly convex, which confers stability and resists subluxation at the joint during knuckle-walking. This convex architecture is more prominent in *Gorilla* compared to *Pan troglodytes* and, in conjunction with a relatively larger hamate-MC5 joint surface area in *Gorilla* compared with *Pan troglodytes*, reflects the palm-back mode of knuckle-walking employed by *Gorilla*, in which the fifth metacarpal, and by extension carpometacarpal joint, incurs a greater proportion of load relative to that of *Pan troglodytes*, who varyingly knuckle-walk with a palm-back posture where the fifth digit is not loaded, or a rolling side-palm posture during which the fifth digit incurs substantially less loads than the fourth to fifth digits (Inoyue, 1992). The fifth carpometacarpal joint of *Pongo* is less complex than those of the African non-human great apes, having no convex curvature of the dorsum. This is likely a reflection of their palm-walking mode of terrestrial locomotion, which is minimally employed, and in which the fifth ray is positioned obliquely to the substrate, and remediation against mediolateral subluxation has not been adapted for. Nevertheless, the hamate-MC5 joint surfaces of *Pongo* are strongly bevelled at their palmar portion, and such

morphologies would effectively resist torsional forces acting on the joint during arboreal locomotion.

10.1.3 The hamate-MC4 joint surfaces of extant taxa

Differences in the shape of the hamate-MC5 joint surfaces are consistently dominated by adaptations of the human hand for increased force transmission and mobility. For the fourth carpometacarpal joint, however, shape differences appear to be dictated by adaptations that restrict movement, especially in *Pan troglodytes* and *Pongo*, while this joint in *Homo sapiens* is simple and more planar. The fourth carpometacarpal joint is the most variable of all the carpometacarpal joints in the hominoid hand, and results of the hamate-MCIV surface studies reflect this increased variability. Of the first five principal components studied for the hamate-MCIV surface, three (PCs 1, 3, and 4) were not particularly informative in exploring the human morphology, with the modern human sample being distributed evenly between the negative and positive halves, and with a mean value approximating zero. The first principal component distinguished between a highly irregular surface, with a strong distal, bevelled projection of the palmar surface on its medial edge and a prominent distally-projecting ballooning of the laterodorsal surface, from a simpler articular surface that, while still exhibiting a palmar bevelling and laterodistal ballooning, was much more subtle, and a mediolaterally wider surface. The first principal component distinguished between the highly irregular articular surfaces of *Pan troglodytes* and *Pongo* from the less complex surface of *Gorilla*. The second principal component, which accounted for 15.8% of the variation, was more effective in distinguishing the human sample. Nevertheless, along this axis there was considerable overlap of the modern human sample with non-human groups, and principal components three to four displayed a high degree of overlap between taxa and were of limited utility in identifying differences in shape between taxa.

The significance of the morphology of the fourth carpometacarpal joint in human dexterous activities, and the utility of assessing the joint's articular surface morphology, has been questioned by Kivell *et al.* (2015), who queried the significance of the surface morphology of the fourth carpometacarpal joint given its high morphological variation in both modern humans and

non-human great apes, and the restraints of soft tissues acting upon it. The results obtained in this study reinforce such observations, and interpretation of the results of the hamate-MC4 joint surfaces, and the relationship of hominin joint morphologies, were challenging.

The highly modified morphology of the hamate-MCIV joint of *Pan* and *Pongo* relative to the less complex form seen in *Gorilla* has been previously commented upon (Marzke, Wullstein & Viegas, 1994; Selby, Simpson & Lovejoy, 2016). Marzke, Wullstein & Viegas (1994) argued that the differences in the fourth carpometacarpal joint morphology between *Pan troglodytes* and *Gorilla* reflected the differences in knuckle walking strategies of the two African apes. The *Pan troglodytes* mode of knuckle-walking primarily involves digits three and four (Inoyue, 1992), and the complex and interlocking surface of the fourth carpometacarpal joint of *Pan troglodytes*, Marzke, Viegas & Wullstein (1994) argued, would enhance stability at the focus of load. Conversely, gorillas knuckle-walk with all four non-pollical digits making contact with substrate, therefore increasing the number of supports bearing the bodyweight during knuckle-walking and reducing the need for a complex interlocking of the joint (Inouye, 1992; Marzke, Wullstein & Viegas, 1994). The interlocking topography of the medial carpometacarpal joints was also argued to be adaptations for knuckle-walking by Richmond, Begun and Strait (2001) and Begun (2004). Selby, Simpson, and Lovejoy (2016), however, argued that the interlocking nature of the hamate-MC4 joint surfaces in chimpanzees is an adaptation for climbing and/or suspension, as the complex joint morphology would maximize stability of the joint during suspension and vertical climbing by greatly reinforcing the joint's resistance to torsion. The polarization of the *Gorilla* sample from the clustering of the *Pan troglodytes* and *Pongo* samples along the first principal component suggests that, as *Pongo* does not engage in knuckle-walking, and is almost exclusively arboreal, the arguments of Selby, Simpson, and Lovejoy (2016) that the complex interlocking nature of the fourth carpometacarpal joint in *Pan troglodytes* is an adaptation for the resistance of torsional and extensional forces during arboreal locomotion, bear more weight. Conversely, gorillas actually have a less complex fourth carpometacarpal joint morphology than chimpanzees and orangutans, being intermediate between the modern human form and those of the more arboreal great apes. The fact that several fossil hominins were classified as *Gorilla* by the canonical variate analysis and had closer Procrustes distances to the *Gorilla* mean shape than to *Homo sapiens* reflects the intermediate nature of the joint in these fossil taxa, hinting that while

the fourth carpometacarpal joint retained features to resist torsional and extensional forces, such selection was being relaxed in favour of an increased range of mobility.

In contrast to the great ape taxa, the articular surfaces of the fourth carpometacarpal joint of modern humans are generally flat and featureless, though display high variation. While the PCA of the hamate's articular surface for the fourth metacarpal primarily distinguished differences between the non-human taxa, the first principal component of the fourth metacarpal proximal articulation isolated the modern human sample from non-human taxa, as did the canonical variate analysis. The overall morphology of this joint in modern humans is flat both mediolaterally and palmodorsally, with only a very slight bevelling of the surface at the palmar portion. The surfaces of both the hamate and the fourth metacarpal for this joint are also notably palmodorsally long and mediolaterally narrow, reflecting the proportionately smaller surface area of the joint compared to that of the fifth carpometacarpal joint. The flat and narrow form of the modern human fourth carpometacarpal joint is indicative of a mobile joint with limited loads transmitted across it, and, contrary to the fifth carpometacarpal joint, no notable degree of a sellar morphology is observed. It is likely therefore that conjunct rotation of the fourth metacarpal is not functionally important, certainly not to the extent it is at the fifth carpometacarpal joint, and any supination of the fourth metacarpal during flexion is a consequence of the fourth metacarpal being "carried along" by movements of the fifth metacarpal. Indeed, flexion and abduction of the fourth metacarpal is limited by an absence of musculature capable of such movements acting upon the bone, contrasting with the powerful musculature associated with the fifth metacarpal. A further indication of reduced loading of the fourth carpometacarpal joint is the gracile appearance of the fourth metacarpal, which is the least robust of all the metacarpals in the modern human hand (Marzke, Wullstein & Viegas, 1994).

The principal component axes for the hamate-MC4 joint surfaces which isolated the human sample from non-human taxa comprised a proportionately smaller share of the total variation than those of the fifth carpometacarpal joint – PC 2 of the hamate-MCIV study represented 15.8% of the total variance, while PC 1 of the fourth metacarpal proximal surface accounted for 22.6% - compared with 40.4% and 42.3% for the fifth CMC joint, both of which were represented by the 1st PC. This weaker signal in the human 4th CMC joint relative to the 5th

is likely a result of several factors. The most obvious factor is that shape differences between great ape taxa at this joint is dictated by the highly complex joint surfaces of non-human great apes, primarily *Pan troglodytes* and *Pongo*, which result from the obligations of the hand in these taxa for locomotory use. However, the fourth carpometacarpal joint of modern humans is also highly variable (the most variable of all the carpometacarpal joints), with as much as six different forms of this joint observed in humans (El-Bacha, 1981; Viegas *et al.,* 1991). The lack of a highly specialized joint morphology of the fourth carpometacarpal joint in humans would naturally lessen the strength of signal found in studies focused on the hamate-MC4 joint surfaces. Thirdly, and complementing both previous statements, the human fourth carpometacarpal joint may simply not have been subject to the same selective pressures as those of non-human taxa, nor of the fifth carpometacarpal joint of humans. Rather, any morphological features (or lack thereof) of the joint surfaces in humans are simply the result of a necessity for not impeding on the movement of the fifth metacarpal at its proximal joint.

Nevertheless, the morphology of the fourth carpometacarpal joint of modern humans does appear to be adapted to facilitate movement at the joint, as it is generally lacking the features seen in *Pan troglodytes*, *Pongo*, and *Gorilla* that confer stability and rigidity. The first canonical axes of both carpometacarpal surfaces demonstrated that the shape of the joint surfaces between modern humans and other great apes represented the greatest shape difference between the groups, and reflects the importance of freedom of movement of the fourth metacarpal in human manual behaviours. Flexion at the fourth carpometacarpal joint is much less pronounced than at the fifth, allowing about 10° of flexion (Dubousset, 1981). It has been shown that movement of the fifth metacarpal is restricted when the fourth metacarpal is held rigid (Dubousset, 1981). The planar nature of the fourth carpometacarpal joint therefore allows the passive fourth metacarpal to move in concert with the active fifth metacarpal without restricting its movement, thereby enhancing the fifth digit's ability to oppose the thumb, cup the palm, and powerfully flex during power squeeze grips.

It has been previously reported that very little flexion of the fourth metacarpal at its carpometacarpal joint is permitted in non-human African apes (Marzke, 1983; Domalain, Bertin and Daver, 2017), and while measurements of movement at the fourth and fifth carpometacarpal joints of non-human apes have not been identified in the literature (Selby, Simpson & Lovejoy,

2016), the articular surfaces of these joints appear to corroborate these assertations. The fourth carpometacarpal articulations in all three non-human taxa are more complex and irregular than in modern humans, with the two surfaces of the fourth carpometacarpal joint having corresponding, mirroring, and interlocking morphologies. In all three non-human great ape taxa, the surface of the hamate's MC-4 articulation is, as with that for MC-5, strongly palmodorsally concave, with a radioulnarly concave palmar portion. Conversely, this joint in humans is strikingly flat, featureless, and planar, and is also proportionately smaller than the hamate-MCV joint. This reflects not only a decreased loading of the fourth carpometacarpal joint, but a requirement of the joint not to impede the freedom of movement enjoyed by the fifth metacarpal at its proximal articulation.

Table 10.1: Summary of notable features of extant great ape groups

	Gorilla	*Homo sapiens*	*Pan troglodytes*	*Pongo*
Hamate-MC	-Strong palmodorsal curvature with acute apex Mediolaterally-narrow surface relative to palmodorsal length -Palmar edge of MC5 surface projects more distally than MC4 surface -Mediolaterally-enlarged MC4 surface with constricted MC5 surface -Both surfaces face distally	-Moderate palmodorsal curvature -Palmodorsally squat -Longer mediolaterally than palmodorsally -Mediolaterally-enlarged MC5 surface relative to MC4 surface -Divergence of MC4 and MC5 surfaces -MC5 surface angled medially relative to MC4 surface	-MC4 surface larger than MC5 surface -Increased mediolateral width of MC4 surface relative to MC5 surface -Step between the two surfaces, most notable on the dorsal edge -MC5 surface is positioned more distally than MC4 surface	- Continuity between the two MC articular surfaces
Hamate-MC4	-Ballooning of dorsolateral surface Erratic and uneven surface -Rectangular from distal view -Medial border longer than lateral border -Palmar border shorter than dorsal border -Curved medial border with distomedially-protruding mediodistal corner -Mediolaterally concave palmar border -Strong distal ballooning of laterodorsal surface	-Smooth and lacking distal ballooning -Longer in palmodorsal plane than mediolateral plane -Palmar edge gently curves distally, most notably at the mediopalmar corner -Moderately bevelled surface which is gently concaved palmodorsally Mildly mediolaterally concaved -Mild laterodorsal distal protrusion -Medial border is longer than lateral border -Mediopalmar and mediodorsal corners protruding further distally than corresponding lateral corners	-Prominent distally-projecting ballooning of dorsolateral portion of surface -Erratic and irregular surface -Strongly concave palmar portion -Dorsal portion sloped towards the laterodorsal corner -Distally-projecting mediopalmar corner -Strong scooping bevelling of mediolateral quadrant -Prominent ballooning of lateral surface, which is situated more palmarly than in other taxa -Medial edge is palmodorsally longer than lateral edge	-Pronounced lateral bulge -Strongly sloping and proximolaterally-projecting laterodorsal corner -Straight medial edge Lateral edge bulges laterally in palmar and dorsal portion
Hamate-MC5	-Mediolaterally narrow -Palmodorsally long -Strongly mediolaterally arched dorsal half -Flat palmar half	-Saddle-shaped morphology -More medially facing -Mediolaterally convex -Gently palmodorsally concave, with no clear apex	-Dorsal portion of the surface slopes proximally towards its medial edge -Strong apex separating palmar and dorsal halves of surface, resulting in strong palmodorsal bevelling	-Mediolaterally narrow and palmodorsally long -Curved mediopalmar and mediodorsal corners -Prominent distal projection of palmar edge

	Strong bevelled surface, with prominent apex of dorsopalmar curvature -Constricted mediolateral waist			-Strong apex separating palmar and dorsal halves of surface, resulting in strong palmodorsal bevelling -Medial and dorsal edges slope proximally
MC4	-Pronounced palmodorsal bevelling of surface	-Flat and featureless -Palmar border is minimally curved -Surface slopes medially and dorsally relative to the shaft of the bone	-Prominent divot on lateral portion of surface -Mediopalmar corner projects medially and distally -Acute palmodorsal bevelling is concentrated on the medial side	-Asymmetrical bevelling of palmar edge -Distal depression positioned more centrally
MC5	-Dorsal half is strongly concave mediolaterally Slightly convex mediolateral half -Palmar and dorsal portions separated by strong bevelling of surface -Surface is both wide and long	-Mediolaterally wide and palmodorsally squat -Saddle-shaped morphology corresponding to the Hamate-MC5 surface -Gently and uniformally mediolaterally concave -Palmodorsally convex	-Mediolaterally narrow -Asymmetrical mediolateral concavity of surface, with flatter lateral side and proximally flaring medial side -Hockey-stick profile of bevelling -Shallow bulge at palmar portion	Narrow and elongate surface Lateral and medial borders contracted towards the midline -Exaggerated palmodorsal bevelling

10. 2 Fossil Specimens

Australopithecus

Australopithecus afarensis

The fossil material attributable to *Australopithecus afarensis* used in this study comprised of one hamate (A.L. 333-50), one fourth metacarpal (A.L. 333-56) and two fifth metacarpals (A.L. 333w-89; A.L. 333-14). The hamate-metacarpal surface of A.L. 333-50 exhibits an intermediate morphology, exhibiting some features that are distinct from all extant non-human taxa, and some that more closely resemble non-human great apes than modern humans. The surface for the fifth metacarpal is smaller than that for the fourth (corroborating the observations of Orr *et al*. (2013)), and is not angled mediodistally as in modern humans, but rather faces distally in a similar plane to the fourth carpometacarpal surface. Further, the fourth carpometacarpal surface displays the laterodorsal ballooning of the surface that is characteristic of non-human taxa and confers stability and rigidity of the joint, and the fifth carpometacarpal surface lacks a distinctly-human sellar morphology. However, the distal edge of the *Australopithecus afarensis* A.L. 333-50 hamate is not as strongly palmodorsally curved as in non-human great ape taxa, nor does it display the acute bevelling of its palmar border, which is characteristic of non-human taxa. In this respect, the *Australopithecus afarensis* hamate-metacarpal surface is more similar to modern humans, having a gentler palmodorsal curvature, which would have enabled greater flexion at the hamate-metacarpal joints than in extant non-human taxa.

This intermediate nature of the A.L. 333-50 hamate's distal articular surface is reflected in its positioning both in the principal component and canonical variates analyses. Its PC value was more than one standard deviation from the mean values of all extant taxa along all three principal components studied (table 5.2.2) Along the first canonical variate axis, A.L. 333-50 did not fall within the range of any extant taxa, but rather was intermediate between modern humans and non-human great apes. And while the CVA placed A.L. 333-50 within the *Homo sapiens* sample with a probability of 66.8%, it had a probability of 33.2% of being a member of the *Pan troglodytes* sample, and with the exception of *Homo floresiensis*, was the least *Homo*-like fossil specimen. In terms of absolute Procrustes distances, A.L. 333-50 was closer to a greater

percentage of the *Pan troglodytes* and *Gorilla* samples to their respective mean shapes than it was to the mean shape of the *Homo sapiens* sample (section 5.5).

The architecture of the proximal articular surface of the A.L. 333-56 fourth metacarpal is similarly complex, with a corresponding indentation of the laterodorsal surface in which the bulbous distal projection of the corresponding hamate surface would nest. And while the articular surface does not expand distally onto the palmar surface of the fourth metacarpal to the same extent as non-human taxa, it does display a prominent palmar curvature that would nest in the corresponding palmar surface of the hamate-MCIV surface. These non-human features are again reflected in the results of the canonical variate analysis, in which the A.L. 333-56 fourth metacarpal was classified into the *Gorilla* sample with a confidence of 99.9%. Along the first canonical variate axis, this specimen was within the ranges of *Pan troglodytes* and *Gorilla.* The articular surfaces of the *Australopithecus afarensis* fourth carpometacarpal joint are therefore highly interlocking, and retained a morphology primarily adapted for stability of the joint rather than for freedom of movement. Furthermore, the greater surface area of the fourth carpometacarpal joint relative to the fifth suggests a greater loading of the fourth ray relative to the fifth and demonstrates that the fourth and fifth metacarpals were subject to loads more similar to *Pan* and *Pongo* than to modern humans, and indicate a retention of a feature considered to be advantageous for arboreal locomotion.

While the fourth carpometacarpal joint of *Australopithecus afarensis* is unambiguously un-human-like and appears to have retained adaptations for load transmission and stability at the expense of freedom of movement, interpretation of the fifth carpometacarpal joint is more complex. The base of the two *Australopithecus afarensis* fifth metacarpals used in this study are clearly closer to the human form than to non-human taxa. Both A.L. 333-14 and A.L. 333w-89 are radioulnarly wide and palmodorsally squat, with a palmodorsal convex curvature only slightly more acute than the human average, with no sharp bevelling of the palmar surface common to non-human taxa. Similarly, when compared in isolation, the hamate-MCV surface of *Australopithecus afarensis* appears medially expanded at its palmodorsal midsection, resulting in a radioulnarly expanded and palmodorsally squat surface, though not to the same extent as modern humans. However, while the palmodorsal curvature of the surface is less acute than in non-human taxa, with a palmar edge that does not extend as distally, it is nevertheless stronger

than the *Homo sapiens* curvature. The strength of palmodorsal curvature is therefore intermediate between humans and non-human taxa. Perhaps most significantly, the fifth carpometacarpal joint is not sellar/saddle-shaped. The base of the fifth metacarpal is not radioulnarly concave, and the corresponding hamate-MCV surface is not radioulnarly convex. Contrary, the A.L. 333-50 surface is both radioulnarly and palmodorsally concave, while the two metacarpal surfaces (A.L. 333-14; A.L. 333w-89) are varyingly radioulnarly convex, resulting in a more condyloid joint.

When viewed in isolation, both the fourth and fifth carpometacarpal joints of *Australopithecus afarensis* confer morphologies intermediate to modern humans and extant non-human great apes, and though movements at these joints do not appear to have been restricted to the same extent as in non-human taxa, there does not appear to have been a freedom of movement comparable to modern *Homo sapiens*. The more distal projection of the MCV joint surface on the metacarpal's palmar portion relative to modern humans, and its deeper concave palmodorsal curvature, reflect Marzke's (1983) observations that the hamate-MCV surface of *Australopithecus afarensis* continued onto the hamulus. Flexion of the fifth metacarpal would have been further compounded by a more rigid fourth carpometacarpal joint, with indications that the two joints were not as independent from each other as in modern humans due to the lack of divergence of the two joint surfaces on the distal hamate. Further, the lack of a saddle-shaped morphology of the fifth carpometacarpal joint indicates that any flexion that was permitted at this joint was not accompanied by conjunct supination. Such conclusions are supported by the observations of Marzke (1983, 1997, 2005) and Marzke *et al.,* (1992), who were also of the opinion that, compared to modern humans, *Australopithecus afarensis* lacked the flexional and rotational capacities of the fifth digit.

Taken holistically, the morphology of the fourth and fifth carpometacarpal joints of *Australopithecus afarensis* indicate a limited ability of the fourth and fifth metacarpals to move with the freedom of movement associated with modern humans, or for the fifth finger to absorb and resist the greater external and internal loads associated with human stone tool-making behaviours. Nevertheless, the absence of a sheer bevelling morphology of the hamate-metacarpal joints, and the less complex nature of the hamate-fifth metacarpal surfaces, may indicate that a degree of flexion was permitted at the joint, albeit checked by a restrictive fourth

carpometacarpal joint. Further, when the fifth carpometacarpal surfaces are viewed in isolation, the width relative to length ratios are more similar to that of modern humans, with the fifth carpometacarpal surfaces being ulnarly-expanded at their waists, resulting in radioulnarly broad surfaces, and unlike the narrower and more elongated surface of non-human great apes. The expanded mediolateral surface of the fifth carpometacarpal joint is reflected in the results of this study, which strongly reflected certain human-like features. Both the proximal surfaces of A.L. 333-14 and A.L. 333w-89 fifth metacarpals were within one standard deviation of the *Homo sapiens* mean value along PC1, and both were within the interquartile range of the group. The CVA assigned both specimens as *Homo sapiens* with a confidence of greater than 99%, and they were closer to the mean shape of *Homo sapiens* in terms of absolute distance than more than 10% of the human sample. This may indicate an increased loading on the ulnar surface of the joint. The more palmarly-projecting nature of the hamulus, as noted by Marzke (1983), may also not have impeded flexion to the same extent as in extant non-human apes. The hamate-metacarpal joints of *Australopithecus afarensis* therefore appear intermediate between the rigid and restricted nature of non-human great apes, and the mobile nature of these joints in modern humans, with evidence of increased flexion of the fifth metacarpal which is not accompanied by supination, and increased loading of the joint.

The intermediate nature of the fourth and fifth carpometacarpal joints of *Australopithecus afarensis* between the modern human form and those of non-human taxa reflect several other features of the species' hand. For example, Marzke (1983) determined, using composite hand measurements, that the thumb of *Australopithecus afarensis* was closer in relative length to the modern human thumb than to the chimpanzee thumb, though debate continues regarding the finger/thumb ratio of *Australopithecus afarensis* (Alba, Moya-Sola and Kohler, 2003; Almecija and Alba, 2014; Marzke, 1983; Rolian and Gordon, 2013; Rolian, Gordon and Hallgrimson, 2011). Despite such debate, it is unlikely that the thumb/finger ratio of this species would have precluded manipulation of objects (Marzke, 2013). Further, the shape of the second carpometacarpal joint of *Australopithecus afarensis* resembles that of modern humans, being curved and continuous between the second metacarpal and the capitate, and orientated more proximally and coronally and transversely, and also lacks a carpometacarpal ligament between the capitate and the second metacarpal. These features have been interpreted as evidence of pronation of the second metacarpal during manipulation (Drapeau, 2012; Drapeau

et al., 2005; Marzke, 2005; Marzke and Shackley, 1986; Tocheri *et al*., 2003, 2005). The second metacarpal head of *Australopithecus afarensis* is also asymmetrically tapered and would therefore have further facilitated pronation of the second digit during flexion, allowing for the index finger to conform to the shape of a manipulated object (Drapeau, 2012). A human-like thumb-to-finger length ratio and a second metacarpal capable of slight pronation would likely have enhanced movement of the second metacarpal towards the centre of the palm during flexion (Marzke, 1983; Drapeau, 2012). These forelimb traits of *Australopithecus afarensis* have been interpreted as adaptations for increased manipulatory abilities (Marzke, 1983, 1997, 2005; Marzke and Shackley, 1986; Alba, Moya-Sola and Köhler 2003).

Despite these human-like features, the hand of *Australopithecus afarensis* retained several features more similar to living apes that can be considered as retentions of features compatible with arboreality, and not conducive for enhanced dexterity. For example, the distal phalanges are characterized by slender apical tufts, rather than the broad tufts characteristic of human distal phalanges (Stern and Susman, 1983), and longitudinally curved proximal phalanges with well-developed flexor sheath ridges on the proximal and middle phalanges suggest that arboreal locomotion remained prominent (Stern, 2000; Stern and Susman, 1983; Susman, Stern and Jungers, 1984). The diminutive nature of the fifth carpometacarpal joint relative to the fourth reflects a similarly small first carpometacarpal joint that was also less mobile, and associated with a pollical metacarpal that was more gracile and less powerful than modern humans, and a smaller and robust fifth metacarpal (Marzke, 2005; Susman, 1994; Tocheri *et al.,* 2008). The absence of a styloid process on the base of the third metacarpal is further indication that the *Australopithecus afarensis* hand was not subjected to extensional forces associated with the hard-hammer percussive activities of stone tool making, or with stresses associated with spherical and squeeze power grips (Marzke & Marzke, 1987). Further, *Australopithecus afarensis* had a relatively greater intermembral index than modern humans (Stern and Susman, 1983), and the orientation of the glenoid surface of the scapula is intermediate between *Pan* and humans (Alemseged *et al*., 2006; Bush *et al*., 1982). A rod-like pisiform, more similar to chimpanzees, is a further feature more closely resembling a non-human form (Bush *et al*., 1982; Stern, 2000; Susman, Stern and Jungers, 1984).

Previous investigations have concluded that the hand of *Australopithecus afarensis* exhibited a combination of derived features consistent with advanced manipulative abilities while retaining features indicative of a degree of arboreal behaviour. The results of this research are broadly consistent with such interpretations. The fifth, and especially the fourth, carpometacarpal joints of *Australopithecus afarensis* did not allow for the degree of mobility seen in the human joints and would therefore have likely restricted the ability of the species' hypothenar area to cup the palm, movements which are necessary for powerful and effective execution of precision grips and the power "squeeze" grip, though it is likely that the fifth metacarpal was more mobile than those of extant non-human great apes. It has been suggested that the human-like second carpometacarpal joint of *Australopithecus afarensis* and a human-like thumb-to-finger length ratio is indicative of a hand well-adapted to pad-to-pad, pad-to-side, and three-jaw-chuck grips (Alba *et al*., 2003; Marzke and Shackley, 1986). If *Australopithecus afarensis* was indeed making and using stone tools such as those from Lomekwi, as has been suggested by Harmand *et al.* (2015), it is unlikely that the fourth and fifth digits were used in a human-like manner, and the species' capacity for power squeeze and palm grips with strong recruitment of the fifth digit would have been restricted by a less mobile fifth metacarpal. The diminutive size, deep condyloid morphology, and distal-facing orientation of the fifth carpometacarpal joint, as identified and reinforced by this research, suggest that the joint was not only less mobile than the modern human form but was not loaded to the same extent or in the same manner as modern humans. Nevertheless, the increased mediolateral width of the fifth carpometacarpal joints surfaces, especially that of the fifth metacarpal, is suggestive of an increased loading of the joint, and may be consistent with the suggestions of Harmand *et al.* (2015) that the artifacts of Lomekwi were not produced through hard-hammer percussive knapping, but rather through a pounding or throwing technique.

These conclusions are supported by musculoskeletal modelling of the fifth digit of *Australopithecus afarensis* conducted by Domalain, Bertin and Daver (2017) who determined that the hamate's articular surface for the fifth metacarpal inhibited supination of the fifth digit, precluding the digit from applying a strong grip force to any large object held in the hand, and that the pulp of the fifth ray would have been unable to adequately face the surface of large-sized objects, thus limiting the species' ability to exert sufficient force to hold lithic blocks such as those of Lomekwi 3. Nevertheless, a medial expansion of the fifth carpometacarpal joint is

noteworthy, and hints that increased loads were being incurred by the lateral base of the fifth metacarpal. Such human-like traits, accompanied by asymmetry of the distal head of the second and fifth metacarpal heads of *Australopithecus afarensis* accompanied by a relatively long thumb and features consistent with rotation of the second metacarpal (Drapeau, 2012; Marzke, 1983, 1997), may hint at incipient adaptations for a more derived utilization of the fifth ray in *Australopithecus afarensis.* Lastly, the complex and enlarged structure of the fourth carpometacarpal joint of *Australopithecus afarensis* is indicative of adaptations for resistance of extensional loads associated with arboreal locomotory behaviour such as clambering or climbing. The retention of this feature is consistent with other traits in the upper limb of *Australopithecus afarensis* that are adaptations to arboreality, mentioned above (Alemseged *et al.*, 2006; Bush *et al.,* 1982; Stern, 2000; Stern and Susman, 1983; Susman, Stern and Jungers, 1984), and any adaptations for stone tool related behaviour in the *Australopithecus afarensis* hand was likely checked by continued use of the hand for arboreal locomotion.

Australopithecus cf. Australopithecus afarensis

The KNM-WT-22944-I hamate was assigned by Ward *et al.* (1999) as belonging to *Australopithecus afarensis*, though this taxonomic categorization is disputed, and KNM-WT-22944-I has also been attributed to or compared with *Kenyanthropus platyops* (Brown, McDougall and Gathogo, 2013; Grine *et al.,* 2022; Leakey *et al.,* 2001; Wood and Leakey, 2011). The results of this study demonstrate that the KNM-WT-22944-I hamate-metacarpal surface is overall more human-like than the A.L. 333-50 *Australopithecus afarensis* hamate. The fifth carpometacarpal surface on the KNM-WT-22944-I hamate comprises a proportionately larger area of the hamate-metacarpal surface than in A.L. 333-50 and is more medio-proximally angled than the *Australopithecus afarensis* hamate. The surface for the fourth metacarpal is also more uniform and less complex, and the fifth carpometacarpal surface is mediolaterally convex, resulting in a mild sellar-morphology of the joint surface. The three canonical variate analysis of the joints (hamate-metacarpal; hamate-MC4; hamate-MC5) assigned KNM-WT-22944-I as *Homo sapiens* with a 100% probability, and within all canonical variate axes of each test, it was within the range of modern humans. The hamate-metacarpal and hamate-MC5 surfaces were within one standard deviation of the mean value of modern humans and within the group's interquartile

range along the first principal components, and were both closest to the mean shape of *Homo sapiens* when absolute Procrustes distance was considered, with the hamate-metacarpal surface being closer to the mean shape of the modern human sample than 16.77% of the group specimens, and the hamate-MC5 surface closer than 68.11% of the human sample. Results of the hamate-MC4 are more varied. Along the first principal component, it was within one standard deviation of the mean value of *Gorilla*, though within the ranges of gorilla and modern humans. The canonical variate analysis again classified the KNM-WT-22944-I specimen as *Homo sapiens* with a probability of 100%, and along all three canonical variate axes it was within the range of *Homo sapiens.* It was closest in terms of Procrustes distance to the human mean shape, followed closely by *Gorilla*.

Several features of the hamate-metacarpal complex of KNM-WT-22944-I are human-like, certainly more so than the *Australopithecus afarensis* A.L. 333-50 hamate specimen. A proportionately larger MC5 surface than the MC4 suggest the fifth metacarpal was loaded to a greater extent, and a sellar morphology of the joint surface would have facilitated a degree of supination during flexion of the fifth metacarpal, enhancing the fifth digit's ability to oppose the thumb and act in a human-like manner during precision and power grips. A simple and relatively featureless fourth metacarpal joint surface, and divergence of the two surfaces, would have further facilitated movement of the fifth metacarpal by not impeding it, and would have widened the distal metacarpal arch and realigned axial loading of the fifth metacarpal towards the centre of the carpal complex. While the KNM-WT-22944-I hamate has a distal articular surface for the fourth and fifth metacarpal that is overall more akin to modern humans than to extant non-human great apes, there are some features of the specimen's articular surface that differ significantly from the modern human condition. A palmolateral expansion of the hamate-MCIV surface, and a radioulnar waisting of the hamate-MCV surface results in the fourth metacarpal surface still being of proportionally greater area size than that of the fifth metacarpal. The hamate-MCIV surface itself is more complex than those of modern humans, with a deeper palmodorsal and radioulnar concave curvature resulting in a more condylar and bowl-like morphology, similar to A.L. 333-50. Nevertheless, the hamate-MCIV surface is quite unlike the non-human extant great ape taxa and does not have the ballooning of its laterodorsal portion that is characteristic of non-human taxa.

Overall, the hamate-metacarpal surface of the KNM-WT-22944-I hamate is more similar to modern humans than that of A.L.333-50 and displays several derived features that can be regarded as adaptations to increased mobility, and reorientation of axial loading, of the fifth metacarpal. However, the taxonomic ambiguity associated with this specimen complicates assessment of its relation to contemporary hominins, and the archaeological record of the earliest stone tools. If KNM-WT-22944-I is indeed an *Australopithecus afarensis* specimen, then the hamate-metacarpal joints of the species are highly variable. However, if, as has been suggested, KNM-WT-22944-I is associated with *Kenyanthropus platyops*, then it is reasonable to argue, based on the results of this study, that this species was more adept at human-like power "squeeze" grips and powerful precision grips using the hypothenar digits than *Australopithecus afarensis* was. Additional manual fossil material associated with the KNM-WT-22944 hand is sparse, comprising of only a capitate, lunate, and a fragmentary third metacarpal, further compounding interpretations of hand use in this species. Until further fossil material associated with the manus of *Kenyanthropus platyops* is discovered, interpretation of the KNM-WT-22944-I hamate, and its taxonomic classification, must be conducted with caution. Nevertheless, the presence of derived human-like features in a hamate both chronologically and geographically contemporaneous with the stone tools of Lomekwi is intriguing and warrants further investigation.

Australopithecus africanus

No hamate specimens attributed to *Australopithecus africanus* were available for inclusion in this study, and as such, interpretations of human-like movement of the hamate-metacarpal joints in this hominin taxon is limited to the proximal articular surfaces of the metacarpals. Nevertheless, comparisons of the proximal articulations of the fourth (StW-330; StW-65) and fifth (StW-63) metacarpals of *Australopithecus africanus* with extant hominoid taxa and other fossil hominin specimens provided insights into the function of the fourth and fifth carpometacarpal joints of *Australopithecus africanus*.

The two fourth metacarpal specimens indicate a great deal of variation in the shape of the bone's proximal articular surface in *Australopithecus africanus.* StW-330 is strikingly human-

like, being notably flat in both the radioulnar and palmodorsal plane, with no expansion of the surface on to the palmar surface of the bone and only a mild lateral indentation, suggesting that the distal ballooning of the lateral portion of the corresponding surface on the hamate would have been reduced. The human-like shape of the StW-330 proximal surface resulted in the specimen being categorized as modern *Homo sapiens* with a confidence of 100% by the canonical variates analysis, and its PC 1 score was within one standard deviation of the average score of the *Homo sapiens* sample. In contrast, StW-65 was classified as *Gorilla* by the CVA with a confidence of 83.3%. There was a likelihood of 13.1% of this specimen belonging to *Pan troglodytes,* and only a 3.6% likelihood of StW-65 belonging to the *Homo sapiens* sample, though the specimen was more than one standard deviation from the mean values of all groups along PC 1. This is likely due to a prominent distal expansion of the palmar edge, resulting in a non-human-like palmar bevelling, and a very prominent divot on the distolateral portion of the surface, which may indicate that the corresponding articulation of the hamate had a characteristically non-human-like ballooning of the surface. Such features confer stability of the joint and would have restricted freedom of movement of the fourth metacarpal relative to modern humans. However, the distal expansion of the palmar surface is not as expansive as in the non-human great ape form, and overall, the StW-65 MC4 proximal articular surface is intermediate between modern humans and other great apes.

The subtle yet noteworthy variation in the shape of the proximal articular surfaces of the *Australopithecus africanus* fourth metacarpal surfaces StW-330 and StW-65 confound attempts at interpreting their significance. Kivell *et al.* (2020) also remarked on the variable shape of the two specimens, notably the radioulnarly broad surface of StW-330 relative to its midshaft breadth compared to a radioulnarly narrow surface for StW-65 (a feature that would not have been identified in this study). As mentioned above, Kivell *et al*. (2020) questioned the functional significance of subtle variations in the articular morphology (both within and between taxa) of a joint that has relatively limited mobility, and which is bound by carpometacarpal ligaments. Given the clear variation between the two specimens, interpretation of any general functional significance of the MC-IV proximal articular surface in *Australopithecus africanus* is challenging and brings into question any conclusions made regarding the functional significance of the morphologies of the fourth carpometacarpal joint in extinct hominins. Nevertheless, features that confer stability at the joint appear to be intermediate between modern humans and extant

non-human taxa and may indicate that factors resulting in selection for stability at the fourth carpometacarpal joint was being relaxed in *Australopithecus africanus.*

The proximal articulation of the *Australopithecus africanus* StW-63 fifth metacarpal, as with the fourth metacarpal proximal articulation, exhibits both modern human-like and non-human great ape-like morphologies. The articulation is clearly medially-expanded, resulting in an articulation that has a mediolateral-palmodorsal length ratio similar to modern humans, as opposed to the mediolaterally narrow and palmodorsally elongated articulation common to the extant non-human great apes. The medial expansion of the StW-63 proximal articular surface complements interpretations that the rugosity along the ulnar shaft of the metacarpal signifies a human-like insertion of the *opponens digiti minimi* muscle along the full length of its shaft (Kivell *et al.,* 2020). Furthermore, while the palmodorsal convex curvature of the fifth metacarpal proximal articular surface of *Australopithecus africanus* is slightly more acute than that of modern humans, it does not exhibit a flat dorsal area transforming sharply to a prominent bevelling onto the palmar surface of the bone, as is the case with *Pan* and *Pongo.* However, the palmar edge of the surface does project more distally than in *Homo sapiens*, especially centrally, and in this respect is more similar to the *Gorilla* condition than to that of modern humans. Marzke (1983) also highlighted the ventral continuation of the hamate facet of StW-63 being slightly more developed than in modern humans, and based on these observations, Ricklan (1987) concluded that the Stw-63 fifth metacarpal would have been capable of a similar range of flexion as *A. afarensis*, and slightly less than that in modern humans.

The proximal articulation of the StW-63 fifth metacarpal is very slightly mediolaterally convex, and does not display the gentle, mediolateral concavity that is a prominent and important feature of the modern human surface. This suggests that, while the fifth carpometacarpal joint of *Australopithecus africanus* was subject to increased loading on its medial edge, rather than having the saddle-shaped morphology associated with *Homo sapiens*, the articulation is likely to have been more condyloid, similar to *Australopithecus afarensis*. Without the corresponding hamate-metacarpal surface, it is not possible to ascertain whether the fifth carpometacarpal joint of *A. africanus* is proximomedially diverged relative to the fourth, thereby facilitating more independent movements of the fourth and fifth metacarpals. Nevertheless, the overall structure of the carpometacarpal joint surfaces available for analysis in this study suggest that the fifth

carpometacarpal joint of *Australopithecus africanus* lacked capacities for the same degree of flexion, and certainly supination, that augment distinctly-human grips and hand postures.

Several features of the *Australopithecus africanus* hand indicate a pattern that should have been compatible with forming and securing forceful precision grips and accommodating external forces at the centre of the palm associated with tool making (Marzke, 2013). For example, it has been suggested that, based on the length ratio of the first and third metacarpals, *Australopithecus africanus* had a thumb-to-finger length similar to those of modern humans (Green and Gordon, 2008). Additionally, broad distal phalangeal tuberosities, and evidence of deep extrinsic muscles to the thumb, as well as the architecture of the second carpometacarpal joint, indicate that *Australopithecus africanus* had the capacity to rotate the 2nd metacarpal during flexion. These features are similar to those seen in *Australopithecus afarensis*, and a similar fifth carpometacarpal joint morphology indicates that, though *Australopithecus africanus* may have been capable of forming and securing forceful precision grips, especially between the thumb and second and third digits (Marzke, 2013; Ricklan, 1987), its capacity for power (squeeze) gripping would have been similarly limited.

Such a conclusion challenges those of Skinner *et al.* (2015) who concluded that the distribution of trabecular morphology in the metacarpals of *Australopithecus africanus* (e.g. an asymmetrical distribution of trabeculae in the third and fifth metacarpal heads) was consistent with habitual and forceful opposition of the thumb and fingers during precision and power (squeeze) gripping that are used during tool-related behaviours. Ricklan (1987) was also of the opinion that there was a capacity for rotation of the fifth digit during flexion, and that *Australopithecus africanus* was capable of a firm power grip. However, Ricklan's (1987) rationale that the fifth metacarpal was capable of supination was based purely on the conclusion that any amount of flexion would be accompanied by supination, stating that "*StW 63 would* […] *have been capable of* […] *flexion and hence automatic rotation of the CMJ5*" (Ricklan, 1987, *p.* 649). While the results of this study suggest that the fifth carpometacarpal joint of *Australopithecus africanus* was not adapted to enable supination during flexion, a capacity for human-like wrist extension, and a styloid process on the base of the third metacarpal, are evidence of human-like adaptations to increased production and resistance of power in the *Australopithecus africanus* hand (Richmond & Strait, 2000; Ricklan, 1983), and does not directly contradict Skinner *et al.*'s

(2015) conclusions that *Australopithecus africanus* was capable of making and using stone tools. Rather, this study suggests that the hypothenar portion of the palm would have been used in a different manner by the *Australopithecus africanus* hand relative to modern humans during tool-related behaviours, with a fifth metacarpal that, while being capable of some flexion, and exposed to increased axial loads, such movement was not accompanied by supination. An *Australopithecus africanus* hamate is yet to be discovered, and as such, interpretation if the flexional and rotational capacity of the fifth metacarpal in the species is limited. Needless to say, the discovery and analysis of an *Australopithecus africanus* hamate would prove invaluable to interpretations of the utility of the fourth and fifth metacarpals in this species.

Australopithecus sediba

The distal articular surface of the *Australopithecus sediba* U.W. 88-1729 hamate displays a combination of human-like and non-human great ape-like features. The surface for the fourth metacarpal is of greater surface area than the fifth metacarpal surface, having a greater palmodorsal length and comparable mediolateral width. However, the angulation between the two surfaces is human-like, with the hamate-MCV joint surface being distomedially oriented relative to the distally-facing fourth. Further, the hamate-MCV joint surface is expanded medially, and both surfaces are only gently palmodorsally concave, with the fourth carpometacarpal surface lacking, for the most part, any great complexity to its surface. Along the first and second principal components, the U.W. 88-1729 hamate was more than one standard deviation from the mean values of every extant group and was only within one standard deviation of the *Pan troglodytes* mean value along the third principal component, though was within the range of the *Homo sapiens* sample along the first principal component. The canonical variates analysis classified U.W. 88-1729 as human with a probability of 100%, and the specimen was within the human range along the first two canonical variate axes, while along PC 3 and CV 3, the specimen was within the range of *Pan troglodytes.* The hamate-metacarpal surface of U.W. 88-1729 had an absolute Procrustes distance closest to the *Homo sapiens* mean shape, but the specimen was further from the mean shape of each group than every specimen of the respective groups (tables 5.4.2 & 5.4.4).

Both surfaces of the *Australopithecus sediba* fifth carpometacarpal joint display several distinctly-human features. The PC 1 value of the U.W. 88-118 fifth metacarpal was within the interquartile range of the *Homo sapiens* group, and within the group's first quartile along the second principal component. The joint surface was categorised as *Homo sapiens* with a probability of 98.7% by the CVA, and along each CV axis it was within the range of *Homo sapiens.* Nevertheless, in terms of absolute Procrustes distance, U.W. 88-118 was the fossil furthest from the mean shape of modern humans, though was closer to the human mean shape than to any other extant group. Likewise, along the first two principal components of the hamate-MCV surface, W.U. 88-95 was within the human range and had the strongest negative PC1 score of all fossils, being at the extreme negative end, reserved for the first quartile of modern humans (figure 7.2.2). The CVA assigned U.W. 88-95 as *Homo sapiens* with a confidence of 100%, and the specimen was in the human range along all CV axes. However, as with the MC5 surface, in terms of absolute distance, U.W. 88-95 was the furthest from the *Homo sapiens* average shape, though was again closest to the average shape of the group. These results are explained by the medially expanded and palmodorsally squat profile of the joint. However, the joint surfaces do not display a human-like sellar morphology. Rather, the surface for the fifth metacarpal of the U.W. 88-1729 hamate is concave both in the mediolateral and dorsopalmar plane, while the fifth metacarpal proximal articulation of U.W. 88-117 is convex in both planes. As such, rather than having a saddle-shaped morphology, the fifth carpometacarpal joint of *Australopithecus sediba* more closely resembles a condyloid joint.

The hamate-MC4 joint surfaces of *Australopithecus sediba* are both overwhelmingly flat and featureless, and similar to the general *Homo sapiens* condition, albeit mediolaterally wider, comparatively, especially the hamate's articular surface for the fourth metacarpal. Along the first principal component, the MC4 surface of U.W. 88-1729 was within one standard deviation of the mean shapes of *Gorilla* and *Homo sapiens* and within the range of both groups, which is explained by its wider mediolateral width. The U.W. 88-117 fourth metacarpal's proximal surface was in the *Homo sapiens* range along all three studied PC axes, though was more than one standard deviation from the group's mean value along the first two. Canonical variates analysis classified both surfaces as *Homo sapiens* with a confidence of 100%, and both surfaces were closest to the mean shape of *Homo sapiens* when absolute Procrustes distances were assessed, though they were comparatively further from the mean shape than the modern human sample itself. The U.W.

88-95 hamate's fourth metacarpal surface was within one SD of the *Homo sapiens* mean shape along the first principal component and was classified as *Homo sapiens* by the CVA.

Overall, the morphologies of the *Australopithecus sediba* hamate-metacarpal joint surfaces display a mosaic of human and non-human traits. The surfaces of both the fourth and fifth carpometacarpal joints are relatively simple, and it is unlikely that flexion would have been restricted to any great extent. The hamate-MCV joint surfaces suggest that the joint was exposed to increased loads, being mediolaterally expanded as well as mediolaterally angled relative to the fourth carpometacarpal joint. However, the hamate-MCV joint surfaces, while exhibiting some traits akin to modern humans, were not saddle-shaped, and flexion of the metacarpal was therefore unlikely to have been accompanied by supination.

It has been previously stated that the MH2 hand exhibits a unique mosaic of features indicating that, while it was likely capable of enhanced dexterity, it would still have been capable of powerful flexion during locomotory grasping (Kivell *et al.*, 2022; Marzke, 2013). Despite the absence of a saddle-shaped morphology of the fifth carpometacarpal joint and a larger fourth metacarpal articulation of the hamate relative to the fifth, all other features of the ulnar carpometacarpal joints of *Australopithecus sediba* are human-like, and the overall morphology is consistent with hypothenar digits that were capable of flexion. Neither the fourth nor fifth carpometacarpal joints would have precluded movement at the joints, exhibiting as they do a mild and gentle palmodorsal curvature. The palmarly-projecting hamulus would have likewise facilitated flexion at the hamate-metacarpal joints (Kivell, *et al.,* 2011). The high angle of proximo-ulnar divergence of the fifth carpometacarpal joint relative to the fourth may also have allowed greater mobility of the fifth metacarpal, as it would have lessened obstruction of movement of the fifth metacarpal by the fourth. The mediodistal facing fifth metacarpal surface is also indicative of a human-like direction of load transmission from the fifth metacarpal to the hamate, although the diminutive nature of the surface suggests that any such loads would have been less than is experienced by the modern human hand.

A mobile and ulnarly divergent fifth carpometacarpal joint would have facilitated flexion of the digit and enhanced its opposition to the thumb, and is consistent with other features of the *Australopithecus sediba* hand. Proportionately short fingers relative to a particularly long

thumb would have enhanced opposition of the fingers to the pollex and pad-to-pad precision grasping, leading to greater control and manipulation of small objects (Kivell, 2015; Marzke, 1997). An unusually long thumb may even have compensated for a lack of supination of the fifth metacarpal due to an absence of a sellar joint at its base by enhancing the range of pollical movement towards the hypothenar area of the palm. Although the pollical metacarpal is gracile, the morphology of the distal pollical phalanx and carpometacarpal morphology are evidence of forceful precision grip capabilities of the hand, and bone and joint shape and sizes would have accommodated stresses generated by forceful pinch and grasp by the thumb and fingers (Marzke, 2013). Despite the diminutive size of the fifth carpometacarpal joint relative to the fourth, the base of the fifth metacarpal itself is robust, suggesting that the extrinsic and intrinsic musculature to the fifth finger was well developed and consistent with forceful use of the ray (Kivell, 2015; Kivell *et al*., 2015).

Nevertheless, as with *Australopithecus afarensis* and *Australopithecus africanus*, the MH2 *Australopithecus sediba* hand retains morphological features indicative of a retention of arboreal locomotion. The proximal phalanges are moderately curved, and both the proximal and intermediate phalanges have well-developed flexor sheath ridges (Kivell *et al.,* 2015). The phalangeal morphology of MH2, and its palmarly-projecting hamulus, has been interpreted as indicative of powerful flexion of the fingers during grasping, and is consistent with upper limb and shoulder girdle morphologies adapted for above-head use of the arm (Churchill *et al.,* 2013, 2018; Kivell, *et al.,* 2011; Syeda *et al.,* 2021). A *Pongo*-like grasping signal in the trabecular structure of the metacarpals support this functional interpretation, combined with a modern human-like loading pattern within the first metacarpal (Dunmore *et al.,* 2020; Kivell *et al.*, 2022). A proportionately larger fourth carpometacarpal joint is also consistent with overhead grasping in *Australopithecus sediba*, although the absence of complex interlocking structures in this joint suggest that the fourth digit was likely loaded in a manner distinct from *Pan troglodytes* and *Pongo* during such behaviour, or that the behaviour was utilized less frequently. Again, the variable nature of the hominoid fourth carpometacarpal joint morphology renders its interpretation challenging.

Australopithecus sediba is contemporaneous with stone tools that would have been manufactured with bimanual striking of hammerstones on cores (Marzke, 2013). Previous work

has interpreted morphological features of the hand of this species to be indicative of capabilities of precision grips and handling and effective power grips, and by extension an ability to make and use the associated bimanually-produced stone tools, while retaining abilities for arboreal locomotory behaviours. The results of this study generally corroborate these observations and indicate that flexion of the fifth metacarpal was not impeded to the same extent as in extant non-human great apes. Nevertheless, flexion of the fifth metacarpal was likely not accompanied by supination, and while the base of the fifth metacarpal is angled in a human-like manner, the fifth digit would not have been utilized in an entirely comparable manner if *Australopithecus sediba* was making and using early stone tools.

Homo

Paranthropus robustus/early *Homo*

The proximal surface of the SKW 2954 fourth metacarpal is relatively flat both in the palmodorsal and radioulnar plane, although, again, is generally more complex than that of modern humans, suggesting that the fourth carpometacarpal joint of the associated SKW 2954 skeleton, though more flexible than extant non-human taxa, was more rigid and restrictive than the modern human condition. In the absence of corresponding hamate and fifth metacarpal material, and the lack of a definitive taxonomic assignment, interpretation of this specimen is challenging. Furthermore, SKW 2954 originated from Member 2 from Swartkrans, and is dated to between 1.8 and 1.0 Ma (Gibbon *et al.,* 2014), and is therefore not contemporaneous with Lomekwian tools. Its inclusion in this study was therefore of limited utility when considering earlier lithic artefacts.

Along the first principal component, SKW 2954 was more than one standard deviation from the mean value of all groups, though it was within the range of all extant taxa. Along the second principal component it was within one standard deviation of the mean value of the *Pan troglodytes* sample, and within the interquartile range of *Pan troglodytes.* Nevertheless, the canonical variate analysis assigned the specimen as *Homo sapiens* with a confidence of 93.7%, and with regards to absolute Procrustes distance, was closest to the mean shapes of *Homo*

sapiens and *Pan troglodytes.* If anything can be discerned from interpretation of this specimen, it is that a non-human-like morphology of the fourth carpometacarpal joint was still retained in hominins that may have been adept tool-users (Backwell and d'Errico, 2001). Though, to reiterate, in the absence of associated osteological material and definitive taxonomic assignment, and in interpreting such a variable joint surface, any conclusions must be considered highly speculative.

Homo floresiensis

The hamate-metacarpal articulations of *Homo floresiensis* are among the most intriguing of the fossil hominin specimens examined in this study. Along the first principal component, the Liang Bua composite hamate was within one standard deviation of the human mean value and within the group's interquartile range. Along the second principal component it was within one standard deviation of the *Gorilla* mean value, and within the ranges of the African non-human great apes. Along the third principal component, the Liang Bua hamate was within one standard deviation of the mean values of both modern humans and gorillas, and within the ranges of both groups. The intermediate shape between *Homo sapiens* and *Gorilla* is reflected in its classification as *Homo sapiens* with a probability of 54.3%, and as *Gorilla* with a probability of 45.4% by the canonical variates analysis, and it being closest to the mean shapes of both groups in terms of absolute Procrustes distance - though all samples of all groups are closer to their relative mean shapes than Liang Bua is. The intermediate nature of the Liang Bua composite hamate between *Homo sapiens* and *Gorilla* likely results from the relative sizes of the two metacarpal surfaces being more equal than the modern human condition, a feature also commented on by Orr *et al.* (2013).

The shape of the hamate-MCV surface, when viewed in isolation, is notably unhuman-like, and displays several features more reminiscent of *Gorilla*. The palmar portion of the *Homo floresiensis* hamate-MCV surface is strongly directed distally onto the hamulus, particularly along its midline, resulting in a palmodorsal concave curvature that is stronger than modern humans and very similar in shape to gorillas. Orr *et al.* (2013) noted that the MCV facet extends a considerable way onto the long and distally-inclined hamulus, and these results corroborate this

observation. As with *Gorilla,* the radioulnar waist of the surface is narrower than its palmar and dorsal edges, and the surface lacks the obvious radioulnar convexity that produces the saddle-shaped morphology of the surface associated with modern *Homo sapiens,* further corroborating Orr *et al.*'s (2013) observations. The similarity of the *Homo floresiensis* hamate-MCV joint surface on the hamate to that of *Gorilla* was reflected in the results of the canonical variates analysis, which classed the Liang Bua composite hamate's fifth metacarpal surface as *Gorilla* with a confidence of 73%, and as *Homo sapiens* with a confidence of less than 3%. However, the surface was within one standard deviation of *Homo sapiens* and within the range of all African species along the first and second principal components, and within one standard deviation of the mean value of gorilla along the second principal component. The Procrustes distance of the Liang Bua composite hamate was of similar distance from *Homo sapiens*, *Gorilla* and *Pan troglodytes*, being approximately equally dissimilar from all African great ape taxa, though closest to the *Homo sapiens* mean shape.

The Liang Bua composite hamate's hamate-MC4 joint surface also returned intriguing results. Visual assessment of the joint shows a relatively flat joint that does not display the complex morphology which confers stability in the non-human and some earlier hominin taxa. However, while the palmar surface is not bevelled distally, there is a slight ballooning of its laterodorsal surface. The canonical variate analysis classified the specimen as *Homo sapiens* (92.9%, with a 7.1% probability of belonging to *Gorilla*). However, it was within the range of *Gorilla* along all CV axes, within one standard deviation of *Gorilla* along the two first principal components, and within the range of that group along the first two and the fifth principal component. Its Procrustes distance was also closest to the gorilla mean shape.

The hamate-metacarpal articulations of *Homo floresiensis* reflect the rest of the hand and wrist in exhibiting a combination of derived and primitive characters (Orr *et al.,* 2013). The fifth carpometacarpal surface is of approximately equal surface area relative to the fourth, unlike *Pan troglodytes* and *Pongo* and several earlier hominins. However, there is no indication that the joint was adapted for greater freedom of motion. The morphology of the fifth carpometacarpal joint of *Homo floresiensis* is likely to have inhibited flexion and any associated supination at the joint given the strong distal projection of the surface onto a distally projecting hamulus (Orr *et al.,* 2013). The relative inflexibility of the fifth CMC joint, and the absence of features that would

facilitate flexion and supination of the fifth metacarpal at its proximal articulation, complement the conclusions of Orr *et al.* (2013) that the less oblique orientation of the MC-II facet on the capitate of *Homo floresiensis* would have compromised the capacity of the second metacarpal to pronate, and thus corroborates previous observations that the hand of *Homo floresiensis* lacked modern human morphologies relating to both the cupping of the palm and for accommodating stresses across the wrist (Marzke, 2013). The similarity of the hamate-MCV surface to non-human African taxa further complements previous research that concluded that the morphology of the scaphoid, trapezoid and capitate of *Homo floresiensis* are *Pan*-like and show none of the features associated with committed tool-use in modern humans, or a hamulus which lacks the oval-shaped cross sectional characteristic of modern humans and Neanderthals (Orr *et al.,* 2013; Tocheri *et al.,* 2007). On the contrary, the highly curved palmar surface of the joint and its constricted and radioulnarly-flat midportion suggest that the joint was rigid.

Nevertheless, the archaeological record unequivocally shows that *Homo floresiensis* was making and using Oldowan-like stone tools. Given that the hamate-metacarpal joints of the species appear less mobile than modern humans, the use of the fifth digit of the *Homo floresiensis* hand during such behaviour was clearly distinct from the function of the digit in modern humans. Whether this is a unique adaptation of the hand of the species due to their diminutive stature, and the smaller size of their hands relative to their environment, might warrant further analysis. The morphology of the *Homo floresiensis* carpometacarpal articulations highlight the fact that the evolution of the hominin hand was not linear, and a fossil species' ability or inability to make and/or use stone tools cannot, and should not, be inferred from the presence or absence of a single feature.

Homo naledi

The overall morphology of the metacarpal articulation of the U.W. 101-1729 *Homo naledi* hamate displays several unambiguously modern human-like characteristics. The surfaces for the fourth and fifth metacarpals are clearly divergent from one another, with the hamate-MC5 surface angled to face distomedially relative to the hamate-MC4 surface. The surface for the fifth metacarpal is radioulnarly convex resulting in a saddle-shaped morphology, and the surface for

the fourth metacarpal is relatively flat and featureless. These similarities to the modern human form are reflected in the placement of U.W. 101-1729 within one standard deviation of the modern human mean value along the first principal component, and within the range of *Homo sapiens* along the first principal component. However, the hamate-MCV surface is not expanded medially, and the two articulations are approximately similar in terms of surface area. In this respect it is more similar to the form of *Gorilla*, and is reflected in the specimen's PC 2 value, which is within one standard deviation of the *Gorilla* sample alone, and outside the range of the *Homo sapiens* sample. These shared similarities between *Homo sapiens* and *Gorilla* result in U.W. 101-1729 being positioned intermediately between the *Homo sapiens* and non-human great ape samples along the first canonical variate axis. Nevertheless, the canonical variate analysis of the hamate-metacarpal surface placed U.W. 101-1729 within the modern human sample with a confidence of 99.9%, and the specimen was within the range of *Homo sapiens* along both the second and third CV axes. Furthermore, analysis of Procrustes distances showed that the specimen's shape was more similar to the mean shape of the *Homo sapiens* sample than to any other group, and closer to that sample's mean shape than 4.66% of *Homo sapiens* specimens.

When considered in isolation, the articular surfaces of the fifth carpometacarpal joint of *Homo naledi* is more similar to modern humans than to any other taxa. While the surface does not extend medially to the same extent as in modern humans, the joint is smoothly palmodorsally concave with no abrupt bevelling, and is also mediolaterally convex, resulting in the saddle-shaped morphology associated with modern humans. The hamate-MCV surface of U.W. 101-1729 was within the range of *Homo sapiens* along the first two principal component axes and was within one standard deviation of the *Homo sapiens* first principal component mean value. However, along the second principal component, U.W. 101-1729 was more than 1 SD from the *Homo sapiens* mean value but within 1 SD of *Gorilla*, and while the CVA classified the specimen as *Homo sapiens* with a confidence of 88.2%, there was a 10.6% affinity to the *Gorilla* sample, and the specimen was positioned intermediately between modern humans and non-human taxa along the first canonical variate axis. These results are likely due to a lack of a notable medial expansion of the joint surface, resulting in the palmar edge being proportionately wider relative to the rest of the surface, and a more distal projection of the palmar surface, as is seen in *Gorilla.* Nevertheless, the MC5 surface of U.W. 101-1729 was closer to the mean shape of the *Homo*

sapiens sample than any other groups when the upper-tail cumulative distribution of Procrustes distances were measured, being closer than 20.6% of human specimens.

Similar to the hamate-MCV joint surface of U.W. 101-1729, the proximal articular surface of the U.W. 102-028 *Homo naledi* fifth metacarpal exhibits some non-human features, though overall, clearly most closely resembles a modern human morphology. It is consistently and uniformly palmodorsally convex, with no bevelling of the palmar surface. However, both the palmar and dorsal edges project distally, resulting in a highly curved surface in the palmodorsal plane. The palmar edge of the surface is also radioulnarly wide relative to the rest of the surface, and there is no medial expansion of the joint surface as is present in modern humans, with the palmodorsal length of the joint being slightly longer than it is radioulnarly width. Nevertheless, the joint is mediolaterally concave, and the overall shape therefore mirrors the saddle-shaped morphology of the corresponding surface on the hamate. U.W. 101-1309 was within one standard deviation of the mean value of *Homo sapiens* along the first two principal components and was within the range of that group along the first three principal components. Similarly, it was within the *Homo sapiens* range along the first and third canonical variate axis and was classified by the CVA as *Homo sapiens* with a confidence of 74.4%. Its placement within the ranges of the non-human African apes along CV 2, and a 25.5% likelihood of belonging to the *Gorilla* sample, is likely due to a distally-projecting laterodistal corner, and a relatively high rate of palmodorsal curvature. In terms of absolute Procrustes distance, the U.W. 101-1309 fifth metacarpal proximal surface was closest to the mean shape of the *Homo sapiens* sample, though was further than 93.44% of human specimens to the mean shape.

As with the fifth carpometacarpal joint, the hamate-MC4 joint surfaces of *Homo naledi* displayed a mixture of human and non-human features. The MC4 surface of the U.W. 101-1729 hamate is more mediolaterally wide than would be expected of a modern human specimen, and while being for the most part relatively flat and featureless, does exhibit a subtle ballooning of the dorsolateral surface, and extremely mild bevelling of the mediopalmar corner, reminiscent of the stabling and interlocking features of the *Pan troglodytes* surface, albeit much less prominent. The intermediate nature of the surface is reflected in its PC 1 value being more than one standard deviation from the mean value of every extant group, though within the first quartile of *Gorilla.* Nevertheless, the canonical variate analysis classified the hamate-MC4 surface of U.W. 1010-

1729 as *Homo sapiens* with a 100% confidence and was within the range of modern humans along all three canonical variate axes. Conversely, due to its mediolaterally broad and mildly complex surface, its Procrustes distance from the mean shape of *Gorilla* was less than its distance to *Homo sapiens*, though it was comparably far from both compared to the samples of each.

Of the two *Homo naledi* proximal MC4 surfaces studied, U.W. 101-1318 was more similar to the modern human form than U.W. 102-028, being mediolaterally narrower with a less complex surface. U.W. 102-028 exhibited mild proximal bevelling of its mediopalmar corner, and undulation of its laterodorsal surface, reminiscent of, but not to the same extent as, the *Pan troglodytes* surface. Both specimens were within the *Homo sapiens* range along all principal components, though U.W. 101-028 was consistently at the extremes of the *Homo sapiens* sample, and outside its interquartile range. Both *Homo naledi* metacarpals were assigned to the *Homo sapiens* extant group with a confidence of 100% and were closer to the mean shape of modern humans than to any other extant taxa. However, U.W. 102-028 was closer to *Pan troglodytes* than U.W. 101-1318 was when absolute Procrustes distances were considered, likely due to the distal projection of the mediopalmar corner of the joint surface and a more irregular dorsolateral surface. These subtle variations between the morphology of two specimens of the same species again reflect the highly variable nature of the fourth carpometacarpal joint in hominoids, and the challenges associated in interpreting the function of such a variable joint.

The combination of “primitive” and derived human-like traits of the fourth and fifth carpometacarpal joints reflects a wider pattern throughout the *Homo naledi* hand. The presence of a sellar fifth carpometacarpal joint with evidence of reduced loading mirrors a relatively small first carpometacarpal joint that also likely lacked the capacity for human-like loading of the joint (Bowland *et al.,* 2021; Kivell *et al.*, 2015). However, the radial carpus and pollex of *Homo naledi* also possess a suite of derived features considered advantageous to high external loading of the thumb during tool-related behaviours, and which are only found in taxa known to produce and utilize complex tools, including a trapezium-trapezoid facet that extends onto the scaphoid tubercle, and a palmarly-expanded trapezoid (Kivell, 2015; Kivell *et al.,* 2015, 2022). The pollical distal phalanx is radioulnarly broad with a clear gabled attachment for the *flexor pollicis longus* muscle, and the thumb itself is long relative to the fingers (Kivell *et al.,* 2015). While these features suggest a long, robust, and powerful thumb capable of pad-to-pad forceful precision

grips (Kivell *et al.,* 2023), the highly curved non-pollical proximal and intermediate phalanges of *Homo naledi*, coupled with a cranially-oriented shoulder and extremely low humeral torsion, suggest that the hand was still habitually recruited for grasping during arboreal locomotion (Feuerriegel *et al.,* 2017; Kivell *et al.,* 2015, 2022). Furthermore, the base of the third metacarpal lacks the styloid process present in modern humans which acts as a buttress against hyper expansion of the third carpometacarpal joint (Kivell *et al.,* 2015).

Kivell (2015) considered that the presence of a saddle-shaped morphology of the fifth carpometacarpal joint indicated a capacity for efficient precision and precision pinch grips and would have enhanced opposition of the fifth finger to the thumb. The ulnar divergence of the joint relative to the fourth carpometacarpal joint is likely to have further enabled opposition of the fifth digit to the thumb by not only altering the axis of longitudinal rotation, but also relaxing limitations to flexion of the fifth metacarpal imposed upon it by the fourth. Further, this orientation of the joint would have more efficiently directed loads transmitted across the joint towards the carpal complex. The surfaces of the fourth carpometacarpal joint, while relatively flat and featureless, are more complex than the modern human condition, and the increased mediolateral width of these surfaces suggest that the fourth carpometacarpal joint was exposed to proportionately higher loads than in the modern human hand. The retention of such features in the hand of *Homo naledi* correspond with other features that are consistent with arboreal grasping and indicate that the fourth carpometacarpal joint of *Homo naledi* retained at least partial adaptations to resist extensional stresses at this joint. A relatively flat and featureless fourth carpometacarpal joint would facilitate flexion at the fifth carpometacarpal joint simply by not restricting its movement, and the divergence of the two joint surfaces would further free the fifth metacarpal to flex and supinate. However, discrepancies between the two fourth metacarpal surfaces studied complicate interpretation of this joint's function in *Homo naledi*.

The fourth and fifth carpometacarpal joints of *Homo naledi* are, for the most part, human-like. The sellar morphology of the fifth carpometacarpal joint, the flat morphology of the fourth, and the particularly robust general morphology of the fifth metacarpal, with its well-developed crest for *opponens digiti minimi* (Kivell, *et al.,* 2015), infer a human-like ability to flex and supinate the fifth metacarpal, thus facilitating the capacity for distinctively human movements and postures such as the cupping of the palm, pinch precision grips and the ability to manipulate

objects with the fingers of a single hand (Kivell *et al.,* 2015). And while the fifth carpometacarpal joint is not medially expanded, suggesting that, as with the first carpometacarpal joint, the joint was not exposed to, nor was it able to withstand, the same magnitude of external stresses as in modern humans, the results of this study corroborate previous assessments that the fifth digit of *Homo naledi* was capable of flexion and supination, therefore enhancing the hand's ability to cup the palm, and to effectively execute power "squeeze" grips.

Homo neanderthalensis

Unsurprisingly, the overall morphologies of the hamate-metacarpal articular surfaces of *Homo neanderthalensis* are most similar to contemporary humans. All *Homo neanderthalensis* specimens were classified into the *Homo sapiens* sample with a confidence of 100% when the entire hamate-metacarpal surface was considered, and overall, the hamate-metacarpal surface of Neanderthals and modern humans are very similar, with a hamate-MCIV surface that is comparable in size and overall shape. The mean shapes of the hamate-MCIV surfaces of the *Homo sapiens* and *Homo neanderthalensis* samples used in this study are almost identical, with only the laterodorsal edge showing any noticeable difference, being very slightly more proximal in Neanderthals than in modern humans. Interestingly, all four *Homo neanderthalensis* specimens had a closer absolute Procrustes distance to the mean shape of *Homo sapiens* than the early modern human Tianyuan-1.

Any difference between the hamate-metacarpal articular surfaces of modern humans and Neanderthals are concentrated on the hamate-MCV surface, with the hamate-MCIV surfaces of both groups being morphologically identical. However, the ulnar divergence of the fifth carpometacarpal joint relative to the fourth does appear to be less acute in Neanderthals than in modern humans. The relative orientations of the hamate-metacarpal joints of Neanderthals suggest that not only were movements at both hamate-metacarpal joints less independent from each other than in modern humans, but also that the fifth metacarpals of Neanderthals were not as ulnarly deviated as in modern humans (*contra* Musgrave, 1971).

The hamate-MCV surface of Neanderthals is notably longer in the palmodorsal plane and narrower in the radioulnar plane than the mean shape of modern humans and does not display the proximomedial extension of the medial edge of the surface common in modern humans. This results in the hamate-MCV facet of the Neanderthal hamate comprising proportionately less of the hamate's total radioulnar breadth compared with the modern human condition. These observations corroborate the work of Niewoehner (2007), who concluded that this implied that Neanderthals experienced primary axial loads at both the fourth and fifth metacarpal bases equally, whereas modern humans are adapted for reduced axial loads at the fourth carpometacarpal joint and an increase at the fifth. The palmar edge of the surface projects slightly more distally, resulting in a slight increase in the dorsopalmar concavity of the facet in Neanderthals. The degree of radioulnar convexity of the hamate-MCV surface characteristic of modern humans is generally lacking in Neanderthals, with only Tabun-1 exhibiting only a mild sellar morphology of the joint surface, while Regourdou-1 and Kebara-2 are generally flat in that plane, and Shanidar-4 displaying a concave radioulnar curvature, resulting in a more condyloid than sellar morphology. Niewoehner (2007) also noted a radioulnar flattening of the hamate's facet for the base of the fifth metacarpal. The palmodorsally narrower and deeper, and radioulnarly flatter hamate articulation for the fifth metacarpal complements Trinkaus's (2006) and Niewoehener's (2007) assessments that the corresponding facet on the base of the fifth metacarpal is more of a condyloid morphology and lacks the radioulnar concavity notable in modern humans.

Overall, the morphology of the Neanderthal hamate-metacarpal articulation suggests that the fourth carpometacarpal joint was exposed to proportionately greater axial loading, and the fifth proportionally less, relative to modern humans, given the differences in relative sizes of the joint surfaces between the two species. This increased relative size of the fourth carpometacarpal surface compared to the fifth is either a retention of the primitive condition, or an indication that the joint was loaded to a proportionately greater extent than in modern humans. The fact that Neanderthals were habitual and accomplished tool users would suggest that the hamate-metacarpal joints were subject to different loading regimes than is the case in modern humans, and/or that these joints are uniquely derived relative to the modern human form.

The ability of the fifth metacarpal to supinate during flexion appears to have been reduced in Neanderthals compared to modern humans, reflected in the less ulnarly-oriented MCV facet relative to the MCIV facet, a lack of medial expansion of the hamate-MCV surface, and a reduction/absence of the radioulnar convex curvature and associated sellar morphology of the surface. The absence, or reduction, of features that would have facilitated conjunct rotational movements of the Neanderthal fifth metacarpal reflects the absence of such features on the corresponding and opposite surface morphology of the fifth metacarpal base, and a metacarpal-V head morphology that also would have reduced the capacity of the fifth proximal phalanx to supinate and ulnarly-deviate during flexion (Niewoehner, 2007; Trinkaus, 2006). While such morphological differences between modern humans and Neanderthals is slight compared to the differences between modern humans and extant non-human taxa and earlier hominins, the overall morphologies of the articulations of the fifth carpometacarpal joint, in conjunction with those of the fifth metacarpophalangeal joint, suggest that Neanderthals, while undeniably dexterous, lacked the characteristically modern-human fine-tuned capacity for supination and radial rotation of the fifth ray during flexion and opposition to the thumb. However, evidence of hypertrophy throughout the Neanderthal hand, and in particular the increased mechanical advantage of the hypothenar muscles as indicated by an enlarged and palmarly-projecting hamulus and prominent crests on the fifth metacarpal shaft for the attachment of the *opponens digiti minimi* muscle (Trinkaus, 1983), suggest that the fifth metacarpal was likely strongly recruited during Neanderthal tool-using behaviours, and the less optimal rotational capacity of the fifth carpometacarpal joint may have been compensated for by such hypertrophy of the hypothenar region of the Neanderthal hand.

Early *Homo sapiens*

As with the *Homo neanderthalensis* sample, the overall hamate-metacarpal surfaces of the two early modern *Homo sapiens* specimens (Qafzeh-9 and Tianyuan) unambiguously resemble modern *Homo sapiens*, with both specimens having mediodistally-facing MCV surfaces that are saddle-shaped and proportionately larger than the MCIV surfaces. Both were classified as *Homo sapiens* with an extremely high degree of certainty by the three canonical variate analysis to which they were subject to. There does not appear to be any feature of either of the

early-modern specimens to suggest that the mobility of their fourth and fifth carpometacarpal joints differed markedly from that seen in later modern *Homo sapiens*.

Table 10.2: Summary of notable features of the fossil hominin specimens

	Hamate	Hamate-MC4	Hamate-MC5	MC4	MC5
Australopithecus afarensis	- Hamate-MC5 surface smaller than hamate-MC4 surface - Surfaces do not diverge in direction	- Ballooning of laterodorsal surface, reminiscent of non-human great apes, with corresponding topography on MC4 base, resulting in highly interlocking joint	- Condyloid CMC-V joint surfaces – surface is not radioulnarly convex (not saddle-shaped) - Surface is gently palmodorsally curved, and not bevelled - Surface is medially expanded at its palmodorsal midsection, resulting in a radioulnarly expanded and palmodorsally squat surface - Palmodorsal curvature is intermediate between modern humans and non-human taxa - Surface is distally-projecting, suggesting continuation onto the hamulus	- Indentation of laterodorsal surface corresponding to ballooning of the hamate surface	- Condyloid CMC-V joint surfaces - surface is not radioulnarly concave - Radioulnarly wide and palmodorsally squat - Palmodorsal convex curvature only slightly more acute than modern humans - No sharp bevelling of the palmar surface
cf. *Australopithecus afarensis*	- Ham-MC4 surface is proportionately larger than the Ham-MC5 surface -	- Surface is palmolaterally expanded - Surface is uniform and smooth, though is condylar and bowl-shaped - No laterodorsal ballooning of surface	- Ham-MC5 surface is angled medioproximally relative to the ham-MC4 surface - Surface is radioulnarly waisted - Surface is mediolaterally convex, and mildly saddle-shaped		
Australopithecus africanus				- Highly variable surface – from a flat surface to a highly-bevelled surface with a divot on the dorsolateral portion	- Medially expanded surface - Palmodorsal convex curvature more acute than in modern humans, and expanded on the palmar shaft,

					though does not exhibit non-human-like bevelling - Condyloid – not saddle-shaped
Australopithecus sediba	- Surface is only slightly palmodorsally concaved - Ham-MC4 surface is proportionately greater in size than Ham-MC5 surface - Ham-MC5 surface is distomedially orientated relative to the distally-facing Ham-MC4 surface - Human-like angulation between the two surfaces	- Flat and featureless CMC-4 surfaces, similar to modern humans, though mediolaterally wider	- Surface is expanded medially - Surface is condyloid rather than saddle-shaped		
Australopithecus robustus/early *Homo*			- Surface is flat and featureless	- Flat surface relative to non-human great apes, though less so than modern humans	
Homo naledi	- Divergent MC4 and MC5 surfaces – ham-MC5 surface angled distomedially relative to distally-angled ham-MC4 surface	- Surface is mediolaterally wide - Mild ballooning of dorsolateral surface and bevelling of palmar surface, but is otherwise flat and featureless	- Surface is saddle-shaped owing to radioulnar convex curvature -Gently palmodorsally curved - Medial surface is not medially expanded	- Variable MC4 base surfaces	- CMC5 surfaces do not exhibit palmar bevelling - Surface is mediodorsally convex resulting in a saddle-shaped morphology - Highly curved in palmodorsal plane
Homo floresiensis		- Surface is relatively flat and featureless - No bevelling of palmar edge	- Palmar edge projects distally onto the hamulus, resulting in a strong palmodorsal concave curvature		

		- Slight distal ballooning of dorsolateral edge	- Radioulnarly narrow midsection -Surface lacks a saddle-shaped morphology		
Homo neanderthalensis	- Ulnar deviation of Ham-MC5 surface relative to ham-MC4 surface less pronounced than in modern humans	- Surface is comparable to modern humans in overall size and shape	- Ham-MC5 surface is longer in palmodorsal plane and narrower in radiodorsal plane – thus comprising a proportionately smaller area than in modern humans		- Stronger palmodorsal curvature in Neanderthals than in modern humans - High variability in degree of radioulnar curvature of ham-mc5 surface, but generally lacking in saddle-shaped morphology - Flat-to-condyloid

10. 3 Summary

The aim of this project was to explore morphological variation in the fourth and fifth carpometacarpal joints of extant great apes including modern humans, and selected fossil specimens in an effort to identify morphological adaptations conducive to the production and use of early stone tools. The fifth carpometacarpal joint of modern humans is the most mobile of the non-pollical carpometacarpal joints, while those of non-human great apes are generally considered to be immobile. The fifth metacarpal, and to a lesser extent the fourth as well, is capable of substantial amounts of flexion accompanied by abduction and axial supination, which is vital for the effective execution of some precision grips, the power "squeeze" grip, opposition of the fifth digit to the thumb, and the cupping of the palm. Without such motions, human manual dexterity would be severely restricted. Several features have previously been identified in the hamate-metacarpal joints of humans which are considered to facilitate the movements of the fourth and fifth metacarpals. The human joints are gently palmodorsally curved, and the fifth carpometacarpal joint is proportionately larger than the fourth and is also saddle-shaped. These features are not only conducive of a high degree of flexile and rotational movement, but also reflect the increased loads transmitted across the fifth carpometacarpal joints of humans. The joints in non-human primates generally display an acute bevelling of the palmar surface, with a fourth carpometacarpal joint that is proportionately larger than the fifth carpometacarpal joint, and which does not have a gentle sellar morphology. While these features have been previously assessed in fossil hominin taxa, previous research has been limited to qualitative assessments. This project aimed to quantitatively assess variation in the fourth and fifth carpometacarpal joints through use of three-dimensional geometric morphometric analysis.

In addition to the aforementioned features, the results of this project also highlighted the significance of divergence of the fifth carpometacarpal joint relative to the fourth. The fifth carpometacarpal joint in humans is diverged medially and proximally so that the longitudinal axis of the fifth metacarpal is angled more transversely than the sagittally-oriented fourth. Conversely, both joints in non-human great apes are sagittally orientated. This feature, while largely overlooked or unnoticed in previous work, is considered by the conclusions of this research to be functionally important for several reasons. It not only increases the independence of movement of the fifth metacarpal from any restrictions posed upon it by the more restrictive fourth

metacarpal, but also widens the distal palm, and enhances the oblique orientation of the metacarpal heads, which in turn enhances effectiveness of the power “squeeze” grip and cradle grip when the fingers are powerfully flexed around a cylindrical object. Furthermore, the more transverse orientation of the joint more effectively transfers the substantial loads incurred on the fifth metacarpal during manipulative behaviours to the central carpal complex, where it may then be dissipated through the forearm. The fifth carpometacarpal joint of modern humans shows clear and unambiguous adaptations for increased mobility and force resistance. The human fourth carpometacarpal joint is likewise adapted for increased mobility, being more uniform and simpler than the complex interlocking joint of non-human taxa. Furthermore, the human fourth carpometacarpal joint is smaller than the fifth, indicating a decrease in load transmission across the joint, likely due to the redundancy of the hand in any locomotory strategy, and the increased importance of the fifth digit during manual manipulation. However, the fourth carpometacarpal joint of both modern humans and extant non-human taxa is highly variable, and the significance of any morphological signal at this articulation has been brought into question (Kivell *et al.,* 2022; Marzke *et al.,* 1994; Viegas *et al.,* 1991). This subtle variation in articular morphology both within and across taxa suggests that there may be limited functional consequences for this varying morphology, especially across joints with limited mobility which are bound by carpometacarpal ligaments. The highly variable nature of this joint is reflected in the results of this study, and interpretation of the functional significance of morphologies seen in fossil hominin specimens was challenging.

Species of both *Australopithecus* and *Kenyanthropus* have been recovered in chronological and geographical proximity to the Lomekwi site. The fourth carpometacarpal joint of *Australopithecus afarensis* is complex and suited for stability and resistance of extensional torsional loading, displaying an interlocking form. And while the fifth metacarpal of *Australopithecus afarensis* was capable of greater flexion than those of extant non-human great apes, such movement was not accompanied by supination. Furthermore, the fifth ray was not diverged medially, nor was the joint subject to the significant loads associated with modern human tool use. While the fifth digit of *Australopithecus afarensis* was capable of greater mobility than extant non-hominin taxa, the hypothenar portion of the hand is unlikely to have been used in a recognisably human-like manner if these hominins were making and using Lomekwian stone tools. The taxonomic affinity of the KNM-WT-22944-I hamate is contentious, belonging either to

Australopithecus afarensis or *Kenyanthropus platyops*. The KNM-WT-22944-I hamate is overall more human-like than the A.L. 333-50 *Australopithecus afarensis* hamate, displaying a fifth carpometacarpal surface that comprises a proportionately larger area of the hamate-metacarpal articular surface and which is proximo-medially diverged. The surface for the fourth metacarpal is also more uniform and less complex, and the hamate-MC5 surface is mediolaterally convex, resulting in a mild sellar-morphology of the joint surface. These features indicate that the fifth metacarpal corresponding to the KNM-WT-22944-I hamate was capable of flexion accompanied by supination, enhancing the fifth digit's ability to oppose the thumb during precision and power grips, and allowing effective transmission of loads from the fifth metacarpal through the carpus. In the absence of additional hand fossil material associated with the hamate, and the uncertainty regarding its taxonomic affiliation, it is difficult to contextualize these observations. However, the morphology of the distal articulation of the KNM-WT-22944-I hamate suggests that some human-like use of the hypothenar digits were within the capabilities of some hominin species contemporaneous with the earliest known stone tools found at Lomekwi.

The morphology of the fourth carpometacarpal joint of *Australopithecus africanus* appears to be highly variable,. The fifth carpometacarpal surface studied displays a mosaic of primitive and derived features, and while the fifth carpometacarpal joint of *Australopithecus africanus* was subject to increased medial loading, its mobility was limited similarly to *Australopithecus afarensis.*

The hamate-metacarpal joints of *Australopithecus sediba* also display a mosaic of features. As with other australopithecines, the surface for the fourth metacarpal is larger than the fifth metacarpal surface on the *Australopithecus sediba* hamate. However, the angulation between the two surfaces is human-like, indicating a medial deviation of the fifth digit. The hamate-MC4 joint lacks any great complexity, and the fifth metacarpal would have been capable of considerable flexion, though likely without any accompanying supination. While no stone tool artefacts are directly associated with the MH 2 skeleton, its notably long thumb may be indicative of a capacity for precision gripping, which is important in creating and using stone tools. An abducted fifth metacarpal capable of human-like flexion (though unaccompanied by supination) in the hand of *Australopithecus sediba* would enhance this ability.

The fifth carpometacarpal joint of *Homo naledi* is diverged medially with respect to the fourth and is saddle-shaped, with a fourth metacarpal surface that is more flat and featureless than in extant great apes, though both surfaces are approximately similar in size. The mosaic morphology of these joints compliments the rest of the *Homo naledi* hand. *Homo naledi* post-dates the earliest archaeological record by almost three million years and is therefore not directly pertinent when considering authorship of Lomekwian stone tools. Furthermore, no lithic artefacts have been discovered in direct association with *Homo naledi*, and if they did make and use stone tools, the sophistication of their culture is unknown. Nevertheless, the overall morphology of the hand of *Homo naledi* suggests capabilities for efficient precision and precision pinch grips, and enhancing the hand's ability to cup the palm, and to effectively execute power "squeeze" grips.

Three of the *Homo* species included in this study are unambiguously associated with the manufacture and use of stone tools. *Homo floresiensis* is associated with Oldowan-like stone tool technology (Brumm *et al.,* 2006; Moore and Brumm, 2009). The *Homo neanderthalensis* specimens and Qafzeh-9 early *Homo sapiens* are associated with Mousterian lithic culture, and while no cultural remains were discovered with the Tianyuan early *Homo sapiens* skeleton, this individual was undoubtably capable of making and using relatively sophisticated tools. There is high variability in the morphology of the hamate-metacarpal joints of these three tool-using *Homo* species. The morphology of the *Homo floresiensis* hamate's distal articulation indicates an approximately equal loading of both joints, and while the fourth carpometacarpal joint is simple and featureless, the fifth likely lacked human-like mobility, being constrained in flexion and supination. The association of Oldowan-like tools with a hand in which the fifth carpometacarpal joint lacks many of the derived features seen in modern humans brings into question the utility of mobile and robust hypothenar digits in the production and use of early stone tools, and whether the early hominin taxa posited to have been early stone tool users were even using derived human-like grips and postures to make these artefacts. The Neanderthal specimens assessed likewise raise interesting questions. The distal surface of the Neanderthal hamate is highly variable, and as with *Homo floresiensis*, the fourth and fifth metacarpal joint surfaces are more equal in terms of surface area than is observed in modern humans. The surface for the fifth metacarpal of the hamate is generally deeper proximodistally, and lacks a sellar morphology, indicating that flexion and supination of the fifth metacarpal was not as important for

Neanderthal dexterity as it is to modern humans. The decreased ulnar divergence of the surface also suggests that any loads transmitted across the joint were not directed laterally in a human-like manner, but rather more proximally, and also that, when cylindrical tools were being utilized, they were handled more transversely across the palm, rather than obliquely, as in modern humans (Niewoehner, 2001, 2005, 2007). The full suite of modern human-like features in the hamate-metacarpal joints of hominins, comprising of a planar fourth carpometacarpal joint accompanied by an enlarged, saddle-shaped, and proximo-medially divergent and expanded fifth carpometacarpal joint does not appear in the fossil record until the advent of early *Homo sapiens.* The late advent of a complete suite of human-like adaptations may reflect more advanced behaviours, such as an increased reliance on hafted tools used during hammering-like behaviour, in which a medially diverged fifth digit can powerfully flex and rotate around a tool handle positioned obliquely across the palm while simultaneously transferring considerable loads proximolaterally towards the central carpal complex to be dissipated along the forearm.

10. 4 Limitations of this project and scope for future research

The scope of this research was constrained by the limited number of comparative taxa used in the study. While a small number of *Hylobatidae* and *Cercopithidae* were digitized with the intention of including them in the study, the poor quality of these scans precluded this. The inclusion of more diminutive primate taxa in this study through utilization of micro-CT scanning, including *Hylobatidae*, *Cercopithidae* and *Cebidae* (which are known to use their hands not only for various locomotory behaviours but also for lithic tool-use) would provide a deeper insight into the adaptive significance of morphological variation of the hamate-metacarpal joints in terms of hominin adoption of habitual tool-making and tool-using behaviours and arboreal locomotion. The inclusion of *Pan paniscus* would also have been of great benefit to this study, not only as the species is our closest living relative, but also as they are generally considered to be more arboreal than chimpanzees (Kivell *et al.,* 2023), and would therefore have provided comparisons of fossil hominin taxa with a more arboreal close relative. An increase in the number of certain taxa used in the study would also have been of great benefit. This study did not identify morphological differences in the hamate-metacarpal joints of various sub-species of *Pan troglodytes.* This is worthy of note given that *Pan troglodytes verus*, the Taï Forest, or western chimpanzee, are

distinguished by their use of stone tools in a bipolar manner for access to nutrients. There may simply be no morphological variation in the hamate-metacarpal joints between *Pan troglodytes verus* and other sub-species of chimpanzee. Alternatively, the small number of *Pan troglodytes verus* specimens used in this study (three) may have precluded any signal being identified relative to the greater number of other *Pan troglodytes* species, as well as other genera. A comparative assessment of the fourth and fifth carpometacarpal joints comprising of a greater number of this sub-species of chimpanzee may (or may not) identify significant differences in the joint morphology relating to their use of lithic material as tools.

An obvious omission of this study is that, while the fourth and fifth metacarpals articulate with the hamate at their respective carpometacarpal joints, they also interact with each other at the intermetacarpal joint. It has been stated in previous chapters that the fourth and fifth metacarpals rarely move independently of each other, and the human fifth metacarpal is restricted in its flexion-extension plane when the fourth metacarpal is held stationary. It is therefore reasonable to conclude that the intermetacarpal joint of the fourth and fifth rays display derived morphologies or angles relative to the carpometacarpal joints in modern humans to facilitate such flexibility. This study did not consider these articulations for various reasons: the digitizing and additional statistical analysis was not feasible due to time restraints; and any consideration of the morphology of the fourth metacarpal's articulation with the fifth would, by extension, necessitate consideration of its articulation with the third metacarpal, and by further extension the capitate-metacarpal articulations. Such considerations were therefore beyond the scope of this study. However, future research into not only the morphology of the intercarpal joints, but also the respective angles of the hamate-metacarpal and intercarpal surfaces (see Orr *et al*., 2013) would provide further insight into the freedom of motion permitted for the fourth and fifth metacarpals of fossil hominin taxa, and may shed light on medial divergence of the fifth metacarpal of fossil taxa where the hamate is not available for analysis, for example in *Australopithecus africanus*.

In addition to the limitations and shortcomings of this project, there is considerable scope for further lines of inquiry regarding the functionality of the hamate-metacarpal joints of extant and extinct primate taxa. There is currently no quantitative information on the range of motion of the fourth and fifth carpometacarpal joints of extant non-human taxa. Movement at the fifth

carpometacarpal joints of non-human great apes have traditionally been considered to be null (Domalain *et al.,* 2017). In-vivo measurements of movement at the fourth and fifth carpometacarpal joints of non-human taxa will confirm or disprove this assumption, and would further inform interpretations of the significance of hamate-metacarpal joint morphologies in terms of the human hand's unique propensity for performing distinctive forceful precision and precision-pinch grips and power "squeeze" grips, and to what degree the joint morphology in extant non-human taxa restrict movements compared to modern humans. This information would further inform interpretations of movement at these joints in fossil hominin taxa.

Investigating the internal bone structure of the hamate and fourth and fifth metacarpal bases would also provide valuable information on human-like manual behaviours in early hominins. The interpretation of external bone morphology is often ambiguous, and interpretations of the functional significance of some features can be challenging given that they may be retentions of an ancestral condition and may not in fact be functionally significant (Skinner *et al*., 2015; Ward, 2002; *contra* Almecija *et al.,* 2015). This is highlighted by the results of the hamate-MC4 joint surfaces in this study. Trabecular bone, however, remodels throughout an individual's life in response to mechanical loading, and variations in locomotor and manipulative behaviours across extant and extinct hominoids may therefore be reflected in differences in trabecular bone structure (Ruff, Holt and Trinkaus, 2006; Tsegai *et al.,* 2013). Recent advances in the internal imaging of osteological material have enabled comparisons in the trabecular bone morphology of extant and fossil specimens and can provide additional information regarding behavioural adaptations during the life of individuals in both extant and fossil taxa, as trabeculae remodel in response to habitual load during an individual's lifetime (Skinner *et al.,* 2015). The analysis of trabecular bone structure can therefore provide direct morphological evidence of forceful precision and tool-use in hominins prior to the first recognizable stone tools and offers a method for linking archaeological evidence with particular hominin taxa (Dunmore *et al.,* 2020, 2024; Skinner *et al.,* 2015; Stephens *et al.,* 2018; Syeda *et al.,* 2021, Tsegai *et al.,* 2017). Assessment of the concentration of trabecular bone in the hamate and proximal joints of the fourth and fifth metacarpals of extant primates and fossil hominins would complement and develop upon the results of this study.

Lastly, this research was limited by the fossil hominin specimens available for interpretation. The inclusion of additional fossil material, such as the associated hamate and metacarpals of the ARA-VP-6/500 *Ardipithecus ramidus* skeleton, and Miocene hominoids, would provide a greater understanding of the evolutionary development and functional significance of the hamate-metacarpal joint of fossil hominins, and the role of the hypothenar area of the hand in the development of hominin tool-use and locomotory repertoires in basal hominins. It also goes without saying that the discovery and evaluation of additional hominin fossil material would be of considerable value for further research into this topic. Research into the evolutionary development of the human hand is restricted by the sparce recovery of relevant material from the Early and Middle Pleistocene (Trinkaus, 2016). Manual skeletal material from this period is rare, localized in time and space, and consist of isolated bones rather than associated hand skeletons (Richmond *et al.,* 2016; Trinkaus, 2016). Nevertheless, the more sophisticated Acheulean stone tools, which are dated to *circa* 1.7 Ma, are first found in association with *Homo erectus* (Lepre *et al.,* 2011). As such, the recovery of hand fossils securely attributed to *Homo erectus* and other Middle Pleistocene *Homo* species would be invaluable in interpreting the timing, context, and potential selective pressures responsible for the development of a more human-like hand morphology (Richmond *et al.,* 2016).

Conclusions

The development of stone tools has been instrumental in the evolutionary success of the hominin lineage. However, in the absence of direct associatory evidence, identifying authorship of the earliest-known stone tools to specific hominin taxa remains elusive and somewhat speculative. The flexibility of the fifth, and to a lesser extent fourth, metacarpals at their respective carpometacarpal joints are instrumental for the effective use of hand grips and postures unique to modern humans among extant taxa. However, despite the importance of these joints in modern human manual behaviours, their functional morphology is under-explored.

This study quantified and compared the morphologies of the fourth and fifth carpometacarpal joints of modern humans, non-human great apes, and selected hominin fossil specimens using landmark-based three-dimensional geometric morphometric analysis for two primary purposes: to identify morphological features of these joints which are unique to *Homo sapiens* among extant great-ape taxa, and which can reasonably be considered to facilitate the freedom of movement of these joints which are unique to humans; and to identify such features in the hominin fossil record in order to inform research into the capabilities of fossil hominin taxa to make and use early stone tools.

Despite its variable nature, the fourth carpometacarpal joint of modern humans is planar and simple compared with the complex and irregular structure of this joint in other great apes. The fifth carpometacarpal joint of *Homo sapiens* displays several adaptations for increased mobility, most notably a shallow saddle-shaped morphology which facilitates flexion and accompanying rotation of the fifth metacarpal. An enlarged fifth carpometacarpal joint relative to the fourth also reflects the increased loads incurred upon the fifth metacarpal of humans during tool-use and manual dexterous behaviours. The results of this project highlighted the distinctiveness of the orientation of the fifth carpometacarpal joint relative to the fourth in modern humans, which is positioned more transversely relative to a saggitally-oriented fourth carpometacarpal joint. This unique orientation not only exaggerates supination of the fifth metacarpal during flexion and the spread of the distal palm but also ensures that movement of the fifth metacarpal at its carpometacarpal joint is not impeded by the position of the fourth

metacarpal. Furthermore, this orientation is more efficient in transferring the significant loads incurred upon the fifth ray during manipulative behaviours to be dissipated through the carpal complex and the upper forearm.

While several Australopith species had fifth carpometacarpal joints that would have enabled a considerable amount of flexion of the fifth metacarpal and increased loading across the fifth carpometacarpal joint, a saddle-shaped surface of the hamate-fifth metacarpal articular surface does not appear until relatively late in the hominin lineage, and remains absent in species known to make and use stone tools, such as *Homo floresiensis* and some *Homo neanderthalensis* specimens. The results of this study demonstrate that the full suite of human features of the fourth and fifth carpometacarpal joints that facilitate the enhanced flexibility of the hypothenar palm was not fully present until the emergence of *Homo sapiens*, and that hominin taxa responsible for the production and use of the earliest-known lithic technologies were likely to have used the hypothenar rays of the hand in a manner distinct from modern humans.

Bibliography

Adams, D., Collyer, M., Kaliontzopoulou, A., Baken, E. 2023. Geomorph: Software for geometric morphometric analyses. R package version 4.0.6. https://cran.r-project.org/package=geomorph.

Adams, D., Otarola-Castillo, E. 2013. Geomorph: An R package for the collection and analysis of geometric morphometric shape data. *Methods in Ecology and Evolution*. **4**: 393-399.

Adams, D. C., Rohlf, F. J., Slice, D. E. 2004. Geometric morphometrics: Ten years of progress following the 'revolution'. *Italian Journal of Zoology* **71**(1): 5-16.

Adams, D. C., Rohlf, F. J., Slice, D. E. 2007. A field comes of age: geometric morphometrics in the 21st century. *Hystrix, the Italian Journal of Mammalogy* **24**(1): 7-14.

Adobe Inc., 2019. *Adobe Photoshop*. https://www.adobe.com/products/photoshop.html.

AgiSoft PhotoScan Professional (Version 1.2.6) (Software). (2016). Retrieved from http://www.agisoft.com/downloads/installer/.

Aiello, L., Dean, C. 2006. *An Introduction to Human Evolutionary Anatomy.* London: Academic Press.

Alba, D. M., Moya-Sola, S., Köhler, M. 2003. Morphological affinities of the *Australopithecus afarensis* hand on the basis of manual proportions and relative thumb length. *Journal of Human Evolution* **44**(2): 225-254.

Alemseged, Z., Spoor, F., Kimbel, W. H., Bobe, R., Geraads, D., Reed, D., Wynn, J. G. 2006. A juvenile early hominin skeleton from Dikika, Ethiopia', Nature, 443(7109): 296–301.

Almecija, S., Alba, D. M. 2014. On manual proportions and pad-to-pad precision grasping in *Australopithecus afarensis. Journal of Human Evolution* **73**: 88-92.

Almécija, S., Orr, C. M., Tocheri, M. W., Patel, B. A., Jungers, W. L. 2015. Exploring phylogenetic and functional signals in complex morphologies: the hamate of extant anthropoids as a test-case study. *Anatomical Record* **298**(1), 212–229.

Almecija, S., Smears, J. B., Jungers, W. L. 2015. The evolution of human and ape hand proportions. *Nature Communications* **6**(7717): 1-11.

Ambrose, S. H. 2001. Paleolithic technology and human evolution. *Science* **291**(5509): 1748-1753.

Anderson M. J. 2006. Distance-based tests for homogeneity of multivariate dispersions. *Biometrics* **62**(1): 245–253.

Ankel-Simons, F. 2007. *Primate Anatomy: An Introduction. 3rd Edition.* San Diego Elsevier Academic Press.

Asfaw, B., White, T., Lovejoy, O., Latimer, B., Simpson, S., Suwa, G. 1999. *Australopithecus garhi:* A new species of early hominid from Ethiopia. *Science* **284**(5414): 629-635.

Avis, V. 1962. Brachiation: The crucial issue for man's ancestry. Southwestern *J. Anthropol.* **18**: 119-148.

Backwell, L. R., d'Errico, F. 2001 Evidence of termite foraging by Swartkrans early hominids. *Proceedings of the National Academy of Sciences of the United States of America* **98**(4): 1358–1363.

Bade, H., Koebke, J., Bilger, H. 1993. Functional anatomy of the fifth carpometacarpal joint. *Handchirurgie, mikrochirurgie, plastische chirurgie* **25**(3): 116–120.

Balter, M. 2015. World's oldest stone tools discovered in Kenya. *Science* doi: 10.1126/science.aab2487.

Balter, V., Blichert-Toft, J., Braga, J., Telouk, P., Thackeray, F., Albarède, F. 2008. U–Pb dating of fossil enamel from the Swartkrans Pleistocene hominid site, South Africa. *Earth and planetary science letters* **267**(1-2): 236–246.

Bandini, E., Motes-Rodrigo, A., Archer, W., Minchin, T., Axelsen, H., Hernandez-Aguilar, R. A., McPherron, S. P., Tennie, C. 2021. Naïve, unencultured chimpanzees fail to male and use flaked stone tools. *Open Research Europe*. **1**(20): 2021

Barrett, B. J., Monteza-Moreno, C. M., Dogandžić, T., Zwyns, N., Ibáñez, A., Crofoot, M. C. 2018. Habitual stone-tool-aided extractive foraging in white-faced capuchins, *Cebus capucinus. Royal Society Open Science* **5**: 181002.

Bardua, C., Felice, R. N., Watanabe, A., Fabre, A. C., Goswami, A. 2019. A Practical Guide to Sliding and Surface Semilandmarks in Morphometric Analyses. *Integrative Organismal Biology* **1**(1): obz016.

Basmajian, J. V. 1979. Muscles alive. Their functions revealed by electromyography, 4th Edition. Baltimore: Williams & Wilkins.

Batmanabane, M., Malathi, S. 1985. Movements at the carpometacarpal and metacarpophalangeal joints of the hand and their effect on the dimensions of the articular ends of the metacarpal bones. *The Anatomical record* **213**(1): 102–110.

Beck, B. B. 1972. Tool use in captive hamadryas baboons. *Primates* **13**(3): 276-296.

Begun, D. R. 2004. Knuckle-walking and the origin of human bipedalism. In: DJ Meldrum and CE Hilton (Eds.) *From Biped to Strider: The emergence of modern human walking*. New York: Kluwer Press: 9-33.

Bentley-Condit, V. K., Smith, E. O. 2010. Animal tool use: Current definitions and an updated comprehensive catalog. *Behaviour* **147**(2): 185–32A

Berger, L. R., de Ruiter, D. J., Churchill, S. E., Schmid, P., Carlson, K. J., Dirks, P. H., Kibii, J. M. 2010. Australopithecus sediba: a new species of Homo-like australopith from South Africa. *Science* **328**(5975): 195–204.

Blumenschine, R. J., Marean, C. W., Capaldo, S. D. 1996. Blind tests of inter-analyst correspondence and accuracy in the identification of cut marks, percussion marks, and carnivore tooth marks on bone surfaces. *Journal of Archaeological Science* **23**(4): 493-507.

Boesch, C., Boesch, H. 1989. Hunting behavior of wild chimpanzees in the Taï National Park. *American Journal of Physical Anthropology* **78**(4): 547-573.

Boesch, C., Boesch, H. 1990. Tool use and tool making in wild chimpanzees. *Folia primatologica; international journal of primatology*, **54**(1-2): 86–99.

Boesch, C., Boesch, H. 1993. Different hand postures for pounding nuts with natural hammers by wild chimpanzees. In: Preuschoft, H., Chivers, D.J. (Eds.) *Hands of Primates*. Vienna: Springer: 31-43.

Boesch-Achermann, H., Boesch, C. 1994. Hominization in the rainforest: the chimpanzee's piece of the puzzle. *Evolutionary Anthropology.* **3**: 9–16.

Boesch, C., Boesch-Achermann, H. 2000. *The chimpanzees of the Taï Forest: Behavioural ecology and evolution*. Oxford: Oxford University Press.

Boinski, S. 1988. Sex differences in the foraging behavior of squirrel monkeys in a seasonal habitat. *Behavioral Ecology and Sociobiology,* **23**(3): 177–186.

Bookstein, F. L. 1986. Size and Shape Spaces for Landmark Data in Two Dimensions. *Statistical Science* **1**(2): 181-222.

Bookstein, F.L. 1991. *Morphometric Tools for Landmark Data Geometric and Biology*. Cambrige: Cambrige University Press.

Bookstein, F.L. 1996. Combining the Tools of Geometric Morphometrics. In: Marcus, L. F., Corti, M., Loy, A., Naylor, G. J. P., Slice, D. E. (Eds.). *Advances in Morphometrics.* New York: Springer: 131-151.

Bookstein, F. L. 1997. Landmark methods for forms without landmarks: morphometrics of group differences in outline shape. *Medical image analysis* **1**(3): 225–243.

Bookstein, F. L. 1998. A hundred years of morphometrics. *Acta Zoologica Academiae Scientiarum Hungaricae* **44**: 7-59.

Bookstein, F. L. 2014. *Measuring and Reasoning: Numerical Inference in the Sciences.* Cambridge: Cambridge University Press.

Bookstein, F. L. 2018. *A Course in Morphometrics for Biologists.* Cambridge: University Press.

Bookstein, F. L., Chernoff, B., Elder, R. L., Humphries, J. M. Jr., Smith, G. R., Strauss, R. E. 1985. Morphometrics in evolutionary biology. *Special publication 15. Academy of Natural Sciences Press,* Philadelphia.

Bower, B. 2011. Gone fishing, orangutan style. [online] Borneo Orangutan Survival Australia. Available at: https://www.orangutans.com.au/news-orangutan-behaviour/gone-fishing-orangutan-style/ [Accessed 28 Feb. 2024].

Bowland, L. A., Scott, J. E., Kivell, T. L., Patel, B. A., Tocheri, M. W., Orr, C. M. 2021. *Homo naledi* pollical metacarpal shaft morphology is distinctive and intermediate between that of australopiths and other members of the genus Homo. *Journal of Human Evolution* **158**: 103048.

Braun, D. R., Aldeias, V., Archer, W., Arrowsmith, J. R., Baraki, N., Campisano, C. J., Deino, A. L., DiMaggio, E. N., Dupont-Nivet, G., Engda, B., Feary, D. A., Garello, D. I., Kerfelew, Z., McPherron, S. P., Patterson, D. B., Reeves, J. S., Thompson, J. C., Reed, K. E. 2019. Earliest known Oldowan artifacts at >2.58 Ma from Ledi-Geraru, Ethiopia, highlight early technological diversity. *Proceedings of the National Academy of Sciences of the United States of America* **116**(24): 11712–11717.

Breuer, T., Ndoundou-Hockemba, M., Fishlock, V. 2005. First Observation of Tool Use in Wild Gorillas. *PLoS Biology* **3**(11): 2041–2043

Brown, F. E., McDougall, I., Gathogo, P. N. 2013. Age Ranges of *Australopithecus* Species, Kenya, Ethiopia, and Tanzania. In: Reed, K. E., Fleagle, J. G., Leakey, R. E. (Eds.) *The Paleobiology of Australopithecus.* New York: Springer: 7-20.

Brumm, A., Aziz, F., van den Bergh, G. D., Morwood, M. J., Moore, M. W., Kurniawan, I., Hobbs, D. R., Fullagar, R. 2006. Early stone technology on Flores and its implications for *Homo floresiensis. Nature* 441(7093): 624–628.

Bush ME, Lovejoy CO, Johanson DC, Coppens Y. 1982. Hominid carpal, metacarpal, and phalangeal bones recovered from the Hadar Formation—1974–1977 Collections. *American Journal of Physical Anthropology* **57**: 651–677.

Byrne, R. W., Russon, A. E. 1998. Learning by imitation: a hierarchical approach. *The Behavioral and brain sciences* **21**(5): 667–721.

Callaway, E. 2015. Oldest stone tools raise questions about their creators. *Nature* **520**(7548): 421.

Campisano, C. J., Feibel, C. S. 2008. Depositional environments and stratigraphic summary of the Pliocene Hadar Formation at Hadar, Afar Depression, Ethiopia. In: Quade, J., Wynn, J. G. (Eds.) *The Geology of Early Humans in the Horn of Africa*. The Geological Society of America.

Canale, G. R., Guidorizzi, C. E., Kierulff, M. C. M., Gatto, C. A. F. R. 2009. First record of tool use by wild populations of the yellow-breasted capuchin monkey (*Cebus xanthosternos*) and new records for the bearded capuchin (*Cebus libidinosus*). *American Journal of Primatology* **71**(5): 366-372.

Carlson, K. J., Doran-Sheehy, D. M., Hunt, K. D., Nishida, T., Yamanaka, A., Boesch, C. 2006. Locomotor behavior and long bone morphology in individual free-ranging chimpanzees. *Journal of Human Evolution* **50**(4): 394–404.

Carvalho, S., Biro, D., McGrew, W. C., Matsuzawa, T. 2009. Tool-composite reuse in wild chimpanzees (Pan troglodytes): archaeologically invisible steps in the technological evolution of early hominins? *Animal Cognition* **12**(Supplement 1): S103–S114.

Carvalho, S., Cunha, E., Sousa, C., Matsuzawa, T. 2008. Chaînes opératoires and resource-exploitation strategies in chimpanzee (Pan troglodytes) nut cracking. *Journal of Human Evolution* **55**(1): 148–163.

Carvalho, S., Matsuzawa, T., McGrew, W. C. 2013. From pounding to knapping: How chimpanzees can help us to model hominin lithics. In: Sanz, C. M., Call, J., Boesch, C. (Eds.) *Tool Use in Animals*. Cambridge: Cambridge University Press: 225-241.

Carvalho, S., McGrew, W. C. 2012. The origins of the Oldowan: Why chimpanzees (*Pan troglodytes*) still are good models for technological evolution in Africa. In: Dominguez-Rodrigo, M. (Ed.) *Stone Tools and Fossil Bones: Debates in the Archaeology of Human Origins.* Cambridge: Cambridge University Press: 201-221.

Copeland, L. 2002. Thumbs Up. *Washington Post.* https://www.washingtonpost.com/archive/lifestyle/2002/06/24/thumbs-up/05cd36f1-653f-44da-bc6d-b96cb92753a6/

Collyer, M. L., Sekora, D. J. and Adams, D. C. 2015. A method for analysis of phenotypic change for phenotypes described by high-dimensional data. *Heredity* **115**(4): 357–365.

Christel, M. 1993. Grasping techniques and hand preferences in Hominoidea. In: Preuschoft, H., Chivers, D.J. (Eds.) *Hands of Primates*. Vienna: Springer: 91-108.

Churchill, S. E., Gree, D. J., Feuerriegel, E. M., Macias, M. E., Mathews, S., Carlson, K. J., Schmid, P., Berger, L. R. 2018. The Shoulder, Arm, and Forearm of Australopithecus sediba. *PaleoAnthropology 2018*: 234-281.

Churchill, S.E., Holliday, T.W., Carlson, K.J., Jashashvili, T., Macias, M.E., Mathews, S., Sparling, T.L., Schmid, P., de Ruiter, D.J., and Berger, L.R. 2013. The upper limb of Australopithecus sediba. *Science* **340**: 1233477.

Darwin, C. 1871. *The Decent of Man and Selection in Relation to Sex.* Cambridge: University Press.

Daver, G., Détroit, F., Berillon, G., Prat, S. 2014. Fossil hominins, quadrupedal primates and the origin of human bipedalism: a 3D geometric morphometric analysis of the Primate hamate. *Bulletins et Mémoires de la Société d anthropologie de Paris* **26**: 121–128.

de Heinzelin, J., Clark, J. D., White, T., Hart, W., Renne, P., Woldegabriel, G., Beyene, Y., Vrba, E. 1999. Environment and Behavior of 2.5-Million-Year-Old Bouri Hominids. *Science* **284**(5414): 625-629.

Deino, A. L. 2011. 40Ar/39Ar Dating of Laetoli, Tanzania. In Harrison, T. (Ed.) *Paleontology and Geology of Laetoli: Human Evolution in Context*. New York: Springer: 77-97.

Delagnes, A., Roche, H. 2005. Late Pliocene hominid knapping skills: the case of Lokalalei, West Turkana, Kenya. *Journal of Human Evolution* **48**(5): 435-472.

Diogo, R., Richmond, B. G., Wood, B. 2012. Evolution and homologies of primate and modern human hand and forearm muscles, with notes on thumb movements and tool use. *Journal of Human Evolution* **63**(1): 64–78.

Domalain, M., Bertin, A., Daver, G. 2017. Was Australopithecus afarensis able to make the Lomekwian stone tools? Towards a realistic biomechanical simulation of hand force capability in fossil hominins and new insights on the role of the fifth digit. Comptes Rendus Palevol 16(5-6): 572-584.

Dominguez-Rodrigo, M., de Juana, S., Galán, A., Rodriguez, M. 2009. A new protocol to differentiate trampling marks from butchery cut marks. *Journal of Archaeological Science* **36**(12): 2643-2654.

Dominguez-Rodrigo, M., Pickering, T. R., Bunn, H. T. 2010. Configurational approach to identifying the earliest hominin butchers. *Proceedings of the National Academy of Sciences of the United States of America* **107**(49): 20929-20934.

Dominguez-Rodrigo, M., Pickering, T. R., Bunn, H. T. 2011. Reply to McPherron *et al.*: Doubting Dikika is about data, not paradigms*. Proceedings of the National Academy of Sciences of the United States of America* **108**(21): 117.

Dominguez-Rodrigo, M., Pickering, T. R., Bunn, H. T. 2012. Experimental study of cut marks made with rocks unmodified by human flaking and its bearing on claims of w3.4-million-year-old butchery evidence from Dikika, Ethiopia. *Journal of Archaeological Science* **39**(2): 205-214.

Doran, D. M. 1992. The ontogeny of chimpanzee and pygmy chimpanzee locomotor behavior: A case study of paedomorphism and its behavioral correlates. *Journal of Human Evolution* **23**(2): 139-158.

Doran, D. 1993. Sex differences in adult chimpanzee positional behaviour: the influence of body size on lococmotion and posture. *American Journal of Physical Anthropology* **91**(1): 99-116.

Doran, D.M., 1996. The comparative positional behavior of the African apes. In: McGrew, W., Nishida, T. (Eds.) *Great Ape Societies*. Cambridge: Cambridge University Press: 213-224.

Doran, D. 1997*a*. Ontogeny of locomotion in mountain gorillas and chimpanzees. *Journal of Human Evolution* **32**: 323-344.

Doran, D. 1997*b.* Influence of seasonality on activity patterns, feeding behavior, ranging, and grouping patterns in Taï chimpanzees. *International Journal of Primatology* **18**(2): 183–206.

Doran, D., Hunt, K. D. 1996. Comparative Locomotor Behavir of Chimpanzees and Bonobos: Species and habitat differences. In Wrangham, R. W., McGrew, W. C., de Waal, F. B. M., Heltne, P. G. (Eds.) *Chimpanzee Cultures.* Cambridge, MA.: Harvard University Press: 93-108.

Drapeau, M. S. M., Ward, C. V., Kimbel, W. H., Johanson, D. C., Rak, Y. 2005. Associated cranial and forelimb remains attributed to *Australopithecus afarensis* from Hadar, Ethiopia. *Journal of Human Evolution* **48**(6): 593-642.

Drapeau, M. S. M. 2012. Forelimb adaptation s in *Australopithecus afarensis.* In: Reynolds, S. C., Gallagher, A. (Eds.) *African Genesis: Perspecitves on Hominin Evolution.* Cambridge: University Press: 223-247.

Dryden, I.L., Mardia, K.V. 1998. *Statistical Analysis of Shape.* Chichester: John Wiley & Sons.

Dubosset, J. F. 1981. Finger rotation during prehension. In: Tubiana, R. (Ed.) *The Hand*. Philadelphia: W.B. Saunders Company: 202-206.

Dunmore, C. J., Bachmann, S., Synek, A., Pahr, D. H., Skinner, M. M., Kivell, T. L. 2024. The deep trabecular structure of first metacarpals in extant hominids. *American Journal of Biological Anthropology.* **183**(3): e24695.

Dunmore, C. J., Skinner, M. M., Bardo, A., Berger, L. R., Hublin, J.-J., Pahr, D. H., Rosas, A., Stephens, N. B. and Kivell, T. L. 2020. The position of Australopithecus sediba within fossil hominin hand use diversity', *Nature Ecology and Evolution*. Springer Nature: 911-918.

El-Bacha, A. 1981. The carpometacarpal joints (excluding the trapeziometacarpal). In: Tubiana, R. (Ed.) *The Hand. Volume 1*. Philadelphia: Saunders.

El-shennawy, M., Nakamura, K., Patterson, R. M., Viegas, S. F. 2001. Three-dimensional kinematic analysis of the second through fifth carpometacarpal joints. *The Journal of Hand Surgery* **26**(6): 1030-1035.

Falotico, T., Ottoni, E. B. 2016. The manifold use of pounding stone tools by wild capuchin monkeys of Serra da Capivara National Park, Brazil. *Behaviour* **153**(4): 421-442.

Feuerriegel, E. M., Green, D. J., Walker, C. S., Schmid, P., Hawks, J., Berger, L. R., Churchill, S. E. 2017. The upper limb of Homo naledi. *Journal of Human Evolution* **104**: 155–173.

Fernández, P. J. Almécija, S., Patel, B. A., Orr, C. M., Tocheri, M. W., Jungers, W. L. 2015. Functional aspects of metatarsal head shape in humans, apes, and Old World monkeys. *Journal of Human Evolution* **86**: 136–146.

Fleagle, J. 1998. *Primate Adaptation and Evolution 2nd Edition.* London: Academic Press.

Fox, E. A., Sitompul, A. F., Van Schaik, C. P. 1999. Intelligent tool use in wild Sumatran orangutans. In: Parker, S. T., Mitchell, R. W., Miles, H. L. (Eds.) *The mentalities of gorillas and orangutans: Comparative perspectives*. Cambridge: Cambridge University Press: 99–116

Fragaszy, D. M., Biro, D., Eshchar, Y., Humle, T., Izar, P., Resende, B., Visalberghi, E. 2013. The fourth dimension of tool use: temporally enduring artefacts aid primates learning to use tools. *Philosophical transactions of the Royal Society of London. Series B. Biological sciences* **368**(1630): 20120410–20120410.

Fragaszy, D., Izar, P., Visalberghi, E., Ottoni, E.B., de Oliveira, M.G., 2004. Wild capuchin monkeys (Cebus libidinosus) use anvils and stone pounding tools. *American Journal of Primatology* **64**: 359-366.

Galletta, L., Stephens, N. B., Bardo, A., Kivell, T. L., Marchi, D. 2019. Three-dimensional geometric morphometric analysis of the first metacarpal distal articular surface in humans, great apes and fossil hominins. *Journal of Human Evolution* **132**: 119–136.

Garrod, D. A., Bate. D. M. A. 1937. *Excavations at the Wady El-Mughara, Volume 1*. Oxford: Clarendon Press.

Gibbon, R. J., Pickering, T. R., Sutton, M. B., Heaton, J. L., Kuman, K., Clarke, R.J., Brain, C.K., Granger, D.E. 2014. Cosmogenic nuclide burial dating of hominin-bearing Pleistocene cave deposits at Swartkrans, South Africa. *Quaternary geochronology* **24**: 10–15

Gibbs, S. 1999. Comparative soft tissue morphology of the extant Hominoidea, including man. Ph.D. dissertation, University of Liverpool.

Goodall, J. 1963. Feeding behaviour of wild chimpanzees: a preliminary report. *Symp. zool. Soc. Lond.* **10:** 39-48.

Goodall, J. 1964. Tool-Using and Aimed Throwing in a Community of Free-Living Chimpanzees. Nature **201**: 1264-1266

Goodall, C. 1991. Procrustes Methods in the Statistical Analysis of Shape. *Journal of the Royal Statistical Society. Series B, Methodological* **53**(2): 285–339.

Gower, J.C. 1975. Generalized procrustes analysis. *Psychometrika* **40**: 33–51

Green, D. J., Gordon, A. D. Metacarpal proportions in *Australopithecus africanus. Journal of Human Evolution* **54**(5): 705-719.

Grine, F. E., Mongle, C. S., Fleqgle, J. G., Hammond, A. S. 2022. The taxonomic attribution of African hominin postcrania from the Miocene through the Pleistocene: Associations and assumptions. *Journal of Human Evolution* **173:** 103255.

Grueter, C. C., Robbins, M. M., Ndagijimana, F., Stoinski, T. S. 2013. Possible tool use in a mountain gorilla. *Behavioural processes* **100**: 160–162.

Grun, R., Stringer, C. B. 1991. Electron spin resonance dating and the evolution of modern humans. *Archaeometry* **33**(2): 153-199.

Gumert, M. D., Kluck, M. Malaivijitnond, S. 2009. The physical characteristics and usage patterns of stone axe and pounding hammers used by long-tailed macaques in the Andaman Sea region of Thailand. *American Journal of Primatology*. **71**(7): 594–608.

Gunz, P., Mitteroecker, P. 2013. Semilandmarks: A method for quantifying curves and surfaces. *Hystrix, the Italian Journal of Mammalogy* **24**(1): 103-109.

Gunz, P., Mitteroecker, P. Bookstein, F. L. 2005. Semilandmarks in Three Dimensions. In: Slice, D. E. (Ed.): *Modern Mrphometrics in Physical Anthropology.* New York: Plenum Publishers: 73-98.

Haile-Selassie, Y., Melillo, S. M., Su, D. F. 2016. The Pliocene hominin diversity conundrum: Do more fossils mean less clarity? *Proceedings of the National Academy of Sciences of the United States of America* **113**(23): 6364–6371.

Harcourt-Smith, W. E. H., Tallman, M., Frost, S. R., Wiley, D. F., Rohlf, F. J., Delson, E. 2008. Analysis of Selected Hominoid Joint Surfaces Using Laser Scanning and Geometric Morphometrics: A Preliminary Report. In: Sargis, E. J., Dagosto, M. (Eds.) *Mammalian Evolutionary Morphology: A Tribute to Frederick S. Szalay.* New York: Springer: 373-383.

Harmand, S., Lewis, J. E., Felbel, C. S., Lepre, C. J., Prat, S., Lenoble, A., Boes, X., Quinn, R. L., Brenet, M., Arroyo, A., Taylor, N., Clement, S., Daver, G., Brugal, J., Leakey, L., Mortlock, R. A., Wright, J. D., Lokorodi, S., Kirwa, C., Kent, D. V., Roche, H. 2015. 3.3-million-year-old stone tools from Lomekwi 3, West Turkana, Kenya. *Nature* **521**(7552): 310-315.

Harris, J. W. K. 1983. Cultural Beginnings: Plio-Pleistocene Archaeological Occurrences from the Afar, Ethiopia. *The African archaeological review*, **1**(1): 3–31.

Haslam, M., Hernandez-Aguilar, A., Ling, V., Carvalho, S., de la Torre, I., DeStefano, A., Du, A., Hardy, B., Harris, J., Marchant, L., Matsuzawa, T., McGrew, W., Mercader, J., Mora, R., Petraglia, M., Roche, H., Visalberghi, E., Warren, R. 2009. Primate archaeology. *Nature* **460**(7253): 339–344.

Hawks, J., Elliott, M., Schmid, P., Churchill, S. E., de Ruiter, D. J.,Roberts, E. M., Hibert-Wolf H., Garvin, H. M., Williams, S. A.,Delezene, L. K., Feuerriegel, E. M., Randolph-Quinney, P., Kivell, T. L.,Laird, M. F., Tawane, G., DeSilva, J. M., Bailey, S. E., Brophy, J. K.,Meyer, M. R., Matthew M Skinner, M. W., Tocheri, M. W., VanSickle, C., Walker, C. S., Campbell, T. L., Kuhn, B., Kruger, A., Tucker, S., Gurtov, A., Hlophe, N., Hunter, R., Morris, H., Peixotto, B., Ramalepa, M., van Rooyen, D., Tsikoane, M., Boshoff, P., Dirks, P. H. G. M., Berger, L. R. 2017. New fossil remains of *Homo naledi* from the Lesedi Chamber, South Africa. *eLife* **6**: e24232.

Herries, A. I. R., Curnoe, D., Adams, J. W. 2009. A multi-disciplinary seriation of early *Homo* and *Paranthropus* bearing palaeocaves in southern Africa. *Quaternary International* **202**(1-2): 14-28.

Hill, A., Ward, S., Deino, A., Curtis, G., Drake, R. 1992 Earliest *Homo. Nature* **355**(6362): 719-722.

Hirt, B., Seyhan, H., Wagner, M., Zumhasch, R. 2017. *Hand and wrist anatomy and biomechanics: a comprehensive guide*. Stuttgart: Thieme.

Hovers, E. 2015. Archaeology: Tools go back in time. *Nature*, **521**(7552): 294–295.

Hunt, D. R., Albanese, J. 2005. History and demographic composition of the Robert J. Terry anatomical collection. *American journal of physical anthropology* **127**(4): 406–417.

Inouye, S. E. 1992. Ontogeny and allometry of African ape manual rays. *Journal of Human Evolution* **23**(2): 107-138.

Johanson, D. C., Lovejoy, O., Kimbel, W. H., White, T. D., Ward, S. C., Bush, M. E., Latimer, B. M., Coppens, Y. 1982. Morphology of the Pliocene partial hominid skeleton (A. L. 288-1) from the Hadar formation, Ethiopia. *American Journal of Physical Anthropology* **57**(4): 403-451.

Jungers, W. L., Godfrey, L. R., Simons, E. L., Chatrath, P. S. 1997. Phalangeal curvature and positional behavior in extinct sloth lemurs (Primates, Palaeopropithecidae). *Proceedings of the National Academy of Sciences of the United States of America* **94**(22): 11998–12001.

Kapandji, I. A. 1982. *The Physiology of the Joints. Volume One: Upper Limb.* Churchill Livingstone.

Keeley, L. H., Toth, N. 1981. Microwear polishes on early stone tools from Koobi Fora, Kenya. *Nature* **294**: 464-465.

Kendall, D. G. 1977. The diffusion of shape. *Advances in Applied Probability*. **9**(3):428-430.

Kendall, D. G. 1984. Shape-manifolds, Procrustean metrics and complex projective spaces. *Bulletin of the London Mathematical Society* 16: 81-121.

Kendall, D. G. 1989. A survey of the statistical theory of shape. *Statistical Sciences* **4**(2): 87-99.

Key, A. J. M., Dunmore, C. J. 2015. The evolution of the hominin thumb and the influence exerted by the non-dominant hand during stone tool production. *Journal of Human Evolution* **78**:60- 69

Key, A. J. M., Dunmore, C. J., Marzke, M. W. 2019. The unexpected importance of the fifth digit during stone tool production. *Scientific reports* **9**(1): 16724.

Key, A.J.M., Merritt, S.R., Kivell, T.L. 2018. Hand grip diversity and frequency during Lower Palaeolithic stone tool use. *Journal of Human Evolution* **125**:137-158.

Kimbel, W. H., Rak Y., Johanson, D. C. 2004. The Skull of Australopithecus afarensis. Oxford: Oxford University Press.

Kinani, J.-F., Zimmerman, D. 2014. Tool use for food acquisition in a wild mountain gorilla (*Gorilla beringei beringei*). *American Journal of Primatology* **77**(3): 353-357.

Kivell, T. L. 2015. Evidence in hand: recent discoveries and the early evolution of human manual manipulation. *Philosophical Transactions of the Royal Society B-Biological Sciences* **370**(1682): e1-e11.

Kivell, T.L. 2016. The Primate Wrist. In: Kivell, T., Lemelin, P., Richmond, B., Schmitt, D. (eds) *The Evolution of the Primate Hand. Developments in Primatology: Progress and Prospects.* Springer, New York, NY: 17-54.

Kivell, T. L., Baraki, N., Lockwood, V., Williams-Hatala, E. M., Wood, B. A. 2022. Form, function and evolution of the human hand. *Yearbook of Biological Anthropology 2023* **181**(Suppl. 76): 6-57.

Kivell, T. L., Churchill, S. E., Kibii, J. M., Schmid, P., Berger, L. R. 2018. The hand of *Australopithecus sediba. PalaeoAnthropology Special Issue:* Australopithecus sediba: 282-333.

Kivell, T. L., Deane, A.S., Tocheri, M. W., Orr, C. M., Schmid, P., Hawks, J., Berger, L. R., Churchill, S. E. 2015. The hand of Homo naledi. *Nature communications* **6**(1): 8431–8431

Kivell, T. L., Guimont, I., Wall, C. E. 2013. Sex-related shape dimorphism in the human radiocarpal and midcarpal joints. *Anatomical record* **296**(1): 19–30.

Kivell, T. L., Kibii, J. M., Churchill, S. E., Schmid, P., Berger, L. R. 2011. *Australopithecus sediba* hand demonstrated mosaic evolution of locomotor and manipulative abilities. *Science* **333**(6048): 1411-1417.

Kivell, T. L., Ostrofsky, K. R., Richmond, B. G., Drapeau, M. S. 2020. Metacarpals and manual phalanges. In: Zipfel. B., Richmond, B. G., Ward, C. V. (*Eds.*) *Hominin postcranial remains from Sterkfontein, South Africa, 1936-1995* Oxford: University Press. 106-143.

Klingenberg, C. P. 2016. Size, shape, and form: concepts of allometry in geometric morphometrics. *Development Genes and Evolution* **226**(3): 113–137.

Lamarck, J. -B. 1809. *Philosophie Zoologique*. Flammarion. André Pichot (1994).

Landsmeer, J. M. 1962. Power grip and precision handling. *Annals of the rheumatic diseases* **21**(2): 164–170.

Landsmeer, J. M., Long, C. 1965. The mechanism of finger control, based on electromyograms and location analysis. *Acta Anatomica* **60**(3): 330–347.

Leakey, L. S. B. 1959. A new fossil skull from Olduvai. *Nature* **184**(4685): 491-493.

Leakey, L. S. B. 1960. Recent discoveries at Olduvai Gorge. *Nature* **188:** 1050-1052

Leakey, L. S., Tobias, P. V., Napier, J. R. A. 1964. A new species of the genus *Homo* from Olduvai Gorge. *Nature* **6**(4): 424-427.

Leakey, M. G., Spoor, F., Brown, F. H., Gathogo, P. N., Kiarie, C., Leakey, L. N., Mcdougall, I. 2001. New hominin genus from eastern Africa shows diverse middle Pliocene lineages. *Nature* **410**(6827): 433-440.

Lemelin, P., Diogo, R. 2016. Anatomy, function, and evolution of the primate hand musculature. In: Kivell, T., Lemelin, P., Richmond, B., Schmitt, D. (eds) The Evolution of the Primate Hand. Developments in Primatology: Progress and Prospects. Springer, New York, NY: 155-193.

Lepre, C. J., Roche, H., Kent, D. V., Harmand, S., Quinn, R. L., Brugal, J. P., Texier, P. J., Lenoble, A., & Feibel, C. S. 2011. An earlier origin for the Acheulian. *Nature* **477**(7362): 82–85.

Lewis, O. J. 1974. Wrist articulations of *Anthropoidea.* In: Jenkins, F. A. (Ed.). *Primate Locomotion.* New York: Academic Press: 143- 169.

Lewis, O. J. 1977. Joint remodeling and the evolution of the human hand. *Journal of Anatomy* **123**(1): 157-201.

Lewis, O. J. 1989. *Functional Morphology of the Evolving Hand and Foot.* Oxford: Oxford University Press.

Lewis, J. E., Harmand, S. 2016. An Earlier Origin for Stone Tool Making: Implications for Cognitive Evolution and the Transition to Homo. *Philosophical Transactions of the Royal Society B: Biological Sciences 371: Philosophical Transactions of the Royal Society B: Biological Sciences* **371**: 20150233**.**

Lockwood, C. A., Lynch, J. M. and Kimbel, W. H. 2002. Quantifying temporal bone morphology of great apes and humans: an approach using geometric morphometrics. *Journal of anatomy* **201**(6): 447–464

Long, C. II, Conrad, P. W., Hall, E. A., Furler, S. L. 1970. Intrinsic-extrinsic muscle control of the hand in power grip and precision handling. *Journal of Bone Joint Surgery* **52A**(5): 853–857.

Luncz, L. V., Arroyo, A., Falótico, T., Quinn, P., Proffitt, T. 2022. A primate model for the origin of flake technology. *Journal of Human Evolution* **171**: 103250–103250.

Maki, J., Trinkaus, E. 2011. Opponens Pollicis Mechanical Effectiveness in Neandertals and Early Modern Humans. *PaleoAnthropology 2011*: 62-71.

Malaivijitnond, S., Lekprayoon, C., Tandavanittj, N., Panha, S., Cheewatham, C., Hamada, Y. 2007. Stone-tool usage by Thai long-tailed macaques (*Macaca fascicularis*). *American Journal of Primatology* **69**(2):227–233

Marchi, D. Proctor, D.J., Huston, E., Nicholas, C. L., Fischer, F. 2017. Morphological correlates of the first metacarpal proximal articular surface with manipulative capabilities in apes, humans and South African early hominins. *Comptes rendus. Palevol* **16**(5-6): 645–654.

Marchi, D., Ruff, C.B., Capobianco, A., Rafferty, K.L., Habib, M.B., Patel, B.A., 2016. The locomotion of Babakotia radofilai inferred from epiphyseal and diaphyseal morphology of the humerus and femur. *Journal of morphology* **277**(9): 1199–1218.

Marcus, L. F. 1990. Traditional morphometrics. In: Rohlf, F. J., Bookstein, L. (Eds.), *Proceedings of the Michigam morphometrics workshop, Special Publication No. 2*. Ann Arbor: University of Michigan Museum of Zoology: 77-122.

Marzke, M. W. 1971. Origins of the human hand. *American Journal of Physical Anthropology* **34**(1): 61-84.

Marzke, M. W. 1983. Joint functions and grips of the Australopithecus afarensis hand, with special reference to the region of the capitate. *Journal of Human Evolution* **12**(2): 197-211.

Marzke, M. W. 1997. Precision grips, hand morphology, and tools. *American Journal of Physical Anthropology* **102**(1): 91-110.

Marzke, M. W. 2005. Who made stone tools? In: Rouz, V., Bril, B. (Eds.) *Stone Knapping: The Necessary Conditions for a Uniquely Hominin Behaviour.* Cambridge: McDonald Institute for Archaeological Research: 243-255.

Marzke M. W. 2009. Upper-limb evolution and development. *The Journal of Bone and Joint Surgery. American volume* **91**(4): 26–30.

Marzke, M. W. 2013. Tool making, hand morphology and fossil hominins. *Philosophical Transactions of the Royal Society B* **368**(1630): 20120414.

Marzke, M. W., Marzke, R. F. 1987. The third metacarpal styloid process in humans: origin and functions. *American journal of physical anthropology* **73**(4): 415–431.

Marzke, M. W., Marzke, R. F. 2000. Evolution of the human hand: approaches to acquiring, analysing and interpreting the anatomical evidence. *Journal of anatomy*, **197**(1): 121–140.

Marzke, M. W., Marzke, R. F., Linscheid, R. L., Smutz, P., Steinberg, B., Reece, S., An, K. N. 1999. Chimpanzee thumb muscle cross sections, moment arms and potential torques, and comparisons with humans. *American journal of physical anthropology* **110**(2): 163–178.

Marzke, M. W., Tocheri, M. W., Steinberg, B., Femiani, J. D., Reece, S. P., Linscheid, R. L., Orr, C. M., Marzke, R. F. 2010. Comparative 3D quantitative analyses of trapeziometacarpal joint surface curvatures among living catarrhines and fossil hominins. *American journal of physical anthropology* **141**(1): 38–51.

Marzke, M. W., Toth, N., Schick, K., Reece, S., Steinberg, B., Hunt, K., Linscheid, R. L. 1998. EMG study of hand muscle recruitment during hard hammer percussion manufacture of Oldowan tools. *American Journal of Physical Anthropology* **105:** 315-332.

Marzke, M. W., Shackley, S. 1986. Hominid hand use in the pliocene and pleistocene: Evidence from experimental archaeology and comparative morphology. *Journal of Human Evolution* **15**(6): 439-460.

Marzke, M. W., Wullstein, K. L. 1996. Chimpanzee and human grips: a new classification with a focus on evolutionary morphology. *International Journal of Primatology* **17**(1): 117-139.

Marzke, M. W., Wullstein, K. L., Viegas, S. F. 1992. Evolution of the power ("squeeze") grip and its morphological correlates in hominids. *American journal of physical anthropology* **89**(3): 283–298.

Marzke, M. W., Toth, N., Schick, K., Reece, S., Steinberg, B., Hunt, K., Linscheid, R. L. 1998. EMG study of hand muscle recruitment during hard hammer percussion manufacture of Oldowan tools. *American Journal of Physical Anthropology* **105:** 315-332.

Matarazzo S. 2008. Knuckle walking signal in the manual digits of Pan and Gorilla. *American journal of physical anthropology* **135**(1): 27–33.

Matsuzawa, T. 1991. Nesting cups and metatools in chimpanzees. Behavioural and Brain Sciences **14**: 570–571.

Matsuzawa, T. 2001. Primate foundations of human intelligence: A view of tool use in nonhuman primates and fossil hominids. In: Matsuzawa, T. (Ed.), *Primate origins of human cognition and behaviour.* Springer-Verlag Publishing: 3-25.

McFadden, D., Bracht, M. S. 2005. Sex differences in the relative lengths of metacarpals and metatarsals in gorillas and chimpanzees. *Hormones and behavior* **47**(1): 99–111.

McGrew, W. C. 1979. Evolutionary implications of sex differences in chimpanzee predation and tool use. In: Hamburg, D. A., McCown, E. R. (Eds.) *The Great Apes.* Benjamin Staples: 441-463.

McGrew, W. C. 1991. Manual laterality in anvil use: wild chimpanzees cracking strychnos fruits. *Laterality: Asymmetries of Brain, Behaviour, and Cognition* **4**(1): 79-87.

McGrew, 2004. *The Cultured Chimpanzee: Reflections of Cultural Primatology.* Cambridge; Cambridge University Press.

McGrew, W. C. 1992. *Chimpanzee Material Culture: Implications for Human Evolution.* Cambridge: University Press.

McHenry H. M. 1983. The capitate of Australopithecus afarensis and A. africanus. *American journal of physical anthropology* **62**(2): 187–198.

McPherron, S. P., Alemseged, Z., Marean, C. W., Wynn, J. G., Reed, D., Geraads, D., Bobe, R., Bearat, H. A. 2010. Evidence for stone-tool-assisted consumption of animal tissues before 3.39 million years ago at Dikika, Ethiopia. *Nature* **466**(7308): 857-860.

McPherron, S. P., Alemseged, Z., Marean, C. W., Wynn, J. G., Reed, D., Geraads, D., Bobe, R., Bearat, H. A. 2011. Tool-marked bones from before the Oldowan change the paradigm. *Proceedings of the National Academy of Sciences - PNAS*, 108(21): E116–E116.

Mercader, J., Barton, H., Gillespie, J., Harris, J., Kuhn, S., Tyler, R., Boesch, C. 2007. 4,300-year-old chimpanzee sites and the origins of percussive stone technology. *Proceedings of the National Academy of Sciences of the United States of America*, **104**(9): 3043–3048.

Mercader, J., Panger, M., Boesch, C. 2002. Excavation of a chimpanzee stone tool site in the African rainforest. *Science* **296**(5572): 1452–1455.

Meulman, E. J. M., van Schaik, C. P. 2013. Orangutan tool use and the evolution of technology In: Sanz, C. M., Call, J., Boesch, C. (Eds.) Tool Use in Animals. Cambridge: Cambridge University Press: 176-202.

Meyer, V., Jaroslav, B., Couture-Veschambre, C., Madelaine, S. 2011. Un nouveau bassin Néandertalien: description morphologique des restes pelviens de Regourdou 1 (Montignac, Dordogne, France). *Paléo* **22**(22): 207-222

Mitteroecker, P., Gunz, P., Windhager, S., Schaefer, K. 2013. A brief review of shape, form, and allometry in geometric morphometrics, with applications to human facial morphology', *Hystrix* **24**(1): 59-66.

Mittra, E. S., Smith, H. F., Lemelin, P., Jungers, W. L. 2007. Comparative morphometrics of the primate apical tuft. *American journal of physical anthropology* **134**(4): 449–459.

Moore, M. W., Brumm, A. 2009. *Homo floresiensis* and the African Oldowan. In: Hovers, E., Braun, D. R. (Eds.) *Interdisciplinary Approaches to the Oldowan.* New York: Springer: 61-69.

Moura, A. C. 2007. Stone banging by wild capuchin monkeys: an unusual auditory display. *Folia Primatologica* **78**: 36–45.

Murdoch, D., Adler, D. 2023. rgl: 3D Visualization Using OpenGL. R package version 1.2.8. <https://CRAN.R-project.org/package=rgl>.

Musgrave, J. 1971. How Dextrous was Neanderthal Man? *Nature* **233**: 538–541

Nakamura, K., Patterson, R. M., Viegas, S. F. 2001. The ligament and skeletal anatomy of the second through fifth carpometacarpal joints and adjacent structures. *The Journal of Hand Surgery* **26**(6): 1016–1029.

Nanno, M., Buford, W. L., Jr, Patterson, R. M., Andersen, C. R., Viegas, S. F. 2007. Three-dimensional analysis of the ligamentous attachments of the second through fifth carpometacarpal joints. *Clinical anatomy* **20**(5): 530–544.

Napier, J. R. 1955. The form and function of the carpo-metacarpal joint of the thumb. *Journal of anatomy* **89**(3): 362–369.

Napier, J. R. 1956. The prehensile movements of the human hand. *The Journal of Bone and Joint Surgery* **38-B**(4): 902-913.

Napier, J. R. 1960. Studies of the hands of living primates. *Proceedings of the Zoological Society of London* **134**(4): 647-657.

Napier, J. R. 1961. Prehensility and opposability in the hands of primates. *Symposium of the Zoological Society of London* **5**: 115-132.

Napier, J. R. 1962. Fossil hand bones from Olduvai Gorge. *Nature* **196**: 409-411.

Napier, J. R. 1980. *Hands.* London: George Allen & Unwin.

Napier, J. R. 1993. *Hands* (revised edition). Chichester: Princeton University Press.

Neufuss, J., Robbins, M. M., Baeumer, J., Humle, T., Kivell, T. L. 2017. Comparison of hand use and forelimb posture during vertical climbing in mountain gorillas (*Gorilla beringei beringei*)

and chimpanzees (*Pan troglodytes*). *American journal of physical anthropology* **164**(4): 651–664.

Newman, S. L. 2016. *The Growth of a Nation: Child health and development in the Industrial Revolution in England, c. AD 1750-1850*. Ph.D. Dissertation, University of Durham.

Niewoehner, W.A. 2001. Behavioral inferences from the Skhul/Qafzeh early modern human hand remains. *Proceedings of the National Academy of Sciences* **98**(6):2979-84

Niewoehner, W.A. 2005. A Geometric Morphometric Analysis of Late Pleistocene Human Metacarpal 1 Base Shape. In: Slice, D. E. (Ed.) *Modern Morphometrics in Physical Anthropology.* New York: Springer: 285-298.

Niewoehner, W.A. 2007. Neanderthal hands in their proper perspective. In: Hublin, JJ., Harvati, K., Harrison, T. (Eds.) Neanderthals Revisited: New Approaches and Perspectives. Vertebrate Paleobiology and Paleoanthropology. Dordrecht: Springer: 157-198.

Nystrom, P., Ashmore, P. 2011. *The life of primates*. Eastern economy edition. New Delhi, India: PHI Learning Private Limited.

O'Higgins, P. 2000. The study of morphological variation in the hominid fossil record: biology, landmarks and geometry. *Journal of anatomy* **197**(1): 103–120.

Oakley, K. 1956. The earliest tool-makers. *Antiquity* **30**(117): 4-8.

Orr, C. M. 2012. Kinematics and morphometrics of the radiocarpus in anthropoids with implications for reconstructing the evolution of hominin wrist mechanics. *American Journal of Physical Anthropology* **147**: 229-230.

Orr, C. M., Tocheri, M. W., Burnett, S. E., Awe, R. D., Saptomo, E. W., Sutikna, T., Jatmiko, Wasisto, S., Morwood, M. J., Jungers, W. L. 2013. New wrist bones of Homo floresiensis from Liang Bua (Flores, Indonesia). *Journal of Human Evolution* **64**(2): 109–129.

Ottoni, E. B., Izar, P. 2008. Capuchin monkey tool use: overview and implications. *Evolutionary Anthropology* **17**(4): 171-178.

Perez, S. I., Bernal, V. and Gonzalez, P. N. 2006. Differences between sliding semi-landmark methods in geometric morphometrics, with an application to human craniofacial and dental variation. *Journal of anatomy* **208**(6): 769–784.

Pickering, T. R., Dirks, P. H., Jinnah, Z., de Ruiter, D. J., Churchil, S. E., Herries, A. I., Woodhead, J. D., Hellstrom, J. C., Berger, L. R. 2011. Australopithecus sediba at 1.977 Ma and implications for the origins of the genus Homo. **333**(6048): 1421–1423.

Pickering, T. R., Heaton, J. L., Clarke, R. J., Sutton, M. B., Brain, C. K., Kuman, K. 2012. New hominid fossils from Member 1 of the Swartkrans formation, South Africa. *Journal of Human Evolution* ***62***(5): 618–628.

Plummer, T. 2004. Flaked stones and old bones: Biological and cultural evolution at the dawn of technology. *American journal of physical anthropology* **125**(S39): 118–164.

Plummer, T. W., Oliver, J. S., Finestone, E. M., Ditchfield, P. W., Bishop, L. C., Blumenthal, S. A., Lemorini, C., Caricola, I., Bailey, S. E., Herries, A. I.R., Parkinson, J. A., Whitfield, E., Hertel, F., Kinyanjui, R. N., Vincent, T. H., Li, Y., Louys, J., Frost, S. R., Braun, D. R., Reeves, J. S., Early, E. D.G., Onyango, B., Lamela-Lopez, R., Forrest, F. L., He, H., Lane, T. P., Frouin, M., Nomade, S., Wilson, E. P., Bartilol, S. K., Rotich, N. K., Potts, R. 2023. Expanded geographic distribution and dietary strategies of the earliest Oldowan hominins and Paranthropus. Science (American Association for the Advancement of Science), **379**(6632): 561–566.

Proctor, D.J., 2010. Morphometric analysis of MT 2 with Pan, Gorilla, Homo (recent and Holocene), and South African fossil hominins. *American Journal of Physical Anthropology* **143**(3): 192-193.

Proctor, D. J., Broadfield, D., Proctor, K. 2008. Morphometric analysis of MT 2 with Pan, Gorilla, Homo (recent and Holocene), and South African fossil hominins. American Journal of Physical Anthropology **135**(2): 216-224.

Proffit, T., Reeves, J. S., Pacome, S. S., Luncz, L. V. 2022. Hunting behavior of wild chimpanzees in the Taï National Park. *Royal Society Open Science* **9**(9): 220826.

Proffitt, T., Luncz, L. V., Falótico, T., Ottoni, E. B., de la Torre, I., Haslam, M. 2016. Wild monkeys flake stone tools. *Nature* **539**(7627): 85–88.

Proffitt, T., Reeves, J. S., Braun, D. S., Malaivijitnond, S., Luncz, L. V. 2023. Wild macaques challenge the origin of intentional tool production. *Science Advances* **9**(10): eade8159.

Pruetz, J. D., Bertolani, P. 2007. Savanna chimpanzees, *Pan troglodytes verus,* hunt with tools. *Current Biology* **17:** 412-417.

Putt, S. S. 2015. The origins of stone tool reduction and the transition to knapping: An experimental approach. *Journal of Archaeological Science: Reports* **2**: 51-60.

R Core Team, 2015. R: A language and environment for statistical computing. R Foundation for Statistical Computing, Wien.

Rak Y. 1990. On the differences between two pelvises of Mousterian context from the Qafzeh and Kebara caves, Israel. *American journal of physical anthropology* **81**(3): 323–332.

Rein T. R. 2011. The correspondence between proximal phalanx morphology and locomotion: implications for inferring the locomotor behavior of fossil catarrhines. *American journal of physical anthropology* **146**(3): 435–445.

Rein T. R. 2019. A geometric morphometric examination of hominoid third metacarpal shape and its implications for inferring the precursor to terrestrial bipedalism. *Anatomical record* **302**(6): 983–998.

Remis, M. J. 1998. The Gorilla Paradox: The Effects of Body Size and Habitat on the Positional Behavior of Lowland and Mountain Gorillas. In: Strasser, E., Fleagle, J. G., Rosenberger, A. L.,McHenry, H. M. (Eds.) *Primate Locomotion: Recent Advances.* New York: Springer: 95-106.

Richmond, B. G., Begun, D. R., Strait, D. S. 2001. Origin of human bipedalism: The knuckle-walking hypothesis revisited. *American Journal of Physical Anthropology*, *Suppl* **33**: 70–105.

Richmond, B. G., Roach, N. T., Ostrofsky, K. R. 2016. Evolution of the early hominin hand. In: Kivell, T., Lemelin, P., Richmond, B., Schmitt, D. (eds) The Evolution of the Primate Hand. Developments in Primatology: Progress and Prospects. Springer, New York, NY: 515-543.

Richmond, B. G., Strait, D. S. 2000. Evidence that humans evolved from a knuckle-walking ancestor. *Nature* **404**(6776): 382–385.

Ricklan, D. E. 1987. Functional anatomy of the hand of *Australopithecus africanus. Journal of Human Evolution* **16**(7-8): 643-664.

Robinson, C., Terhune, C. E. 2017. Error in geometric morphometric data collection: Combining data from multiple sources. *American journal of physical anthropology* **164**(1): 62–75.

Roche, H., Blumenschine, R. J., Shea, J. J. 2009. Origins and adaptations of early *Homo:* What archaeology tells us. In: Grine, F. E., Fleagle, J. G., Leakey, R. E. (Eds.), *The First Humans: Origin and Early Evolution of the Genus* Homo. London: Springer: 135-147.

Rohlf, F. J. 2010. tpsRelw: Relative warps analysis. Version 1.49. Department of Ecology and Evolution, State University of New York at Stony Brook, Stony Brook, NY.

Rohlf, F. J., Marcus, L. F. 1993. A revolution morphometrics. *Trends in ecology & evolution* **8**(4): 129–132.

Rolian, C., Gordon, A. D. 2013. Reassessing manual proportions in Australopithecus afarensis. *American Journal of Physical Anthropology* **152**(3): 393-406.

Rolian, C., Gordon, A. D., Hallgrimson, B. 2011. Assessing manual proportions in *Australopithecus afarensis* using Monte Carlo resampling. *American Journal of Physical Anthropology* **52**(Suppl.): 256.

Rohlf, F. J., Slice, D. 1990. Extensions of the Procrustes Method for the Optimal Superimposition of Landmarks. *Systematic zoology* **39**(1): 40–59.

Rose, M. D. 1988. Functional anatomy of the cheiridia. In: Schwartz, H. D. (Ed.) *Orang-utan Biology.* Oxford: Oxford University Press: 299-310.

Rosenberg, K. R. 1988. The Functional Significance of Neandertal Pubic Length. *Current Anthropology* **29**(4): 595-617.

Roy, T. A., Ruff, C. B. and Plato, C. C. 1994. Hand dominance and bilateral asymmetry in the structure of the second metacarpal. *American Journal of Physical Anthropology* **94**(2): 203–211.

Ruff, C., Holt, B., Trinkaus, E. 2006. Who's afraid of the big bad Wolff?: "Wolff's law" and bone functional adaptation. *American journal of physical anthropology* **129**(4): 484–498.

Sakura, O., Matsuzawa, T. 1991. Flexibility of wild chimpanzee nut-cracking behaviour using stone hammers and anvils: an experimental analysis. *Ethology* **87**(3-4): 237-248.

Sanz, C. M., Morgan, D. B. 2007. Chimpanzee tool technology in the Goualougo Triangle, Republic of Congo. *Journal of Human Evolution* **52**(4): 420–433.

Sanz, C. M., Morgan, D. B. 2007. Flexible and Persistent Tool-using Strategies in Honey-gathering by Wild Chimpanzees. *International Journal of Primatology* **30**: 411-427.

Sarringhaus, L. A., Stock, J. L., Marchant, L. F., McGrew, W. C. 2005. Bilateral asymmetry in the limb bones of the chimpanzee (*Pan troglodytes*). *American Journal of Physical Anthropology* **128**(4): 840–845.

Schick, K., Toth, N. 2006. An overview of the Oldowan industrial complex: the sites and the nature of their evidence.

Schick, K., Toth, N. 2013. The Origins and Evolution of Technology. In: Begun, D. R. (Ed.), A Companion to Palaeoanthropology. Oxford: Blackwell Publishing Ltd. 265-305.

Schick, K. D., Toth, N., Garufi, G., Savage-Rumbaugh, E. S., Rumbaugh, D., Sevcik, R. 1999. Continuing Investigations into the Stone Tool-making and Tool-using Capabilities of a Bonobo (Pan paniscus). *Journal of Archaeological Science* **26**(7): 821-832.

Schlager, S. 2017. Morpho and Rvcg - Shape Analysis in R. In: Zheng, G., Li, S., Szekely, G. (Eds.) *Statistical Shape and Deformation Analysis.* Academic Press: 217-256.

Schmitt, D., Zeininger, A., Granatosky, M. C. 2016. Patterns, Variability, and Flexibility of Hand Posture During Locomotion in Primates. In: Kivell, T., Lemelin, P., Richmond, B., Schmitt, D. (eds) *The Evolution of the Primate Hand. Developments in Primatology: Progress and Prospects.* Springer, New York, NY: 345-369.

Schmitt, D. 2010. Primate Locomotor Evolution: Biomechanical Studies of Primate Locomotion and Their Implications for Understanding Primate Neuroethology. In: Platt, M., Ghazanfar, A. (Eds.) *Primate Neuroethology*. Oxford: Oxford University Press: 31-63.

Schrenk, F. 2013. In: Begun, D. (Ed.), Earliest Homo. A Companion to Paleoanthropology. Oxford: Blackwell Publishing Ltd. 479-496.

Selby, M. S., Simpson, S. W., Lovejoy, C. O. 2016. The Functional Anatomy of the Carpometacarpal Complex in Anthropoids and Its Implications for the Evolution of the Hominoid Hand. *Anatomical Record* **299**(5): 583–600.

Semaw, S. 2006. The Oldest Stone Artefacts from Gona (2.6-2.5 Ma), Afar, Ethiopia: Implications for Understanding the Earliest Stages of Stone Knapping. In; Schick, K., Toth, N. (Eds.), *The Oldowan: Case Studies into the Earliest Stone Age.* Gossport: Stone Age Institute Press: 247-265.

Semaw, S., Renne, P. Harris, J. W. K., Feibel, C. S., Bernor, R. L., Fesseha, N., Mowbray, K. 1997. 2.5-million-year-old stone tools from Gona, Ethiopia. *Nature* **385**: 333-336.

Semaw, S., Rogers, M. J., Quade, J., Renne, P. R., Butler, R. F., Dominguez-Rodrigo, M., Stout, D., Hart, W. S., Pickering, T., Simpson, S. W. 2003. 2.6-Million-year-old stone tools and associated bones from OGS-6 and OGS-7, Gona, Afar, Ethiopia. *Journal of Human Evolution* **45**(2): 169-177.

Shang, H., Tong, H., Zhang, S., Chen, F., Trinkaus, E. 2007. An early modern human from Tianyuan Cave, Zhoukoudian, China. *Proceedings of the National Academy of Sciences* **104**(16): 6573-6578.

Shearer, B. M. Cooke, S. B., Halenar, L. B., Reber, S. L., Plummer, J. E., Delson, E., Tallman, M. 2017. Evaluating causes of error in landmark-based data collection using scanners. *PLoS ONE* **12**(11): e0187452–e0187452.

Shrewsbury, M. M., Marzke, M. W., Lindscheid, R. L., Reece, S. P. 2003. Comparative morphology of the pollical distal phalanx. *American Jounral of Physical Anthropology* **121**(1): 30-47.

Skinner, M. M., Stephens, N. B., Tsegai, Z. J., Foote, A. C., Nguyen, N. H., Gross, T., Pahr, D. H., Hublin, J. J., Kivell, T. L. 2015. Human-like hand use in *Australopithecus africanus*. Science **347**(6220): 395-399.

Slice, D. E. 2005. Modern Morphometrics. In: *Slice, D. E.* (Ed.): *Modern Mrphometrics in Physical Anthropology.* New York: Plenum Publishers.

Slice, D. E. 2007. Geometric Morphometrics. *Annual Review of Anthropology* **36**(1): 261-281.

Solecki, R. S. 1975. Shanidar IV, a Neanderthal Flower Burial in Northern Iraq. *Science* **190**(4217): 880-881.

Sollaccio, D. R., Navo, P., Ghiassi, A., Orr, C. M., Patel, B. A.., Lewton, K. L. 2019. Evaluation of Articular Surface Similarity of Hemi-Hamate Grafts and Proximal Middle Phalanx

Morphology: A 3D Geometric Morphometric Approach *The Journal of hand surgery (American ed.)* **44**(2): 121–128.

Stephens, N. B., Kivell, T. L., Pahr, D. H., Hublin, J. J., Skinner, M. M. 2018. Trabecular bone patterning across the human hand. *Journal of Human Evolution* **123**: 1–23.

Stern, J. T., Jr. 2000. Climbing to the top: A personal memoir of *Australopithecus afarensis. Evolutionary anthropology* **9**(3): 113–133.

Stern, J. T., Jr, Susman, R. L. 1983. The locomotor anatomy of Australopithecus afarensis. *American journal of physical anthropology* **60**(3): 279–317.

Stratovan Corporation. (2018). Stratovan Checkpoint (Version 2018.08.07). (Software). Sacramento, CA: Stratovan Corporation Incorporated.

Sugardjito, J., Cant, J. G. 1994. Geographic and sex differences in positional behaver of orang-utans. *Treubia* **31**: 31-41.

Sugardjito, J., van Hooff, J. A. 1986. Age-sex class differences in the positional behaviour of the Sumatran orang-utan (*Pongo pygmaeus abelii*) in the Gunung Leuser National Park, Indonesia. *Folia primatologica; international journal of* primatology **47**(1): 14–25.

Surujnarain, R. 2019. New we must redefine man, or accept chimpanzees as … humans? [online]. Available at https://news.janegoodall.org/2019/07/24/now-we-must-redefine-man-or-accept-chimpanzees-ashumans/ (accessed 28 February 2024).

Susman, R. L. 1979. Comparative and functional morphology of hominoid fingers. *American Journal of Physical Anthropology* **50**(2): 215-236.

Susman, R. L. 1989. New hominid fossils from the Swartkrans formation (1979-1986 excavations): Postcranial specimens. *American Journal of Physical Anthropology* **79**: 451-474.

Susman, R. L. 1994. Fossil evidence for early hominid tool use. *Science* **265**(5178): 1570-1573.

Susman, R. L. 1998. Hand function and tool behavior in early hominids. Journal of Human Evolution **35**(1): 23-46.

Susman, R. L., Stern, J.T. Jungers, W. L. 1984. Arboreality and bipedality in the Hadar hominids. *Folia primatologica* **43**(2-3): 113-156.

Syeda, S. M., Tsegai, Z. J., Dunmore, C. J., Cazenave, M., Skinner, M. M. and Kivell, T. L. 2021. Inferring hand use in Australopithecus sediba: Analysis of the external and internal morphology of hominin proximal and intermediate phalanges. *11th Annual Meeting of the European Society for the Study of Human Evolution*.

Tallman, M. 2016. Shape ontogeny of the distal femur in the hominidae with implications for the evolution of bipedality. *PloS one* **11**(2): e0148371–e0148371.

Tallman, M. Almécija, S., Reber, S. L., Alba, D. M., Moyà-Solà, S. 2013. The distal tibia of Hispanopithecus laietanus: More evidence for mosaic evolution in Miocene apes. *Journal of Human Evolution* **64**(5): 319–327.

Thorpe, S. K., Crompton, R. H. 2006. Orangutan positional behavior and the nature of arboreal locomotion in *Hominoidea*. *American journal of physical anthropology* **131**(3): 384–401.

Tobias, P. V. 1971. *The brain in hominid evolution.* New York ; London: Columbia University Press.

Tocheri, M. W. 2007. Three-dimensional riddles of the radial wrist: Derived carpal and carpometacarpal joint morphology in the genus *Homo* and the implications for understanding the evolution of stone tool-related behaviours in hominins. Ph.D. Dissertation, Arizona State University.

Tocheri, M. W., Marzke, M. W., Liu, D., Bae, M., Jones, G. P., Williams, R. C., Razdan, A. 2003. Functional capabilities of modern and fossil hominid hands: three-dimensional analysis of trapezia. *American Journal of Physical Anthropology* **122**(2): 101-112.

Tocheri, M. W., Orr, C. M., Larson, S. G., Sutikna, T., Jatmiko, Saptomo, E. W., Due, R. A., Djubiantono, T., Morwood, M. J., Jungers, W. L. 2007. The primitive wrist of *Homo floresiensis* and its implications for hominin evolution. *Science* **317**(5845): 1743–1745.

Tocheri, M. W., Orr, C. M., Jacofsky, M. C., Marzke, M. W. 2008. The evolutionary history of the hominin hand since the last common ancestor of Pan and Homo. *Journal of Anatomy* **212**(4): 544–562.

Tocheri, M. W., Razdan, A., Williams, R. C., Marzke, M. W. 2005. A 3D quantitative comparison of trapezium and trapezoid relative articular and nonarticular surface areas in modern humans and great apes. *Journal of Human Evolution* **49**(5): 570–586.

Tocheri, M. W., Solhan, C. R., Orr, C. M., Femiani, J., Frohlich, B., Groves, C. P., Harcourt-Smith, W. E., Richmond, B. G., Shoelson, B., Jungers, W. L. 2011. Ecological divergence and medial cuneiform morphology in gorillas. *Journal of Human Evolution* **60**(2): 171–184.

Toth, N., Schick, K. 2015. Evolution of Tool Use. In: Muehlenbein, M. P. (Ed.) *Basics in human evolution*. Academic Press, New York: 193–208.

Toth, N., Schick, K., Rumbaugh, E. 1993. Pan the Tool-Maker: Investigations into the Stone Tool-Making and Tool-Using Capabilities of a Bonobo (Pan paniscus). *Journal of Archaeological Science* **20**(7):821-832

Trinkaus, E. 1983. *The Shanidar Neanderthals.* London: Academic Press.

Trinkaus, E. 2006. Modern human versus Neandertal evolutionary distinctiveness. *Current Anthropology* **47**(4): 597-620.

Trinkaus, E. 2016. The evolution of the hand in Pleistocene *Homo.* In: Kivell, T., Lemelin, P., Richmond, B., Schmitt, D. (eds) *The Evolution of the Primate Hand. Developments in Primatology: Progress and Prospects.* Springer, New York, NY: 545-571.

Tsegai, Z. J., Kivell, T. L., Gross, T., Nguyen, N. H., Pahr, D. H., Smaers, J. B., Skinner, M. M. 2013. Trabecular bone structure correlates with hand posture and use in hominoids. *PloS one* **8**(11): e78781.

Tsegai, Z. J., Stephens, N. B., Treece, G. M., Skinner, M. M., Kivell, T. L., Gee, A. H. 2017. Cortical bone mapping: An application to hand and foot bones in hominoids. *Comptes Rendus Palevol*. **16** (5–6): 690-701.

Tubiana, R., Thomine, J.-M., Mackin, E. 1996 *Examination of the hand and wrist*. 2nd ed. London: Dunitz.

Tuttle R. H. 1969. Knuckle-walking and the problem of human origins. *Science* **166**(3908): 953–961.

Tuttle, R. H., Watts, D. P. 1985. The positional behavior and adaptive complexes of *Pan gorilla*. In: S. Kondo (Ed.) *Primate Morphophysiology, Locomotor Analyses and Human Bipedalism.* Tokyo: University of Tokyo Press: 261-288.

Valladas, H., Joron, J., Valladas, G., Arensburg, B., Bar-Yosef, O., Belfer-Cohen, A., Goldberg, P., Laville, H., Meignen, L., Rak, Y., Tchernov, E., Tillier, A. M., Vandermeersch, B. 1987. Thermoluminescence dates for the Neanderthal burial site at Kebara in Israel. *Nature* **330**: 159–160.

van der Hulst, F. P. J., Schatzle, S., Preusche, C., Schiele, A. 2012. A Functional Anatomy Based Kinematic Human Hand Model with Simple Size Adaptation. *2012 IEEE International Conference on Robotics and Automation*: 5123-5129.

van Schaik, C. P., Fox, E. A., Sitompul, A. F. 1996. Manufacture and use of tools in wild Sumatran orangutans. Implications for human evolution. *Naturwissenschaften* **83**(4): 186-188.

Vandermeersch, B. 1963. Position stratigraphique et chronologie relative des restes humains du Paléolithique moyen du sud-ouest de la France. *Annales de Paléontologie humaine (vertébrés)* **51**: 90-92.

Vandermeersch, B, 1981. *Les Hommes Fossiles de Qafzeh (Israël).* Paris: C.N.R.S.

Vandermeersch B, Trinkaus E. 1995. The postcranial remains of the Regourdou I Neandertal: the shoulder and arm remains. *Journal of Human Evolution* 28: 439–476.

Vanhoof, M. J. M., Galletta, L., De Groote, I., Vereecke, E. E. 2021. Functional signals and covariation in triquetrum and hamate shape of extant primates using 3D geometric morphometrics. *Journal of morphology* **282**(9): 1382–1401.

Villmoare, B., Kimbel, W. H., Chalachew, S., Campasino, C. J., Dimaggio, E. N., Rowan, J., Braun, D. R., Arrowsmith, J. R., Reed, K. E. 2015. Palaeoanthropology. Early *Homo* at 2.8 Ma from Ledi-Geraru, Afar, Ethiopia. *Science* **347**(6228): 1352-1355.

Vereecke and Wunderlich, 2016. Experimental research on hand use and function in Primates. In: Kivell, T., Lemelin, P., Richmond, B., Schmitt, D. (eds) *The Evolution of the Primate Hand. Developments in Primatology: Progress and Prospects.* Springer, New York, NY: 259-284.

Viegas, S. T., Crossley, M., Marzke, M., Wullstein, K. 1991. The fourth carpometacarpal joint. *Journal of Hand Surgery*, **16**(3): 525-533.

Visalberghi, E., Fragaszy, D. 2013. The Etho-Cebus Project: Stone-tool use by wild capuchin monkeys. In: Sanz, C. M., Call, J., Boesch, C. (Eds.) *Tool Use in Animals*. Cambridge: Cambridge University Press: 203-222.

Visalberghi, E., Limongelli, L. 1996. Acting and understanding: Tool use revisited through the minds of capuchin monkeys. In: Russon, A. E., Bard, K. A., Parker, S. T. (Eds.) *Reaching into Thought: The Minds of the Great Apes.* Cambridge: Cambridge University Press. 57-79.

Visalberghi, E., Trinca, L. 1989. Tool use in capuchin monkeys: Distinguishing between performing and understanding. *Primates* **30**(4): 511–521.

Volpato, V., Macchiarelli, R., Guatelli-Steinberg, D., Fiore, I., Bondioli, L., Frayer, D. W. 2012. Hand to mouth in a neandertal: right-handedness in Regourdou 1. *PloS one* **7**(8): e43949.

Walker, A., Leakey, R. E. F., Harris, J., Brown, F. 1986. 2.5-Myr Australopithecus boisei from west of Lake Turkana, Kenya. Nature 322:517–522.

Ward, C. V. 2002. Interpreting the posture and locomotion of Australopithecus afarensis: Where do we stand? *American journal of physical anthropology* Suppl **35**: 185–215.

Ward, C. V., Leakey, M. G., Brown, B., Brown, F., Harris, J., Walker, A. 1999. South Turkwel: A noew Pliocene hominid site in Kenya. *Journal of Human Evolution* **36**: 69-95.

Washburn, S. 1960. Tools and human evolution. *Scientific American* **203:** 62-75.

Watanabe, A. 2018. How many landmarks are enough to characterize shape and size variation? *PloS one* **13**(6): e0198341–e0198341.

Weber, G.W., Bookstein, F.L. 2011. Virtual Anthropology: A Guide to a New Interdisciplinary Field. Wien: Springer.

Webster, M., Sheets, A.D. 2010. A Practical Introduction to Landmark-Based Geometric Morphometrics*. Quantitative Methods in Paleobioogy* **16**: 163-188.

Whiten, A., Schick, K., Toth, N. 2009. The evolution and cultural transmission of percussive technology: integrating evidence from palaeoanthropology and primatology*. Journal of Human Evolution* , **57**(4): 420–435.

Wiley, D. F. , Amenta, N., Alcantara, D. A., Ghosh, D., Kil, Y. J., Delson, E., Harcourt-Smith, W., Rohlf, F. J. , St John, K., Hamann, B. 2005. Evolutionary morphing. *Proc IEEE Vis 2005*: 431–438.

Williams, E., Gordon, A., Richmond, B. 2012. Hand pressure distribution during Oldowan stone tool production. *Journal of Human Evolution* **62**(4): 520-532.

Williams-Hatala, E. M. 2016. Biomechanics of the Human Hand: From Stone Tools to Computer Keyboards. In: Kivell, T., Lemelin, P., Richmond, B., Schmitt, D. (eds) *The Evolution of the Primate Hand. Developments in Primatology: Progress and Prospects*. Springer, New York, NY: 285-312.

Wood, B., Leakey, M. 2011. The Omo-Turkana Basin Fossil Hominins and Their Contribution to Our Understanding of Human Evolution in Africa. *Evolutionary anthropology* **20**(6): 264–292.

Wolpoff, M. H. 1999. *Paleoanthropology, 2nd edn*. Boston: McGraw-Hill.

Westergaard, G. C., Suomi, S. J. 1997. Capuchin monkey (*Cebus apella*) grips for the use of stone tools. *American Journal of Physical Anthropology* **103**(1): 131-135.

Wright, R. V. S. 1972. Imitative Learning of a Flaked Stone Technology—The Case of an Orangutan. The Australian Journal of Anthropology **8**(4): 296-306.

Wunderlich, R. E., Jungers, W. L. 2009. Manual digital pressures during knuckle-walking in chimpanzees (*Pan troglodytes*). *American journal of physical anthropology* **139**(3): 394–403.

Young, R. W. 2003. Evolution of the human hand: the role of throwing and clubbing. *Journal of Anatomy* **202**(1):165-74.

Zelditch, M. L., Swiderski, D. L., Sheets, H. D., Fink, W. L. 2004. *Geometric morphometrics for biologists : a primer*. London: Academic Press.

Zelditch, M. L., Swiderski, D. L., Sheets, H. D., Fink, W. L. 2012. *Geometric morphometrics for biologists: A primer*. London: Academic Press.

Appendices

Appendix A: Dataset Spreadsheets

Homo sapiens			
Specien Catalogue name/no.	Collection	Sex	Side
1010	MNMH	F	Right
1023	MNMH	M	Left
106r	MNMH	U	Right
1073RR	MNMH	F	Right
1075r	MNMH	M	Right
125	MNMH	F	Right
1341	MNMH	F	Right
1390	MNMH	F	Right
1512	MNMH	F	Right
1523	MNMH	F	Right
1555	MNMH	M	Right
1569	MNMH	M	Right
1602	MNMH	F	Right
161	MNMH	F	Right
1617	MNMH	F	Right
171r	MNMH	F	Right
208	MNMH	M	Right
211	MNMH	M	Right
213	MNMH	M	Right
233	MNMH	M	Right
235	MNMH	M	Right
261	MNMH	F	Right
289r	MNMH	F	Left
293r	MNMH	M	Right
324	MNMH	M	Right
362	MNMH	M	Right
377	MNMH	F	Right
39	MNMH	M	Right
405	MNMH	M	Right
414	MNMH	M	Right
468	MNMH	M	Right
49r	MNMH	F	Right
522	MNMH	M	Right
567	MNMH	F	Right
645	MNMH	F	Right
815	MNMH	M	Right

880	MNMH	F	Right
88rr	MNMH	F	Right
929	MNMH	M	Right
943	MNMH	F	Right
94r	MNMH	U	Right
970	MNMH	U	Right
989	MNMH	M	Right
GLR91010	UoS	U	Right
SK2404	UoS	M	Right
SK2659	UoS	U	Left
SK2886	UoS	M	Right
SK2997	UoS	M	Right
SK3028	UoS	M	Right
SK3048	UoS	M	Right
SK3052	UoS	M	Right
SK3054	UoS	F	Right
SK3090	UoS	M	Right
SK3310	UoS	U	Left
SK3632	UoS	F	Right
SK3861	UoS	M	Right
SK368	UoS	F	Right
Y3307	UoS	F	Right
Y3354	UoS	F	Right
Y3650	UoS	F	Right
	UoS	F	Left

Pan trogloytes				
Specien Catalogue name/no.	Sub species	Collection	Sex	Side
FC100	P. t. ellioti	PCM	M	Right
M273	P. t. ellioti	PCM	F	Right
M440	P. t. ellioti	PCM	M	Right
M677	P. t. ellioti	PCM	F	Right
M720	P. t. ellioti	PCM	F	Right
M742	P. t. ellioti	PCM	F	Right
M78	P. t. ellioti	PCM	M	Right
51376	P. t. schweinfurthii	NMNH	F	Right
236971	P. t. schweinfurthii	NMNH	F	Right
51376	P. t. schweinfurthii	NMNH	F	Right
236971	P.t. spe.	NMNH		Right
Cami147	P.t. spe.	PCM	F	Right
Cami206	P.t. spe.	PCM	F	Right
Cami228	P.t. spe.	PCM	M	Right

Camii301	P.t. spe.	PCM	F	Right
M249	P.t. spe.	PCM	F	Right
M272	P.t. spe.	PCM	M	Right
M712	P.t. spe.	PCM	M	Right
M724	P.t. spe.	PCM	M	Right
M984	P.t. spe.	PCM	M	Right
M986	P.t. spe.	PCM	F	Right
Zvi25	P.t. spe.	PCM	M	Right
Zvi34	P.t. spe.	PCM	M	Right
176226	P. t. troglodytes	NMNH	U	Right
176227	P. t. troglodytes	NMNH	F	Right
176228	P. t. troglodytes	NMNH	M	Right
176229	P. t. troglodytes	NMNH	F	Right
17622	P. t. troglodytes	NMNH	U	Left
176230	P. t. troglodytes	NMNH	U	Right
FC116	P. t. troglodytes	PCM	M	Right
M144	P. t. troglodytes	PCM	M	Right
M254	P. t. troglodytes	PCM	M	Right
M450	P. t. troglodytes	PCM	F	Right
M501	P. t. troglodytes	PCM	F	Right
M743	P. t. troglodytes	PCM	F	Right
M86	P. t. troglodytes	PCM	F	Right
M873	P. t. troglodytes	PCM	F	Right
M967	P. t. troglodytes	PCM	F	Right
M988	P. t. troglodytes	PCM	M	Right
Zix49	P. t. troglodytes	PCM	M	Right
Zvii24	P. t. troglodytes	PCM	M	Right
477333	P. t. verus	NMNH	F	Right
481803	P. t. verus	NMNH	F	Right
481804	P. t. verus	NMNH	M	Right

Gorilla beringei			
Specien Catalogue name/no.	Collection	Sex	Side
395636	NMNH	M	Right
396934	NMNH	M	Right
396935	NMNH	F	Right
396936	NMNH	F	Right
396937	NMNH	M	Right
397351	NMNH	F	Right
545045	NMNH	M	Left

Gorilla gorilla			
Specien Catalogue name/no.	Collection	Sex	Side
176225	NMNH	M	Right
2767	NMNH	U	Left
Cami106	PCM	M	Right
Cami134	PCM	M	Right
Cami139	PCM	F	Right
Cami149	PCM	F	Right
Cami150	PCM	F	Right
Cami231	PCM	M	Right
Cami41	PCM	M	Right
Cami42	PCM	F	Right
Cami48	PCM	M	Right
Cami95	PCM	F	Right
Cami96	PCM	F	Right
FC123	PCM	M	Right
FC130	PCM	M	Right
M119	PCM	M	Right
M135	PCM	M	Right
M150	PCM	F	Right
M20	PCM	M	Right
M264	PCM	M	Right
M470	PCM	F	Right
M720	PCM	M	Right
M729	PCM	M	Right
M755	PCM	F	Right
M789	PCM	F	Right
M799	PCM	M	Right
M835	PCM	F	Right
M89	PCM	F	Right
M962	PCM	M	Right
M96	PCM	F	Right
M962	PCM	M	Right
Mii23	PCM	M	Right
ZI30	PCM	M	Right
Zvi30	PCM	M	Right
Zvi33	PCM	F	Right

Pongo abelii			
Specien Catalogue name/no.	Collection	Sex	Side
143587	NMNH	M	Right
143588	NMNH	M	Right

143590	NMNH	M	Right
143593	NMNH	M	Right
143601	NMNH	F	Left
267325	NMNH	M	Right
270807	NMNH	M	Right
A22937	NMNH	M	Right
Pongo pygmaeus			
Specien Catalogue name/no.	Collection	Sex	Side
142169	NMNH	F	Left
145301	NMNH	M	Right
145302	NMNH	F	Right
145304	NMNH	M	Right
145305	NMNH	M	Right
145308	NMNH	F	Right
145309	NMNH	F	Right
145310	NMNH	M	Right
153821	NMNH	F	Right
153822	NMNH	M	Right
153823	NMNH	F	Right
588109	NMNH	F	Right
UoS1	UoS	U	Right

Appendix B: Synopsis of human manual dexterity

John Napier (1956, 1960, 1961, 1980, 1993) was among the first to categorize the wide range of movements, postures and grips used by the human hand to manipulate the external environment. Napier divided hand movements into two primary categories: nonprehensile and prehensile movements. Nonprehensile movements are relatively simple movements that do not require any degree of manual dexterity, and are by no means exclusive to humans, nor indeed to primates. They involve non-grasping movements in which objects are simply pushed or tapped and include pushing or lifting movements of the hand as a single unit, or the pushing, lifting, tapping, and punching movements of the fingers (Aiello and Dean, 2006; Williams-Hatala, 2016). Prehensile movements are more complex and are defined as manipulative behaviours in which objects are held either between the digits or between the digits and the palm of a single hand (Napier, 1956, 1993). Prehensile movements can be divided into of four different primary grips: hook grips; scissor grips; power grips; and precision grips (Napier, 1980, 1993).

Hook and Scissor grips

Hook and scissor grips are relatively simple and uncomplicated. The hook grip (figure 2.6 (*a*)) is achieved by simply flexing the second to fifth fingers to form a hook, with the thumb being passive and uninvolved. The hook grip is commonly used when carrying an object with a handle such as a briefcase or a bag (Napier, 1956). The scissor grip (figure 2.6 (*b*)) is similarly simple, and is used to hold objects between the sides of two adjacent fingers, such as is commonly used if smoking a cigarette.

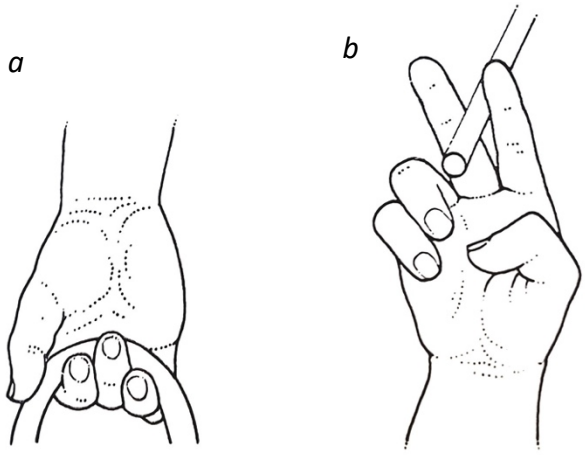

Figure 2.6: The hook (*a*) and scissor (*b*) grips. From Aiello and Dean, 2006.

Power grips

The remaining two grips (power and precision) require more complex movements of the hand. Power grips are those in which an object is secured between the flexed fingers and the palm of the hand, with the thumb acting as a buttress, further securing the object in the hand (Napier, 1956, 1962, 1993). The power grip can be subdivided into three variants: the squeeze, disc, and spherical grips.

During the squeeze grip, a cylindrical object is held diagonally across the palm, with the second to fifth digits flexed around the object, and the fourth and fifth digits flexed around the object to a greater extent than the second and third digit. The thumb is either extended along the longitudinal axis of the object or wrapped around it, and the object itself is braced securely against the bases of the fifth digit and the thumb (figure 2.7 (*a*)). During the disc grip, pressure is applied against a manipulated object while the slightly flexed thumb and fingers grasp its circumference, as is used when handling a discus (figure 2.7 (*b*)). The spherical grip is utilized when handling large spherical objects, which is clamped against the palm of the hand by the flexed fingers and thumb (figure 2.7 (*c*)).

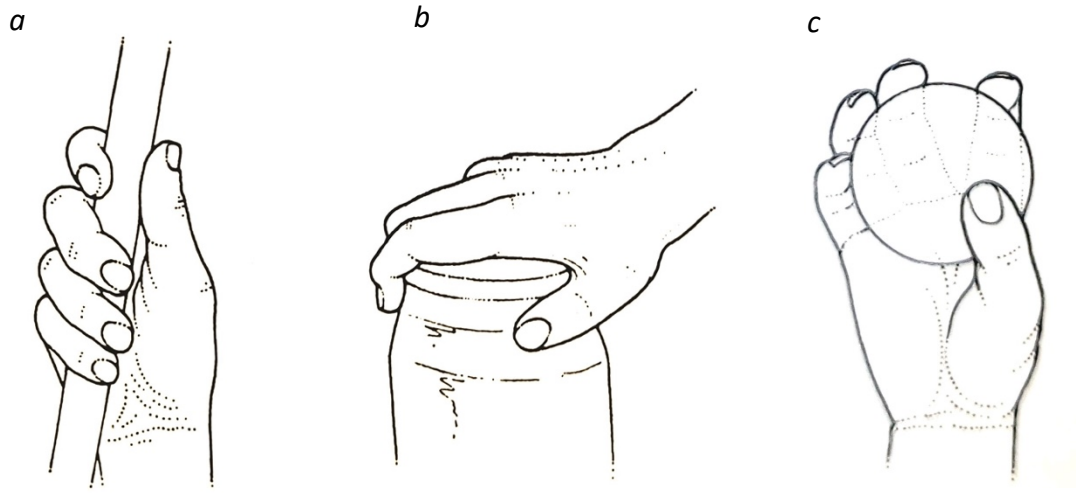

Figure 2.7: The power "squeeze" grip (*a*), disc grip (*b*), and spherical grip (*c*). From Aiello and Dean, 2006.

Precision grips

Precision grips require the use of the thumb and one or more of the fingers, with no active involvement of the palm, and are executed between the palmar surfaces of one or more of the fingers and the pollical distal phalanx, with the distal ends of the digits used in any combination (Landsmeer, 1962). During precision grips, the thumb, which is abducted and rotated to face the palm to oppose the other digits, plays the main supportive role, in contrast to the power grips, where it has a buttressing obligation (Napier, 1956, 1993). The palm may occasionally be passively involved in the execution of precision grips, although this is not a requirement (Marzke, 1997; Williams-Hatala, 2016).

As with the power grip, the precision grip can be subdivided into more specialized definitions. When a large object is held between the palmar surfaces of all five fingers and the thumb, the five-jaw-chuck grip is employed (figure 2.8 (*a*)). When a smaller object is handled, the three-jaw-chuck grip is used, where the object is held between the palmar surfaces of the first, second and third digits. The three-jaw-chuck grip (figure 2.8 (*b*)) is a variation on the precision grip and is termed a forceful precision grip (Marzke and Wullstein, 1996; Marzke, 1997). Another forceful precision grip is the cradle grip (figure 2.8 (*c*)), in which an object is cupped by the thumb and finger pads (Marzke, 2013). Alternatively, the pad-to-pad grip (figure 2.8 (*d*)) utilises the palmar surfaces of the thumb and a single finger, while the pad-to-side grip (figure 2.8 (*e*)), where

the terminal digit pad of the thumb is opposed to the radial side of the index finger, is the typical grip utilized when inserting and turning a key in a lock (Aiello and Dean, 2006).

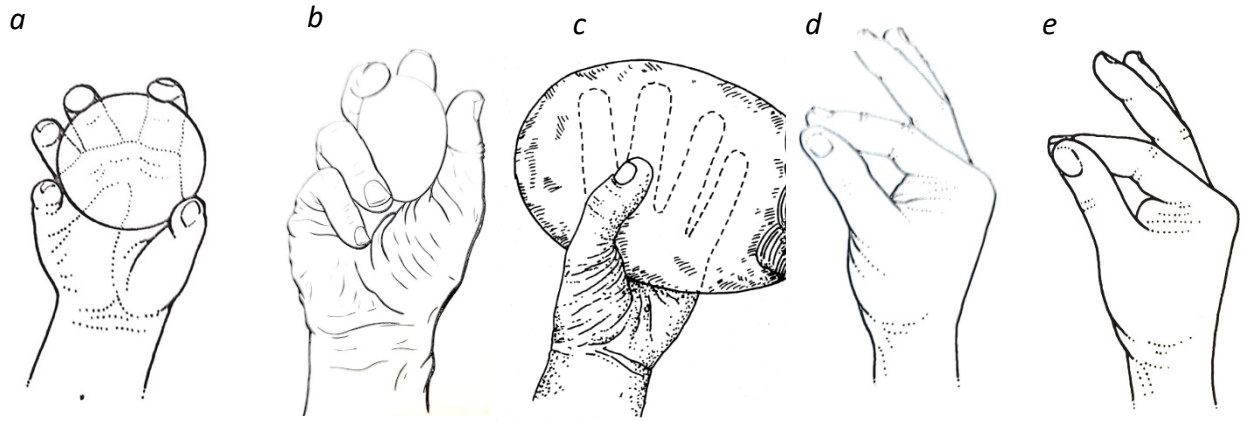

Figure 2.8: The five-jaw chuck grip (*a*), three-jaw chuck grip (*b*), cradle grip (c),pad-to-side grip (*d*), and pad-to-pad grip (*e*). From Aiello and Dean, 2006, Kapandji, 1982, and Marzke, 2013.

Opposition

In addition to, and complementing, the various power and precision grips described above, two movements – or postures – of the hand are essential to the prehensile abilities of modern humans, and which are instrumental in the effective execution of the human repertoire of hand grips: opposition and cupping. Opposition was defined by Napier (1980) as the ability to place the pulp surface of the thumb squarely in contact with, or diametrically opposed to, the terminal pads of one or all of the remaining digits (figure 2.9 (*a*)). Opposition of the thumb to the second to fifth digits is instrumental in achieving pad-to-pad contact between the thumb and fingers, and is employed extensively during various precision grips (Napier, 1955, 1956). Cupping of the palm of the hand is the movement whereby the hypothenar and thenar portions of the palm are migrated towards the centre of the palm (figure 2.9 (*b*)). Forceful cupping of the palm is an essential movement in several grips, specifically the power, cradle, and five-jaw-chuck grips, where the tip of the fifth digit must be placed in fine adjustment to the size and shape of objects manipulated by the fingertips (Aiello and Dean, 2006).

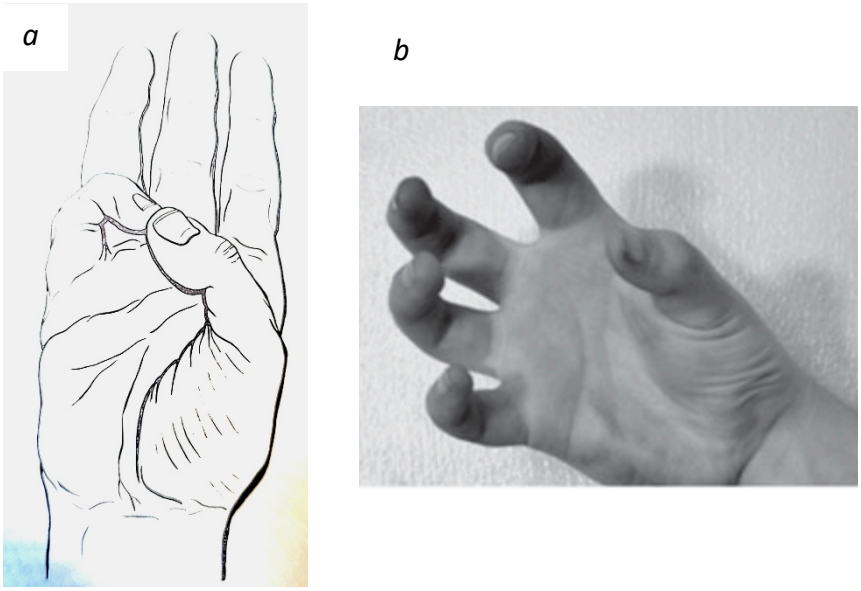

Figure 2.9: Opposition of the thumb to the fifth digit (*a*) and the cupping posture of the hand (*b*). From Marzke, 2013 and Kapandji, 1982.

Appendix C: Basic anatomical terminology and movements of the human hand

Anatomical terminology

The human hand, while extremely derived in some respects, is generally primitive, and despite having derived and specialized features, it remains among the most primitive anatomical regions in the human body (Richmond et al., 2016). The human hand demonstrates a primitive Bauplan that is universal to most primates, and the anatomical terminology discussed below is applicable to most non-human primate taxa, particularly the *Catarrhini* and *Hominoidea.* As such, the anatomy of the human hand alone will be discussed at the expense of the myriad subtle variations on a common form seen in the wider *Primate* order.

The hand, or manus, originates at the wrist, which generally corresponds to the skin creases at the base of the palm and separates the two bones of the forearm (brachium), the ulna and radius, from the hand itself. The hand is supinated in anatomical position, with the palm facing upwards and the thumb furthest away from the body (figure 2.11). In anatomical position, a proximal direction is towards the forearm, while a distal direction is towards the fingertips. The side closest to the body, where the little finger is found, is variably termed the medial or ulnar side, while the side of the thumb is towards the lateral or radial side of the hand. The front of the hand is termed the palmar, volar, or anterior surface, while the back of the hand is the dorsal or posterior surface. Following from the wrist, moving distally, is the palm, from which emanates the thumb (pollex) on the radial side, and four non-pollical digits distally. The thumb is also termed the first digit, while the index finger is the second digit, progressing to the little finger, which is the fifth digit of the hand. Each ray is comprised of the corresponding bones of the palm (metacarpal) and fingers (phalanges) of each digit. The hand is compartmentalized in the sagittal plane by its midline, which progresses from the centre of the writs and distally along the centre of the third digit (figure 2.11). On the radial/lateral side of the palmar surface of the hand can be found the thenar eminence, which is formed by the concentration of intrinsic hand muscles that operate the thumb, and from which the thumb itself emanates from. This side of the hand is also termed the thenar side. Correspondingly, on the ulnar side of the palm is the hypothenar eminence, which is composed of the intrinsic muscles of the fifth digit, and this side of the hand is variably called the ulnar, medial, or hypothenar side.

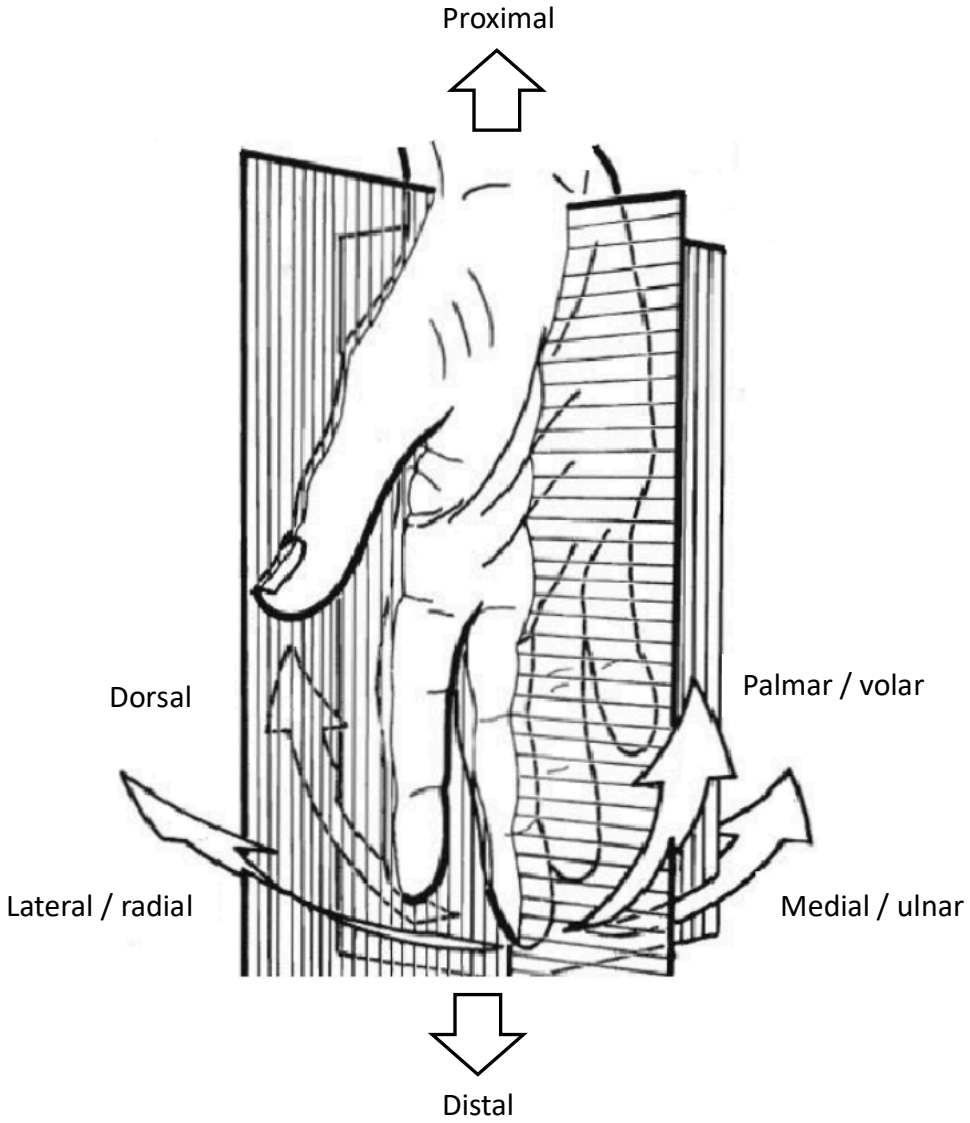

Figure 2.11: Diagram of a right hand in anatomical position with directional terminology. Adapted from van der Hulst *et al.,* 2012.

Movements of the hand

Basic movements of the hand predominantly occur at the wrist, the joints of the fingers, and the first ray. The hand is capable of flexion (bending the palm towards the forearm) and extension (bending the dorsum of the hand towards the forearm) when the wrist is moved in the transverse axis (figure 2.12). Adduction (ulnar deviation) is achieved by moving the hand towards the side of the fifth digit (ulnar/medial/hypothenar side), while abduction (radial deviation) is

achieved by moving the hand along its sagittal axis towards the side of the thumb (radial/lateral/thenar side) (figure 2.12). Circumduction is a combination of the movements of flexion-extension and adduction-abduction of the wrist, which results in a circling movement of the hand (figure 2.13). Very simplistically, the second to fifth digits have two degrees of freedom, being flexion-extension and abduction (away from the hand's midline) and adduction (towards the midline) (figure 2.15). The third digit, being situated along the midline of the hand, is technically incapable of adduction, rather performing radial/lateral abduction and ulnar/medial abduction. Similar to the wrist, the fingers can combine movements in the two planes to achieve circumduction, which is a circular movement of the finger around an axis centred on the relevant metacarpal head. Movement at the interphalangeal joints of all digits (including the thumb) are restricted to the flexion-extension plane (figure 2.15). However, due to the asymmetric morphologies of the distal heads of several metacarpals and proximal phalanges, a very small degree of accessory supination-pronation is observed at the metacarpophalangeal and proximal interphalangeal joints of several rays (Shrewsbury *et al.*, 2003).

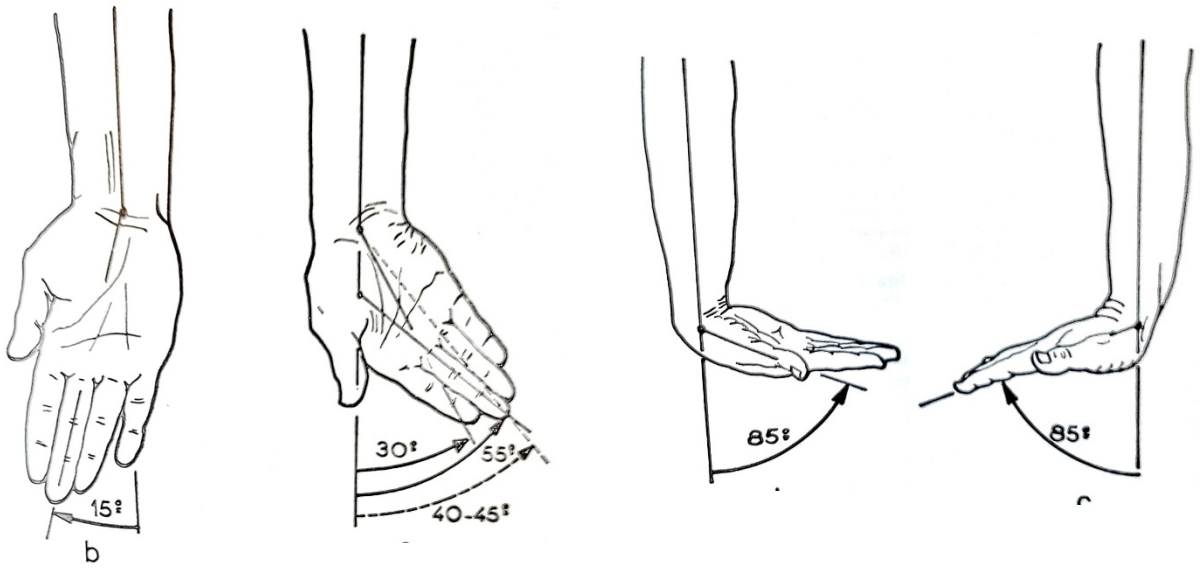

Figure 2.12: Movements of the hand at the wrist, from left: abduction, adduction, flexion, and extension. From Kapandji, 1983.

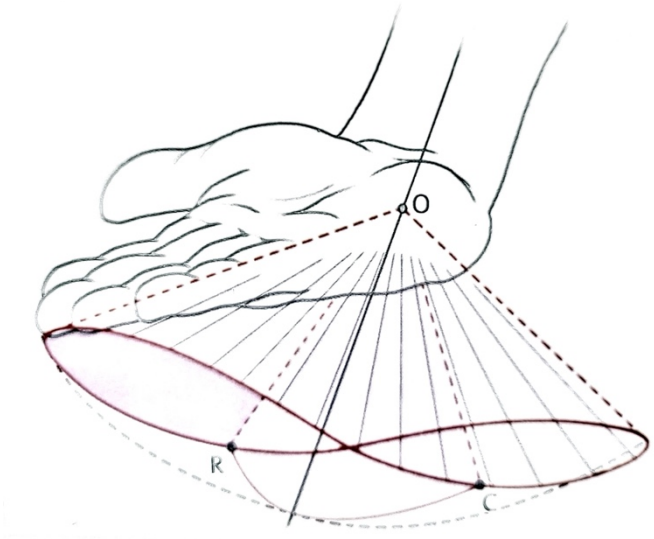

Figure 2.13: Circumduction of the wrist. From Kapandji, 1983.

The human thumb is the most versatile digit of the hand in terms of movements among the primates. However, the great majority of the thumb's movement occur at its carpometacarpal joint (described below). While movements of the second to fifth carpometacarpal joints are variably restricted, the first carpometacarpal joint is capable of adduction-abduction, flexion-extension, and opposition, in which the carpometacarpal joint is abducted and flexed in concert with flexion of the pollical metacarpophalangeal and interphalangeal joints so that the palmar surface of the thumb faces the palm and the palmar surfaces of the second-to-fifth digits. While an extraordinary range of motion is capable at the pollical carpometacarpal joint, both the metacarpophalangeal and interphalangeal joints of the thumb are overwhelmingly restricted to flexion-extension (figure 2.14).

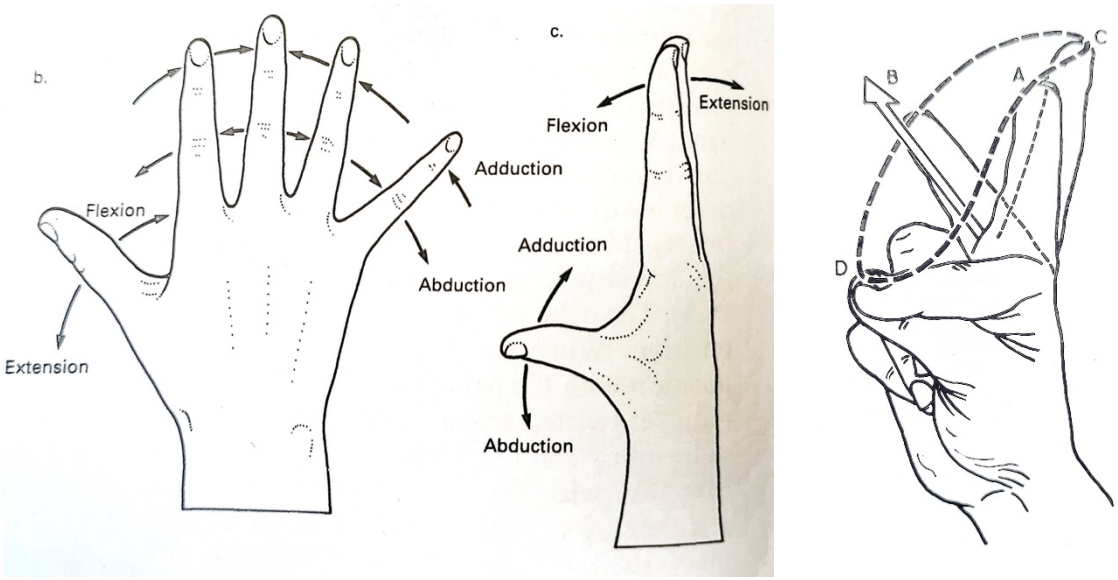

Figure 2.14: Movements of the thumb and fingers, with circumduction of the index finger to the right. From Aiello and Dean, 2006 and Kapandji, 1982.

Appendix D: Skeletal anatomy of the hand

The human hand contains 27 bones (in addition to numerous sesamoid bones within various tendons), with 36 articulations and 39 active muscles (Hirt *et al.* 2017). These bones can be divided into bones of the wrist; bones of the palm; and bones of the fingers (figure 2.15). The wrist bones are called the carpals and are located between the bones of the forearm (radius and ulna) proximally, and the bones of the palm (metacarpals) distally. There are two rows of carpal bones consisting of four carpals each. The proximal carpal row is composed of, moving from a radial to ulnar direction: the scaphoid, lunate, triquetrum, and pisiform; while the distal carpal row is formed of (from radial to ulnar): the trapezium trapezoid, capitate, and hamate. Moving distally, the four bones of the distal carpal row articulate with the five metacarpals of the palm at the first to fifth carpometacarpal joints. The trapezium articulates with the pollical, or first, metacarpal, and minimally the second, the trapezoid articulating with the second metacarpal, the capitate articulating primarily with the third metacarpal, but also variably and minimally with the second and fourth, and the hamate articulating with the fourth and fifth metacarpals. The fingers of the hand have their origins at the metacarpophalangeal joints, which are the articulations between the distal metacarpal heads and the proximal bases of the corresponding proximal phalanx. While digits two to five have three phalanges in each finger (proximal, intermediate, and distal), resulting in two interphalangeal joints for each finger, the thumb is only possessed of a proximal and distal phalanx, thereby having one interphalangeal joint.

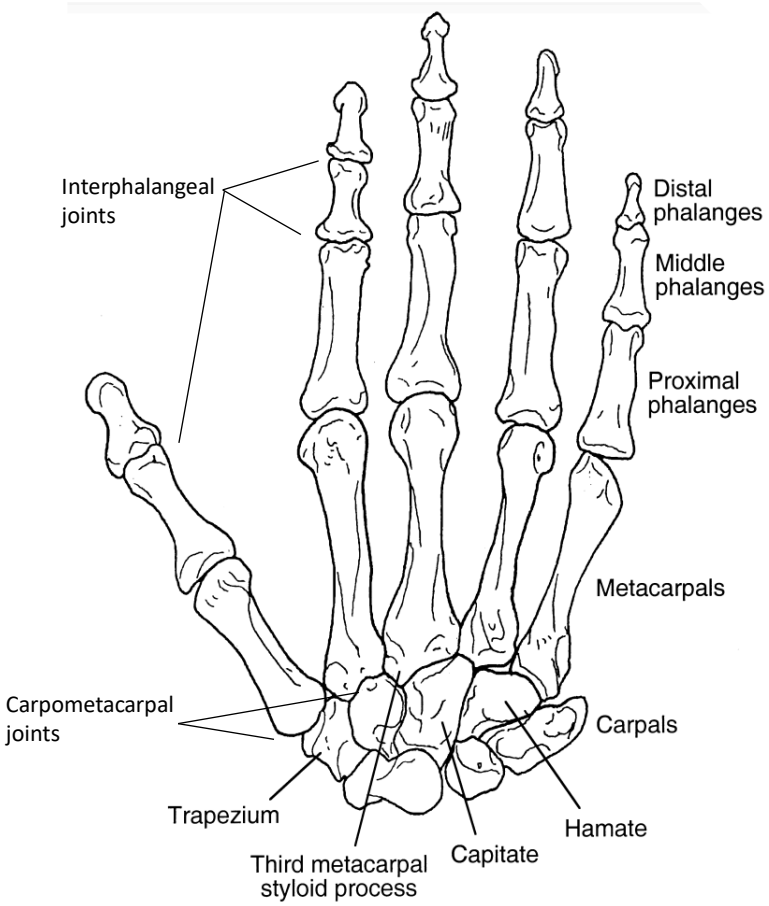

Figure 2.15: Osteological structure of the hand with bones and joint names indicated. Adapted from Marzke and Marzke, 2000.

Appendix E: Muscular anatomy of the hand

For a complete understanding of the muscles that play a role in the complex movements of the primate hand, we must begin at the forearm – or the antebrachium. The muscles that move the hand is divided into two major groups: the extrinsic muscles of the hand (long muscles which originate in the forearm and insert into the hand) and intrinsic muscles (shorter muscles with their origin and insertion points both within the hand itself). The extrinsic muscles originate from the epicondyles of the humerus or from the shafts of the long antebrachial bones – the humerus and radius – as well as the interosseus membrane of the forearm. They insert onto the carpal bones, the metacarpals, or the phalanges, and are responsible for the movements of extension, flexion, adduction, abduction, and circumduction of the wrist, and flexion and extension of the fingers.

The extrinsic and intrinsic muscles are divided into three compartments: the dorsal compartment of the forearm; the ventral compartment of the forearm; and the ventral compartment of the hand. The dorsal and ventral compartments of the forearm, which are innervated by radial nerve (C5-T1) and median nerve (C5 or 6-T1) respectively, contain the extrinsic muscles, whilst the intrinsic muscles of the hand are to be found in the ventral compartment of the hand, innervated mostly by the ulnar nerve and some by the median nerve (Lemelin and Diogo, 2016).

The muscles found in the dorsal compartment of the forearm are involved primarily in extension of the hand, and as such, the term extensor compartment is commonly used (Lemelin and Diogo, 2016). The dorsal compartment is further divided into two layers: the superficial and the deep layers. The superficial layer of this compartment comprises five extrinsic muscles, all of which originate from the radial epicondyle of the humerus: *extensor carpi radialis longus, extensor carpi radialis brevis, extensor carpi unlaris, extensor digitorum,* and *extensor digiti minimi*. Three of these extrinsic muscles, *extensor carpi radialis longus, extensor carpi radialis brevis,* and *extensor carpi unlaris,* all cross the radiocarpal joint to insert onto the bases of the second, third, and fifth metacarpals respectively (Lemelin and Diogo, 2016). The primary function of these three muscles is to extend the hand at the wrist, however the *extensor carpi radialis longus* and *extensor carpi radialis brevis* also work to abduct the hand, while the *extensor carpi*

ulnaris aids in adducting the hand at the wrist. Both of these muscles insert onto the middle and distal phalanges of the three-joint-fingers via the extensor expansion. *Extensor digitorum* works to extend the second to fifth digits, while the *extensor digiti minimi* extends the fifth digit.

The deep layer of the dorsal compartment of the forearm is composed of four extrinsic muscles which originate from the ulna, radius, and the interosseous membrane, a fibrous connective band between the two bones (Lemelin and Diogo, 2016). Three of these muscles act upon the thumb. *Abductor pollicis longus* originates from the posterior surface of the ulna and radius and the interosseous membrane, inserts onto the base of the first metacarpal, and abducts, laterally rotates, and extends the first digit at the carpometacarpal joint. *Extensor pollicis longus* originates from the posterior surface of the ulna and the interosseous membrane, inserts onto the base of the distal pollical phalanx, and extends the thumb at the carpometacarpal, metacarpophalangeal, and interphalangeal joints. *Extensor pollicis brevis,* which has its origin at the posterior surface of the radius and interosseous membrane and inserts onto the trapezium and the base of the pollical proximal phalanx, extends the pollex at the carpometacarpal and metacarpophalangeal joints only. The fourth muscle in the deep layer of the posterior compartment of the forearm is the *extensor indicis.* Its origin is on the posterior surface of the ulna, and it inserts as a tendon that blends with the extensor expansion of the index finger (2nd digit). *Extensor indicis* extends the second digit at its metacarpophalangeal and interphalangeal joints and provides the index finger with greater independence during extension compared to the third and fourth digits, which can only be extended by the extensor digitorum (Lemelin and Diogo, 2016).

The muscles of the ventral compartment of forearm are responsible for the flexion of the hand and fingers. As with the posterior compartment of the forearm, the ventral compartment is subdivided into superficial and deep layers. The superficial layer is comprised of four muscles, while two extrinsic muscles are to be found in the deep layer. In the superficial layer are found *flexor carpi ulnaris*, *flexor carpi radialis*, *palmaris longus*, and *flexor digitorum superficialis.* All four muscles have a common origin from the ulnar epicondyle of the humerus, while *flexor carpi ulnaris* has a second origin point at the olecranon process of the ulna, and *flexor digitorum* has additional origins at the coronoid process of the ulna and the anterior border of the radius. Of the three main long flexors of the wrist – *flexor carpi radialis, flexor carpi ulnaris*, and *palmaris*

longus – *flexor carpi ulnaris* alone inserts onto the base of the fifth metacarpal. The *flexor carpi ulnaris* muscle arises from two heads. The humeral head originates from the medial epicondyle of the humerus and the antebrachial fascia, while the ulnar head originates from the dorsal aspect of the olecranon and the proximal two-thirds of the posterior border of the ulna (Hirt *et al.* 2017). *Flexor carpi ulnaris* inserts onto the hook of the hamate and the palmar base of the fifth metacarpal, and its tendon contains the pisiform. The *flexor carpi ulnaris* muscle is the strongest flexor of the wrist, and along with the *extensor carpi ulnaris* and *extensor digitorum* muscles, adducts the hand at the wrist, while *flexor carpi radialis,* with its insertion onto the base of the second and third metacarpals, flexes and abducts the hand at the wrist. *Extensor carpi ulnaris* also arises with two heads – the humeral head originating at the lateral epicondyle, the radial collateral ligament, and the ulnar ligament of the radius. The ulnar head from the olecranon, posterior surface and border of the ulna, and the antebrachial fascia, inserts onto the dorsal base of the fifth metacarpal.

Palmaris longus is a thin muscle with a long tendon that blends with the palmar aponeurosis, skin and facia of the palm, and acts as a weak flexor of the hand at the radiocarpal joint, and also tightens the palmar aponeurosis, a triangular fibrous sheet deep to the skin of the palm. *Palmaris longus* is absent in between 5 and 20% of the modern human population (Gibbs, 1999; Lemelin and Diogo, 2016). *Flexor digitorum superficialis*, which has two distinct heads originating from each of its two origin points, branches off distally into four distinct tendons (two from each head) (Lemelin and Diogo, 2016). Each of these four tendons travel to one of the four three-joint digits, splitting in two to insert on the anterior border of the middle phalanges of digits two to five. The splitting of the tendons allows for the tendon of *flexor digitorum profundus* to pass between.

The two muscles of the deep layer of the ventral compartment, *flexor digitorum profundis* and *flexor pollicis longus*, have their origin on the proximal two thirds of the anterio-medial ulnalr shaft, and the anterior shaft of the radius, the anterior interosseous membrane, and the medial epicondyle of the humerus, respectively. *Flexor digitorum profundus*, as with *flexor digitorum superficialis*, splits into four tendons, each of which travel between the split tendons of *flexor digitorum superficialis* to insert onto the palmar aspect of the base of the second to fifth distal phalanges. *Flexor pollicis longus* inserts onto the palmar base of the pollical distal phalanx. By virtue of their traverse along the palmar side of the rays, *flexor digitorum profundus* and *flexor*

pollicis longus have the ability to flex the carpometacarpal, metacarpophalangeal, and interphalangeal joints of their respective rays – the first ray in the case of *flexor digitorum profundus,* and the second to fifth (which includes the proximal and distal interphalangeal joints) in the case of *flexor pollicis longus.*

As with the ventral and dorsal compartments of the antebrachium, the ventral compartment of the hand is composed of a superficial and a deeper layer. All of these muscles are intrinsic muscles of the hand, that is to say, both their origins and insertions are to be found distal to the radiocarpal joint. In addition to the *palmaris brevis, adductor pollicis*, lumbrical, and interosseous muscles, the intrinsic muscles of the human hand include two groups: the thenar and hypothenar muscles. The thenar eminence is the prominent bulge at the base of the thumb, and is comprised of the *abductor pollicis brevis,* the *flexor pollicis brevis*, and *opponens pollicis*. *Abductor pollicis brevis*, the most superficial of these three muscles, attaches from the flexor retinaculum, the scaphoid and the trapezium to insert onto the base of the first pollical phalanx and the dorsal aponeurosis of the thumb (Lemelin and Diogo, 2016). The *flexor pollicis brevis,* which is more ulnar to the *abductor pollicis brevis,* has two heads: the superficial and deep heads, which are separated at their origin by the tendon of *flexor pollicis longus* (Lemelin and Diogo, 2016). Both heads originate at the trapezium, with the superficial head also having a second origin point at the flexor retinaculum,and proceeds to the radial side of the first metacarpophalangeal joint, to attach at the base of the proximal first phalanx, thus flexing the pollex at the metacarpophalangeal joint. The *opponens pollicis* muscle is the deepest muscle of the thenar eminence. This muscle crosses the trapeziometacarpal joint from its origin at the flexor retinaculum and trapezium, to the radial side of the pollical metacarpal shaft, and in contraction, acts to oppose the thumb. Each muscle of the thenar eminence can produce independent action at the thumb – abduction, flexion and medial rotation. However, when acting in tandem and in synergy with one another, the compound action of the thenar muscles produces opposition (Long *et al.,* 1970).

On the opposite side of the palm, at the base of the fifth digit, is the hypothenar eminence. Of the intrinsic muscles of the hand, three make up the hypothenar eminence: *abductor digiti minimi, flexor digiti minimi brevis,* and *opponens digiti minimi*. Additionally, *palmaris brevis*, a thin muscle just deep to the skin of the palm on the ulnar side, is also located

in this vicinity. *Palmaris brevis,* which originates on the flexor retinaculum and inserts onto the skin of the medial (ulnar) border of the palm, is a subcutaneous muscle that overlies the other muscles of the hypothenar eminence. In contraction, it creases the skin of the palm at the hypothenar region and aids in gripping by deepening the central hollow of the palm (Aiello and Dean, 2006). The three muscles of the hypothenar eminence originate from the bones and ligaments of the ulnar side of the hand. *Opponens digiti minimi brevis* and *flexor digiti minimi brevis* both originate from the flexor retinaculum and hamate, while *abductor digiti minimi* has its origin on the pisiform. Both *flexor digiti minimi brevis* and *abductor digiti minimi* insert onto the base of the fifth proximal phalanx, and both flex the fifth digit at its metacarpophalangeal joint, with *abductor digiti minimi* also a synergist for abduction of the fifth digit. *Opponens digiti minimi* also flexes the fifth digit, however its action point is at the carpometacarpal joint, as it inserts onto the medial (ulnar) shaft of the fifth metacarpal, where it adducts and rotates the first metacarpal during flexion, thereby deepening the palm of the hand. The hypothenar muscles move the fifth digit in planes similar to the thumb, albeit with more limited ranges of motion (Lemelin and Diogo, 2016), and as with their thenar counterparts, the hypothenar muscles show a progressive increase in activity as the thumb opposes the more ulnar fingers, with the *opponens digiti minimi* showing a disproportionately higher activity level as the tip of the thumb touches the side and distal tip of the fifth digit (Basmajian, 1979).

In addition to the thenar and hypothenar muscles, three more muscles are to be found intrinsically within the human hand. The lumbrical muscles, of which there are four, originate from the lateral side of the tendons of *flexor digitorum profundus*. These small muscles insert into the radial side of their respective extensor expansion. The actions of the lumbricals are seen on digits two to five, where they are weak flexors of the fingers at the metacarpophalangeal joints and assist in extension at the interphalangeal joints. Deep to the *flexor digitorum profundis* tendons and the lumbrical muscles on the thenar side of the palm, at the base of the thumb, is the *adductor pollicis* muscle. *Adductor pollicis* has two heads, a transverse head, which originates from the shaft of the third metacarpal, and an oblique head, which has its origin on the capitate and the bases of the second to fourth metacarpals. Both heads of *adductor pollicis* merge to insert onto the base of the ulnar side of the proximal phalanx of the thumb. As its name suggests, *adductor pollicis* adducts the thumb from an abducted position. It also flexes the thumb at its carpometacarpal and metacarpophalangeal joints (Lemelin and Diogo, 2016). Adduction and

abduction of the three-joint fingers at the metacarpophalangeal joints are the primary function of the interosseous muscles, which comprise the deepest intrinsic muscles of the palm. There are three palmar and four dorsal *interosseous* muscles, and as their names suggest, they are to be found between the metacarpal bones, on the shafts of various metacarpals. A palmar interosseous muscle can be found for each of the three-joint digits, except for the third (Lemelin and Diogo, 2016). The palmar *interossei* originate from the palmar surface of the second, fourth and fifth metacarpals, and insert onto the extensor expansion of the second (ulnar side), fourth (radial side), and fifth (radial side) digits, to adduct these digits to the midline of the hand, while aiding in flexion at the metacarpophalangeal, and extension at the interphalangeal joints of these fingers.

The dorsal *interossei* are the deepest muscles of the palm. A total of four dorsal interosseous muscles are present: one for the second digit on its radial side, two for the third digit – one either side of the third digit, and a fourth for the ulnar side of the fourth digit. The dorsal interossei are bipennate muscles with attachments on adjacent metacarpal shafts – for example, the first dorsal interosseous muscle attaches onto the shafts of the first and second metacarpals, while the second interosseous muscle attaches onto the second and third metacarpal shaft. They also have two compartments: a dorsal (deep) compartment with attachment onto the base of a proximal phalanx of a finger, and a superficial (palmar of volar) compartment with attachment onto the extensor expansion. The dorsal interossei primarily act to abduct the second, third, and fourth digits from the midline of the hand, and as with the palmar interossei, they are also synergists in the flexion of their respective digits at the metacarpophalangeal joint, and extensors at the interphalangeal joints.

Appendix F: Synopsis of Geometric Morphometrics

Landmarks

Geometric morphometric analysis utilizes the cartesian coordinates of discrete landmarks to describe shape. Landmarks are points of correspondence on each specimen that match between and within populations or, equivalently, biologically homologous anatomical loci recognizable on all specimens in the study (Bookstein, 1991; Dryden and Mardia, 1998; Webster and Sheets, 2010). The landmarks used for geometric morphometric analysis are selected based on their adequate representation of the shape of the structure under investigation (Webster and Sheets, 2010). The choice of landmarks used in a study is dependent on matters of practicality, and by necessity landmarks are points that can be precisely and consistently identified on each specimen, clearly corresponding in a one-to-one manner from one specimen to another, and repeatedly digitized with a high degree of accuracy and confidence.

Bookstein (1991) developed a classification scheme which defined three principal types of landmarks used in geometric morphometrics, based on anatomical and geometric criteria (type I, II, and III). Bookstein's (1991) original categorisation scheme was further developed and redefined by Bookstein (1997, 2018).

- **Type I: Discrete juxtaposition of tissues.** These are points in space where there occurs an intersection of three structures or surfaces, a curve, and a surface through which it passes, or any other combination of constraints on Cartesian coordinates that add up to the correct count, such as triple points of suture intersections.
- **Type II: Maxima of curvature characterizing a single structure or other local morphogenetic processes.** Points classically called vertices (extremes of one-dimensional curvature). Located at curvature minima and maxima associated with local structures.

- **Type III: Extremal points.** Landmark points characterized locally by information from multiple curves and by symmetry. These are "deficient" in that they contain meaningful information only in line with remotely defined structures.

Type I landmarks are optimal landmarks and are generally considered the most reliable and interpretable as they capture points with clear definitions (Baruda *et al*., 2019). Type II landmarks are less optimal, and some might not consider Type III landmarks to be landmarks at all (Zeldich *et al.,* 2004).

A major limitation of landmark-based morphometrics is the method's traditional reliance on easily recognisable and identifiable landmarks such as processes or sutures that have been extensively used in traditional morphometrics (Baruda *et al*., 2019). The reliance of geometric morphometric analysis on traditional landmarks not only restrict the number of available points, due to the necessity of biological homology across specimens, but also restricts analysis to biological structures where discrete points of clear homology are present. Many areas of anatomical interest, such as the surface morphologies of limb bones, the articular surfaces of joints, and sites of muscle attachment, are deficient in any clearly-definable landmarks, let alone those which are homologous across populations. The result is that, without innovation, structures between landmarks remain undefined, leaving large anatomical regions unsampled, and leading to a loss of morphological information (Gunz and Mitteroecker, 2013; Baruda *et al*., 2019).

A solution to this issue is the development and utilization of semilandmarks (Bookstein, 1991; Gunz, Mitteroeker and Bookstein, 2005; Gunz and Mitteroeker, 2013). The use of semi-landmarks enables the representation of structures that are generally lacking in observable landmarks, such as curves or joint surfaces, and therefore allows integration of the shape of these structures with more easily-definable landmarks that would otherwise be unattainable through traditional morphometrics. Semilandmarks make it possible to quantify two- or three-dimensional homologous curves and surfaces, and to analyse them in conjunction with traditional landmarks (Gunz and Mitteroeker, 2013). Semilandmarks greatly improve the representation of morphology and alleviate the issues above by densely sampling regions that do not have many discrete points of homology within or between them, but represent homologous

structures across specimens (Baruda *et al*., 2019). Bookstein and Weber (2011) elaborated on Bookstein's (1991, 1998, 2018) original categorisation scheme to include a further three types of landmarks, which defined semilandmarks (type IV, V, and VI).

- **Type IV: Semilandmarks on curves.** The number of semilandmarks needs to be sufficient to capture the spatial nature of variation or covariation that will ultimately emerge from multivariate analysis of their shape coordinates.
- **Type V: Semilandmarks on surfaces.** Semilandmarks constrained to surfaces can slide with respect to any combination of point landmarks and curve semilandmarks.
- **Type VI: Constructed semilandmarks**. A portmanteau category collecting various familiar loci that appear not to qualify for any of the preceding categories. Includes projections from one structure onto another, places where a curve comes nearest to another, loci of greatest width of bilaterally symmetrical structures, and other special circumstances.

Semilandmarks come in two forms: curve and surface semilandmarks. Curve sliding semilandmarks are used to define outlines (Bookstein, 1997), and form "curves" of landmarks along a structure, such as the margins of bones, with each curve being demarcated by two homologous, traditional landmarks (Gunz, Mitteroecker and Bookstein, 2005). Surface sliding semilandmarks define entire surfaces which are bound by traditional landmark points and curves (Baruda *et al*., 2019). The notion of homology is not redundant in the application of semilandmarks, so long as the number of surface and curve semilandmarks remain constant for each corresponding surface or curve across the studied population and are bound by the same homologous "traditional" landmarks. Although Bookstein (2018) and Bookstein and Weber (2011) elaborated on Bookstein's (1991) original classification scheme, the three original Type I, II, and III landmark categorizations remain in common parlance, with Type IV and V landmarks commonly referred simply as curve and surface sliding semilandmarks, respectively.

Sliding semi-landmarks

Following placement of any landmark and surface- and curve- semilandmark configuration on all specimens within a population of interest, it is necessary to optimize the distances between these arbitrarily-placed semilandmarks on any given curve or surface though a process called sliding. Sliding establishes geometric correspondence of the semilandmarks by removing the effect of random positioning in their initial placement on a surface or curve so as to minimize shape differences between each specimen and the average shape in the sample (Harcourt-Smith *et al*., 2008; Gunz and Mitteroeker, 2013). Two alternative computational approaches to sliding semilandmarks are available: bending energy (Bookstein, 1997; Gunz, Mitteroecker and Bookstein, 2005) and Procrustes distances (Rohlf, 2010). These two approaches differ in the way that shape differences are quantified, and therefore in what is being minimized. Minimizing bending energy only considers local shape deformation, with uniform shape differences such as stretching and shearing having no effect on bending energy and the sliding process. Bending energy is based on all landmarks and semilandmarks and the smoothness of the shape deformation as a whole.

By contrast, minimizing the Procrustes difference is a least-squares procedure and more closely resembles the usual sum-of-squares decomposition in statistics. When minimizing Procrustes distance, each landmark slides separately and the sliding is not influenced by other landmarks and semilandmarks. The nature of sliding through minimizing Procrustes distance means that curve semilandmarks can potentially slide beyond the endpoint of its curve, or pass another semilandmark, while surface semilandmarks may slide beyond the fixed landmarks or curve landmarks that bound the surface or pass beyond other surface semilandmarks (this scenario is almost impossible when minimizing bending energy). Sliding semilandmarks by minimizing bending energy is the most common and widely used method of the two. However, in most scenarios, the results obtained through the two sliding methods are comparable and yield similar results if shape variation is small, and excessive sliding of landmarks is not necessary (Perez, Bernal and Gonzalez, 2006; Gunz and Mitteroeker, 2013). After sliding, landmarks and semilandmarks can be treated indifferently in any subsequent statistical analysis (Gunz and Mitteroeker, 2013).

Generalized Procrustes Analysis

Following the application of landmarks and semilandmarks to the population of interest, and removing variation caused by arbitrary placement of semilandmarks, the first step in any geometric morphometric analysis is to superimpose all the coordinates that represent each specimen in a dataset to a common coordinate system. The purpose of superimposing the landmark coordinates to a common coordinate system is to ensure that variation associated with differences in location, orientation, and size of specimens are minimized so that it is differences in shape that is the only variable being scrutinized (though information on size is retained in the Centroid size) (Slice, 2005; Webster and Sheets, 2010). Once landmark configurations are superimposed to a common coordinate system, these superimposed coordinates are used as shape variables (Slice, 2005; Webster and Sheets, 2010).

Several methods are available to use for superimposing landmark configurations (two-point registration; full Procrustes superimposition; resistant-fit methods; Bookstein registration; sliding baseline registration), each differing in how, and in the degree to which, differences in location, scale and size are removed (Webster and Sheets, 2010). The most widely used superimposition method is the Procrustes superimposition. Procrustes superimposition is a least-squares method that estimates the parameters for location and orientation that minimize the sum of squared distances between corresponding points on two configurations (Slice, 2005). Procrustes superimposition comes in two "flavours": a full Procrustes fit, and a partial Procrustes fit. A full Procrustes fit is when a least-squares estimate of scale is used. However, such a least-squares estimate for scale does not lead to symmetric results between configurations of different size, so all specimens are most often scaled to a standard size. A partial Procrustes fit is when configurations are scaled to a common size (centroid size 1). While the difference between partial and full Procrustes fit is negligible in most biological applications, the partial Procrustes fit is the most commonly used method of Procrustes superimposition and forms the basis for many operations carried out further downstream (Slice, 2005). As such, the partial Procrustes fit will be discussed here at the expense of other superimposition methods.

The superimposition of one configuration of landmarks onto another specified configuration is termed an ordinary Procrustes fit, and involves only two specimens (Goodall, 1991). However, most research is interested in the analysis of samples of more than two

specimens. The Procrustes superimposition of landmark configurations of more than two specimens is known as generalized Procrustes analysis (GPA) (Gower, 1975), and it is Generalized Procrustes analysis that is used for most geometric morphometric analysis (Slice, 2005). The first step in a generalized Procrustes superimposition is to calculate the centroid of each configuration within the sample. The centroid of a landmark configuration is simply its centre: the x, y, (and z in three-dimensions) coordinates of the configuration's centroid are simply the mean values of the x and y (and z) coordinates for all the landmarks in a given configuration, and is, in a sense, the "centre of gravity" of a specimen's landmark configuration (figure 3.1) (Webster and Sheets, 2010). The centroids of all the specimens within a population are then transported to a common locale, so that the landmark configurations of all specimens within a population share a common centroid – (0, 0) in two-dimensions, or (0, 0, 0) in three-dimensions (figure 3.2 (b)).

Differences in size between configurations are then removed by scaling all the landmark configurations to have a centroid size of 1. Centroid size is defined as the square root of the sum of squared distances between each landmark of a configuration and its centroid (Bookstein, 1991; Klingenberg, 2016), and it is the retention of Centroid size that allows for assessment of size variation in geometric morphometrics.

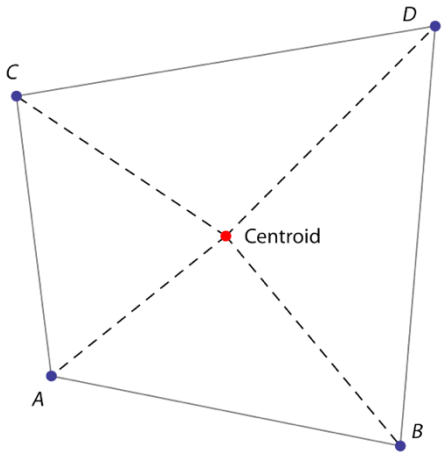

Figure 3.1: A configuration of four landmarks (A-D) with their centroid, which is equal to the average landmark position. Centroid size, the size measure used in geometric morphometrics, is equal to the square root of the summed squared distances between the landmarks and their centroid (square root of the summed squared lengths of the dashed lines). From Mitteroecker *et al.,* 2013.

Lastly, differences in orientation between configurations are removed by rotating them around the common centroid so that the sum of squared distances between corresponding landmarks is reduced to a minimum, and an overall best-fit is achieved (figure 3.2 (d)) (Rohlf and Slice, 1990; Dryden and Marida, 2016; Klingenberg, 2016). Optimizing alignment of samples of more than two specimens requires knowledge of the mean configuration. However, the mean coordinates of the sample cannot be computed prior to superimposition (Slice, 2005). The solution to this Catch-22 situation is an iterative process, in which a specimen is randomly selected to represent the mean (usually the first specimen in a sample), and all other configurations are fitted to that reference. Then, a new mean is computed as the arithmetic average location of the individual landmarks in the sample and scaled to unit centroid size. This process is repeated, fitting the sample to the new estimate, and finishes when the sum-of-squared deviations of the sample configurations around the estimated mean no longer decreases by a critical value, or when the change in mean estimate from one iteration to the next is deemed negatable (Slice, 2005).

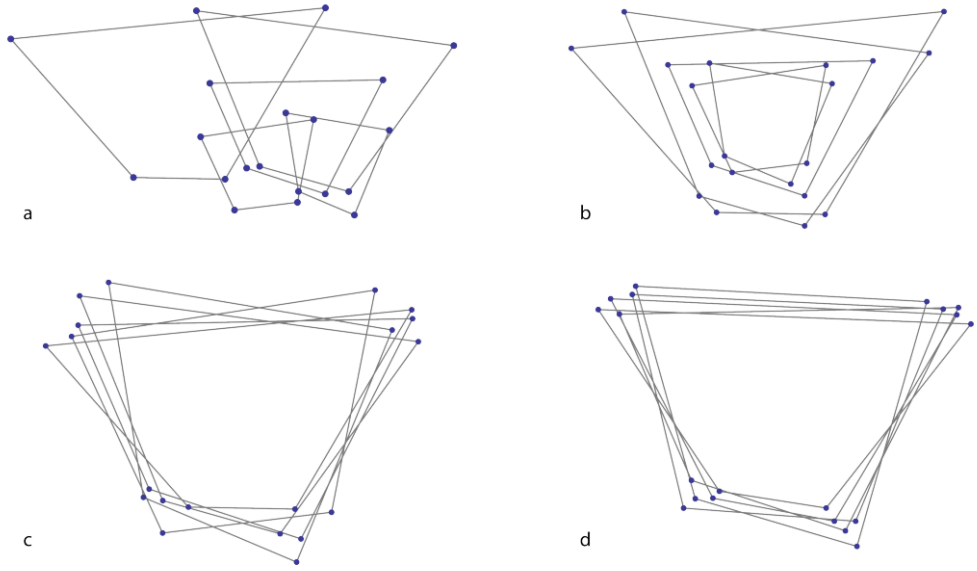

Figure 3.2: A graphical representation of Procrustes superimposition. Raw landmark coordinates (a) are translated so that they all have the same centroid (*b*). The centred configurations are then scaled to the same centroid size (*c*) and iteratively rotated until the summed squared distances between the landmarks and their corresponding sample average position is a minimum. From Mitteroecker *et al.,* 2013.

Translating all landmark configurations to a common location, rescaling all to unit centroid size, and rotating them all into an optimal least-squares alignment with an iteratively estimated mean reference form is called Generalized Procrustes Analysis (Webster and Sheets, 2010). Because all differences in location, scale, and orientation have been removed, any differences in coordinates of corresponding landmarks between configurations must be the result of differences in shape between those configurations. Generalized Procrustes analysis produces a new set of optimized coordinates for each specimen in the analysed population. The differences left between coordinates of corresponding landmarks after superimposition are the differences in shape between the configurations, the total magnitude of which provides a measure of shape difference. These resultant aligned coordinates are termed Procrustes coordinates, and it is these coordinates which are used in subsequent analysis. Following a generalized Procrustes analysis, shape differences between configurations are measured as the square root of the sum of squared distance between a specified Procrustes coordinate configuration and the sample mean (Slice, 2005), a unit known as the Procrustes distance.

Procrustes coordinates are aligned in a complex, non-Euclidean curved space, known as Kendall's shape space (Kendall, 1977, 1984; Rohlf and Slice 1990; Bookstein 1991, 1996). This shape space describes all the possible shape configurations for the particular number of landmarks and dimensions used in the study. Each individual landmark configuration within a Procrustes-aligned sample can therefore be thought of as occupying a single point in Kendall's shape space, with more similar shapes (i.e. representing members of the same species) being in closer proximity to each other in shape space relative to samples with less similar morphologies. It is therefore possible to describe differences between groups in a population (e.g. species or genera) based on general similarities and differences of the shape space configurations. The geometry of Kendall's shape space and that of generalized Procrustes analysis is non-linear. However, the theory underlying many multivariate methods assume a linear, Euclidean space (Slice, 2005). It is therefore necessary to project the Procrustes coordinates of a population onto a linear space which is tangent to the Kendall's shape space, and which is centred around the average shape (figure 3.3.) (Dryden and Marida, 1993; Rohlf, 1999; Webster and Sheets, 2010). The projection of Procrustes coordinates onto a Euclidean space tangent to Kendall's shape space then allows for multivariate analysis.

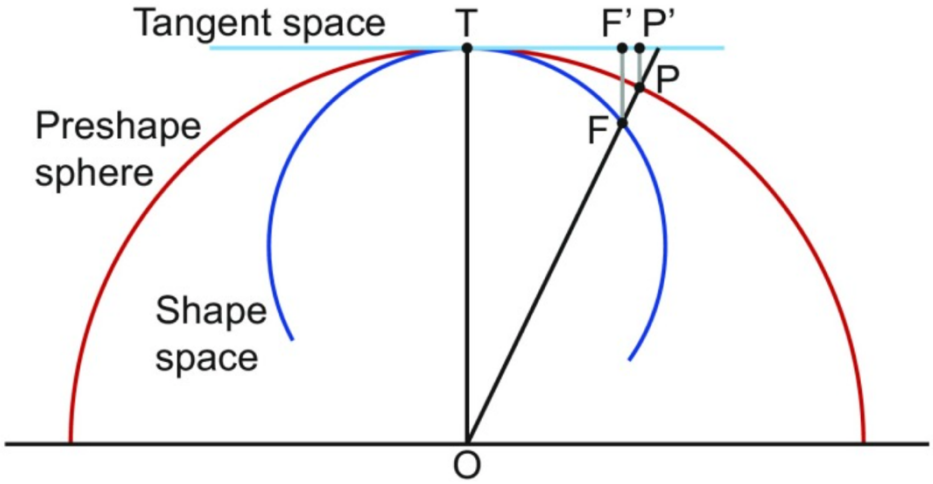

Figure 3.3: The connection between Procrustes superimposition and Kendall's shape space for triangles. From Klinenberg, 2016.

A significant advantage of using geometric morphometric analysis to study changes in shape is that following Procrustes superimposition, not only is it possible to investigate such changes using multivariate analysis, but differences, associations, variability etc. can be

represented visually. Shape changes within a population can be explored and explained as transformation vectors between two coordinate configurations (Rohlf and Marcus, 1993; Gunz and Mitteroeker, 2013), as a thin plate spline which visualizes the difference in shape between a reference form and a target form, deformation grids, and even by warping three-dimensional meshes from one specified coordinate system to another. This visual representation of shape change is a major appeal of geometric morphometric methods and is a major factor as to why the method is so useful in addressing a wide array of biological inquiry.

Appendix G: Repeatability Test Results

Hamate landmark repeatability test

Results of the multivariate correspondent of Levene's test to verify repeatability of the bounding landmarks chosen to represent the hamate are shown in table B.1.1, with graphical representations in the form scatterplots of PC 1 scores against PC 2 scores shown in in figure B.1.1. For all taxa, repeated measures were closely clustered relative to the parent population, and easily distinguishable. The results of the multivariate correspondent of the Levene's test were significant ($p < 0.05$) for each taxon for the first four principal components. It was therefore concluded that the landmarks selected for representation of the proximal articular surface of the hamate were repeatable and suitable for the purposes of this study.

Table B.1.1: Results of the multivariate correspondent of Levene's test along the first four principal components of PCAs conducted on the Procrustes-aligned coordinates of five repeated landmark coordinates of the hamate pooled with their respective parent population.

Taxon	Levene's Test (Anderson, 2006)
Gorilla	**<0.001**
Homo sapiens	**<0.001**
Pan troglodytes	**<0.001**
Pongo	**0.003**

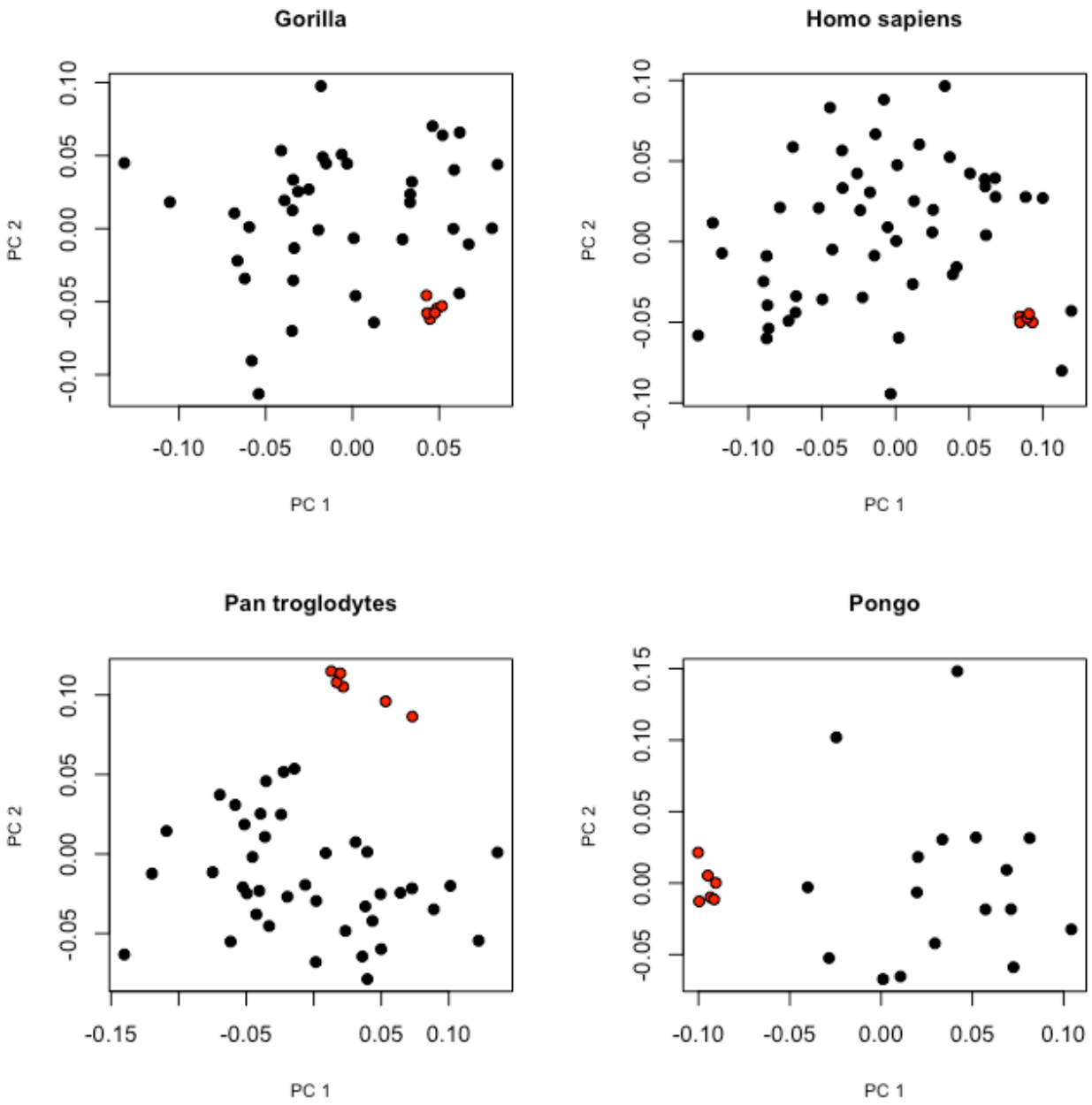

Figure B.1.1: Scatterplots of PC1 against PC2 for the PCA of Procrustes-aligned landmarks used to define the landmark grids placed on the hamate's articular surfaces for metacarpals four and five. Black circles represent individuals of the parent (group) samples, while red circles represent repeated measures.

5.2 Metacarpal-4 landmark repeatability test

Graphical outputs of the repeatability testing for the proximal articular surface of the fourth metacarpal are shown as scatterplots of PC 1 scores against PC 2 scores in figure B.2.1, with results of the multivariate Levene's test shown in table B.2.1. For all taxa, repeated measures were clustered in the morphospace relative to the un-repeated population, and easily distinguishable from the rest of the sample. Results of the multivariate correspondent of the Levene's test were significant ($p < 0.05$) for each taxon along the first four principal components. It was therefore concluded that the landmarks selected for representation of the proximal articular surface of the fourth metacarpal were repeatable and suitable for the purposes of this study.

Table B.2.1: Results of the multivariate correspondent of Levene's test along the first four principal components of PCAs conducted on the Procrustes-aligned coordinates of five repeated landmark coordinates of the fourth metacarpal proximal articular surface pooled with their respective parent population.

Taxon	Levene's Test (Anderson, 2006)
Gorilla	**<0.001**
Homo sapiens	**<0.001**
Pan troglodytes	**<0.001**
Pongo	**0.007**

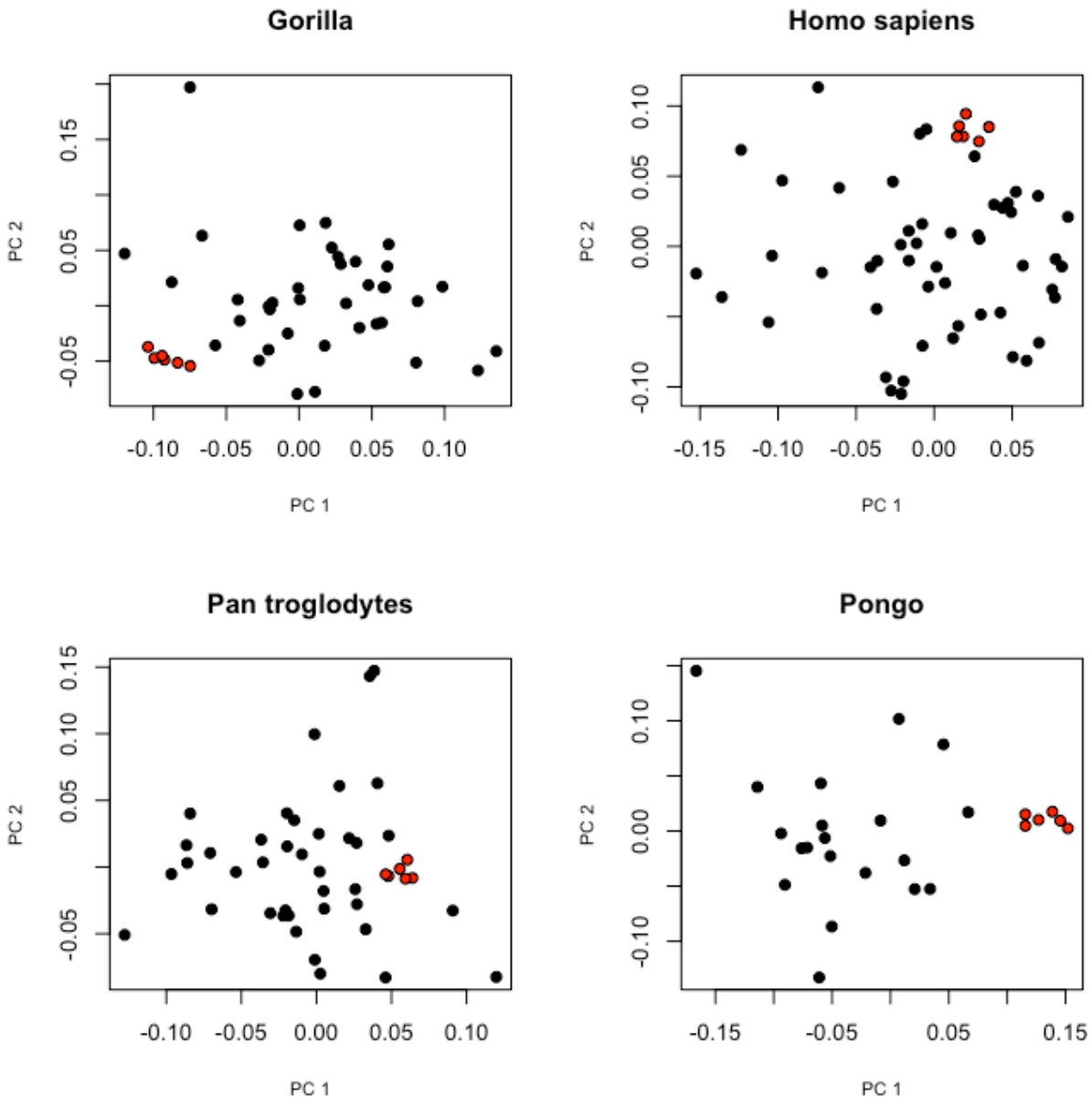

Figure B.2.1: Scatterplots of PC1 against PC2 for the PCA of generalized Procrustes-aligned landmarks used to define the landmark grids placed on the fourth metacarpal's proximal articular surface. Black circles represent individuals of the parent (group) populations, while red circles represent repeated measures.

5.3 Metacarpal-5 landmark repeatability test

Graphical outputs of the repeatability testing for the proximal articular surface of the fifth metacarpal are shown as scatterplots of PC 1 scores against PC 2 scores in figure B.3.1, with results of the multivariate Levene's test shown in table B.3.1. Again, for all taxa, repeated measures were tightly-clustered relative to the respective parent population and easily distinguishable from the unrepeated sample. The results of the multivariate correspondent of the Levene's test were significant ($p < 0.05$) for each taxon for the first four principal components, indicating that the landmarks selected for representation of the proximal articular surface of the fifth metacarpal were repeatable and suitable for the purposes of this study.

Table B.3.1: Results of the multivariate correspondent of Levene's test along the first four principal components of PCAs conducted on the Procrustes-aligned coordinates of five repeated landmark coordinates of the fifth metacarpal proximal articular surface pooled with their respective parent population.

Taxon	Levene's Test (Anderson, 2006)
Gorilla	**<0.001**
Homo sapiens	**<0.001**
Pan troglodytes	**<0.001**
Pongo	**0.003**

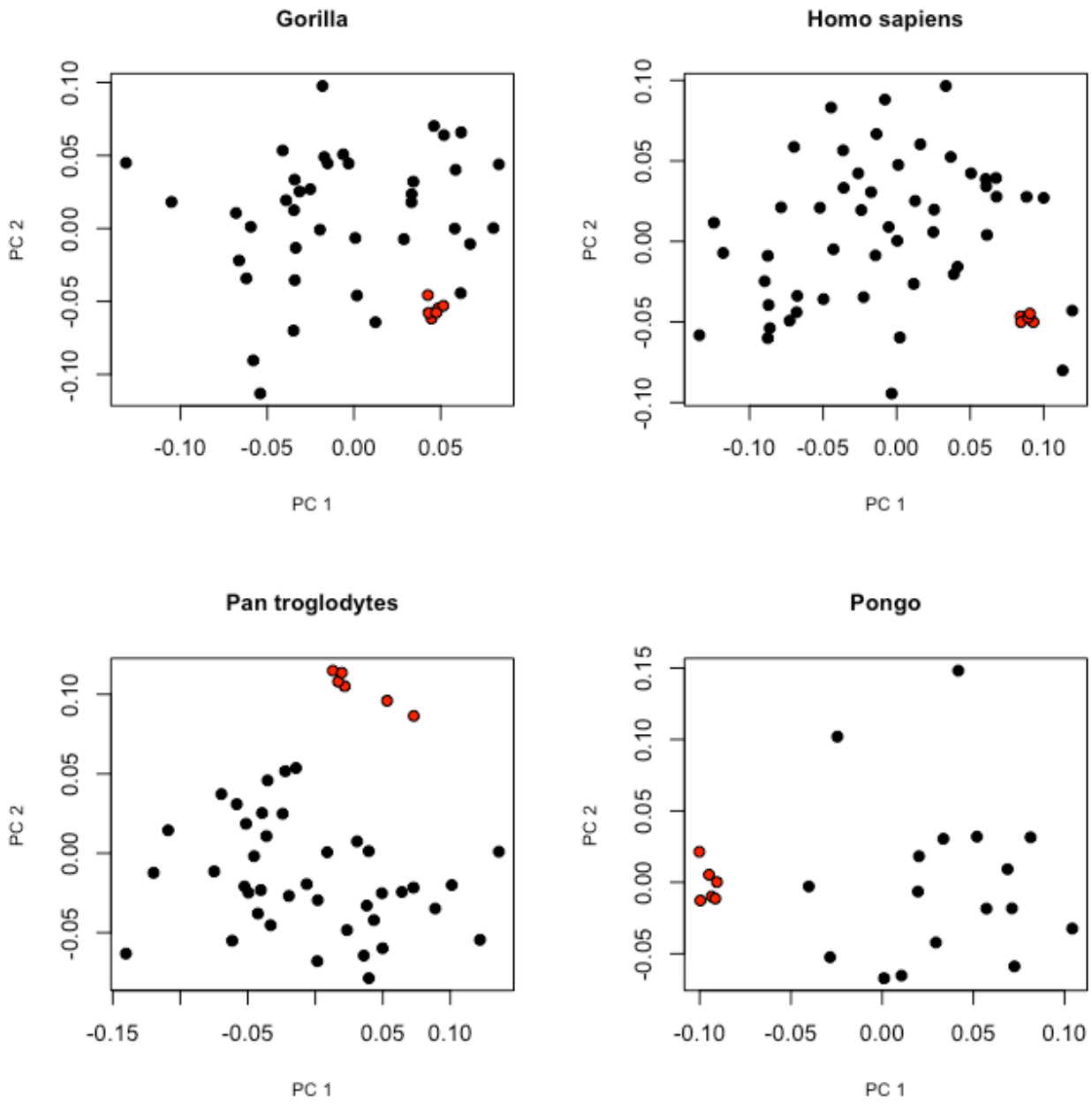

Figure B.3.1: Scatterplots of PC1 against PC2 for the PCA of generalized Procrustes-aligned landmarks used to define the landmark grids placed on the fifth metacarpal's proximal articular surface. Black circles represent individuals of the parent (group) populations, while red circles represent repeated measures.

Appendix H: Allometry Tests Results

Hamate-metacarpal surface allometry test

Table C.1: Results of regression analysis of principal component scores one through four on log centroid size for the hamate-metacarpal surface.

PC	Adjusted R^2	*p*	F
PC1	-0.006	0.701	0.142
PC2	0.262	**<0.001**	53.27
PC3	0.083	**<0.001**	14.22
PC4	-0.005	0.633	0.230

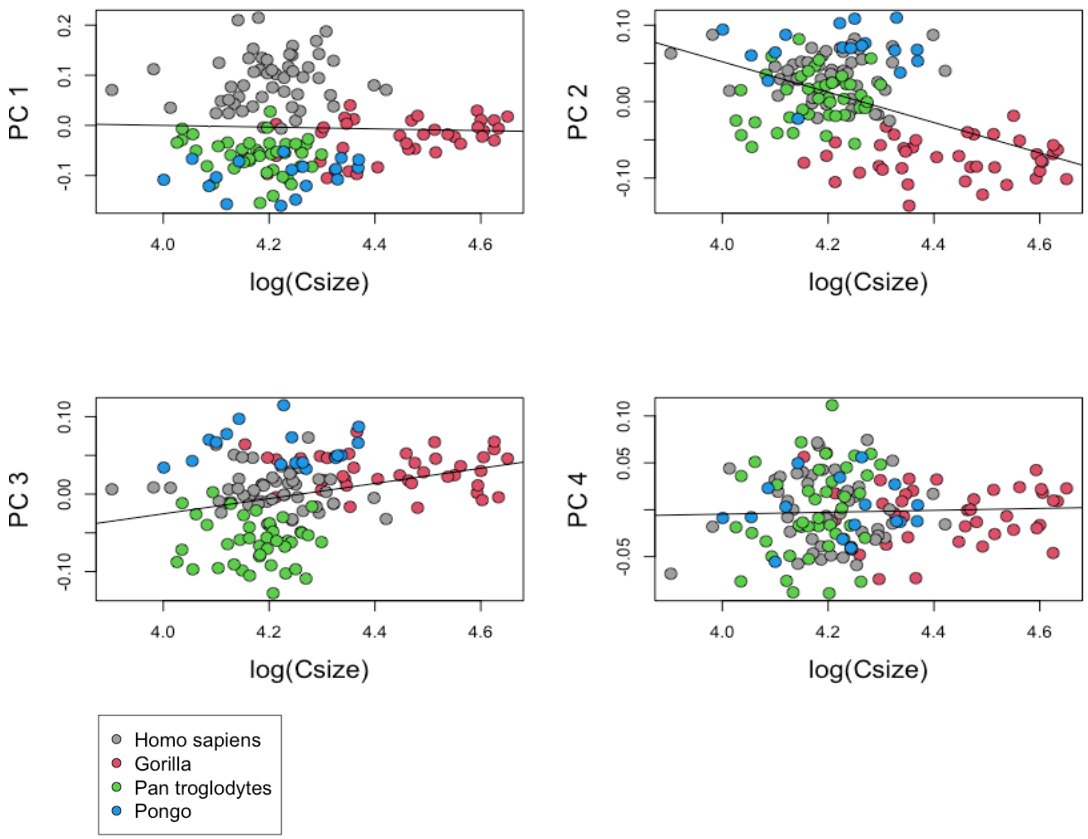

Figure C.1: Boxplots of principal component scores against log centroid size for principal components 1-4 for the hamate's articulation with the fourth and fifth metacarpal.

Hamate-MC4 surface allometry test

Table C.2: Results of regression analysis of principal component scores one through four on log centroid size.

PC	Adjusted R^2	*p*	F
PC 1	0.06094	**0.0015**	10.54
PC 2	0.1206	**<0.001**	21.16
PC 3	-0.006403	0.7995	0.06475
PC 4	0.01875	0.05287	3.81
PC 5	0.1611	**<0.001**	29.23
PC 6	0.002837	0.2356	1.418

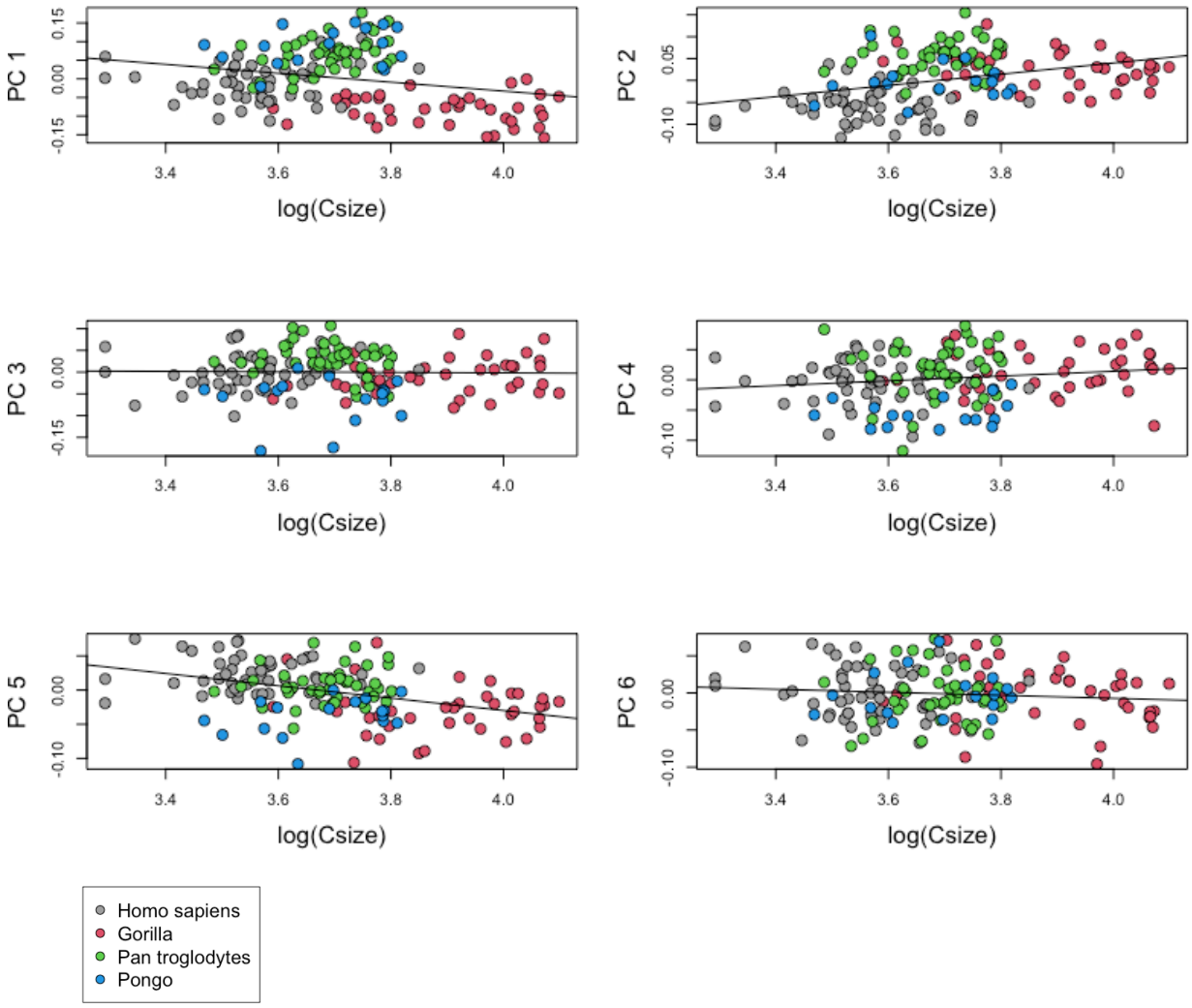

Figure C.2: Boxplots of principal component values against log centroid size among the extant population for principal components 1-6. There was a slight significant correlation between principal component value and log centroid size in the first, second, and fifth principal components.

Hamate-MC5 surface allometry test

Table C.3: Results of regression analysis of principal component scores one through four on log centroid size.

PC	Adjusted R^2	*p*	F
PC1	0.0058	0.176	1.851
PC2	0.293	**<0.001**	67.84
PC3	0.024	0.033	4.643
PC4	-0.0054	0.64	0.215
PC5	-0.00666	0.868	0.028

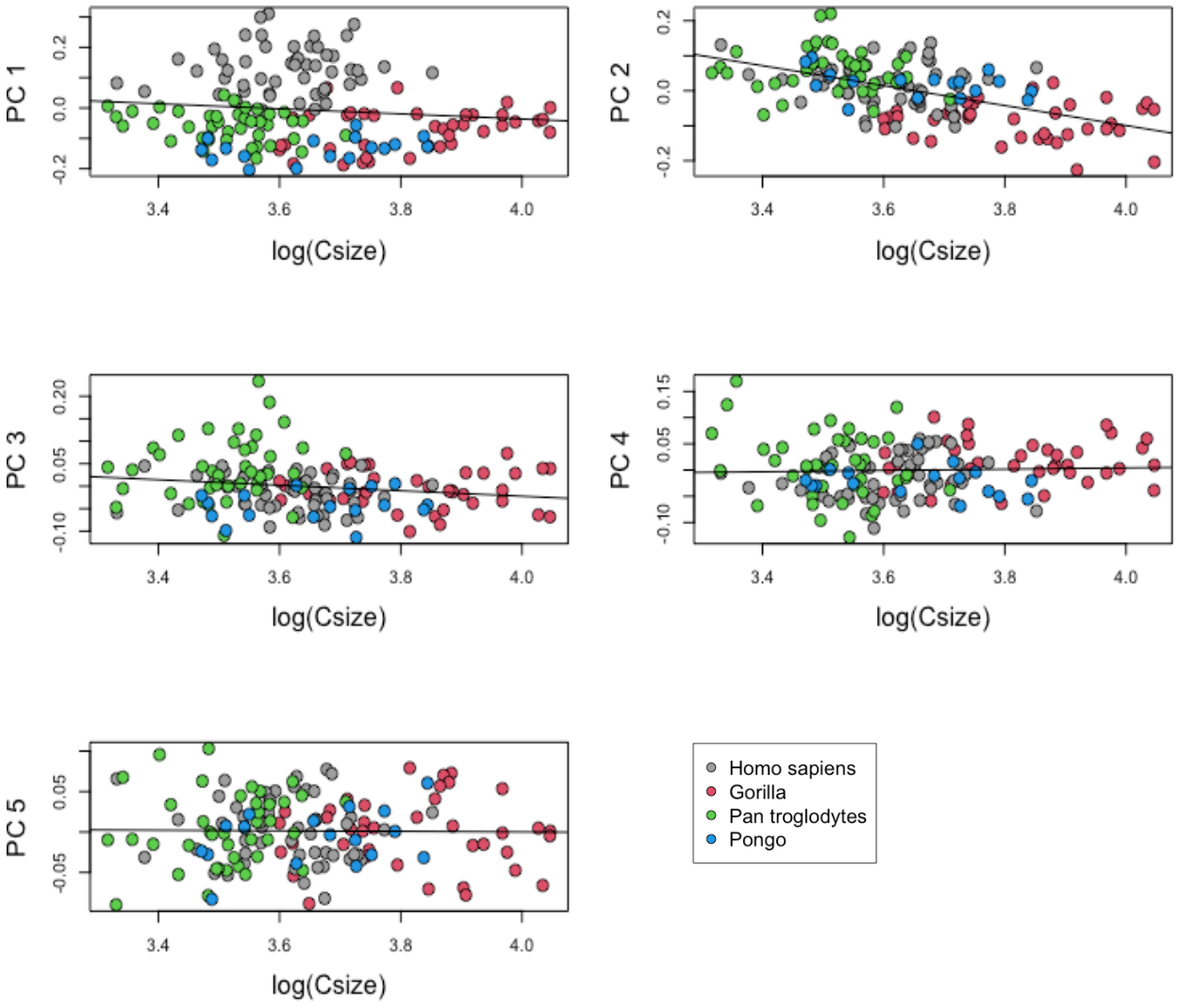

Figure C.3: Boxplots of principal component scores against log centroid size for principal components 1-5.

MC4 proximal articular surface allometry test

Table C.4: Results of regression analysis of the first five principal component scores on log centroid size.

PC	Adjusted R^2	*p*	F
PC1	0.2576	**<0.001**	52.35
PC2	0.1316	**<0.001**	23.43
PC3	0.0338	**0.0149**	7.54
PC4	-0.0006	0.342	0.912
PC5	0.0056	0.1777	1.834

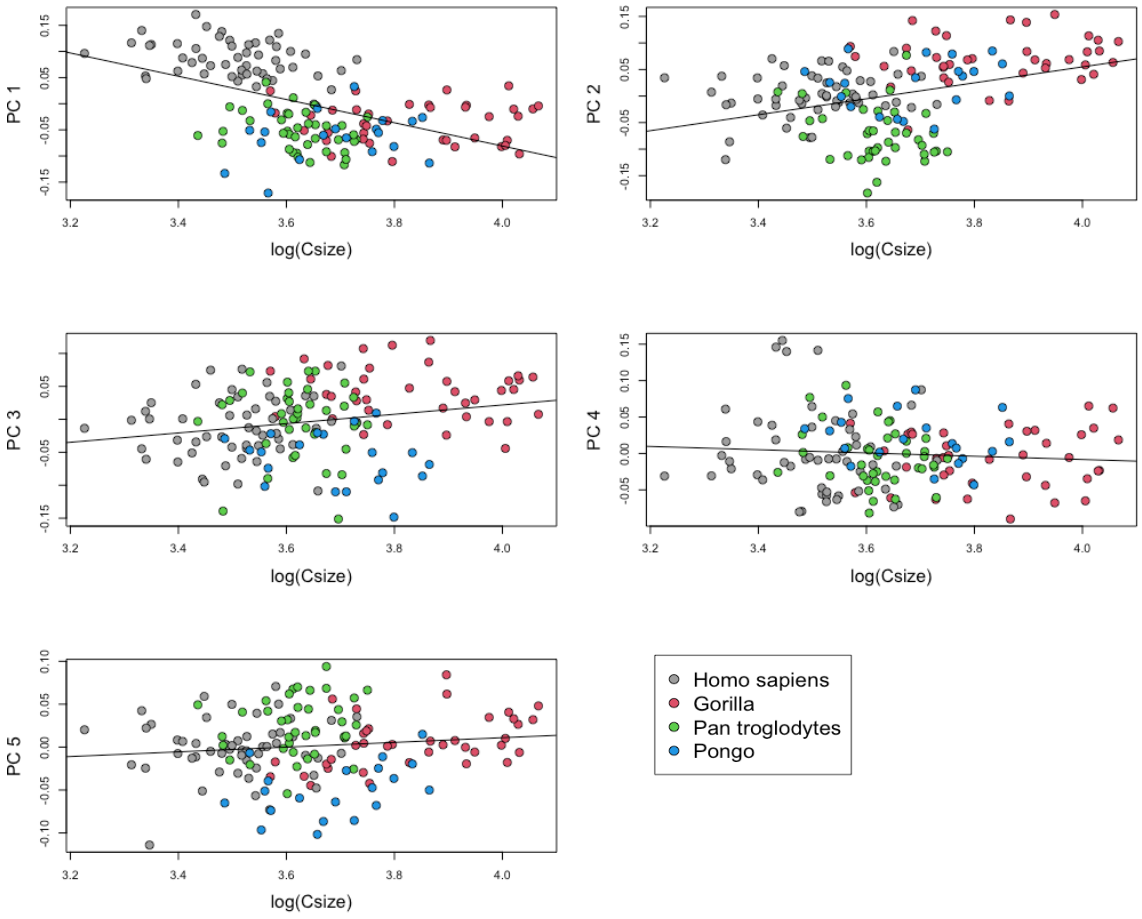

Figure C.4: Boxplots of principal component scores against log centroid size for principal components 1-4.

MC5 proximal articular surface allometry test

Table C.5: Results of regression analysis on the scores of the first three principal components on log centroid size.

PC	Adjusted R^2	*p*	F
PC 1	0.0227	**0.036**	4.484
PC 2	0.0319	**0.016**	5.943
PC 3	0.0238	**0.032**	4.660

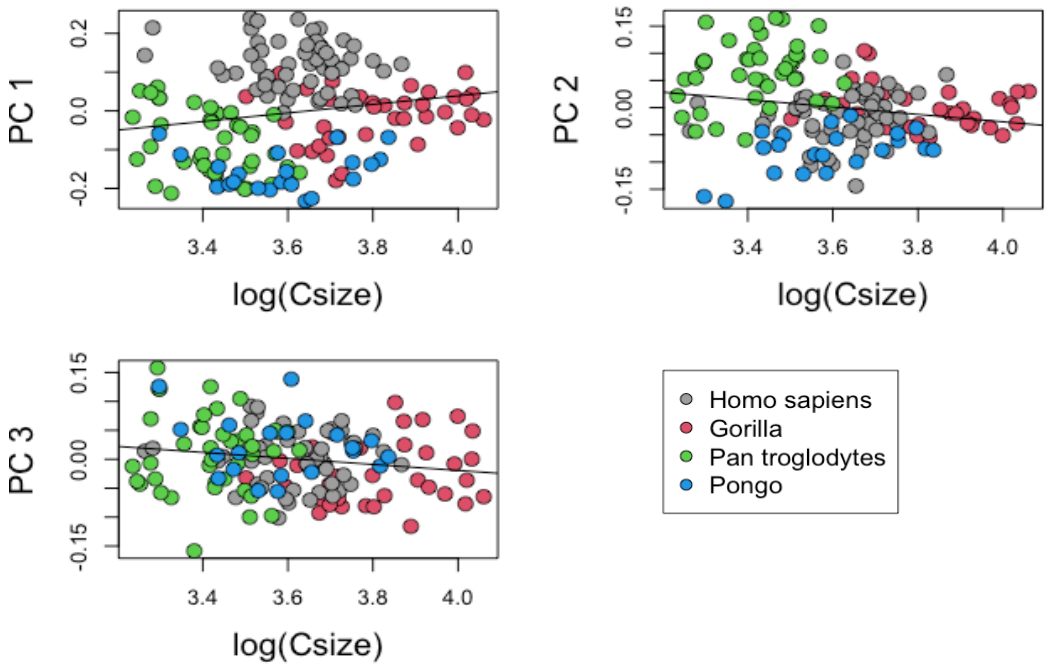

Figure C.5: Boxplots of principal component scores against log centroid size for principal components 1-3.

Appendix I: The bivariate scatterplots of PCs 2v3, 2v4, 3v4, 3v5, and 4v5 of the hamate-MC4 surface.

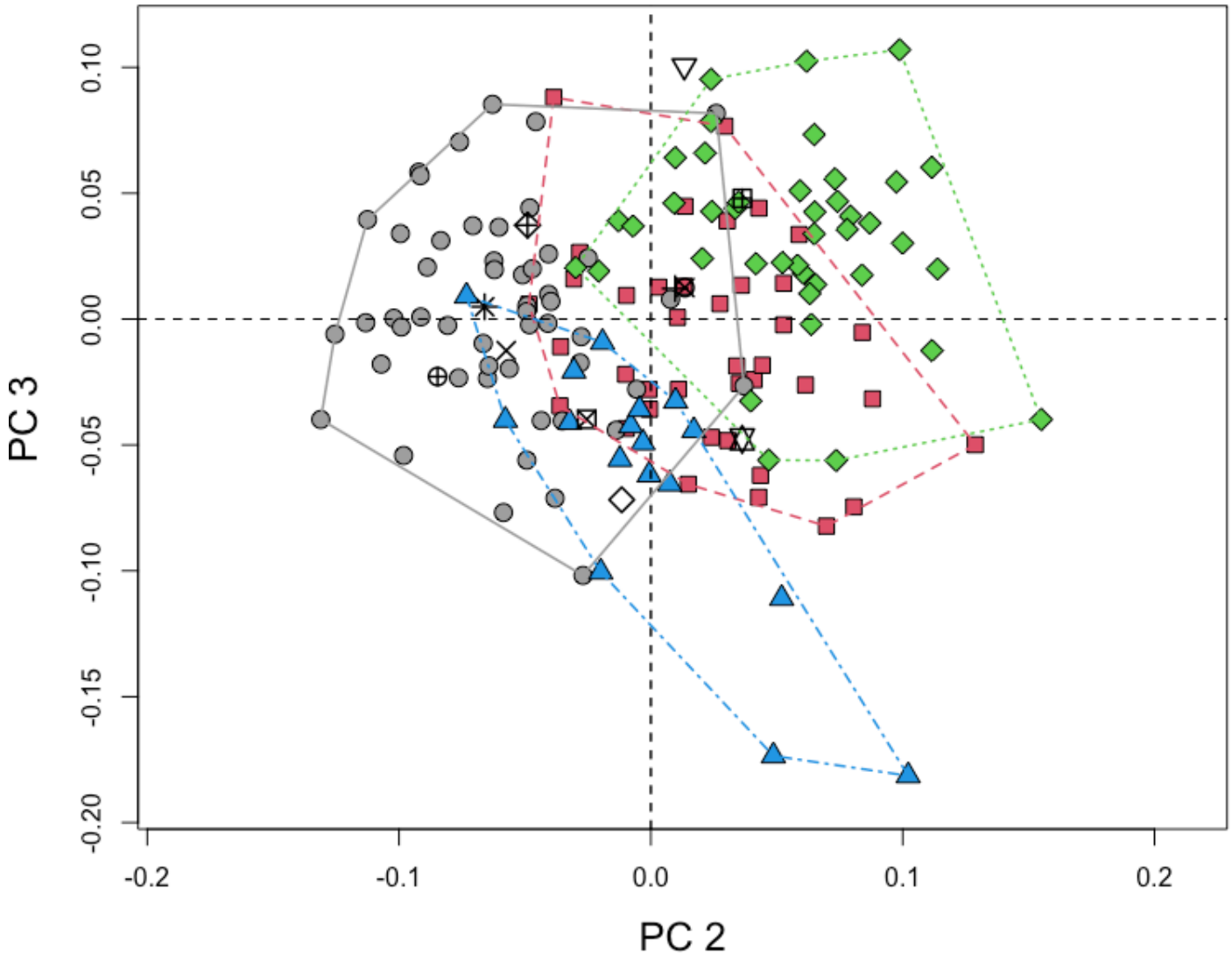

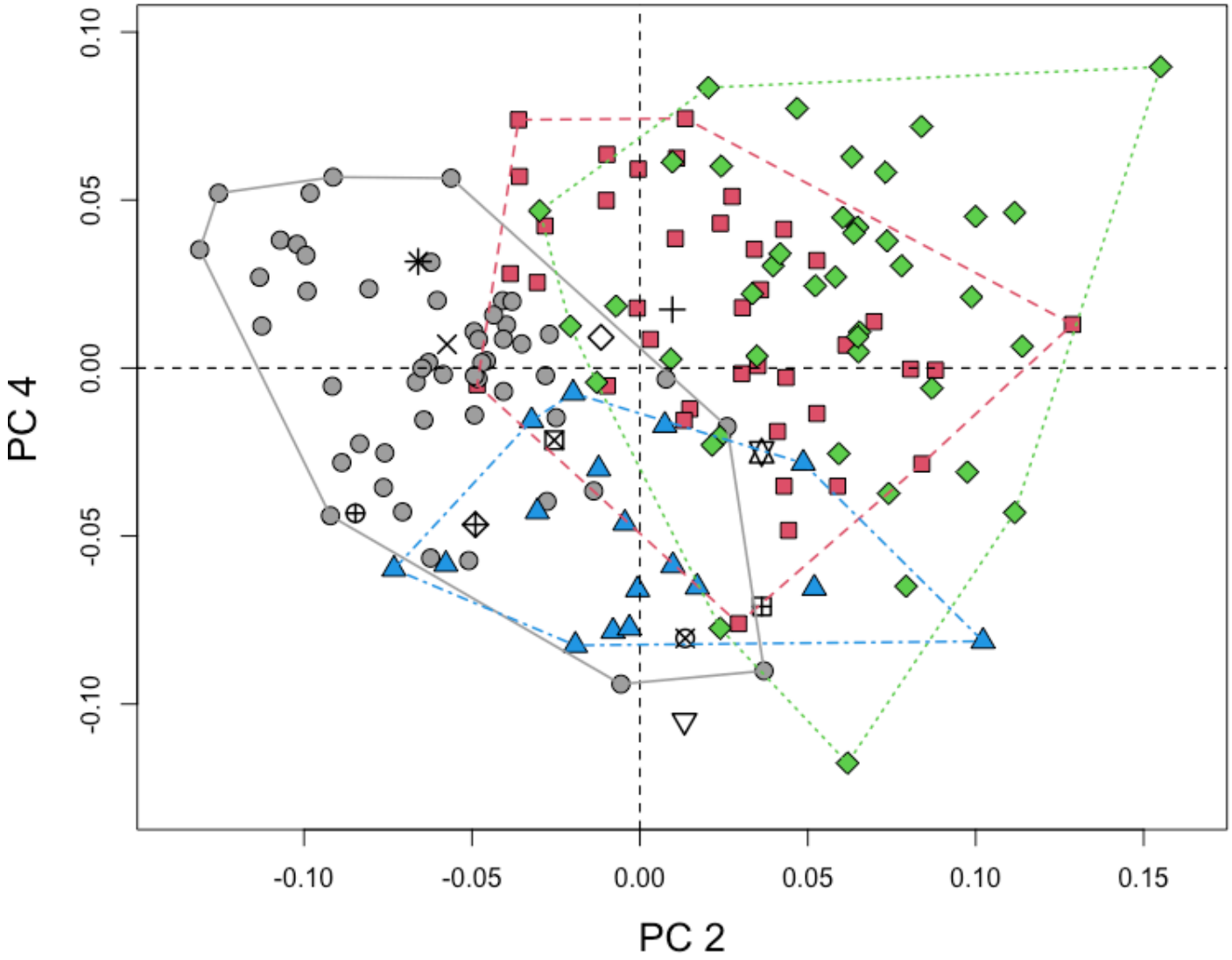
PC 4
0.10
0.05
0.00
-0.05
-0.10
-0.10
-0.05
0.00
0.05
0.10
0.15
PC 2

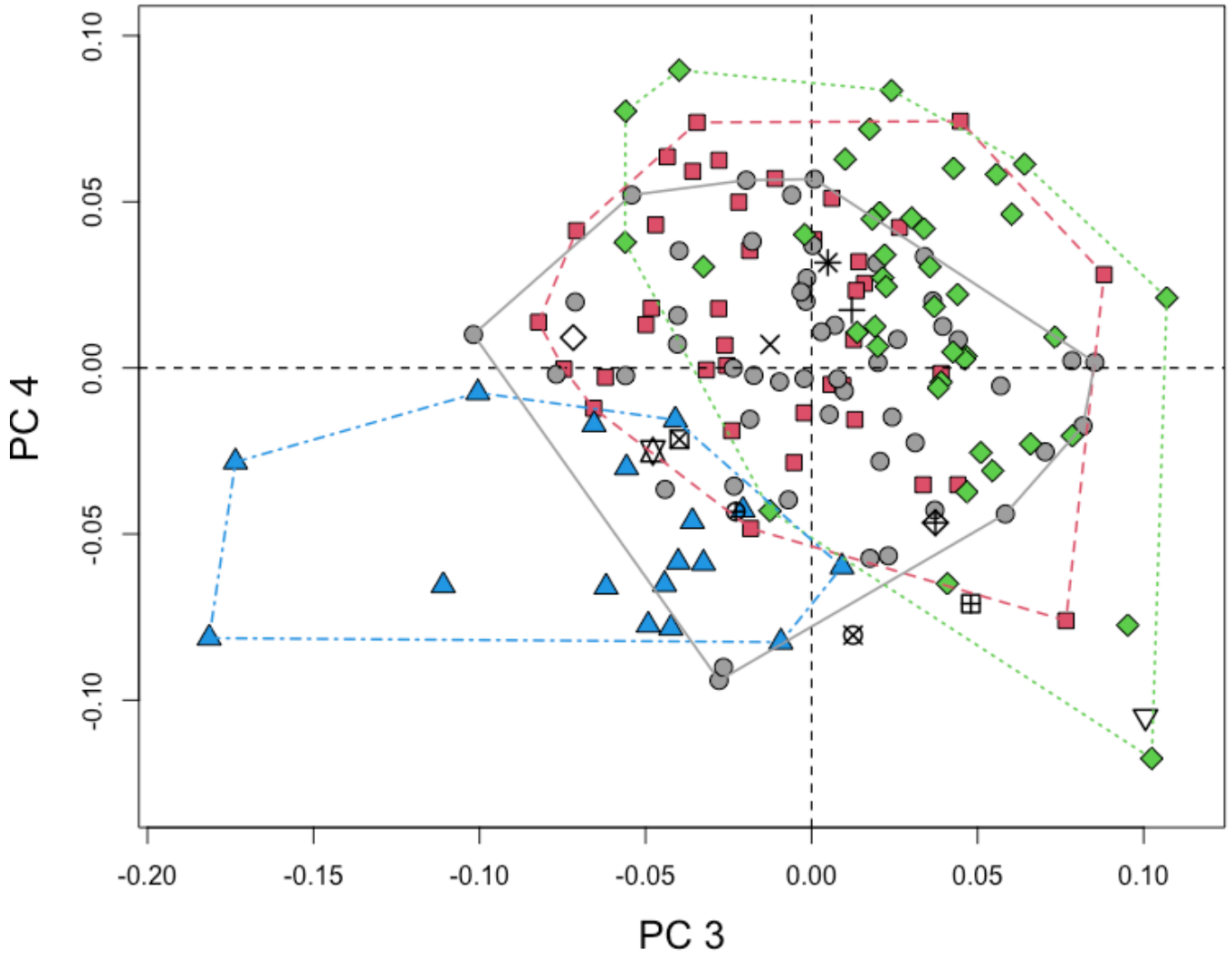
PC 4
0.10
0.05
0.00
-0.05
-0.10
-0.20
-0.15
-0.10
-0.05
0.00
0.05
0.10
PC 3

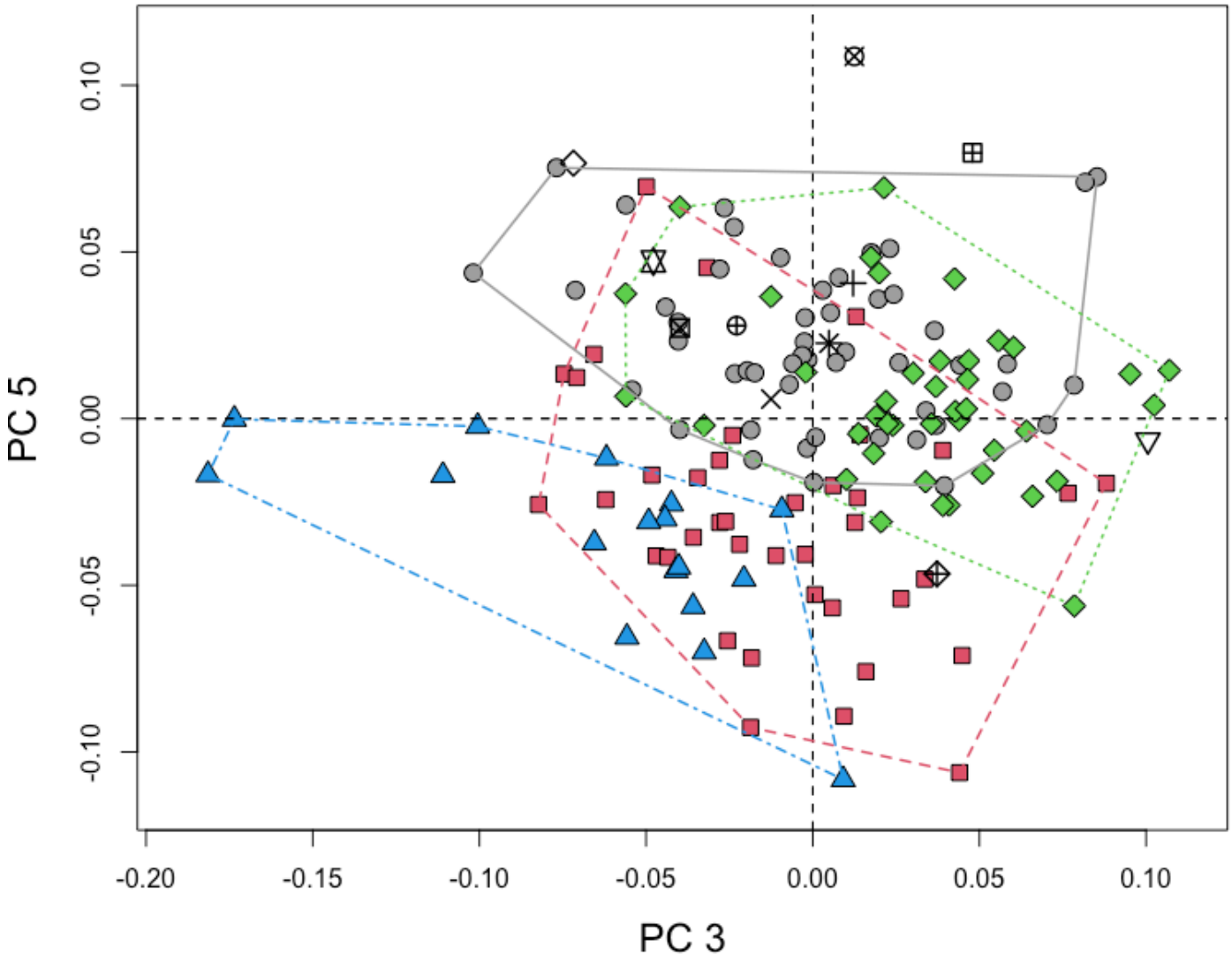
PC 5
0.10
0.05
0.00
-0.05
-0.10
-0.20
-0.15
-0.10
-0.05
0.00
0.05
0.10
PC 3

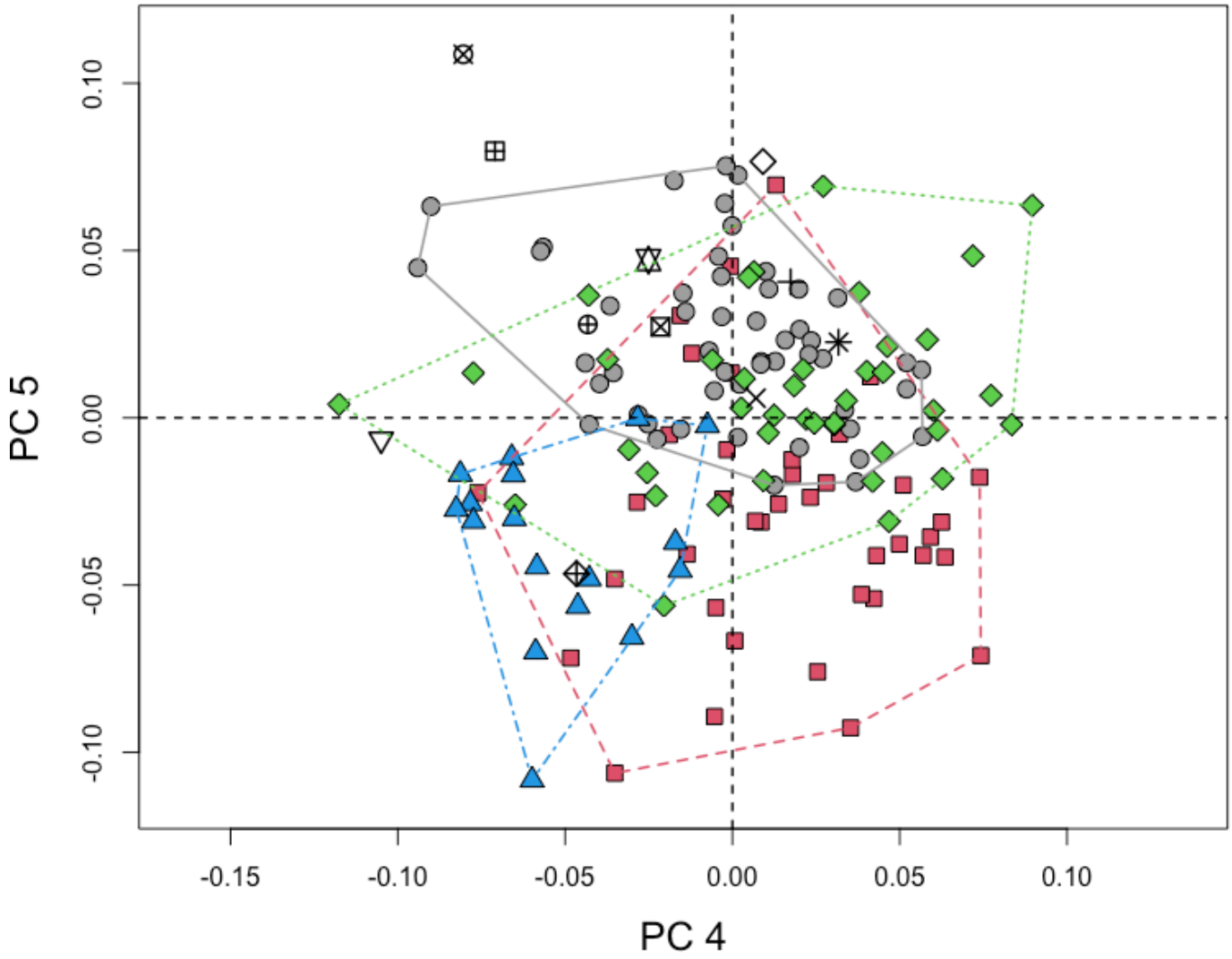
PC 5
0.10
0.05
0.00
-0.05
-0.10
-0.15
-0.10
-0.05
0.00
0.05
0.10
PC 4